BEHAVIOUR OF CAISSON FOUNDATION UNDER STATIC AND SEISMIC CONDITIONS

Ph.D. Thesis

by

MOHIT KUMAR

DEPARTMENT OF CIVIL ENGINEERING
INDIAN INSTITUTE OF TECHNOLOGY ROORKEE
ROORKEE - 247667, INDIA
JULY, 2022

BEHAVIOUR OF CAISSON FOUNDATION UNDER STATIC AND SEISMIC CONDITIONS

A THESIS

Submitted in partial fulfilment of the

requirements for the award of the degree

of

DOCTOR OF PHILOSOPHY

in

CIVIL ENGINEERING

by

MOHIT KUMAR

DEPARTMENT OF CIVIL ENGINEERING
INDIAN INSTITUTE OF TECHNOLOGY ROORKEE
ROORKEE - 247667, INDIA
JULY, 2022

INDIAN INSTITUTE OF TECHNOLOGY ROORKEE

STUDENT'S DECLARATION

I hereby certify that the work presented in the thesis entitled "**BEHAVIOUR OF CAISSON FOUNDATION UNDER STATIC AND SEISMIC CONDITIONS**" is my own work carried out during a period from JULY, 2017 to MAY, 2022 under the supervision of Dr. Kaustav Chatterjee, Assistant Professor, Department of Civil Engineering, Indian Institute of Technology Roorkee, Roorkee.

The matter presented in the thesis has not been submitted for the award of any other degree of this or any other Institute.

Mohit

Dated: June 01, 2022 **(MOHIT KUMAR)**

SUPERVISOR'S DECLARATION

This is to certify that the above-mentioned work is carried out under my supervision.

Kaustav Chatterjee

Dated: June 01, 2022 **(KAUSTAV CHATTERJEE)**

The Ph.D. Viva-Voce examination of Mr. Mohit Kumar, Research Scholar, has been held on **July 28, 2022**

Bappaditya Manna

Chairman, SRC

(BAPPADITYA MANNA)
Signature of External Examiner

This is to certify that the student has made all the corrections in the thesis.

Kaustav Chatterjee
Signature of Supervisor

28/7/22
Head of Department

ABSTRACT

Bridges have been part of human civilization for many centuries now as they connect two locations separated by a river or any difficult terrain. Therefore, bridges facilitate trade, transportation and passage to locations which would otherwise be obscure and thus act as lifeline structures. Most bridges are supported by caissons which are massive and rigid foundation systems and is equipped to resist wide variety of loads like high magnitudes of vertical load, lateral load, uplift load and moments. Because of this virtue, caissons were supposed to be completely safe against any loading combination. However, The Great Hanshin earthquake of 1995 exposed the vulnerability of caissons against earthquake loads. An extensive literature review revealed several research gaps, such as lack of studies with consideration of combined failure wedge formed in front of caisson due to various resisting components, modified pseudo-dynamic study of caissons in layered soil, which could be addressed through the present study. Therefore, the present study attempts to study various aspects of caisson under static and seismic conditions.

Numerical study has been performed, using finite element method-based computer program ABAQUS, to model the behaviour of caisson embedded in layered soil and subjected to different combinations of vertical load and lateral load and moment in order to obtain generalized interaction diagrams relating vertical load, lateral load and moment at failure. Failure is assumed to occur when tensile stresses are developed in soil below the base of caisson. The numerical modelling has been done to take effect of geometric, material and contact non-linearity and pore water pressure into account. Different soil responses (maximum and minimum stresses in soil at base of caisson) and caisson responses like displacement (tilt, shift and depth of point of rotation of caisson) and stresses on various faces (lateral soil pressure, horizontal and vertical skin friction, base friction and base pressure) has been studied in response to different magnitudes of vertical load, lateral load, soil-wall friction angle and horizontal and vertical seismic acceleration coefficients. Based on the magnitudes of various stresses, shear force and moment of resistance profile for caissons in vertical plane has been developed. The moment of resistance developed due to sides and base of caissons has been determined for a series of input parameters and based on the data-set obtained, empirical correlation has been developed to determine load shared by sides of caisson. The results indicate that higher magnitude of vertical load is required to safely carry increasing magnitudes of lateral load. It is also found that at higher magnitudes of seismic acceleration coefficients, lower magnitude of normalized lateral load is required to cause failure.

Theoretical parametric studies have been conducted to study caissons embedded in cohesive frictional (c-ϕ) soil, considering realistic shape of failure wedge obtained from numerical study, to obtain seismic passive earth pressure coefficients due to cohesion, surcharge and unit weight component. The studies have been conducted considering both, individual failure surface for each resisting component using principle of superposition and for combined failure surface due to all resisting components acting together. Comparison of results from the two studies revealed significant difference in magnitude of seismic passive earth pressure coefficient due to cohesion component. The difference in magnitude of seismic passive earth pressure coefficient due to surcharge component is found to be less sensitive than cohesion component while that for unit weight component is even less affected by relative actions of other components. Empirical correlations to obtain centre of log-spiral defining the failure wedge is obtained from the present study based on results of the theoretical analyses.

Limit equilibrium analysis using modified pseudo-dynamic method is conducted to obtain seismic passive earth pressure coefficient considering soil as a Kelvin-Voigt solid. Acceleration profile with depth is obtained from the study which is used to calculate seismic inertial forces. Seismic passive earth pressure coefficient for dry soil as well as submerged soil with free water and restrained water is obtained for multitude of input parameters. The increment of volume of wedge per unit width of caisson with reducing width of caisson and subsequent increase in seismic passive earth pressure coefficient has been studied. The study is further extended to propose analysis of caisson embedded in generalized n-layered cohesionless soil considering polylinear failure wedge. Parametric variation in extent of failure wedge formed in front of caisson is studied in addition to the effect of variation of relative depths and relative magnitudes of soil friction angle in different soil layers on seismic passive earth pressure coefficient. Transfer function relating acceleration amplitude in various layers has also been studied.

The study presented in the thesis presents a series of design charts for seismic passive earth pressure coefficients under a plethora of conditions by cutting down on many assumptions and simulating actual field conditions closely. The numerical study also provides detailed behaviour of caisson foundation under static and seismic conditions which might be useful for practicing engineers and academicians alike.

Keywords: *Caisson; numerical analysis; interaction diagram; log-spiral failure wedge; c-ϕ soil; principle of superposition; seismic passive earth pressure coefficient; modified pseudo dynamic method; layered soil*

ACKNOWLEDGEMENT

This thesis marks the end of my journey in obtaining Ph.D. from IIT Roorkee, which has been kept on track and been seen through to completion with the encouragement and support of my extended family at IIT Roorkee. Although only my name appears on the cover of this thesis, many friends and well-wishers have contributed to its production. It is a pleasant task for me to express thanks to all those who are involved in the success of this study and because of whom my stay in IIT Roorkee for the last five years has been a memorable experience and one that I will cherish forever. To start with, I express sincere gratitude to my supervisor Dr. Kaustav Chatterjee for giving me the opportunity to work under his expert supervision and motivating me to choose this very topic for my Ph.D. research work. I am sincerely thankful to him for his invaluable suggestions, mental support, constant guidance and encouragement which he bestowed upon me throughout the course of my research work and without which this work would not have been possible. I thank him for all his precious time that he has spent with me during the course of preparation of this thesis and the critical suggestion that he made for its improvement. I will always remain grateful to him for allowing me access to the valued references in his personal library. His interactive and cordial nature with eminent stalwarts in the field of geotechnical engineering provided me the opportunity to interact with them and gain valuable knowledge and advice. His integral view on research and focus on 'high quality work for communicating to top class journals' has left behind a deep long-lasting impression on my mind. I am grateful to the Student Research Committee (SRC) members Prof. N. K. Samadhiya, Prof. V. A. Sawant and Prof. Yogendra Singh who were very supportive of my research work and provided me with critical remarks, encouragements and invaluable modifications during the course of my research. The final shape of the thesis would not have been possible without their distinguished comments and suggestions. I also owe a great deal of appreciation and gratitude to Prof. Manohar Viladkar, Prof. Mahendra Singh, Prof. Satyendra Mittal, Prof. Priti Maheshwari, Prof. Bal Krishna Maheshwari, Dr. Akanksha Tyagi, Dr. Anumita Mishra and Dr. Aditya Singh for enlightening me with extensive knowledge during my work at IIT Roorkee.

I would like to take the opportunity to thank my colleagues from Civil Engineering Department Dr. Siddharth Mehndiratta, Dr. Ashish Gupta, Dr. Dipaloke Majumder, Dr. Chandaluri Vinay Kumar, Dr. Aparna, Dr. Anant Konkane, Dr. Vidya Tilak B., Dr. Godas

Srikar, Dr. Akshay Pratap Singh, Dr. Avinash Kumar Singh, K. Sai Kumar, Pavan Kumar Meena, Somdutt Pathak, Tapobrata Lodh, Rahul Verma, Siddalingeshwara D.H., Kirtika Samanta, Ashna K.N., Phibe Khalkho, Hansraj Vashishtha, Pankaj Rawat, Lalhruaikima, Kami Venkata Balaiah and Kavan Modha for the stimulating discussions and all the help and support they provided me without any hesitations during my research work at IIT Roorkee.

I would be failing in my duties if I do not acknowledge Waibhaw Kumar, Shweta Singh, Sonam Ladol, Sushant Rahul, Manisha Yadav and Rashi Singh for providing an invigorating and fun filled environment. They have helped me stay sane through the difficult times with their support and care and have helped me to overcome setbacks while staying focused on my research work. I also thank my other friends Hunny Verma and Gurdeep Singh for their valuable help and support. The value of friendship I received from all of you is immeasurable and I deeply appreciate their belief in me.

Most importantly, the thesis would not have been possible without the love and patience of my family. This thesis is dedicated to my parents Shri Amarendra Kumar and Smt Lata Kumari who motivated me to go ahead with my decision of pusuing Ph.D. at IIT Roorkee. I am indebted to my brother Shankar Shekhar, Dhruv Kumar, sister Kumari Varsha, sister-in-law Aparna Kumari and fiancé Kirtika Samanta for being a constant source of encouragement, inspiration and strength throughout this endeavour. I would like to express my heart–felt gratitude to them for helping me uphill in this phase of life. Last but not the least, I am grateful to God for giving me good health, sense of wellbeing and divine nudges at difficult times that was necessary to complete this thesis.

Mohit

June 1, 2022 **Mohit Kumar**

CONTENTS

LIST OF FIGURES

LIST OF TABLES

LIST OF SYMBOLS

Symbol	**Description**
Chapter 3	
B	caisson base width
D	caisson embedment depth
H	height of lateral load application above scour level
V	applied vertical load
V_a	allowable vertical load
V_n	normalizing vertical load
Q	applied lateral load
M	applied moment
M_n	normalizing moment
γ	unit weight
μ	Poisson’s ratio
ϕ	soil friction angle
δ	wall friction angle
Q_a	allowable bearing pressure
Q_n	normalizing lateral load
N	corrected value of standard penetration resistance
k_h	horizontal seismic coefficient
k_v	vertical seismic coefficient
κ	slope of swelling line
λ	slope of virgin compression line
s	shift of caisson
p_{max}	maximum base pressure
p_{min}	minimum base pressure
p_0	overburden pressure at base of caisson
d	caisson displacement
p	lateral soil pressure
z	depth under consideration

Symbol	**Description**
Chapter 4	
d_p	depth of point of rotation of caisson from scour level
V	applied vertical load
Q	applied lateral load
M	applied moment
σ_{xx}	normal stress in X-direction
F_{xx}	force due to normal stress in X-direction
M_{xx}	moment due to normal stress in X-direction
z_p	depth of point of rotation of caisson from infinitesimal strip at depth z
x_n	nodal spacing in X-direction
y_n	nodal spacing in Y-direction
z_n	nodal spacing in Z-direction
σ_{xy}	horizontal shear stress on side faces
F_{xy}	force due to horizontal shear stress on side face
M_{xy}	moment due to horizontal shear stress on side face
σ_{zy}, σ_{zx}	vertical shear stress on side and front face respectively
F_{zy}, F_{zx}	force due to vertical shear stress on side and front face respectively
M_{zy}, M_{zx}	moment due to vertical shear stress on side and front face respectively
σ_{zz}	normal stress on base of caisson
F_{zz}	force due to normal stress on base of caisson
M_{zz}	moment due to normal stress on base of caisson
σ_{zx}	shear stress on base of caisson
F_{zx}	force due to shear stress on base of caisson
M_{zx}	moment due to shear stress on base of caisson
B	caisson base width
D	caisson embedment depth
ϕ	soil friction angle
δ	wall friction angle
k_h	horizontal seismic coefficient

Symbol	Description
k_v	vertical seismic coefficient
M_{sides}	resisting moment due to stresses on sides of caisson
M_{base}	resisting moment due to stresses on base of caisson
LS_{sides}	resisting moment shared by sides of caisson
M_{base}	resisting moment shared by base of caisson
H	height of lateral load application above scour level
V	applied vertical load
Q	applied lateral load
f	frictional force
N	normal reaction
SF	shear force
M_R	resisting moment

Chapter 5 and 6

c	cohesion
q	surcharge acting on failure wedge
K_{spc}	seismic passive earth pressure coefficient due to cohesion component
K_{spq}	seismic passive earth pressure coefficient due to surcharge component
$K_{sp\gamma}$	seismic passive earth pressure coefficient due to unit weight component
L	length of rectangular caisson
B	width of rectangular caisson
d	embedment depth
r_o	initial radius of log-spiral
ϕ_m	mobilized soil-soil interface friction angle
α	angle subtended at the center of log-spiral between r_o and radius r
α_o	angle subtended by initial radius r_o with vertical at the center of log-spiral
r_f	final radius of log-spiral
α_f	angle subtended by r_f with vertical at the center of log-spiral

Symbol	**Description**
$m(z)$	extent of log-spiral in front of caisson at any depth z
x	angle subtended by radius of side wedge with chord m
θ	angle subtended by circular segment in front of caisson at the center of circle
δ_m	mobilized soil-wall interface friction angle
$p(z)$	reaction force per unit depth exerted by caisson on soil at any depth z
ΔF	tangential force acting on vertical portion of wedge due to side wedges
ΔW	self-weight of the passive wedge
γ	unit weight of the soil inside the passive wedge
$A(z)$	area of horizontal wedge at depth z
k_h	horizontal seismic acceleration coefficient
k_v	vertical seismic acceleration coefficient
ϕ_m	mobilized soil-soil interface friction angle
R	stress applied by soil surrounding the passive wedge
x_o	horizontal distance of caisson face from the center of log-spiral
y_o	vertical distance of caisson face from the center of log-spiral
A_s	area of side wedge
A_r	area of rectangular portion of wedge
A_r	area of wedge in front of rectangular portion
$Q(z)$	overburden pressure force at depth z
$N(z)$	normal reaction at depth z
λ	tangential stress coefficient
W_{sides}	weight of the side wedges
V_{sides}	volume of side wedges
R_H	horizontal component of reaction force due to R
R_V	vertical component of reaction force due to R
HD	denominator of equation containing horizontal force components
VD	denominator of equation containing vertical force components
P_p	total force applied by caisson face on soil wedge
p_p	seismic passive earth pressure
V_a	allowable vertical load in numerical study
V	applied vertical load in numerical study

Symbol	Description
Chapter 7	
$K_{sp\gamma}$	seismic passive earth pressure coefficient due to unit weight component
L	length of rectangular caisson
B	width of rectangular caisson
H	embedment depth of caisson
v_p	primary wave velocity
v_s	shear wave velocity
τ	shear stress
G	shear modulus
η_s	soil viscosity
ρ	dry bulk density of soil
λ, G	Lame’s constants
ω	angular frequency of seismic wave
$F_{j,p}$	transfer function relating displacement amplitude of j^{th} layer with p^{th} layer
r_o	initial radius of log-spiral
ϕ_m	mobilized soil-soil interface friction angle
α	angle subtended at the center of log-spiral between initial radius r_o and radius r
α_o	angle subtended by initial radius r_o with vertical at the center of log-spiral
r_f	final radius of log-spiral
α_f	angle subtended by r_f with vertical at the center of log-spiral
$l(z)$	extent of log-spiral in front of caisson at any depth z
x	angle subtended by radius of side wedge with chord l
β	angle subtended by circular segment in front of caisson at the center of circle
δ_m	mobilized soil-wall interface friction angle
$p(z)$	reaction force per unit depth exerted by caisson on soil at any depth z
T	force due to tangential stress

Symbol	**Description**
ΔF	horizontal component of T
ΔW	self-weight of the infinitesimal failure wedge at any depth
γ	dry unit weight of the soil
γ_{sub}	submerged unit weight of the soil
γ_{sat}	saturated unit weight of the soil
γ_w	unit weight water
H	depth of wall
p_{hdyn}	hydrodynamic pressure
p_{hst}	hydrostatic pressure
$A(z)$	area of horizontal wedge at depth z
k_h	horizontal seismic acceleration coefficient
k_v	vertical seismic acceleration coefficient
Q_h	horizontal seismic inertial force
Q_v	vertical seismic inertial force
ξ	damping ratio of soil
r_u	excess pore pressure ratio
ϕ_m	mobilized soil-soil interface friction angle
R	stress applied by soil surrounding the passive wedge
A_s	area of side wedge
A_r	area of rectangular portion of wedge
A_f	area of wedge in front of rectangular portion
V/B	volume per unit width of failure wedge
$Q(z)$	overburden pressure force at depth z
$N(z)$	normal reaction at depth z
λ_t	tangential stress coefficient
R_H	horizontal component of reaction force due to R
R_V	vertical component of reaction force due to R
HD	denominator of equation containing horizontal force components
VD	denominator of equation containing vertical force components
$P_{p\gamma}$	total force applied by caisson face on soil wedge
V	volume of failure wedge

Symbol	Description
Chapter 8	
L	length of caisson
B	width of caisson
H	embedment depth of caisson
h_j	depth of j^{th} layer
γ_j	unit weight of j^{th} layer
ξ_j	damping ratio of j^{th} layer
ϕ_j	mobilized soil friction angle
α_j	inclination of failure wedge in j^{th} layer with horizontal
θ_j	fanning angle of j^{th} layer
$m(z)$	extent of failure wedge at any depth z
V_j	volume of j^{th} layer
$A(z)$	area of horizontal wedge at depth z
k_h	horizontal seismic acceleration coefficient
k_v	vertical seismic acceleration coefficient
Q_h	horizontal seismic inertial force
Q_v	vertical seismic inertial force
ξ	damping ratio of soil
r_u	excess pore pressure ratio
R	stress applied by soil surrounding the passive wedge
$Q(z)$	overburden pressure force at depth z
$N(z)$	normal reaction at depth z
λ_t	tangential stress coefficient
P_j	total force applied by caisson face on soil wedge in j^{th} layer
$K_{sp\gamma}$	seismic passive earth pressure coefficient due to unit weight component
W_j	weight of the failure wedge in soil layer j
n	number of soil layers
v_p	primary wave velocity
v_s	shear wave velocity
ω	angular frequency of seismic wave

Chapter 1

INTRODUCTION

1.1 General

Caissons are massive foundation systems with high stiffness and rigidity. This equips the caisson to support excessive vertical load, lateral load and applied moments and thus a suitable foundation system to support lifeline structures like bridge piers and abutments. In addition, the mass of caisson enables it to easily withstand the uplift forces in submerged conditions. Lifeline structures are critical to human and economic resources. Therefore, safe design and performance of these structures is a vital cog in the working of an affluent nation. Design of bridge substructure is as important as the design of superstructure from the safety point of view. The resistance generated by sides of caissons is quite significant compared to base of caissons in presence of lateral loads and hence, they are treated as deep foundation. Based on the installation mechanism, caissons are of following three major types as shown in Fig. 1.1.

- *Open caisson or well foundation*: Open caisson is hollow at the time of installation. It is sunk on site by virtue of self-weight with the help of cutting edge at the foot. As the caisson is sunk, the soil within is dredged out and further sequential construction in upward direction is done. After sinking the well to the required depth, the top and bottom of caisson is sealed with concrete and the body is filled with sand.
- *Box caisson or floating caisson*: This type of caisson is installed at a previously levelled foundation site. The caisson is constructed off-site and sunk to the foundation base. It finds its application in situations where loads are not excessive, and a bearing stratum is reached at a shallow depth [Ranjan and Rao (2004)]. Box caissons are to be protected from scouring action.
- *Pneumatic caisson*: It comprises of a dry working chamber at the bottom which enables better control in sinking. The caisson sinks as excavation is made and upon reaching the required depth, the working chamber is sealed off with concrete. Despite providing most control in sinking, this type of caisson is very costly, and the depth of sinking is limited to about 35m below water level since the air pressure inside the chamber below this depth is dangerous for human body.

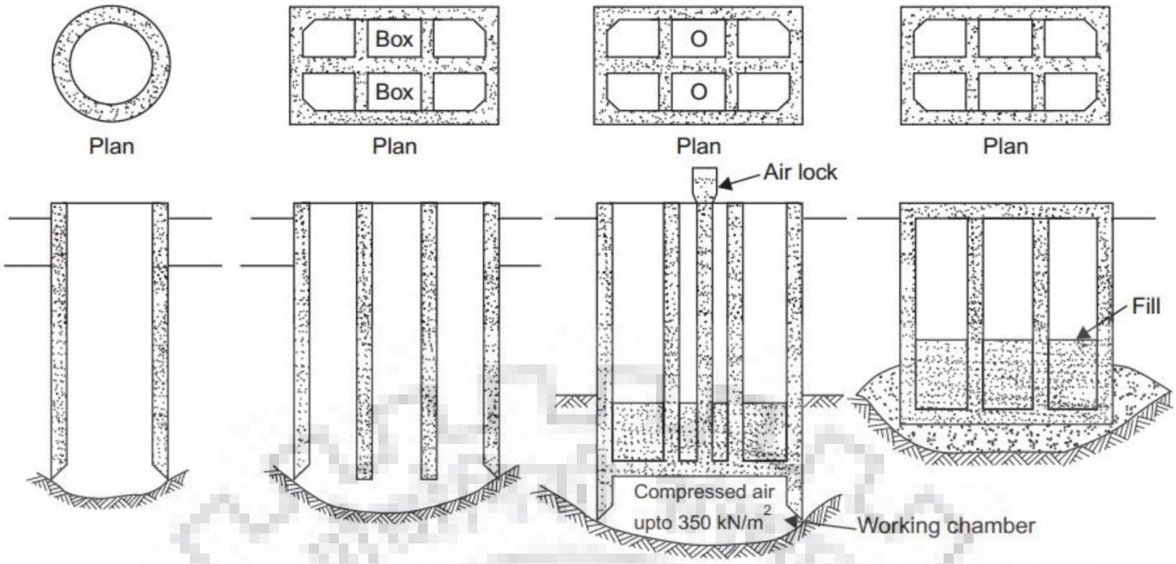

(a) Pile-type open caisson

(b) Box-type open caisson

(c) Pneumatic caisson

(d) Box (floating) caisson

Fig. 1.1 Schematic diagram of different types of caissons

(https://gcekbpatna.ac.in)

The prime examples of engineering structures which employ caisson as foundation system are Taj Mahal in India and San Francisco-Oakland Bay bridge in USA. Both these structures are engineering marvels and have boldly faced the test of time, withstanding multiple earthquakes. The western span of the San Francisco-Oakland Bay bridge between San Francisco and Yerba Buena Island is two suspension bridges joined by a common anchorage. The chief engineer of the project, Charles H Purcell consulted with deep water foundation expert, Daniel E Moran to reach on a decision to build one of the largest caissons, Moran-Purcell caisson to support the anchorage at Yerba Buena Island as shown in Fig. 1.2. The size of the caisson used in San Francisco-Oakland bridge is 29.6 m × 60.1 m in section and depth of 74 m (Murthy, 2016).

1.1.1 Caisson loads and stresses

Caisson foundation is commonly subjected to three types of external loading, i.e., vertical load (V), lateral load (Q) and applied moment (M). These are result of plethora of individual loads like dead load, live load, wind load, earthquake load, load due to water current, load due to vehicular traffic, buoyancy etc. Under the application of these loads, variety of resistive forces act on the caisson as shown in Fig. 1.3. These resistive components are lateral soil pressure on front and rear face of caisson, horizontal skin friction on side faces of caisson (parallel to direction of applied lateral load), vertical skin friction on all the vertical faces of caisson, base pressure and base friction. The distribution of stresses is guided by the point of rotation of the caisson under the action of these loads. The magnitude of resistive forces is also affected by soil properties, soil-wall interface properties and seismic conditions.

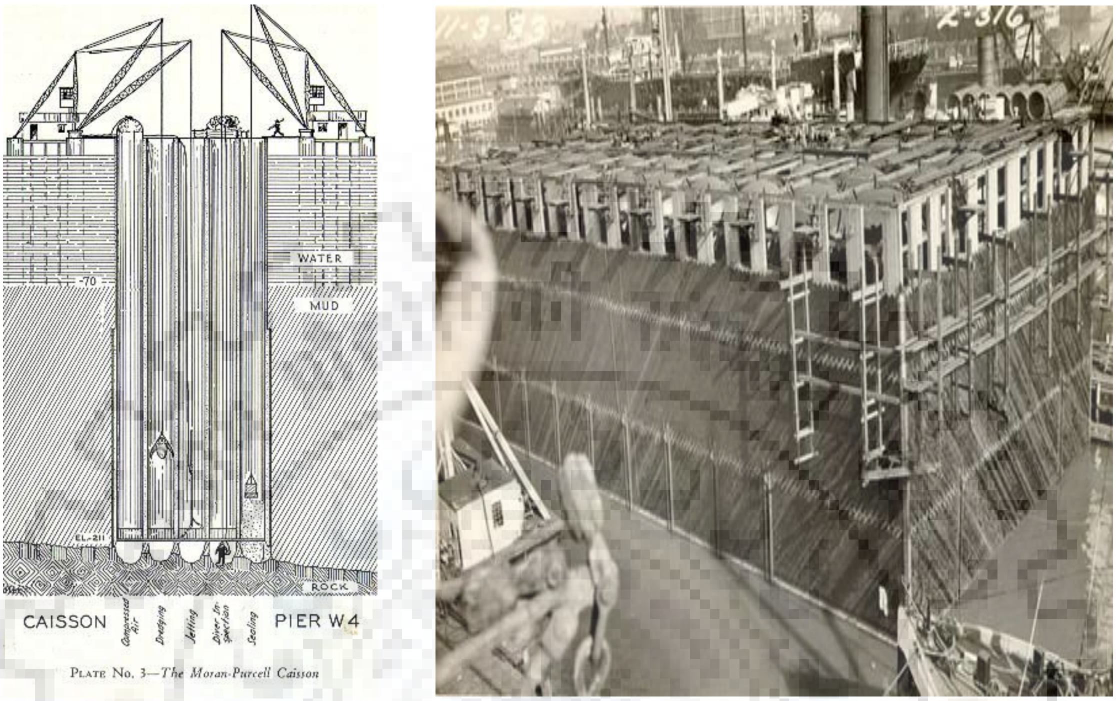

(a) (b)

Fig. 1.2 Moran-Purcell caisson (a) illustration from "Facts About the San Francisco - Oakland Bay Bridge" (b) construction

(https://www.lib.berkeley.edu/news_events/bridge/bb_dc006.html)(https://calisphere.org/item/78d3aaae7e91a95bbb64721e1c090856) (Source: San Francisco Public Library)

The effectiveness of caisson foundation lies in their ability to generate resistive forces for a wide variety of load combinations. This made them automatic choice for foundation system for bridge piers and abutments. Caisson foundations were thought to be immune to seismic loads because of their high stiffness, but the failure of bridges in the Great Hanshin-Awaji earthquake of 1995 illustrated that the analysis of caissons under seismic conditions cannot be neglected. The damage to bridges supported by caisson foundation (Kobe bridge, Portpia bridge, Second Maya bridge and Nishinomiya-Ko bridge [as shown in Fig. 1.4]) was mainly due to lateral spreading of subsoils which caused movement and inclination towards water. Lateral spreading also caused the failure of four caissons at Barcelona harbour in November 2001 [Puzrin et al. (2009)].

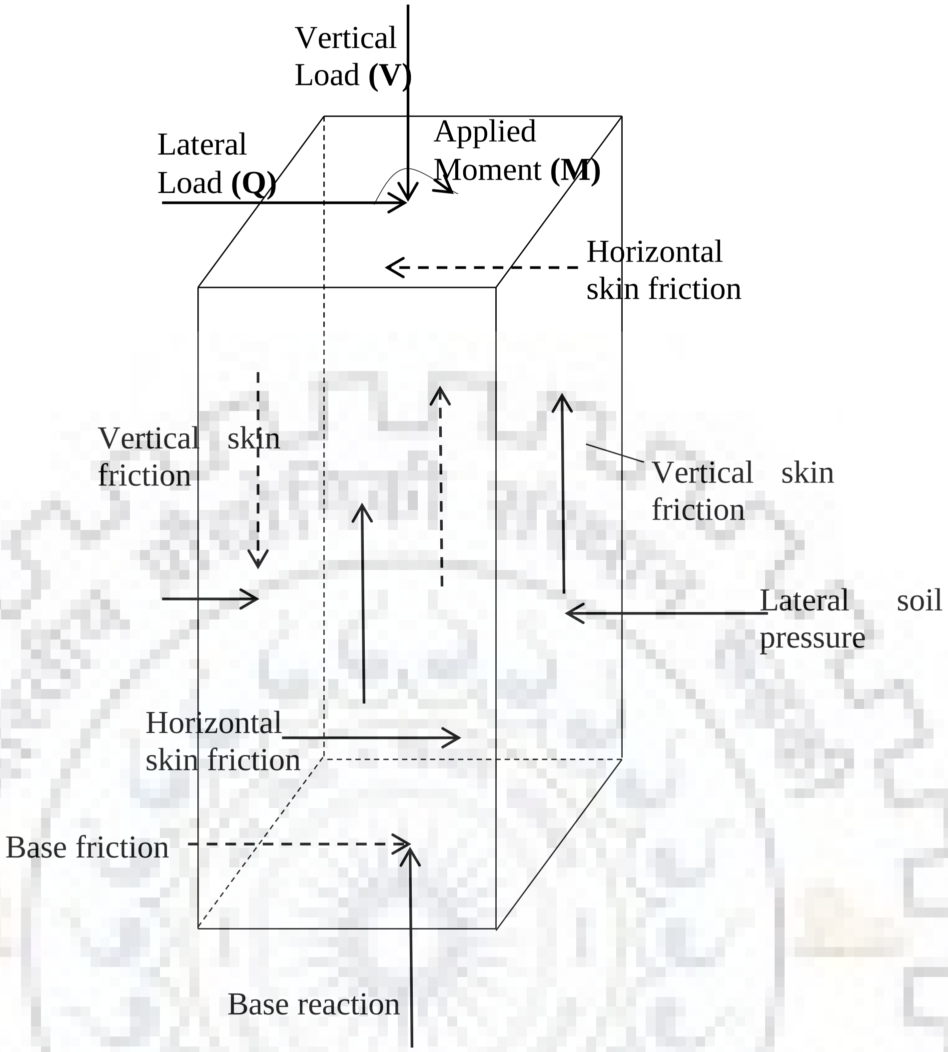

Fig. 1.3 Stresses acting on various faces of caisson for applied loads *V*, *Q* and *M*

1.2 Aim of the Study

A great variety of loads is transferred to caisson foundation by different superstructures it is used for. As mentioned in the previous section, despite their high stiffness, failure of caisson foundation cannot be ruled out under seismic conditions. The present study aims to provide safe design guidelines for caissons by means of numerical and analytical studies which improve upon the assumptions made by previous researchers as mentioned in the next chapter. The finite element based numerical analysis aims to obtain the relative magnitudes of vertical load, lateral load and applied moment at failure and to determine the load sharing between base and sides of caisson for various loading and site conditions. The analytical studies use limit equilibrium analysis to determine seismic passive resistance acting on a caisson by considering a novel 3D logarithmic spiral failure wedge.

Fig. 1.4 Failure of Nishinomiya-Ko bridge during 1995 the Great Hanshin-Awaji Earthquake

(Image source: https://www.shutterstock.com/es/editorial/image-editorial/elevated-sections-hanshin-expressway-nishinomiya-western-japan-7283970a)

The study determines seismic resistance by considering both individual failure surfaces for different resisting components and combined failure surface for all the components acting together using pseudo-static approach. Furthermore, modified pseudo-dynamic approach has been used for caisson embedded in layered soil to account for amplification of earthquake waves through various soil layers. The proposed study allows for safe design of caissons and earth retaining structures using the interaction diagrams and design charts presented in subsequent chapters.

1.3 Motivation Behind the Study

Caissons are huge foundations with unparalleled stiffness and rigidity among foundation systems. This makes them reliable for supporting structures subjected to various loading combinations. However, The Great Hanshin-Awaji earthquake of 1995 exposed the vulnerability of caissons in seismic conditions. Since, the primary application of caissons is as foundation to bridge piers and abutments, its failure can be catastrophic. An extensive literature review revealed the lack of numerical studies by taking pore water pressure into account [Varun et al. (2009), Gerolymos et al. (2015)]. In addition, all the previous analytical studies considered either 2D failure wedge [Soubra (2000), Soubra and Macuh (2002), Liu et al. (2018)] or non-realistic planar 3D wedge [Biswas and Choudhury (2019), Biswas and Choudhury (2021)]. Moreover, the modified pseudo-dynamic method of analysis [Rajesh and Choudhury (2017)] had been used to study mostly homogeneous soil which can be extended for layered soil. Thus, it was essential to conduct realistic study for a foundation system of great importance to the society.

1.4 Organization of Thesis

A summary of the contents of this thesis is presented in this section. The chapter wise contents of the thesis are as follows:

The first chapter introduces caisson, its importance and the basic working mechanism. The aim of the study and motivation behind the study have also been briefly discussed.

The second chapter gives an account of in-depth literature review about the studies pertaining to caissons. Few studies related to piles and retaining structures, which may have substantial bearing on the present study have also been explored and the critical appraisal of the literature has been done. Based on the critical appraisal of literature, objectives for the present study have been chosen.

The third chapter presents the finite element method-based numerical study for caisson embedded in layered submerged soil. Static and pseudo-static analysis has been performed and various generalized interaction diagrams have been developed relating V-Q-M at failure for various seismic acceleration coefficients and soil-wall friction angles.

The fourth chapter deals with the stress (soil pressure and skin friction) response of caisson under various soil, interface and seismic conditions. The load-sharing between base and sides of caisson for different cases have been presented.

The fifth chapter proposes a novel geometry of 3D failure wedge formed behind a caisson. The seismic passive earth pressure coefficients due to unit weight component, surcharge component and cohesion component have been determined using limit equilibrium method of analysis and principle of superposition. Empirical correlation for the centre of log-spiral with respect to top of scour level has been presented. Design charts for different seismic passive earth pressure coefficients have been presented.

The sixth chapter extends the theoretical analysis of the fifth chapter. The failure wedge considered in this chapter is obtained by considering all the resistive components working together instead of individual components in previous chapter. Design charts have been developed for a combination of resistive components.

The seventh chapter deals with the limit equilibrium analysis of cohesionless soil under dry and submerged conditions using modified pseudo-dynamic method. The caisson is assumed to be embedded in layered soil; however, the entire failure wedge lies in a single layer. Linear analysis has been performed to obtain various design charts considering different input parameters.

The eighth chapter assumes polylinear failure wedge for caisson embedded in layered soil. Limit equilibrium method of analysis has been adopted to return the seismic passive resistance offered by the strata with varying depths and properties of layers. Design charts have been developed for the entire set of input parameters.

The ninth chapter reveals the major conclusions drawn from the entire study. The scope for future work, contribution of the present study and the limitations of the study have also been discussed in this chapter.

Chapter 2

LITERATURE REVIEW

2.1 General

The analysis of caissons is very different from analysis of other geotechnical structures like retaining walls or piles. This stems from the fact that caisson is a finite-width, 3-dimensional structure unlike retaining wall and it behaves in a predominantly rigid manner unlike piles. However, theoretical analysis of caissons has been derived and updated from the assumptions made during analysis of retaining walls and piles. Therefore, the present literature review also encompasses the research pertaining to walls and piles. Researchers have studied the behaviour of caissons for more than a century now. A plethora of experimental, numerical and theoretical studies have been performed in this duration. This chapter gives a brief account of the various studies performed over the years in chronological order.

2.2 Experimental Studies

A number of experimental studies have been performed over the years that helped researchers understand behaviour of embedded piers and piles subjected to static and dynamic loading. Several model load tests were performed on caissons and piers during the start of experimental program [Lazard (1957), Roscoe (1957), Kondner and Cunningham (1963), Sharda (1975)]. Few studies have also been conducted to demonstrate the ground response to dynamic excitation [Kumar et al. (2017), Chaudhary et al. (2018)]. Furthermore, dynamic load tests have been conducted on piles [Bhattacharya et al. (2004), Manna and Baidya (2009), Manna and Baidya (2010a), Manna and Baidya (2010b), Chandrasekaran et al. (2013), Biswas and Manna (2018), Ralli et al. (2022)] and retaining walls [Boominathan et al. (2004), Fukumoto et al. (2014)] to observe their behaviour during earthquakes. The centrifuge tests [Gadre and Dobry (1998), Muszynski et al. (2014), Olson et al. (2017)] and other field tests [Kelly et al. (2006), Loli et al. (2011)] conducted over the years have clarified the failure patterns and response of caissons to variety of field conditions. The detail of these studies is mentioned in this section.

2.2.1 Lazard (1957)

The author performed model tests on piers of diameter 3 feet and depth 9 feet to study overturning moment at limiting condition. The author reported that passive earth pressure is the most prominent parameter associated with limit state and therefore all the factors that affect the magnitude of passive earth pressure (such as, ground configuration, direction of pull) should be taken into consideration during formulation of overturning moment at limit state.

2.2.2 Roscoe (1957)

The author performed field test by applying lateral pull to saw-tooth portal frames supported by reinforced cement concrete pier foundation. The test piers used by the authors were 1.5 feet in diameter and 3 feet deep. Provision for application of vertical load was also provided by means of loading chamber. The piers had been constrained to rotate about the base by the author. The average moment required to cause failure and the extent of failure wedge formed in front of pier was measured by the author and compared with available theoretical studies. The author also reported the 3-dimensional failure geometry obtained from the study as shown in Fig. 2.1.

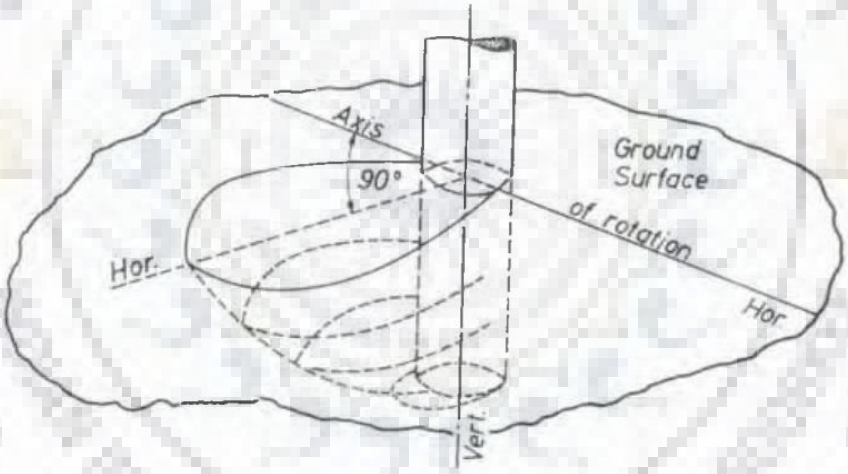

Fig. 2.1 Actual failure wedge geometry for laterally loaded pier [after Roscoe (1957)]

2.2.3 Kondner and Cunningham (1963)

The authors studied the performance of a rigid circular pole in dry, dense sand having uniform properties under horizontal loading, which is applied above the ground line for varying distances. A relationship between the moment-deflection characteristics of the soil-pole system was developed by the authors using the hyperbolic function method.

2.2.4 Sharda (1975)

A series of laboratory and field tests for well foundations embedded in sand was conducted by the author. Test set-up for lateral load test has been depicted in Fig. 2.2. The author studied the effects of size of well, embedment depth, vertical and lateral loads, stiffness of subgrade at base and soil-wall friction angle in the model tests. The author also developed a theory for analysing the lateral resistance of caissons by taking non-linear pressure versus displacement characteristics of surrounding soil. The results of theoretical and experimental studies are reported to be in excellent agreement by the author.

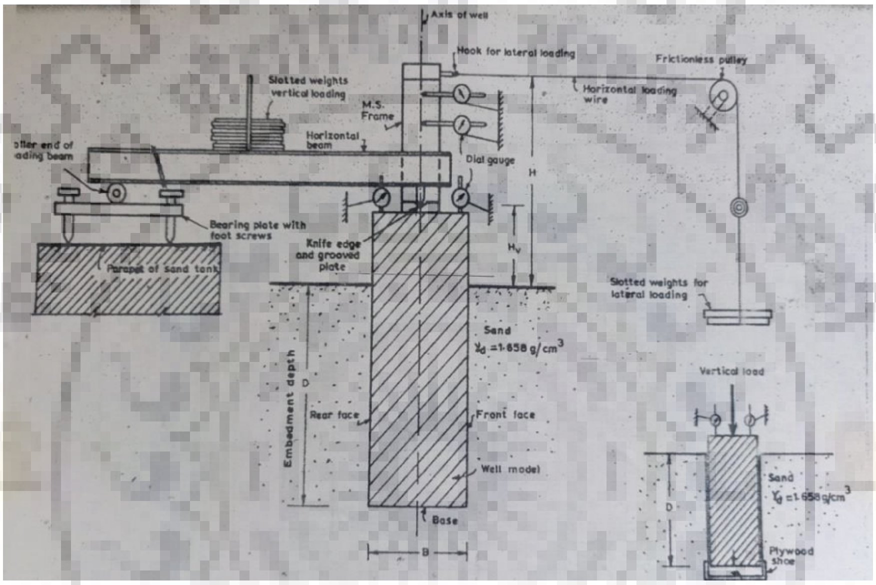

Fig. 2.2 Lateral load test set-up for laboratory well models [after Sharda (1975)]

2.2.5 Gadre and Dobry (1998)

The authors conducted a series of centrifuge tests, including seven soil-foundation configurations on an embedded pile cap foundation, to calculate the ultimate lateral capacity, material damping, and secant stiffness. A square footing model of 1.14 m×1.14 m×0.84 m inserted in dense dry sand with a relative density of 75% was used for the tests. The authors assessed the contributions and possible interactions of base and side shear, and active and passive forces to the lateral response of the foundation. The authors observed the contribution of the passive forces in the total lateral resistance of the system to be most substantial.

2.2.6 Bhattacharya et al. (2004)

The authors proposed buckling mode of failure of piles in liquefiable soil caused due to earthquake loading. The authors conducted dynamic centrifuge test to verify the proposed failure mechanism based on 14 case studies of pile performance during earthquake. It was concluded that slenderness ratio can be used to distinguish pile behaviour in liquefiable soil.

2.2.7 Boominathan et al. (2004)

The authors conducted laboratory tests using laminar shake boxes to study the behaviour of pile walls installed in sandy soil strata. The authors considered both rigid and flexible pile walls embedded in dry loose sand (15% and 23% relative density) as well as saturated sandy layers. The magnitude of static load applied was also varied by the authors. The authors varied initial displacement amplitude to model different levels of severity of earthquakes. The authors reported that the maximum acceleration was recorded at the surface and that the maximum pile wall displacement in liquefied state for wall in loose saturated sand was found to be 30-40% higher than wall in dry loose sand.

2.2.8 Kelly et al. (2006)

The authors studied the dynamic behaviour of suction caissons embedded in sand and clay subjected to vertical and moment loading. Comparisons were drawn by the authors between the laboratory tests and field tests for caisson foundations concerning the stiffness and strength by establishing a scaling relationship. The results from the tests were presented in a dimensionless manner by the authors. The authors reported that the field tests could be used to scale the results of the laboratory tests of caissons under moment loading. On the contrary, a noteworthy difference in the results between the laboratory and field tests for caissons under vertical loading was observed by the authors.

2.2.9 Manna and Baidya (2009)

The authors conducted static and forced vibration tests in the vertical direction to predict the natural frequencies and peak amplitudes of reinforced concrete piles considering varying eccentricities. Further, the experimental results were compared with two-dimensional finite element analysis and Novak’s continuum theory (1978). The authors reported that the maximum amplitude of the pile predicted from the finite element analysis was in reasonable agreement with that of the experiment results.

2.2.10 Manna and Baidya (2010a)

The authors studied the dynamic characteristics of piles against vertical vibrations considering non-linearity. For this, forced vibration tests on both single and group piles were performed by the authors for varying frequencies of excitation and pile cap embedment. Subsequently, the authors compared the experimental results with continuum theory. A weak boundary zone surrounding the pile was used in the analysis by the authors to consider the effects of nonlinearity in the response of the soil-pile system.

2.2.11 Manna and Baidya (2010b)

The authors conducted field vibration tests and theoretical analysis using a continuum approach to examine the dynamic response of piles subjected to coupled excitations. The authors observed a decrease in the pile stiffness and damping with the increase in the excitation frequency for both horizontal and rocking modes. Further, the results from the experimental and theoretical analysis by the authors were found to be in reasonable agreement when pile-soil separation was considered.

2.2.12 Loli et al. (2011)

The authors conducted experimental and numerical studies to predict the behaviour of embedded caisson foundations against reverse faulting. The authors found that the rigid caisson foundation brings about a diversion in the rupture, which then progresses around the foundation edges. The authors observed that the failure pattern and its influence on the foundation response depend on the exact position of the caisson with respect to the fault. Therefore, a parametric study to highlight the effect of the position of the caisson corresponding to the rupture fault was conducted numerically.

2.2.13 Chandrasekaran et al. (2013)

The authors conducted dynamic lateral load tests on laboratory scale models of piles embedded in clay. The authors modelled elastic half space in the test set up to ensure that the stress waves are not reflected by the test container as shown in Fig. 2.3. Hollow aluminium tubes were used by the authors to model test piles in groups of 1×2, 2×2 and 3×3. The extensive test program was conducted by the authors for varying consistency index of clay, length to diameter ratio of piles, spacing of piles, dynamic load and frequency of loading. The authors reported that the displacement of pile group subjected to dynamic lateral load is highly non-linear. The authors also observed that the dynamic lateral loading produced higher magnitude of maximum bending moment and active length of pile as compared to static loading.

2.2.14 Fukumoto et al. (2014)

The authors performed numerical and experimental analyses to study the behaviour of dry-stone retaining walls under seismic loadings by focusing on the shape effect of the stone blocks. The discrete element method employed in the analysis by the authors was found to replicate the behavior of the stone walls as obtained from the centrifuge tests. The authors reported a higher seismic performance of the wedge-shaped blocks as compared to the cuboid blocks which was attributed to the difference in the friction at the interface.

2.2.15 Muszynski et al. (2014)

The authors conducted four centrifuge tests on a massive foundation with high rigidity embedded in liquefiable soil. The repeatability of the test in terms of coefficient of variation of parameters like base input excitation, porewater pressures and shift of foundation. The authors advised for meticulous control over input motion, as it is the guiding parameter controlling the repeatability of tests.

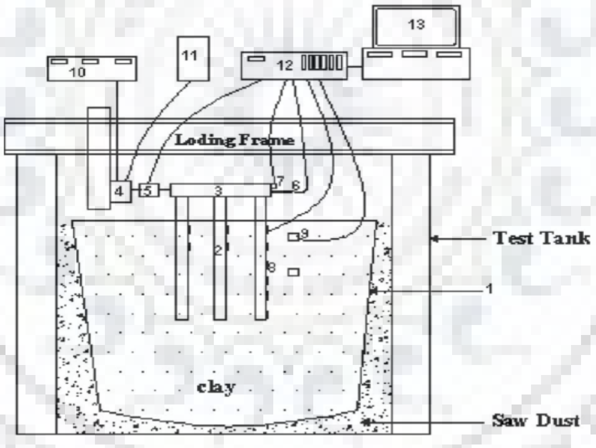

1	M.S. basket with geomembrane	8	Strain gauge
2	Model pile	9	Pore pressure transducer
3	Pile cap	10	Excitation amplifier
4	Exciter	11	Blower
5	Load cell	12	DAS (MGC + and Spider 8)
6	LVDT	13	PC with Catman software
7	Accelerometer		

Fig. 2.3 Experimental set-up for dynamic lateral load test [after Chandrasekaran et al. (2013)]

2.2.16 Kumar et al. (2017)

A new methodology for obtaining dynamic soil properties (DSP), based on asymmetrical hysteresis loop at high shear strain has been proposed by the authors. A series of cyclic triaxial test was conducted by the authors at different initial conditions. The authors inferred that most of the DSP obtained from both asymmetrical and symmetrical hysteresis loops were similar in magnitude, but damping ratio was significantly lower when evaluated using symmetrical loop compared to asymmetrical loop.

2.2.17 Olson et al. (2017)

The authors conducted four centrifuge tests to evaluate the lateral spreading loads imposed on a stiff caisson due to seismic conditions in liquefiable soil. The authors considered pressures on both the upslope and downslope sides of the caisson and calculated them using tactile sensors. Additionally, a hybrid approach considering a passive wedge factor (PWF) that is variable, was developed by the authors to evaluate the ultimate lateral earth pressure distribution due to lateral spreading. The authors considered a three-dimensional upslope passive wedge, the depth, size, and shape of which were depicted with respect to an oval-shaped passive wedge formed ahead of the caisson as shown in Fig. 2.4. The authors reported that the results from the newly proposed method were in accordance with the centrifuge test results.

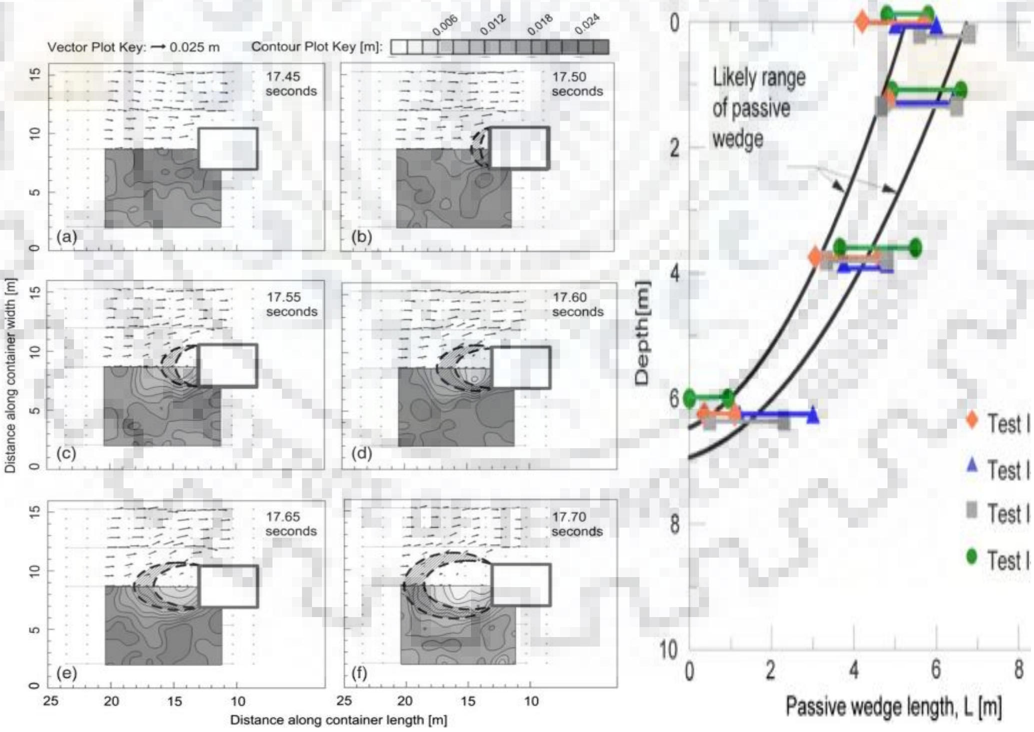

(a) (b)

Fig. 2.4 Shape of passive wedge in (a) horizontal plane and (b) vertical plane determined from strong shaking [after Olson et al. (2017)]

2.2.18 Biswas and Manna (2018)

The authors carried out dynamic field tests to study the non-linear behavior of a soil-pile system subjected to coupled vibrations from machine foundations. From the test results, the authors presented frequency-amplitude plots for varying eccentricities. Furthermore, a numerical analysis using continuum theory was executed by the authors which studied the stiffness and damping variation of piles with frequency.

2.2.19 Chaudhary et al. (2018)

The authors used geogrid and sheet piles to reinforce the breakwater foundations and investigated the response of these foundations against various earthquake loadings. Further, the authors assessed the resilience of the proposed reinforced model by performing shake table tests and numerical analysis using the finite difference method. A significant decrease in the lateral displacement and settlement of the reinforced foundation under earthquake foreshocks and mainshock was observed by the authors.

2.2.20 Ralli et al. (2022)

The authors carried out dynamic field tests to study the nonlinear response of single vertical and inclined piles subjected to machine loadings. The authors observed an increase in the resonant frequency with the increase in the batter angle thereby highlighting the influence of the batter angle on the pile response. Additionally, theoretical analysis was also performed by the authors which compared well with the test results. The authors found the dependency of the loading direction of batter piles on the stiffness and damping of the pile-soil system.

2.3 Numerical Studies

Finite element analysis has been the most popular modes of numerical study for a long period of time because of its effectiveness in modelling complex geometry and loading and has been adopted by a plethora of researchers for studies pertaining to caissons [Mita and Luco (1989), Varun et al. (2009), Karapiperis and Gerolymos (2014), Gerolymos et al. (2015), Gaudio and Rampello (2016), Gaudio and Rampello (2020), Al-Ramthan and Aubeny (2020), Biswas and Choudhury (2020), Fu et al. (2020)] and other geotechnical problems [Zaman et al. (1984), Murakami et al. (2005), Boominathan (2008), Chatterjee et al. (2014), Krishna and Bhattacharjee (2017), Jalbi et al. (2018)]. An account of several other numerical methods was given by Murakami (2010) which was also adopted by Murakami et al. (2005) and Shuku et al. (2012).

2.3.1 Zaman et al. (1984)

The authors used the finite element method to study the interface deformation behaviour of a thin layer element under the action of dynamic loading. An elastic-plastic hardening model was used by the authors to account for the non-linear behaviour of the soil. The results observed by the authors were verified with the response obtained from field tests on a model nuclear power plant. Finally, the authors concluded that the proposed model accurately represented the interface behaviour.

2.3.2 Mita and Luco (1989)

The authors conducted the dynamic response analysis of a 3D square embedded foundation by utilizing an elastic half-space. The authors applied a hybrid technique to obtain the impedance function of the rigid embedded foundation by combining the boundary element approach in the frequency domain and the finite element method. It was reported by the authors that a cylindrical foundation having an equal circular base and depth of embedment could be used as an estimate in the response analysis of square foundations. Moreover, the authors observed a decrease in the coefficient of horizontal stiffness in the higher frequency range, particularly for Poisson’s ratio value of 0.4 and square base foundations.

2.3.3 Murakami et al. (2005)

The authors introduced formulations for a soil-water coupled problem by employing a mesh-free strategy and validated it with undrained soil tests. Further, the authors studied the punch problem of a foundation resting on a soft saturated soil having problems of stress singularity, utilizing the mesh-free Galerkin method. The forward difference approximation was used by the authors in the discretization of time domain.

2.3.4 Boominathan (2008)

The authors performed numerical analysis of ventilation stack of a nuclear power plant using computer program SASSI 2000. The authors employed flexible volume substructure method to conduct soil-structure interaction analysis for varying relative stiffness of the layers of strata, thickness of soil layer and embedment of foundation. The study revealed that the spectral accelerations and displacement at top reduce with increasing embedment ratio (ratio of depth of embedment to radius of footing) due to soil structure interaction. The reduction in spectral acceleration was reported by the authors to be as high as 35% for embedment ratio of 2.5 compared to surface footing.

2.3.5 Varun et al. (2009)

The authors used a four-spring Winkler model to predict the static and dynamic response of a rigid caisson foundation. The authors obtained spring stiffness by employing a macroscopic model of the well foundation for rigid and semi-rigid foundations, comparing the same with finite element analysis, which was found to be in very good agreement with each other.

2.3.6 Murakami et al. (2010)

The authors compiled various numerical methods that may be useful in field of geotechnical engineering. The authors discussed various aspects of nonlinear finite element method, micromechanics and discrete element method, inverse analysis etc. The authors also shed light on methods like limit analysis (upper and lower bound), limit equilibrium method, smoothed particle hydrodynamics, mesh free analysis and finite volume method which can be used for solving various geotechnical problems.

2.3.7 Shuku et al. (2012)

The authors highlighted the importance of data assimilation method of “particle filter” (PF) in geotechnical applications. It is observed that using the method on numerical experiments and model tests identifies the elasto-plastic geomaterials very well. The authors reported that the parameters identified by PF, based on sampling method ‘SIS’ for a numerical test, converged into their true value.

2.3.8 Chatterjee et al. (2014)

The authors modelled undrained response of skirted shallow foundations using FEM based computer program ABAQUS. The authors have considered alteration of embedment depth and mobilized shear strength of local soil with increased translation of foundation by using large deformation FEM analysis. The authors drew comparisons between results of the numerical study with centrifuge test results of circular model of skirted foundation and concluded that the proposed model is capable of replicating the foundation response to a variety of loading accurately even after yielding.

2.3.9 Karapiperis and Gerolymos (2014)

The authors investigated the lateral response of a massive caisson foundation in undrained clay subjected to externally applied combined vertical, horizontal, and moment loading. Using three different D/B (depth to width) ratios ranging from 1–3, the response of the caisson was obtained by the authors, and every possible failure mode was identified for different load paths by conducting a 3D finite element analysis as illustrated in Fig. 2.5. The results from the numerical study were used to scale the parameters of a four-spring Winkler model. It was observed that the lateral soil resistances depend on the various loading paths and factors of safety to vertical loading, apart from being a function of the soil strength properties and geometry of caisson.

2.3.10 Gerolymos et al. (2015)

The author used a thorough 3D finite element analysis to study the response of a cuboid caisson foundation with varying embedment depths in cohesive soil under combined loading. The analysis considers the influence of the embedment depth, vertical loading, and soil interface friction coefficient on the bearing capacity of the caisson. A generalized failure envelope developed in the vertical load-lateral load-moment (N-Q-M) space, capturing every response aspect, was used to determine the displacement vector of the caisson head under post-failure conditions. Furthermore, low-frequency and high-frequency dynamic tests were used to validate the obtained failure envelope for caissons. The radiation damping was found to have a negligible influence on the caisson response under failure conditions.

2.3.11 Gaudio and Rampello (2016)

The authors conducted a 3D numerical analysis in the time domain for a bridge pier supported by a caisson foundation to evaluate its seismic behaviour. The soil behaviour was represented by an elastic-plastic hardening model taking into account soil non-linearity and hysteretic behaviour. The authors carried out the analysis for varying slenderness ratio of caissons and pier height, wherein its influence on the rotation of caisson and permanent deformation of bridge pier was highlighted. Furthermore, the equivalent horizontal seismic coefficient $k_{h,eq}(t)$ was developed by the authors by dividing the caisson into n horizontal discs and is given as follows:

$$k_{h,eq}(t) = \frac{\sum_i k_{h,i}(t).W_i}{W} = \frac{\sum_i k_{h,i}(t).h_i}{H} \tag{2.1}$$

where H is the caisson height and W is the weight of caisson; h_i is the height of the horizontal disks having weight W_i; $k_{h,i}(t)$ is the estimated seismic acceleration coefficient at a particular time instant. The equivalent horizontal seismic coefficient can be adopted in the pseudo-static analysis of caissons.

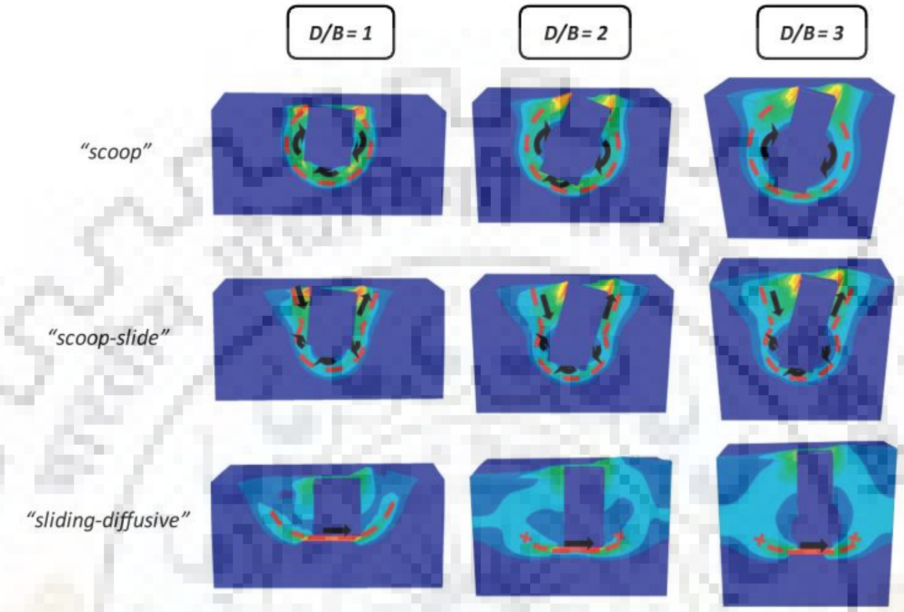

Fig. 2.5 Failure mechanisms for the three different embedment ratios [after Karapiperis and Gerolymos (2014)]

2.3.12 Han et al. (2016)

The authors estimated the earth pressure of a retaining wall supporting a layered backfill for static and dynamic conditions by utilizing the horizontal slice technique considering limit equilibrium analysis. The failure surface was assumed to be both linear and curved by the authors, for the analysis. The authors observed the consequential effect of the soil-wall interface friction angle (δ) on the earth pressure magnitudes and failure surface shape. Further, it was reported by the authors that the active earth pressure could be calculated using the linear failure surface, while the passive earth pressure uses the curved failure surface for both static and dynamic conditions.

2.3.13 Krishna and Bhattacharjee (2017)

The authors studied the response of reinforced soil retaining wall to scaled ground motion. The numerical model was calibrated with the results of shake table test and was further updated to study the response to 5 scaled earthquake motion. The authors reported formation of two deformation zones. The constant strain zone extended beyond the reinforced soil while the high strain zone lied close to the wall face. The authors concluded that seismic excitations during earthquake is a complex phenomenon and knowledge of peak ground acceleration (PGA) or predominant frequency are not sufficient to predict the effect of ground motion on structures.

2.3.14 Jalbi et al. (2018)

The authors presented closed-form solutions to evaluate the foundation stiffness of suction caissons on three different soil profiles using the finite element method. The authors modeled the soil as linearly elastic. The stiffness parameter was used by the authors to predict the natural frequency. The authors reported the significant influence of the Poisson’s ratio on the lateral stiffness of a homogeneous soil profile. It was observed by the authors that the increase in the Poisson’s ratio up to a value of 0.4 causes a reduction in the lateral stiffness after which it was found to increase.

2.3.15 Gaudio and Rampello (2020)

The authors evaluated the caisson inertia under earthquake loading, represented by an equivalent horizontal k_h and rotational seismic coefficient k_{rot}, by conducting an extensive 3D numerical analysis considering 14 different soil-caisson-pier-deck systems subjected to 6 strong ground motions. The seismic coefficients are described by empirical relationships depending on the dynamic properties of the soil-structure system and also on the seismic input. Using these seismic coefficients, the authors applied the pseudo-static analysis to check the safety of caissons against bearing capacity for stiff and flexible systems.

2.3.16 Al-Ramthan and Aubeny (2020)

The authors conducted a finite-element investigation by employing an axisymmetric Fourier analysis to predict the permanent deformation of caissons in clay under the action of cyclic loading. The authors used a nonlinear hardening model that simulates plastic deformations at loading lower than the soil strength. A parametric study of caissons to evaluate the influence of various soil properties and loading conditions on the predicted displacement subjected to cyclic loading shows significant effects.

2.3.17 Biswas and Choudhury (2020)

The authors investigated the moment capacity of circular caisson embedded in layered cohesive soil, using three-dimensional numerical study. Parametric study was performed by the authors to study the effect of various input parameters on lateral soil pressure profile. Various tilt and shift combination under the action of applied lateral load have been addressed by the authors.

2.3.18 Fu et al. (2020)

Undrained bearing capacity of a side-rounded caisson foundation in clay subjected to uniaxial and combined loading was investigated by the authors. The side-rounded foundation has a rectangular section in the middle, placed between the two halves of a circular foundation. A thorough finite element investigation using ABAQUS was conducted, and the influence of the foundation shape, depth of penetration, and soil strength profile on the bearing capacity of caissons were analysed. The authors adopted an equivalent dimensionless embedment ratio and an equivalent soil strength heterogeneity ratio for the side-rounded foundation to describe its bearing capacity by the groundwork determined for a circular foundation.

2.4 Theoretical Studies

Terzaghi (1943) pioneered the theoretical study for caissons by analysing pier foundations followed by studies by Pender (1947) and Banerjee and Gangopadhyay (1960). Most of the theoretical studies to determine earth pressure coefficients considered 2-dimensional failure wedge for the analysis using pseudo-static [Subba Rao and Choudhury (2005), Choudhury and Ahmad (2007), Caltabiano et al. (2012)] and pseudo-dynamic [Choudhury and Nimbalkar (2005), Ahmad and Choudhury (2009), Bellezza et al. (2012), Bellezza (2014)] or modified pseudo-dynamic approach [Bellezza (2015), Pain et al. (2015), Rajesh and Choudhury (2017), Santhoshkumar et al. (2019)]. Several other researchers [Gerolymos and Gazetas (2006a,b,c), Mylonakis et al. (2006), Tsigginos et al. (2008), Varun et al. (2009), Zhong and Huang (2013)] adopted 2-dimensional Winkler’s model for the analysis of caissons. Ashour (1998) adopted the strain wedge model proposed by Norris (1986) to study the resistance to piles considering 3D planar failure wedge behind laterally loaded pile. The same model was later adopted by Biswas and Choudhury (2019,2021) to model passive resistance to caissons in cohesionless soil. However, these studies have been conducted for homogeneous soil. Few researchers [Kumar and Samui (2006), Qin and Chian (2017), Hazari et al. (2020), Santhoshkumar and Ghosh (2021a,b)] have attempted to study the response of layered soil in 2D. The studies pertaing to theoretical analysis has been discussed in this section in detail.

2.4.1 Terzaghi (1943)

The author suggested that full mobilization of skin friction on vertical faces should be considered as the pier would not sink into the strata until frictional resistance is completely mobilized. The author proposed a formula for the determination of ultimate bearing capacity for pier foundation under this assumption. The author also recommended that this analysis be extended for rigid bulkhead under lateral loads and suggested that contribution of side friction on parallel faces to the plane of tilt should not be considered in the analysis but included the contribution of base friction and base resistance. Terzaghi's theory turned out to be the central idea for many of the succeeding analyses by various authors.

2.4.2 Pender (1947)

The author was the pioneer in analyzing well foundations subjected to lateral load extensively. The author established that special considerations must be taken into account while theoretical analysis of massive foundation with high stiffness as opposed to previous studies of light and slender foundations like piles [Stobie (1930); Wolf (1933)]. The author considered the cohesionless soil surrounding the well foundation to act as linear springs with linearly increasing stiffness with depth. The author studied the problem using two approaches:

- Smooth, weightless well rotating about an axis above the base
- Heavy well rotating about centroidal axis on base and considering base friction

2.4.3 Banerjee and Gangopadhyay (1960)

The authors derived expressions for calculating lateral load-carrying capacity of well foundation embedded in cohesionless soil. The authors made use of the modulus of subgrade reaction assumption of Pender (1947) and combined it with the rigid bulkhead analysis by Terzaghi (1943). The authors also assumed front and rear face to be rough and thus used Coulomb's (1776) earth pressure coefficients in the formulation.

2.4.4 Beredugo and Novak (1972)

The authors developed closed-form solutions to determine the response of embedded foundations to coupled horizontal and rocking vibrations. The theoretical curves obtained from the analytical solution were compared with results obtained from field tests. Frequency independent damping and stiffness were developed by the authors for design. The authors observed that the response of the embedded footings was dominated by the first resonant peak and hence is of utmost importance. Furthermore, it was also observed that the embedment increases the resonant frequencies and decreases the resonant amplitudes significantly.

2.4.5 Ashour et al. (1998)

The authors used strain wedge model to study passive wedge formed in front of flexible piles. The authors considered 3-dimensional planar failure wedge developed in front of single pile embedded in homogeneous and layered strata. The study explored the nonlinear variation of modulus of subgrade reaction and also reflected the dependence of *p-y* curves on soil and pile properties. The author used effective stress theory and reported that the parameters required in the proposed model used fundamental soil properties for solving laterally loaded pile problem.

2.4.6 Choudhury and Nimbalkar (2005)

The authors proposed an improvement in pseudo-dynamic method to obtain the passive earth pressure distribution considering both horizontal and vertical seismic accelerations as shown in Fig. 2.6. A constant shear modulus was considered with depth throughout the backfill. Additionally, the influence of various parameters like horizontal and vertical seismic coefficient, angle of soil and wall friction, shear wave velocity, and lateral shaking period was investigated. The authors compared the adopted pseudo-dynamic method with the existing pseudo-static method from the literature, showing a highly nonlinear earth pressure distribution for the former case.

2.4.7 Subba Rao and Choudhury (2005)

The authors conducted a pseudo-static analysis to predict the seismic passive earth pressure coefficient for a rigid retaining wall with homogeneous backfill using the limit equilibrium method. Primarily, the passive earth pressure coefficient considering the self-weight, cohesion, and surcharge condition was calculated separately and then using the superposition principle the minimum passive earth pressure was calculated by summation of the minimum values of each of these components. The authors considered a combined log spiral and straight line to be the failure surface. An increase in the passive earth pressure coefficient with an increase in the seismic vertical and horizontal acceleration coefficients was reported by the authors.

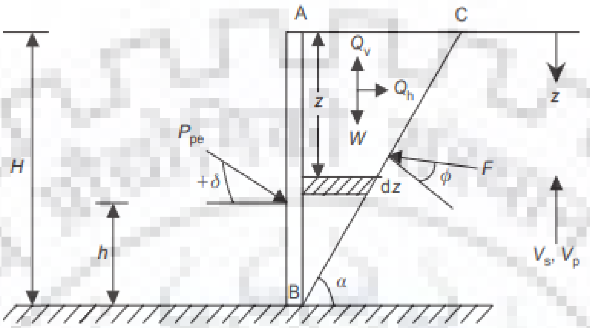

Fig. 2.6 Passive earth pressure model [after Choudhury and Nimbalkar (2005)]

2.4.8 Choudhury and Chatterjee (2006)

The authors proposed 2-degree of freedom (DoF), dynamic MSD (mass-spring-dashpot) model to calculate earth pressure in active conditions. The 2 DoF considered in the study are translations of soil mass at the back of retaining wall and that of the wall itself under dynamic loading. The authors determined extent of influence zone for the dynamic earth pressure and the magnitude of translation of wall. The authors also proposed generalized design charts required to obtain total dynamic force due to earth pressure.

2.4.9 Gerolymos and Gazetas (2006a)

The authors proposed a multi-spring Winkler model to study response of caisson foundations in homogeneous, elastic soil, having a variety of shapes (square, circular or rectangular) in plan, under static and dynamic loading. The authors used 4 different types of spring to relate caisson translation and rotation with soil resistance in form of stresses and moments acting on various faces of caisson. The authors coupled each spring with a dashpot to effectively model dynamic problem and formulated closed form solution for all the springs and dashpots and conducted parametric study. The authors compared the results of the proposed model with results of 3D finite element study to confirm its reliability.

2.4.10 Gerolymos and Gazetas (2006b)

The authors incorporated the effect of soil nonlinearity and slippage and separation at caisson-soil interface and base uplifting. The authors also considered the effect of radiation damping using visco-plastic approach and degradation of strength and stiffness of soil with higher number of load cycles. The authors developed finite-difference method-based, time-domain code and calibrated the parameters associated with the proposed model using experimental and analytical data.

2.4.11 Gerolymos and Gazetas (2006c)

The authors developed a methodology to determine the response of non-linear caisson embedded in layered strata with nonlinear soil behavior. The response of static, cyclic and dynamic loading has been investigated by the authors considering 4-spring Bouc-Wen-Gerolymos-Gazetas model wherein inelastic springs and dashpots have been used to model soil stiffness and damping properties. The authors established the efficacy of the model using the results from 1/3 scale model subjected to lateral loading in field. The authors presented the results of the parametric study based on the proposed model.

2.4.12 Mylonakis et al. (2006)

The authors proposed a methodology to study spread footing under bridge piers. The authors studied the dynamic stiffness of foundation, computation of kinematic response, assessment of proper embedment effect. Comparison was drawn by the authors between kinematic and inertial response and radiation damping effect has also been explored. The authors presented the results in graphical and tabular form for stiffness and damping in different modes of vibration.

2.4.13 Kumar and Samui (2006)

The authors assessed the stability of slopes consisting of cohesive-frictional soil with two layers by upper bound analysis. Different arcs of a logarithmic spiral having a common focus were used by the authors as the failure surface. Subsequently, the authors established a set of stability charts giving the values of stability numbers N_s which can evaluate the factor of safety of the layered soil slope, considering the pore water pressure and horizontal seismic forces. With the increase in pore water pressure coefficient and seismic horizontal pressure coefficient, the authors reported a decrease in the value of stability numbers.

2.4.14 Choudhury and Ahmad (2007)

The authors applied the pseudo-static approach in assessing the stability of waterfront retaining walls subjected to the combined effect of tsunami and earthquake forces. The passive earth pressure was considered on the wall by the authors. Additionally, the authors emphasized the influence of the hydrodynamic pressure on the stability analysis of the retaining wall which is generated during earthquake shaking. The authors presented factor of safety of the retaining wall in sliding and overturning failure modes.

2.4.15 Solov'ev (2008)

The author suggested a method for computation of bearing capacity of soil stratum supporting well foundation for varying geometry of cutting edge. The author performed the analyses for caissons in both cohesionless and cohesive soil. Limit equilibrium method of analysis was employed by the author to study the effects of shape and taper of the blades on limiting bearing capacity. Correction factor ξ_o was introduced to obtain the width of blade in terms of its shape and embedment in the stratum.

2.4.16 Tsigginos et al. (2008)

The authors carried out a dynamic soil-structure interaction analysis of a pier-caisson foundation system embedded in an elastic half-space subjected to earthquake loading. The Winkler model was used by the authors to evaluate the elastic response of the caisson foundation in the frequency domain. The authors used a model comprising four individual dashpots and springs that represents the lateral loads and moments at the caisson shaft and translational loads in shear and moments at the base of the caisson as shown in Fig. 2.7. The authors observed the dependency of the equivalent system period on the relative mass and stiffness of the structure and soil and slenderness. An increase in the system period was reported by the authors for lower slenderness ratio values.

2.4.17 Ahmad and Choudhury (2009)

The authors proposed methodology for obtaining seismic design factors for translation of waterfront retaining wall. Pseudodynamic method for determination of seismic acceleration profile was used considering dynamic soil properties. The authors reported that the difference in water level at either side of wall poses challenges to design of wall. The authors also recognized the parameters affecting the design factors.

2.4.18 Varun et al. (2009)

The author proposed Winkler model to develop analytical solutions for caisson foundation considering resistance due to both base and sides of caisson. The calibration of various parameters has been done based on the results of 3D finite element numerical analysis. The authors confirmed the applicability of the model by verifying the results for strata with soil properties varying with depth.

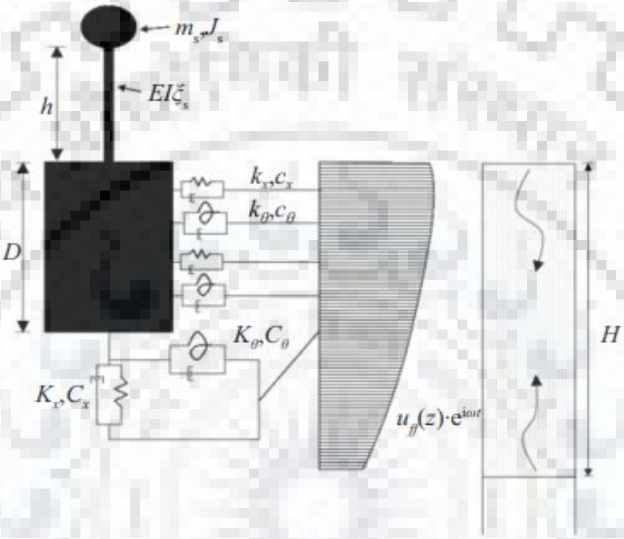

Fig. 2.7 Four spring and dashpot Winkler model [after Tsigginos et al. (2008)]

2.4.19 Bellezza et al. (2012)

The author proposed the use of pseudo-dynamic approach for determination of seismic inertial forces in homogeneous submerged backfill wherein, pore water could be either free or restrained. The authors then carried out parametric study to understand the effect of dynamic soil properties on active thrust on walls. The effect of soil amplification was also studied by the authors.

2.4.20 Caltabiano et al. (2012)

The authors employed limit equilibrium method to obtain analytical expressions for the active slip surface angle, the critical acceleration coefficient, and the active earth pressure coefficient under static and seismic conditions. The authors carried out the analysis considering the retaining wall to be smooth and vertical, with a backfill having no surcharge, infinite surcharge, and limited surcharge as shown in Fig. 2.8. The authors assumed the pore water pressure to be zero.

2.4.21 *Jawaid and Madhav (2013)*

The authors proposed a rigid composite open caisson foundation by replacing the soil within the caisson with granular fill as depicted in Fig. 2.9 to increase its overall stability for use in land with high water table. The settlement of the proposed caisson foundation to axial loading was studied by the authors using the continuum approach. Furthermore, the authors conducted a parametric analysis to study the effect on load sharing, settlement, and stress distribution. A decrease in the foundation settlement was reported by the authors for an increase in the ratio of length to diameter (L/d_0), for all diameter ratios.

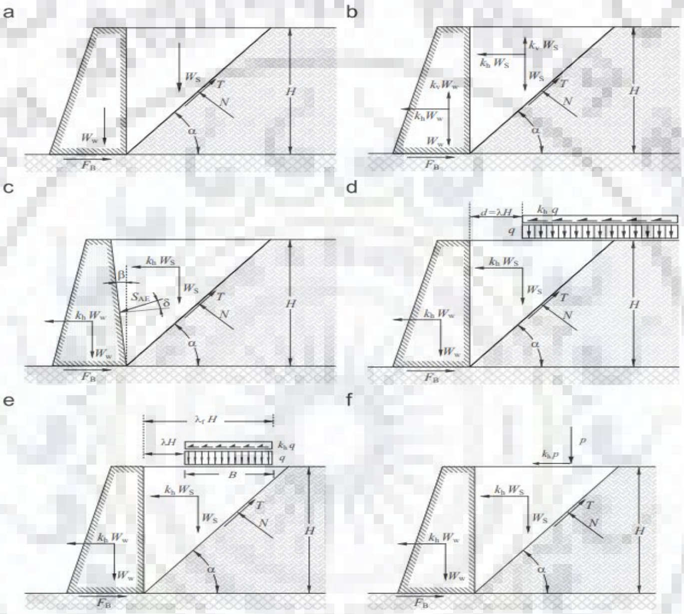

Fig. 2.8 Different surcharge loading conditions: wall with no surcharge in (a) static conditions, (b) seismic conditions with $\beta=\delta=0$ (c) seismic conditions with $\beta\neq0$ and $\delta\neq0$; (d) wall with an infinite surcharge; (e) wall with a limited surcharge or, (f) equivalent linear surcharge [after Caltabiano et al. (2012)]

2.4.22 *Zhong and Huang (2013)*

The authors studied the dynamic behaviour of a composite caisson pile foundation, the upper part of which comprised of caisson and the lower part comprised of grouped piles. The authors adopted a four spring Winkler model that accounts for the varying physical and mechanical properties of layered soils. A modified rotational embedment factor was utilized by the authors in the calculation of spring coefficients of caissons. The authors observed the significant influence of the piles beneath the caissons in increasing the foundation resistance against dynamic loads.

2.4.23 Bellezza (2014)

The author introduced a variation of traditional pseudo-dynamic method wherein both amplitude and phase of the seismic wave changes with depth as opposed to only phase variation in case of previous method. The author considered soil as a viscoelastic material and formulated closed-form solutions for seismic active soil pressure distribution with depth. Constraint on shear stress at ground surface was imposed by the author and parametric study was conducted to check the sensitivity of various soil and seismic parameters.

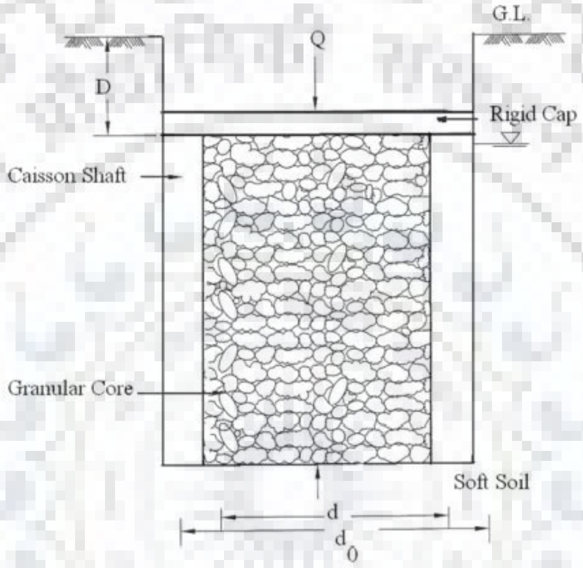

Fig. 2.9 Proposed rigid open caisson foundation [after Jawaid and Madhav (2013)]

2.4.24 Liu (2014)

For a circular retaining wall, the authors calculated the lateral active earth pressure by applying the slip line method, taking into account the tangential stress and movement of the wall. The authors assumed that the soil's internal friction and friction of the wall would vary with wall rotation. The dependency of the active earth pressure on the shape of the wall and its displacement magnitudes was observed by the authors. Additionally, the authors observed a non-linear active earth pressure distribution across the wall height. Subsequently, the authors reported an exponential decrease in the earth pressure with increased wall movement.

2.4.25 Bellezza (2015)

The author proposed modified pseudo-dynamic methodology by considering vertically propagating standing primary and shear waves through viscoelastic media. The method returned both horizontal and vertical seismic acceleration profile considering various dynamic soil properties. Extensive parametric study has been performed by the author to check the response of seismic active soil thrust on input parameters.

2.4.26 Chatterjee et al. (2015)

The authors proposed a finite element method-based analytical technique to obtain the bending moment and deflection profile of a single pile under the influence of vertical and transverse seismic loading. The authors conducted the study for both, dry and submerged and uniform and layered soil. Pseudo-static approach was employed to compute seismic inertial forces in both liquefiable and non-liquefiable soils.

2.4.27 Pain et al. (2015)

The authors used a modified pseudo-dynamic limit equilibrium method to study the retaining wall in sliding conditions for seismic cases. The authors considered the retaining wall to support a cohesionless backfill in active earth pressure conditions as depicted in Fig. 2.10. It was observed that the wall-soil interaction may or may not occur simultaneously for maximum sliding in active failure mode, under seismic conditions. The authors calculated the critical seismic acceleration coefficient at the sliding failure edge and Newmark's method was employed to calculate the extent of sliding of the wall.

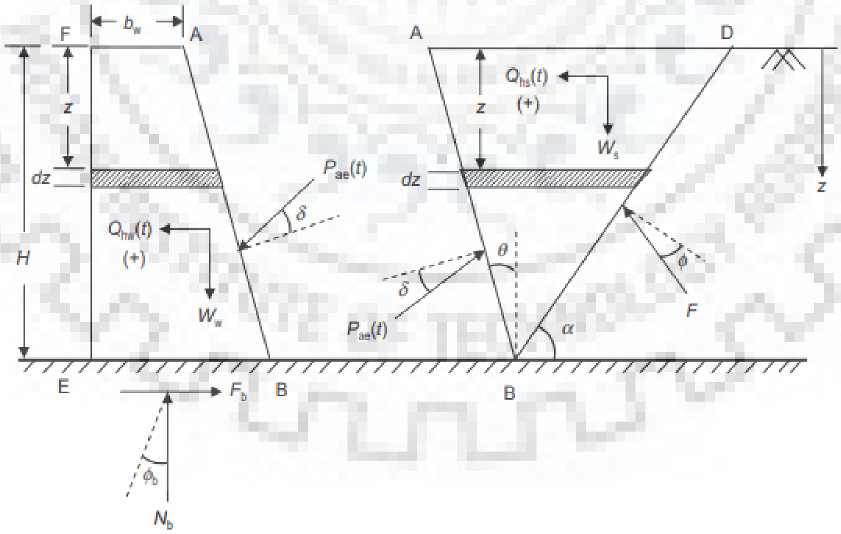

Fig. 2.10 Inertia forces on the active soil wedge of the wall [after Pain et al. (2015)]

2.4.28 Chowdhury et al. (2017)

The authors presented an analytical model for the seismic analysis of a well foundation supporting a pier that illustrates the limitations of the existing literature. The authors highlighted the importance of the soil-structure interaction effect of the well and pier. A generalized model considering the well as a rigid, semi-rigid, and flexible body was developed taking into account the liquefaction effects.

2.4.29 Rajesh and Choudhury (2017)

The authors presented a closed-form solution for the evaluation of the seismic passive earth pressure resistance (P_{pe}) of an inclined retaining wall having a submerged backfill by employing the modified pseudo-dynamic method. The authors assumed the failure surface as a logarithmic spiral at the base of the wall and linear close to the ground surface as depicted in Fig. 2.11. Furthermore, the influence of the seismic acceleration coefficients (k_h and k_v), angle of soil-wall friction and soil friction (δ and ϕ), excess pore water pressure ratio (r_u), and angle of inclination of the wall (θ) on the seismic passive resistance were investigated by the authors.

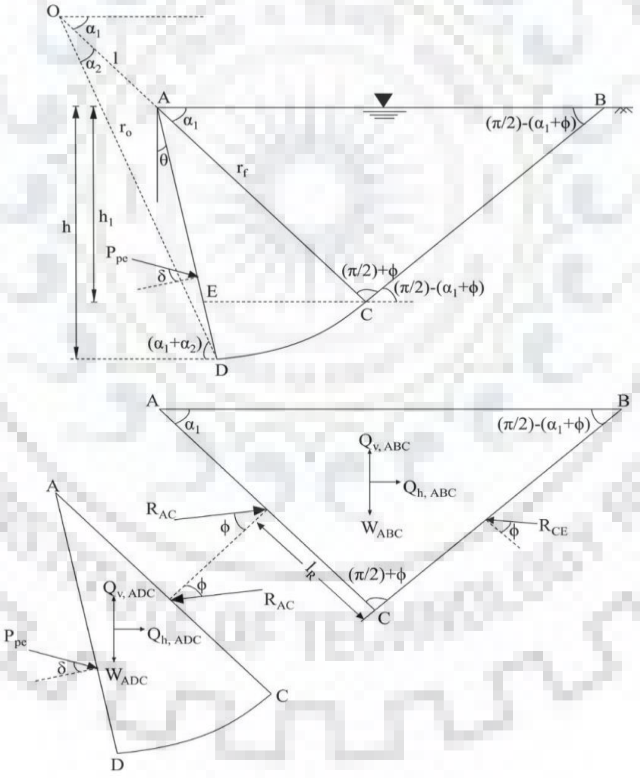

Fig. 2.11 Curved failure surface represented by α_1 and α_2 [after Rajesh and Choudhury (2017)]

2.4.30 Qin and Chian (2017)

The authors used the pseudo-static method to study the stability of a two-layered slope having a strip footing at its edge by employing the upper-bound analysis. The vertical and horizontal seismic coefficients were used by the authors to describe the inertia forces generated during earthquakes. The authors assumed the failure surface to be a logarithmic spiral in the drained condition and circular in the undrained condition. Analytical expressions were presented by the authors to evaluate the dimensionless ultimate bearing capacity and yield seismic coefficient. Subsequently, the authors conducted a parametric analysis to investigate the influence of the geometry parameters of the slope, non-homogeneity of soil cohesion, self-weight of soil, and seismic coefficients on the stability of the slope. The authors reported that with the increase in the strength of soil and its parameters the stability of the slope increases, while an increase in the self-weight of soil decreases the slope stability.

2.4.31 Liu et al. (2018)

The authors used the limit equilibrium technique to calculate the passive earth pressure of a rigid retaining wall supporting a sloping backfill, by adopting a composite curved failure surface with a logarithmic spiral as the curved portion. The authors assumed the soil of the backfill to follow the Mohr-Coulomb failure criteria. The passive earth pressure, as obtained by the authors, by varying the wall geometry, properties of backfill soil, and soil-wall internal friction. Furthermore, the authors compared the proposed analysis with finite element results. The authors reported that the proposed method cannot be used for a cohesive backfill.

2.4.32 Biswas and Choudhury (2019)

The authors presented a formulation for rectangular caissons embedded in cohesionless soil, considering a planar 3D passive wedge in front of the caisson under seismic loading as shown in Fig. 2.12. The authors proposed a tangential stress coefficient λ corresponding to the forces acting on the vertical wedge side. The authors reported that the seismic earth pressure coefficient value was as much as 62.7% lower than that in the static state for the same range of input parameters. Furthermore, an increase in the seismic passive earth pressure coefficient was observed on increasing the length, D of the caisson. The authors found the analytical solution of the study to agree well with the results of centrifuge tests from the literature.

2.4.33 Santhoshkumar et al. (2019)

The authors studied the seismic earth pressure in active condition for an inclined cantilever retaining wall by utilizing the stress characteristic method combined with the modified pseudo-dynamic method. A predefined failure surface was not considered by the authors for the analysis. Further, the authors compared the results from the proposed study with that of the literature and observed an underestimation of the value of the earth pressure coefficient by the pseudo-dynamic approach considering a planar failure surface.

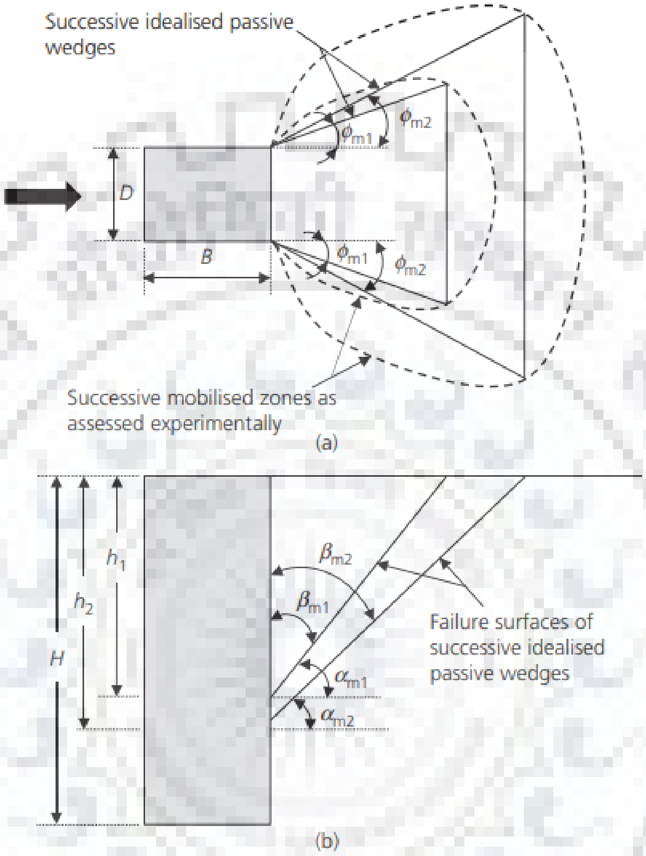

Fig. 2.12 Passive failure wedge development: (a) Plan view (b) Sectional view of the rectangular caissons ($B \times D \times H$) [after Biswas and Choudhury (2019)]

2.4.34 Hazari et al. (2020)

The authors performed a slope stability analysis employing the limit equilibrium pseudo-dynamic method considering the slope non-homogeneity and damping. The authors evaluated the slope to consist of a two-layered cohesive-friction soil. The failure surface for the analysis was assumed to be a logarithmic spiral by the authors. A thorough parametric investigation was conducted by the authors by varying the damping ratio, seismic acceleration coefficients, cohesion and angle of internal friction at various soil layers and earthquake loading conditions. The authors reported an increase in the slope stability with a considerable increase in the cohesion, damping ratio, unit weight, and angle of internal friction, and a decrease in the overall factor of safety of slopes on increasing the seismic acceleration coefficients.

2.4.35 Biswas and Choudhury (2021)

The authors conducted limit equilibrium analysis on simplified 3D planar failure wedge. Modified pseudo-dynamic method was adopted by the authors to obtain seismic acceleration at any depth in cohesionless, homogeneous soil surrounding rectangular caisson. The authors conducted parametric study to study the effect of width of caisson, seismic acceleration coefficients and damping ratio of soil. The authors extended the study for submerged soil and studied the effects of soil-wall friction, soil-soil friction angle and excess pore pressure ratio.

2.4.36 Santhoshkumar and Ghosh (2021a)

The authors derived closed-form solutions for a bilinear retaining wall supporting a cohesionless backfill to calculate the active and passive earth pressure coefficients for static and seismic conditions. The authors used the stress characteristic method to obtain the solutions. A parametric study to determine the influence of seismic acceleration coefficients, friction of soil, and wall parameters (inclination, roughness, and height ratio) on the earth pressure of the retaining wall was conducted by the authors.

2.4.37 Santhoshkumar and Ghosh (2021b)

The authors used the stress characteristic method combined with the pseudo-static approach to calculate the passive seismic thrust on a cantilever retaining wall supporting a layered horizontal backfill of height H. The authors considered a cohesionless backfill of dense sand underlying a loose sand stratum, wherein the effect of this two-layered backfill on the passive earth pressure was analysed. The layered backfill passive earth pressure coefficient as given by the authors:

$$K_{p\gamma} = \frac{P_{p\gamma}}{0.5\gamma_{avg}H^2} \tag{2.2}$$

where γ_{avg} is the backfill average unit weight along wall height. The authors reported a decrease in the passive earth pressure coefficient with the increase in the depth of the topmost layer having loose sand. Stress contours were used by the authors to represent the stress distribution in the layered soil.

2.5 Codal Provisions Adopted in Various Countries

2.5.1 Indian Standards

IRC 78 (2014): Section VII provides recommendations and specifications regarding foundations of road bridges while Indian Railway Standards (1985) employ a separate manual for design and construction of well and pile foundation for railway bridges. Fig. 2.13 depicts the diagram recommended by Indian Railway Standards (1985) which gives maximum depth of pier in water below highest flood level (HFL) and minimum depth of foundation below greatest possible scour for well foundations in sand. IRC 78 (2014) gave an empirical correlation for mean scour below HFL in terms of design discharge for foundation and a suitable silt factor mentioned in Eqn. 2.3. The depth of caisson is decided by both, depth of scour level and the forces acting on the caisson.

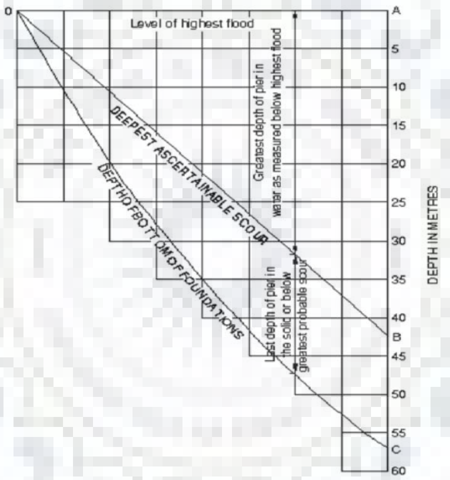

Fig. 2.13 Depth of bridge pier and foundation in river and river bed [after Indian Railway Standards (1985)]

$$d_{sm} = 1.34 \left(\frac{D_b^2}{K_{sf}} \right)^{1/3} \tag{2.3}$$

where, d_{sm} is the mean scour depth below HFL; D_b is the design discharge for foundation per meter effective width of waterway in cumecs and K_{sf} is the silt factor. Special design recommendations have been mentioned in the code for consideration of maximum scour depths at different sections of channels. Apart from this, IRC 78 (2014) recommends minimum embedment of caissons in strong rocks as 0.6 m and in weak rocks as 1.5 m.

The allowable bearing pressure, Q (in kg/m^2), suggested by Indian Railway Standards (1985), is mentioned in Eqn. 2.4.

$$Q = 5.4N^2B + 16(100 + N^2)D \tag{2.4}$$

where, N is the standard penetration resistance, B is the smaller cross section dimension in meter and D is the depth of foundation below scour level in meter. The manual also provides the magnitudes of skin friction for various soil types. The maximum settlement for well foundations is recommended as less than 25mm and tilt and shift of well is restricted to a magnitude of 1 in 100 and $D/40$ respectively, where D is the width or diameter of the well.

On the other hand, IRC 78 (2014) recommends determination of allowable bearing pressure and settlement characteristics under different loads based on sub-soil exploration and testing. The maximum allowable differential settlement for well foundations is recommended as 1 in 400. The Indian Roads Congress has given a detailed set of guidelines for the procedure for calculating soil resistance (resistance due to both sides and base of caisson) offered to well foundations in IRC 45 (1972). The code provides soil resistance by two approaches namely, elastic theory method and ultimate resistance method. Both IRC 78 (2014) and Indian Railway Standards (1985) recommend possible load combinations, to obtain critical load combination, to be considered for the design and analysis of well foundations.

2.5.2 American Standards

Federal Highway Administration (FHWA) has adopted the recommendations of Hydraulic Engineering Circular No. 18 (HEC-18) for the evaluation of scour at bridges. The total scour has been sub-divided into 3 parts, i.e., long term degradation of river beds, contraction scour at bridge and local scour at piers and abutments. While the long-term degradation is obtained from past records and with the help of computer programs, separate empirical expressions have been recommended to obtain contraction scour and local scour.

The American Standards consider more possible types of loads that could act on the bridges and transferred to the substructure, like ice load, uniform temperature, creep and shrinkage, vehicular collision force, vessel collision force etc. National Highway Institute (NHI) recommended load and resistance factor design (LRFD) which states that the factored resistance should not be affected by factored loads for all limit states. Multiple limit states of strength, service, fatigue and extreme events has been considered by NHI to obtain the critical loading combination. Similar to Indian Standards, NHI recommends different load factors for different loads. However, while IRC 45 (1972) recommends a single resistance factor of 0.7 for sum of all resistive moments, NHI recommends separate resistance factors for resistance developed in various parts of drilled shaft. The response of drilled shaft to lateral load is modelled using Broms' model (1964). The computation of moments and stresses is performed using non-linear analysis with computer programs.

2.5.3 Eurocode

Eurocode EN 1991-1-6 (2005) or Eurocode 1 reflects on the effects of various external actions on structures. It divides the total scour depth due to channel flow into two sub-categories, i.e., general scour depth and local scour depth. General scour is defined as the river flow-scour independent of any obstacle and depends solely on flood magnitudes. Local scour depth, on the other hand, is the scour due to water vortices next to an obstruction.

Eurocode 1990 (2002) recommends guidelines for basics of structure design. It terms external loading as "actions" and sub-classifies it into three categories.

- Permanent actions (G), which are likely to act throughout a given period in which its magnitude remains unaltered.
- Variable actions (Q), for which variation in magnitude over time is neither negligible, nor monotonic.
- Accidental actions (A), which are usually of short duration but significant magnitude.

Critical load combinations are then selected using different factors (ψ) and sub-factors (γ) in combination with characteristic and representative values of different actions. EN: 1997-1 (2004), i.e., Eurocode 7 deals with the geotechnical design guidelines for structures. It recommends the use of either spread footing or pile foundation to be used as foundation system for bridge piers and abutments.

2.6 Critical Appraisal of Literature

The critical appraisal of literature summarizes the major shortcomings in the works of various previous authors and different aspects that were not considered during the course of previous research.

- ***Lack of 3D failure wedge consideration in theoretical studies*:** Most of the studies modelled the soil surrounding the caisson either as a 2D plane-strain element or a 1D spring-dashpot model and not as a 3D continuum. Since, caisson is a finite width foundation system, assumption of 2D plane strain model is highly conservative.
- ***Lack of empirical correlation for load sharing behaviour*:** Many researchers in the past 5-6 decades have computed effect of loading and seismic parameters on resisting

components of caisson, neglecting one or more resisting components. However, no empirical correlation is available to obtain load shared by sides and base of caisson.

- ***Consideration of planar 3D passive wedge*****:** In the handful of studies that consider 3D passive wedge, it was idealized as planar, which contradicts the recommendations of Terzaghi (1943) and several succeeding researchers, as opposed to actual 3D passive wedge obtained from numerical analysis.
- ***Neglecting pore water pressure in analysis*****:** Despite majority of the structures founded on caissons being in vicinity of water bodies, effect of pore water pressure was considered in only one of the analyses.
- ***Lack of theoretical analyses for caisson embedded in c-ϕ soil*****:** Theoretical studies for caisson embedded in c-ϕ soil is severely lacking in the existing literature. In addition, there is absence of surcharge loading on surrounding soil in almost all the studies concerning caissons.
- ***Limited number of interaction curves*****:** Only one of the authors have derived interaction diagrams for the design and analysis of caissons. More work could be done in this field in order to better understand the loading combination leading to failure.
- ***Consideration of layered strata in theoretical studies*****:** Very few studies on retaining walls and slopes have considered layered soil strata whie carrying out theoretical study. Most of the studies, which have considered layered strata have confined the study to 2, or at most 3-layered strata. So, there is lack of study considering n number of layers.
- ***Study of volume of failure wedge with width of caisson:*** The existing literature which cover the consideration of width of caisson in determination of seismic passive earth pressure coefficient is extremely scarce. In addition, very few studies reflect the change in extent (volume) of failure wedge per unit width with change in width of caisson.

2.7 Proposed Research Objectives

After analysing practical feasibility and resources available to carry out research in the area of interest, the main research objective is “to analyse the static and seismic behaviour of caissons in layered soil”. To complete this objective, following studies need to be carried out:

- Static and pseudo-static numerical analysis of caissons in layered soil taking effects of pore water into account using finite element method-based software ABAQUS.
- Study of the effect of relative magnitude of vertical and lateral loads, soil-wall friction angle and seismic acceleration coefficients in terms of caisson displacement (tilt and shift), depth of point of rotation, maximum and minimum soil pressure, lateral soil pressure, horizontal and vertical skin friction at sides, base friction and base resistance, shear force and resisting moment due to various resistive forces.
- Development of 3D generalized interaction diagrams and empirical correlation for load shared by sides and base of caisson in terms of moment of resistance.
- Determination of seismic passive earth pressure coefficient due to unit weight component ($K_{sp\gamma}$), surcharge component (K_{spq}) and cohesion component (K_{spc}) using limit equilibrium approach-based pseudo-static analysis of caisson embedded in cohesive-frictional (c-ϕ) soil with surcharge (q), by idealizing formation of 3D failure wedge (log-spiral in vertical plane and oval in horizontal plane) obtained from results of numerical analysis, considering individual failure wedge with resisting components acting individually and combined failure wedge by considering all the resisting components acting together.
- Theoretical analysis for caisson embedded in cohesionless soil considering dry and submerged soil condition in homogeneous soil using modified pseudo-dynamic method with determination of seismic wave amplification through various soil layers.
- Modified pseudo-dynamic method based analysis of caisson in layered cohesionless soil considering polylinear 3D failure wedge along with parametric study of shape of failure with parameters like width of caisson, soil-soil friction angle, soil-wall friction angle, horizontal and vertical seismic acceleration coefficients, submergence condition of soil and excess pore pressure ratio.
- Determination of effect of relative depths and relative angle of friction of different soil layers surrounding the caisson.

2.8 Scope of the Study

The study aims to provide design guidelines for caissons through results of numerical and analytical studies. The interaction diagrams and load sharing study aim to provide geotechnical engineers and researchers with load combination that may cause failure for different parameters. The percentage of load shared by base and sides of caisson in conjugation with stress distribution on various faces would allow to properly proportion the width and embedment depth of caisson to avoid failure. The seismic passive earth pressure coefficients due to unit weight, surcharge and cohesion components, considering 3D failure wedge, would also allow determination of maximum passive resistance afforded by soils of different properties surrounding caissons of various widths under various seismic conditions. The formulations proposed in Chapter 5 and 6 of the study can be used to determine seismic passive resistance corresponding to any combination of input parameters. The study will further provide seismic passive resistance and failure wedge profile for caisson embedded in layered soil for a plethora of input parameters. The formulation proposed in the study can be expanded for any number of soil layers while computing the variation of seismic acceleration with depth.

Chapter 3

NUMERICAL MODELLING OF CAISSON IN LAYERED SOIL TO DEVELOP GENERALIZED 3D INTERACTION DIAGRAMS

3.1 General

Caissons are generally employed to support structures of great importance or those which are subjected to a variety of loads like bridge piers and abutments. Typically, a caisson is subjected to a combination of vertical load, lateral load and moment. Numerical studies of caissons subjected to various loading has been performed in the past [Karapiperis and Gerolymos (2014); Gerolymos et al. (2015)] wherein 2D interaction diagrams and failure envelopes have been developed. However, it was found that no such studies have been carried out for layered soil. In addition, most of the caissons are located in submerged ground but none of the previous studies have taken the effect of pore water pressure into consideration. Therefore, in the present study, numerical analyses of caisson embedded in layered soil have been carried out using finite element method-based computer program ABAQUS, wherein, modelling of effects of pore water has been incorporated. The results of the analyses have been used to develop 3D interaction curves relating the magnitudes of applied vertical load (V), lateral load (Q) and moment (M) at failure.

3.2 Numerical Modelling of Caisson in Layered Soil

A square caisson has been modelled to be embedded in layered soil using finite element method-based computer program ABAQUS version 6.14 [SIMULIA (2014)]. The caisson with base dimension (B) 1.5 m × 1.5 m and embedment depth (D) of 2.25 m (D/B = 1.5) is modelled to be embedded in layered strata. The layered soil strata consist of a 4.5 m saturated clay layer sandwiched between top and bottom sand layers, having thickness 3m and 4.5 m, respectively. The water table lies at depth of 3m below ground surface. The aforementioned soil profile has been chosen as per the test site of Sharda's (1975) field tests. The extent of the soil domain in direction of loading has been chosen as 30 m (2×10B) from sensitivity analysis discussed in succeeding section. The extent of soil strata in direction transverse to loading has been chosen to be 20 m as there is no external loading in this direction. The top and bottom sand layers have been modeled as elastic – Mohr-Coulomb plastic material. The intermediate clay layer has been modeled as porous elastic – clay plasticity (Cam-clay) model. 8-noded, 3-dimensional porous continuum brick elements with reduced integration (C3D8RP) have been adopted for all soil layers in order to allow flow of water and hence consolidation of clay layer. 8-noded, 3-dimensional continuum brick elements with reduced integration (C3D8R) have been chosen for caisson modeling. The caisson model along with meshing, boundary conditions and loading used in the present study is shown in Fig. 3.1. The material properties of sand, clay and caisson adopted during material modelling are mentioned in Table 3.1, Table 3.2 and Table 3.3 respectively. The material properties of sand and clay have been obtained from lab tests of soil samples obtained from Sharda's (1975) field test sites.

Table 3.1 Properties of sand used in the present study

Property	Value
Elastic modulus (MPa)	90
Poisson's ratio [μ]	0.3
Unit weight [γ] (kN/m^3)	19
Coefficient of permeability (m/sec)	5×10^{-5}
Initial void ratio	0.8
Friction angle	30°
Dilation angle	1°

Table 3.2 Properties of clay used in the present study

Property	Value
Unit weight [γ] (kN/m^3)	17
Poisson's ratio [μ]	0.45
Slope of swelling line [κ]	0.075
Slope of virgin compression line [λ]	0.12
Coefficient of permeability (m/sec)	6×10^{-8}
Initial void ratio	0.9

Table 3.3 Properties of caisson used in the present study

Property	Value
Unit weight [γ] (kN/m^3)	25
Elastic modulus (MPa)	25000
Poisson's ratio [μ]	0.15

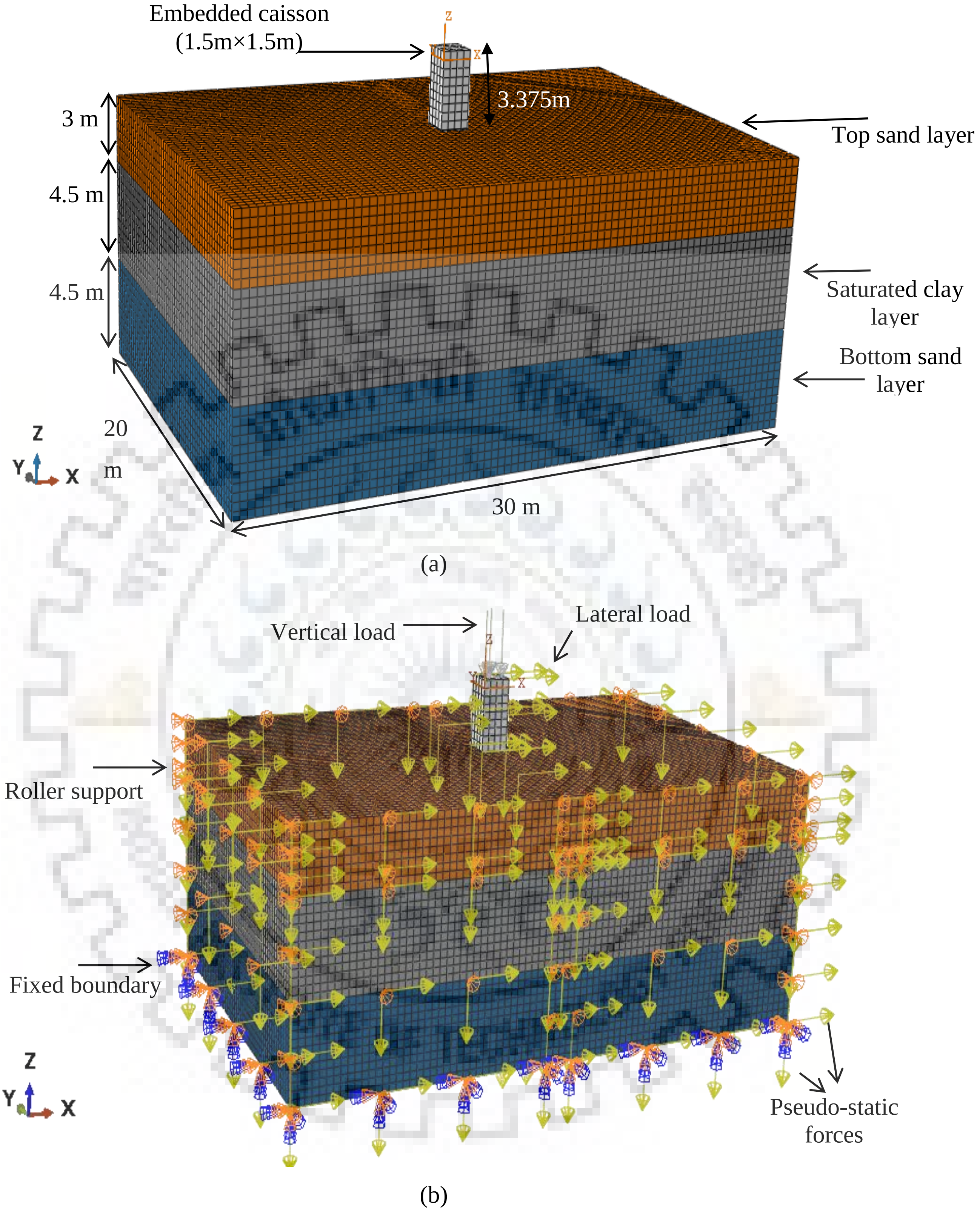

Fig. 3.1 Caisson model showing (a) geometry and meshing of strata and (b) boundary condition and loading

Fixed boundary is applied at the bottom of the soil strata to simulate rigid impermeable stratum whereas roller supports are provided at the side boundaries to allow for settlement of soil but restrict lateral movement of soil. Classical Lagrangian multiplier method of constraint enforcement has been used to establish contact between soil and caisson. Separation of contact between soil and caisson has also been allowed in the current study. Thus, material non-linearity, geometric non-linearity and contact non-linearity have all been incorporated in the present study to simulate the actual field conditions effectively. The effect of pore water has also been modeled in the entire soil mass with water table being located at the soil surface. The entire loading has been applied in 45 steps. Each vertical load step and lateral load step are followed by 4 consolidation steps of increasing time intervals.

3.2.1 Sensitivity analysis

The decision upon the dimensions of strata and mesh size is made by the researcher from own judgement. These two factors affect the accuracy and computational time of the analysis. Sensitivity analysis has been performed to optimize the computational time for the analyses in the present study without compromising with the accuracy of the results. The mesh size for the analyses was optimized by varying the mesh sizes as 1.5 m×1.5 m, 0.75 m×0.75 m, 0.375 m×0.375 m and 0.1875 m×0.1875 m by keeping the length and width of strata as 30m and 20m respectively. Incremental lateral loads have been applied on the caisson under a constant vertical load of 1250kg for the sensitivity analysis. The results for the analysis are plotted in terms of lateral soil pressure vs lateral load as shown in Fig. 3.2(a). It is observed from the figure that results converge as mesh size is reduced to 0.375 m×0.375 m and finer. Therefore, size of the mesh throughout the study has been adopted as 0.375 m×0.375 m. Similarly, the extent of strata in direction of loading has been chosen by varying the length of strata in front of caisson as 6*B*, 8*B*, 10*B* and 12*B*. Again, the difference in magnitude of lateral soil pressure with respect to the previous trial of length is negligible for length of strata in front of caisson as 10*B*, as shown in Fig. 3.2(b), and this magnitude has been adopted for the rest of the study.

3.2.2 Validation of the Present Numerical Model

The accuracy of the model in simulating the actual field conditions has been validated with the experimental work of Sharda (1975). The soil profile and the caisson geometry used in the present study have been kept the same as that adopted by Sharda (1975). Sharda (1975) had presented the observations in the form of lateral soil pressure profile for increasing lateral loads at a constant vertical load of 1250 kg. For validation purpose, same magnitudes of vertical and lateral loads were applied in the proposed model and the response in terms of lateral soil pressure was reported and compared with the experimental results by Sharda (1975), as shown in Fig. 3.3. A maximum variation of 8.78% between the results of numerical analysis of proposed model in the present study and field test results by Sharda (1975) is observed from Fig. 3.3, which shows that the numerical model adopted in present study simulates field conditions quite accurately. Therefore, the proposed model has been adopted for carrying out the numerical study mentioned in the succeeding section.

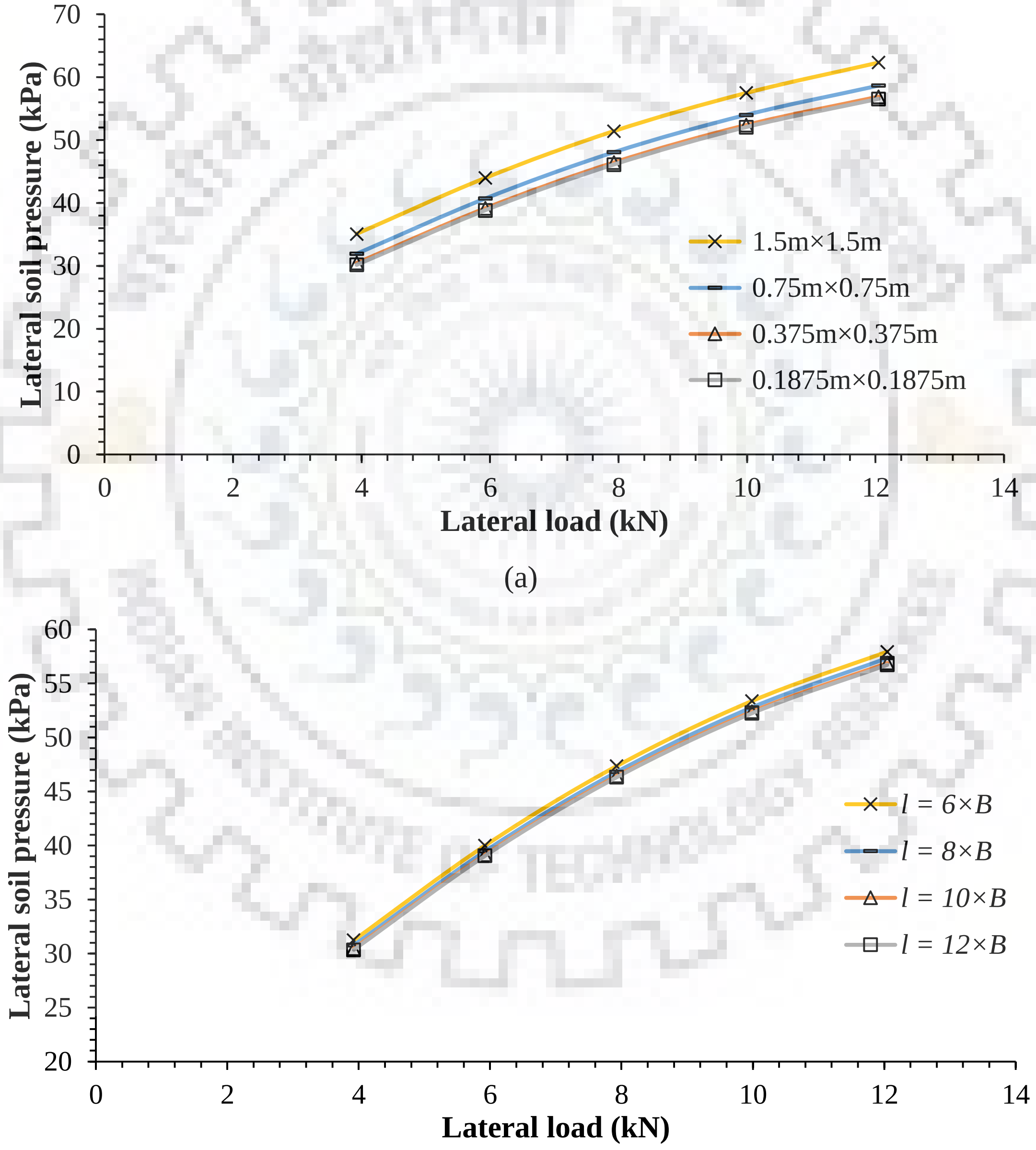

Fig. 3.2 Results of sensitivity analysis for (a) mesh size and (b) extent of strata

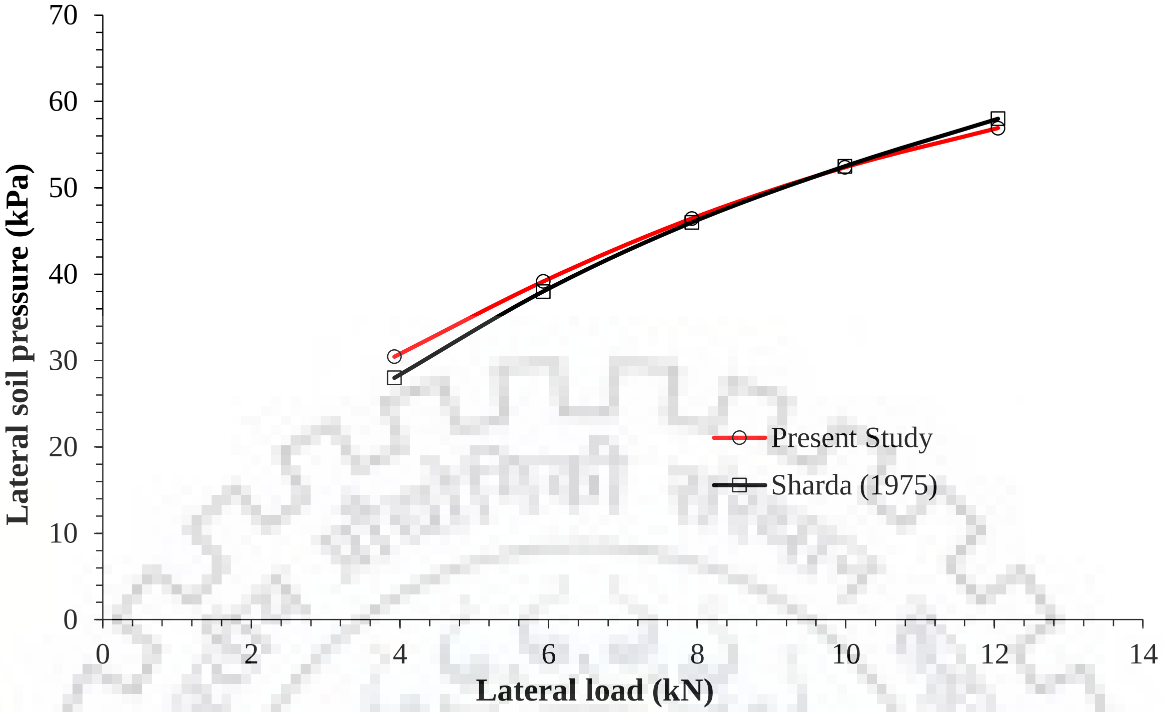

Fig. 3.3 Validation of the present numerical model with the experimental results of Sharda (1975)

3.3 Present Study

In the present study, numerical analyses of caisson embedded in layered soil deposit, for various loading combinations, wall friction angle and seismic acceleration coefficients have been performed using ABAQUS [SIMULIA (2014)] finite element code. The allowable vertical load has been computed by determining the allowable bearing pressure (Q_a) as per IS 3955 (1967) since it considers essential parameters like base dimensions of the caisson, embedment depth and soil strength.

$$Q_a = 5.4N^2B + 16(100 + N^2)D \tag{3.1}$$

where, Q_a is the allowable bearing pressure (kg/m^2), N is corrected value of standard penetration resistance, B is smaller dimension of well section (m) and D is depth of foundation below scour level (m).

In addition to this empirical approach, numerical analysis is also carried out to obtain the stress-strain curve for the soil element below the base of caisson. The load obtained corresponding to the yield stress was factored by a factor of safety of 3 in order to obtain the allowable vertical load. The stress-strain curve obtained from the numerical analysis has been shown in Fig. 3.4. The magnitude of allowable vertical load (V_a) obtained from numerical analysis is 1600 kN and is more critical and therefore has been adopted for the current study.

Fig. 3.5 represent the variation of excess pore pressure with time obtained from numerical study.

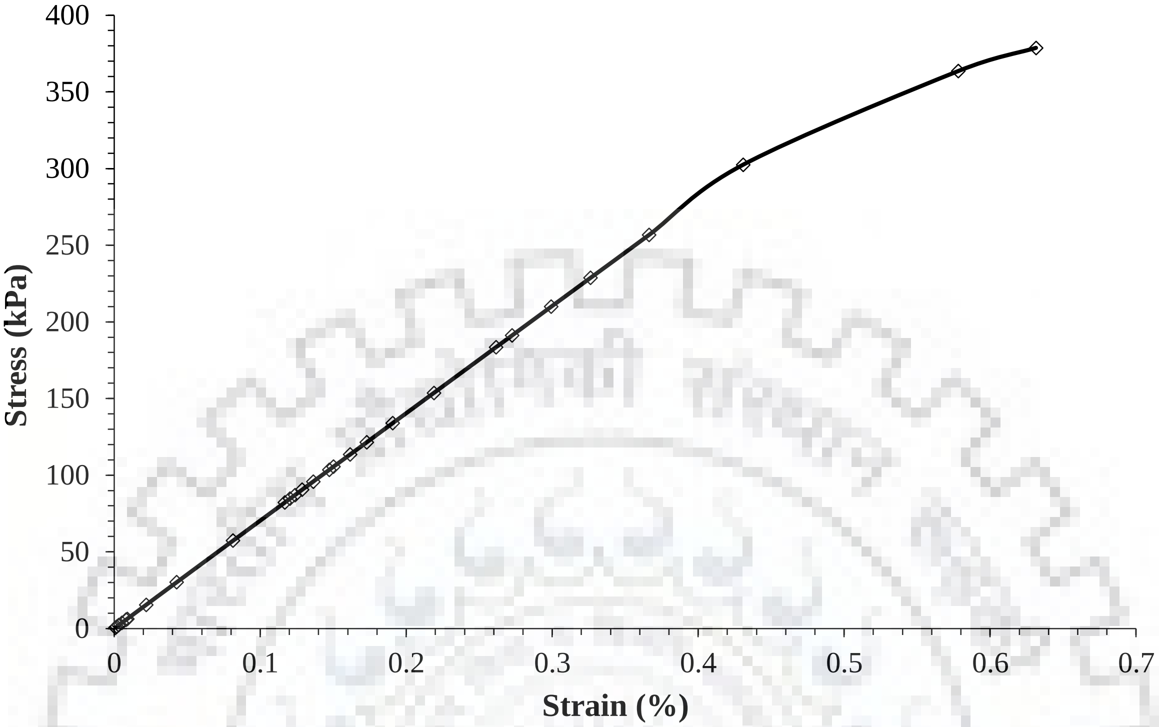

Fig. 3.4 Stress-strain curve for soil element below caisson obtained from numerical analysis

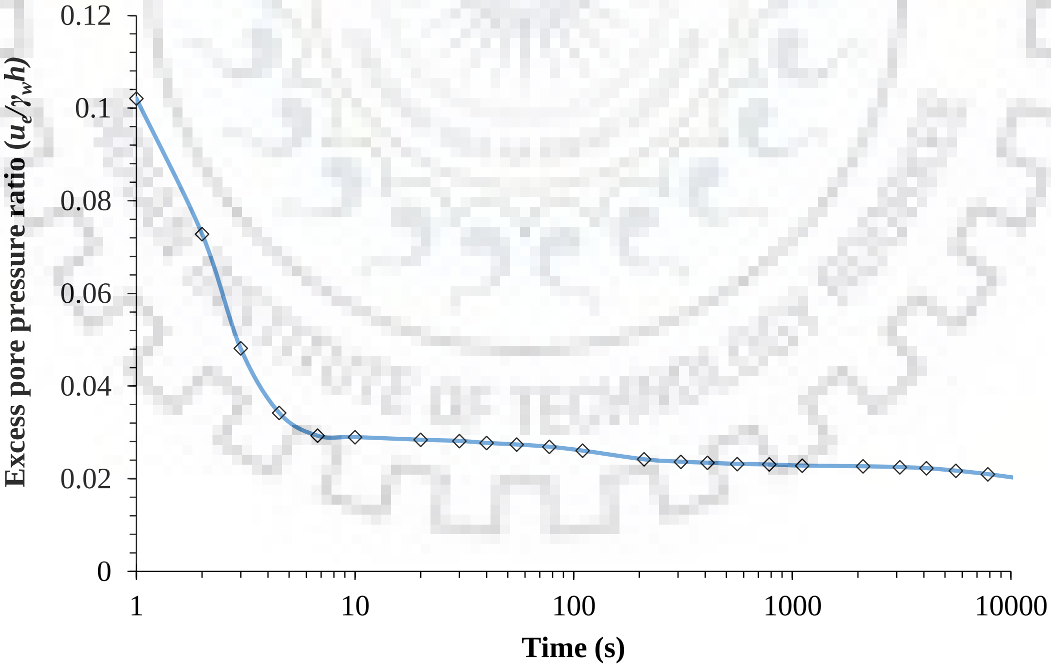

Fig. 3.5 Variation of excess pore pressure ratio with time at the centre of clay layer

After obtaining the magnitude of V_a, vertical load V with magnitudes $V_a/8$, $V_a/4$, $3V_a/8$, $V_a/2$, $5V_a/8$, $3V_a/4$,$7V_a/8$ and V_a, acting on top of the caisson, is varied. For each of these vertical loads, lateral load Q is further varied as $V/8$, $V/4$, $3V/8$, $V/2$, $5V/8$, $3V/4$, $7V/8$ and V. These lateral loads are applied at an elevation of 2.25 times the width of caisson above the scour level. Hence, the applied lateral load and moment are always proportional to each other such that $M/Q = 2.25B = 3.375$ m. The various input parameters considered in the present study have been mentioned in Table 3.4.

Table 3.4 Input parameters considered in the present study

Parameter	**Values**
Base dimension (B)	1.5m ×1.5m
Embedment depth (D)	2.25m
Height of load application above scour level (H)	3.375m
Soil friction angle (ϕ)	30°
Wall friction angle (δ)	$\phi/2$, $2\phi/3$, ϕ
Horizontal seismic acceleration coefficient (k_h)	0, 0.1, 0.2 and 0.3
Vertical seismic acceleration coefficient (k_v)	0,0.5k_h and k_h
Normalized vertical load (V/V_n)	0.2, 0.4, 0.6, 0.8, 1, 1.2, 1.4 and 1.6
Lateral load for each V (Q/V)	0, 0.125, 0.25, 0.375, 0.5, 0.625, 0.75, 0.875, 1

3.3.1 Development of interaction curves

Interaction diagrams are curves relating externally applied load combinations at the time of failure of the caisson. In order to create generalized interaction curves, the vertical load, lateral loads and moments are normalized with respect to certain standard quantities which can be calculated for variety of geometry and soil strength, such that these diagrams can be used for static and seismic conditions. For normalizing the applied lateral loads, normalizing load V_n is calculated to be 1000kN as per IS 3955 (1967), for the current geometry of the caisson and soil profile. The results from ABAQUS analysis are used to calculate lateral soil pressure, maximum and minimum base pressures, tilt, shift and point of rotation of caisson using MATLAB (2021). Finally, the interaction diagrams are developed based on the load combination which gives negative magnitude of minimum base pressure. The normalizing lateral load Q_n and normalizing moments M_n are calculated, as described in the subsequent sections. Thereafter curves are plotted in V-Q-M space for different magnitudes of δ, k_h and k_v.

3.4 Results and Discussions

Numerical analysis of caisson subjected to a variety of loading combinations with different wall friction angle and seismic acceleration coefficients are performed. The results of these analyses are computed using MATLAB (2021), normalized with respect to suitable parameter and the same has been used to develop interaction diagrams in V-Q-M space. The aforementioned results have been presented in this section.

3.4.1 Shape of failure wedge

The shape of failure wedge in vertical and horizontal plane has been obtained from the numerical analysis and presented in Fig. 3.6 From the figure, it can be observed that the shape of wedge in vertical plane is a logarithmic spiral and in horizontal plane, it appears to be section of a circle. The shape in vertical plane is as per the recommendation of Terzaghi (1943) that the shape of failure wedge for rough walls should be considered curved. Additionally, the shape of 3D failure wedge is in perfect agreement with centrifuge test results by Olson et al. (2017).

3.4.2 Lateral soil pressure profile

3.4.2.1 Influence of lateral load on lateral soil pressure profile

Fig. 3.7(a) depicts the variation of lateral soil pressure along width of caisson. It is observed that the magnitude of lateral soil pressure decreases from edge to the center of caisson. This is because of the higher stress concentration that takes place at edges. For a vertical loading of 800kN under static conditions with $\delta=\phi$ (soil friction angle), as the lateral load increases by 25%, the lateral soil pressure increases by 29.11% at center and 29.73% at edges. Fig. 3.7(b) shows the lateral soil pressure variation along depth of caisson. Ideally, the lateral soil pressure at the top should have been maximum, but since the overburden pressure at top of the caisson is zero, the stress generated in that layer is slightly low. The maximum magnitude of lateral soil pressure thus occurs at a depth slightly below the scour level. It is seen from Fig. 3.7(b) that this depth is 0.3 m for all magnitudes of lateral loads. The magnitude of soil pressure decreases with increasing depth, changes sign at a certain depth and then keep increasing in the other direction. Under the same loading conditions as mentioned above, an increase of 25% in lateral load leads to lateral soil pressure increase by 29.61% at the scour level.

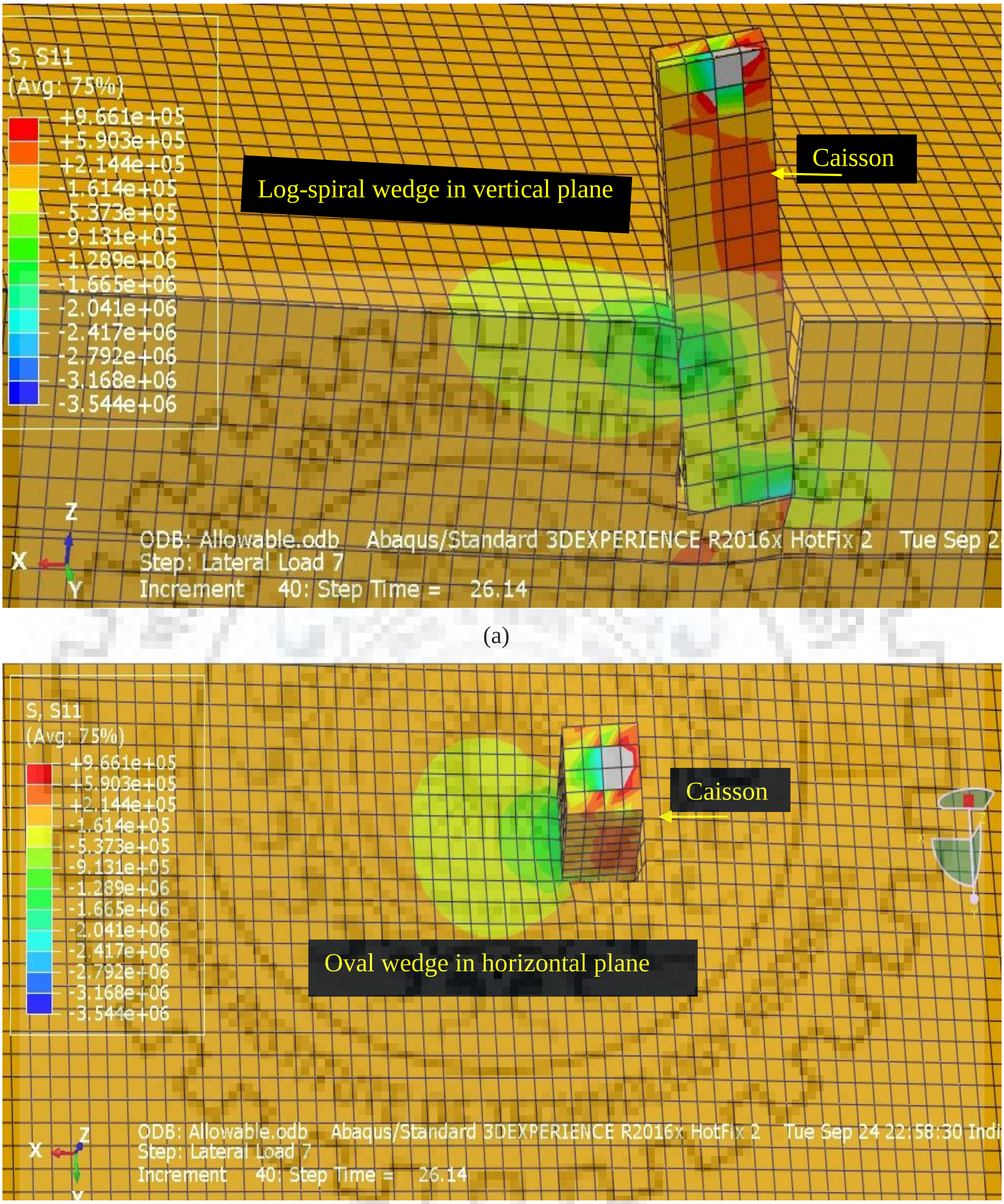

Fig. 3.6 Shape of passive wedge in (a) vertical plane and (b) horizontal plane obtained from numerical analyses of caisson under combination of loading

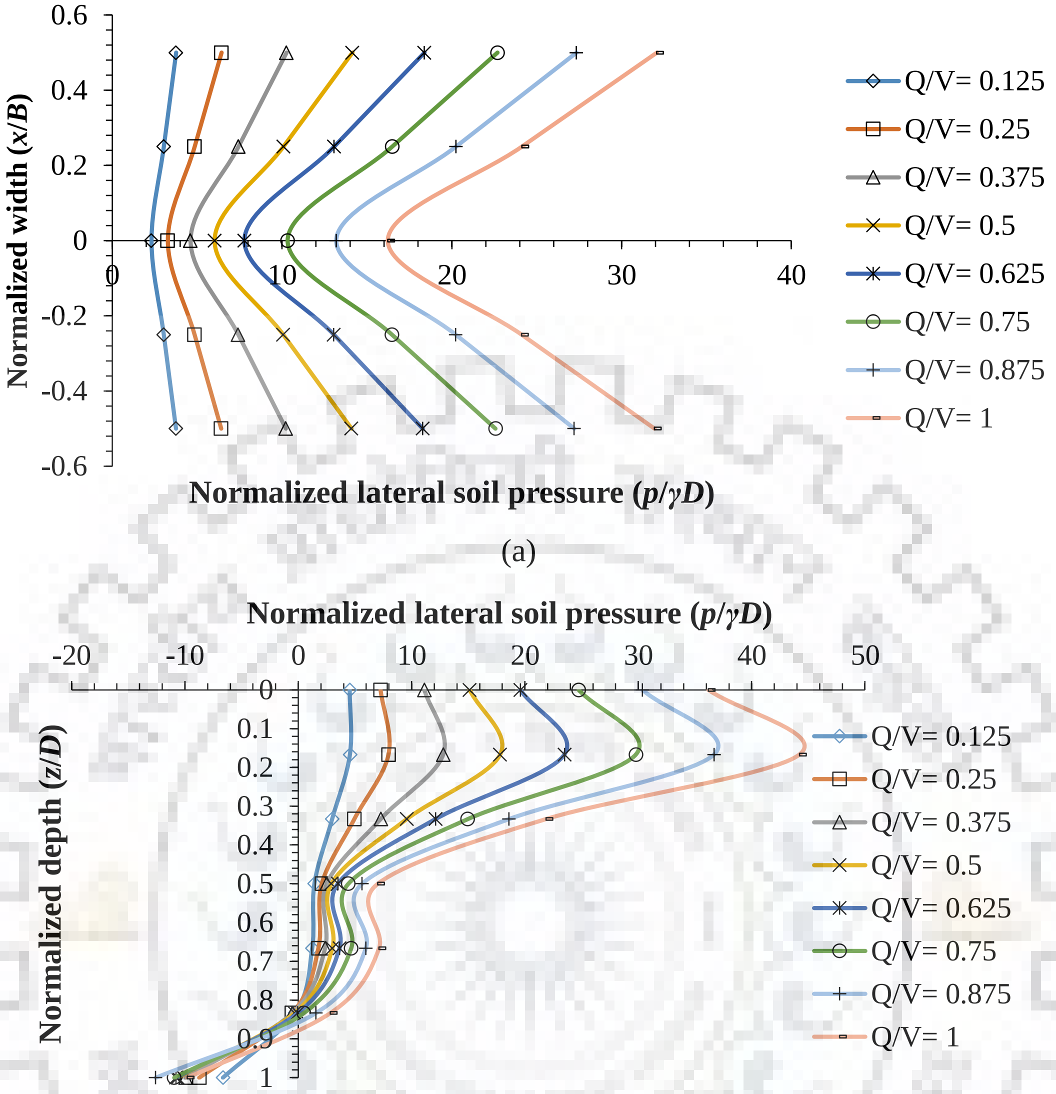

(a)

(b)

Fig. 3.7 Variation of lateral soil pressure along (a) width of caisson and (b) depth of caisson for different *Q/V* ratios when *V*=800 kN, $\delta=\phi$ and $k_v=k_h=0$

3.4.2.2 Influence of soil-wall friction angle on lateral soil pressure profile

The lateral soil pressure produced by surrounding soil on caisson reduces as the magnitude of soil wall friction angle δ increases. Caisson-soil interface with higher magnitude of δ resists displacement, thereby producing lower lateral soil pressure along both width and depth of caisson as shown in Fig. 3.8. As δ increases from $\phi/2$ to $2\phi/3$ and from $\phi/2$ to ϕ under static conditions, for *V*=400 kN and *Q/V*=0.5, the lateral soil pressure along width of caisson reduces by 3.94% and 10.85% respectively. The reduction in lateral soil pressure along depth of caisson for the same increase of δ is found to be 4.92% and 13.48% respectively.

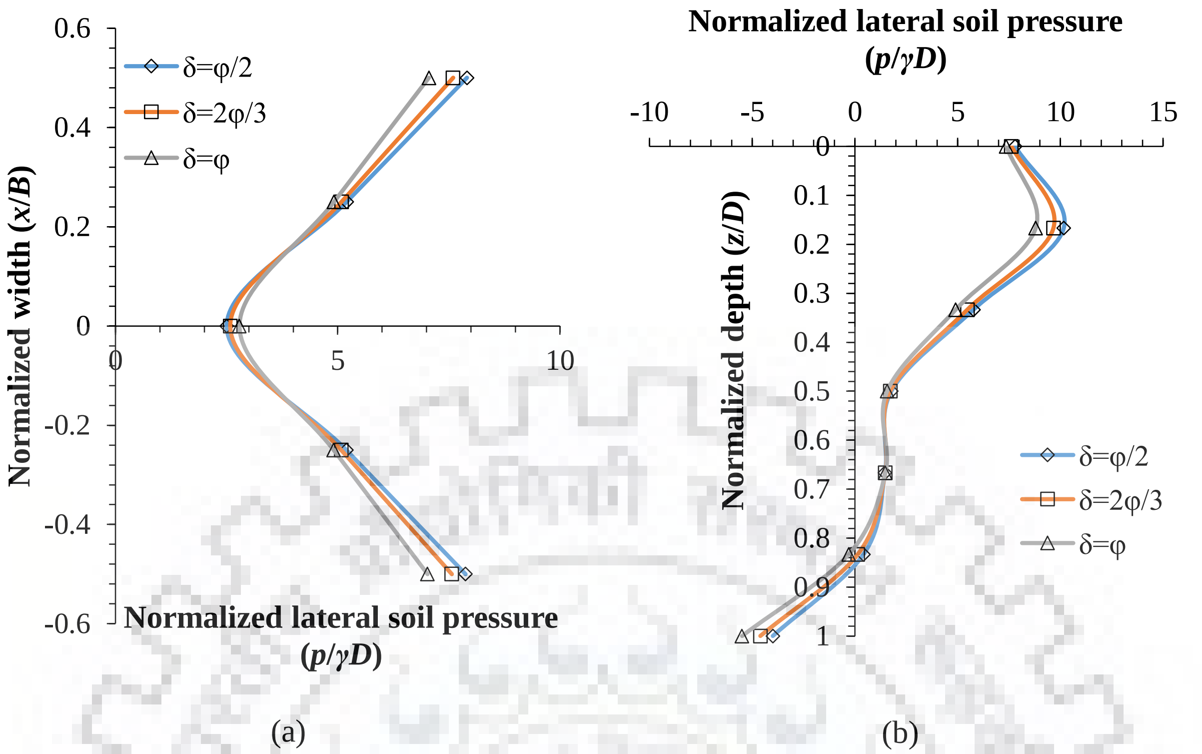

Fig. 3.8 Variation of lateral soil pressure along (a) width of caisson and (b) depth of caisson for varying soil-wall friction angle (δ) when V=400 kN, Q/V=0.5 and k_v=k_h=0

3.4.2.3 Influence of seismic acceleration coefficients on lateral soil pressure profile

Fig. 3.9 and Fig. 3.10 show the effect of k_h and k_v on lateral soil pressure profiles along width and depth of the caisson respectively. It is seen that the magnitude of lateral soil pressure along width and depth of the caisson increases with increase in horizontal and vertical seismic acceleration coefficients. While the increase in magnitude of lateral soil pressure for increasing k_v/k_h ratios is nominal, the effect is more significant for increasing magnitude of k_h. This is because increasing seismic acceleration coefficients causes increase in displacement of caisson, which is also observed in subsequent sections. Further, the soil also gets compressed under the seismic inertia forces. The combination of these two factors leads to a greater soil pressure which is a direct function of displacement and subgrade modulus. For, V=400 kN, Q/V= 0.5, $\delta=\phi$ and k_v/k_h= 0, as k_h increases from 0 to 0.1, 0.2 and 0.3 respectively, the lateral soil pressure increases by 11.39%, 13.69% and 34.87% respectively along width and 11.84%, 14.31% and 36.65% respectively along depth of caisson. On the other hand, for k_h=0.1 as k_v/k_h is increased from 0 to 0.5 and 1, lateral soil pressure increases by 1.02% and 2.17% respectively along width of caisson and 0.94% and 2.08% respectively along the depth.

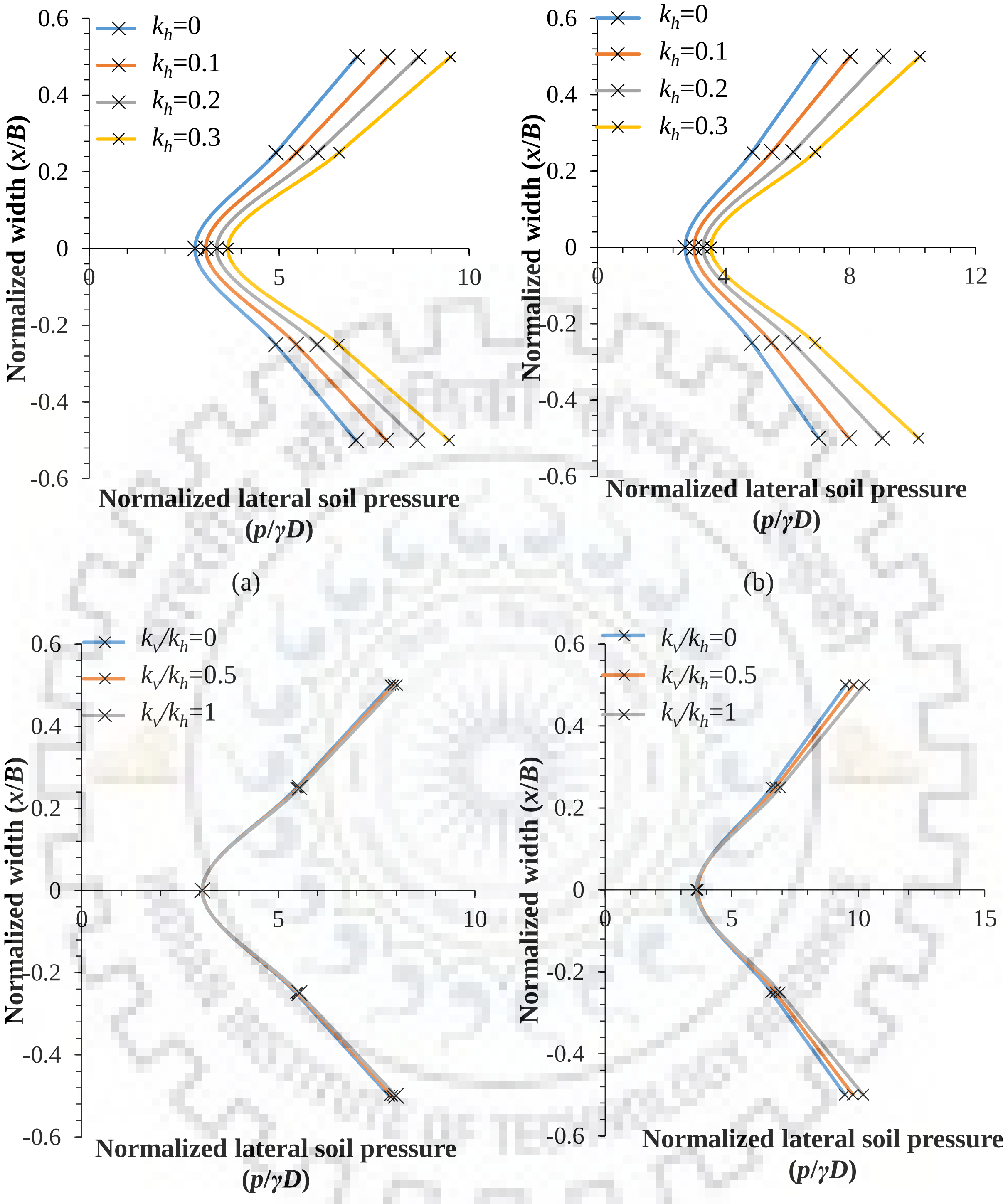

(a) (b)

(c) (d)

Fig. 3.9 Variation of lateral soil pressure with width of caisson for different horizontal seismic acceleration coefficients (k_h) for (a) k_v/k_h=0 and (b) k_v/k_h=1 and for different vertical seismic acceleration coefficients (k_v/k_h) for (c) k_h=0.1 and (d) k_h=0.3 when V=400 kN, Q/V=0.5 and $\delta=\phi$

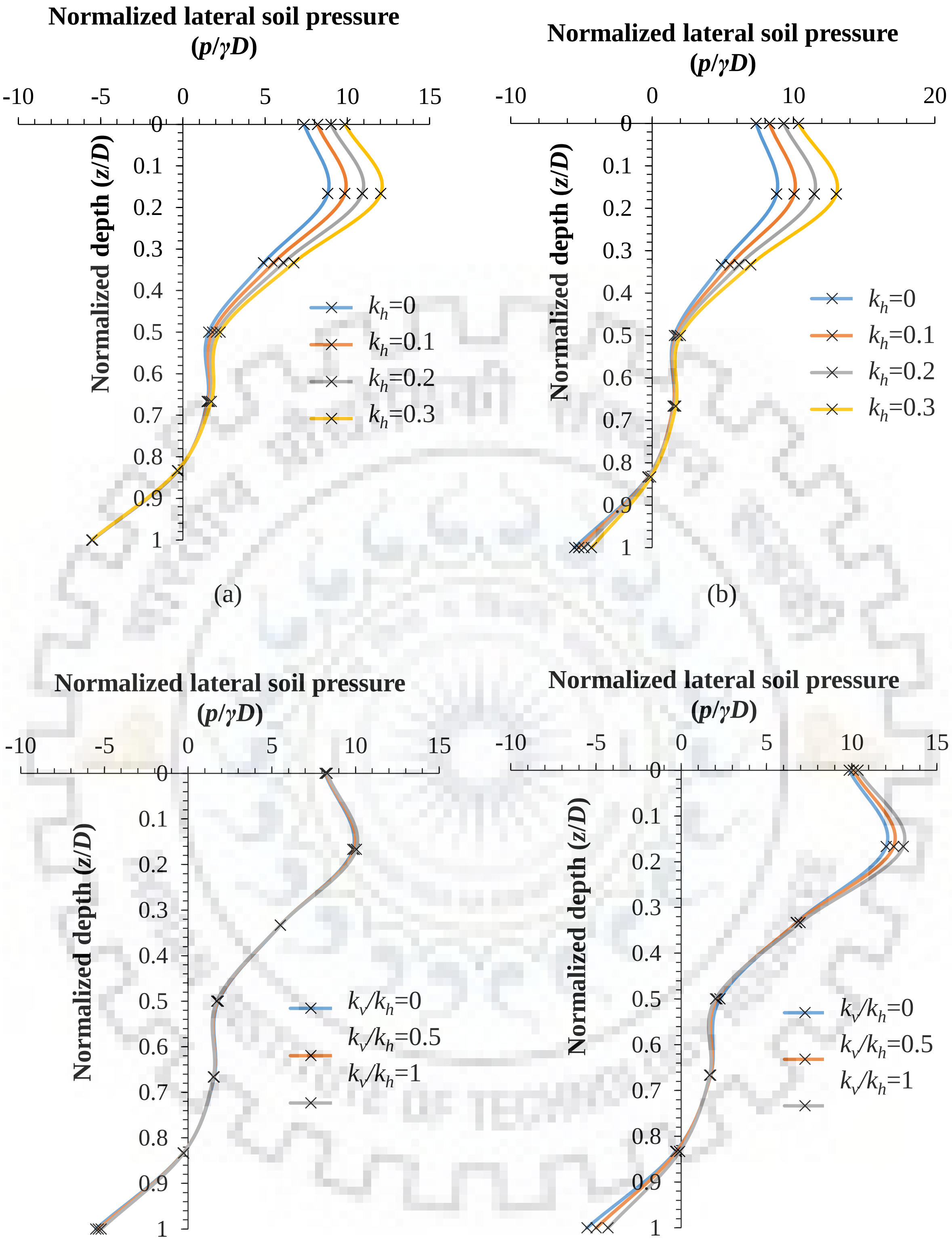

(a) (b)

(c) (d)

Fig. 3.10 Variation of lateral soil pressure with depth for different horizontal seismic acceleration coefficients (k_h) for (a) k_v/k_h=0 and (b) k_v/k_h=1 and for different k_v/k_h for (c) k_h=0.1 and (d) k_h=0.3 when V=400 kN, Q/V=0.5 and $\delta=\phi$

3.4.3 Maximum and minimum base pressure

3.4.3.1 Influence of lateral load on maximum and minimum base pressure

Fig. 3.11(a) and (b) represent the variation of maximum and minimum base pressure produced at the base of the caisson due to the external loading. It is seen that at low magnitudes of vertical load, the magnitude of maximum base pressure increases monotonically with increasing lateral load. However, at higher magnitudes of vertical load, maximum base pressure increases initially, reached the peak value and thereafter decreases. This behavior could be attributed to the fact that at higher magnitudes of lateral load, yielding of soil takes place resulting in reduced magnitude of stress owing to strain softening.

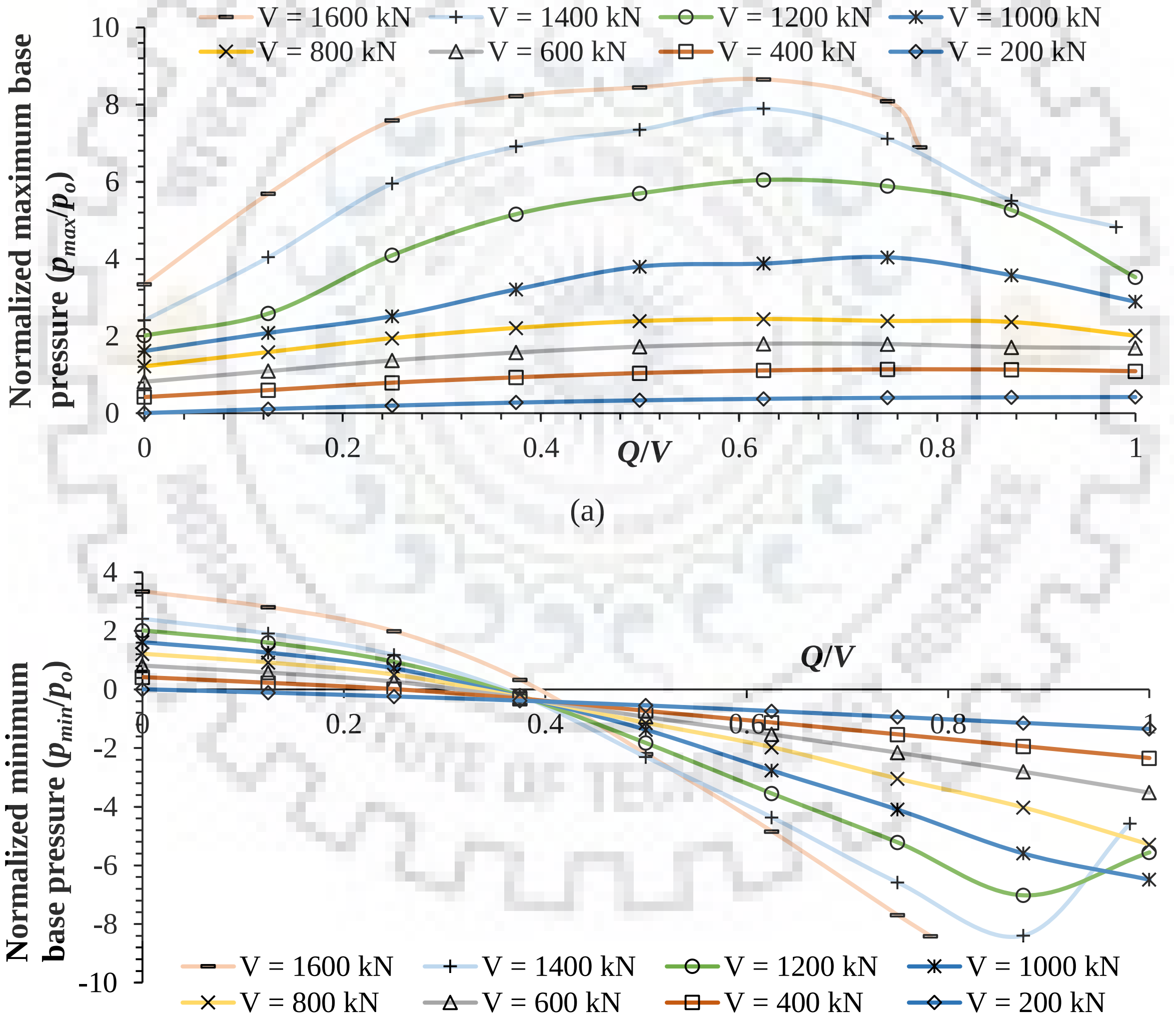

(a)

(b)

Fig. 3.11 Variation of (a) maximum base pressure and (b) minimum base pressure with normalized lateral load for different magnitudes of vertical load when $\delta=\phi$ and $k_v=k_h=0$

Similarly, minimum base pressure decreases monotonically for smaller magnitude of vertical loads and post yielding, the negative magnitude of minimum base pressure decreases. The negative magnitude of base pressure is due to a combination of loss of contact of caisson and soil and the excess pore pressure developed in the soil because of the externally applied loading. The normalizing base pressure, p_o is equal to the vertical load per unit base area. For 600 kN vertical load, increasing the normalized lateral load (Q/V) from 0.25 to 0.375 increases the maximum base pressure by 13.26% whereas increase from 0.75 to 0.875 causes the maximum base pressure to decrease by 2.68% because of strain softening. At greater magnitude of vertical load, the magnitude of lateral load will also be high for the same value of Q/V which causes greater increase in magnitude of maximum base pressure. When the magnitude of vertical load is increased to 1200 kN, increasing Q/V from 0.25 to 0.375 increases the maximum base pressure by 26.02% while increase from 0.75 to 0.875 reduces maximum base pressure by 10.47%.

The influence of vertical load on minimum base pressure for different magnitudes of Q/V is illustrated in Fig. 3.11(b). It is observed that for 600 kN vertical load, increasing Q/V from 0.125 to 0.25 causes minimum base pressure to decrease by 53.27%, while increase of Q/V from 0.875 to 1 cause its negative magnitude to increase by 25.32%. However, in case of 1200 kN vertical load, the minimum base pressure decreases by 40.96% when Q/V is increased from 0.125 to 0.25 but its negative magnitude decreases by 20.85% when Q/V is increased from 0.875 to 1 because of strain softening triggered by yielding. It could also be observed that as the magnitude of vertical load increases, the normalized load (Q/V) required to induce negative base pressure also increases. This indicates that higher magnitude of vertical load causes the caisson to be more stable even at large magnitudes of lateral loads. It is also worth observing that the curves corresponding to V=1600 kN end abruptly before reaching the value Q/V=1. This is because at high magnitude of lateral loads, the soil displacement near base of the caisson is so large that the analysis is terminated in ABAQUS. In the present study, the strain of magnitude 0.4% marks the initiation of yielding and plastic strain being induced in soil, as shown in Fig. 3.4. Therefore, as soon as the magnitude of strain crosses 0.4% in the soil, plastic strain starts accumulating, i.e., the plastic strain increases with small change in stress. Once this plasticity spreads through greater portion of the model, the analysis is aborted in ABAQUS indicating the load is large enough for the material to sustain. Moreover, as soil is weak in tension, the loading combination at which minimum base pressure turns negative is considered as failure load. This load combination is normalized with respect to V_n and has been used for the development of interaction diagrams, as explained in the subsequent section.

3.4.3.2 Influence of soil-wall friction angle on maximum and minimum base pressure

Fig. 3.12(a) and (b) show the effect of varying magnitude of δ on maximum and minimum base pressure respectively. It is seen that higher the magnitude of δ, the safer is the foundation system as it returns lower magnitudes of maximum and minimum base pressure.

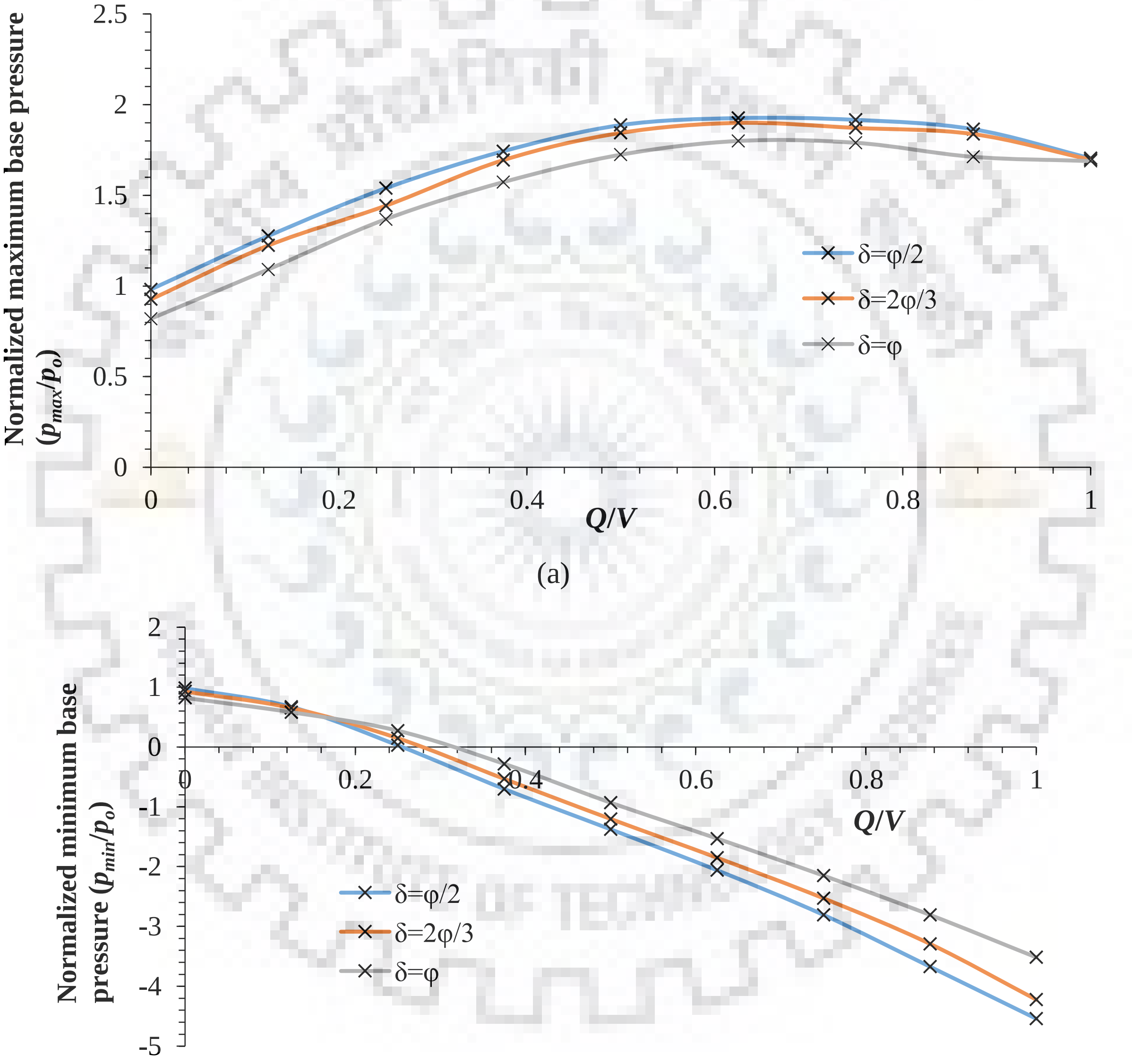

(a)

(b)

Fig. 3.12 Variation of (a) maximum base pressure and (b) minimum base pressure with *Q/V* for different magnitudes of soil-wall friction angle when V=600 kN and $k_v=k_h=0$

For a caisson subjected to 600 kN vertical load and k_v=k_h=0, as δ increases from ϕ/2 to 2ϕ/3, maximum base pressure decreases by 6.27% and when δ increases to ϕ, it further diminishes by 5.17%. The foundation system with larger δ dissipates larger share of the applied load through shear stress development along its boundary which results in lower bearing pressure at base. Similarly, as δ increases from ϕ/2 to 2ϕ/3, minimum base pressure decreases by 12.61% and when δ increases to ϕ, the magnitude again decreases by 22.56%. In this scenario also, higher value of δ gives higher magnitude of normalized lateral load required to generate negative base pressure. This is another indication that larger the value of δ, higher is the load carrying capacity of the foundation system.

3.4.3.3 *Influence of seismic acceleration coefficients on maximum and minimum base pressure*

Fig. 3.13 represents the variation of maximum base pressure and minimum base pressure with normalized lateral load for different combinations of horizontal and vertical seismic acceleration coefficients respectively. It is seen that the magnitude of k_v has a more significant effect on the magnitudes of base pressures. For 600 kN vertical load, Q/V=0.5, δ=ϕ and k_v/k_h=0, as the magnitude of k_h increases from 0 to 0.1, 0.2 and 0.3, the magnitude of maximum base pressure reduces by 0.11%, 2.59% and 5.03% respectively whereas minimum base pressure increases in negative magnitude by 16.03%, 32.3% and 48.91% respectively. Similarly, for 600 kN vertical load, Q/V=0.5, δ=ϕ and k_h=0.1, as the magnitude of k_v/k_h increases from 0 to 0.5 and finally 1, the magnitude of maximum base pressure reduces by 3.49% and 7.05% respectively, whereas minimum base pressure increases in negative magnitude by 6.37% and 12.86% respectively. It is also observed in both Fig. 3.13(a) and (b) that the soil pressure curve corresponding to k_h=0.3 and k_v=k_h does not progress after a small value of Q/V. It may be attributed to the exaggerated displacement taking place for given seismic loading conditions and the ABAQUS algorithm aborts the analysis at this stage, as explained earlier.

3.4.4 *Displacement of caisson*

3.4.4.1 *Influence of lateral load on displacement of caisson*

Caisson displacement is obtained from ABAQUS and further used to determine tilt, shift and point of rotation of the same. The displacement of the caisson for k_h=k_v=0, V=800 kN and δ=ϕ for different combinations of Q/V ratio is shown in Fig. 3.14. The linear nature of the curves for all *Q/V* ratio reveals that caissons behave as rigid foundation system. At scour level, it could be observed that caisson displacement increases with increasing lateral loads. When *Q/V* ratio increases from 0.375 to 0.5, caisson displacement increases by 43.59% whereas for increase in *Q/V* from 0.875 to 1, the increase is 21%.

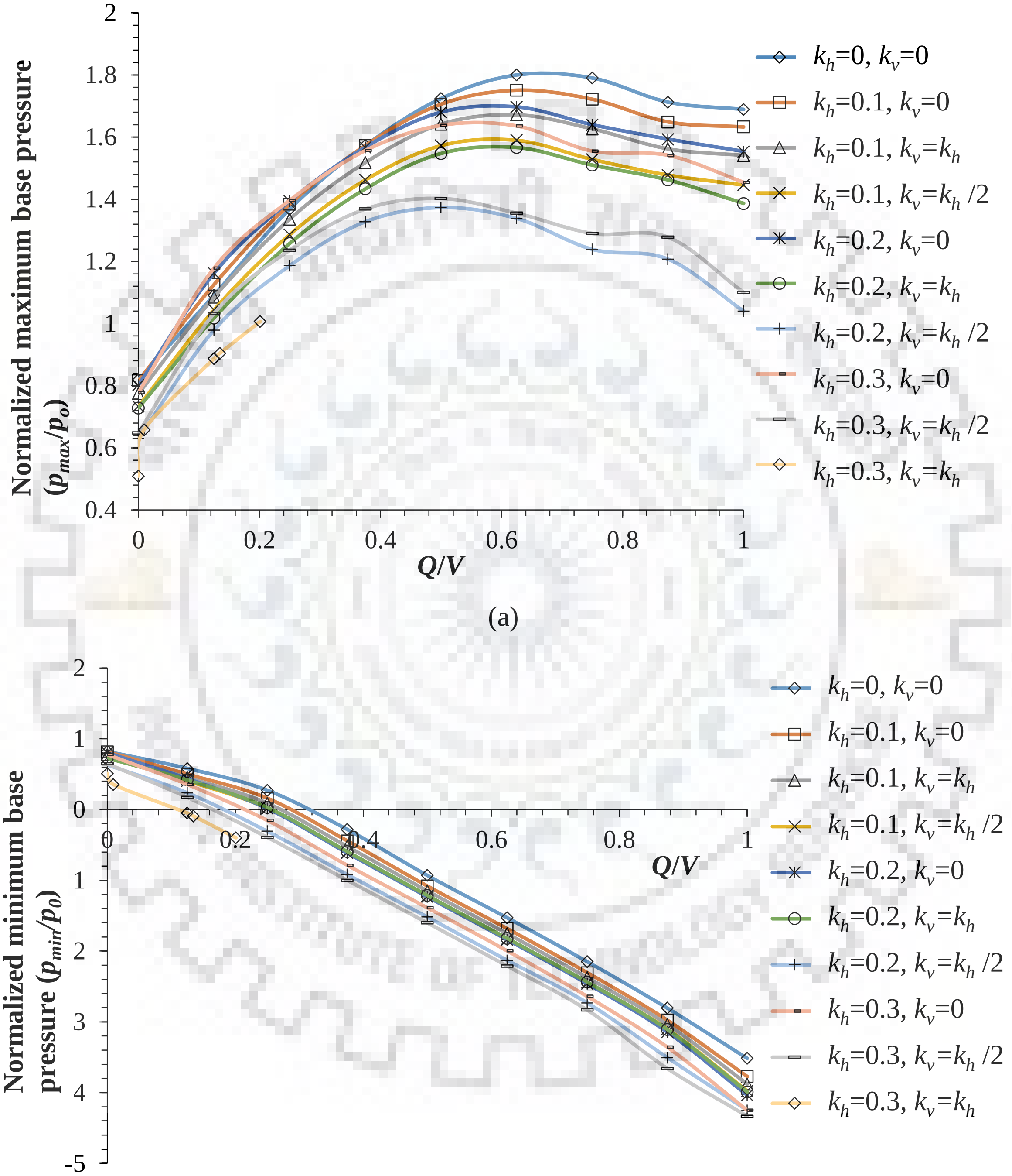

(a)

(b)

Fig. 3.13 Variation of (a) maximum base pressure and (b) minimum base pressure with normalized lateral load for different seismic acceleration coefficients at V=600 kN and $\delta=\phi$

3.4.4.2 *Influence of soil-wall friction angle on displacement of caisson*

It is observed from Fig. 3.15 that by increasing the soil-wall friction, the magnitude of caisson displacement is reduced. This is caused by increased resistance offered by caisson-soil interface against displacement. At scour level, the displacement of caisson diminishes by 5.04% and 13.73% when δ increases from $\phi/2$ to $2\phi/3$ and ϕ respectively, for V=400 kN, Q/V=0.5 and k_h=k_v=0.

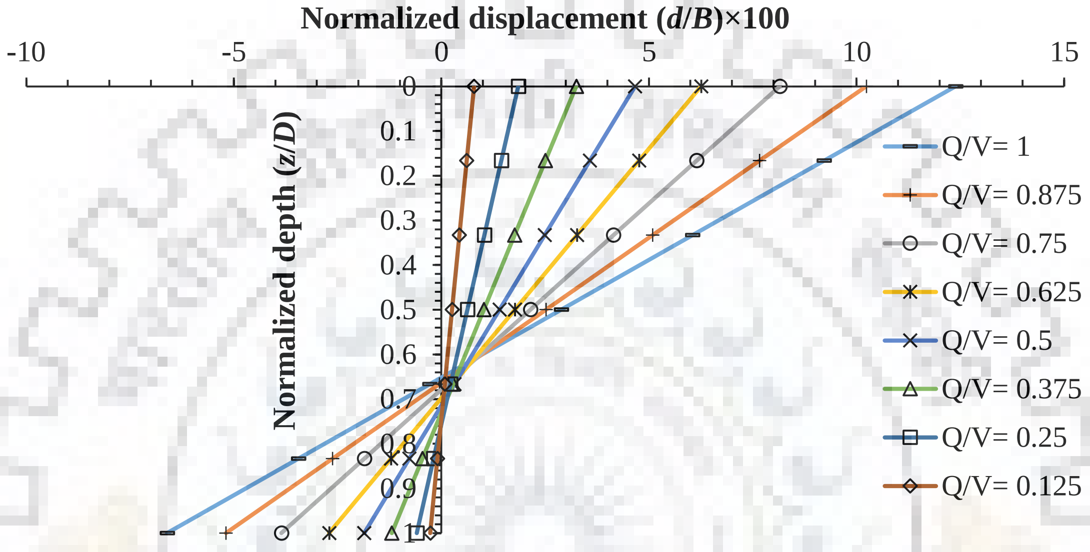

Fig. 3.14 Variation of displacement of caisson along depth for different Q/V ratios when V=800 kN, k_h=k_v=0 and δ=ϕ

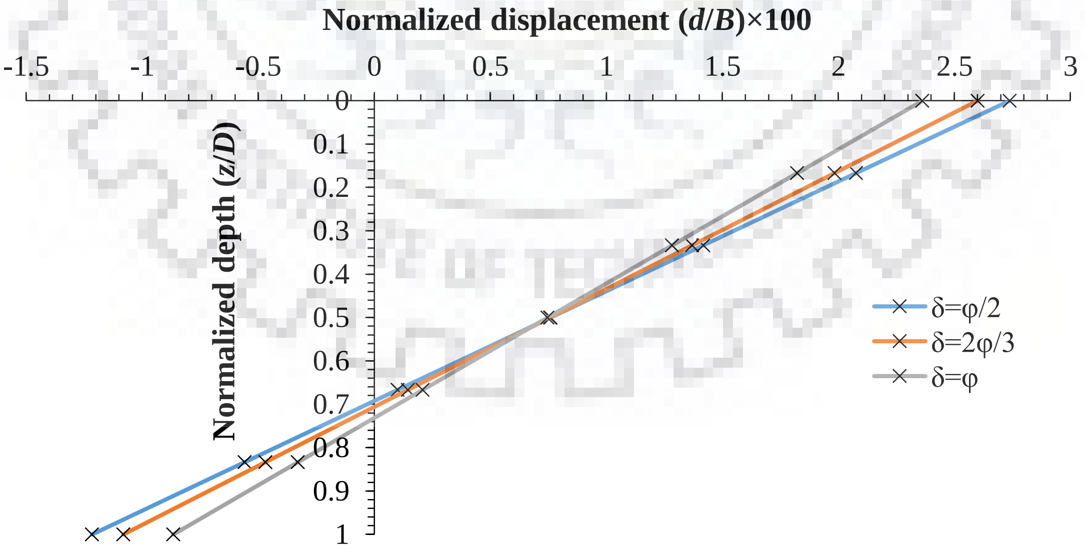

Fig. 3.15 Variation of displacement of caisson along depth for different magnitudes of soil-wall friction angle when V=400 kN, Q/V=0.5 and k_h=k_v=0

3.4.4.3 *Influence of seismic acceleration coefficients on displacement of caisson*

It is seen from Fig. 3.16(a)-(d) that caisson displacement increases with increasing magnitude of seismic acceleration coefficients (k_h and k_v). The horizontal and vertical seismic forces cause the caisson to move significantly. However, the effect of k_h is much more significant than that of k_v because k_h gives rise to the horizontal seismic inertial force, thereby causing the caisson to undergo significant displacement from its original position.

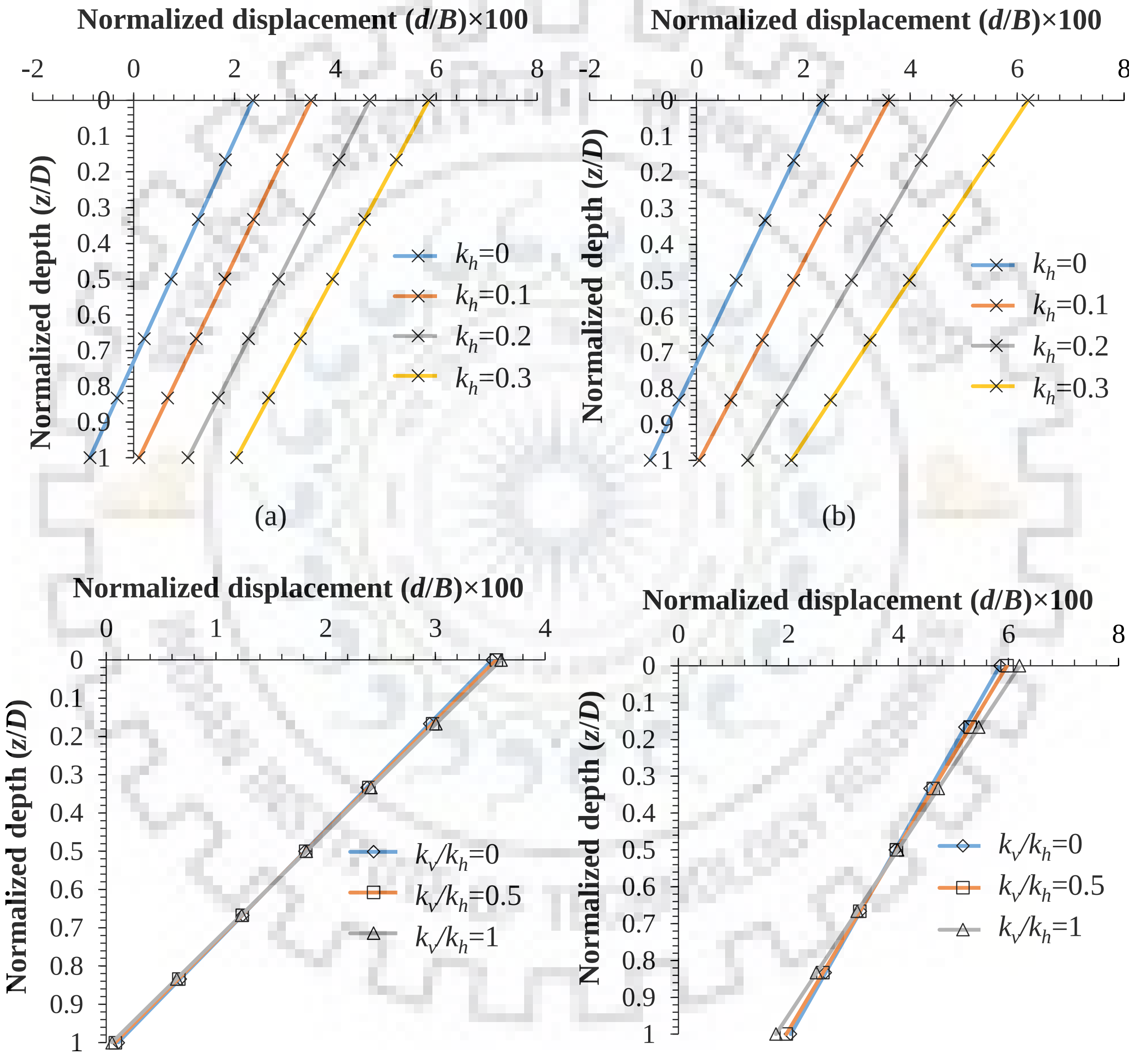

(a)

(b)

(c)

(d)

Fig. 3.16 Variation of caisson displacement with depth for different horizontal seismic acceleration coefficients (k_h) with (a) k_v/k_h=0 and (b) k_v/k_h=1and for different k_v/k_h ratios with (c) k_h=0.1 and (d) k_h=0.3 when V=400 kN, Q/V=0.5 and $\delta=\phi$

For V=400 kN, Q/V=0.5, $\delta=\phi$ and k_v/k_h=0, as k_h increases from 0 to 0.1, 0.2 and 0.3, the caisson displacement increases by 48.9%, 97.97% and 147.52% respectively, whereas for k_h=0.1, increase of 1.08% and 2.29% in caisson displacement is observed when k_v/k_h ratio increases from 0 to 0.5 and 1 respectively.

3.4.5 Tilt and shift of caisson

3.4.5.1 Influence of lateral load on tilt and shift of caisson

Both the tilt and shift of caisson advance with lateral load as shown in Fig. 3.17(a) and (b) respectively. At smaller magnitudes of applied vertical load both tilt and shift of caisson is virtually non-existent because of smaller lateral loads.

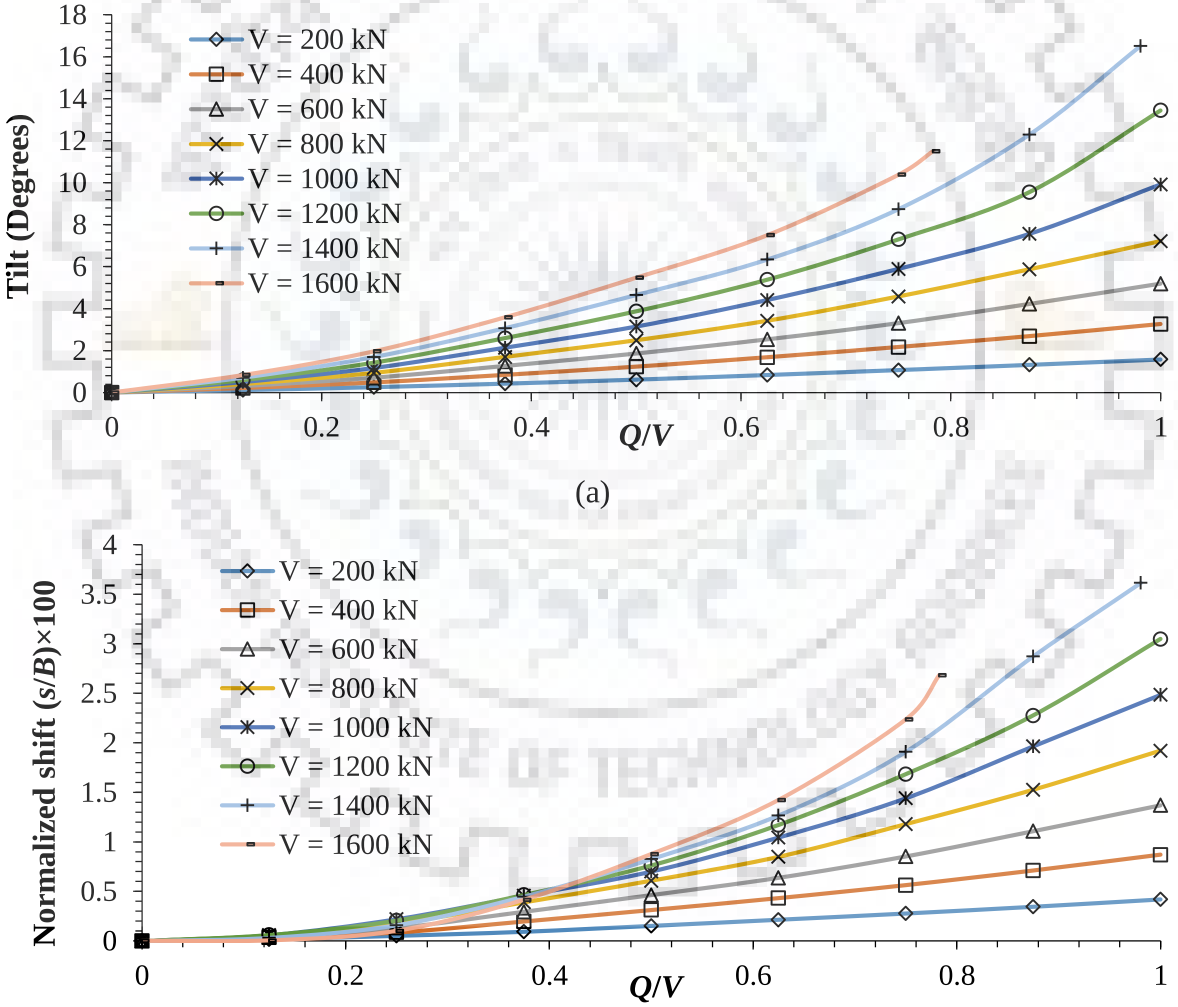

(b)

Fig. 3.17 Variation of (a) tilt of caisson and (b) shift of caisson with normalized lateral load for different magnitudes of vertical load when $\delta=\phi$ and $k_h=k_v$=0

However, at vertical load magnitudes close to allowable vertical load, the lateral loads are also high such that soil reaches plastic state and high values of tilt and shift are obtained. When a vertical load of 200 kN is applied, as normalized lateral load increases from 0.375 to 0.5, tilt of caisson increases by 45.61% and shift increases by 56.2%. Similarly for 1600 kN vertical load and for the same change in normalized lateral load, causes an increase in tilt of 52.6% and shift by 111.33%. Both tilt and shift increase non-linearly with lateral load at higher magnitudes of vertical load.

3.4.5.2 Influence of soil-wall friction angle on tilt and shift of caisson

The effect of δ on tilt and shift of caisson has been illustrated in Fig. 3.18(a) and (b) respectively. Higher magnitude of δ provides larger resistance to tilt of caisson through action on vertical walls of caisson and hence smaller will be the magnitude of tilt and shift. For 800 kN vertical load and normalized lateral load (Q/V) as 0.5 with k_h=k_v=0, as δ increases from ϕ/2 to 2ϕ/3 and ϕ, tilt of caisson reduces by 6.98% and 18.79% respectively, whereas shift of caisson diminishes by 6.88% and 20.44% respectively.

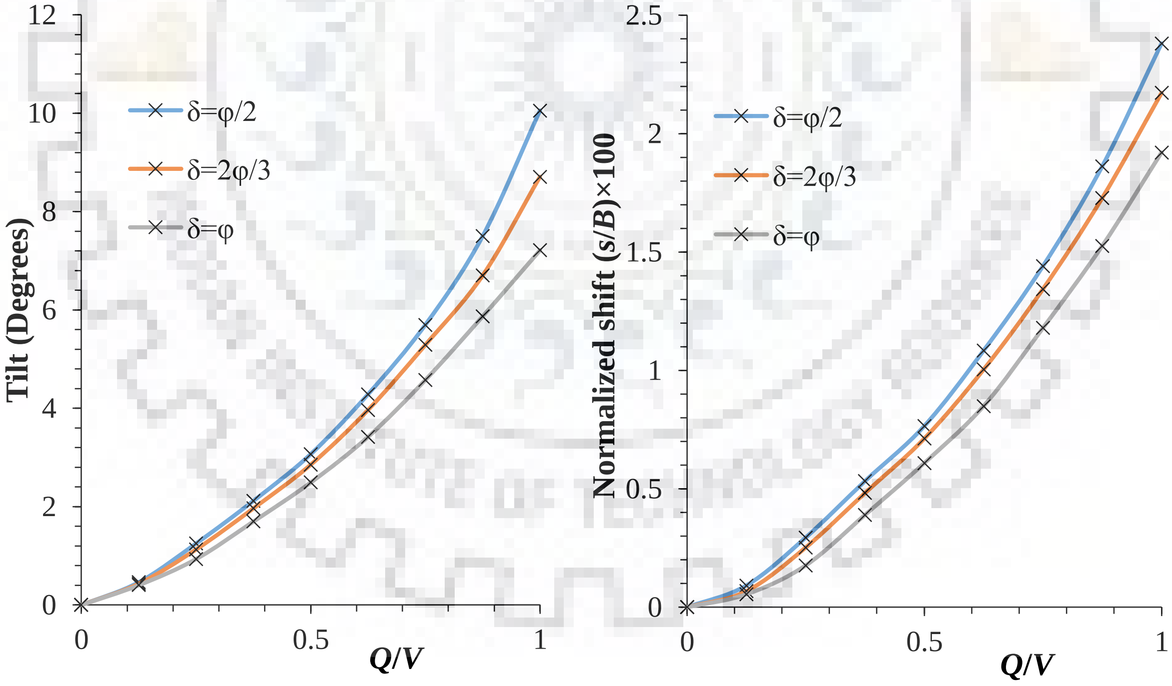

(a) (b)

Fig. 3.18 Variation of (a) tilt of caisson and (b) shift of caisson with Q/V for different magnitudes of δ when V=800 kN and k_h=k_v=0

3.4.5.3 Influence of seismic acceleration coefficients on tilt and shift of caisson

Fig. 3.19(a) and (b) illustrate the influence of k_h on tilt and shift of caisson respectively, at k_v/k_h=0. In all the cases, it could be seen that both tilt and shift of caisson increases with increase in k_h value. The horizontal pseudo-static force causes the direct translation or shift of caisson whereas vertical pseudo-static force reduces the vertical inertia of caisson, thereby making the caisson susceptible to tilt. For k_v=0, V=800 kN and Q/V=0.125, as k_h increases from 0 to 0.1, 0.2 and 0.3 the increase in tilt of caisson is 17.27%, 46.93% and 136.35% respectively, whereas shift in caisson is 20.11 times, 40.93 times and 64.61 times the initial value.

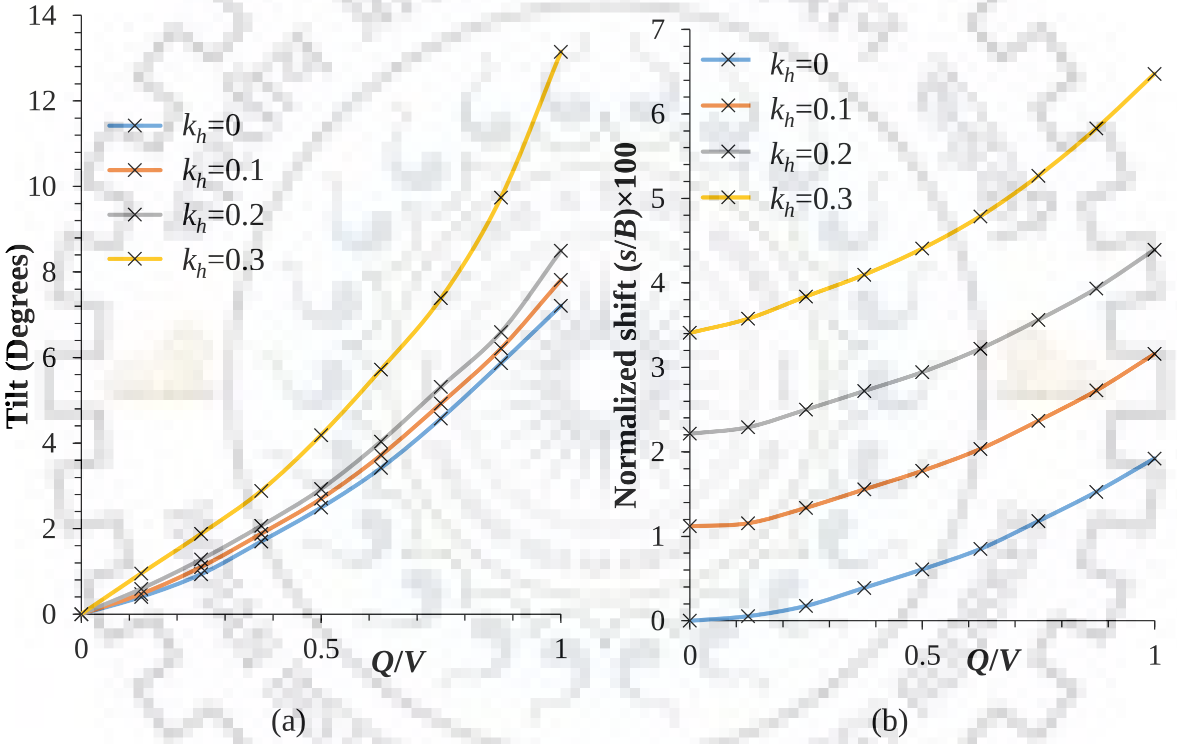

(a) (b)

Fig. 3.19 Variation of (a) tilt of caisson and (b) shift of caisson with normalized lateral loads for different horizontal seismic acceleration coefficients when k_v/k_h=0, $\delta=\phi$ and V=800 kN

On the other hand, Fig. 3.20(a) and (b) show the variation of tilt and shift respectively with normalized lateral load for different k_v/k_h ratio at a given magnitude of k_h. When k_h=0.1, as k_v/k_h increases from 0 to 0.5, tilt increases by 1.46% and shift increases by 0.52% and from 0 to 1, tilt and shift rise by 2.97% and 1.3% respectively. Therefore, it is seen that the effect of increase in magnitude of horizontal seismic acceleration coefficient is more prominent than increase in vertical seismic acceleration coefficient on tilt and shift of caissons.

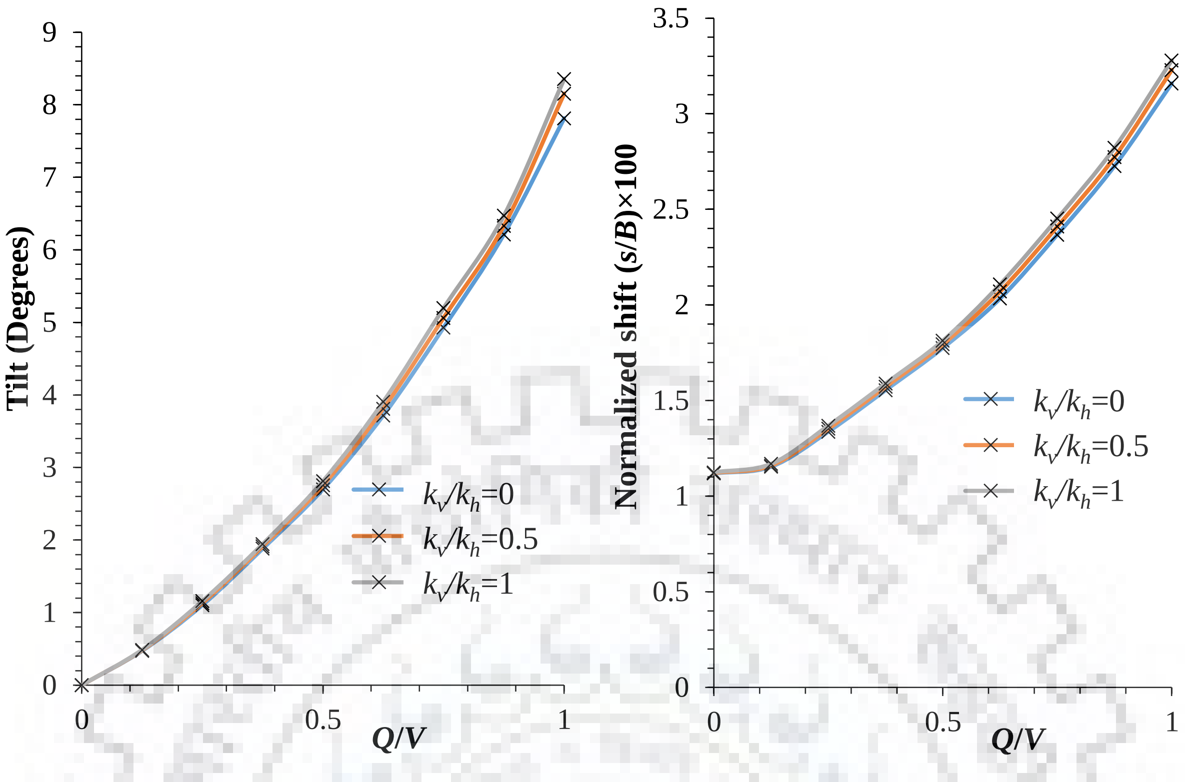

(a) (b)

Fig. 3.20 Variation of (a) tilt of caisson and (b) shift of caisson with normalized lateral loads for different vertical seismic acceleration coefficients when k_h=0.1, $\delta=\phi$ and V=800 kN

3.4.6 Point of rotation of caisson

3.4.6.1 Influence of lateral load on depth of point of rotation of caisson

Depth of point of rotation of caisson plays significant role in determining the resistance offered by soil. Higher the point of rotation, lesser will be the stability of caisson as the portion of soil below the point of rotation will give reaction in the direction of applied lateral load. The non-linear variation of depth of point of rotation with normalized lateral load for $\delta=\phi$ and $k_h=k_v=0$ has been shown in Fig. 3.21. It is observed that as the lateral load increases, the point of rotation moves upwards. Larger magnitude of vertical load tends to stabilize the caisson, thereby, causing the point of rotation to move downwards. However, as the magnitude of lateral load increases, the stability of the caisson reduces as reflected by shifting of point of rotation upwards. The depth of point of rotation reduces by 1.77%, 3.59% and 7.17% when Q/V increases from 0.125 to 0.25, 0.5 and 0.75 respectively for V=600 kN. The depth of point of rotation increases by 4.5% and 6.15% when V increases from 200 kN to 400kN and 800kN respectively for Q=200 kN.

3.4.6.2 Influence of soil-wall friction angle on depth of point of rotation of caisson

Fig. 3.22 highlights the variation of depth of point of rotation with normalized lateral load for different values of δ. It can be observed that because of the additional support by caisson-soil interface, the point of rotation moves further down with increasing δ. Thus, improving the magnitude of δ of caisson-soil interface will add to the stability of caisson. As δ increases from $\phi/2$ to $2\phi/3$ and ϕ, the point of rotation moves downwards by 3.42% and 7.73% respectively for Q/V=0.25 and 2.06% and 3.69% respectively for Q/V=0.75.

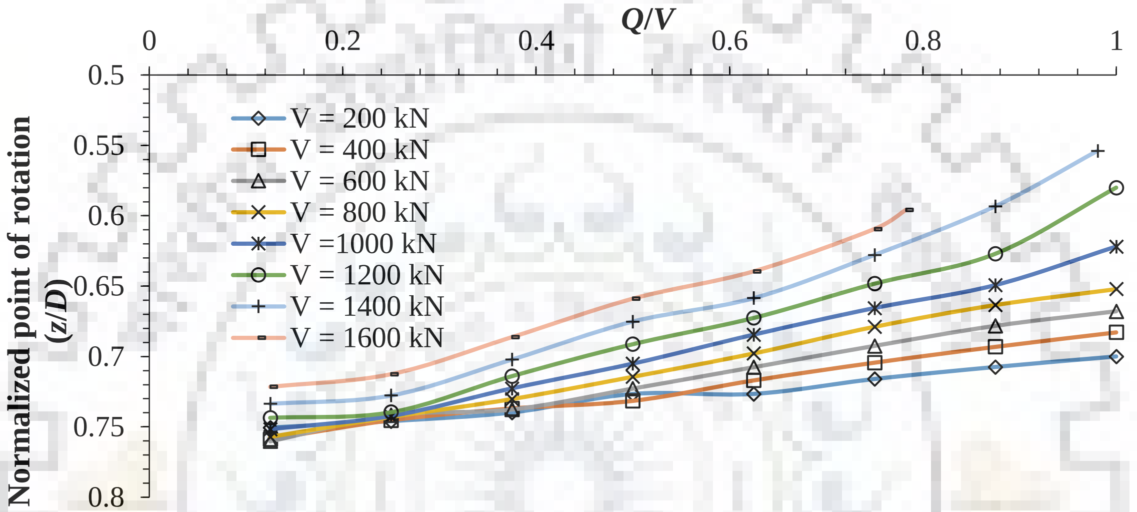

Fig. 3.21 Variation of point of rotation of caisson with normalized lateral loads for different magnitudes of vertical load when $\delta=\phi$ and $k_h=k_v=0$

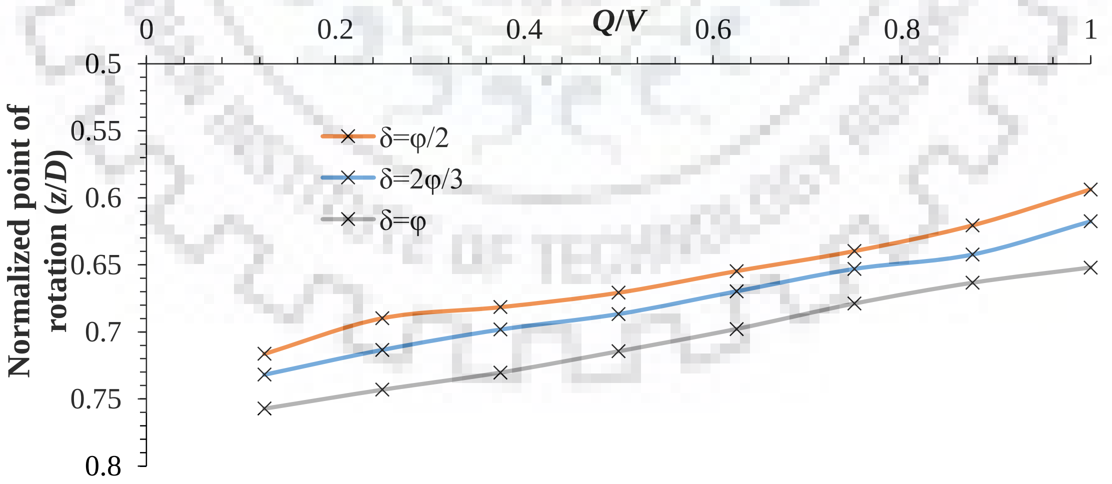

Fig. 3.22 Variation of point of rotation of caisson with Q/V for different magnitudes of δ when V=800kN and $k_h=k_v=0$

3.4.6.3 Influence of seismic acceleration coefficients on depth of point of rotation of caisson

The depth of point of rotation for different magnitudes of horizontal and vertical seismic acceleration coefficients are computed from the displacement data and plotted for V=800 kN and $\delta=\phi$ case. Fig. 3.23(a) show the influence of k_h on depth of point of rotation at different lateral loads for various k_v/k_h values. It is observed that as the magnitude of k_h increases, the point of rotation moves upwards like for $k_v/k_h=0$, the point of rotation moves upward by 5.81%, 7.05% and 10.87% when k_h increases from 0 to 0.1, 0.2 and 0.3 respectively. However, at $Q/V=1$, the upward movement are 0.08%, 1.98% and 7.23% respectively for the same variation of k_h. It is noteworthy that because of the significant pseudo-static forces, the stability of caisson diminishes notably as reflected by larger upward movement of point of rotation in these cases.

Fig. 3.23(b) gives the depth of point of rotation for different k_v/k_h values for various magnitudes of k_h. It is noted that while the depth of point of rotation moves upward with increasing lateral load, it more or less stays unchanged with increasing magnitude of k_v/k_h. Further at $Q/V=1$, the depth of point of rotation almost converges for all magnitudes of k_v/k_h ratios. Hence, depth of point of rotation also reflects that k_h is a more significant parameter than k_v in determining the behavior of caisson.

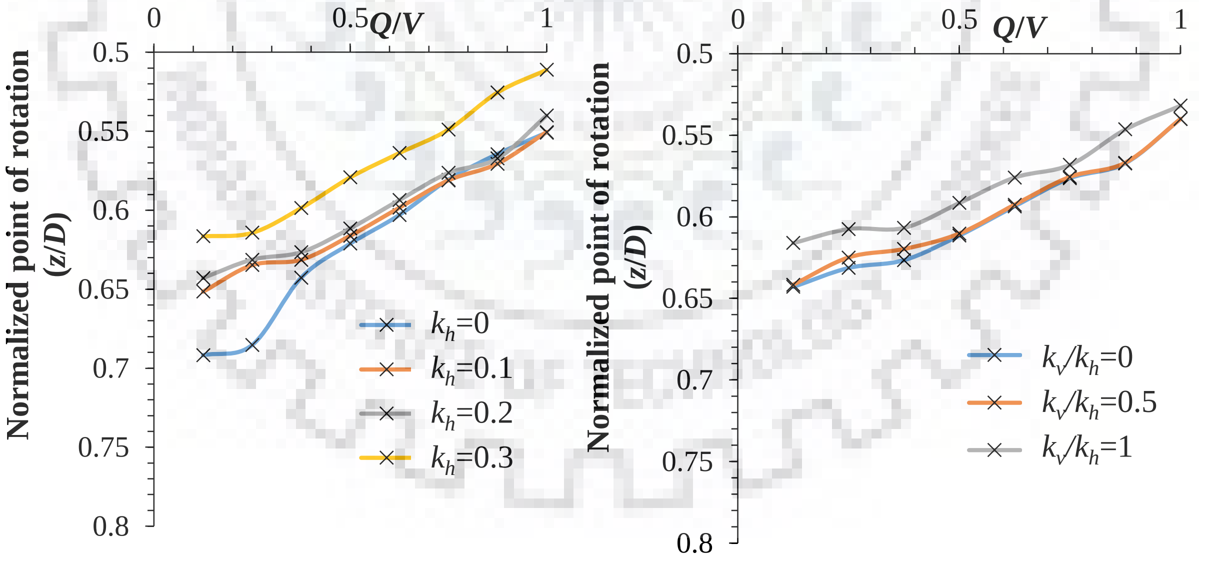

(a) (b)

Fig. 3.23 Variation of depth of point of rotation of caisson with Q/V for (a) different horizontal seismic acceleration coefficients (k_h) when $k_v/k_h=0$ and (b) for different k_v/k_h ratios when $k_h=0.2$ for V=800 kN and $\delta=\phi$

3.4.7 Interaction curves

The present study also deals with development of interaction curves based on the failure obtained from negative magnitude of minimum base pressure. As mentioned in previous sections, a normalizing vertical load V_n is used in order to obtain the interaction curves in normalized form. From the analysis, it is observed that the Q/V value required to develop negative minimum base pressure for even the largest values of vertical load (=1600 kN) bordered around 0.4. Therefore, the normalizing lateral load Q_n was taken as $0.45V_n$, while $Q_n \times (H+D)$ returned the value of normalizing moment M_n.

3.4.7.1 For varying soil-wall friction angle

Fig. 3.24 depicts the interaction diagram in *V-Q-M* space for different magnitudes of δ in static conditions. It can be observed that the interaction curve for larger magnitude of δ lies at the top. The interaction curve for lower magnitudes of δ lies below and to the right of $\delta=\phi$ curve. This indicates that for the same magnitude of vertical load, caisson with lower wall friction angle fail at smaller magnitude of lateral load and moment. Conversely, caissons with smaller wall friction angle subjected to same magnitude of lateral load or moment will require higher magnitude of vertical load to avoid failure. This is because of better load sharing in case of higher magnitude of soil-wall friction angle δ.

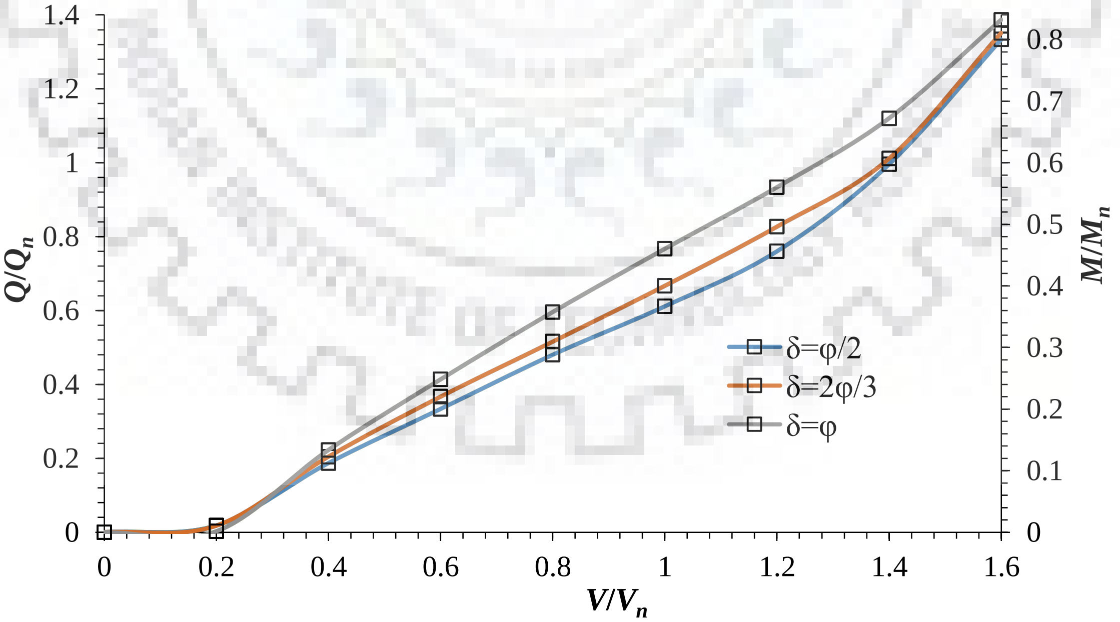

Fig. 3.24 Interaction curves in *V-Q-M* space for caissons with different wall friction angles for static condition ($k_h=k_v=0$)

3.4.7.2 For varying seismic acceleration coefficients

Fig. 3.25 shows the nature of interaction curves in *V*-*Q*-*M* space for varying magnitudes of k_h for $\delta=\phi$. It is observed that for k_v/k_h=0, 0.5 and 1, the interaction curves shift downward and to its right as the magnitude of k_h increases from 0 to 0.3.

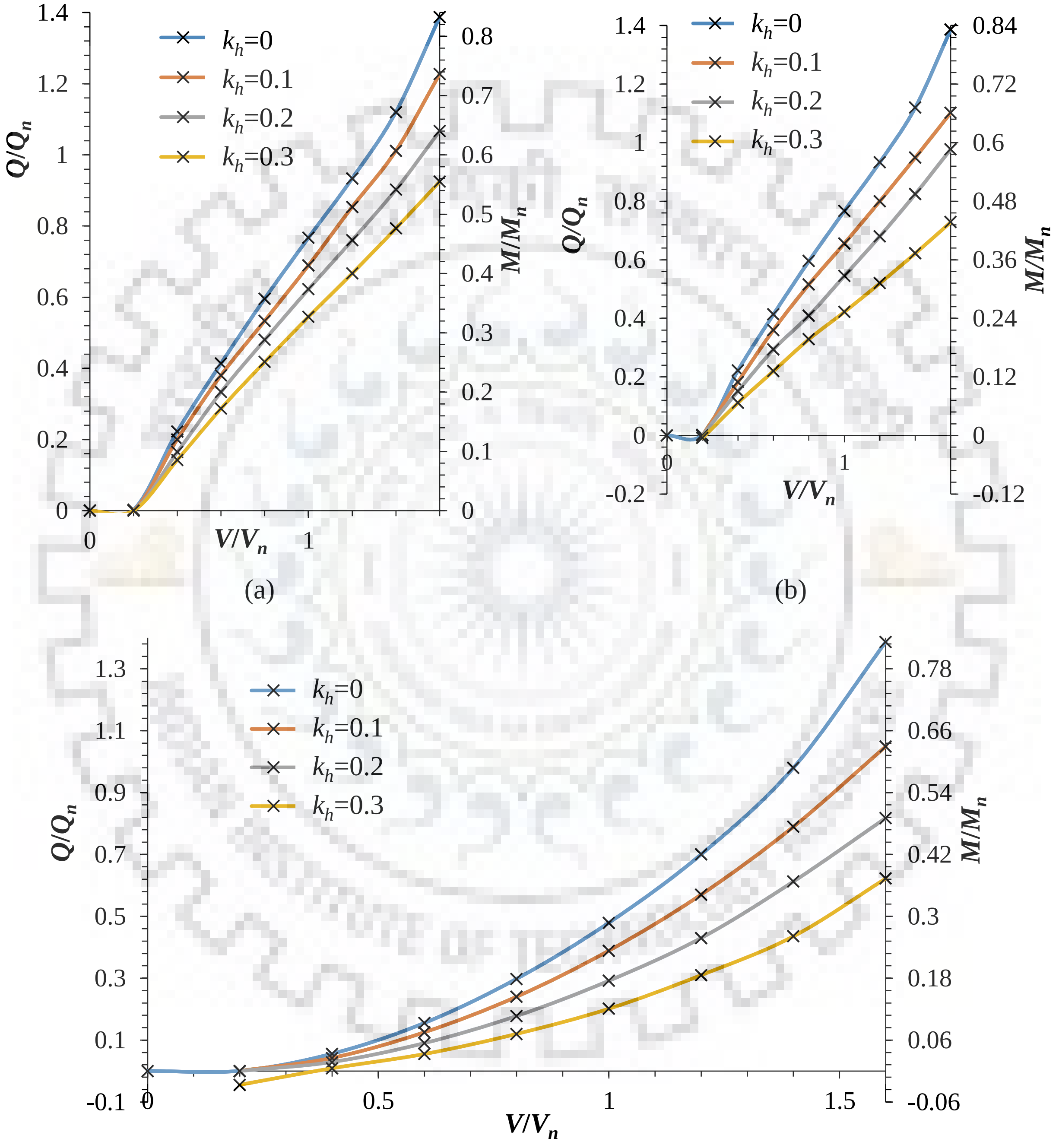

(c)

Fig. 3.25 Interaction curves in *V*-*Q*-*M* space for caissons with different horizontal seismic acceleration coefficients for (a) k_v/k_h=0, (b) k_v/k_h=0.5 and (c) k_v/k_h=1 when $\delta=\phi$

The negative magnitude of Q and M for k_h = 0.3 indicates that load in direction opposite to seismic force must be applied at smaller vertical load level to prevent the system from failing. Similarly, for varying magnitude of k_h, the curves again move downwards and to the right as the magnitude of k_v/k_h increases from 0 to 1 for $\delta=\phi$, as shown in Fig. 3.26. This indicates that ability of caisson to withstand lateral loads and moments reduces for higher magnitudes of k_v.

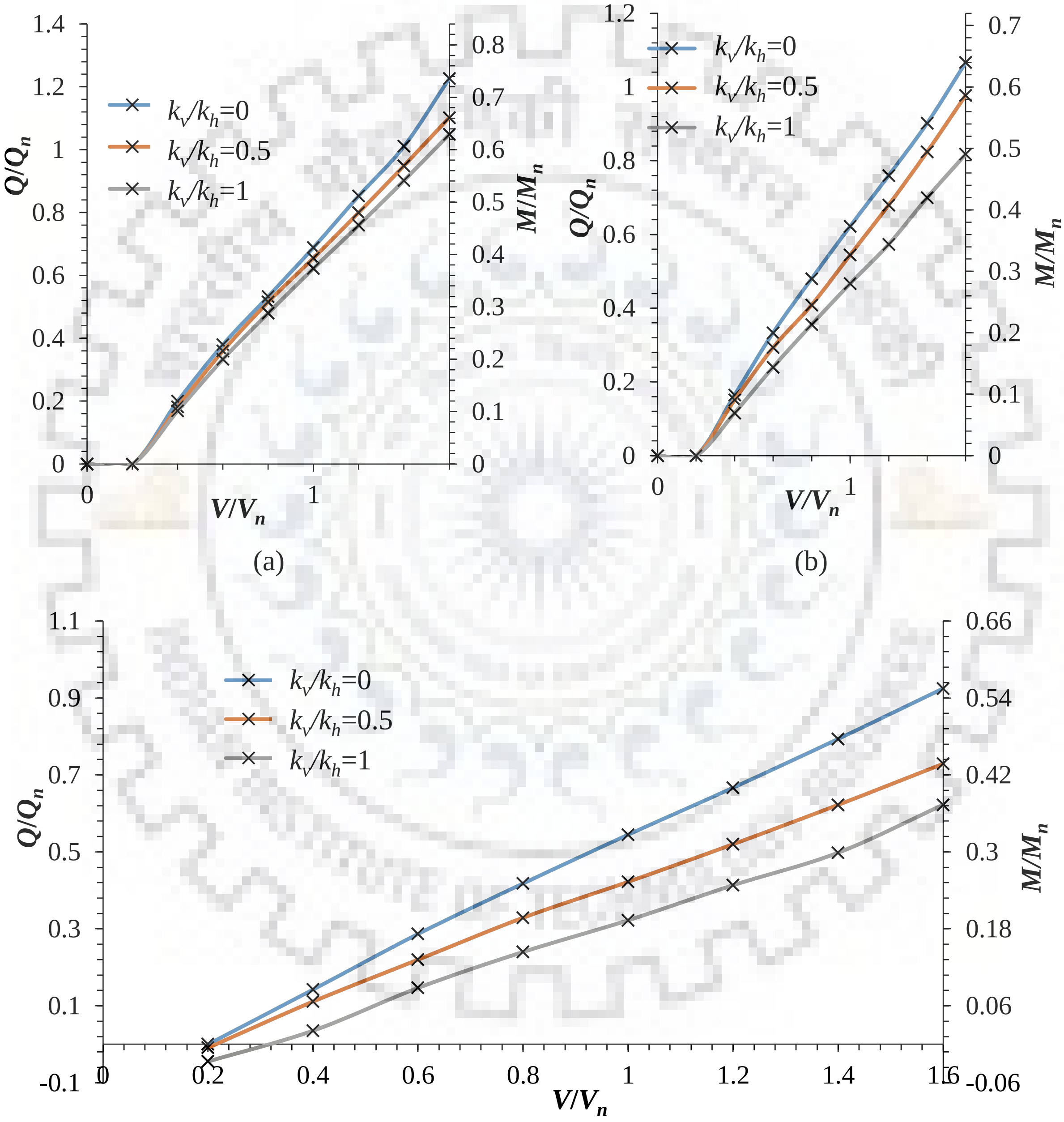

(a)

(b)

(c)

Fig. 3.26 Interaction curves in V-Q-M space for caissons with different k_v/k_h ratios for (a) k_h=0.1, (b) k_h=0.2 and (c) k_h=0.3 when $\delta=\phi$

This is because at higher magnitudes of k_v, the vertical inertia force diminishes which causes the soil beneath to be in tension. However, the interaction curves for varying k_h are more sensitive as they are further apart as compared to the interaction curves for varying k_v. This observation again highlights the fact that the horizontal seismic acceleration coefficient has greater influence on safety of foundation than vertical seismic acceleration coefficient. The interaction diagrams for $\delta=2\phi/3$ and $\delta=\phi/2$ are depicted in Fig. 3.27 through Fig. 3.30.

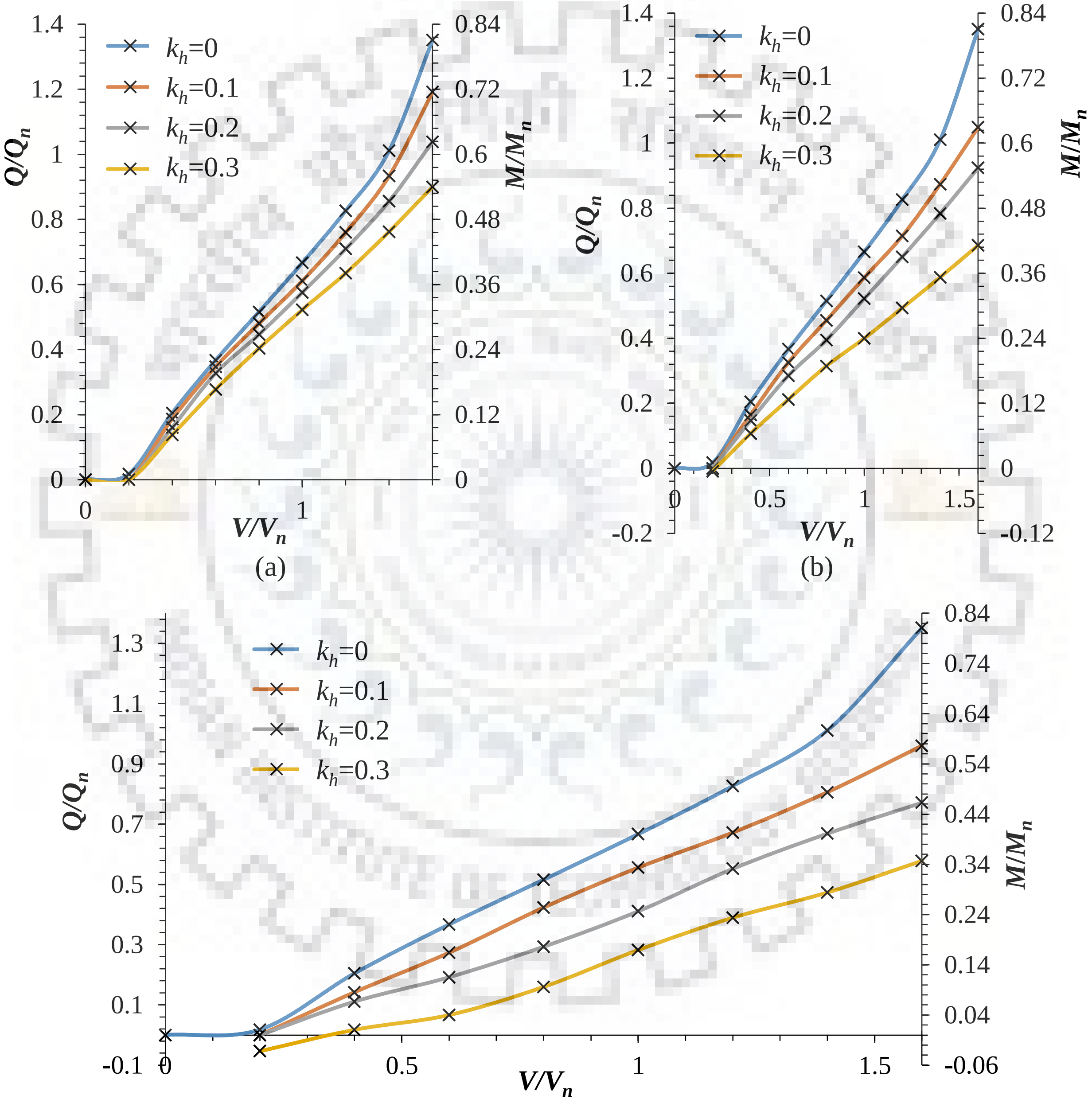

(a) (b)

(c)

Fig. 3.27 Interaction curves in *V-Q-M* space for caissons with different horizontal seismic acceleration coefficients for (a) k_v/k_h=0, (b) k_v/k_h=0.5 and (c) k_v/k_h=1 when $\delta=2\phi/3$

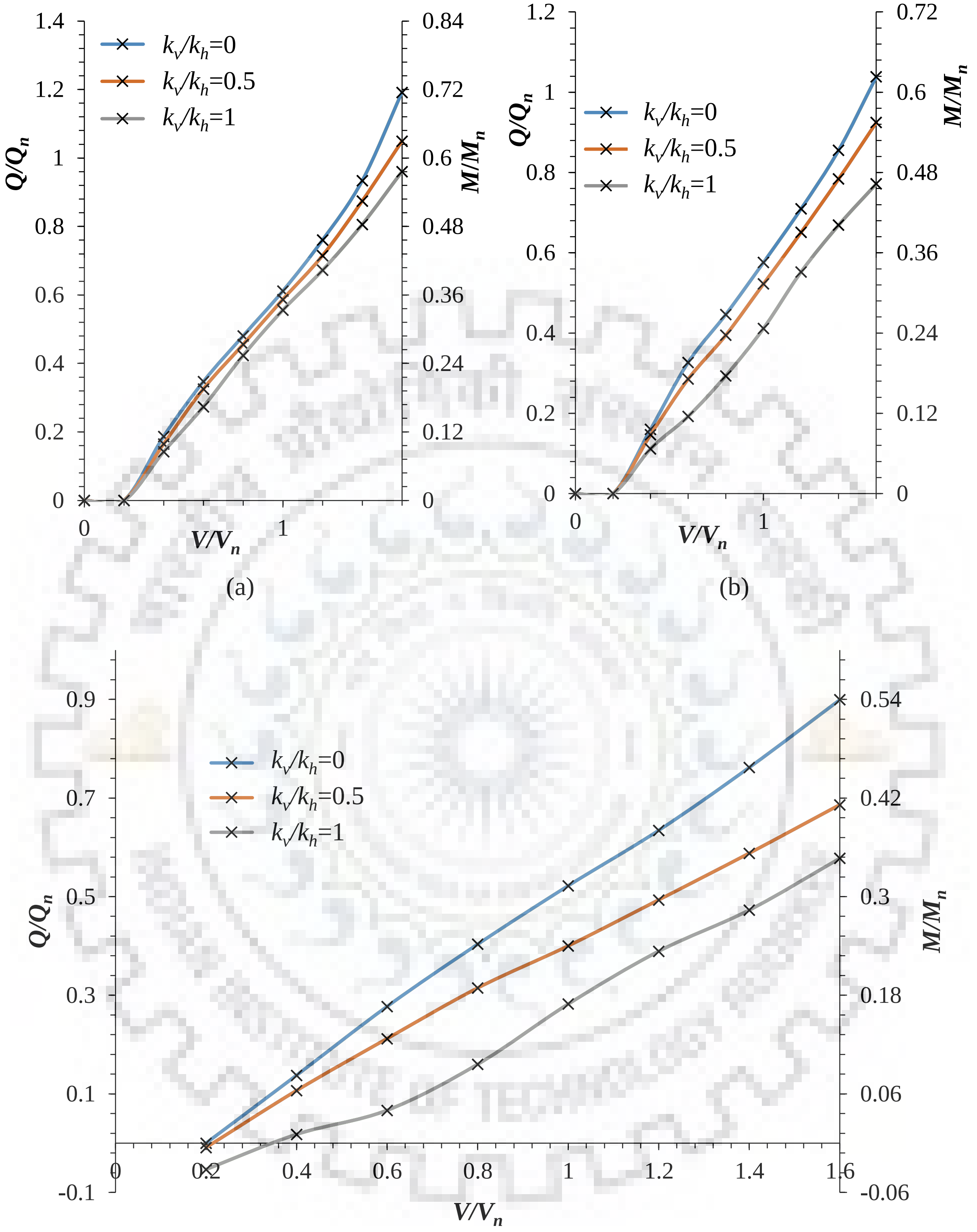

(a) (b)

(c)

Fig. 3.28 Interaction curves in *V*-*Q*-*M* space for caissons with different k_v/k_h ratios for (a) k_h=0.1, (b) k_h=0.2 and (c) k_h=0.3 when δ=2ϕ/3

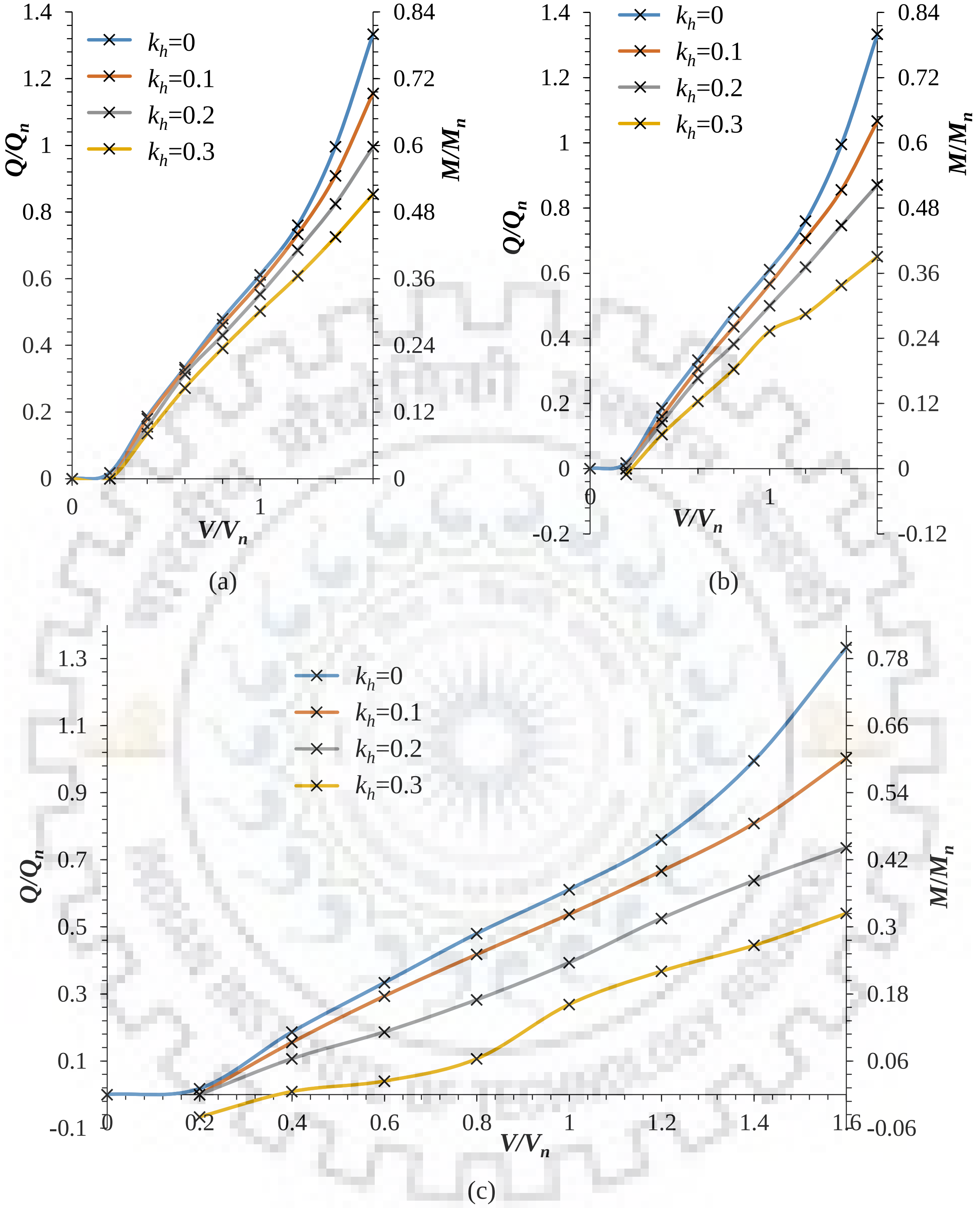

Fig. 3.29 Interaction curves in *V-Q-M* space for caissons with different horizontal seismic acceleration coefficients for (a) k_v/k_h=0, (b) k_v/k_h=0.5 and (c) k_v/k_h=1 when $\delta=\phi/2$

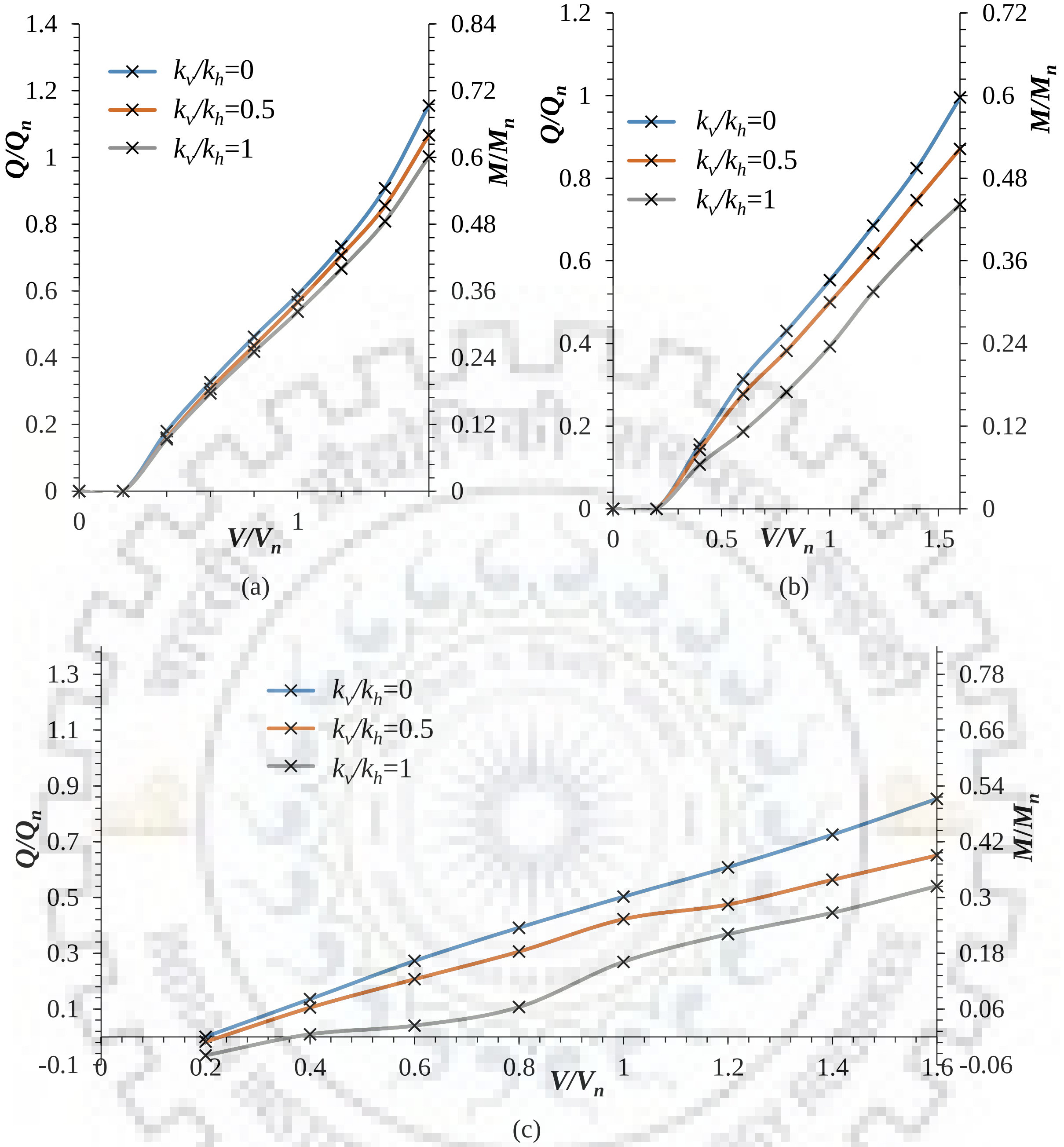

(a)

(b)

(c)

Fig. 3.30 Interaction curves in *V-Q-M* space for caissons with different k_v/k_h ratios for (a) k_h=0.1, (b) k_h=0.2 and (c) k_h=0.3 when $\delta=\phi/2$

3.4.7.3 Calculation of failure loads

The interaction curves are presented in terms of normalized loads at the point of failure. In order to determine the load combination at failure, following steps should be followed:

1. The normalizing vertical load (V_n) is obtained using Eqn. 3.1 based on caisson geometry and soil strength.
2. Q_n and M_n are determined as $0.45V_n$ and $Q_n \times (H+D)$.

3. The design lateral load and moment should be known from the site conditions.
4. The normalized vertical load V/V_n can be obtained based on the various interaction curves presented. The intermediate values can be interpolated from the given interaction diagrams.
5. The vertical load V thus obtained is the minimum required gross weight of caisson-pier-deck system to keep the system from failing.

3.5 Summary

The present numerical study on caissons using ABAQUS finite element code extensively covers the gaps in previous research works by taking into account the effect of layered soil with the provision of pore water in it. The study accounts for material non-linearity, geometric non-linearity and contact non-linearity to accurately model the field conditions. The parametric study considering seismic acceleration coefficients, soil-wall friction angle and varying loading condition attempts to simulate various field conditions. The 3D interaction diagram in addition to the other curves representing lateral soil pressure variation, maximum and minimum base pressure, displacement and tilt and shift of caisson and depth of point of rotation of caisson obtained from this study should be a tool while choosing design loads for the caisson for a variety of loading conditions, site conditions and seismic conditions. Clear steps have been mentioned to use the interaction diagrams as design tools in this chapter.

Chapter 4

NUMERICAL MODELLING OF CAISSON IN LAYERED SOIL TO DETERMINE LOAD SHARING BEHAVIOUR

4.1 General

Caissons are massive foundation system which can be placed under the umbrella of deep foundations as sides of caissons play a major role in resisting the lateral loads acting upon it. The knowledge of load sharing behaviour between base and sides of caisson under any scenario is critical to its design. IRC 45 (1972) proposed methods to determine base and frictional resistance based on elastic theory method and ultimate resistance method. However, very few numerical studies [Jawaid and Madhav (2013)] have been conducted hitherto for determining the load sharing behaviour of caissons. In order to bridge the previous research gaps, the present study aims at finding all the resisting stresses developed on various faces of caisson (lateral soil pressure, horizontal and vertical skin friction, base pressure and base friction) to compute the resisting moments due to these components from the numerical model discussed in Chapter 3. The parametric variation of these components along with shear force diagrams and moment of resistance profile has been reported and finally, regression analysis has been performed to obtain an empirical correlation for the load shared between base and sides of caisson based on various input parameters.

4.2 Proposed Methodology

The details of the numerical model along with material properties and various input parameters have already been discussed in detail in Chapter 3. The stresses developed at different nodes of caisson under applied vertical load (V), lateral load (Q) and moment (M) are obtained, and forces are calculated for entire surfaces using Microsoft Excel [for Microsoft 365 MSO (Version 2204 Build 16.0.15128.20158) 64-bit]. Stresses developed in X-directions, on front and rear face of caisson embedded in soil in direction of loading, as shown in Fig. 4.1 are used to calculate active force and passive resistance developed. Similarly, stresses developed in Z-direction on embedded portion of all the vertical faces of caisson are used to determine vertical skin friction forces. The stresses acting in X-direction on vertical faces, transverse to direction of loading, are used to calculate horizontal skin friction forces which are equal in magnitude due to symmetry of loading and geometry. The stresses acting on base of caisson in X-direction are used to calculate the base friction force and those in Z-direction are used to calculate reaction force on base. All these calculations have been performed using numerical integration of nodal stresses obtained from the numerical analyses using finite element method-based computer program ABAQUS [SIMULIA, (2014)]. The stresses are also used to develop shear force profile and resisting moment profile along the depth of caisson. The resisting moment has been calculated about point of rotation of caisson. The normal and shear nodal stresses have been integrated numerically to obtain resisting forces and moments due to individual components as mentioned in the succeeding section.

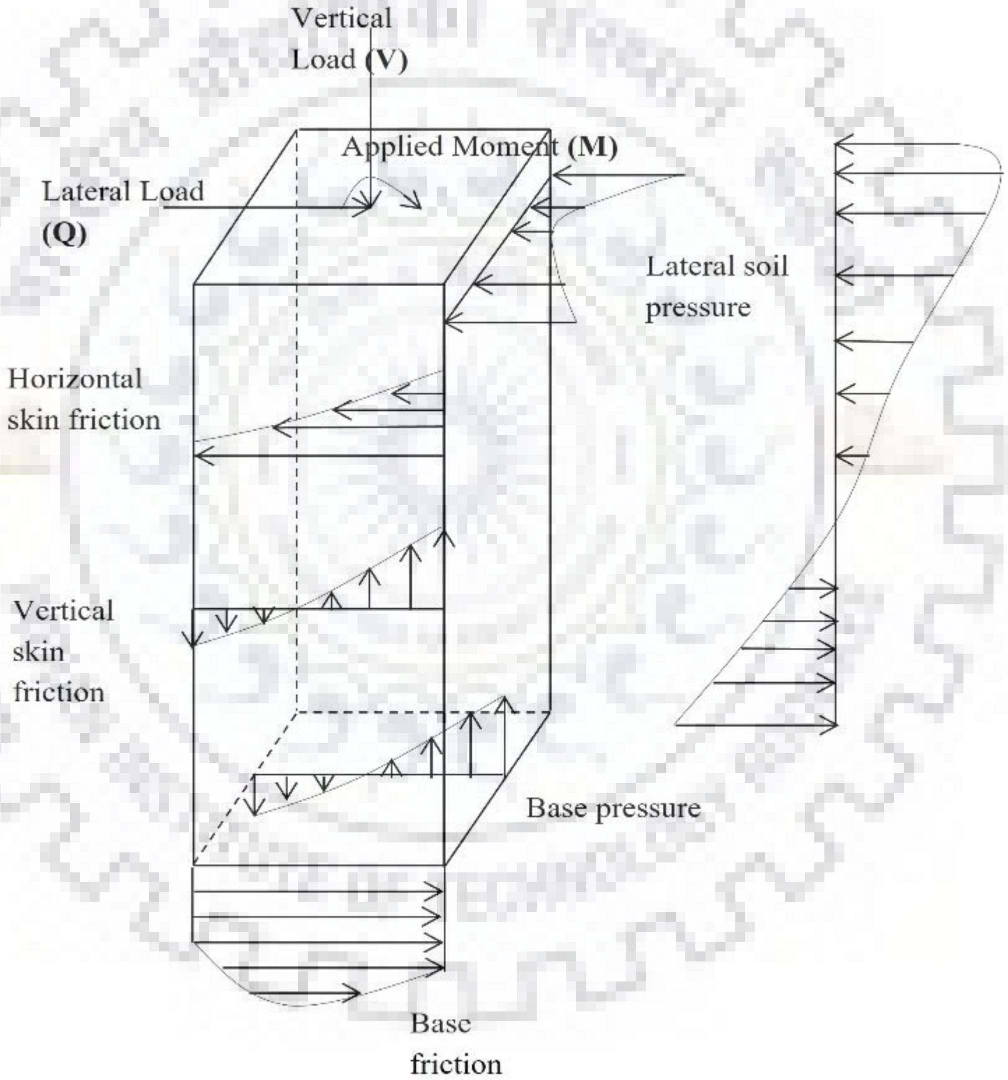

Fig. 4.1 Stresses acting on various faces of caisson under applied loads *V*, *Q* and *M*

4.2.1 Computation of resistive forces and moments

The stresses on the caisson are integrated over area of caisson faces to obtain various resistive forces and moments. Fig. 4.2 illustrates the calculation process for forces and resistive moments due to lateral soil pressure where d_p is the depth of point of rotation from scour level.

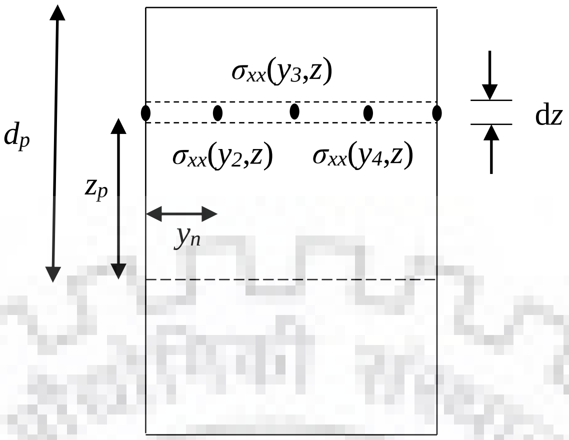

Fig. 4.2 Computation of force and moment due to lateral soil pressure

The surrounding soil applies earth pressure on caisson face. The net resulting force acting on a given portion of caisson face is the volume of the stress profile in the horizontal and vertical plane projected on that portion of caisson face. The volume of the stress profile is obtained using numerical integration (Simpson's 1/3rd rule). From Fig. 4.2, the force (F_{xx}) acting in X-direction on the strip of thickness dz at depth z on plane normal to X-axis is obtained as:

$$F_{xx}(z) = \frac{y_n}{3}\left[\{\sigma_{\mathrm{xx}}(y_1,z) + \sigma_{\mathrm{xx}}(y_5,z)\} + 4\times\{\sigma_{\mathrm{xx}}(y_2,z) + \sigma_{\mathrm{xx}}(y_4,z)\} + 2\times\sigma_{\mathrm{xx}}(y_3,z)\right]\times \mathrm{d}z \qquad (4.1a)$$

where, $\sigma_{xx}(y_i,z)$ are the axial nodal stresses obtained from numerical analysis at depth z and y_n is the horizontal spacing between the nodes. The moment of resistance about point of rotation due to force (F_{xx}) acting at depth z is calculated as product of force acting on a strip of caisson and the vertical distance of its centre of gravity from the point of rotation (z_p).

$$M_{xx}(z) = F_{xx}(z)\times z_p \qquad (4.1b)$$

The horizontal skin friction force acting on side faces of caisson (normal to Y-axis) is obtained as:

$$F_{xy}(z) = \frac{x_n}{3}\left[\left\{\sigma_{\mathrm{xy}}(x_1,z) + \sigma_{\mathrm{xx}}(x_5,z)\right\} + 4\times\left\{\sigma_{\mathrm{xy}}(x_2,z) + \sigma_{\mathrm{xy}}(x_4,z)\right\} + 2\times\sigma_{\mathrm{xy}}(x_3,z)\right]\times \mathrm{d}z \qquad (4.2a)$$

where, $\sigma_{xy}(x_i,z)$ are the shear nodal stresses obtained from numerical analysis at depth z and x_n is the horizontal spacing between the nodes on side faces.

$$M_{xy}(z) = F_{xy}(z) \times z_p \tag{4.2b}$$

Fig. 4.3 shows the procedure for calculating vertical skin friction force $\{F_{zy}(\mathrm{x})\}$ acting on side faces of caisson. Simpson's one third rule is again used to calculate the magnitude of $F_{zy}(\mathrm{x})$ over entire depth of caisson for a strip of thickness dx.

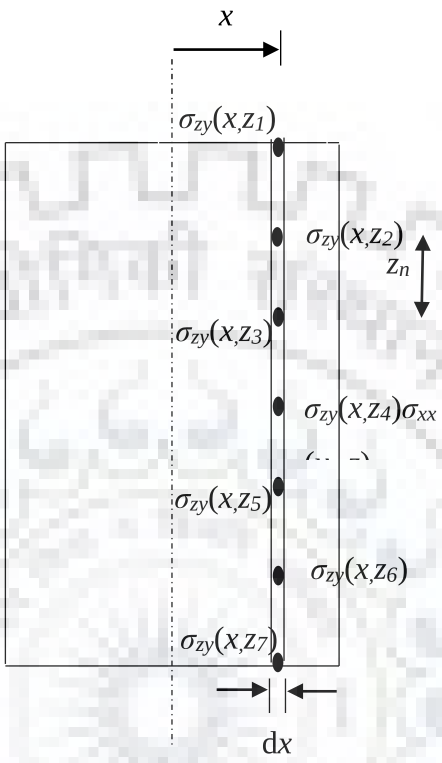

Fig. 4.3 Computation of force and moment due to vertical skin friction

$$F_{zy}(x) = \frac{z_n}{3}\left[\{\sigma_{zy}(z_1,x) + \sigma_{zy}(z_7,x)\} + 4 \times \{\sigma_{zy}(z_2,x) + \sigma_{zy}(z_4,x) + \sigma_{zy}(z_6,x)\} + 2 \times \{\sigma_{zy}(z_3,x) + \sigma_{zy}(z_5,x)\}\right] \times \mathrm{d}x \tag{4.3a}$$

where, $\sigma_{zy}(x,z_i)$ is the nodal shear stress obtained from numerical analysis at horizontal offset x and z_n is the vertical spacing between the nodes. The magnitudes of vertical shear stresses on both the side faces are equal because of symmetry of loading and geometry. If x_p is the horizontal distance between centre of gravity of strip of caisson under consideration and point of rotation in horizontal plane, the resisting moment due to vertical skin friction developed on thin strip on side faces is obtained as:

$$M_{zy}(x) = F_{zy}(x) \times x \tag{4.3b}$$

The vertical skin fiction force on front and rear faces of caisson are calculated in similar manner to that mentioned above. The vertical shear force on front and rear face is found using Eqn. (4.4a). The distance between line of action of shear force and the axis containing point of rotation is always *B*/2, where *B* is the width of the caisson. The resisting moment is thus computed using Eqn. (4.4b).

$$F_{zx}(y) = \frac{z_n}{3}[\{\sigma_{zx}(z_1, y) + \sigma_{zx}(z_7, y)\} + 4 \times \{\sigma_{zx}(z_2, y) + \sigma_{zx}(z_4, y) + \sigma_{zx}(z_6, y)\} + 2 \times \{\sigma_{zx}(z_3, y) + \sigma_{zx}(z_5, y)\}] \times \mathrm{d}y \qquad (4.4a)$$

$$M_{zx}(y) = F_{zx}(y) \times \frac{B}{2} \qquad (4.4b)$$

Similarly, the base reaction {$F_{zz}(x)$} on a strip of caisson at distance *x* from the projection of point of rotation on horizontal plane as shown in Fig. 4.4 is obtained using Eqn. (4.5a) and the resisting moment due to this component is calculated as product of $F_{zz}(x)$ and horizontal distance between centre of gravity of strip and projection of point of rotation (*x*).

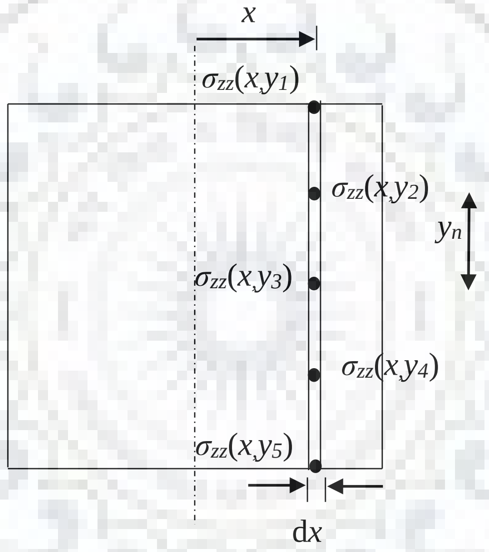

Fig. 4.4 Computation of force and moment due to base reaction

$$F_{zz}(x) = \frac{y_n}{3}[\{\sigma_{zz}(x, y_1) + \sigma_{zz}(x, y_5)\} + 4 \times \{\sigma_{zz}(x, y_2) + \sigma_{zz}(x, y_4)\} + 2 \times \sigma_{zz}(x, y_3)] \times \mathrm{d}x \qquad (4.5a)$$

$$M_{zz}(x) = F_{zz}(x) \times x \qquad (4.5b)$$

where, $\sigma_{zz}(x,y_i)$ is the vertical nodal normal stress acting on base of caisson obtained from numerical analysis at horizontal offset *x*. y_n is the vertical spacing between the nodes in the numerical model and has been obtained as 0.375 m from sensitivity analysis in Chapter 3.

The base friction force {$F_{zx}(y)$} in direction of loading at horizontal offset *y* in transverse direction to loading is obtained using Eqn. (4.6a) and the resisting moment {$M_{zx}(y)$} is computed as product of $F_{zx}(y)$ and normal distance between point of rotation and base of caisson (D-d_p).

$$F_{zx}(y) = \frac{x_n}{3}\left[\{\sigma_{zx}(y, x_1) + \sigma_{zx}(y, x_5)\} + 4 \times \{\sigma_{zx}(y, x_2) + \sigma_{zx}(y, x_4)\} + 2 \times \sigma_{zx}(y, x_3)\right] \times \mathrm{d}y \qquad (4.6a)$$

$$M_{zx}(y) = F_{zx}(y) \times \frac{(D - d_p)}{2} \qquad (4.6b)$$

The magnitudes of all these forces and moments are calculated over entire surface they act upon to determine total force and resisting moment profile due to that force.

4.3 Present Study

The present study deals with calculation of different resistive forces acting on a caisson embedded in layered soil strata for different magnitudes of vertical load (V), lateral load (Q), soil-wall friction angle (δ), and horizontal and vertical seismic acceleration coefficients (k_h and k_v), as listed in Table 3.1. These force components are further used to compute the resisting moment due to individual forces as mentioned in the previous section. The resisting moment due to forces acting on vertical faces of caisson (lateral soil pressure on front and rear face, horizontal skin friction on side faces, vertical skin friction on all the vertical faces) is summed up to obtain the total resisting moment derived from vertical faces of caisson (M_{sides}). Similarly, the resisting moments due to forces acting on base of caisson (base reaction and base friction force) are added up to obtain the resisting moment offered by base of caisson (M_{base}). The load share of sides of caisson (LS_{sides}) and base of caisson (LS_{base}) in percentage is computed as:

$$LS_{sides}(\%) = \frac{M_{sides}}{M_{sides} + M_{base}} \times 100 \qquad (4.7a)$$

$$LS_{base}(\%) = \frac{M_{base}}{M_{sides} + M_{base}} \times 100 \qquad (4.7b)$$

Based on the magnitudes of load shared by sides and base of caisson obtained from the present study for different input parameters, regression analysis has been performed to generate a generalized empirical correlation to obtain load share of sides for any combinations of input parameters. The magnitudes of x_n, y_n and z_n in the present study is equal to the mesh dimension obtained from sensitivity analysis, i.e., 0.375 m. Similarly, the width of caisson (B) is 1.5 m and embedment depth (D) is 2.25 m, as mentioned in previous chapter. Depth of point of rotation from scour level (d_p) is computed in Chapter 3.

4.4 Results and Discussion

Different stress components on various caisson faces have been obtained and used to calculate resistive forces and moments. The variation of lateral soil pressure has already been discussed in the previous chapter. The variation of horizontal skin friction, vertical skin friction on front, rear and side faces, base reaction and base friction force has been discussed in detail in this section. In addition, shear force diagram and moment of resistance variation with depth has been plotted and discussed. Furthermore, empirical correlation between load shared by sides of caisson has been developed based on the results of numerical analysis.

4.4.1 Horizontal skin friction

4.4.1.1 Influence of normalized lateral load (Q/V) on horizontal skin friction profile

Fig. 4.5 and Fig. 4.6 depicts the variation of horizontal skin friction with applied lateral load along depth and width of side face of caisson (face transverse to direction of loading) respectively. It is observed that the magnitude of horizontal skin friction decreases from edge to the center of caisson because of the higher stress concentration that takes place at edges.

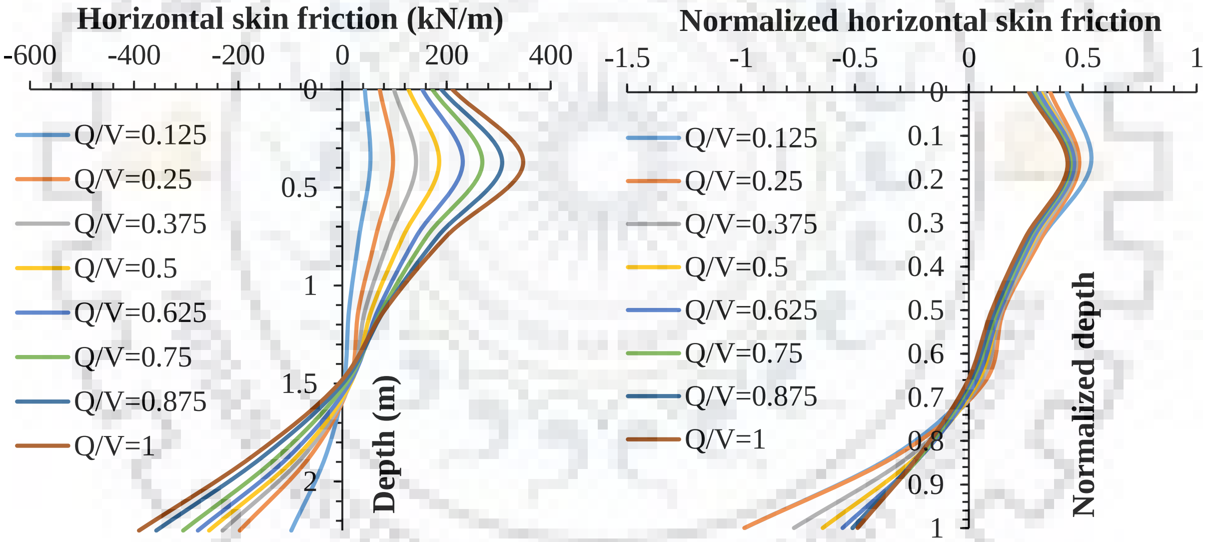

(a) (b)

Fig. 4.5 Variation of (a) horizontal skin friction and (b) normalized horizontal skin friction along depth for different lateral load magnitudes for V=800 kN and $\delta=\phi$

For a vertical loading of 800 kN under static conditions with $\delta=\phi$, as the lateral load increases by 25%, the horizontal skin friction increases by 29.11% at center and 29.73% at edges. Higher magnitude of lateral load directly leads to larger displacement of caisson which generates higher friction force. The horizontal skin friction at any depth is guided by two major factors, i.e., the normal stress acting on caisson due to surrounding soil and the displacement of caisson with respect to soil. The displacement at top of scour level is maximum but the normal stress is negligible because of zero overburden pressure. As the depth increases, the normal stress increases but the displacement decreases. The maximum magnitude of horizontal skin friction thus occurs at a depth slightly below the scour level. It is seen from Fig. 4.5(b) that this depth is 0.2*D* for all magnitudes of lateral loads. The magnitude of horizontal skin friction decreases with increasing depth, changes sign at a certain depth and then keep increasing in the other direction. The change in direction of horizontal skin friction is because of movement of bottom portion of caisson in direction opposite to applied lateral load due to rotation of caisson about a point above the base.

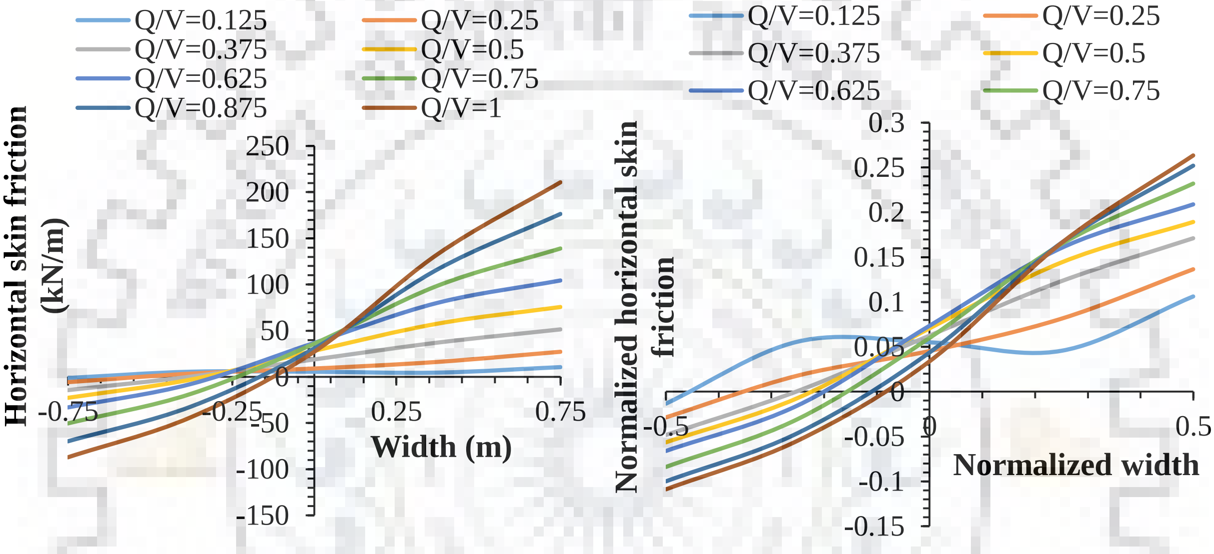

(c) (d)

Fig. 4.6 Variation of (a) horizontal skin friction and (b) normalized horizontal skin friction along width of caisson for different lateral load magnitudes for V=800 kN and $\delta=\phi$

The normalization of horizontal skin friction is done with respect to applied lateral load because it is the direct effect of the displacement caused due to lateral load. It is found that the normalized horizontal skin friction reduces as the lateral load increases which indicates that the horizontal skin friction does not increase linearly with increasing lateral load along depth of caisson. However, the absolute value of normalized horizontal skin friction along width of caisson is found to increase with increasing lateral load for a fixed vertical load.

4.4.1.2 Influence of vertical load (V) on horizontal skin friction profile

Fig. 4.7 and Fig. 4.8 depicts the variation of horizontal skin friction along depth and width of side face of caisson respectively with applied vertical load. As mentioned in the previous section, the skin friction force changes direction at greater depth. It is also observed that the magnitude of horizontal skin friction increases from trailing edge to leading edge of side face of caisson in direction of loading because the leading edge penetrates through undisturbed soil and derives high magnitudes of normal stress and thus higher skin friction. On the other hand, the rear end of side wedge moves through highly disturbed soil and the soil displacement at back end is greater than the caisson displacement which causes negative horizontal skin friction. For a fixed Q/V value, the magnitude of lateral load (Q) increases with increasing vertical load (V). Thus, horizontal skin friction force increases with increasing vertical load since it is a direct effect of applied lateral load. For $Q/V=0.25$ under static conditions with $\delta=\phi$ (soil friction angle), the horizontal skin friction is found to increase by about 25 kN/m as the vertical load increases by 200 kN at a depth of $D/6$.

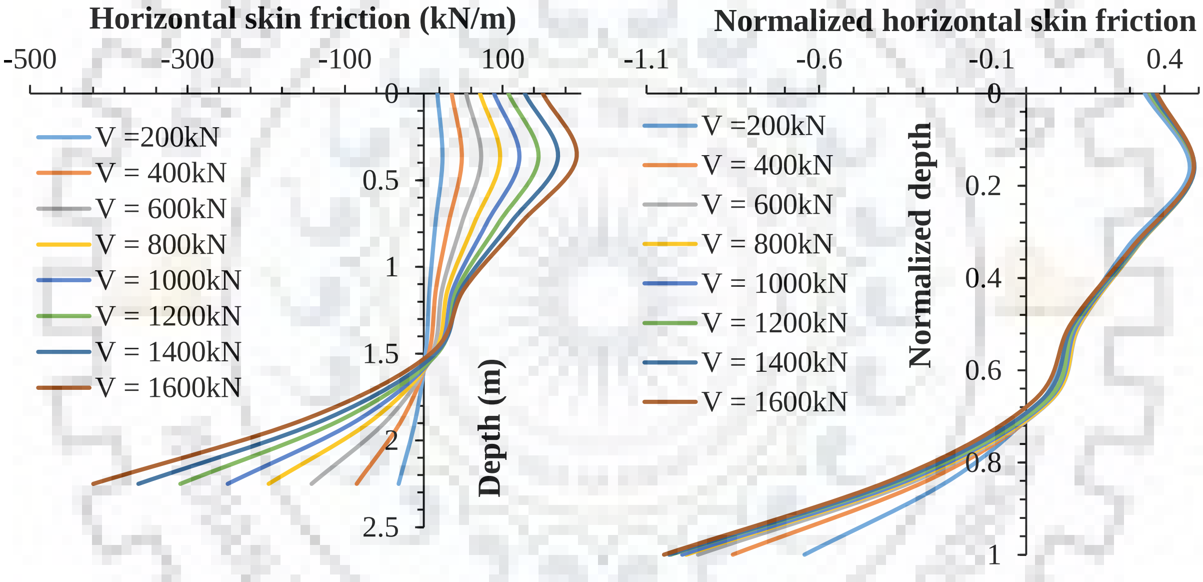

(a) (b)

Fig. 4.7 Variation of (a) horizontal skin friction and (b) normalized horizontal skin friction along depth for different vertical load magnitudes for $Q/V=0.25$ and $\delta=\phi$

The normalization of horizontal skin friction with respect to the lateral load causing it revealed that the horizontal skin friction distribution along depth of caisson reduces to roughly a single curve which suggests that for a constant Q/V value, the horizontal skin friction force profile per unit applied lateral load is roughly independent of magnitude of vertical load. On the other hand, the horizontal skin friction along width of caisson does not increase in proportion to increasing vertical load for a constant Q/V ratio, i.e., as the vertical load increases, the horizontal skin friction, normalized with respect to applied lateral load, reduces as is evident from Fig. 4.8(b).

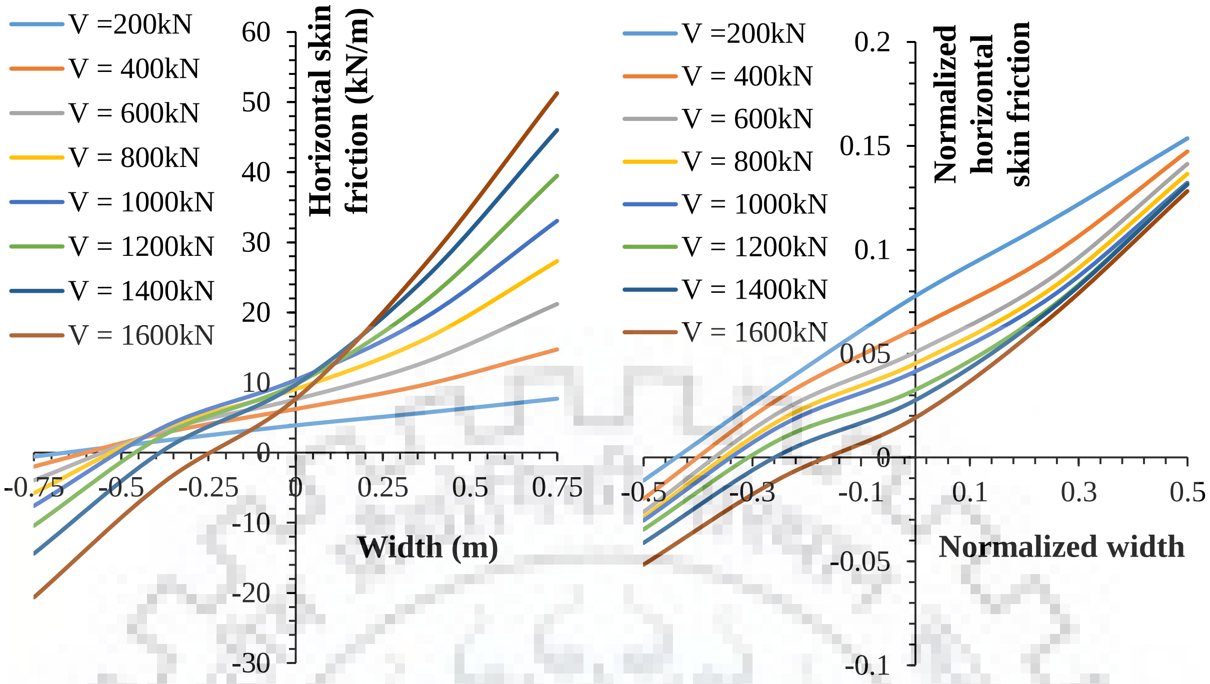

(a) (b)

Fig. 4.8 Variation of (a) horizontal skin friction and (b) normalized horizontal skin friction along width for different vertical load magnitudes for Q/V=0.25 and $\delta=\phi$

4.4.1.3 Influence of soil-wall friction angle (δ) on horizontal skin friction profile

The horizontal skin friction acting over caisson is guided by two aspects of soil-wall friction angle. The higher frictional coefficient for higher soil-wall friction angle and the reduced displacement (as seen in previous Chapter) causing lower mobilization of frictional force for higher soil-wall friction angle. The net effect of these two phenomena is reflected in the normalized horizontal skin friction profile over depth and width of caisson as shown in Fig. 4.9. It is observed that, for V=800 kN, as δ/ϕ increases from 1/2 to 2/3 and 1 under static conditions, the normalized horizontal skin friction force, over entire width of caisson at normalized depth of 1/6, diminishes by 5.48% and 7.58% respectively at Q/V=0.25 and increases by 0.45% and 1.51% respectively at Q/V=0.75. For same set of input parameters, the normalized horizontal skin friction over entire depth at leading edge of caisson decreases by 13.55% and 35.18% respectively for Q/V=0.25 and 7.74% and 21.44% respectively for Q/V=0.75. Therefore, the net effect of increasing soil-wall friction angle over normalized horizontal skin friction is guided by reducing displacement of caisson causing it to decrease for a given set of input parameters.

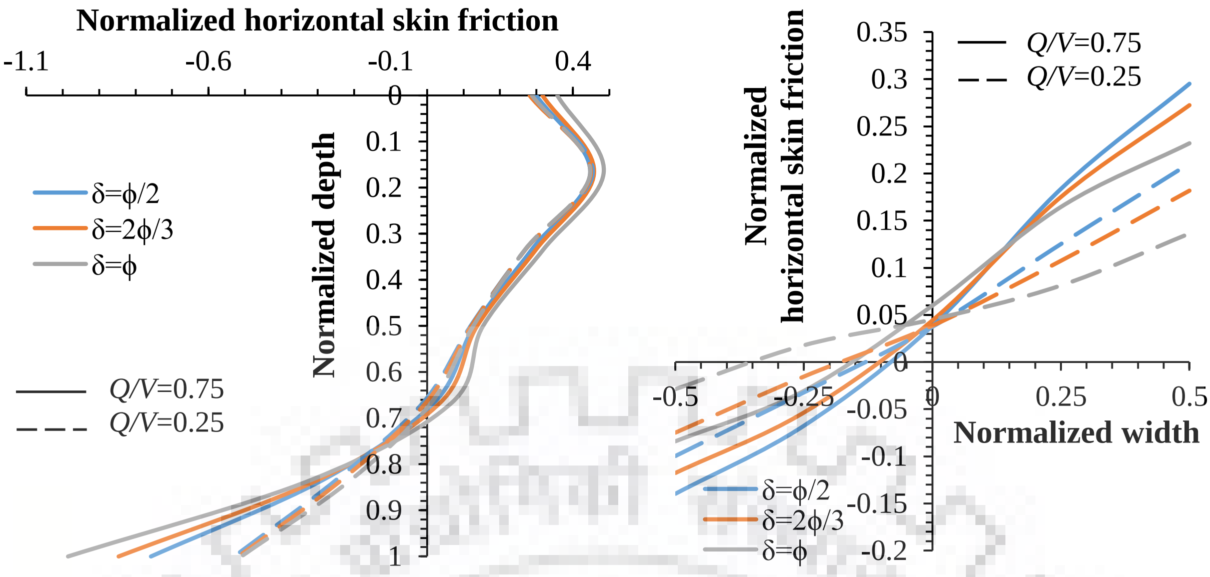

(a) (b)

Fig. 4.9 Variation of normalized horizontal skin friction with soil-wall friction angle along (a) depth and (b) width of caisson

4.4.1.4 Influence of seismic acceleration coefficients (k_h and k_v) on horizontal skin friction profile

Fig. 4.10 to Fig. 4.12 depict the variation of normalized horizontal skin friction with horizontal and vertical seismic acceleration coefficients along width and depth of caisson. It is observed that the magnitude of normalized horizontal skin friction increases along width and depth of caisson with both k_h and k_v. It could also be distinctly observed that increase in normalized horizontal skin friction is significant for increasing k_h values while it is nominal for increasing k_v. As the magnitude of k_h increases, the soil surrounding the caisson densifies in addition to pronounced translation of caisson under seismic inertial force. This causes the magnitude of normalized horizontal skin friction to increase significantly with increasing k_h value. For a vertical loading of 800 kN, k_v=0 and $\delta=\phi$ (soil-wall friction angle), the horizontal skin friction, normalized with respect to applied lateral load, increases by 41.83%, 83.93% and 175.68% at front edge of caisson on side face in direction of loading when k_h increases from 0 to 0.1, 0.2 and 0.3 respectively for Q/V=0.25. The percentage increase is 12.51%, 25.69% and 67.78% respectively for Q/V=0.75 with all other parameters remaining the same. Similarly, the normalized horizontal skin friction force increases by 5.35%, 10.95% and 40.21% respectively at Q/V=0.25 and 18.08%, 35.82% and 91.6% respectively at Q/V=0.75 at normalized depth (z/D) of 1/6.

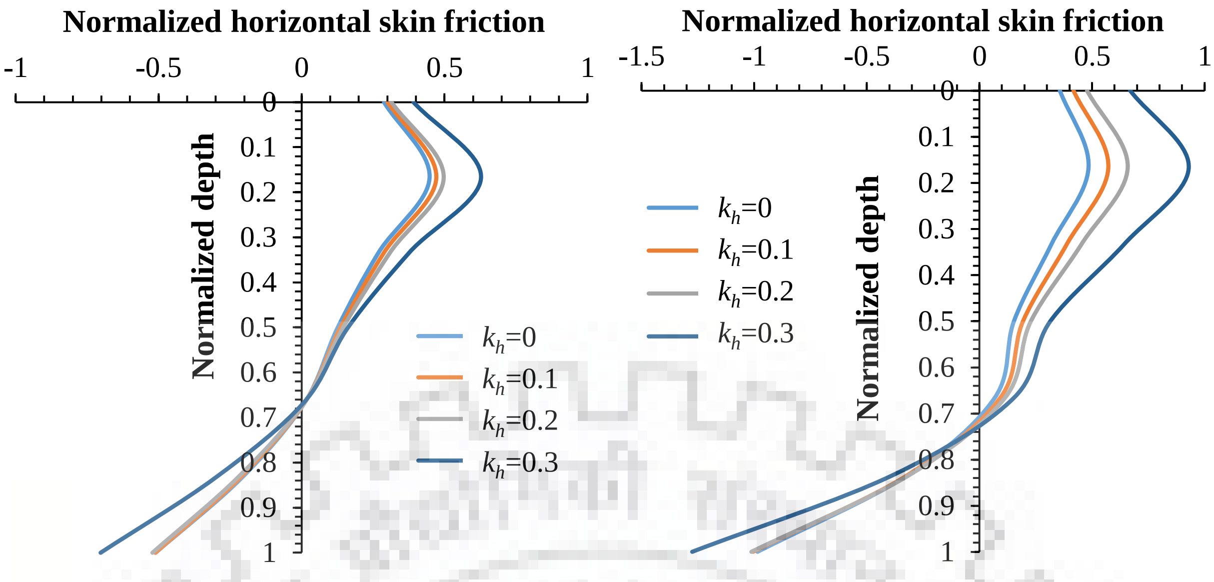

(a) (b)

Fig. 4.10 Variation of normalized horizontal skin friction with horizontal seismic acceleration coefficient along depth of caisson for (a) Q/V=0.25 and (b) Q/V=0.75

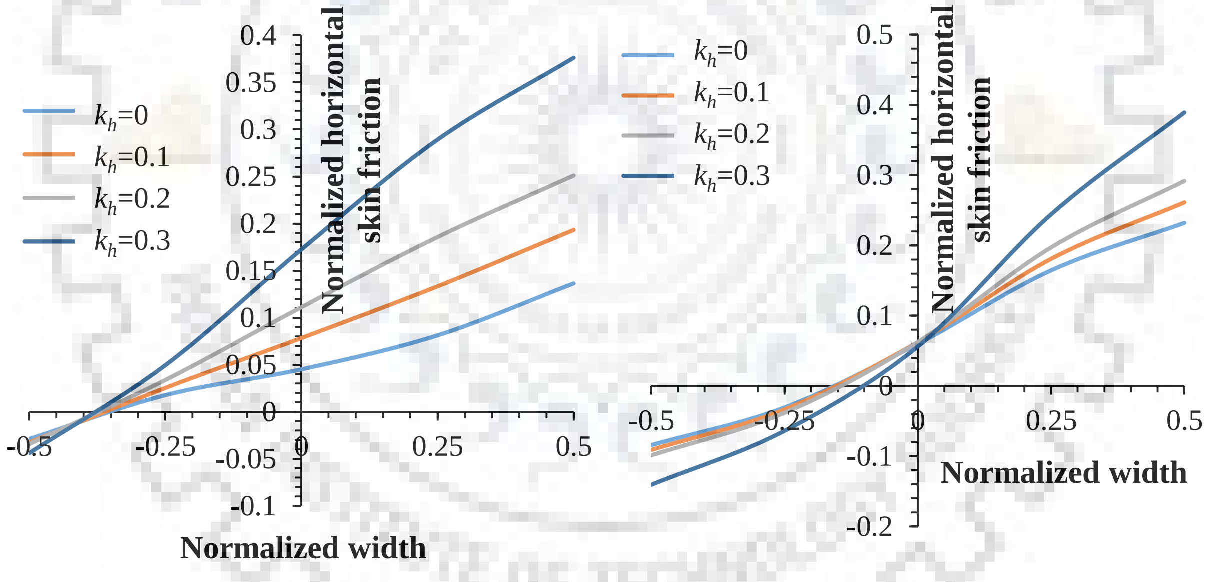

(a) (b)

Fig. 4.11 Variation of normalized horizontal skin friction with horizontal seismic acceleration coefficient along width of caisson for (a) Q/V=0.25 and (b) Q/V=0.75

The effect of k_v, despite being indirect, facilitates the translation of caisson under the action of applied lateral load by reducing base pressure and base friction due to reduced normal reaction. The normalized horizontal skin friction at all depths varies by less than 0.5% as k_v increases from 0 to $k_h/2$ and k_h. The increase in normalized horizontal skin friction is found to be 2.04% and 4.62% as k_v increases from 0 to $k_h/2$ and k_h respectively for Q/V=0.25

and 2.76% and 5.87% respectively for Q/V=0.75 at the front edge of caisson along width of caisson in direction of loading.

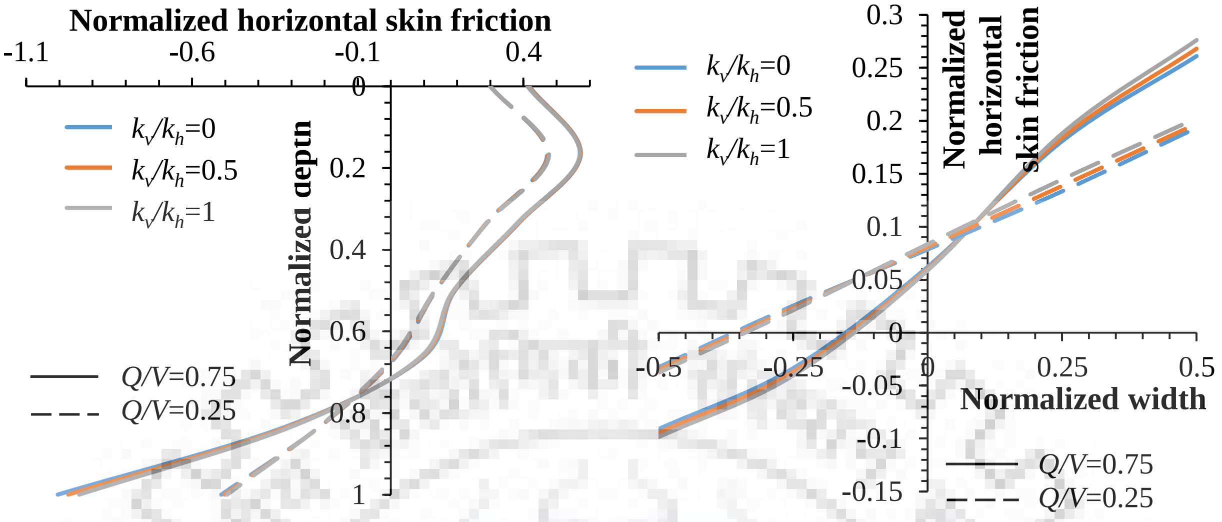

(a) (b)

Fig. 4.12 Variation of normalized horizontal skin friction with vertical seismic acceleration coefficient along (a) depth and (b) width of caisson

4.4.2 Vertical skin friction

Horizontal skin friction is generated on faces transverse to direction of loading (side faces of caisson). Unlike horizontal skin friction, vertical skin friction acts on all the four vertical faces of the embedded portion of caisson. The sensitivity of vertical skin friction to various input parameters has been discussed in this section.

4.4.2.1 Influence of normalized lateral load (Q/V) on vertical skin friction

Fig. 4.13 to Fig. 4.18 illustrate the impact of lateral loading on vertical skin friction acting along embedded depth and width of front face, rear face and side face of caisson. The nature of curves is also observed by normalizing vertical skin friction with respect to applied lateral load, which causes the vertical component of displacement due to the tilt of caisson and thus alters the vertical skin friction under the action of vertical load only. It can be observed that both absolute and normalized vertical skin friction increases with increasing magnitude of lateral load on front and rear vertical faces along depth and width of caisson while it reduces on side face. For vertical load of 800 kN and $\delta=\phi$ under static conditions, an

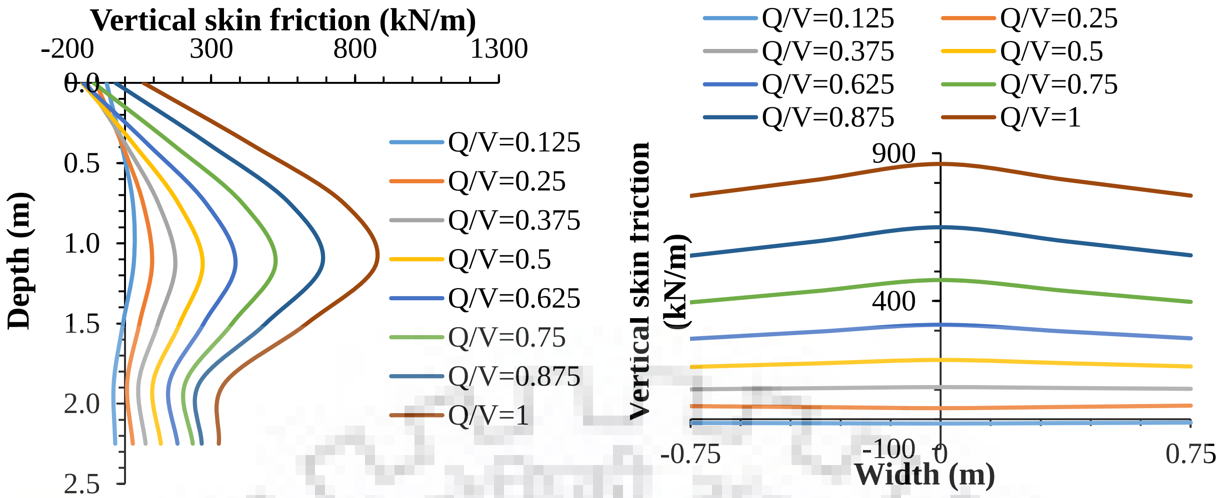

(a) (b)

Fig. 4.13 Variation of vertical skin friction on front face of caisson along (a) depth and (b) width for different lateral load magnitudes for V=800 kN and $\delta=\phi$ under static conditions

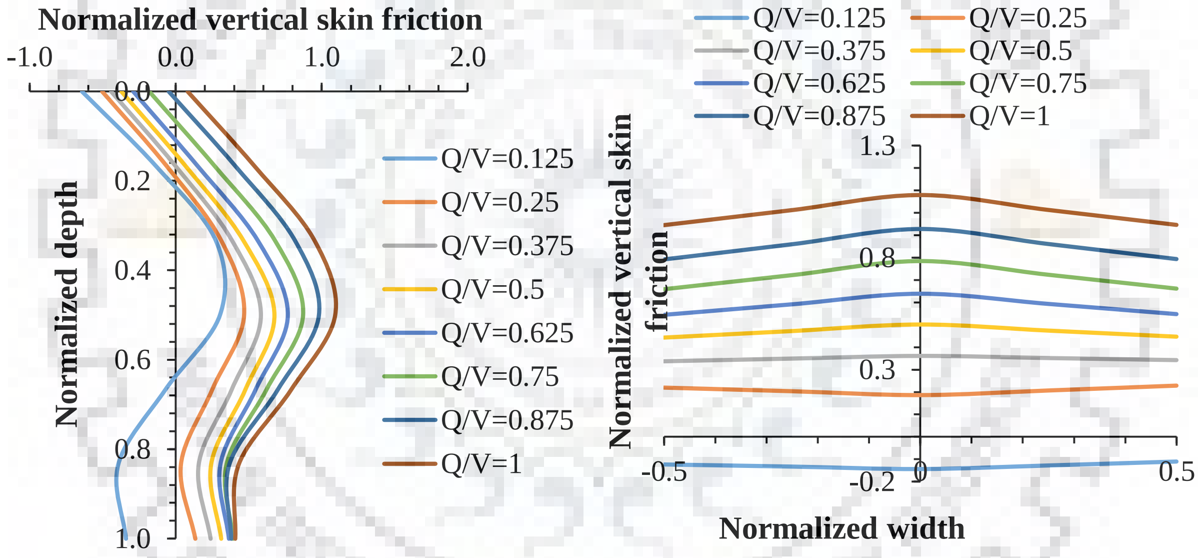

(a) (b)

Fig. 4.14 Variation of normalized vertical skin friction on front face of caisson along (a) depth and (b) width for different lateral loads for V=800 kN and $\delta=\phi$ under static conditions

increase in normalized lateral load from 0.25 to 0.375 and from 0.75 to 0.875 causes the vertical skin friction on front face to increase by 86.27% and 31.32% respectively, while the increase is 102.66% and 44.92% respectively at top of rear face of caisson. For the same set of input parameters, the vertical skin friction remains virtually unaffected by increasing lateral load from Q/V=0.125 to 0.375 while it reduces by 11.8% and 41.14% as Q/V increases from 0.375 to 0.5 and 0.75 to 0.875 respectively. The magnitude of vertical skin friction across width of caisson is observed to increase with increasing lateral loads on all the vertical faces.

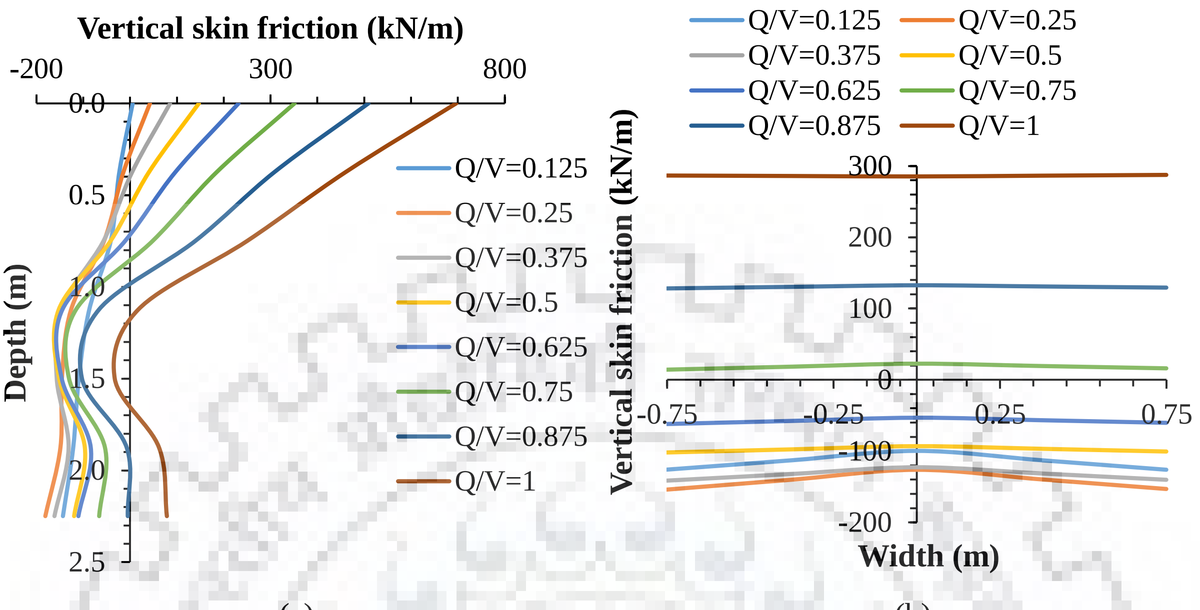

(a) (b)

Fig. 4.15 Variation of vertical skin friction on rear face of caisson along (a) depth and (b) width for different lateral load magnitudes for V=800 kN and $\delta=\phi$ under static conditions

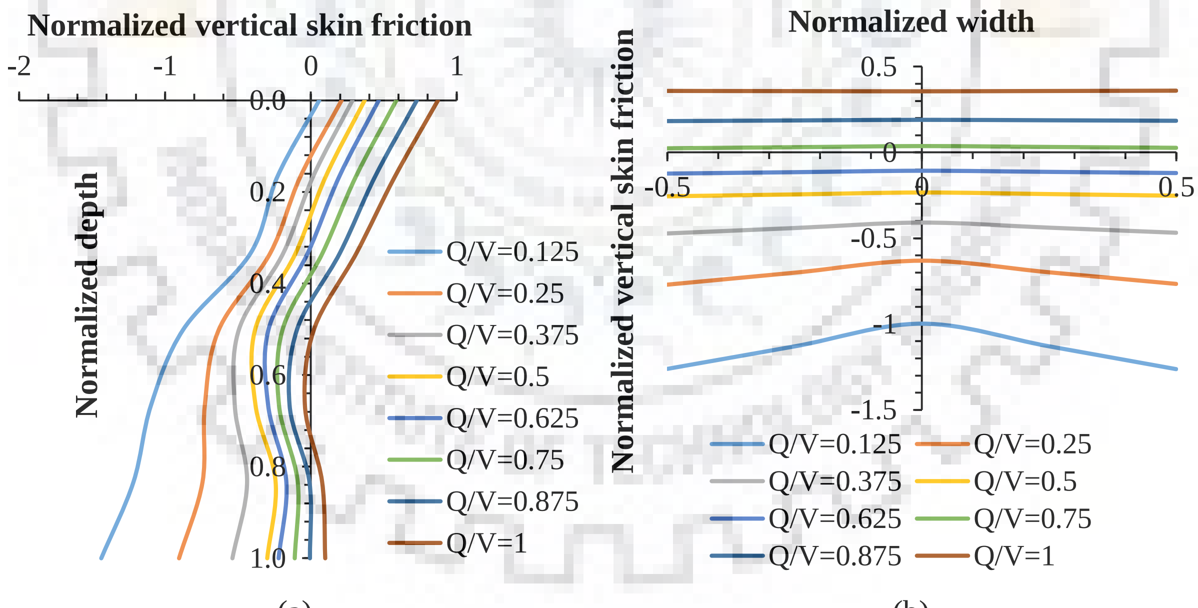

(a) (b)

Fig. 4.16 Variation of normalized vertical skin friction on rear face of caisson along (a) depth and (b) width for different lateral loads for V=800 kN and $\delta=\phi$ under static conditions

The normalization of vertical skin friction with respect to lateral load reveals that the vertical skin friction per unit lateral load increases at a uniform rate on front and rear face with increasing lateral load while the rate of reduction is steep for small lateral load and

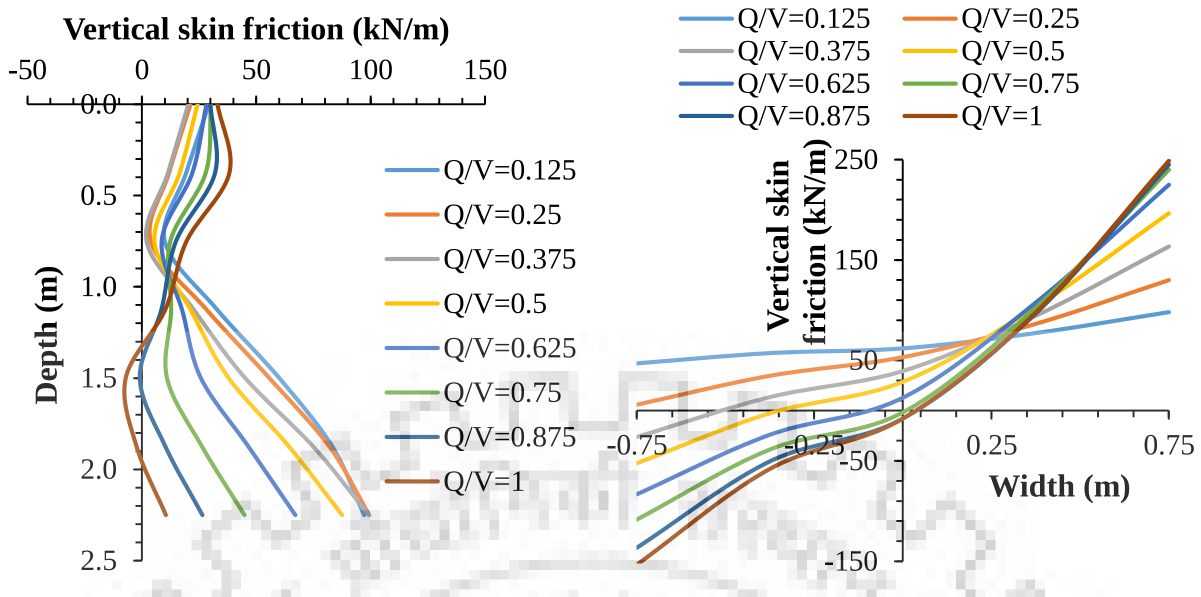

(a) (b)

Fig. 4.17 Variation of vertical skin friction on side face of caisson along (a) depth and (b) width for different lateral load magnitudes for *V*=800 kN and *δ*=*ϕ* under static conditions

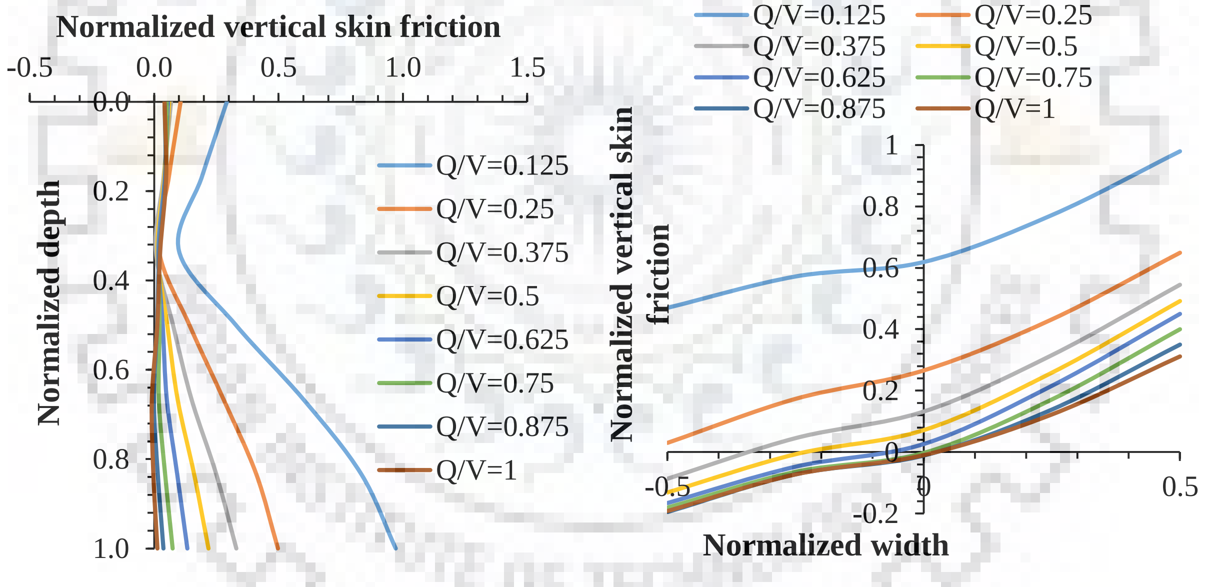

(a) (b)

Fig. 4.18 Variation of normalized vertical skin friction on side face of caisson along (a) depth and (b) width for different lateral loads for *V*=800 kN and *δ*=*ϕ* under static conditions

becomes quite insensitive *Q*/*V*≥0.75. The normalization of vertical skin friction along width of caisson reveals that the vertical skin friction per unit lateral load increases on front face while reduces on rear and side face for increasing lateral load magnitude. Both, increase on front face and reduction on rear and side face, is rapid at lower magnitude of lateral load and becomes smaller as the normalized lateral load (*Q*/*V*) increases in magnitude.

4.4.2.2 Influence of vertical load (V) on vertical skin friction

Vertical load acting on a caisson is a key parameter guiding the magnitude of vertical skin friction acting on vertical faces of caisson. Fig. 4.19 to Fig. 4.24 illustrates the effects of vertical load on vertical skin friction along width and depth of caisson. The vertical skin friction magnitude on all the vertical faces of caisson increases with vertical load along depth of caisson. The magnitude along width of caisson increases on front face and side face while negative vertical skin friction increases at smaller magnitude of vertical load and then decreases in magnitude with increasing vertical load, for V>800 kN, on rear face of caisson. The rear face of caisson experiences contrasting vertical displacements due to vertical load and tilt of caisson under applied lateral load. While the vertical load guides the initial response in terms of vertical skin friction, higher magnitude of lateral load dominates the behaviour of caisson later. However, normalization of vertical skin friction with respect to vertical load reveals uniform increase in vertical skin friction per unit vertical load along depth and width of caisson. The increase in vertical skin friction when vertical load increases from 200 kN to 400 kN and 1200 kN to 1400 kN for Q/V=0.25 and $\delta=\phi$ under static conditions is 87.14% and 33.28% respectively at mid-depth of front face, 84.82% and 31.7% respectively on top of rear face and 64.09% and 20.31% respectively at bottom of side face.

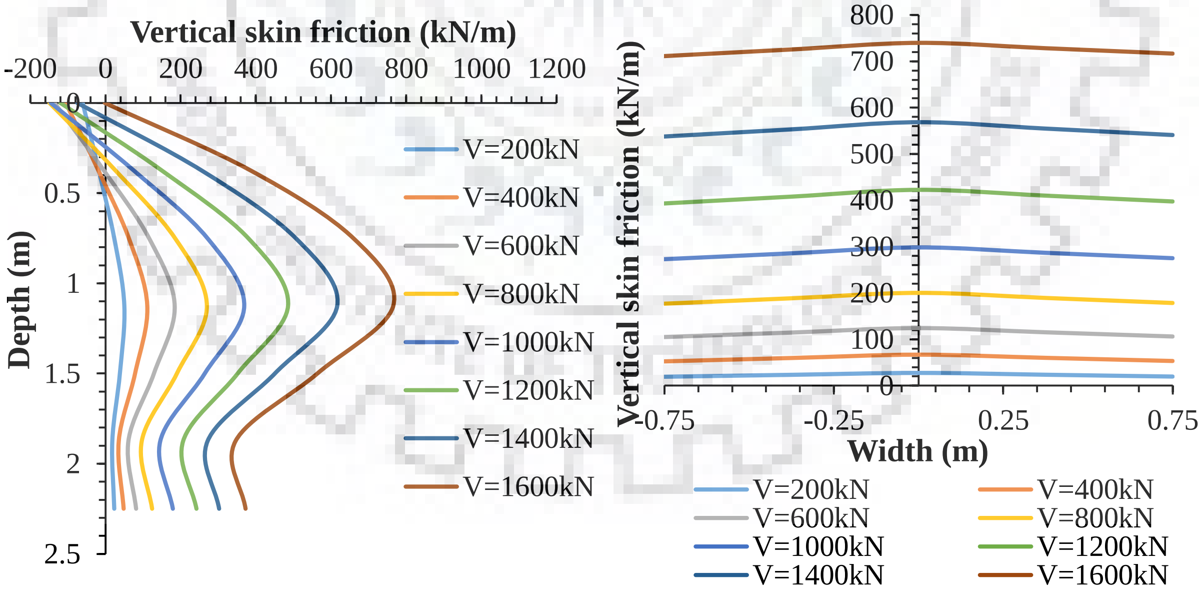

(a) (b)

Fig. 4.19 Variation of vertical skin friction on front face of caisson along (a) depth and (b) width for different vertical loads for Q/V=0.5 and $\delta=\phi$ under static conditions

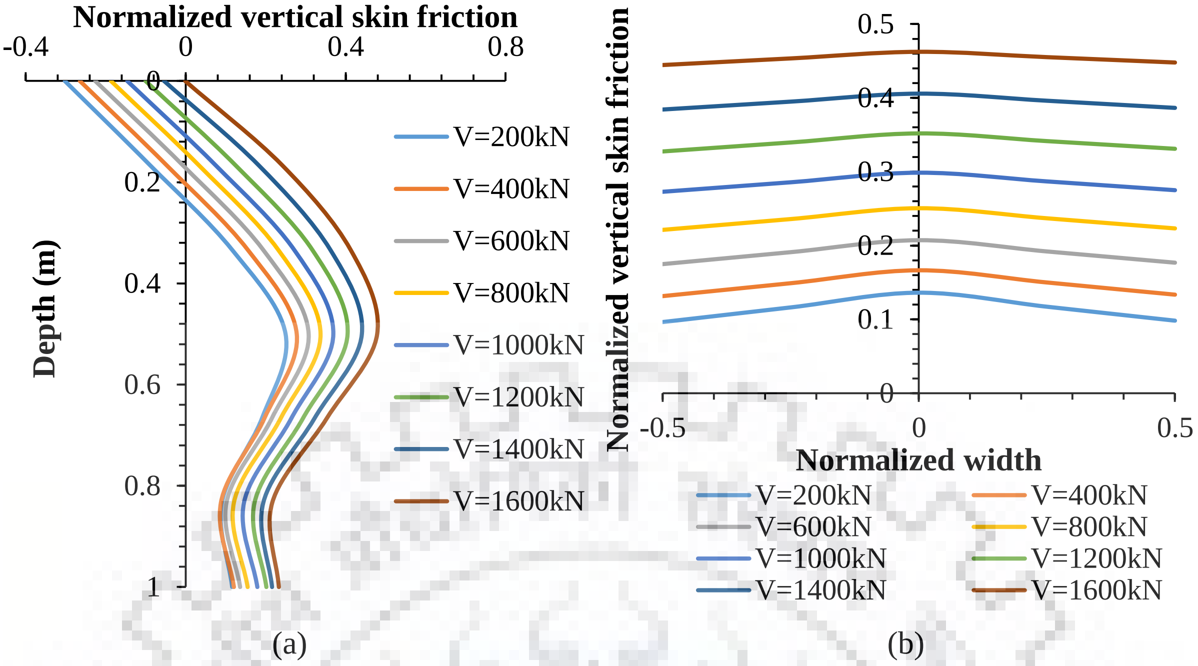

Fig. 4.20 Variation of normalized vertical skin friction on front face of caisson along (a) depth and (b) width for different vertical loads for Q/V=0.5 and $\delta=\phi$ under static conditions

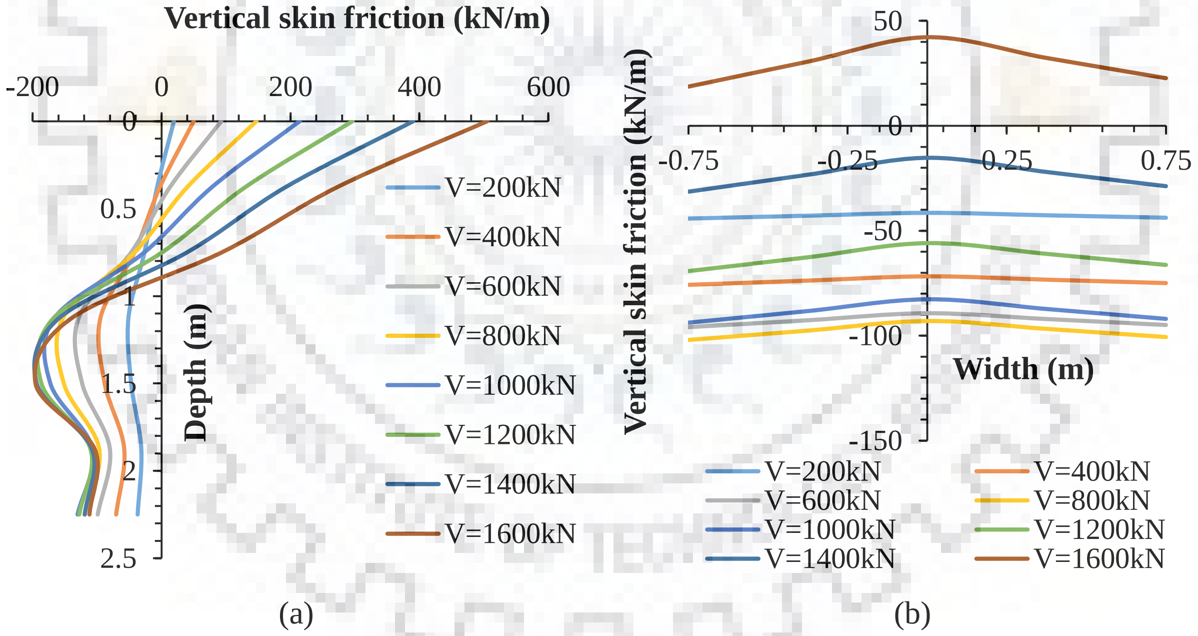

Fig. 4.21 Variation of vertical skin friction on rear face of caisson along (a) depth and (b) width for different vertical loads for Q/V=0.5 and $\delta=\phi$ under static conditions

The vertical skin friction per unit vertical load increases at a steady rate for increasing vertical load as depicted in Fig. 4.20, Fig. 4.22 and Fig. 4.24. The normalized vertical skin friction increases by a magnitude of 0.0296 and 0.0356 respectively on front face at mid-depth of caisson when vertical load increases from 400 kN to 600 kN and 1200 kN to 1400 kN. For same increment of vertical load, the normalized vertical skin friction increases by 0.0291 and 0.0318 respectively at top of rear face and remains insensitive to increased vertical loading on side face. The increase in normalized vertical skin friction, along width of caisson at edges for the vertical load increment, is 0.0433 and 0.0568 respectively on front face and 0.0313 and 0.0361 respectively on rear face.

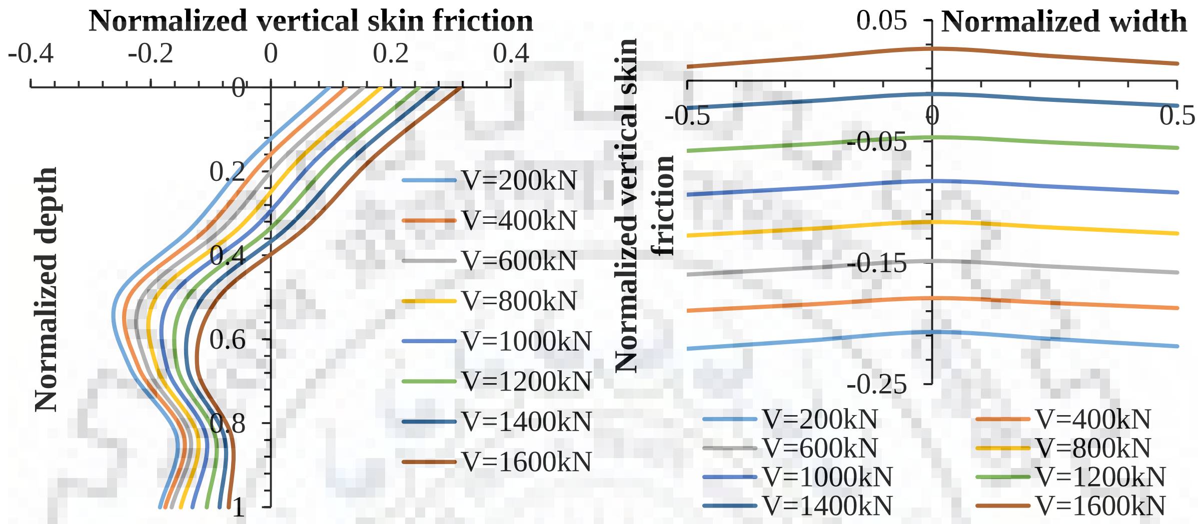

(a) (b)

Fig. 4.22 Variation of normalized vertical skin friction on rear face of caisson along (a) depth and (b) width for different vertical loads for Q/V=0.5 and $\delta=\phi$ under static conditions

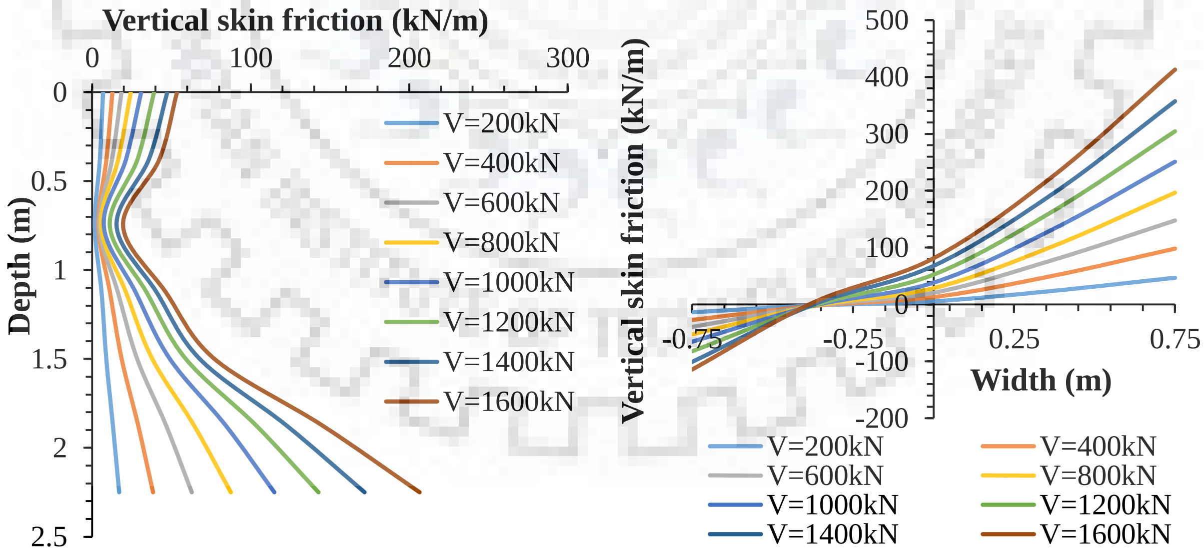

(a) (b)

Fig. 4.23 Variation of vertical skin friction on side face of caisson along (a) depth and (b) width for different vertical loads for Q/V=0.5 and $\delta=\phi$ under static conditions

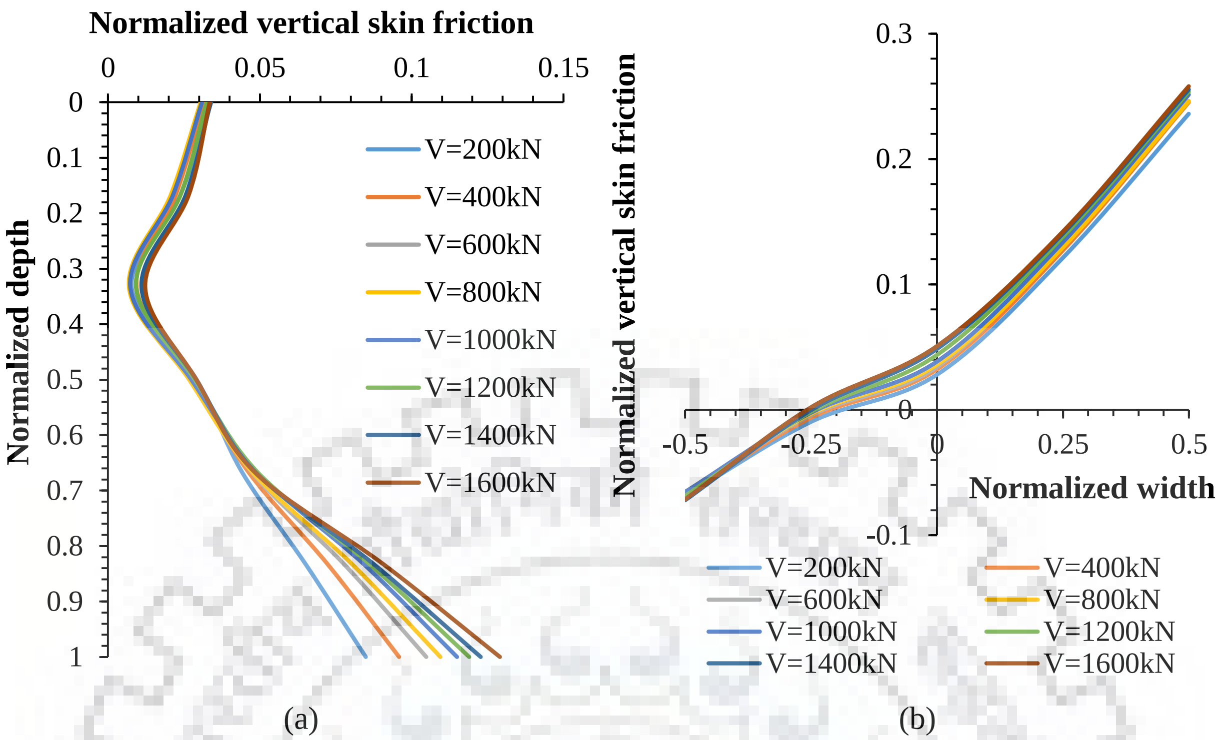

Fig. 4.24 Variation of normalized vertical skin friction on side face of caisson along (a) depth and (b) width for different vertical loads for Q/V=0.5 and $\delta=\phi$ under static conditions

4.4.2.3 *Influence of soil-wall friction angle (δ) on vertical skin friction*

As mentioned in the previous sections, soil-wall friction resists the displacement of caisson through soil under action of externally applied loading. Therefore, in addition to generating higher frictional force for a small displacement of caisson, the soil-wall friction also diminishes the magnitude of displacement and tilt of caisson. Fig. 4.25 to Fig. 4.27 depict the normalized vertical skin friction force acting on front, rear and side face of caisson. The normalization of vertical skin friction force is again done with respect to applied lateral load. It is observed that, for V=800 kN and Q/V=0.25, as δ increases from $\phi/2$ to $2\phi/3$ and ϕ, the normalized vertical skin friction reduces by 10.12% and 26.96% respectively at mid-depth of front face, 5.64% and 16.72% respectively at top of rear face and 5.73% and 20.65% respectively at bottom of side face. It is also observed that the normalized vertical skin friction on front face is much more sensitive to soil-wall friction angle than normalized vertical skin friction on rear face and side face. Furthermore, the normalized vertical skin friction along width of caisson is found to increase in magnitude on rear face of caisson while reduce on front face for increasing δ. Its magnitude is observed to be independent of δ on side face of caisson. The magnitude of normalized vertical skin friction along width of caisson is seen to increase on front face and reduce on rear face proportionally to change in soil-wall friction angle while the magnitude on side face is found to be indifferent to changes in soil-wall friction angle.

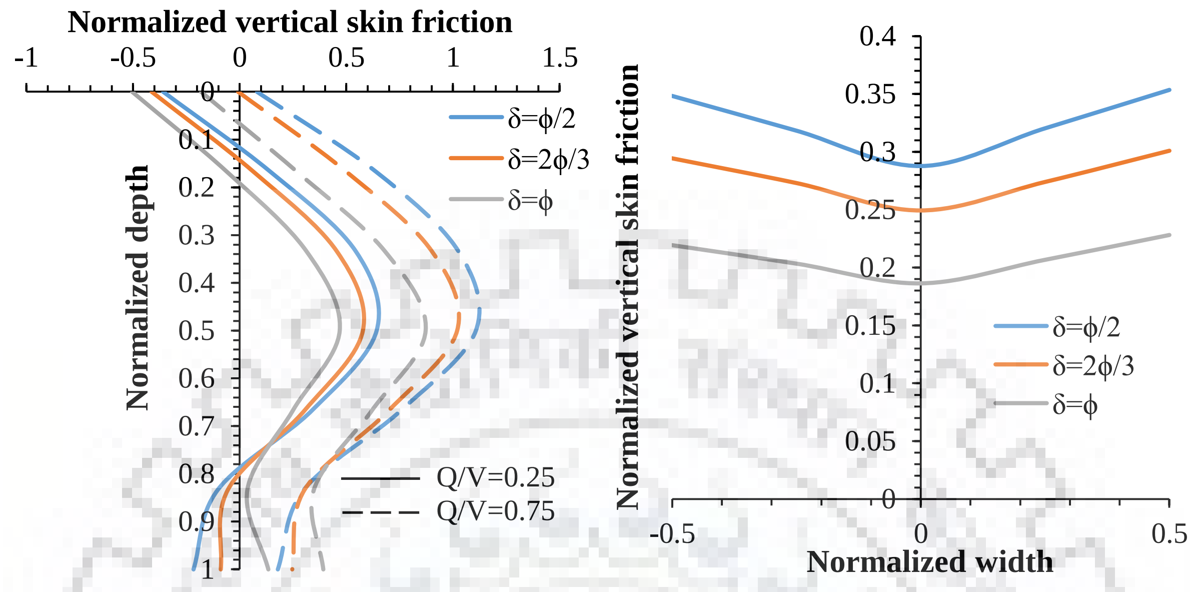

(a) (b)

Fig. 4.25 Variation of normalized vertical skin friction on front face of caisson along (a) depth and (b) width for varying soil-wall friction angle and *V*=800 kN under static conditions

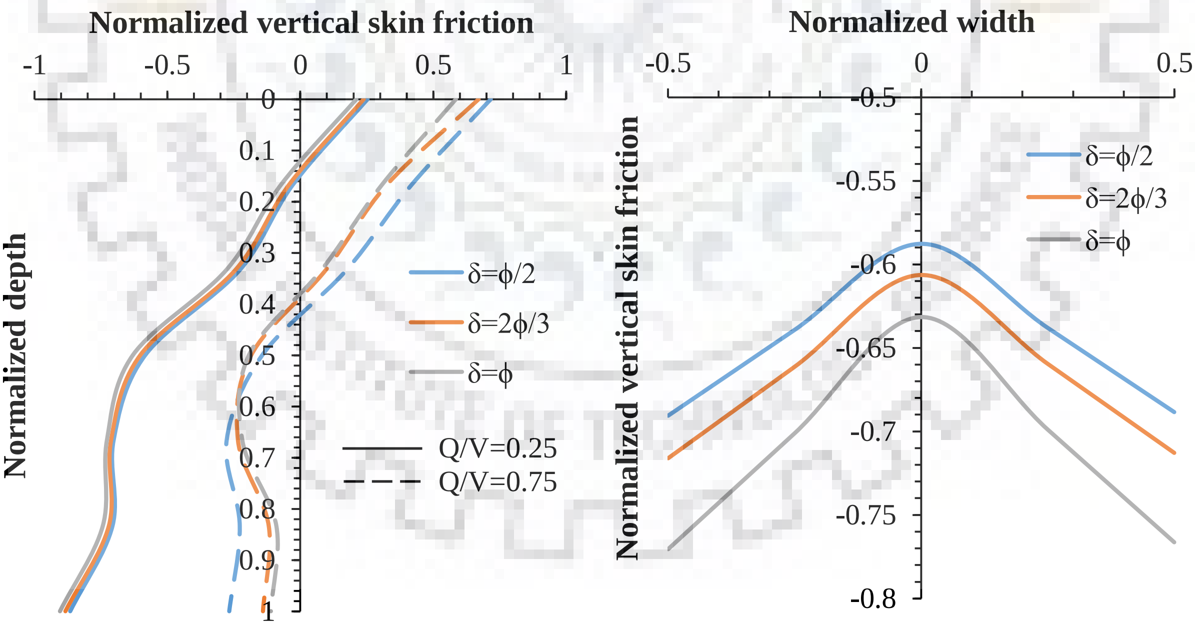

(a) (b)

Fig. 4.26 Variation of normalized vertical skin friction on rear face of caisson along (a) depth and (b) width for varying soil-wall friction angle at *V*=800 kN under static conditions

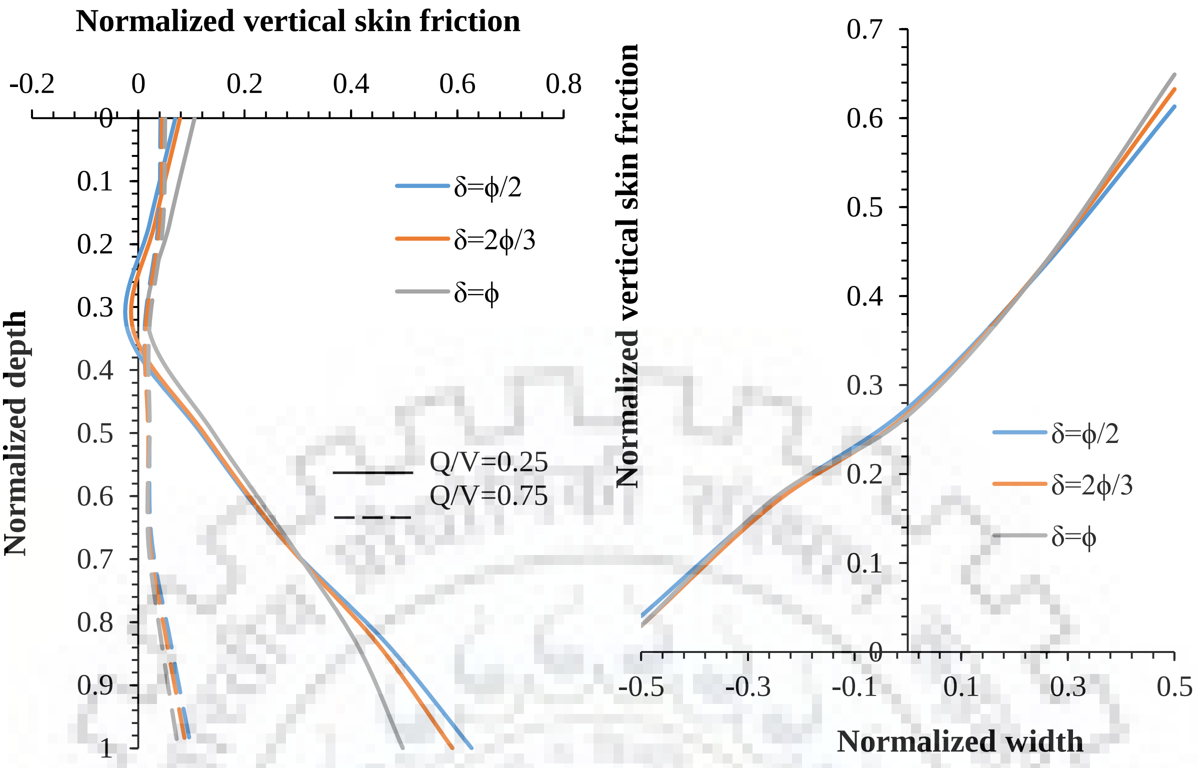

(a) (b)

Fig. 4.27 Variation of normalized vertical skin friction on side face of caisson along (a) depth and (b) width for varying soil-wall friction angle at V=800 kN under static conditions

4.4.2.4 Influence of seismic acceleration coefficients (k_h and k_v) on vertical skin friction

The seismic inertial forces induced in the soil strata leads to densification of soil surrounding the caisson, thereby, increasing the lateral soil pressure on caisson and increasing vertical skin friction ($f=N\tan\delta$; f is frictional resistance, N is normal reaction and $\tan\delta$ is friction coefficient between surfaces). The pronounced displacement under high magnitude of seismic inertial forces may cause this behaviour. The impact of k_h is found to be much more pronounced, along both depth and width of caisson, as k_h increases from 0.2 to 0.3, compared to lower values of k_h as illustrated in Fig. 4.28 to Fig. 4.30. It is observed that for V=800 kN, Q/V=0.75, k_v=0 and $\delta=\phi$, the magnitude of vertical skin friction, normalized with respect to applied lateral load, increases by 7.07%, 14.89% and 74.48% respectively at mid-depth of front face of caisson as k_h increases from 0 to 0.1, 0.2 and 0.3. Similarly, the increase in magnitude at mid-depth of rear face for the above-mentioned increment in k_h is 8.2%, 18.48% and 117.89% respectively while the side face is found to be fairly insensitive to k_h except at k_h=0.3 where the increase is 20.4% at bottom of face. The increase along width of caisson also follows a similar trend.

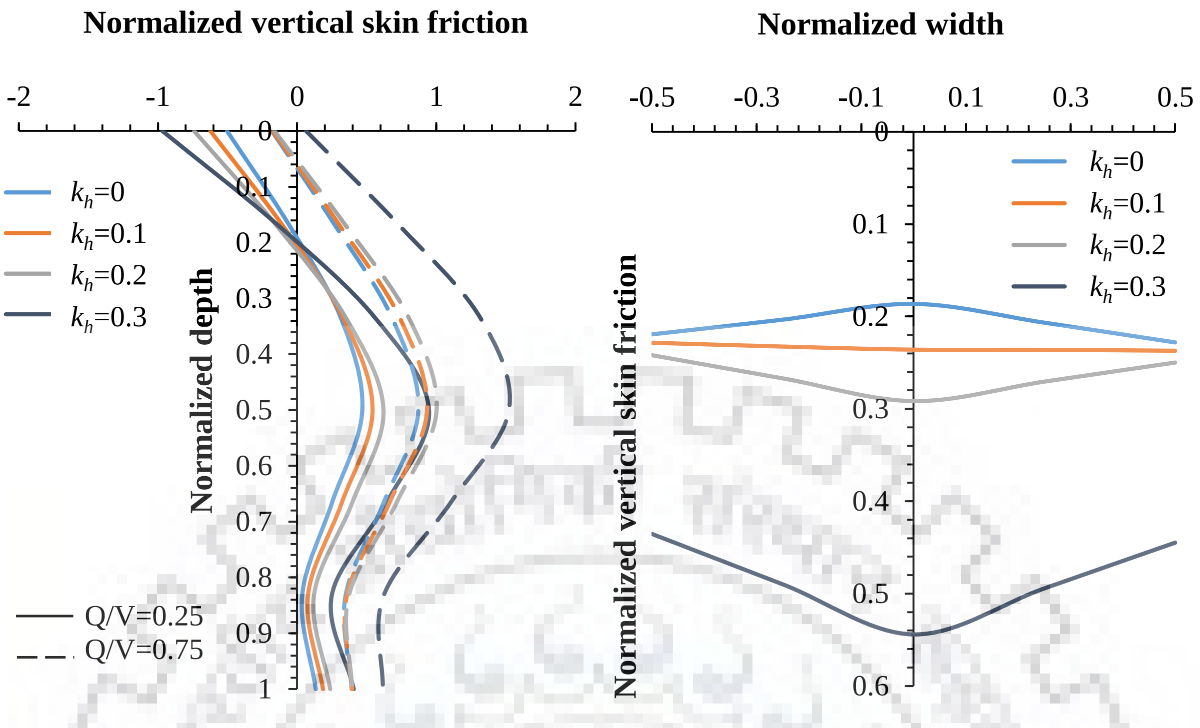

(a) (b)

Fig. 4.28 Variation of normalized vertical skin friction on front face of caisson along (a) depth and (b) width for varying k_h at V=800 kN, k_v=0 and $\delta=\phi$

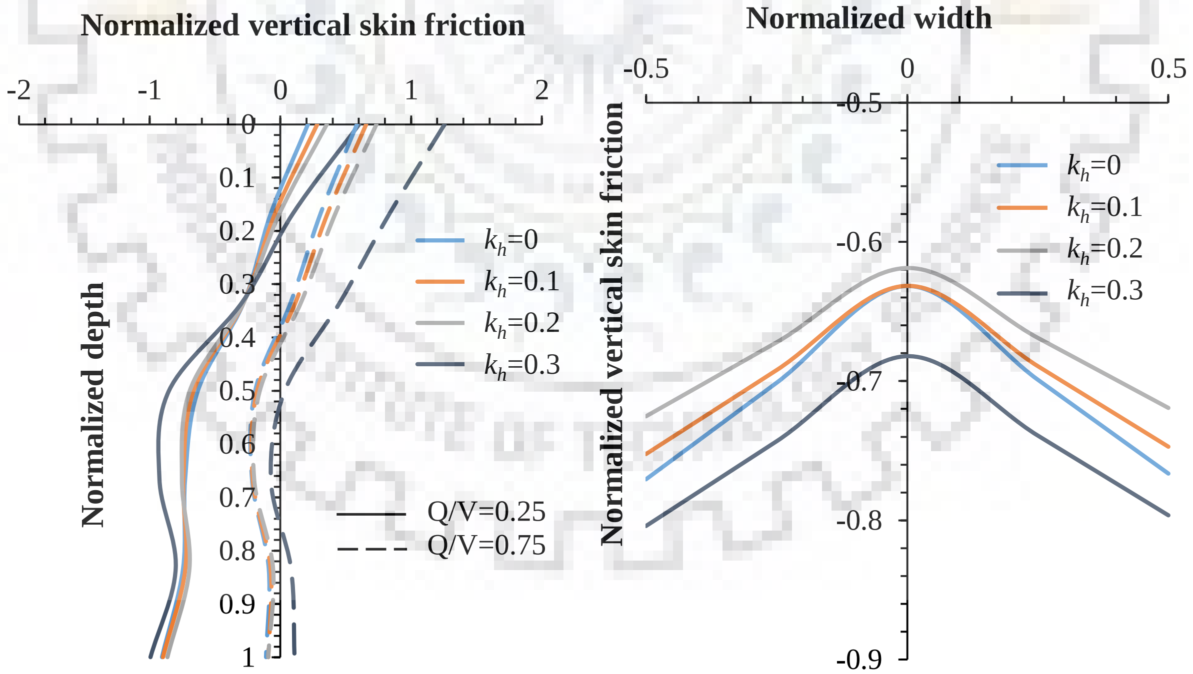

(a) (b)

Fig. 4.29 Variation of normalized vertical skin friction on rear face of caisson along (a) depth and (b) width for varying k_h at V=800 kN, k_v=0 and $\delta=\phi$

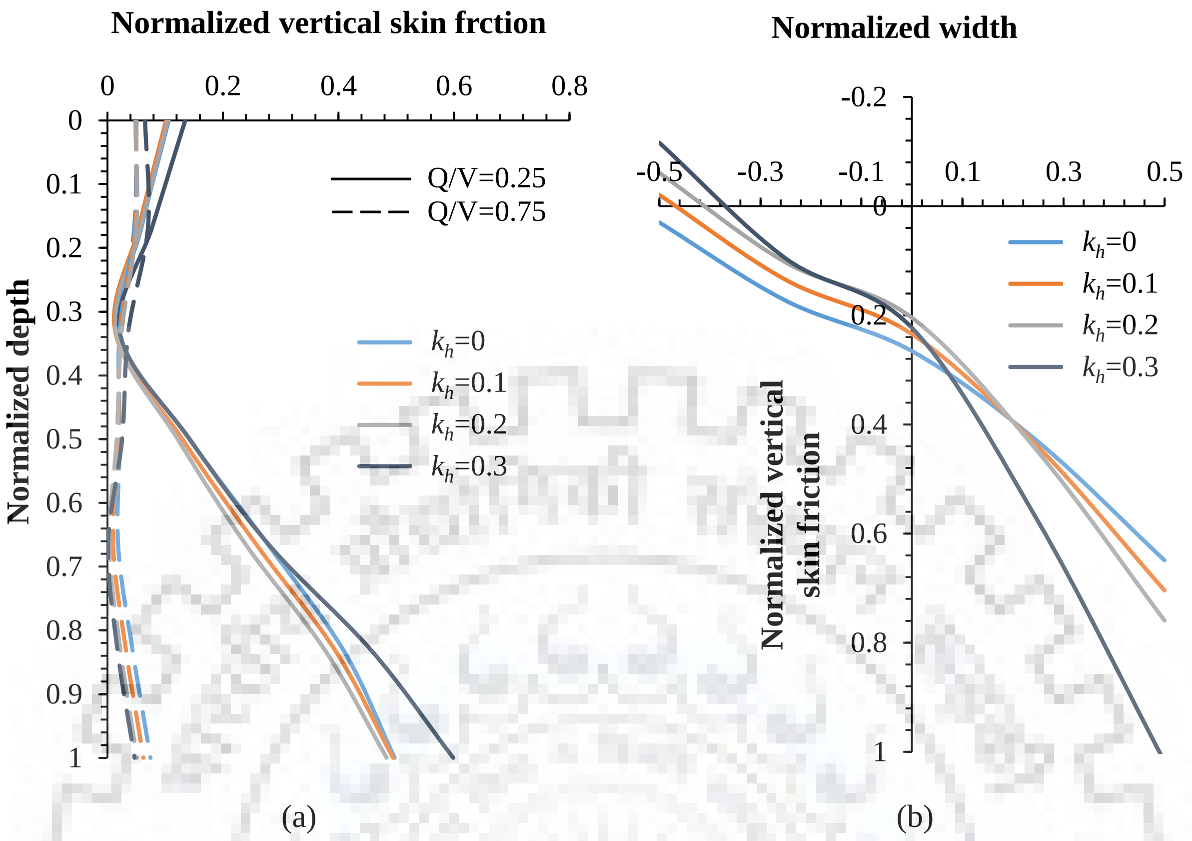

(a) (b)

Fig. 4.30 Variation of normalized vertical skin friction on side face of caisson along (a) depth and (b) width for varying k_h at V=800 kN, k_v=0 and $\delta=\phi$

The normalized vertical skin friction is very mildly affected by changes in vertical seismic acceleration coefficient (k_v) as observed in Fig. 4.31 to Fig. 4.33. A small increase in magnitude of normalized vertical skin friction is observed for increasing k_v values on front face while a minor reduction is observed on rear and side face of caisson. For k_h=0.1, V=800 kN and Q/V=0.25, the increase in normalized vertical skin friction is 1.93% and 3.67% respectively as k_v increases from 0 to $k_h/2$ and k_h at mid-depth of front face. For the same set of input parameters, the reduction in normalized vertical skin friction is 2.1% and 4.31% respectively at mid-depth of rear face and 5.1% and 10.39% respectively at bottom of side face. The variation along width of caisson follows a more linear trend, with percentage increase in normalized vertical skin friction at mid-width of front face being 5.77% and 11.72% respectively for the above-mentioned increase in k_v values. The reduction at mid-width is 4.01% and 8.15% respectively on rear face and 7.81% and 15.6% respectively on side face of caisson, which suggests linear response of normalized vertical skin friction to change in k_v values.

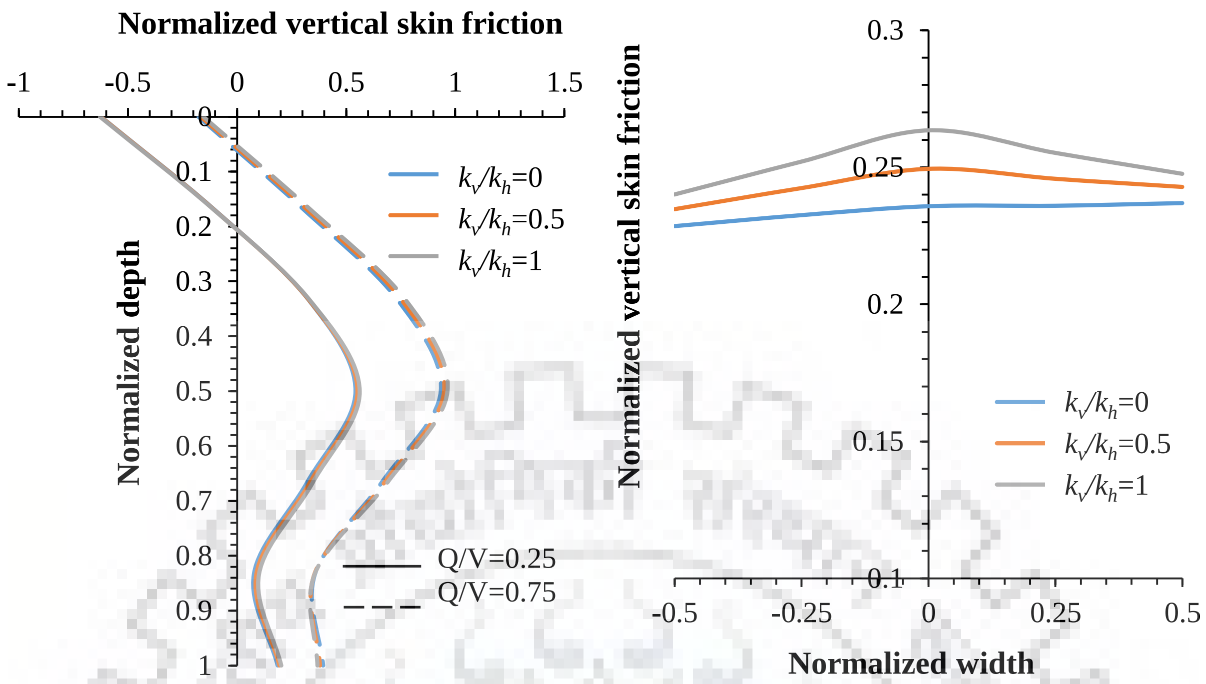

(a) (b)

Fig. 4.31 Variation of normalized vertical skin friction on front face of caisson along (a) depth and (b) width for varying k_v at V=800 kN, k_h=0.1 and $\delta=\phi$

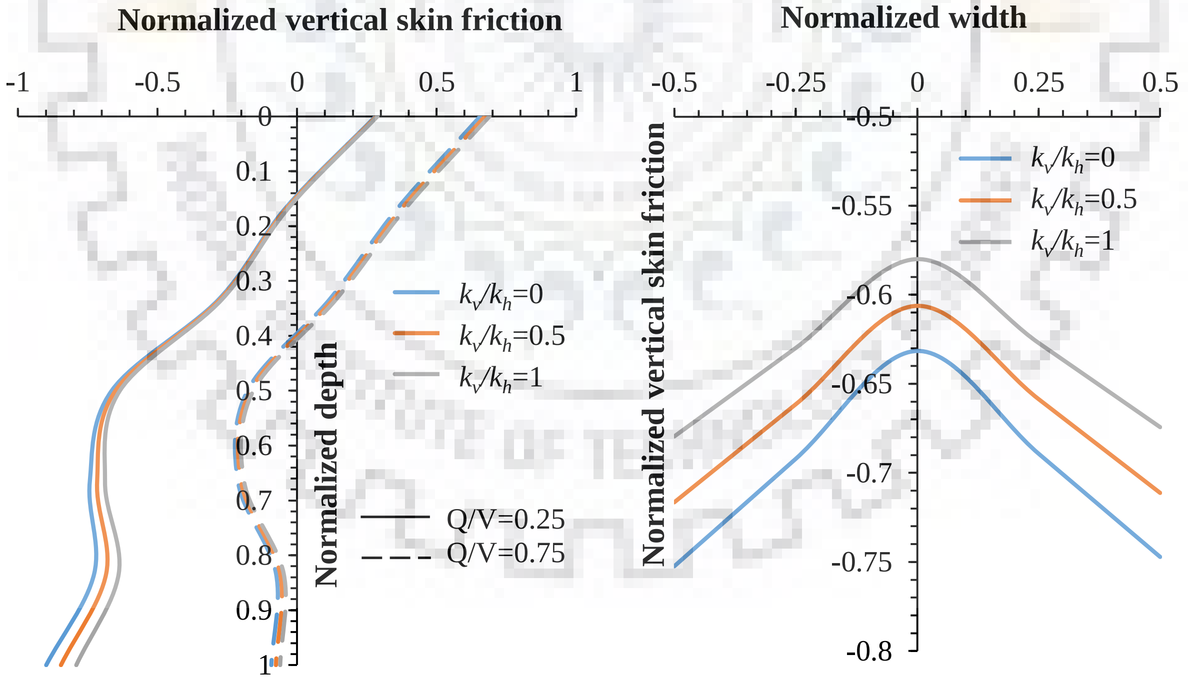

(a) (b)

Fig. 4.32 Variation of normalized vertical skin friction on side face of caisson along (a) depth and (b) width for varying k_v at V=800 kN, k_h=0.1 and $\delta=\phi$

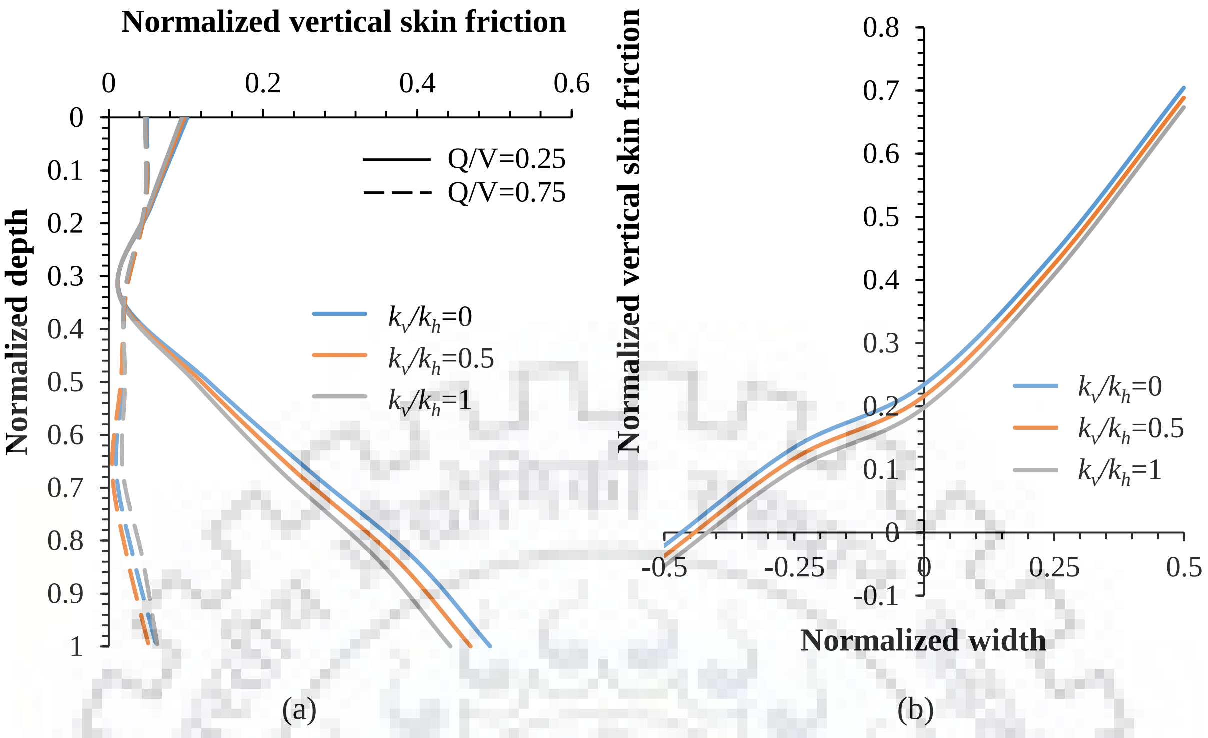

(a) (b)

Fig. 4.33 Variation of normalized vertical skin friction on side face of caisson along (a) depth and (b) width for varying k_v at V=800 kN, k_h=0.1 and $\delta=\phi$

4.4.3 Base friction

Base friction force is developed as caisson tilts or translates under the action of applied external loads and seismic inertial forces. This section describes the effects of various input parameters on the base friction force.

4.4.3.1 Influence of normalized lateral load (Q/V) on base friction

The tilt and shift of caisson both increase with increasing lateral load as mentioned in Chapter 3. While the shift of caisson is in direction of loading, the displacement, by virtue of tilt of caisson, is in opposite direction of loading. The net effect of these two displacements under static conditions is movement of caisson base in opposite direction of loading since the point of rotation lies above the base of caisson. For increasing magnitude of lateral load (Q), the base friction increases in magnitude throughout the length of caisson, however the base friction per unit applied lateral load reduces as shown in Fig. 4.34, which reflects that the rate of development of base friction with applied lateral load reduces with increasing lateral load. For V=800 kN and $\delta=\phi$ under static conditions, the base friction increases by 39.72% and 12.65% as the Q/V increases from 0.25 to 0.375 and 0.75 to 0.875 respectively. The reduction in percentage increase reiterates the point.

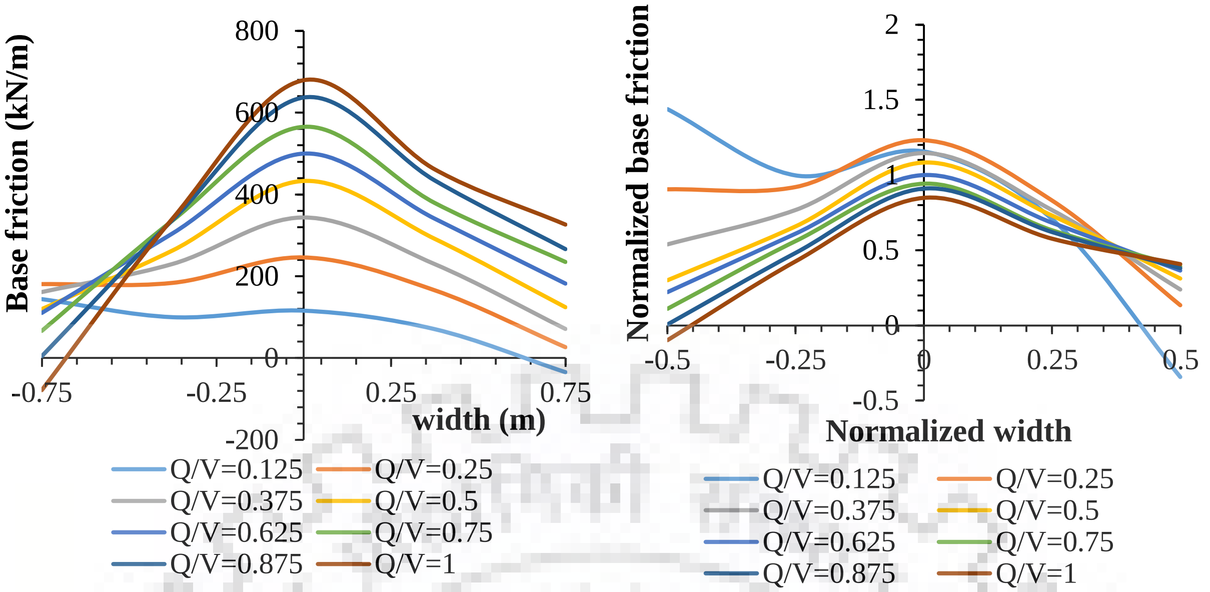

(a) (b)

Fig. 4.34 Variation of (a) base friction force and (b) normalized base friction force for different magnitudes of lateral loads for V=800 kN and $\delta=\phi$ under static conditions

4.4.3.2 Influence of vertical load (V) on base friction

Higher magnitude of vertical load provides higher normal reaction offered by soil strata to caisson, thereby increasing the frictional force at base. In addition, the magnitude of applied lateral load also increases for a given Q/V ratio with increasing vertical load. Fig. 4.35 shows the variation of base friction and normalized base friction along length of caisson for varying vertical load. It is again seen that base friction increases with vertical load but reduces upon normalization with respect to vertical load. The percentage increase in base friction at mid-section for Q/V=0.5 and $\delta=\phi$ under static conditions is 49.78% and 13.73% respectively when vertical load (V) increases from 400 kN to 600 kN and from 1200 kN to 1400 kN.

4.4.3.3 Influence of soil-wall friction angle (δ) on base friction

Increasing magnitude of soil-wall friction angle, as mentioned in the previous sections, has two contradicting effects of increasing the coefficient of friction at soil-wall contact and resisting the displacement of caisson, thereby reducing net frictional force mobilized. In the case of base friction, the second effect is dominant and therefore, the friction force at base of caisson increases with increasing δ for all values of lateral load as shown in Fig. 4.36. The increase in normalized base friction at mid-width of caisson for caisson subjected to V=800 kN and having under static conditions, when δ increases from $\phi/2$ to $2\phi/3$ and ϕ, is found to be 2.69% and 5.69% respectively for Q/V=0.25 and 2.55% and 4.71% respectively for Q/V=0.75.

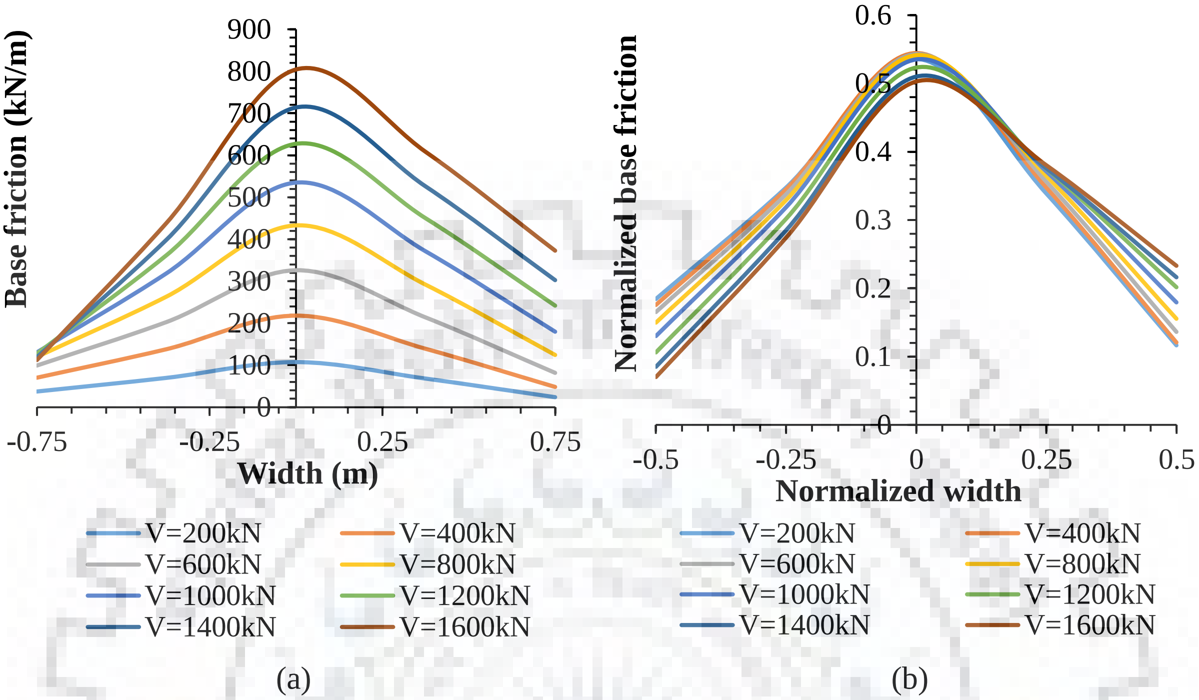

Fig. 4.35 Variation of (a) base friction force and (b) normalized base friction force for different vertical loads for Q/V=0.5 and $\delta=\phi$ under static conditions

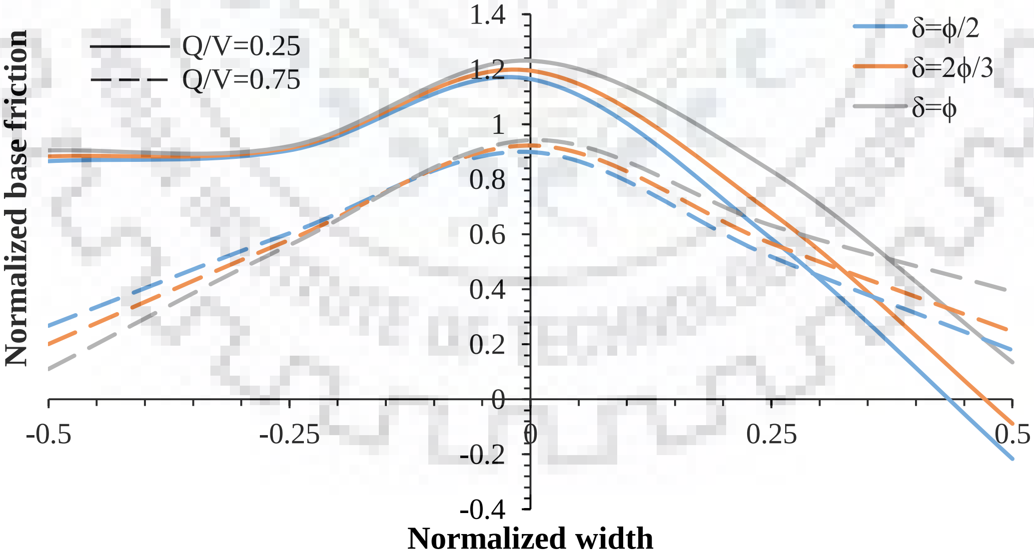

Fig. 4.36 Variation of normalized base friction for different soil-wall friction angles and normalized lateral loads

4.4.3.4 *Influence of seismic acceleration coefficients (k_h and k_v) on base friction*

Horizontal seismic inertial force, caused by seismic acceleration in horizontal direction is responsible for exaggerated displacement and densification of soil. This causes high magnitudes of friction to be mobilized at base of caisson. Therefore, the base friction normalized with respect to applied lateral load is found to increase with increasing k_h as depicted in Fig. 4.37. For V=800 kN, k_v=0 and $\delta=\phi$, the normalized base friction increases by 9.37%, 17.69% and 56.84% respectively for Q/V=0.25 and 287%, 5.77% and 25.89% for Q/V=0.75. The vertical seismic acceleration coefficient contributes to reducing the normal reaction offered to caisson base, which results in reduced base friction. For V=800 kN, k_h=0.1 and $\delta=\phi$, the normalized base friction reduces by 1.22% and 2.4% respectively for Q/V=0.25 and 0.47% and 1.1% respectively for Q/V=0.75 when k_v increases from 0 to k_h/2 and k_h.

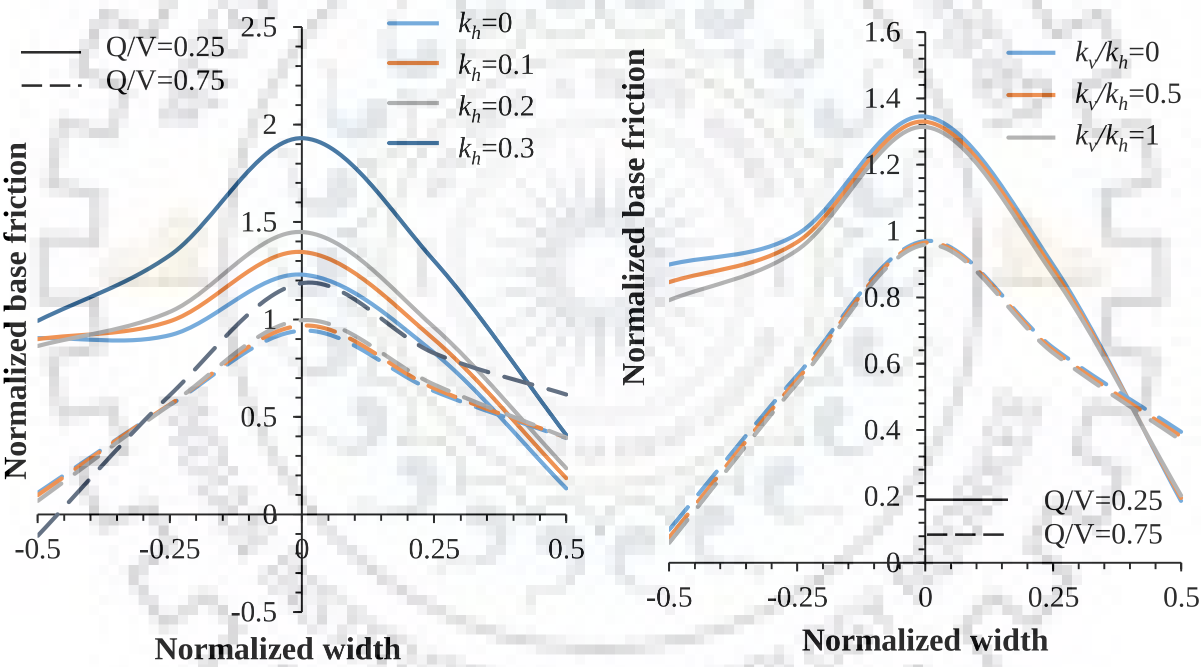

(a) (b)

Fig. 4.37 Variation of normalized base friction for different (a) k_h at k_v=0 and (b) k_v/k_h at k_h=0.1 for V=800 kN and $\delta=\phi$

4.4.4 *Base reaction*

Strata supporting a caisson provides reaction in response to self-weight of caisson and vertical load acting on caisson. Additional soil reaction is generated at toe of caisson, and it keeps diminishing at the heel as caisson starts tilting under the action of applied lateral loads. The variation in base reaction on caisson due to various parameters is discussed below.

4.4.4.1 *Influence of normalized lateral load (Q/V) on base reaction*

An increase in lateral load causes the caisson to tilt, thereby, increasing the normal reaction on base of caisson in one half and reducing it in the other half. Fig. 4.38 illustrates the effect of applied lateral load on base reaction developed. The base reaction is found to increase towards toe of caisson and reduce towards heel of caisson as the magnitude of applied lateral load increases. The base reaction normalized with respect to applied lateral load is found to reduce, over entire width of base, with increasing lateral load. The normalized base reaction reduces by 18.7% and 7.91% as the Q/V increases from 0.25 to 0.375 and 0.75 to 0.875 respectively for V=800 kN and $\delta=\phi$ under static conditions.

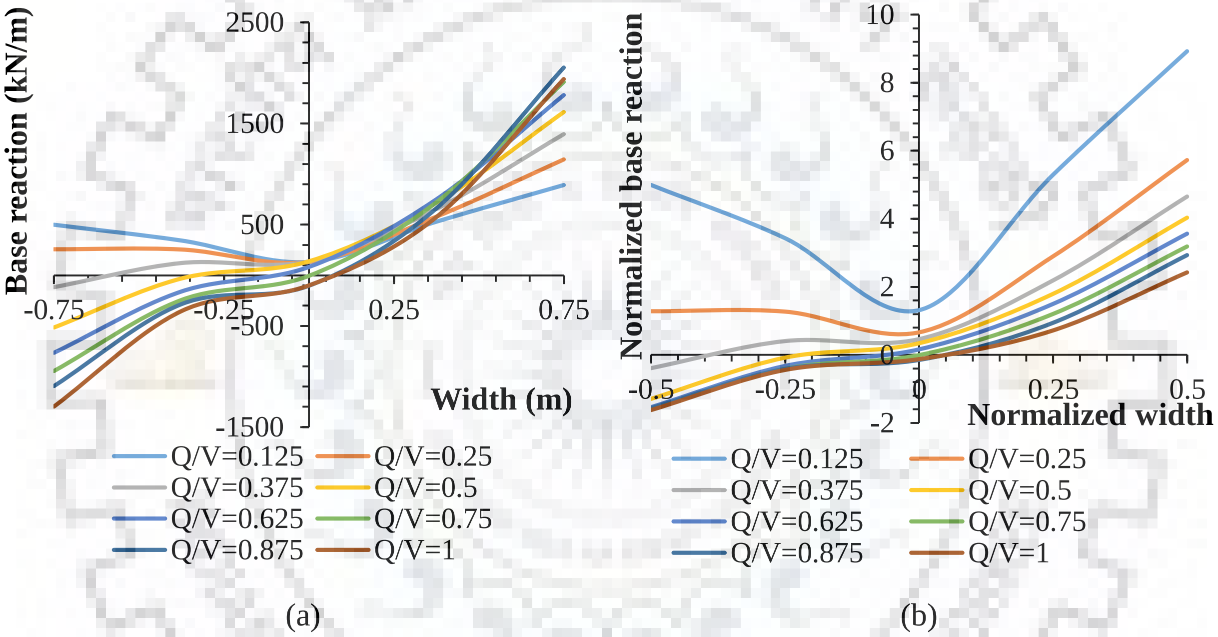

Fig. 4.38 Variation of (a) base reaction and (b) normalized base reaction for different magnitudes of lateral loads for V=800 kN and $\delta=\phi$ under static conditions

4.4.4.2 *Influence of vertical load (V) on base reaction*

An increase in vertical load directly results in development of higher normal reaction offered to base of caisson. Therefore, the base reaction has been normalized with respect to vertical load V to understand the influence of applied vertical load. It is again observed from Fig. 4.39 that the base reaction towards toe of caisson increases while that towards the heel of caisson reduces as vertical load increases for Q/V=0.5 and $\delta=\phi$ under static conditions. The normalized base reaction is found to be insensitive to vertical load magnitude throughout the width of caisson as seen in Fig. 4.39b.

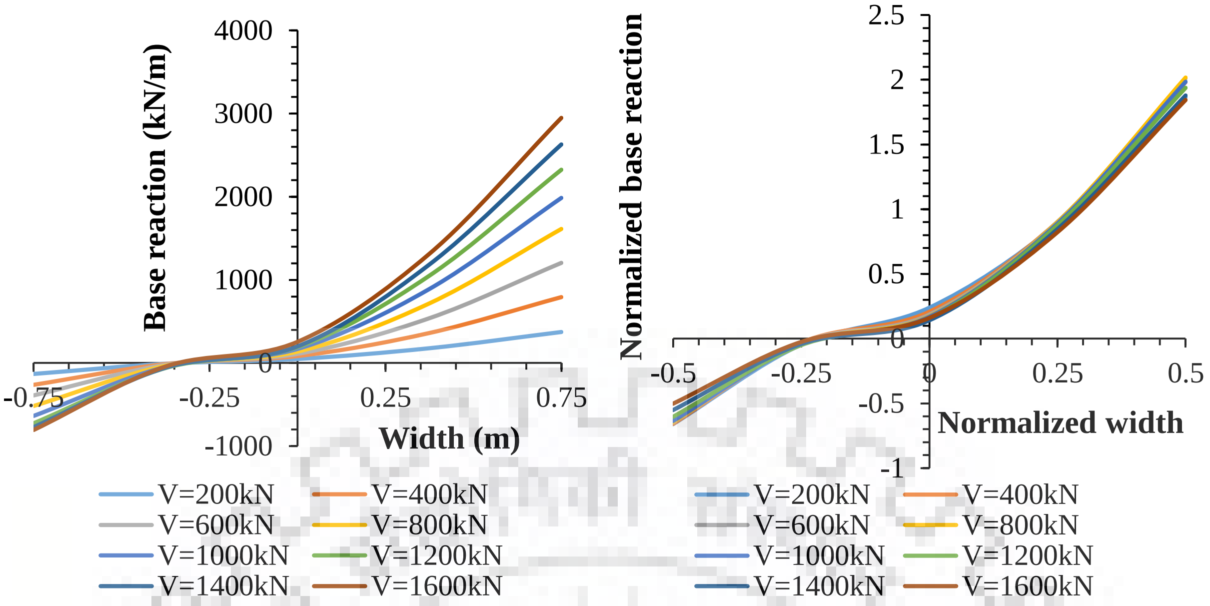

(a) (b)

Fig. 4.39 Variation of (a) base reaction and (b) normalized base reaction for different magnitudes of vertical loads for Q/V=0.5 and $\delta=\phi$ under static conditions

4.4.4.3 *Influence of soil-wall friction (δ) on base reaction*

As mentioned in the previous sections, the vertical component of displacement due to tilt of caisson reduces with increasing soil-wall friction angle (δ). This causes smaller base reaction to be mobilized under the action of applied external loading as seen in Fig. 4.40. For V=800 kN under static conditions, as δ increases from $\phi/2$ to $2\phi/3$ and ϕ, the normalized base reaction at toe of caisson increases by 4.66% and 14.22% respectively for Q/V=0.25 and 2.59% and 14.51% respectively for Q/V=0.75.

4.4.4.4 Influence of seismic acceleration coefficients (k_h and k_v) on base reaction

Horizontal seismic inertial forces cause excessive displacement of soil mass in direction of applied loading (under critical conditions). This causes the soil mass towards toe of caisson to have higher stiffness than that towards heel of caisson. Thus, for a given loading condition, higher the magnitude of k_h, higher is the base reaction developed. However, in case of vertical seismic inertial forces, vertically upwards is the critical loading condition, which reduces the soil reaction at caisson base. The normalized base reaction due to variation of horizontal and vertical seismic acceleration coefficient has been presented in Fig. 4.41. It is observed that, for V=800 kN, k_v=0 and $\delta=\phi$, as k_h increases from 0 to 0.1, 0.2 and 0.3, the normalized base reaction at toe of caisson increases by 4.41%, 8.32% and 41.2% respectively for Q/V=0.25 and 1.49%, 1.86% and 15.09% respectively for Q/V=0.75. On the other hand, increasing the magnitude of k_v from 0 to $k_h/2$ and k_h for V=800kN, $\delta=\phi$ and k_h=0.1, the reduction in normalized base pressure is 2.93% and 5.89% respectively for Q/V=0.25 and 3.31% and 7.1% respectively for Q/V=0.75.

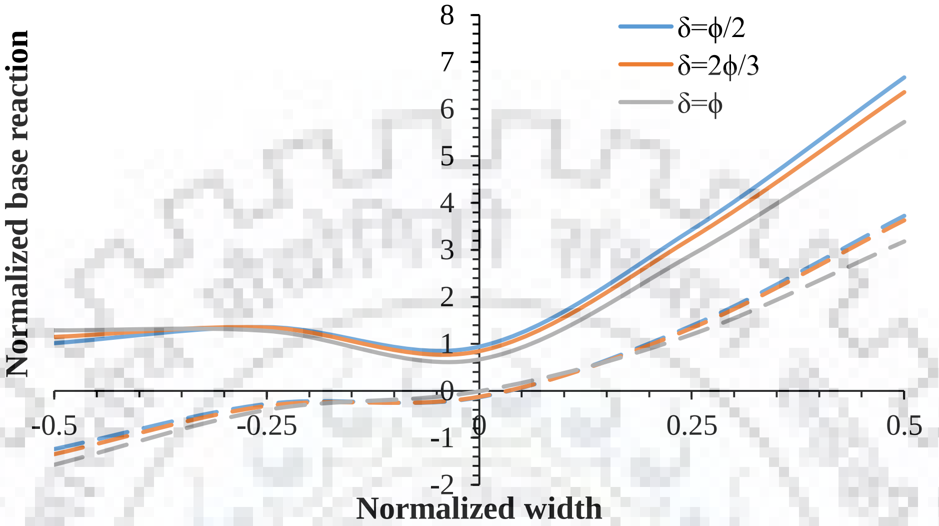

Fig. 4.40 Variation of normalized base reaction for different soil-wall friction angles and normalized lateral loads

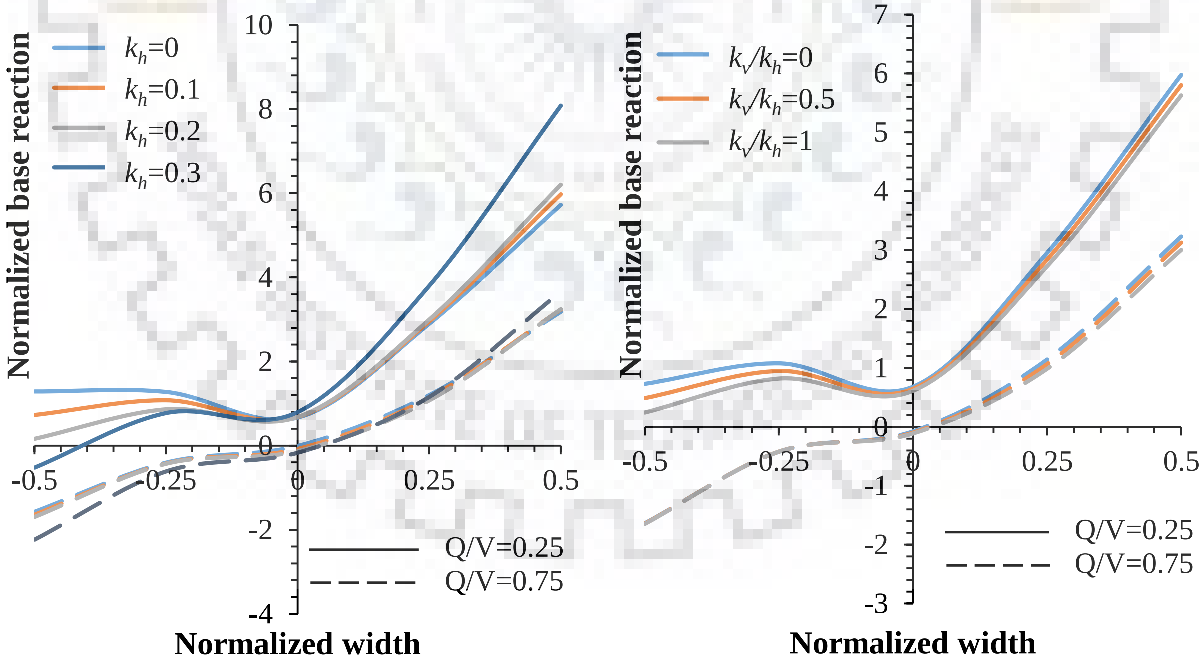

(a) (b)

Fig. 4.41 Variation of normalized base reaction for different (a) k_h at k_v=0 and (b) k_v/k_h at k_h=0.1 for V=800 kN and $\delta=\phi$

4.4.5 *Shear force (SF) and resisting moment (M_R)*

Shear force (*SF*) and resisting moment (M_R) are the indicators of resistive forces acting on a system under the action of applied external loading. Shear force profile identifies the distribution of resisting forces having same line of action as the externally applied load. The shear force profile and moment of resistance profile (due to all the resisting components) on vertical section of caisson has been studied and the effects of various input parameters affecting the *SF* and M_R profiles have been discussed in this section.

4.4.5.1 Influence of normalized lateral load (Q/V) on shear force and resisting moment

Lateral load acting on caisson gives rise to all the resistive stresses acting in horizontal plane opposite to direction of loading. Therefore, the magnitude of lateral load directly affects the shear force (*SF*) on caisson at any depth. The forces in positive X-direction have been considered positive while plotting the shear force diagram. Fig. 4.42 shows the variation of shear force (absolute value as well as *SF* normalized with respect to lateral load) at any depth of caisson. It is observed that, higher the magnitude of applied lateral load, higher is the resistive forces required to counter the applied lateral load.

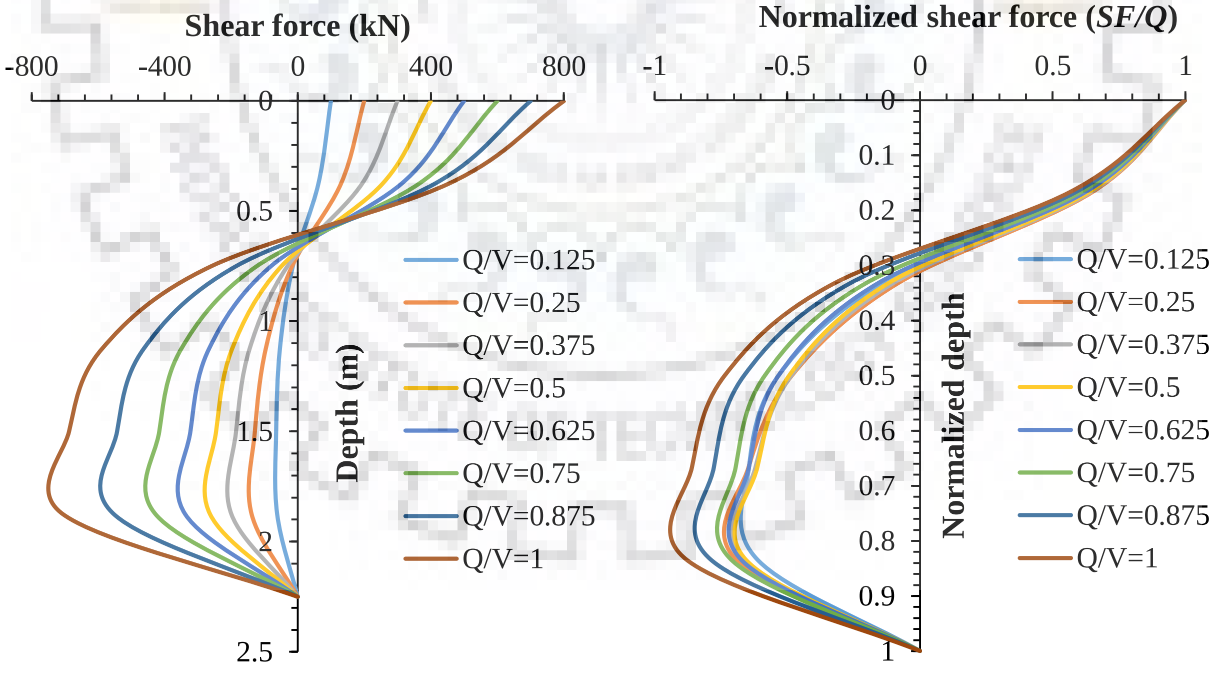

(a) (b)

Fig. 4.42 Variation of (a) shear force and (b) normalized shear force for different magnitudes of lateral loads for V=800 kN and $\delta=\phi$ under static conditions

The normalization of shear force reveals that the sum of resistive forces per unit applied lateral load is constant for Q/V=0.125 to 0.5. On further increasing the lateral load, the resistive forces increase at a higher rate which reflects the non-linear nature of soil at higher loading. Similarly, the resisting moment (M_R) required to withstand higher magnitude of applied lateral load is higher. The variation of M_R is presented by normalizing it with respect to applied moment at scour level (product of applied lateral load and the height of application of lateral load above scour level (H)). In the present study, H has been adopted as 2.25×B, i.e., 3.375 m. It is observed from Fig. 4.43 that the normalized resisting moment marginally increases with increasing lateral load.

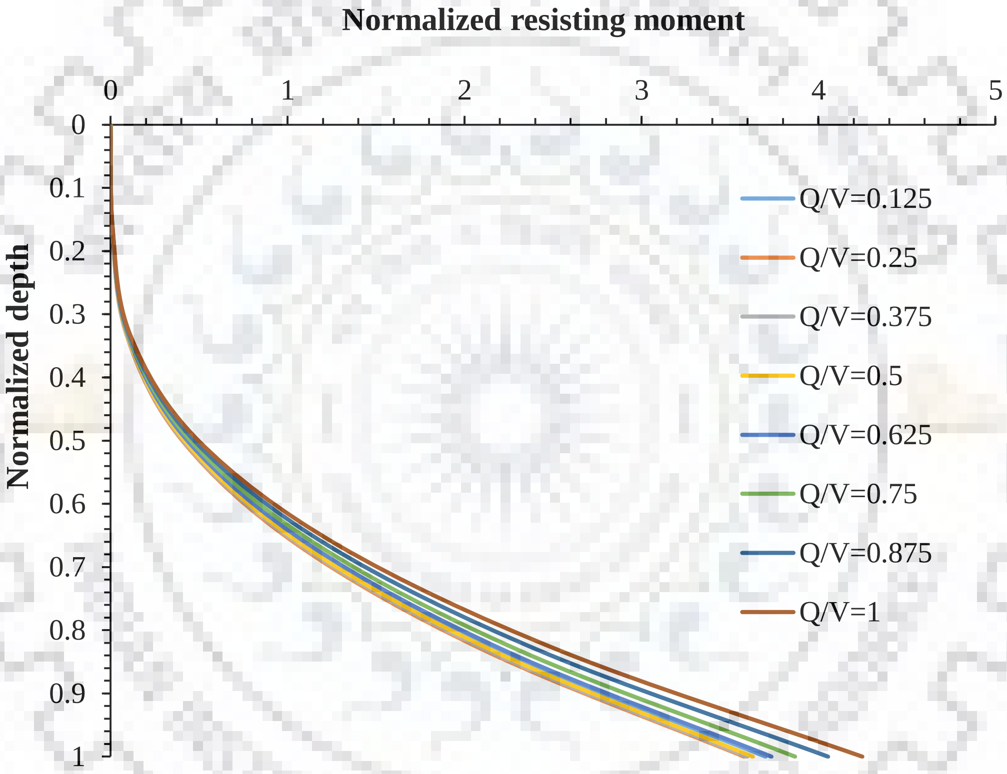

Fig. 4.43 Variation of normalized resisting moment for different magnitudes of lateral loads for V=800 kN and $\delta=\phi$ under static conditions

4.4.5.2 Influence of vertical load (V) on shear force and resisting moment

The vertical load (V) acting on caisson also has significant effect on the resistive forces developed on a caisson. Again, higher is the magnitude of applied vertical load for a fixed Q/V ratio, higher is the lateral load acting on the caisson. Therefore, for increasing vertical load, the normalized shear force follows the same trend as that for varying lateral load as seen in Fig. 4.44. However, the M_R profile for varying vertical load reduces to a single curve as depicted in Fig. 4.45 which suggests that M_R responds linearly to vertical load.

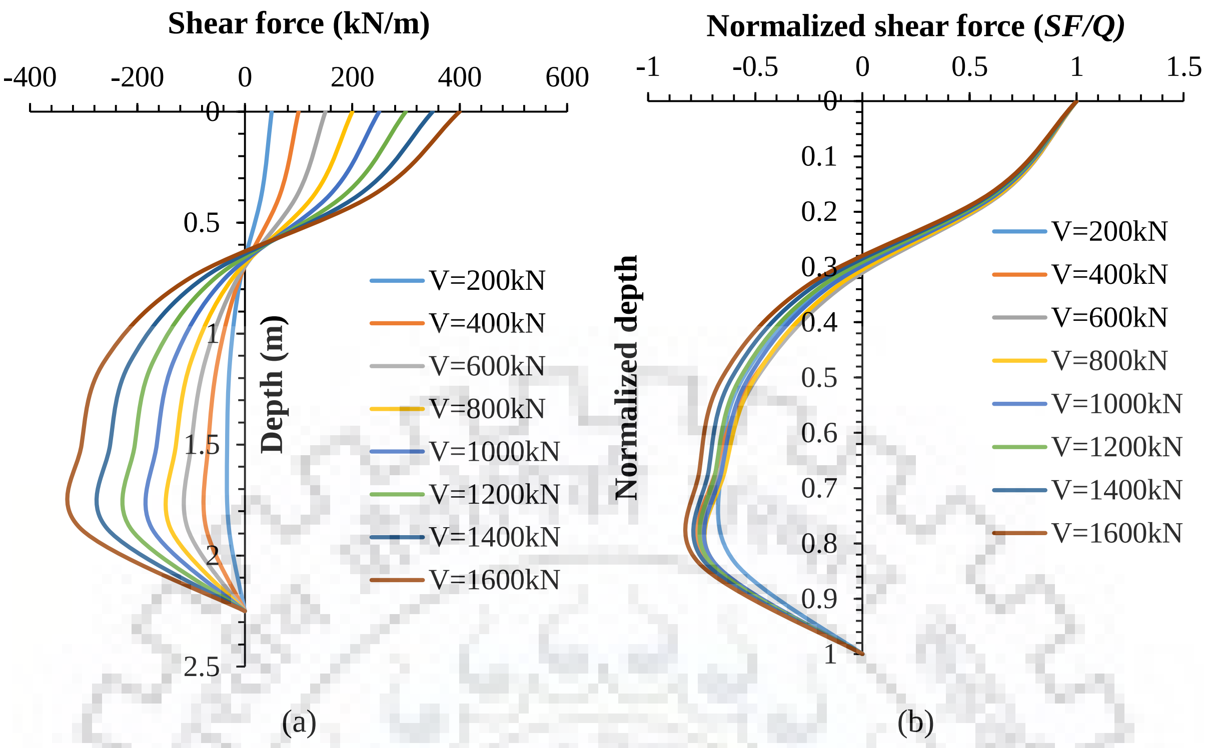

Fig. 4.44 Variation of (a) shear force and (b) normalized shear force for different magnitudes of vertical loads for *Q*/*V*=0.25 and *δ*=*ϕ* under static conditions

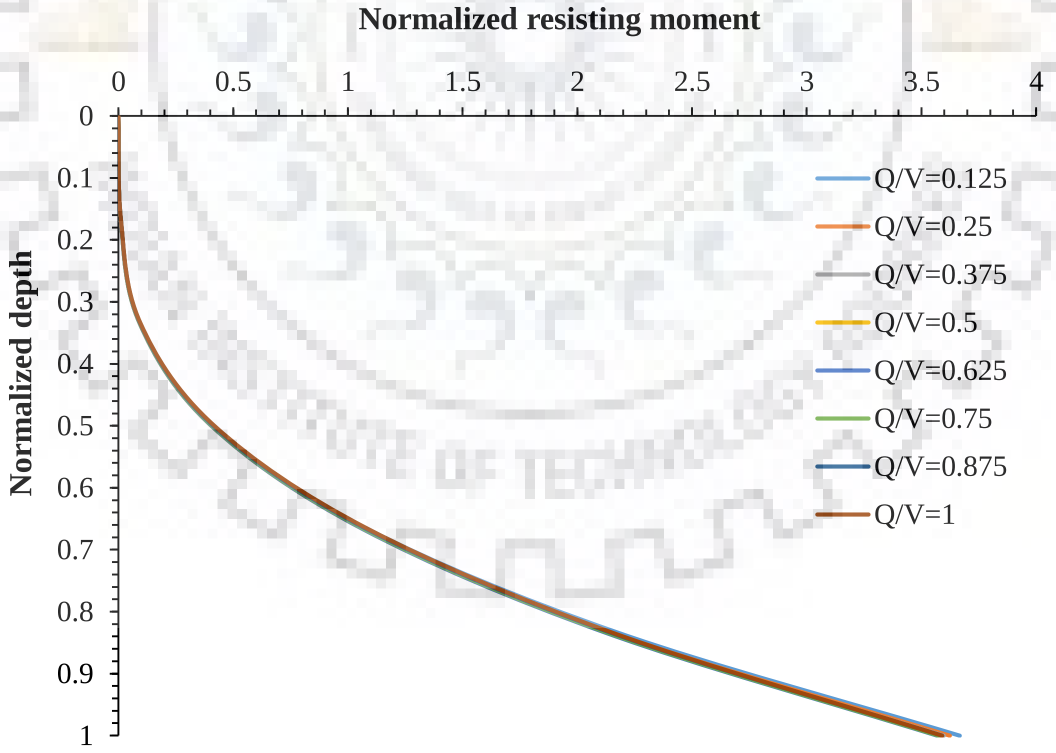

Fig. 4.45 Variation of normalized resisting moment for different magnitudes of vertical loads for *Q*/*V*=0.25 and *δ*=*ϕ* under static conditions

4.4.5.3 *Influence of soil wall friction angle (δ) on shear force and resisting moment*

The variation of various resisting forces with soil-wall friction angle has been observed in the previous section. The resulting shear force diagram reveals that higher is magnitude of δ, smaller is the resisting forces required to be applied to counter the externally applied loading. Fig. 4.46 and Fig. 4.47 represent the variation of normalized shear force and normalized moment of resistance along depth of caisson. It can be confirmed from M_R plot, that smaller moment of resistance is required to be generated at any depth for higher magnitudes of δ.

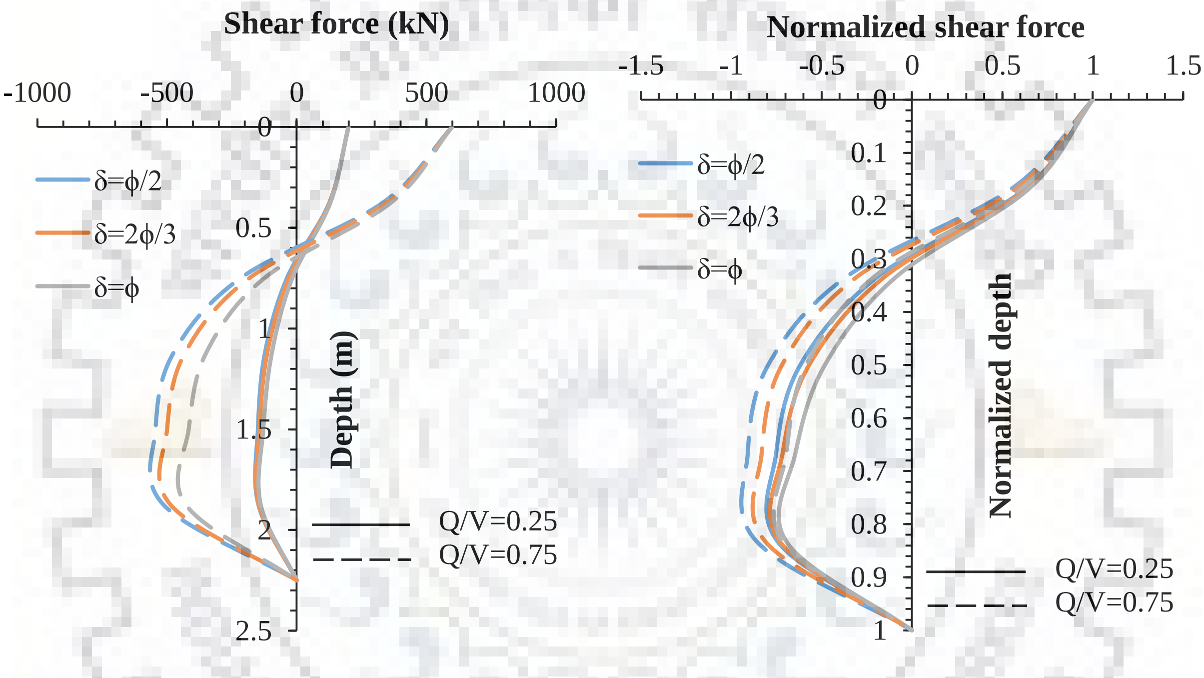

(a) (b)

Fig. 4.46 Variation of (a) shear force and (b) normalized shear force for different magnitudes of soil-wall friction angle at V=800 kN under static conditions

4.4.5.4 *Influence of seismic acceleration coefficients (k_h and k_v) on shear force and resisting moment*

Fig. 4.48 and Fig. 4.49 illustrate the effects of horizontal and vertical seismic acceleration coefficients on shear force profile of caisson. As the magnitude of k_h increases, higher seismic inertial forces are developed and thus, greater magnitudes of resisting forces are mobilized to counter the applied loading. Similarly, vertical seismic acceleration coefficient also has destabilizing effect on caisson-soil system and the shear force diagram reveals the resisting forces developed at any depth.

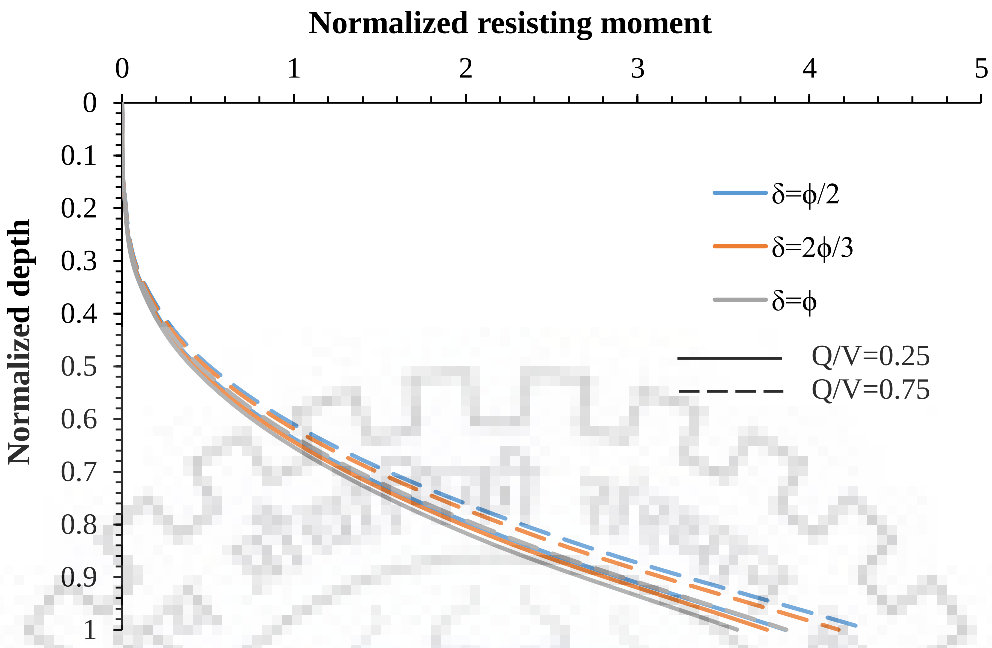

Fig. 4.47 Variation of (a) shear force and (b) normalized shear force for different magnitudes of soil-wall friction angle at V=800 kN under static conditions

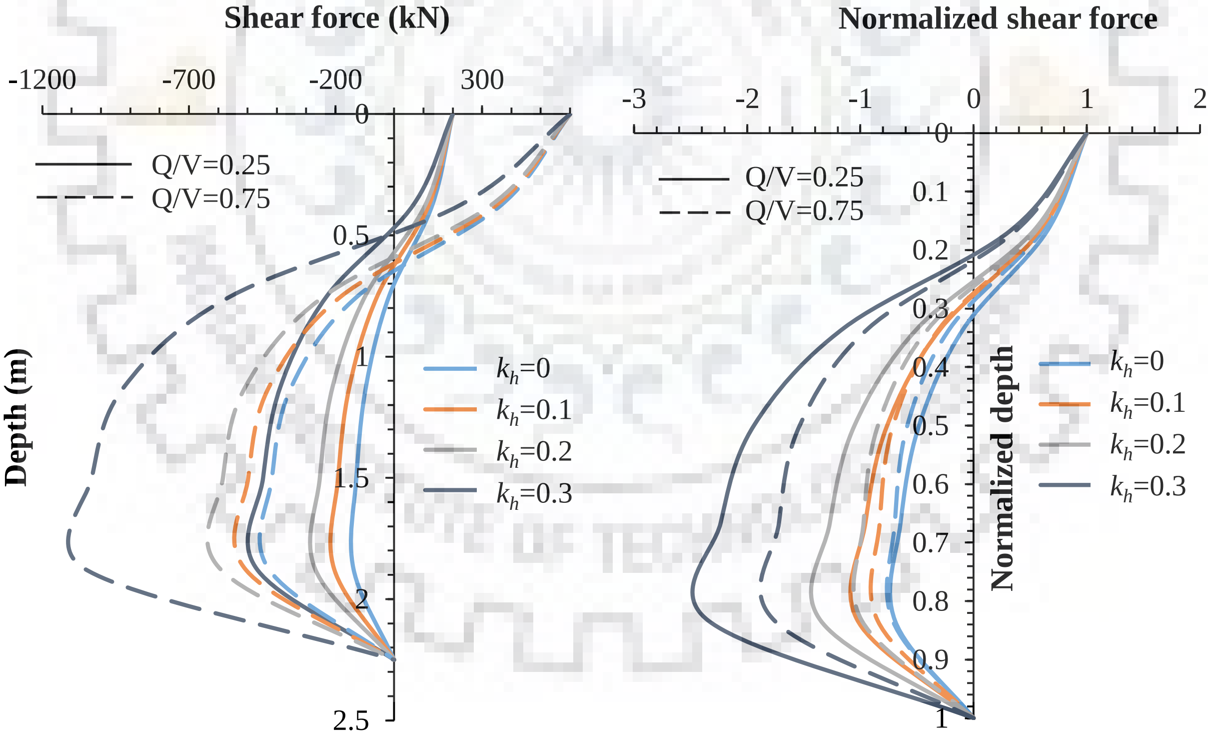

(a) (b)

Fig. 4.48 Variation of (a) shear force and (b) normalized shear force for different magnitudes of k_h at k_v=0, V=800 kN and $\delta=\phi$

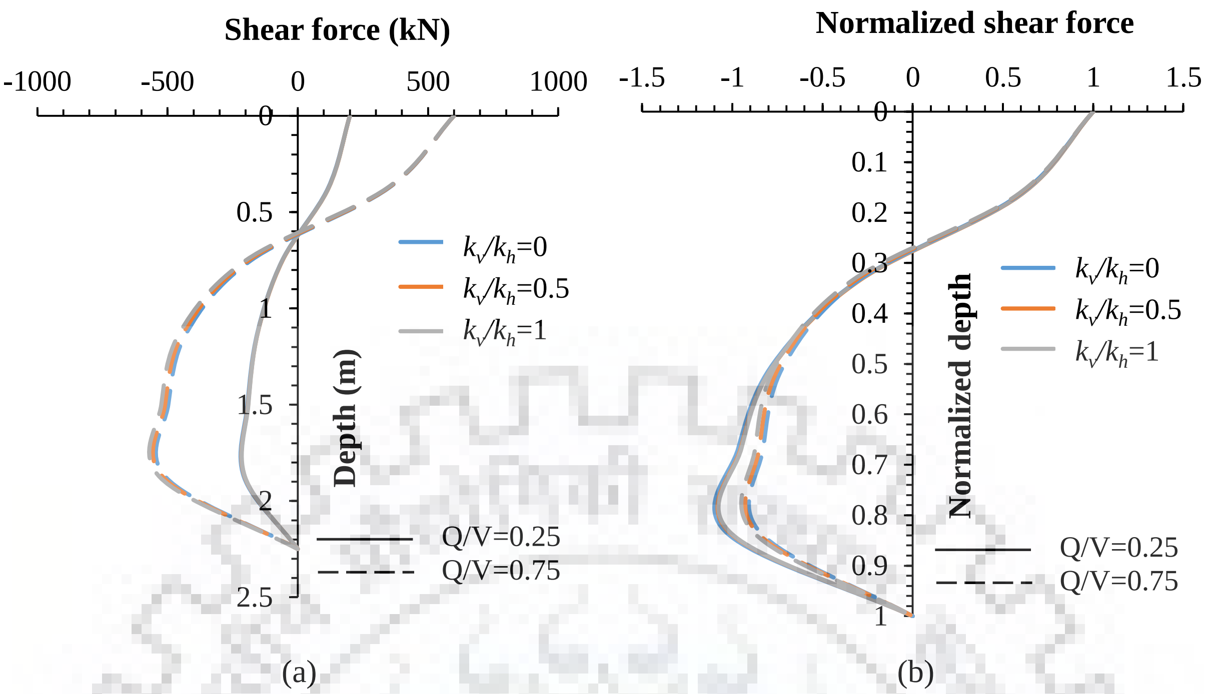

Fig. 4.49 Variation of (a) shear force and (b) normalized shear force for different magnitudes of k_v at k_h=0.1, V=800 kN and $\delta=\phi$

Similarly, Fig. 4.50 and Fig. 4.51 reveal the variation of moment of resistance for various magnitudes of seismic acceleration coefficients. While the normalized M_R is found to be insensitive to the vertical seismic acceleration coefficient, the variation with horizontal seismic acceleration coefficient shows the requirement for higher magnitude of resisting moment at any depth, for different loading and k_h magnitudes.

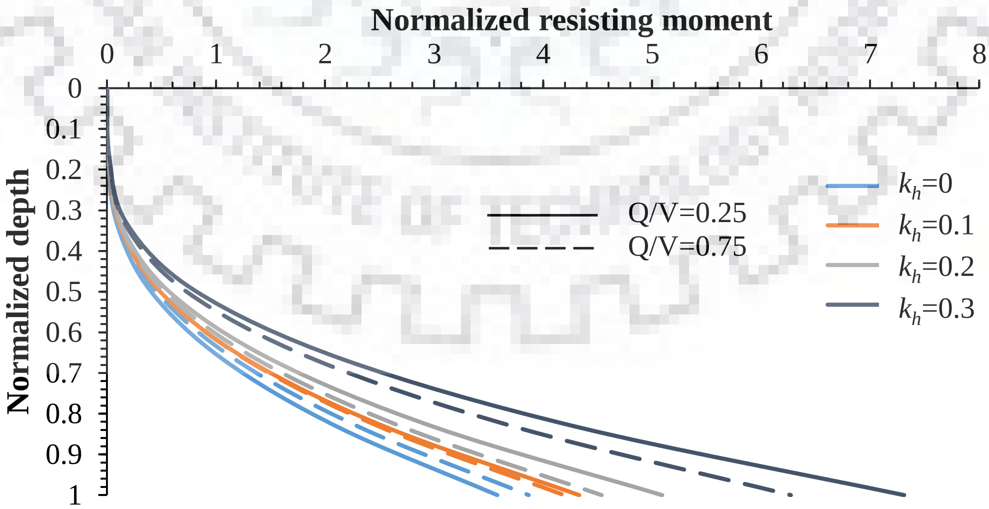

Fig. 4.50 Variation of (a) shear force and (b) normalized shear force for different magnitudes of k_h at k_v=0, V=800kN and $\delta=\phi$

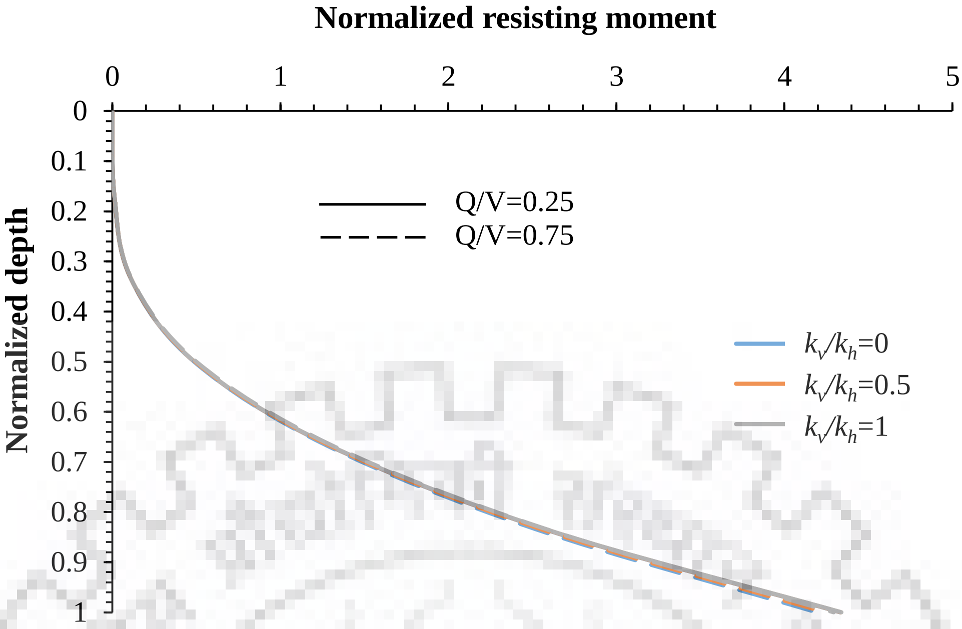

Fig. 4.51 Variation of (a) shear force and (b) normalized shear force for different magnitudes of k_v at k_h=0.1, V=800 kN

4.4.6 Load sharing

The load shared between base (LS_{base}) and sides (LS_{sides}) of caisson in terms of resisting moments is determined based on all the force variations discussed in the preceding sections. The variation of load shared between base and sides of caisson has been discussed with different input parameters.

4.4.6.1 Influence of normalized lateral load (Q/V) on load sharing behaviour

The increasing magnitude of lateral load alters all the resisting components. The net result of these varying resisting forces is that the LS_{sides} first decreases and then increases with increasing lateral load as illustrated in Fig. 4.52. LS_{sides} decreases by 1.27% as Q/V increases from 0.25 to 0.375 and increases by 2.09% when Q/V rises from 0.75 to 0.875. The increase in lateral load increases both lateral soil pressure and base pressure towards toe of caisson. At lower magnitude of lateral load, the increase in side resistance is smaller than base resistance. However, at higher magnitude of lateral load, the side resistance starts dominating.

4.4.6.2 Influence of vertical load (V) on load sharing behaviour

The load shared by sides of caisson reduces with increasing vertical load for a given set of input parameters as seen in Fig. 4.53. It is observed that for Q/V=0.125, LS_{sides} reduces by 0.24% and 0.43% as vertical load increases from V=400 kN to 600 kN and from1000 kN to 1200 kN respectively. At relatively higher magnitudes of vertical loads, the load share of sides is again found to reduce with increasing vertical load. Higher magnitude of vertical load is directly responsible for increasing base pressure and base friction.

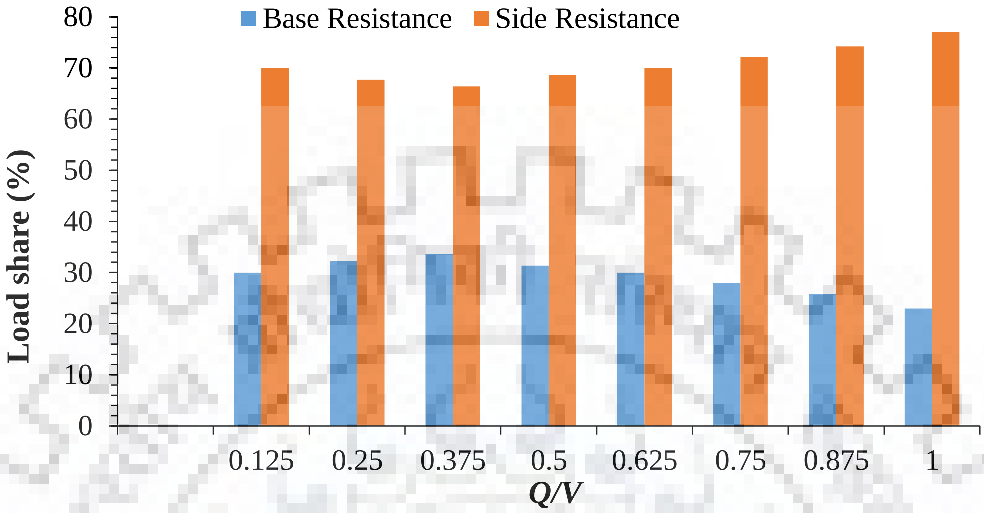

Fig. 4.52 Variation of load share of base and sides with lateral load for V=800 kN and $\delta=\phi$ under static conditions

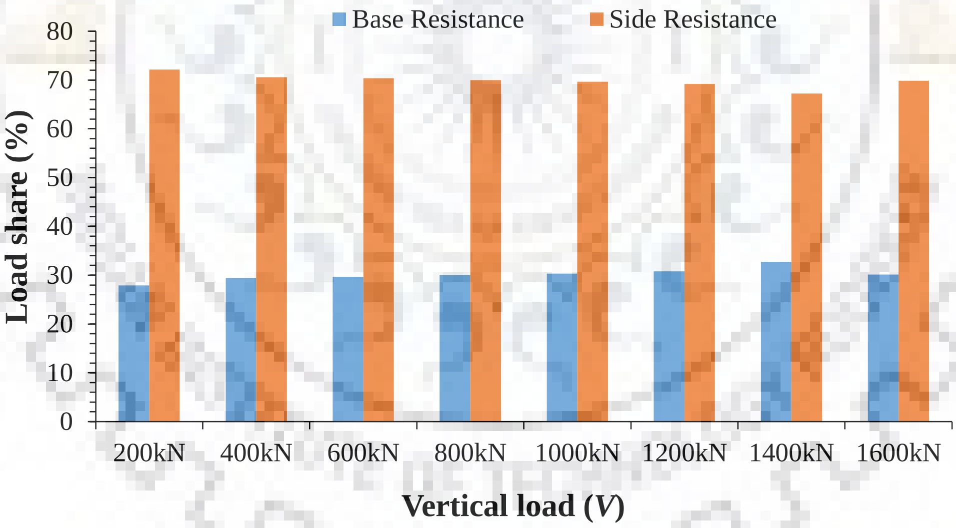

Fig. 4.53 Variation of load share of base and sides with vertical load for Q/V=0.125 and $\delta=\phi$ under static conditions

4.4.6.3 Influence of soil-wall friction angle (δ) on load sharing behaviour

Fig. 4.54 shows the variation of load sharing between base and sides of caisson for varying δ wherein it could be observed that increasing the soil-wall friction angle reduces the percentage of resisting moment provided to sides of caisson. This is because of reduced displacement of caisson under any load combination, which affects the side resistance more than base resistance. As δ increases from $\phi/2$ to $2\phi/3$ and ϕ, the load shared by sides of caisson reduces by 1.09% and 2.58% respectively.

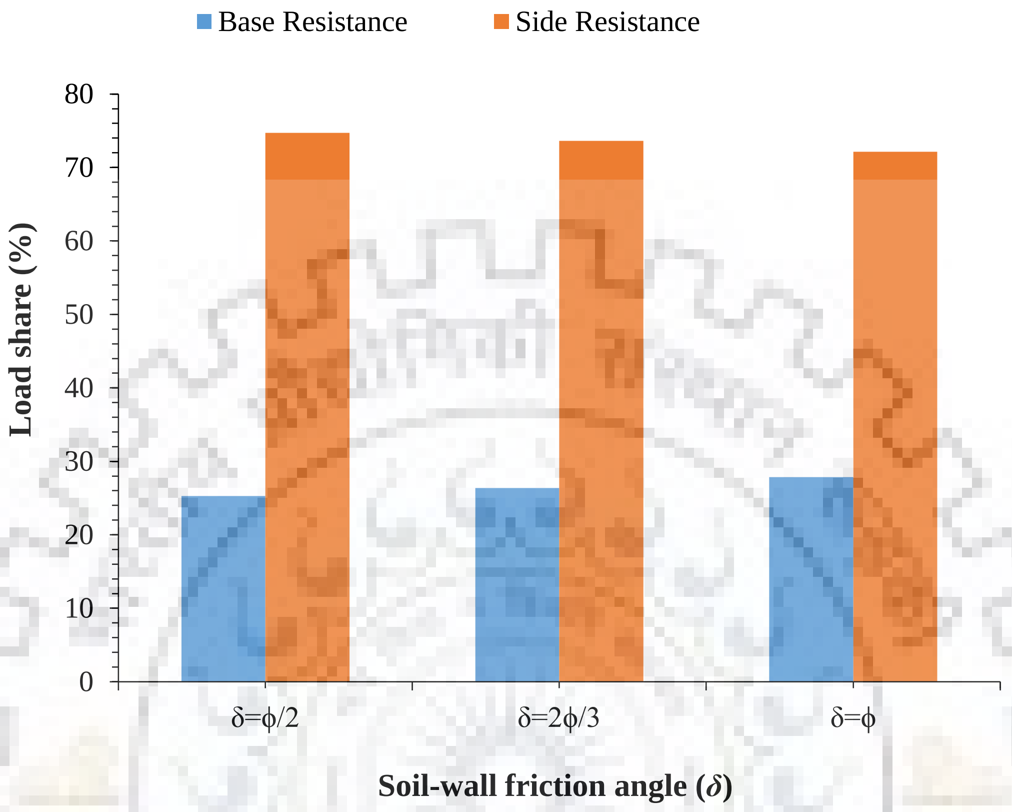

Fig. 4.54 Variation of load share of base and sides with δ for V=800 kN and Q/V=0.75 under static conditions

4.4.6.4 Influence of seismic acceleration coefficients (k_h and k_v) on load sharing behaviour

Both horizontal and vertical seismic acceleration coefficients are found to increase the load shared by sides of caisson. It can be observed from Fig. 4.55 that an increase in k_h from 0 to 0.1, 0.2 and 0.3 increases the load share of sides of caisson by 1.15%, 2.43% and 5.46% respectively for V=800kN, $\delta=\phi$ and Q/V=0.25. Fig. 4.56 reflects the effect of k_v on load sharing behavior. The increase in load sharing by sides when k_v increases from 0 to $k_h/2$ and k_h is found to be 0.73% and 1.5% respectively for the same set of parameters at k_h=0.1. While horizontal seismic acceleration coefficient increases the resisting components acting on sides of caissons much more than they increase the base resisting components, vertical seismic acceleration coefficient reduces the magnitudes of base resistances by individually diminishing both base friction and base reaction.

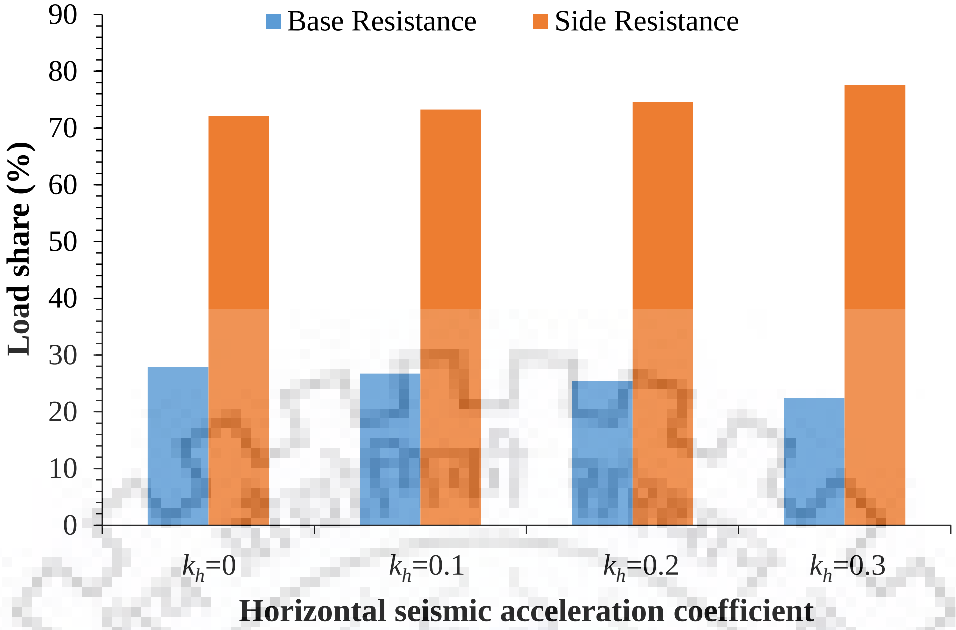

Fig. 4.55 Variation of load share of base and sides with k_h for V=800 kN, Q/V=0.75, k_v=0 and $\delta=\phi$

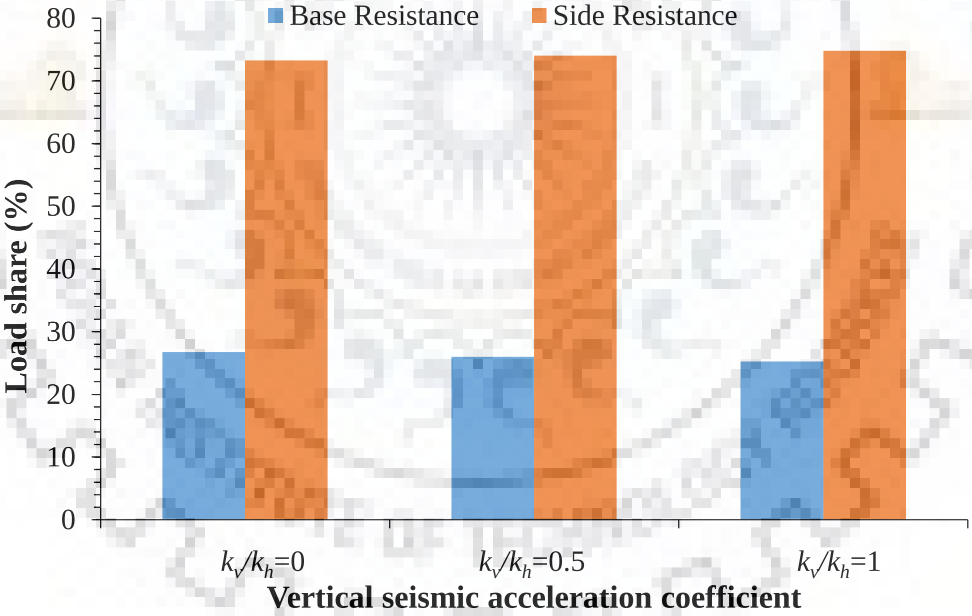

Fig. 4.56 Variation of load share of base and sides with k_v for V=800 kN, Q/V=0.75, k_h=0.1 and $\delta=\phi$

4.5 Regression Analysis

The variation of moment of resistance due to sides of caisson has been mentioned in the previous section. Non-linear regression analysis using Microsoft Excel has been performed on the database comprising the load shared by sides of caisson (LS_{sides}) in terms of resisting moments and the input parameters associated with it. The empirical correlation obtained from regression analysis as mentioned below is valid for the range of input parameters mentioned in Table 3.4.

$$LS_{sides}(\%) = 71.231 - 0.0058V + 0.018Q + 8.767exp(k_h + k_v/3) - 5.589\{\log(Qtan\delta)\} \quad (4.8a)$$

where, the unit of V and Q is kN.

The empirical correlation is found to report the load share with excellent degree of accuracy. The “P-value” testing the accuracy of model is less than 0.02 for all the coefficients suggesting that “null hypothesis” could be rejected. Null hypothesis checks the significance of all the parameters in the model and decides if any parameter could be left out in the model. The load shared by base of caisson (LS_{base}) is thus calculated as:

$$LS_{base}(\%) = 100 - LS_{sides}(\%) \quad (4.8b)$$

4.6 Summary

This chapter deals with the parametric study of different resistive components acting on all the caisson surfaces in contact with the surrounding soil. The absolute and normalized variation of all the resisting components has been presented in this section to better understand the stresses generated on different faces of caisson due to various input parameters. Based on the different resistive components, shear force profile and resisting moment profile along depth of caisson has been generated in both absolute and normalized form. Finally, the load sharing behavior of base and sides of caisson has been explored by performing regression analysis to develop an empirical correlation for the percentage of resisting moment contributed by the sides of caisson for any set of input parameters. The study will help researchers and design engineers in analysis and design of caissons based on the seismic and site conditions that exist.

Chapter 5

PASSIVE EARTH PRESSURE RESISTANCE ON CAISSON EMBEDDED IN c-ϕ SOIL WITH SURCHARGE LOAD USING METHOD OF SUPERPOSITION

5.1 General

Seismic passive resistance offered by soil is the key parameter required for design and analysis of caissons. In the past, multiple studies have been performed for passive earth pressure coefficient for large width structures (Coulomb, 1776; Subba Rao and Choudhury, 2005) and flexible structures like piles (Ashour et al., 1998; Chatterjee et al., 2015). However, determination of seismic passive earth pressure coefficient for finite width structure like caissons is complicated because of formation of 3D failure wedges. Very few studies in the past have considered the width of caisson. In the present study, a novel 3D failure wedge geometry formed behind caisson, embedded in c-ϕ soil (c: cohesion, ϕ: angle of friction) in presence of surcharge loading (q) has been idealized based on the results of numerical study as shown in Fig. 3.6 and experimental study by Olson et al. (2017) as shown in Fig. 2.4. Effect of width of caisson has also been studied for different input parameters. Limit equilibrium method in conjugation with pseudo-static approach has been adopted in the present study. Principle of superposition has been used to determine seismic passive earth pressure coefficients due to different resistive components, i.e., cohesion (K_{spc}), surcharge (K_{spq}) and unit weight ($K_{sp\gamma}$). The seismic passive earth pressure coefficient are the parameters that yield the maximum passive resistance that could be generated by soil at different level of mobilization of strength of soil. These resistances are derived from inertial component of soil ($K_{sp\gamma}$), cohesion of soil (K_{spc}) and the increased confining pressure by virtue of surcharge load (K_{spq}). Design charts for various input parameters have been presented.

5.2 Proposed Theoretical Methodology

A caisson of length L, width B and embedment depth d is assumed to be embedded in homogeneous c-ϕ soil with surcharge of magnitude q acting over failure wedge of depth D. The cohesion and frictional parameters of soil are assumed to be isotropic. The failure wedge in the present study has been chosen to be logarithmic spiral in the vertical plane and sections of circle in horizontal plane as shown in Fig. 5.1 to simulate the actual field conditions more accurately. Limit equilibrium method of analysis has been used in addition to pseudo-static approach for the determination of seismic passive pressure force. The pseudo-static approach of analysis of earth structures was introduced in early 1920s. In this approach, the effects of earthquake motion are represented by constant horizontal and vertical accelerations.

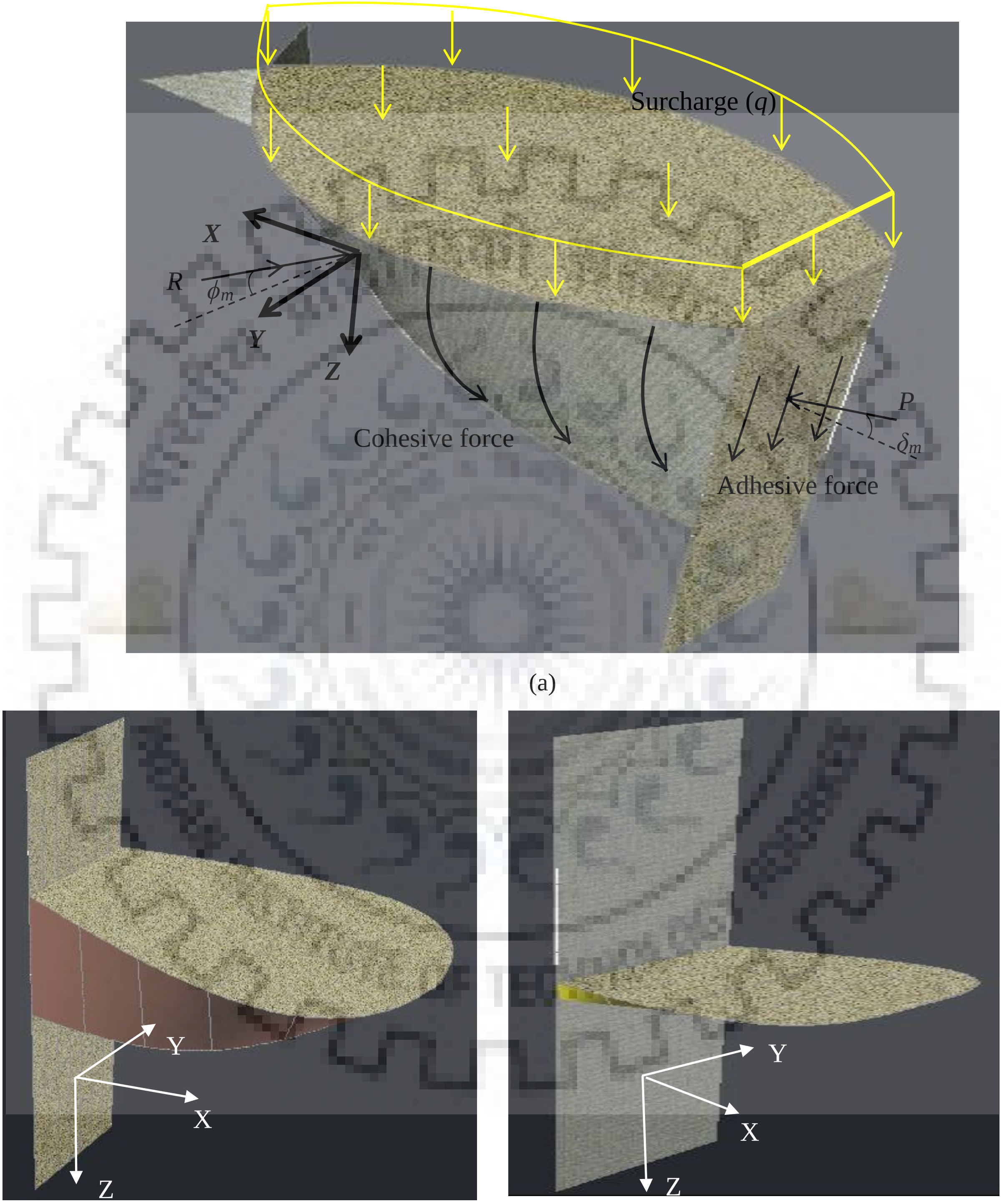

(a)

(b)

(c)

Fig. 5.1 3D failure wedge idealized in the current study with sections at (a) top, (b) mid-depth and (c) near base of failure wedge

Principle of superposition has been used in the present study to find seismic passive earth pressure coefficients due to cohesion (c), surcharge (q) and unit weight components (γ) for the various input parameters as discussed in subsequent section. Principle of superposition states that net effect of all components working together is equal to the sum of effect of individual components acting independently.

5.2.1 Mathematical formulation of the problem

The idealized failure wedge is log-spiral in the vertical plane as illustrated in Fig. 5.2. In the current study, the log-spiral will be described by the equation:

$$r = r_o \mathrm{e}^{\alpha \tan \phi_m} \tag{5.1}$$

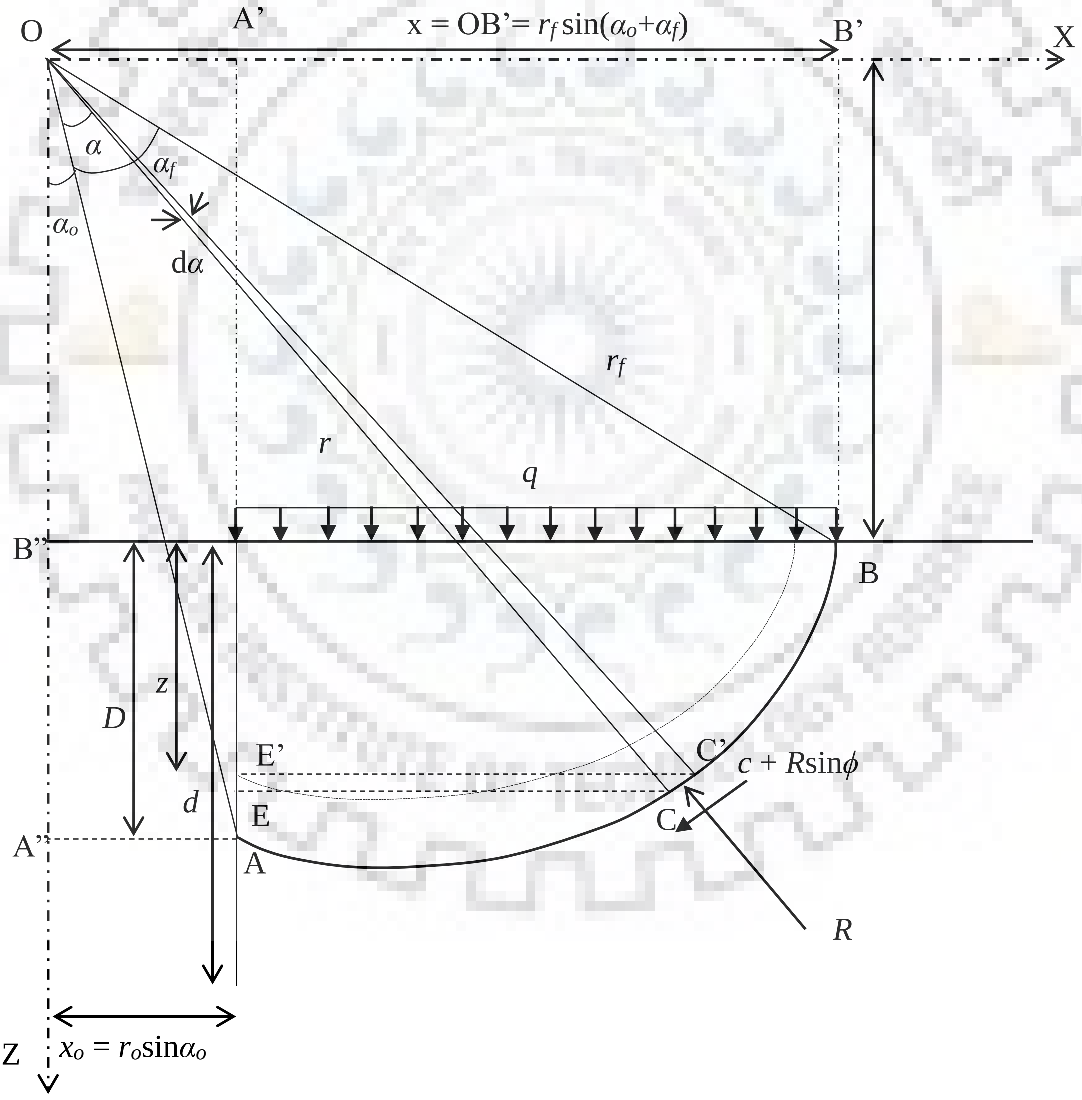

Fig. 5.2 Log-spiral defining the failure wedge in vertical plane

where, r = radius of log-spiral at any angle α at the center from the initial radius r_o

r_o = initial radius of log-spiral

ϕ_m = mobilized soil-soil interface friction angle

As observed from Fig. 5.2, at any depth z,

$$z = r.\cos(\alpha + \alpha_o) - r_f.\cos(\alpha_o + \alpha_f) \tag{5.2a}$$

$$\frac{dz}{d\alpha} = -r.\sin(\alpha + \alpha_o) + r_o.\cos(\alpha + \alpha_o).tan\,\phi_m.e^{\alpha tan\phi_m} \tag{5.2b}$$

$$dz = r.\cos(\alpha + \alpha_o)\,[tan\phi_m - \tan(\alpha + \alpha_o)]d\alpha \tag{5.2c}$$

Fig. 5.3 depicts the geometry of failure wedge in horizontal plane depending on the width of the geotechnical structure. The angle θ defining the shape of the wedge can be obtained as follows:

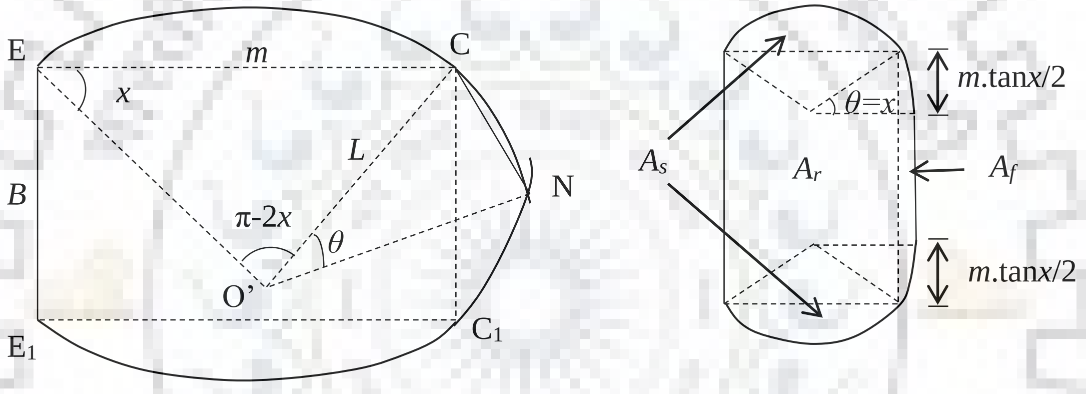

(a) (b)

Fig. 5.3 Idealized passive wedge in horizontal plane for (a) $B \leq m$ tan$x$ and (b) $B > m$ tan$x$

$$m = 2Lcosx \tag{5.3a}$$

$$L = \frac{m}{2\cos x} \tag{5.3b}$$

$$\angle CO'E + 2x = \pi \tag{5.4a}$$

$$\angle CO'E = \pi - 2x \tag{5.4b}$$

Let the angle subtended by half the arc in front of caisson face ($\angle CO'N$) be θ.

Let $\angle CNO' = \angle NCO' = t$

$$2t + \theta = \pi \tag{5.4c}$$

$$t = \frac{\pi}{2} - \frac{\theta}{2} \tag{5.4d}$$

By sine rule,

$$\frac{NC}{\sin\theta} = \frac{L}{\sin t} \tag{5.5a}$$

$$NC = \frac{L\sin\theta}{\sin t} = \frac{2Lsin{}^{\theta}/_{2}cos{}^{\theta}/_{2}}{sin\left(\frac{\pi}{2}-\frac{\theta}{2}\right)} = \frac{2Lsin{}^{\theta}/_{2}cos{}^{\theta}/_{2}}{cos{}^{\theta}/_{2}} = 2Lsin\,{}^{\theta}/_{2} \tag{5.5b}$$

$$\angle O'CE + \angle O'CC_1 = {}^{\pi}/_{2} \tag{5.6a}$$

$$\angle O'CC_1 = {}^{\pi}/_{2} - x \tag{5.6b}$$

$$\angle NCC_1 + \angle O'CC_1 = t \tag{5.6c}$$

$$\angle NCC_1 = t - \left({}^{\pi}/_{2} - x\right) \tag{5.6d}$$

$$NCcos\left(t - \left({}^{\pi}/_{2} - x\right)\right) = \frac{B}{2} \tag{5.7a}$$

$$2Lsin\,{}^{\theta}/_{2}\,cos\left(\left(\frac{\pi}{2} - \frac{\theta}{2}\right) - \left(\frac{\pi}{2} - x\right)\right) = \frac{B}{2} \tag{5.7b}$$

$$2Lsin\,{}^{\theta}/_{2}\,cos\left(x - \frac{\theta}{2}\right) = \frac{B}{2} \tag{5.7c}$$

$$2\,\frac{m}{2\cos x}\,sin\,{}^{\theta}/_{2}\,cos\left(x - \frac{\theta}{2}\right) = \frac{B}{2} \tag{5.8a}$$

$$\frac{2}{\cos x}\,sin\,{}^{\theta}/_{2}\,cos\left(x - \frac{\theta}{2}\right) = \frac{B}{m} \tag{5.8b}$$

$$2sin\,{}^{\theta}/_{2}\left(\cos x\cos\frac{\theta}{2} + \sin x\sin\frac{\theta}{2}\right) = \frac{B\cos x}{m} \tag{5.8c}$$

$$2\sin\frac{\theta}{2}\cos\frac{\theta}{2}\cos x + 2\sin\frac{\theta}{2}\sin x\sin\frac{\theta}{2} = \frac{B\cos x}{m} \tag{5.8d}$$

$$\sin\theta\cos x + 2\sin^2\frac{\theta}{2}\sin x = \frac{B\cos x}{m} \tag{5.8e}$$

$$\sin\theta + 2\sin^2\frac{\theta}{2}\tan x = \frac{B}{m} \tag{5.8f}$$

$$\sin\theta + \tan x\left(2\sin^2\frac{\theta}{2} - 1 + 1\right) = \frac{B}{m} \tag{5.8g}$$

$$\sin\theta + \tan x\left(1 - \left(1 - 2\sin^2\frac{\theta}{2}\right)\right) = \frac{B}{m} \tag{5.8h}$$

$$\sin\theta + \tan x\,(1 - \cos\theta) = \frac{B}{m} \tag{5.9a}$$

$$\sin\theta + \tan x - \cos\theta\tan x = \frac{B}{m} \tag{5.9b}$$

$$\sin\theta - \cos\theta\tan x = \frac{B}{m} - \tan x \tag{5.9c}$$

$$\frac{\sin\theta - \cos\theta\tan x}{\sqrt{1+\tan^2 x}} = \frac{\frac{B}{m} - \tan x}{\sqrt{1+\tan^2 x}} \tag{5.9d}$$

$$\sin\theta\,\frac{1}{\sqrt{1+\tan^2 x}} - \cos\theta\,\frac{\tan x}{\sqrt{1+\tan^2 x}} = \frac{\frac{B}{m} - \tan x}{\sqrt{1+\tan^2 x}} \tag{5.9e}$$

Let $\frac{\tan x}{\sqrt{1+\tan^2 x}} = \sin l$ and $\frac{1}{\sqrt{1+\tan^2 x}} = \cos l$ (5.9f)

$$\tan l = \tan x \tag{5.10a}$$

$$l = x \tag{5.10b}$$

$$\sin\theta\cos x - \cos\theta\sin x = \frac{\frac{B}{m} - \tan x}{\sqrt{1+\tan^2 x}} \tag{5.11a}$$

$$\sin(\theta - x) = \frac{\frac{B}{m} - \tan x}{\sqrt{1+\tan^2 x}} \qquad (5.11b)$$

$$(\theta - x) = \sin^{-1}\left(\frac{\frac{B}{m} - \tan x}{\sqrt{1+\tan^2 x}}\right) \qquad (5.11c)$$

$$\theta(z) = x + \sin^{-1}\left(\frac{\frac{B}{m(z)} - \tan x}{\sqrt{1+\tan^2 x}}\right) \qquad \text{for } B \leq m\tan x \qquad (5.12a)$$

$$\theta = x \qquad \text{for } B > m\tan x \qquad (5.12b)$$

where, *m(z)* = Chord length of the circular sector describing failure wedge at depth *z* along X-direction at edge of caisson

$$m(z) = CE = r(z)\sin(\alpha_o + \alpha_f - \alpha) - x_o \qquad (5.13a)$$

$$x_o = A^{"}A = r_o \sin\alpha_o \qquad (5.13b)$$

$$y_o = OB" = BB' = r_f \cos\left(\alpha_o + \alpha_f\right) \qquad (5.14)$$

where, x_o, y_o are the horizontal and vertical distance of caisson face from the center of log-spiral respectively.

The area of failure wedge in horizontal plane at any arbitrary depth *z* (*A*(*z*)) consists of three components as shown in Fig. 5.3. The magnitudes of these three components at different depths are obtained from the following expressions:

$$A(z) = A_s(z) + A_r(z) + A_f(z) \qquad (5.15a)$$

where, A_s = Area of side wedge as shown in Fig. 5.3b

A_r = Area of rectangular portion of wedge as shown in Fig. 5.3b

A_f = Area of wedge in front of rectangular portion as shown in Fig. 5.3b

$$A_s(z) = \frac{m(z)^2}{4} \times \left[\left(\frac{\pi - 2x}{\cos^2 x}\right) - 2\tan x\right] \qquad (5.15b)$$

$$A_r(z) = B \times m(z) \qquad (5.15c)$$

$B \leq m\tan x$:

$$A_f(z) = \frac{m(z)^2}{4\cos^2 x} \times \left[\theta(z) + \sin\left(x - \theta(z)\right)\cos x - \sin x \cos x\right] \qquad (5.15d)$$

$B > m\tan x$:

$$A_f(z) = \frac{m(z)^2}{4\cos^2 x}(x - \sin x\cos x) + (B - m(z)\tan x)\frac{m(z)}{2}(\sec x - 1) \qquad (5.15e)$$

The resultant of tangential shear force acting on vertical face of failure wedge is given as:

$$\Delta F(z) = 2T \times sin\frac{\phi_m}{2} cos\frac{\phi_m}{2} \qquad (5.16a)$$

where, $T = \lambda\gamma z \times m(z)dz$ (5.16b)

where, λ = tangential stress coefficient. (Prater, 1977)

The angle between radius of log-spiral at any point and the normal to that point is constant and in the current study, this angle is ϕ_m. Thus, the angle of the reaction force with the horizontal plane at any depth z located by sweeping of angle α by the initial radius is $\frac{\pi}{2} - (\alpha + \alpha_o)$. The area of the elemental surface formed by the sweeping angle dξ by the radius of the circle at depth z will be ($\frac{m(z)}{2\cos x} d\xi \times r(z) d\alpha$).

The Y-components (transverse to direction of loading) of soil reaction and cohesion component at soil-soil interface cancel out each other because of geometrical symmetry of the idealized passive wedge about X-axis. The X-component of soil reaction (ΔR_H) and cohesion component (ΔC_H) at depth z is given as:

<u>$B < m\tan x$:</u>

$$dR_H(z) = R\,sin(\alpha + \alpha_o - \phi_m)\,cos\,\phi_m \times \frac{m(z)}{2\,cos\,x} d\xi \times r(z)d\alpha \times cos(x - \xi) \tag{5.17a}$$

$$\Delta R_H(z) = 2\int_0^{\theta} R\,sin(\alpha + \alpha_o - \phi_m)\,cos\,\phi_m \times \frac{m(z)}{2\,cos\,x} d\xi \times r(z)d\alpha \times cos(x - \xi) \tag{5.17b}$$

$$\Delta R_H(z) = Rm(z)r(z)\frac{cos\,\phi_m}{cos\,x} sin(\alpha + \alpha_o - \phi_m) \times d\alpha \times \{sin\,x - sin(x - \theta(z))\} \tag{5.17c}$$

$$dC_H(z) = (c + R\,sin\,\phi_m)\,cos(\alpha + \alpha_o - \phi_m)\frac{m(z)}{2\,cos\,x} d\xi \times r(z)d\alpha \times cos(x - \xi) \tag{5.18a}$$

$$\Delta C_H(z) = 2\int_0^{\theta} (c + R\,sin\,\phi)\,cos(\alpha + \alpha_o - \phi_m) \times \frac{m(z)}{2\,cos\,x} d\xi \times r(z)d\alpha \times cos(x - \xi) \tag{5.18b}$$

$$\Delta C_H(z) = m(z)r(z)d\alpha\frac{cos(\alpha + \alpha_o - \phi_m)\{sin\,x - sin(x - \theta(z))\}}{cos\,x} \times (c + R\,sin\,\phi_m) \tag{5.18c}$$

<u>$B > m\tan x$:</u>

$$\Delta R_H(z) = \left[2\int_0^{x} R\,sin(\alpha + \alpha_o - \phi_m)\,cos\,\phi_m \times \frac{m(z)}{2\,cos\,x} d\xi \times r(z)d\alpha \times cos(x - \xi)\right] + \int_0^{B - m(z)\,tan\,x} R\,sin(\alpha + \alpha_o - \phi_m)\,cos\,\phi_m \times r(z)d\alpha \times dl \tag{5.19a}$$

$$\Delta R_H(z) = \left\{Rm(z)r(z)\frac{cos\,\phi_m}{cos\,x} sin(\alpha + \alpha_o - \phi_m) \times d\alpha \times sin\,x\right\} + \{R\,sin(\alpha + \alpha_o - \phi_m)\,cos\,\phi_m \times r(z)d\alpha \times (B - m(z)\,tan\,x)\} \tag{5.19b}$$

$$\Delta R_H(z) = BRr(z)\,sin(\alpha + \alpha_o - \phi_m)\,cos\,\phi_m\,d\alpha \tag{5.19c}$$

$$\Delta C_H(z) = \left[2\int_0^{x} (c + R\,sin\,\phi_m)\,cos(\alpha + \alpha_o - \phi_m) \times \frac{m(z)}{2\,cos\,x} d\xi \times r(z)d\alpha \times cos(x - \xi)\right] + \int_0^{B - m(z)\,tan\,x} (c + R\,sin\,\phi_m)\,cos(\alpha + \alpha_o - \phi_m) \times r(z)d\alpha \times dl \tag{5.20a}$$

$$\Delta C_H(z) = B(c + R\,sin\,\phi_m)\,cos(\alpha + \alpha_o - \phi_m)rd\alpha \tag{5.20b}$$

The vertical component of soil reaction (ΔR_V) and cohesive resistance (ΔC_V) at depth z is:

<u>$B < m\tan x$:</u>

$$dR_V(z) = R\,cos\,\phi_m\,cos(\alpha + \alpha_o - \phi_m) \times \frac{m(z)}{2\,cos\,x} d\xi \times r(z)d\alpha \tag{5.21a}$$

$$\Delta R_V(z) = 2 \times \int_0^{\pi-2x+\theta(z)} R\cos\phi_m \cos(\alpha+\alpha_o-\phi_m) \times \frac{m(z)}{2\cos x} d\xi \times r(z)d\alpha \qquad (5.21b)$$

$$\Delta R_V(z) = Rmr(z)\frac{\cos\phi_m}{\cos x}\cos(\alpha+\alpha_o-\phi_m)\, d\alpha \times \big(\pi-2x+\theta(z)\big) \qquad (5.21c)$$

$$dC_V(z) = (c+R\sin\phi_m) \times \sin(\alpha+\alpha_o-\phi_m)\frac{m(z)d\xi}{2\cos x} r(z)d\alpha \qquad (5.22a)$$

$$\Delta C_V(z) = 2 \times \int_0^{\pi-2x+\theta(z)} (c+R\sin\phi_m) \times \sin(\alpha+\alpha_o-\phi_m)\frac{m(z)d\xi}{2\cos x} r(z)d\alpha \qquad (5.22b)$$

$$\Delta C_V(z) = m(z)r(z)d\alpha\frac{\{\pi-2x+\theta(z)\}\sin(\alpha+\alpha_o-\phi_m)}{\cos x} \times (c+R\sin\phi_m) \qquad (5.22c)$$

<u>$B > m\tan x$:</u>

$$\Delta R_V(z) = \left[2 \times \int_0^{\pi-x} R\cos\phi_m\cos(\alpha+\alpha_o-\phi_m) \times \frac{m(z)}{2\cos x}d\xi \times r(z)d\alpha\right] +$$

$$\int_0^{B-m(z)\tan x} R\cos\phi_m\cos(\alpha+\alpha_o-\phi_m) \times r(z)d\alpha \times dl \qquad (5.23a)$$

$$\Delta R_V(z) = \left\{Rm(z)r(z)\frac{\cos\phi_m}{\cos x}\cos(\alpha+\alpha_o-\phi_m)\, d\alpha \times (\pi-x)\right\} + \{R\cos\phi_m\cos(\alpha+\alpha_o-$$

$$\phi_m) \times r(z)d\alpha \times (B-m(z)\tan x)\} \qquad (5.23b)$$

$$\Delta R_V(z) = R\cos\phi_m\cos(\alpha+\alpha_o-\phi_m) \times r(z)d\alpha \times \left\{B+\frac{m(z)}{\cos x}(\pi-x-\sin x)\right\} \qquad (5.23c)$$

$$\Delta C_V(z) = \left[2 \times \int_0^{\pi-x} (c+R\sin\phi_m)\sin(\alpha+\alpha_o-\phi_m) \times \frac{m(z)}{2\cos x}d\xi \times r(z)d\alpha\right] +$$

$$\int_0^{B-m(z)\tan x} (c+R\sin\phi_m)\sin(\alpha+\alpha_o-\phi_m) \times r(z)d\alpha \times dl \qquad (5.24a)$$

$$\Delta C_V(z) = r(z)d\alpha\sin(\alpha+\alpha_o-\phi_m)\left\{B+\frac{m(z)}{\cos x}(\pi-x-\sin x)\right\} \times (c+R\sin\phi_m) \qquad (5.24b)$$

5.2.1.1 Formulation for seismic passive earth pressure coefficient due to cohesion component (K_{spc})

Fig. 5.4 depicts the free body diagram of infinitesimally thin soil element of thickness dz at depth *z*. Considering only the cohesion components and soil reaction on failure wedge (*q*=0 and *γ*=0), the horizontal and vertical equilibrium equations can be written as:

<u>$B < m\tan x$:</u>

Considering equilibrium of forces in horizontal direction for the elemental disc:

$$p(z)B\cos\delta\, dz = \Delta C_H(z) + \Delta R_H(z) \qquad (5.25a)$$

$$p(z)B\cos\delta\, dz = m(z)r(z)d\alpha\frac{\cos(\alpha+\alpha_o-\phi_m)\{\sin x-\sin(x-\theta(z))\}}{\cos x} \times (c+R\sin\phi_m) +$$

$$Rm(z)r(z)d\alpha\frac{\cos\phi_m}{\cos x}\sin(\alpha+\alpha_o-\phi_m)\big\{\sin x-\sin\big(x-\theta(z)\big)\big\} \qquad (5.25b)$$

$$p(z)B\cos\delta\, dz = \frac{m(z)r(z)d\alpha\{\sin x-\sin(x-\theta(z))\}}{\cos x} \times \{c\cos(\alpha+\alpha_o-\phi_m) + R\sin\phi_m\cos(\alpha+$$

$$\alpha_o-\phi_m) + R\cos\phi_m\sin(\alpha+\alpha_o-\phi_m)\} \qquad (5.25c)$$

$$p(z)B\cos\delta\, dz\frac{\cos x}{m(z)r(z)d\alpha\{\sin x-\sin(x-\theta(z))\}} - c\cos(\alpha+\alpha_o-\phi_m) = R\sin(\alpha+\alpha_o) \qquad (5.25d)$$

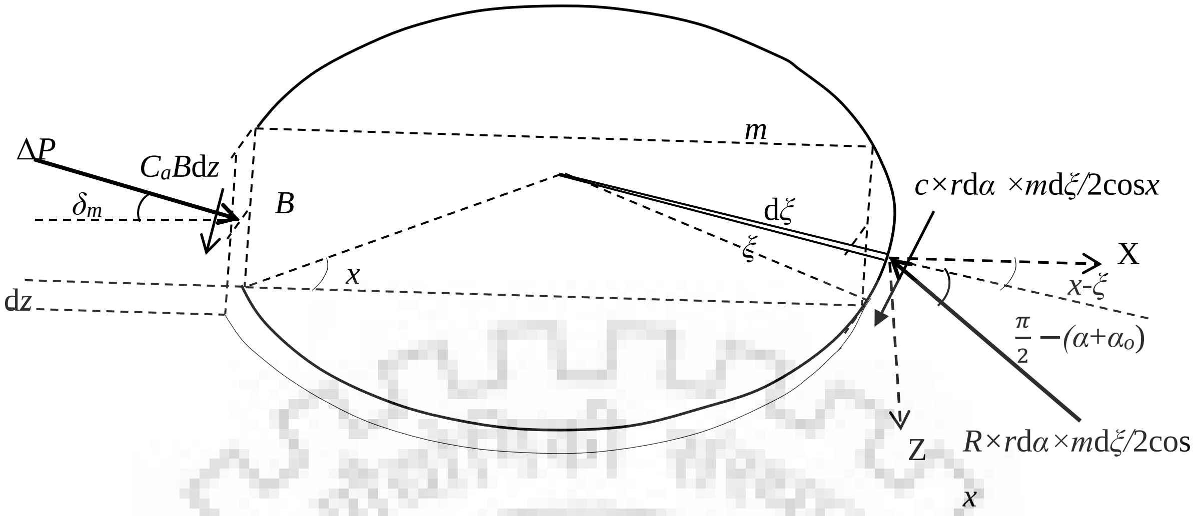

Fig. 5.4 Free body diagram of forces acting on infinitesimal strip of failure wedge in presence of cohesion component only

From equilibrium of forces in vertical direction for the elemental disc:

$p(z)B\sin\delta\,dz + C_aBdz = \delta R_V(z) - \delta C_V(z)$ (5.26a)

$p(z)B\sin\delta\,dz + C_aBdz = Rm(z)r(z)d\alpha\frac{\cos\phi_m}{\cos x}\cos(\alpha+\alpha_o-\phi_m)\{\pi-2x+\theta(z)\} -$

$m(z)r(z)d\alpha\frac{\{\pi-2x+\theta(z)\}\sin(\alpha+\alpha_o-\phi_m)}{\cos x}\times(c+R\sin\phi_m)$ (5.26b)

$p(z)B\sin\delta\,dz + C_aBdz = \frac{m(z)r(z)d\alpha}{\cos x}\{\pi-2x+\theta(z)\}[R\cos\phi_m\cos(\alpha+\alpha_o-\phi_m) -$

$\sin(\alpha+\alpha_o-\phi_m)\,(c+R\sin\phi_m)]$ (5.26c)

$\{p(z)B\sin\delta\,dz + C_aBdz\}\frac{\cos x}{m(z)r(z)d\alpha\{\pi-2x+\theta(z)\}} + c\sin(\alpha+\alpha_o-\phi_m) = R\cos(\alpha+\alpha_o)$

(5.26d)

Dividing Eqn. (5.25d) by Eqn. (5.26d)

$\frac{[p(z)B\cos\delta dz\cos x-c\cos(\alpha+\alpha_o-\phi_m)m(z)r(z)d\alpha\{\sin x-\sin(x-\theta(z))\}][\pi-2x+\theta(z)\}}{[\{p(z)B\sin\delta dz+C_aBdz\}(\cos x)+c\sin(\alpha+\alpha_o-\phi_m)m(z)r(z)d\alpha\{\pi-2x+\theta(z)\}][\sin x-\sin(x-\theta(z))\}} = \tan(\alpha+\alpha_o)$

(5.27a)

$p(z)Bdz\cos x\left[\cos\delta\{\pi-2x+\theta(z)\} - \sin\delta\tan(\alpha+\alpha_o)\{\sin x-\sin(x-\theta(z))\}\right] =$

$cm(z)r(z)d\alpha\{\sin x-\sin(x-\theta(z))\}\{\pi-2x+\theta(z)\}[\cos(\alpha+\alpha_o-\phi_m)+\sin(\alpha+\alpha_o-$

$\phi_m)\tan(\alpha+\alpha_o)] + C_aBdz\cos x\{\sin x-\sin(x-\theta(z))\}\tan(\alpha+\alpha_o)$ (5.27b)

Let $HD(z) = \{\sin x-\sin(x-\theta(z))\}\tan(\alpha+\alpha_o)$ and $VD(z) = \pi-2x+\theta(z)$

$p(z)Bdz\cos x\,[\cos\delta\,VD(z) - \sin\delta\,HD(z)] = cm(z)r(z)d\alpha HD(z)VD(z)\left[\frac{\cos(\alpha+\alpha_o-\phi_m)}{\tan(\alpha+\alpha_o)} +\right.$

$\left.\sin(\alpha+\alpha_o-\phi_m)\right] + C_aBdz\cos x\,HD(z)$ (5.27c)

$$p(z)Bdz = \frac{cm(z)r(z)d\alpha HD(z)VD(z)\left[\frac{\cos(\alpha+\alpha_o-\phi_m)}{\tan(\alpha+\alpha_o)}+\sin(\alpha+\alpha_o-\phi_m)\right]+C_a Bdz\cos x HD(z)}{\cos x[\cos\delta VD(z)-\sin\delta HD(z)]} \tag{5.27d}$$

<u>*B* > *m*tan*x*:</u>

Considering equilibrium of forces in horizontal direction for the elemental disc:

$$p(z)B\cos\delta\, dz = \delta C_H(z) + \delta R_H(z) \tag{5.28a}$$

$$p(z)B\cos\delta\, dz = B(c + R\sin\phi_m)\cos(\alpha+\alpha_o-\phi_m)rd\alpha + BRr(z)\sin(\alpha+\alpha_o-\phi_m)\cos\phi_m\, d\alpha \tag{5.28b}$$

$$p(z)B\cos\delta\, dz = Br(z)d\alpha[R\sin(\alpha+\alpha_o) + c\ \cos(\alpha+\alpha_o-\phi_m)] \tag{5.28c}$$

$$\frac{p(z)B\cos\delta dz - Bc\cos(\alpha+\alpha_o-\phi_m)r(z)d\alpha}{Br(z)d\alpha} = R\sin(\alpha+\alpha_o) \tag{5.28d}$$

From equilibrium of forces in vertical direction for the elemental disc:

$$p(z)B\sin\delta\, dz + C_a Bdz = \delta R_V(z) - \delta C_V(z) \tag{5.29a}$$

$$p(z)B\sin\delta\, dz + C_a Bdz = R\cos\phi_m\cos(\alpha+\alpha_o-\phi_m)\times r(z)d\alpha\times\left\{B+\frac{m(z)}{\cos x}(\pi-x-\sin x)\right\} - r(z)d\alpha\sin(\alpha+\alpha_o-\phi_m)\left\{B+\frac{m(z)}{\cos x}(\pi-x-\sin x)\right\}\times(c+R\sin\phi_m) \tag{5.29b}$$

$$p(z)B\sin\delta\, dz + C_a Bdz = r(z)d\alpha\left\{B+\frac{m(z)}{\cos x}(\pi-x-\sin x)\right\}[R\cos(\alpha+\alpha_o) - c\sin(\alpha+\alpha_o-\phi_m)] \tag{5.29c}$$

$$\frac{p(z)B\sin\delta dz + C_a Bdz + c\sin(\alpha+\alpha_o-\phi_m)r(z)d\alpha\left\{B+\frac{m(z)}{\cos x}(\pi-x-\sin x)\right\}}{r(z)d\alpha\left\{B+\frac{m(z)}{\cos x}(\pi-x-\sin x)\right\}} = R\cos(\alpha+\alpha_o) \tag{5.29d}$$

Dividing Eqn. (5.28d) by Eqn. (5.29d)

$$\frac{\{p(z)B\cos\delta dz - Bc\cos(\alpha+\alpha_o-\phi_m)r(z)d\alpha\}\left\{B+\frac{m(z)}{\cos x}(\pi-x-\sin x)\right\}}{B\left[p(z)B\sin\delta dz + C_a Bdz + c\sin(\alpha+\alpha_o-\phi_m)r(z)d\alpha\left\{B+\frac{m(z)}{\cos x}(\pi-x-\sin x)\right\}\right]} = \tan(\alpha+\alpha_o) \tag{5.30a}$$

Let $HD(z)$ = $B\tan(\alpha+\alpha_o)$ and $VD(z)$ = $B + \frac{m(z)}{\cos x}(\pi - x - \sin x)$

$$p(z)Bdz[\cos\delta\, VD(z) - \sin\delta\, HD(z)] = \left[cr(z)d\alpha HD(z)VD(z)\left\{\sin(\alpha+\alpha_o-\phi_m) + \frac{\cos(\alpha+\alpha_o-\phi_m)}{\tan(\alpha+\alpha_o)}\right\}\right] + C_a BdzHD(z) \tag{5.30b}$$

$$p(z)Bdz = \frac{\left[cr(z)d\alpha HD(z)VD(z)\left\{\sin(\alpha+\alpha_o-\phi_m)+\frac{\cos(\alpha+\alpha_o-\phi_m)}{\tan(\alpha+\alpha_o)}\right\}\right]+C_a BdzHD(z)}{[\cos\delta VD(z)-\sin\delta HD(z)]} \tag{5.30c}$$

Integration of Eqns. (5.27d) and (5.30c) gives the caisson reaction (P_{pc}) for entire depth of failure wedge because of cohesion components. The average seismic passive earth pressure coefficient due to cohesion component (K_{spc}) is determined using the following equations:

$$K_{spc}cBD = P_{pc} \tag{5.31a}$$

$$K_{spc} = \frac{P_{pc}}{cBD} \tag{5.31b}$$

where, *D* is the depth of the failure wedge as shown in Fig. 5.2

5.2.1.2 Formulation of seismic passive earth pressure coefficient due to surcharge component (K_{spq})

Fig. 5.5 shows the forces acting on the infinitesimal failure wedge at depth *z* due to surcharge components acting alone. Considering equilibrium of forces in horizontal direction for the elemental disc due to surcharge component only (*c*=0 and *γ*=0),

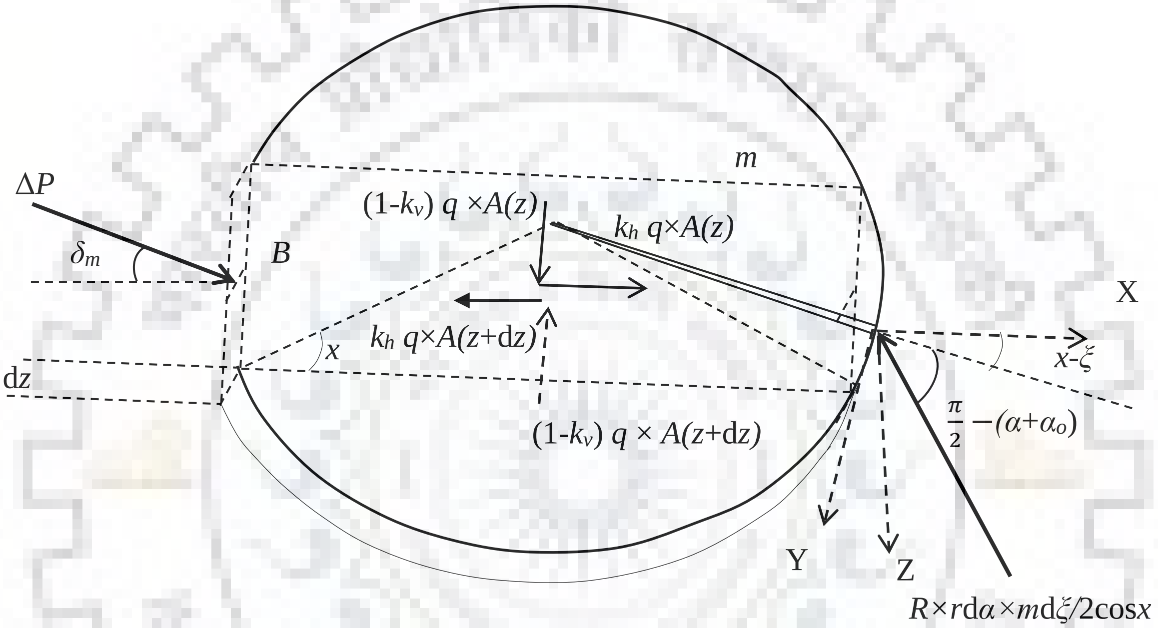

Fig. 5.5 Free body diagram of forces acting on infinitesimal strip of failure wedge in presence of surcharge component only

<u>$B < m\tan x$</u>

$$p(z)B\cos\delta\, dz + k_h qA(z) - k_h qA(z+dz) = \Delta R_H(z) = Rm(z)r(z)\frac{\cos\phi}{\cos x}\sin(\alpha+\alpha_o-\phi_m)\times d\alpha\times\{\sin x - \sin(x-\theta(z))\} \tag{5.32a}$$

From equilibrium of forces in vertical direction for the elemental disc:

$$p(z)B\sin\delta\, dz + (1-k_v)qA(z) - (1-k_v)qA(z+dz) = \Delta R_V(z) = Rm(z)r(z)\frac{\cos\phi_m}{\cos x}\cos(\alpha+\alpha_o-\phi_m)\, d\alpha\times(\pi-2x+\theta(z)) \tag{5.32b}$$

Dividing Eqn. (5.32a) by Eqn. (5.32b)

$$\frac{p(z)B\cos\delta dz + k_h qA(z) - k_h qA(z+dz)}{p(z)B\, sin\,\delta dz + (1-k_v)qA(z) - (1-k_v)qA(z+dz)} = \frac{\tan(\alpha+\alpha_o-\phi_m)\{\sin x - \sin(x-\theta(z))\}}{\pi-2x+\theta(z)} \tag{5.33a}$$

$$p(z)Bdz\left[\sin\delta\left(\pi-2x+\theta(z)\right)-\cos\delta\tan(\alpha+\alpha_o-\phi_m)\left\{\sin x-\sin\left(x-\theta(z)\right)\right\}\right]=\left[k_hq\{A(z)-A(z+dz)\}\tan(\alpha+\alpha_o-\phi_m)\left\{\sin x-\sin\left(x-\theta(z)\right)\right\}\right]-\left[(1-k_v)q\{A(z)-A(z+dz)\}\left(\pi-2x+\theta(z)\right)\right] \tag{5.33b}$$

Let $HD(z)$ = $\tan(\alpha+\alpha_o-\phi_m)\left\{\sin x-\sin\left(x-\theta(z)\right)\right\}$

and $VD(z)$ = $\pi-2x+\theta(z)$

$$p(z)dz=\frac{[k_hq\{A(z)-A(z+dz)\}HD(z)]-[(1-k_v)q\{A(z)-A(z+dz)\}VD(z)]}{(sin\,\delta\times VD(z))-(cos\,\delta\times HD(z))} \tag{5.33c}$$

<u>$B > m\tan x$</u>

$$p(z)B\cos\delta\,dz+k_hqA(z)-k_hqA(z+dz)=\Delta R_H(z)=BRr(z)\sin(\alpha+\alpha_o-\phi_m)\cos\phi_m\,d\alpha \tag{5.34a}$$

$$p(z)B\sin\delta\,dz+(1-k_v)qA(z)-(1-k_v)qA(z+dz)=\delta R_V(z)=R\cos\phi_m\cos(\alpha+\alpha_o-\phi_m)\times r(z)d\alpha\times\left\{B+\frac{m(z)}{\cos x}(\pi-x-\sin x)\right\} \tag{5.34b}$$

Dividing Eqn. (5.34a) by Eqn. (5.34b)

$$\frac{p(z)B\cos\delta dz+k_hqA(z)-k_hqA(z+dz)}{p(z)B\sin\delta dz+(1-k_v)qA(z)-(1-k_v)qA(z+dz)}=\frac{\tan(\alpha+\alpha_o-\phi_m)\times B}{B+\frac{m(z)}{\cos x}(\pi-x-\sin x)} \tag{5.35a}$$

$$(p(z)B\sin\delta\,dz)\{\tan(\alpha+\alpha_o-\phi_m)\times B\}-(p(z)B\cos\delta\,dz)\left[B+\frac{m(z)}{\cos x}(\pi-x-\sin x)\right]=\left[k_hq\{A(z)-A(z+dz)\}\left\{B+\frac{m(z)}{\cos x}(\pi-x-\sin x)\right\}\right]-[(1-k_v)q\{A(z)-A(z+dz)\}\{\tan(\alpha+\alpha_o-\phi_m)\times B\}] \tag{5.35b}$$

$$p(z)Bdz=\frac{[k_hq\{A(z)-A(z+dz)\}\,VD(z)]-[(1-k_v)q\{A(z)-A(z+dz)\}HD(z)]}{(\sin\delta\times HD(z))-(\cos\delta\times VD(z))} \tag{5.35c}$$

where, $HD(z)=\tan(\alpha+\alpha_o-\phi_m)\times B$ and $VD(z)=B+\frac{m(z)}{\cos x}(\pi-x-\sin x)$

Again, the total caisson reaction on soil wedge (P_{pq}) is obtained by carrying out integration of Eqns. (5.33c) and (5.35c). The average magnitude of seismic passive earth pressure coefficient due to surcharge component (K_{spq}) is obtained using following equations.

$$K_{spq}qBD=P_{pq} \tag{5.36a}$$

$$K_{spq}=\frac{P_{pq}}{qBD} \tag{5.36b}$$

5.2.1.3 *Formulation of seismic passive earth pressure coefficient due to unit weight component ($K_{sp\gamma}$)*

Fig. 5.6 depicts the forces acting on infinitesimally thin failure wedge at any depth *z* due to unit weight component of resistance acting alone. The overburden pressure force (*Q*) and normal reaction force (N) acting at wedge interfaces have also been considered. From equilibrium of forces in horizontal direction for the elemental disc,

<u>$B < m\tan x$</u>

$$p(z)\cos\delta_m\,dz - \Delta F(z) + k_h \Delta W(z) = \Delta R_H(z) = Rm(z)r(z)\frac{\cos\phi_m}{\cos x}\sin(\alpha + \alpha_o - \phi_m) \times d\alpha \times \{\sin x - \sin(x - \theta(z))\} \tag{5.37a}$$

From equilibrium of forces in vertical direction for the elemental disc:

$$p(z)\sin\delta_m\,dz + (1 - k_v)\Delta W(z) + Q(z) - N(z + dz) = \Delta R_V(z) = Rm(z)r(z)\frac{\cos\phi_m}{\cos x}\cos(\alpha + \alpha_o - \phi_m)\,d\alpha \times (\pi - 2x + \theta(z)) \tag{5.37b}$$

Let $HD(z) = \tan(\alpha + \alpha_o - \phi_m)\{\sin x - \sin(x - \theta(z))\}$ and $VD(z) = \pi - 2x + \theta(z)$

$$p(z)dz = \frac{\Delta W(z)[\{(1-k_v)\times HD(z)\}-(k_h\times VD(z))]+[\{Q(z)-N(z+dz)\}\times HD(z)]+(\Delta F(z)\times VD(z))}{(\cos\delta_m\times VD(z))-(\sin\delta_m\times HD(z))} \tag{5.38}$$

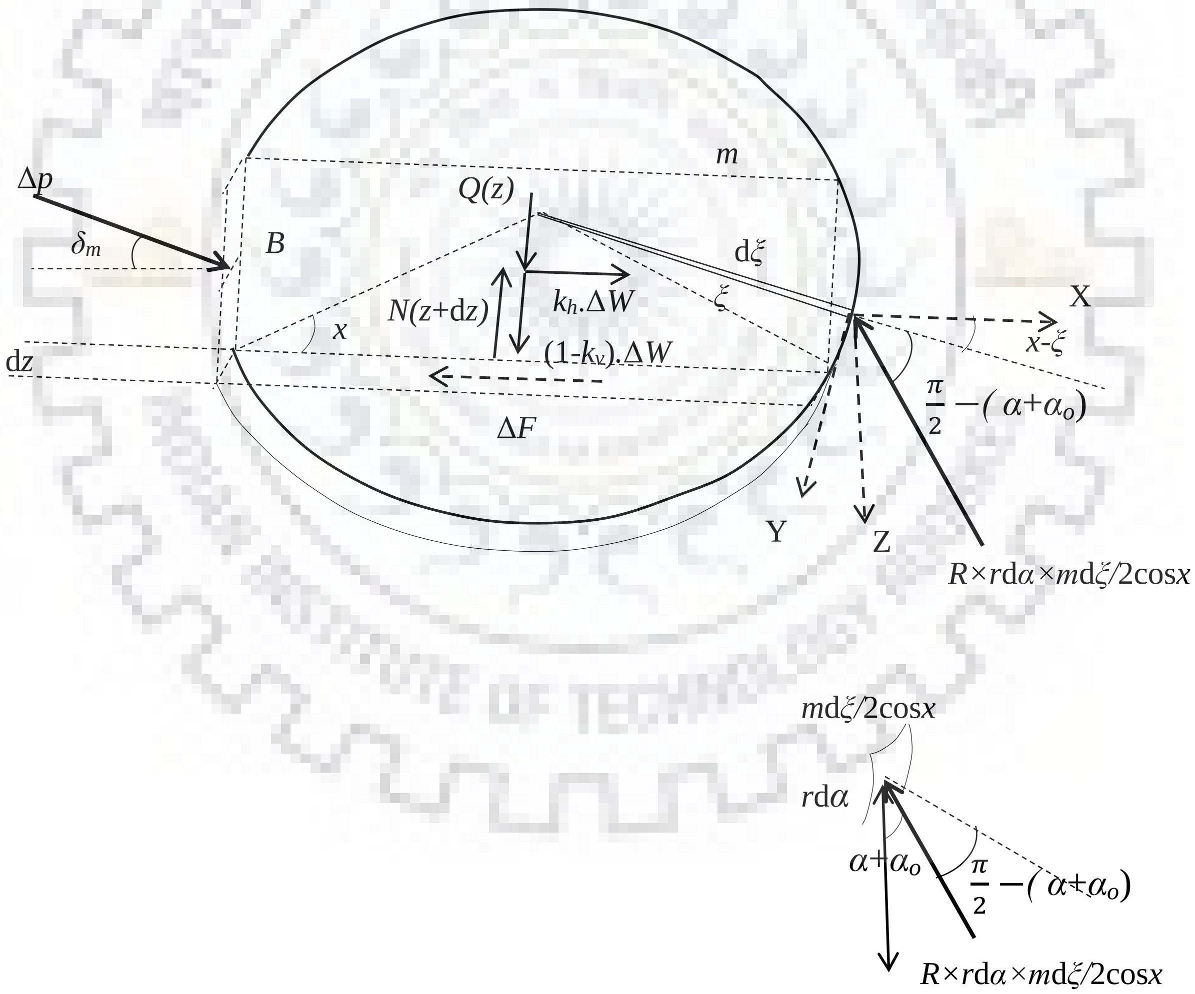

Fig. 5.6 Free body diagram of forces acting on infinitesimal horizontal strip of failure wedge due to unit weight component only

$\underline{B > m\tan x}$

$$p(z)\cos\delta_m\,dz - \Delta F(z) + k_h \Delta W(z) = \Delta R_H(z) = BRr(z)\sin(\alpha + \alpha_o - \phi_m)\cos\phi_m\,d\alpha \tag{5.39a}$$

$$p(z)\sin\delta_m\,dz + (1 - k_v)\Delta W(z) + Q(z) - N(z + dz) = \Delta R_V(z) = R\cos\phi_m\cos(\alpha + \alpha_o - \phi_m) \times r(z)d\alpha \times \left\{B + \frac{m(z)}{\cos x}(\pi - x - \sin x)\right\} \tag{5.39b}$$

Let $HD(z) = \tan(\alpha + \alpha_o - \phi_m) \times B$ and $VD(z) = B + \frac{m(z)}{\cos x}(\pi - x - \sin x)$

$$p(z)dz = \frac{\Delta W(z)[\{(1-k_v)\times HD(z)\} - (k_h \times VD(z))] + [\{Q(z) - N(z+dz)\}\times HD(z)] + (\Delta F(z)\times VD(z))}{(\cos\delta_m \times VD(z)) - (\sin\delta_m \times HD(z))} \tag{5.40}$$

Upon integration of Eqns. (5.38) and (5.40), the total reaction force applied by caisson face on soil wedge in presence of unit weight component of soil reaction ($P_{p\gamma}$) is determined. The average magnitude of seismic passive earth pressure coefficient due to unit weight component ($K_{sp\gamma}$) over the entire depth of passive wedge is obtained using the following equation:

$$\frac{1}{2}K_{sp\gamma}\gamma D^2 \times B = P_{p\gamma} \tag{5.41a}$$

$$K_{sp\gamma} = \frac{2P_{p\gamma}}{\gamma B D^2} \tag{5.41b}$$

5.2.2 *Validation of the proposed method*

Fig. 5.7 shows the variation of total soil pressure with depth obtained from the present study juxtaposed with the results of previous experimental and analytical studies. Olson (2017) conducted a series of centrifuge tests on cohesionless soil with soil properties mentioned in Fig. 5.7. Biswas and Choudhury (2019) proposed a 3D planar failure wedge for computing passive earth pressure in cohesionless soil. Hydrostatic pressure has been added to the pressure obtained from the proposed model to obtain total lateral pressure for the given set of input parameters. The results of the present study are found to be in excellent agreement with the results of the above mentioned experimental and analytical studies. The nature and magnitude of the total soil pressure obtained from the present study is slightly different from that of Biswas and Choudhury's (2019) theoretical study because of the assumption of log-spiral failure wedge as opposed to the planar failure wedge assumed by the authors. The deviation from experimental studies can be attributed to the application of dynamic loads by Olson et al. (2017) in contrast with the pseudo-static analysis conducted in the present study.

Furthermore, Table 5.1, Table 5.2 and Table 5.3 compare the results of seismic passive earth pressure coefficients due to unit weight, surcharge and cohesion component respectively with the results of previous studies (Mononobe and Matsuo, 1929; Soubra, 2000, Soubra and Macuh, 2002, Subba Rao and Choudhury, 2005 and Liu et al., 2018).

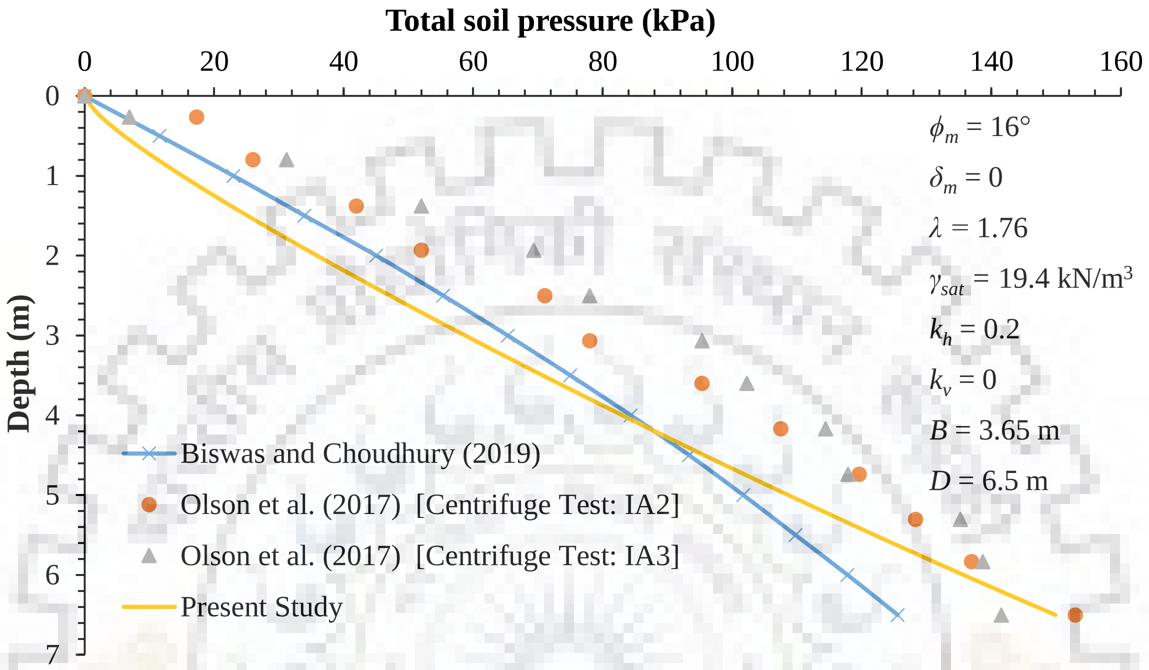

Fig. 5.7 Comparison of total passive earth pressure in present study with centrifuge test results (Olson et al. 2017) and planar wedge idealization (Biswas and Choudhury, 2019)

Table 5.1 Comparison of $K_{sp\gamma}$ in present study with previous literature for B=800 m, D=16 m and k_v=0

Seismic passive earth pressure coefficient due to unit weight component ($K_{sp\gamma}$)							
ϕ_m	k_h	δ_m / ϕ_m	Mononobe – Okabe (1929)	Soubra (2000)	Soubra and Macuh (2002)	Liu et al. (2018)	Present Study
20°	0	1/3	2.41	2.39	2.39	2.38	2.40
		2/3	2.89	2.77	2.75	2.73	2.69
	0.1	1/3	2.19	2.19	-	-	1.88
		2/3	2.59	2.52	-	-	2.25
30°	0	1/3	4.14	4.05	4.03	4.02	3.99
		2/3	6.11	5.40	5.34	5.26	4.98
	0.1	1/3	3.83	3.77	-	-	3.66
		2/3	5.55	5.00	-	-	4.83

- : denotes that study did not present results for seismic cases

Table 5.2 Comparison of K_{spq} in present study with previous literature for B=800 m, D=16 m and k_v=0

			Seismic passive earth pressure coefficient due to surcharge component (K_{spq})			
ϕ_m	k_h	δ_m / ϕ_m	Soubra (2000)	Soubra and Macuh (2002)	Liu et al. (2018)	Present Study
20°	0	1/3	2.37	2.38	2.38	2.35
		2/3	2.65	2.70	2.68	2.64
	0.1	1/3	2.18	-	-	1.84
		2/3	2.45	-	-	2.20
30°	0	1/3	3.95	3.98	4.00	3.91
		2/3	4.93	5.10	5.03	4.88
	0.1	1/3	3.71	-	-	3.59
		2/3	4.63	-	-	4.73

- : denotes that study did not present results for seismic cases

Table 5.3 Comparison of K_{spc} in present study with previous literature for B=800 m and D=16 m

		Seismic passive earth pressure coefficient due to cohesion component (K_{spc})				
ϕ_m	δ_m / ϕ_m	Soubra (2000)	Soubra and Macuh (2002)	Subba Rao and Choudhury (2005)	Liu et al. (2018)	Current Study
20°	0.5	3.24	4.18	3.62	3.68	4.28
	1	5.10	5.31	4.36	4.64	5.80
30°	0.5	12.81	6.05	5.32	5.51	5.94
	1	17.82	8.88	6.84	7.89	11.38

Subba Rao and Choudhury (2005) carried out plane strain limit equilibrium analysis based on pseudo-static approach considering a composite log-spiral-linear failure surface in front of a retaining structure. Soubra (2000) and Soubra and Macuh (2002) used upper bound limit analysis in order to find the seismic earth pressure coefficients in seismic and static conditions respectively for a rigid retaining structure. For comparison of results, width of caisson (B) was chosen as 800 m to simulate plane strain conditions that prevail for retaining structures. In addition, depth of failure wedge (D) was taken as 16 m whereas k_v=0 was adopted for the comparison of results. The magnitudes of K_{spc}, are found to be much smaller compared to results of limit analysis performed by Soubra (2000), Soubra and Macuh (2002) and Liu et al. (2018). However, the results are greater than the limit equilibrium analysis result by Subba Rao and Choudhury (2005). Since the formulation for K_{spc} limit equilibrium method-based study by Subba Rao and Choudhury, 2005 ($P_{pc}=K_{spc}\times 2cBD$) is different than other contemporary studies ($P_{pc}=K_{spc}\times cBD$), the results of Subba Rao and Choudhury (2005) have been doubled ($K_{spc}^{*}=2K_{spc}$) for comparison. This suggests that limit equilibrium method returns more conservative values of K_{spc} than limit analysis. K_{spq} and $K_{sp\gamma}$ values obtained from the present study are found to be smaller than the previous studies. The assumption of the logarithmic spiral failure wedge in the proposed model gives the smaller values.

5.3 Present Study

In the present study, magnitudes of different seismic passive earth pressure coefficients, K_{spc}, K_{spq} and $K_{sp\gamma}$, have been tabulated for different input parameters mentioned in Table 5.4. These coefficients have been obtained corresponding to minimum value of seismic passive earth pressure forces (P_{pc}, P_{pq} and $P_{p\gamma}$). The optimization of these forces is done by varying the initial angle of log-spiral α_o between 0 to $(\pi/2-\phi_m)$ and central angle of log-spiral α_f between 0 to $\{\pi/2-(\phi_m+\alpha_o)\}$. The computation of K_{spc} was carried out corresponding to adhesion (C_a) value of ratio of tangent of δ_m and tangent of ϕ_m ($C_a/c=\tan\delta_m/\tan\phi_m$). The magnitude of K_{spc} is found to be independent of the cohesion magnitude of soil. All the numerical computations including the optimization process are carried out by writing programs in MATLAB (2021). The angle x defining the shape of the failure wedge in horizontal plane has been chosen as $\phi_m\times D/B$ to take width of the caisson into account. Therefore, for smaller width of caisson, the area A_f is significant in comparison to the area A_s whereas for infinite width structures like retaining walls, $A_f\rightarrow 0$. Thus, inclusion of parameter D/B checks the overall volume of wedge. The sequence of steps followed in the present study has been depicted through flow chart in Fig. 5.8.

Table 5.4 Input parameters considered in the present study

Properties	Values
Depth of passive wedge (D)	16 m
Width of caisson (B)	8m, 16m, 32m, 80m, 800m
Adhesion (C_a)	$\tan\delta_m/\tan\phi_m$
Mobilized soil friction angle (ϕ_m)	15°, 20°, 25°, 30°, 35°
Mobilized soil-wall friction angle (δ_m)	$0, \phi_m/3, \phi_m/2, 2\phi_m/3, \phi_m$
Horizontal seismic acceleration coefficient (k_h)	0, 0.1, 0.2
Vertical seismic acceleration coefficient (k_v)	$0, k_h/2, k_h$

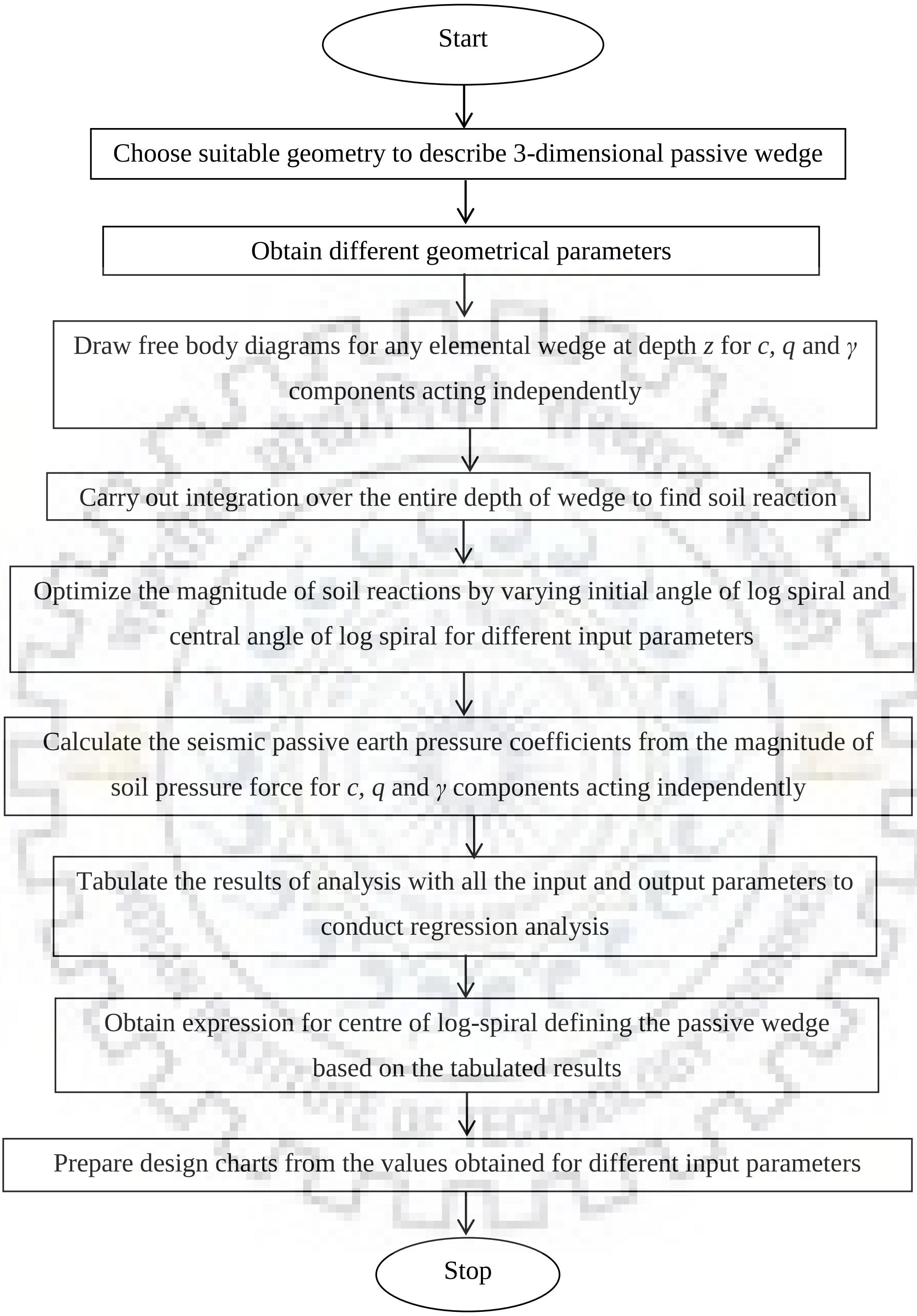

Fig. 5.8 Flow chart representing the sequence of steps in present study

5.4 Results and Discussions

Fig. 5.9 to Fig. 5.24 depict the design charts for K_{spq} and $K_{sp\gamma}$ values under different input parameters. Similarly, Table 5.5 represents the magnitudes of K_{spc} for the given set of parameters. The effects of various input parameters (soil-soil friction angle, soil-wall friction angle, horizontal and vertical seismic acceleration coefficients and width of structure) on the seismic passive earth pressure coefficients have been discussed in the succeeding sections.

Table 5.5 Variation of K_{spc} for different B/D, ϕ_m and δ_m

Seismic passive earth pressure coefficient due to cohesion component (K_{spc})						
B/D	δ_m/ϕ_m	ϕ_m				
		15°	20°	25°	30°	35°
0.5	0	3.158	3.352	3.394	3.482	3.556
50		3.158	3.352	3.394	3.482	3.556
0.5	1/3	3.351	3.888	4.539	5.012	5.777
1		3.339	3.869	4.505	4.953	5.674
2		3.332	3.855	4.479	4.905	5.586
5		3.328	3.845	4.458	4.864	5.507
50		3.304	3.838	4.442	4.832	5.440
0.5	1/2	3.791	4.450	5.394	6.441	8.184
1		3.768	4.405	5.305	6.269	7.819
2		3.753	4.373	5.239	6.135	7.533
5		3.742	4.349	5.187	6.023	7.287
50		3.735	4.332	5.147	5.934	7.082
0.5	2/3	4.061	4.950	6.622	8.904	13.464
1		4.020	4.865	6.435	8.471	12.276
2		3.993	4.806	6.298	8.151	11.427
5		3.974	4.760	6.189	7.889	10.734
50		3.961	4.728	5.824	7.214	9.068
0.5	1	4.651	6.670	8.417	16.525	42.362
1		4.557	6.435	7.861	14.503	32.059
2		4.495	6.274	7.479	13.180	26.090
5		4.451	6.152	7.181	12.164	21.838
50		4.420	6.064	6.958	11.384	18.626

5.4.1 *Effect of mobilized soil-wall interface friction angle (δ_m)*

Fig. 5.9 and Fig. 5.10 reflect the effect of δ_m on $K_{sp\gamma}$ and K_{spq} respectively in static conditions. The seismic passive earth pressure coefficients due to different components were observed to increase with increase in δ_m irrespective of k_h and ϕ_m values.

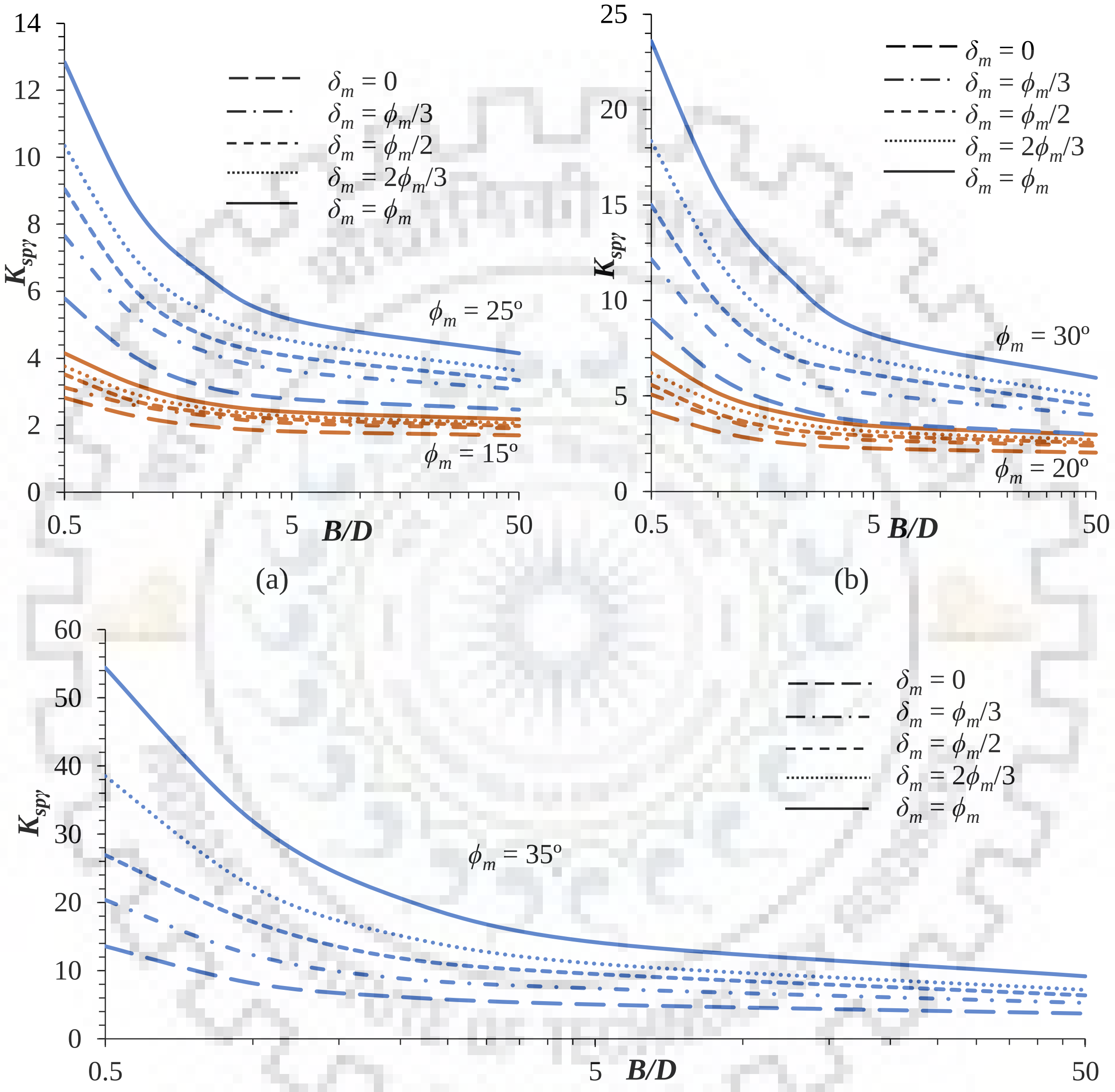

(a) (b)

(c)

Fig. 5.9 Design chart for $K_{sp\gamma}$ under static condition for different soil-wall friction angles for (a) ϕ_m=15°, 25°; (b) ϕ_m=20°, 30° and (c) ϕ_m=35°

This increase is even more prominent for higher value of δ_m. In case of k_h=0.1 and k_v=0.5k_h, for ϕ_m=20°, as δ_m is increased from 0 to ϕ_m/3 and 2ϕ_m/3 to ϕ_m, $K_{sp\gamma}$ increases by 15.04% and 21.46% respectively while for ϕ_m=30°, the increase is 26.41% and 63.4% respectively for 16 m wide caisson. The increase in K_{spq} values for the same increase in δ_m

values was found to be 15.03% and 16.66% respectively for ϕ_m=20° and 24.28% and 64.38% respectively for ϕ_m=30°. The K_{spc} values are even more magnified as they increase by 16.89% and 43.07% respectively for ϕ_m=20° and 27.02% and 71.21% respectively for ϕ_m=30° for the same set of input parameters. Higher magnitude of δ_m indicates higher interface roughness at soil-caisson contact and leads to higher resistance offered to caisson by soil in contact.

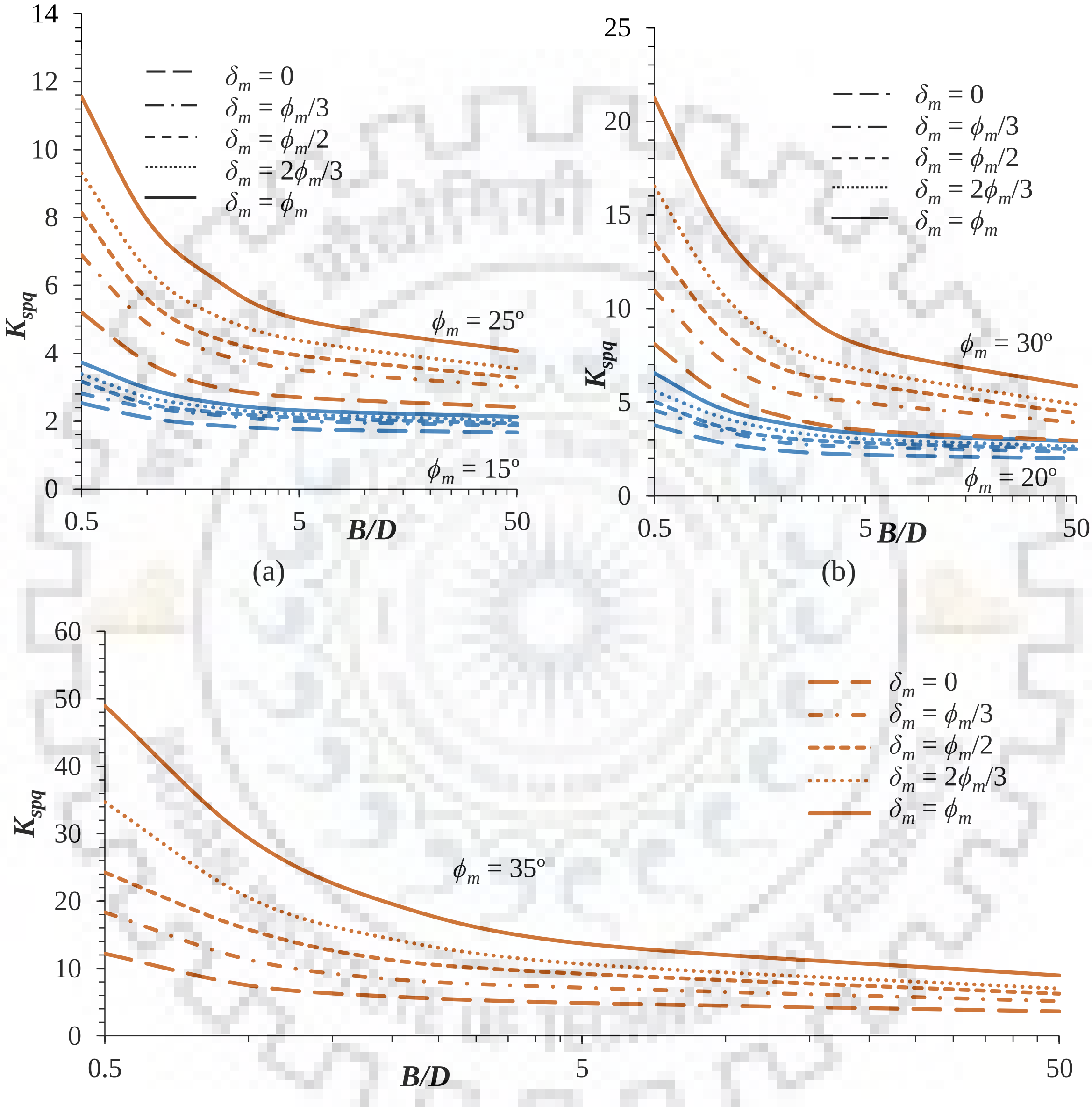

(a)

(b)

(c)

Fig. 5.10 Design chart for K_{spq} under static condition for different soil-wall friction angles for (a) ϕ_m=15°, 25°; (b) ϕ_m=20°, 30° and (c) ϕ_m=35°

Fig. 5.11 illustrates the inflence of δ_m and ϕ_m on the normalized pressure profile due to unit weight component for ϕ_m=25°, k_h=0.1, k_v=k_h/2 and B=800m. The percentage increase in normalized passive earth pressure at mid-depth of wedge formation, when δ_m increased from 0 to ϕ_m/3 and 2ϕ_m/3 to ϕ_m, was found to be 25.64% and 23.26% respectively.

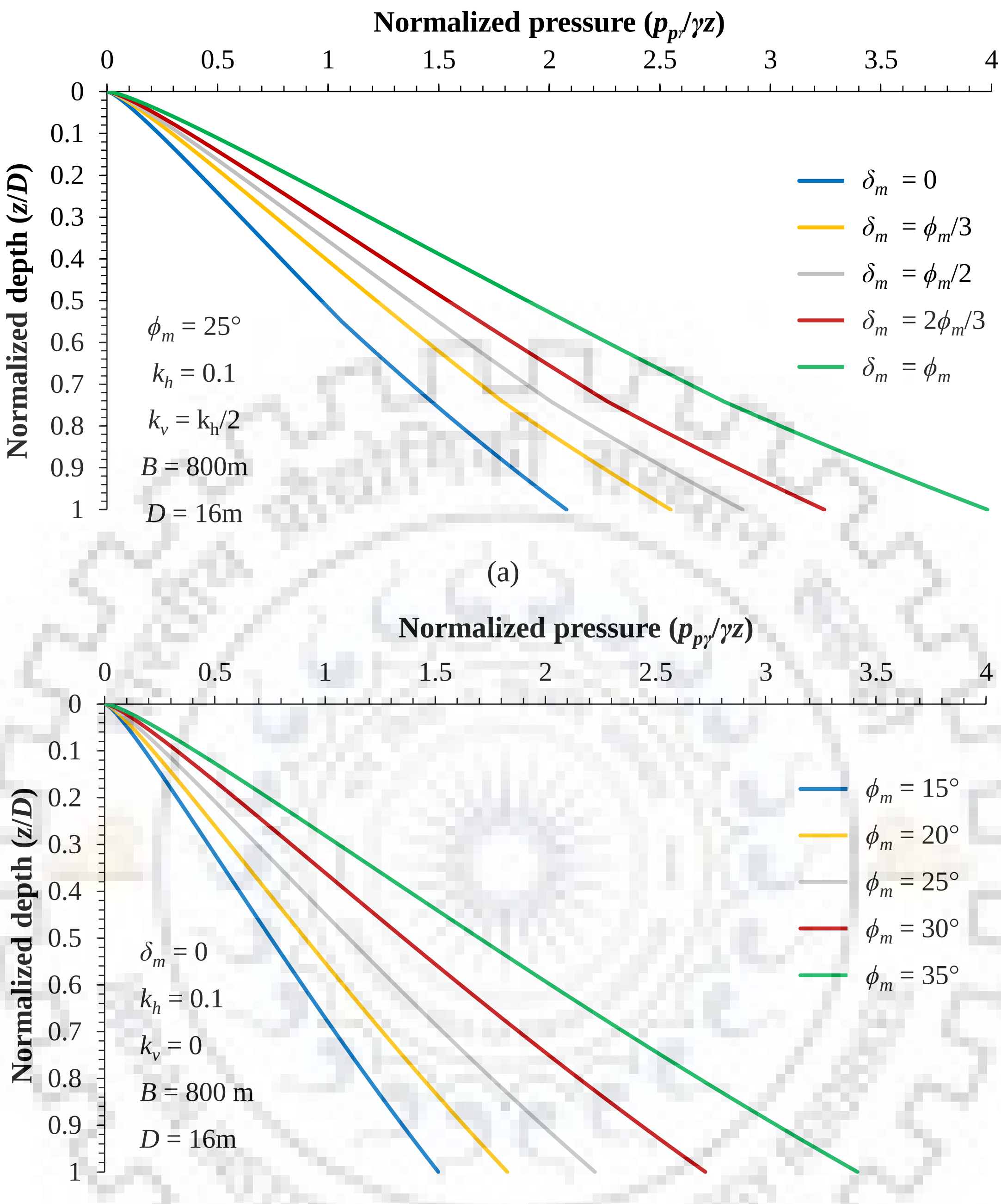

(a)

(b)

Fig. 5.11 Effect of (a) mobilized soil-wall friction angle and (b) mobilized soil-soil friction angle on seismic passive earth pressure profile due to unit weight component

5.4.2 Effect of mobilized soil-soil friction angle (ϕ_m)

Fig. 5.12 and Fig. 5.13 illustrates the effect of ϕ_m on magnitudes K_{spq} and $K_{sp\gamma}$. The increasing trend of all the earth pressure coefficients is evident with increasing soil-soil friction angle. Considering B=16 m, k_h=0.1 and k_v=0, for $\delta_m=\phi_m/3$, with increase in ϕ_m from 15° to 20° and from 30° to 35°, the percentage increase in K_{spq} magnitude was found to be

28.43% and 41.7% respectively and for $\delta_m=2\phi_m/3$, the increase was 37.01% and 42.37% respectively.

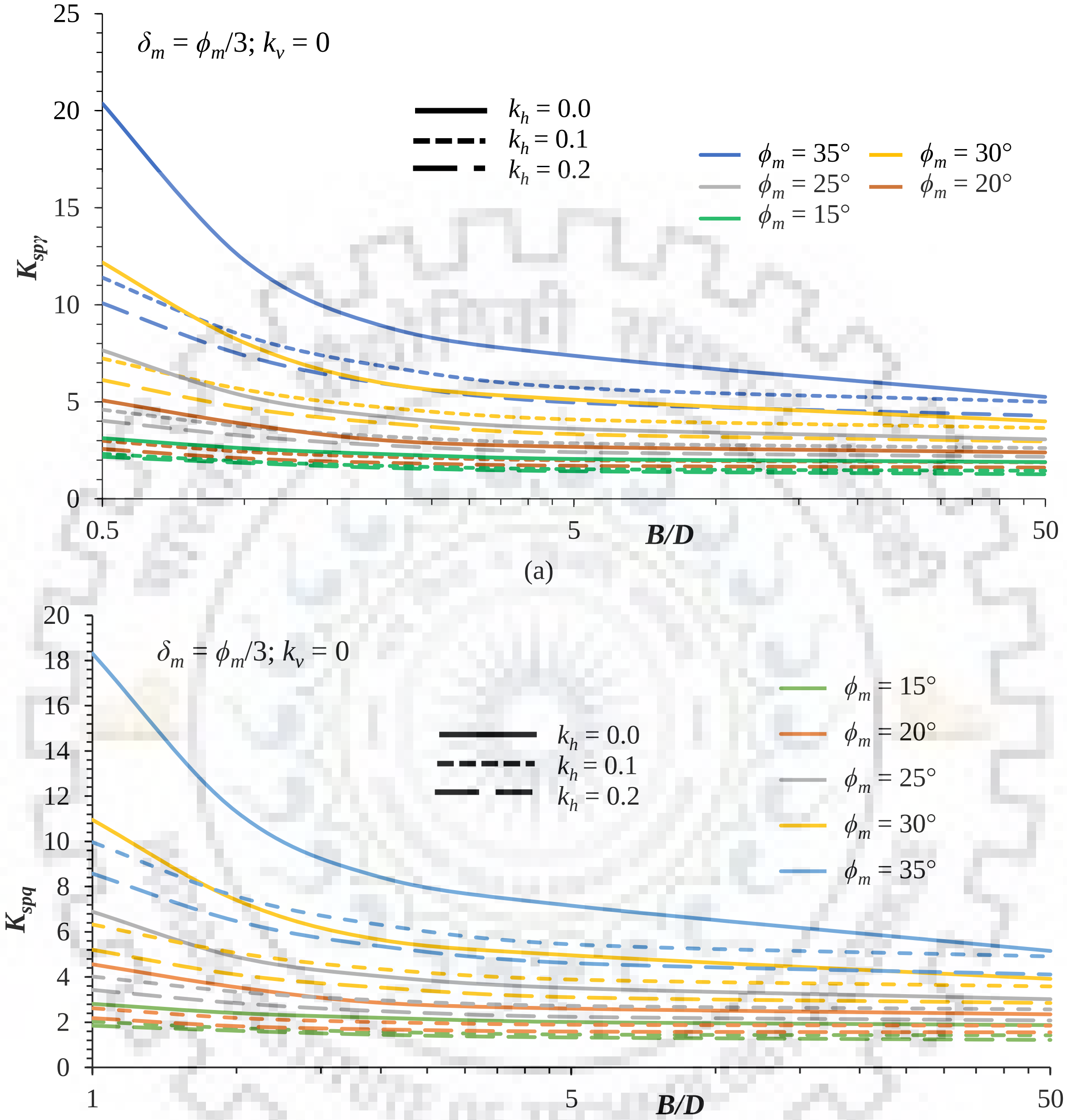

(a)

(b)

Fig. 5.12 Design chart for (a) $K_{sp\gamma}$ and (b) K_{spq} with varying k_h values and different soil-soil friction angles for $\delta_m=\phi_m/3$ and $k_v=0$

Similarly, the increase in K_{spc} magnitude is observed to be 3.43% and 14.56% respectively for $\delta_m=\phi_m/3$ and 20.67% and 44.91% respectively for $\delta_m=2\phi_m/3$. Again, the increase in $K_{sp\gamma}$ magnitude for $\delta_m=\phi_m/3$ case was computed as 27.41% and 40.52% respectively whereas for $\delta_m=2\phi_m/3$, the increase is 33.63% and 46.99% respectively for the same set of input parameters. For $\delta_m=0$, $k_h=0.1$, $k_v=0$ and $B=12$m, the increase in magnitude of pressure at the base of the wedge is 20.59% and 25.34% for increase in ϕ_m from 15° to 20° and from 30° to 35° respectively.

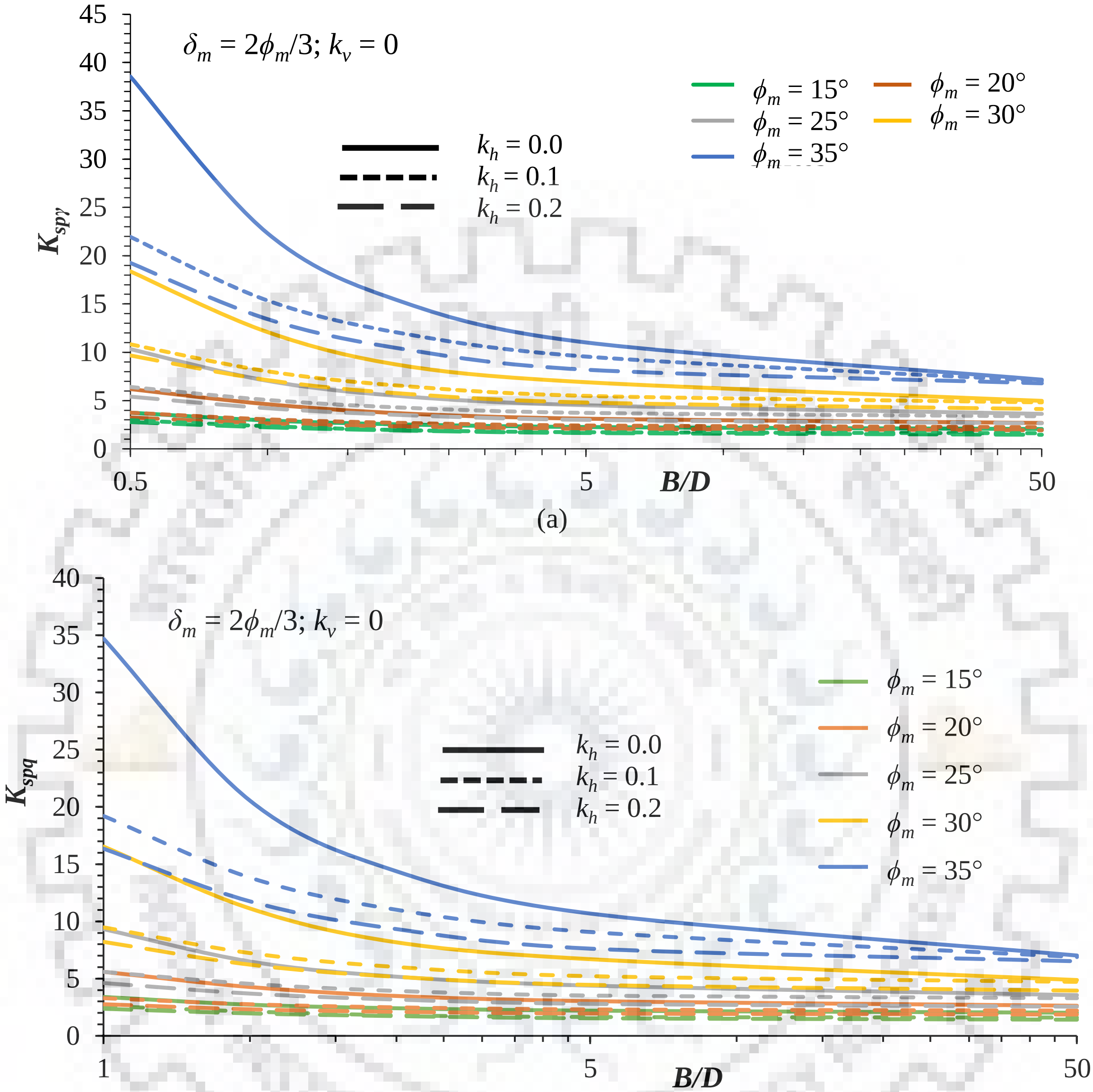

(a)

(b)

Fig. 5.13 Design chart for (a) $K_{sp\gamma}$ and (b) K_{spq} with varying k_h values and different soil-soil friction angles for δ_m=2ϕ_m/3 and k_v=0

As the magnitude of ϕ_m increases, interparticle binding of soil increases which leads to increase in shear strength and hence, higher resistance. In addition, volume of failure wedge also increases with increase in ϕ_m. Therefore, strength from higher volume of soil is mobilized leading to higher resistive force. This increase is further highlighted for higher magnitudes of δ_m since it is direct function of ϕ_m.

5.4.3 *Effect of seismic acceleration coefficients (k_h and k_v)*

Both horizontal and vertical seismic acceleration coefficients have significant impact on the magnitude of K_{spq} and $K_{sp\gamma}$ since they develop destabilizing inertial forces. However, K_{spc} values are observed to be neutral to increasing k_h and k_v values. Fig. 5.12 through Fig. 5.14 showcase the effect of k_h on K_{spq} and $K_{sp\gamma}$. The reduction in magnitudes of earth pressure coefficients is evident from these illustrations.

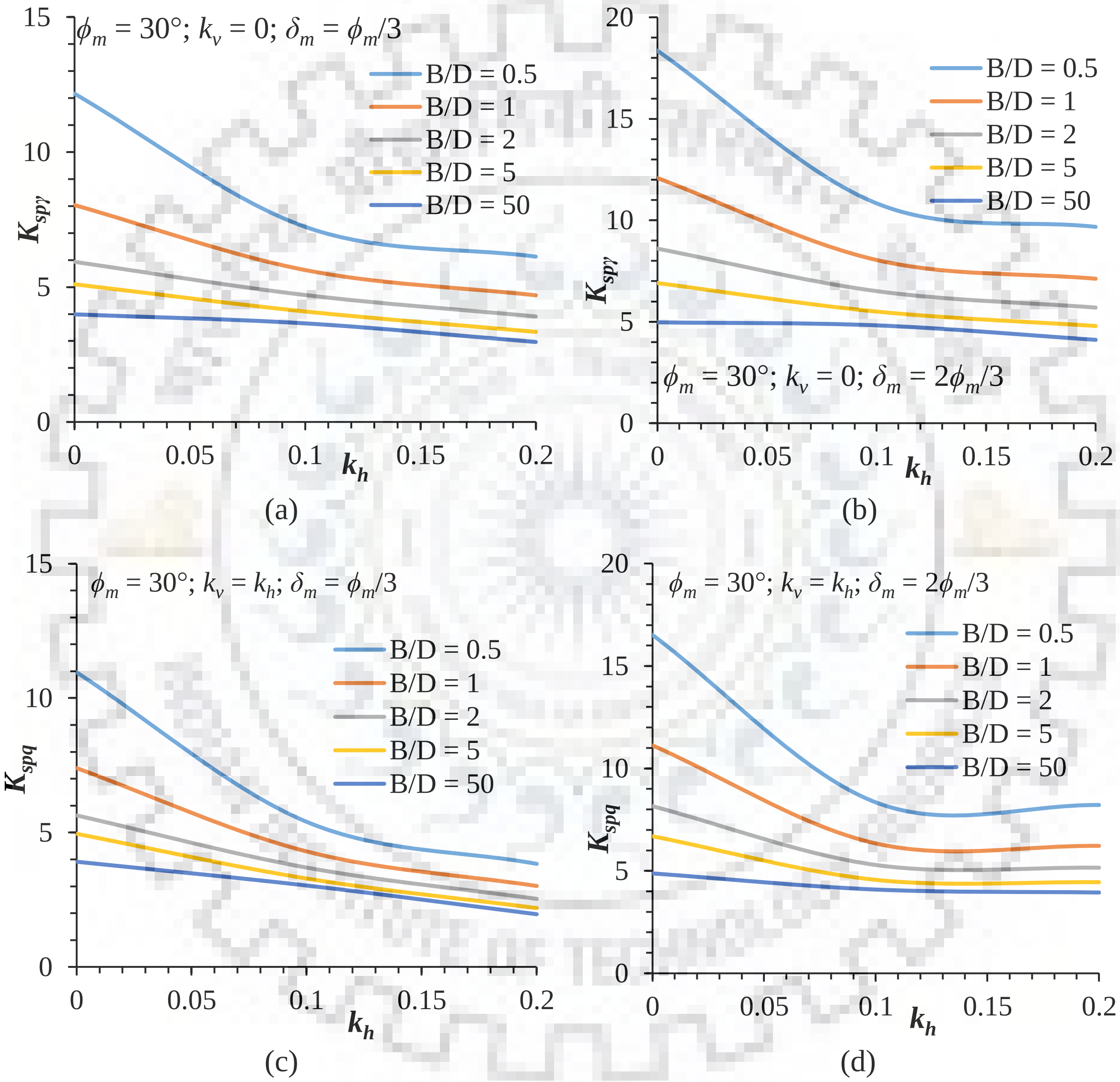

(a) (b)

(c) (d)

Fig. 5.14 Design charts for $K_{sp\gamma}$ for ϕ_m=30°, k_v=0 for (a) $\delta_m=\phi_m/3$ and (b) $\delta_m=2\phi_m/3$; K_{spq} for ϕ_m=30°, $k_v=k_h$ for (c) $\delta_m=\phi_m/3$ and (d) $\delta_m=2\phi_m/3$ with varying *B*/*D* values

For *B/D*=1, $k_v = 0$, ϕ_m=30° and $\delta_m=\phi_m/3$, as k_h is increased from 0 to 0.1 and 0.1 to 0.2, the magnitude of $K_{sp\gamma}$ diminishes by 12.77% and 16.5% respectively. The reduction in K_{spq} magnitudes for the same increase in k_h values are 18.38% and 16.68% respectively for the identical set of parameters. Fig. 5.15 to Fig. 5.24 illustrate the influence of k_v on K_{spq} and $K_{sp\gamma}$.

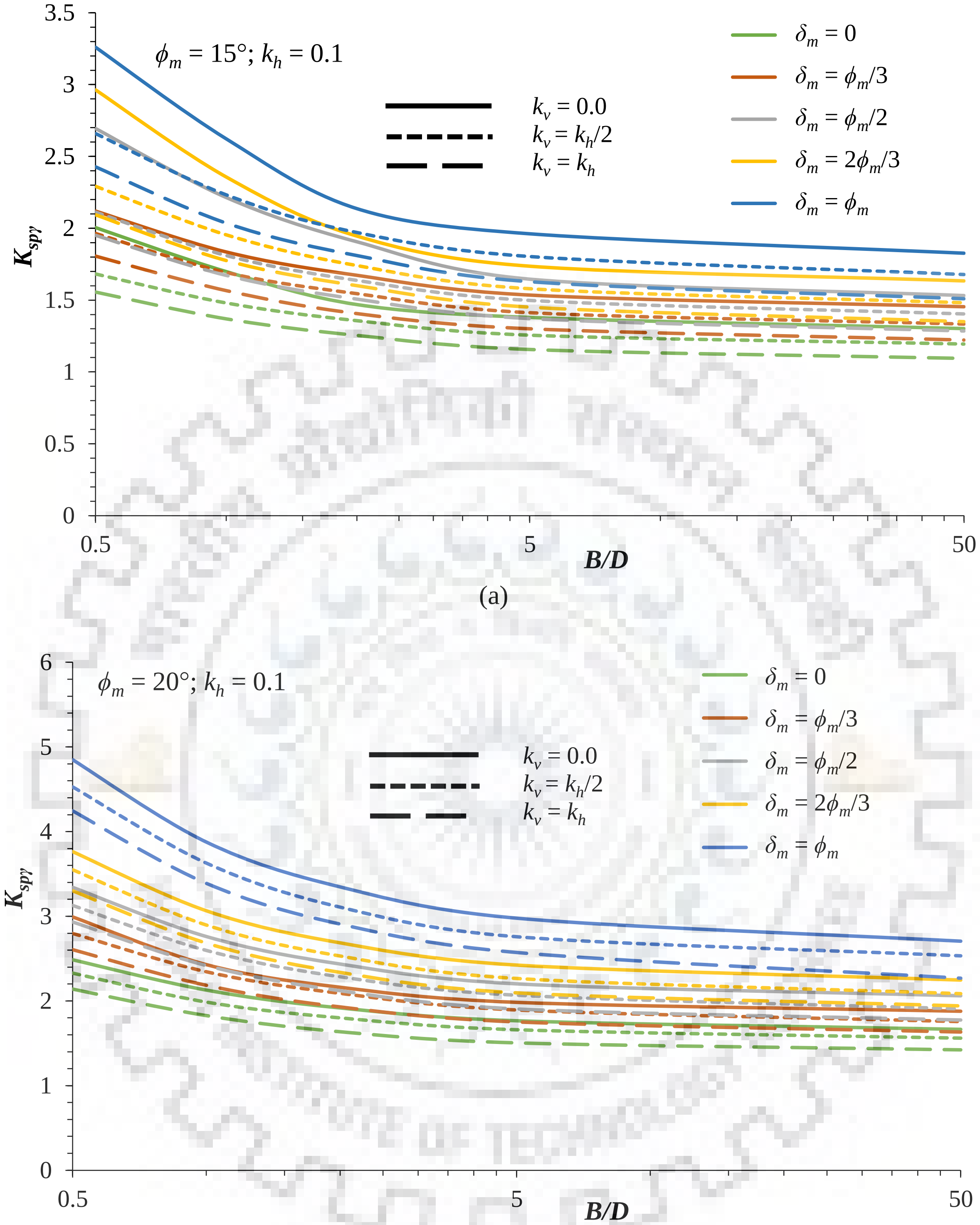

(a)

(b)

Fig. 5.15 Design chart for $K_{sp\gamma}$ for k_h=0.1 for different soil-wall friction angles for (a) ϕ_m=15° and (b) ϕ_m=20°

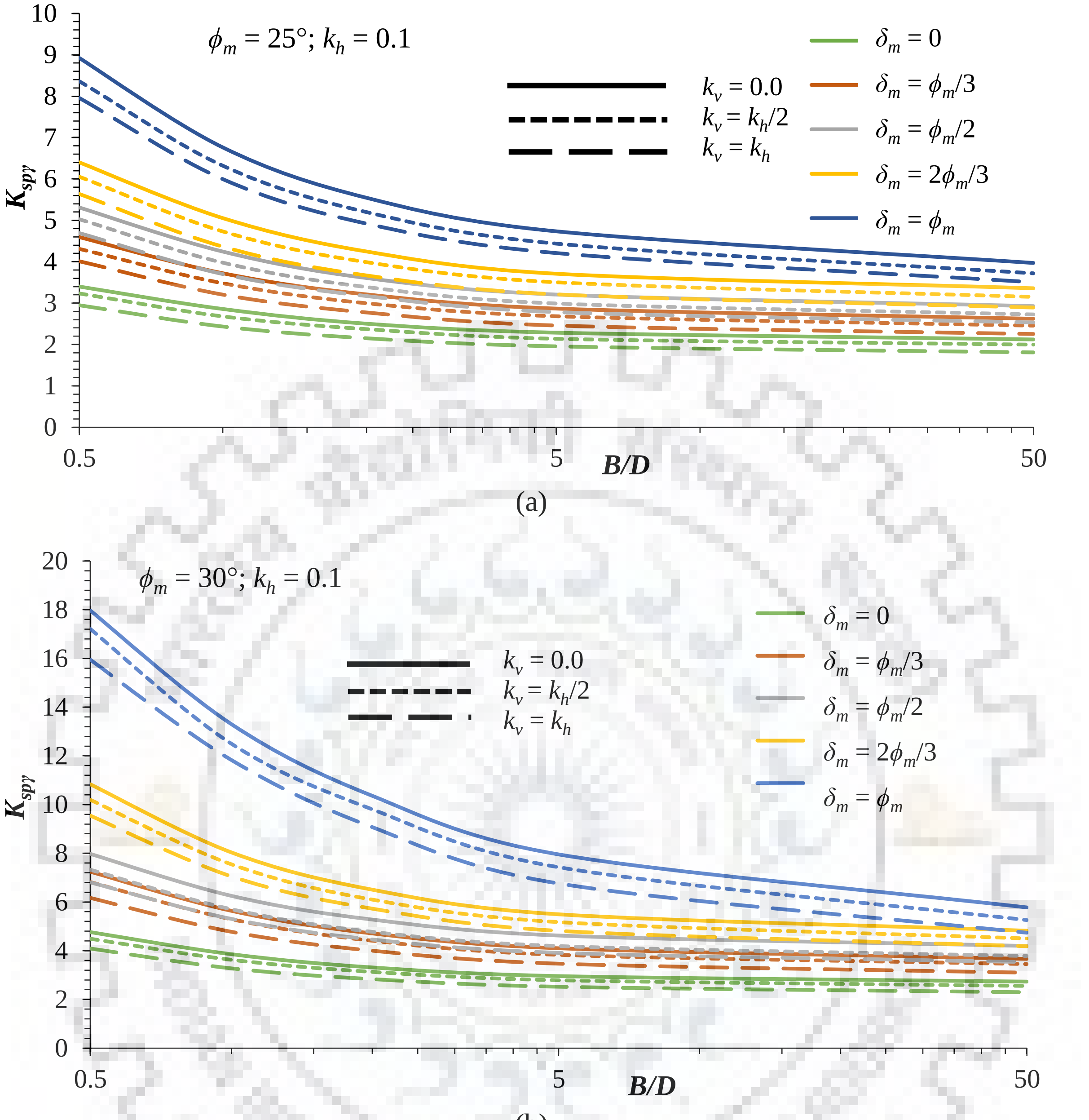

(a)

(b)

Fig. 5.16 Design chart for $K_{sp\gamma}$ for k_h=0.1 for different soil-wall friction angles for (a) ϕ_m=25° and (b) ϕ_m=30°

From the figures, it is evident that the effect of k_v on seismic passive earth pressure coefficients is the same albeit with less severity. In case of ϕ_m=25°, δ_m=ϕ_m/3 and B=16 m, for k_h=0.1, as k_v increases from 0 to k_h/2 and from k_h/2 to k_h, the magnitude of $K_{sp\gamma}$ decreases by 9.43% and 10.22% respectively while K_{spq} diminishes by 9.07% and 9.83% respectively. However, for k_h=0.2, this reduction is much more pronounced for both K_{spq} and $K_{sp\gamma}$, as a reduction of 25.24% and 37.51% respectively is observed in $K_{sp\gamma}$ for the above-mentioned set of input parameters.

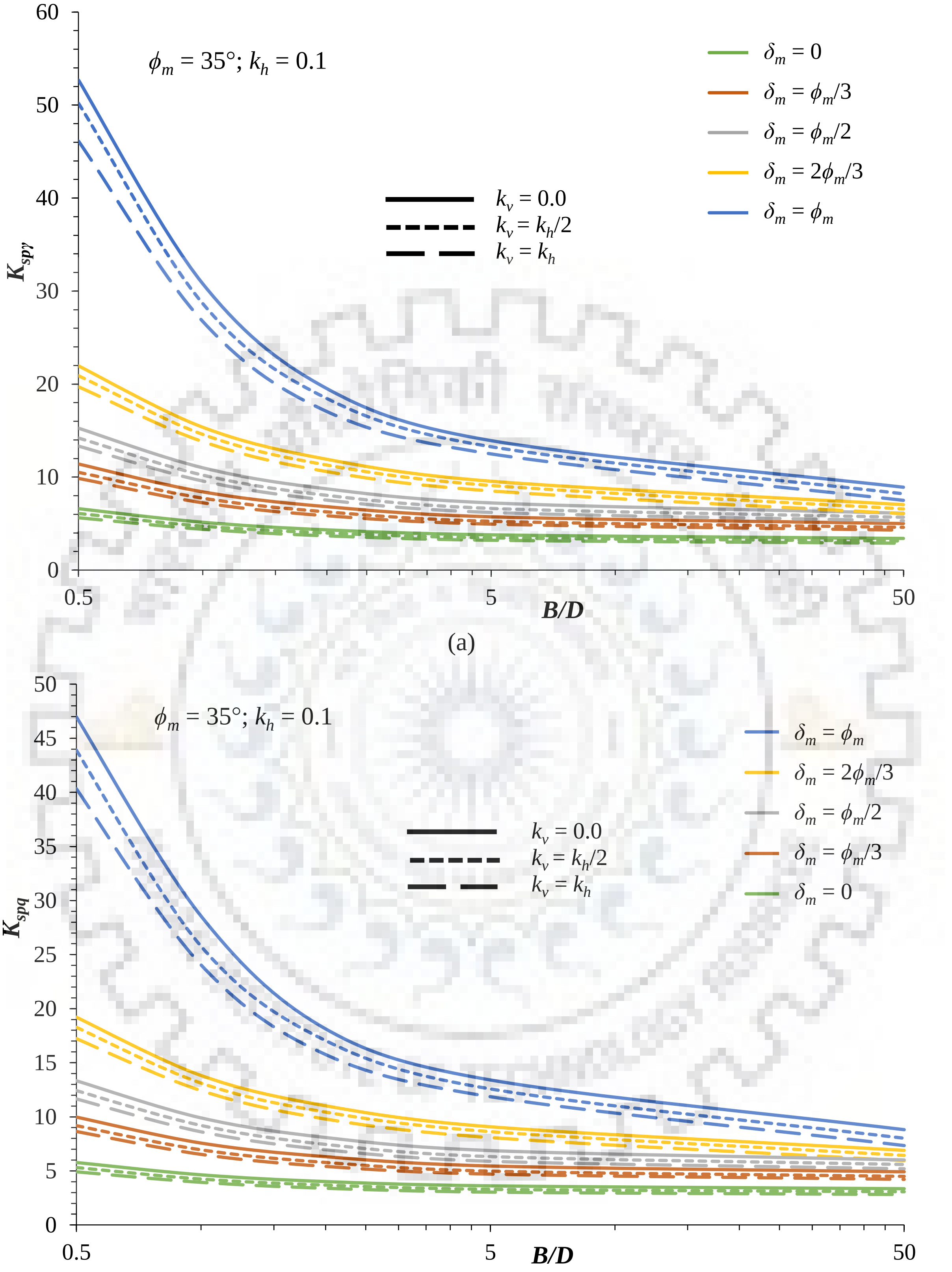

(a)

(b)

Fig. 5.17 Design chart for (a) $K_{sp\gamma}$ and (b) K_{spq} for k_h=0.1 for different soil-wall friction angles for ϕ_m=35°

5.4.4 Effect of width of caisson

Design charts in Fig. 5.9 to Fig. 5.24 and Table 5.5 all showcase the impact of width of caisson on seismic passive earth pressure coefficients. It could be observed that the magnitude of $K_{sp\gamma}$, K_{spq} and K_{spc} decreases as the width of caisson increases irrespective of the input parameters.

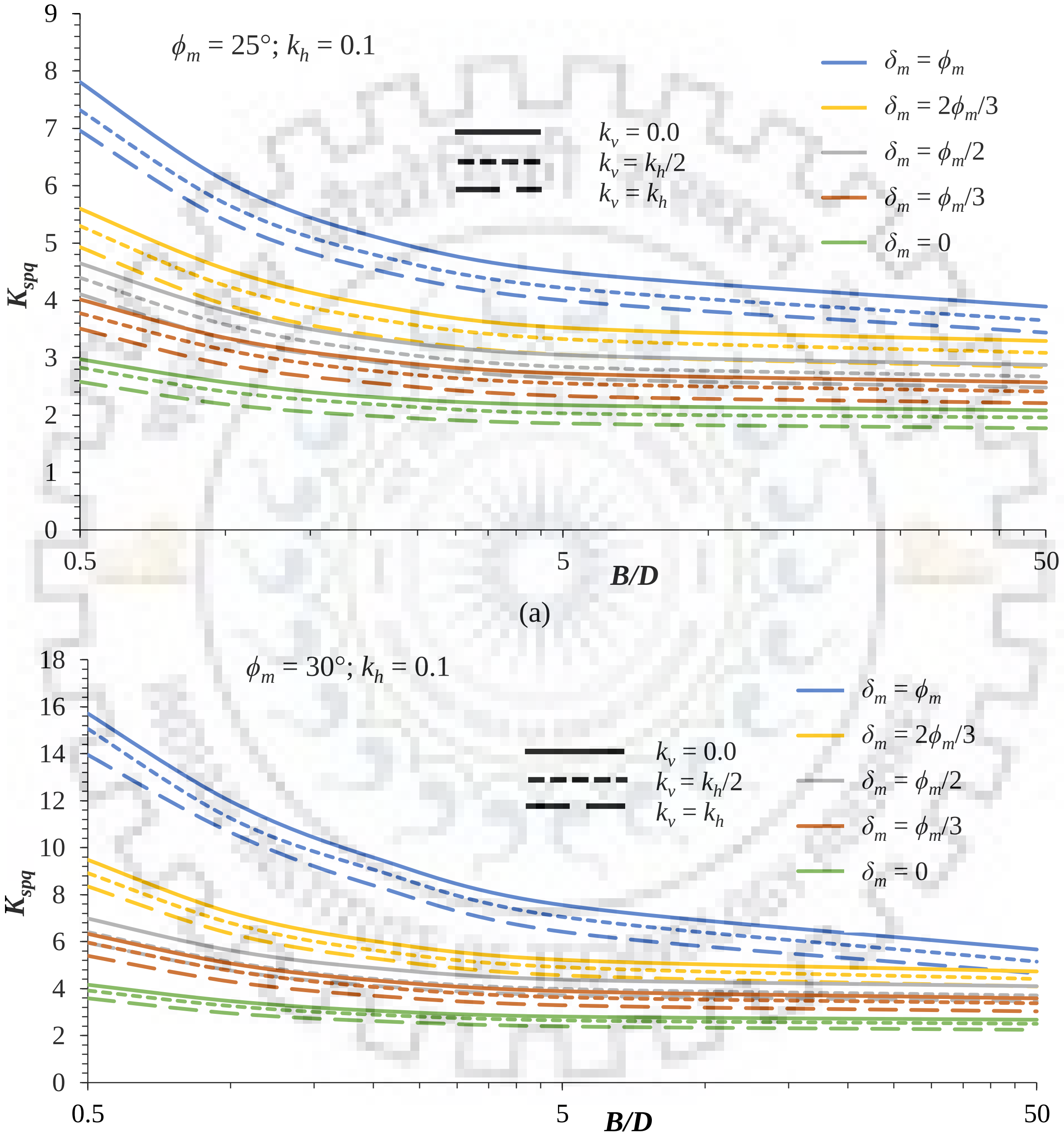

(a)

(b)

Fig. 5.18 Design chart for K_{spq} for k_h=0.1 for different soil-wall friction angles for (a) ϕ_m=25° and (b) ϕ_m=30°

As *B* increases, 3-D behavior tends to convert into plane strain behavior because the volume of soil in side wedges with respect to volume of wedge in front of caisson keeps diminishing. Therefore, the magnitude of extra soil resistance per unit width of caisson keeps decreasing with increase in width of structure. However, at smaller magnitudes of *B*, the volume of soil under side wedge is significant compared to volume of wedge in front of caisson. Therefore, higher the contribution of side wedge volume, higher is the earth pressure coefficient. This trend is observed for all combinations of input parameters.

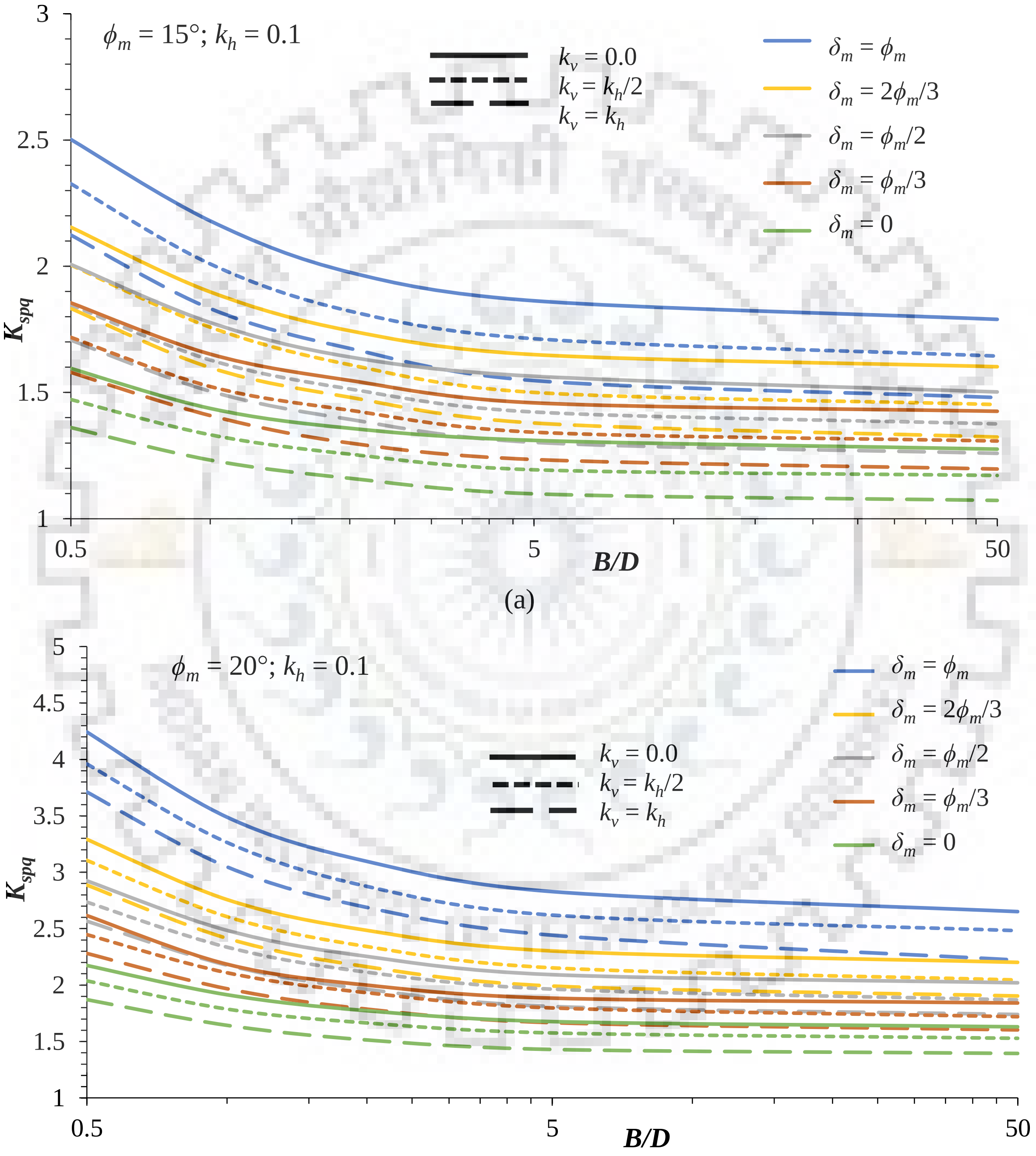

(a)

(b)

Fig. 5.19 Design chart for K_{spq} for k_h=0.1 for different soil-wall friction angles for (a) ϕ_m=15° and (b) ϕ_m=20°

It is seen that the magnitudes of K_{spq} reduces by18.61% and 5.95% as the B/D ratio increases from 0.5 to 1 and from 5 to 50 respectively for ϕ_m=25°, δ_m/ϕ_m=0.5, k_h=0.1 and k_v=k_h/2 while $K_{sp\gamma}$ reduces by 20.87% and 8.83% respectively. For k_h=0.2 and all other parameters remaining the same, the percentage decrease in K_{spq} is 19.67% and 9.41% respectively while the reduction is 21.97% and 12.24% respectively for $K_{sp\gamma}$. These values further highlight that the sensitivity of width of caisson towards seismic passive earth pressure coefficients reduce with increasing width to depth ratio.

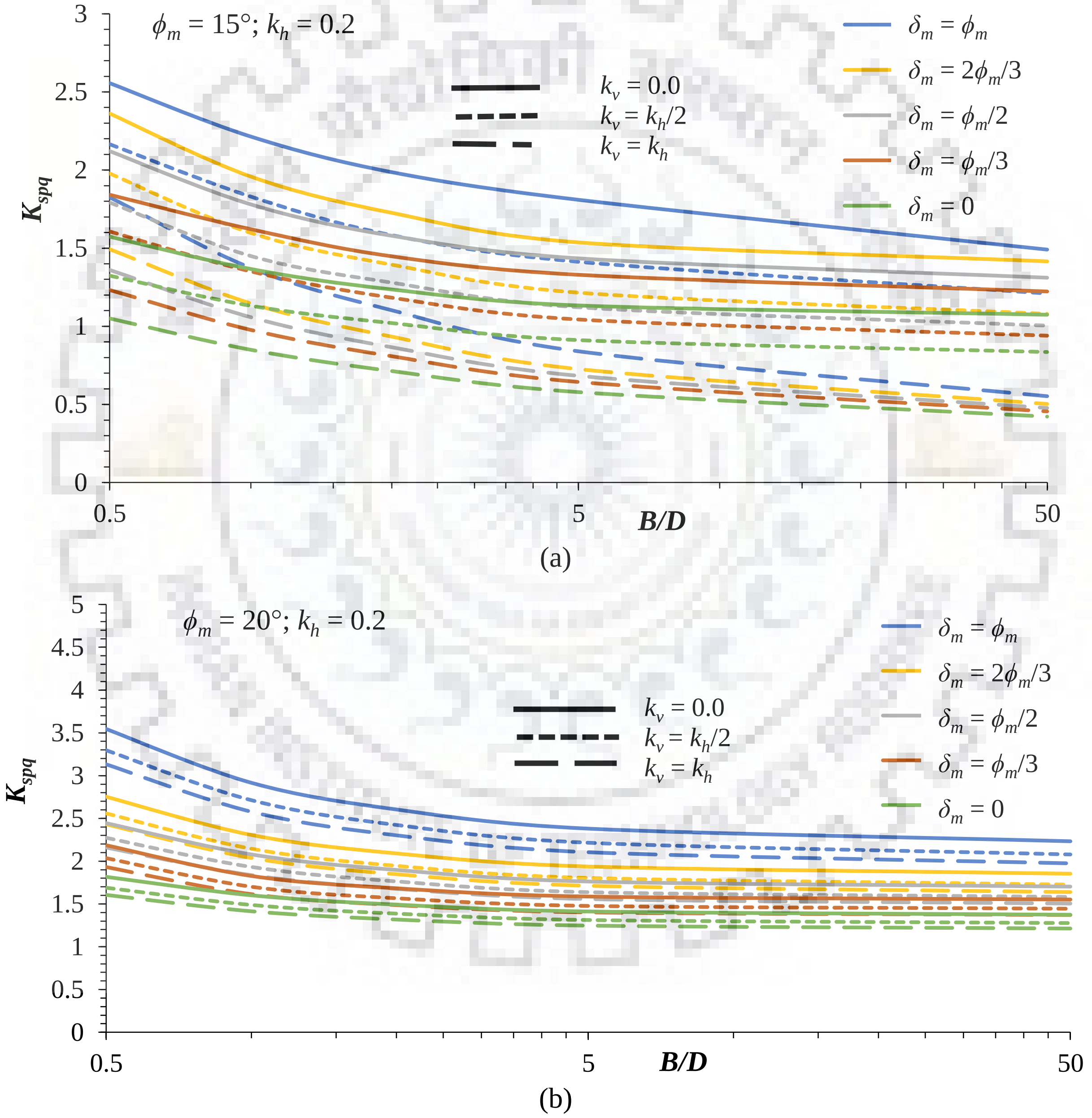

Fig. 5.20 Design chart for K_{spq} for k_h=0.2 for different soil-wall friction angles for (a) ϕ_m=15° and (b) ϕ_m=20°

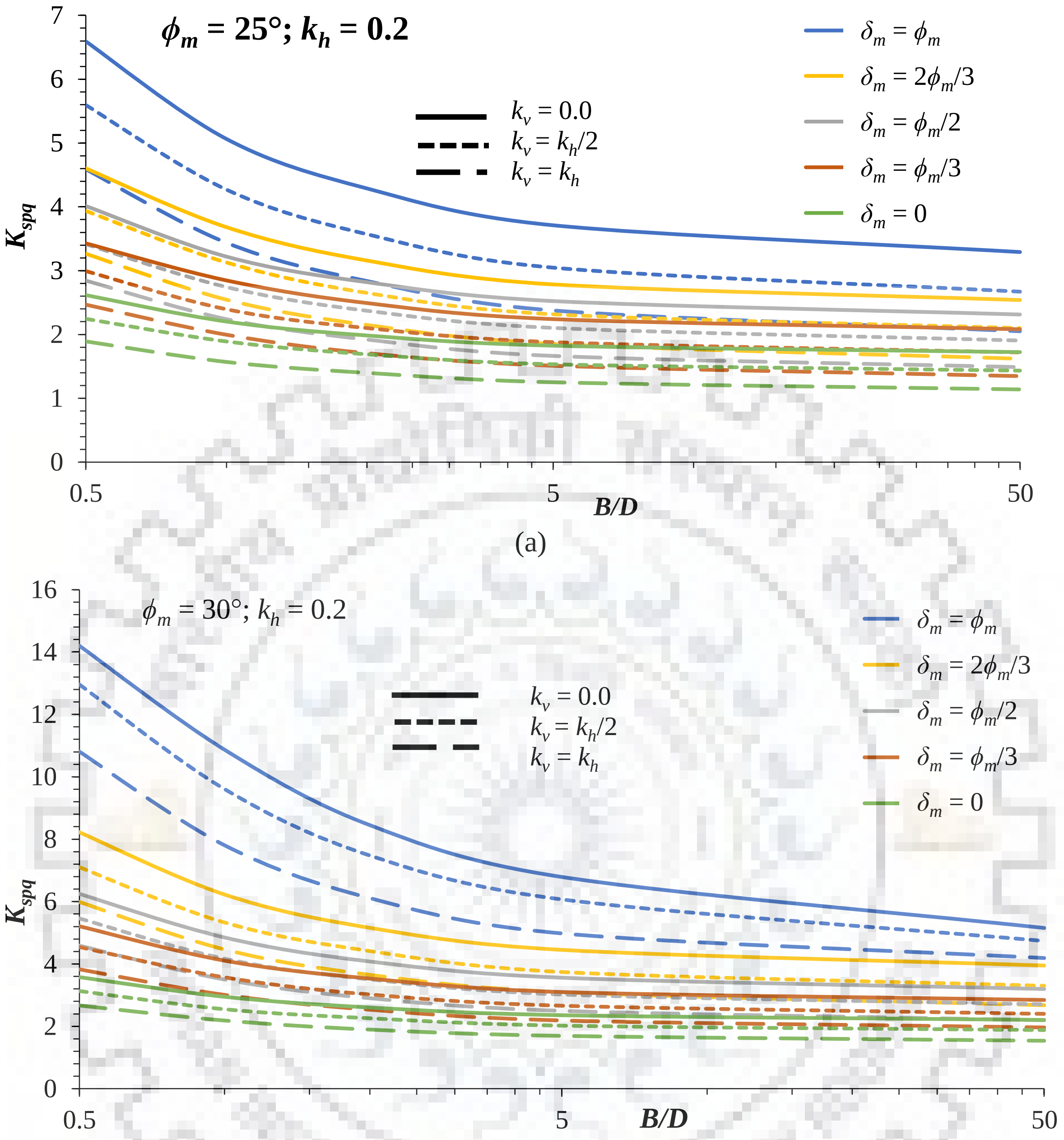

(b)

Fig. 5.21 Design chart for K_{spq} for k_h=0.2 for different soil-wall friction angles for (a) ϕ_m=25° and (b) ϕ_m=30°

5.4.5 *Centre of log-spiral*

Based on the analysis, the results for x_o and y_o were obtained using Eqns. (5.13a) and (5.13b). From the data-set available after the extensive study, multiple regression analysis has been performed in order to locate the centre of the log-spiral defining failure wedge formed in front of caisson embedded in cohesionless soil without surcharge (c=0, q=0). Knowing the depth of passive wedge and equation for log-spiral in addition to x_o and y_o, the entire log-spiral can be obtained. Eqns. (5.42a) and (5.42b) give the empirical correlations for

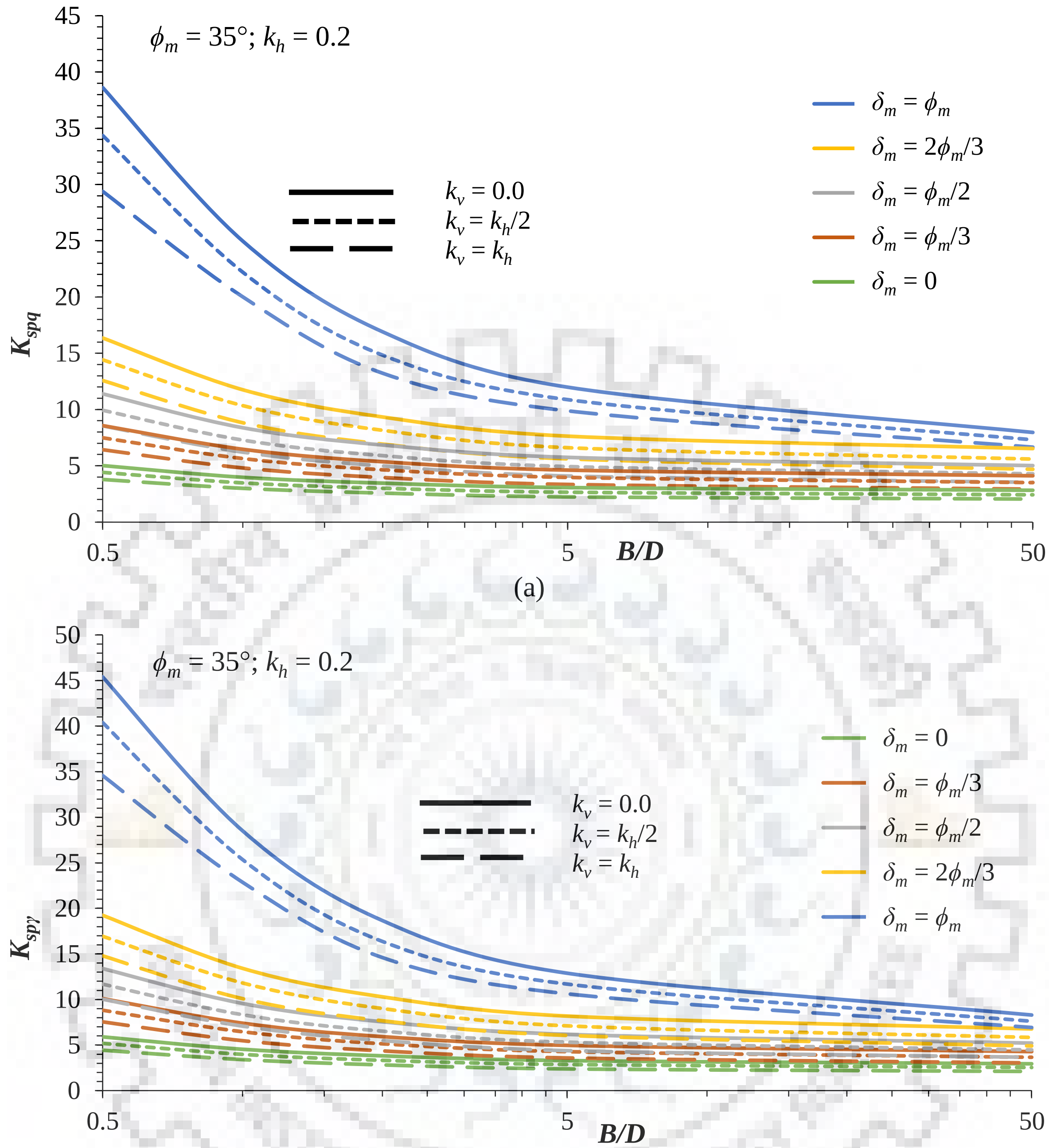

(a)

(b)

Fig. 5.22 Design chart for (a) K_{spq} and (b) $K_{sp\gamma}$ for k_h=0.2 for different soil-wall friction angles for ϕ_m=35°

horizontal and vertical coordinates respectively of the center of log-spiral for different ϕ_m, δ_m, k_h and k_v values. x_o and y_o are expressed in meters. The equations have been derived based on the results for input parameters mentioned in Table 5.4 and therefore, are valid for the values in this range.

$$x_o^{1/3} = -6.81\tan(\delta_m + \phi_m) - 20.865\left(k_h + {k_v}/{3}\right) + 10.176 \tag{5.42a}$$

$$y_o^{1/3} = -6.665\tan(\delta_m + \phi_m) - 4.735\left(k_h + {k_v}/{3}\right) + 8.877 \tag{5.42b}$$

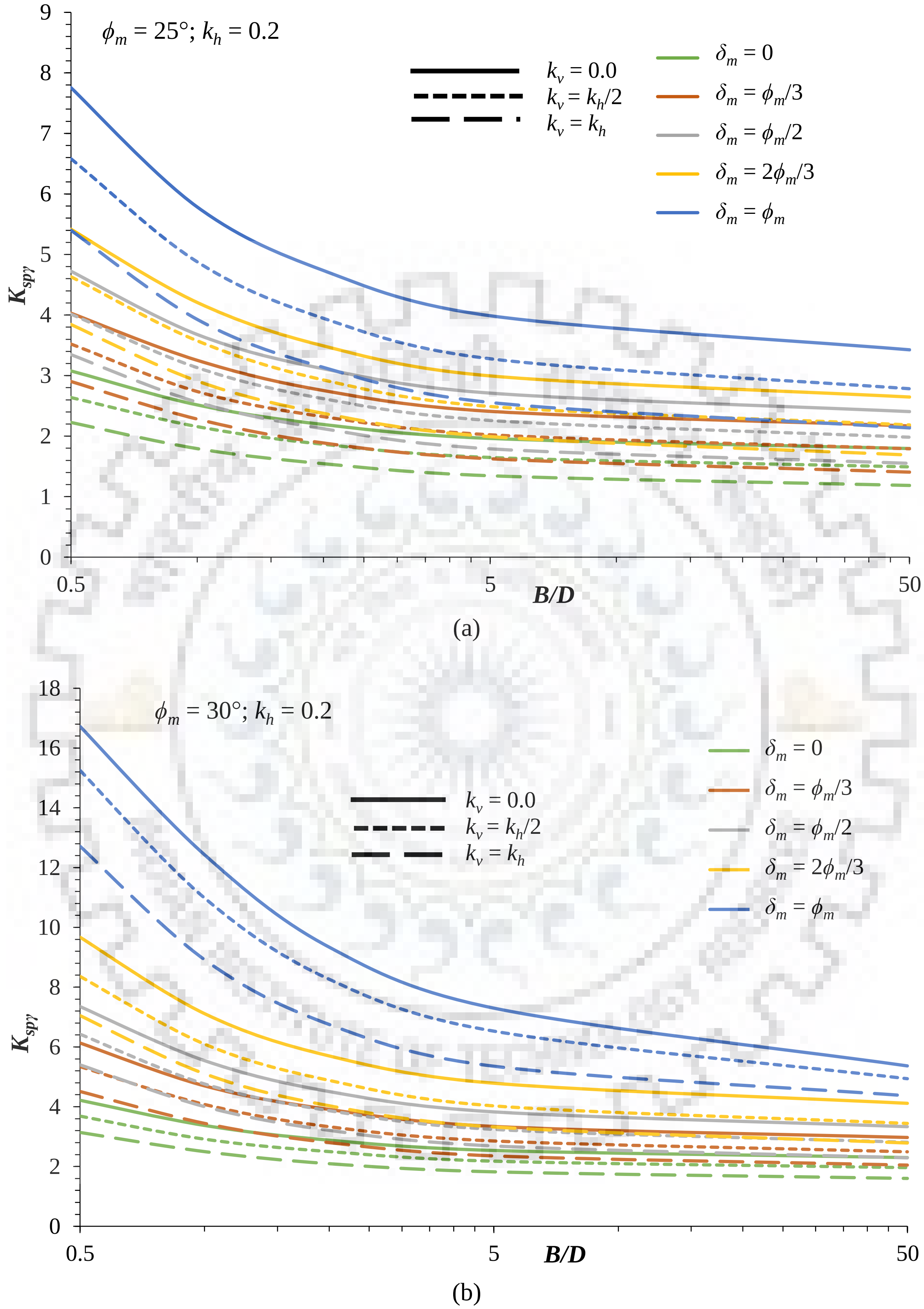

Fig. 5.23 Design chart for $K_{sp\gamma}$ for k_h=0.2 for different soil-wall friction angles for (a) ϕ_m=25° and (b) ϕ_m=30°

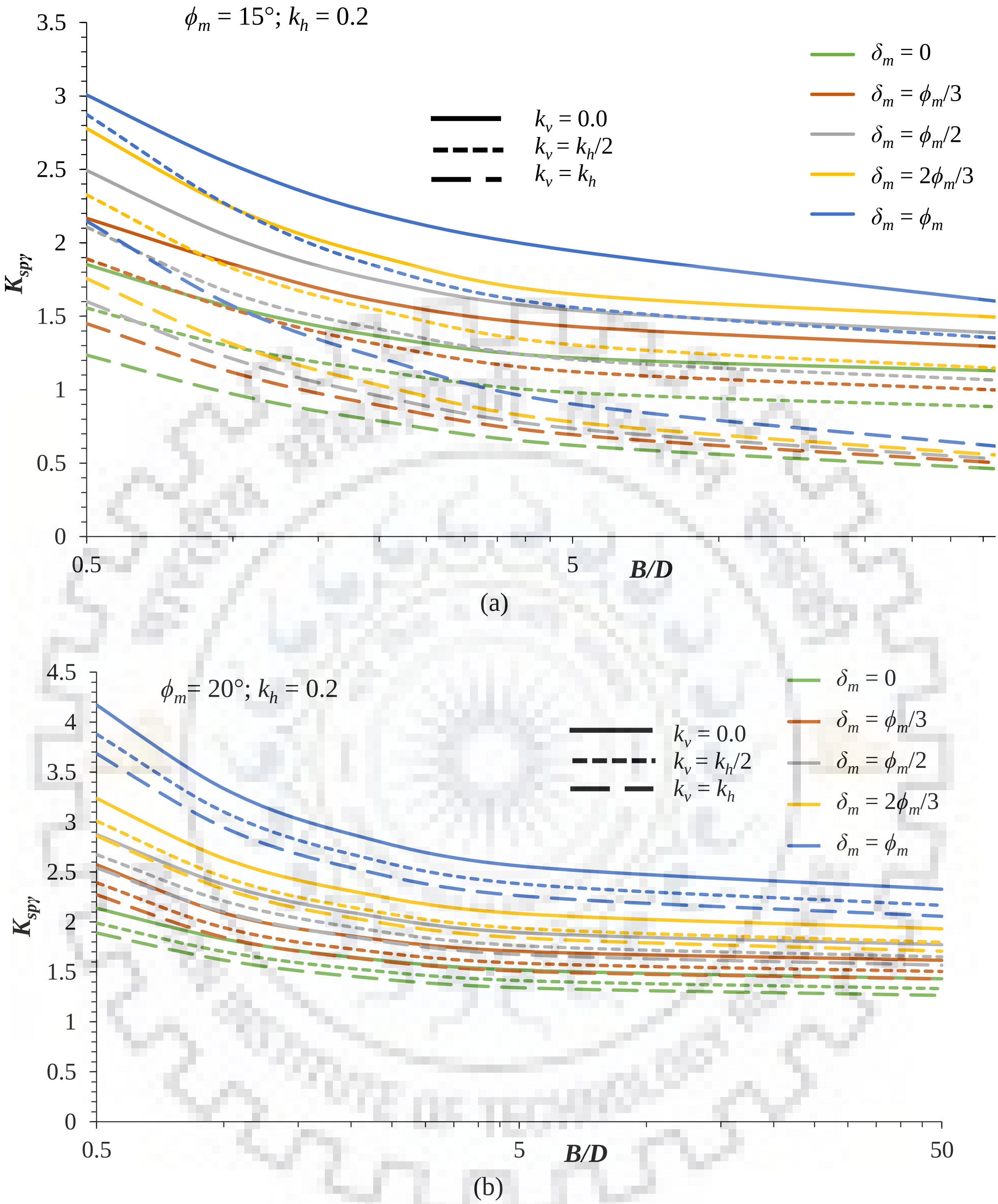

(a)

(b)

Fig. 5.24 Design chart for $K_{sp\gamma}$ for k_h=0.2 for different soil-wall friction angles for (a) ϕ_m=15° and (b) ϕ_m=20°

5.4.6 Use of design curves

The design curves proposed in the present study are used to obtain the seismic passive resistance offered by surrounding soil as follows:

1. The percentage mobilization of strength based on applied lateral load is assumed judiciously by the designer.
2. An initial assumption for the magnitude of embedment depth of caisson is made based on site conditions and presence of hard stratum.
3. Based on the magnitude of externally applied load and other input parameters, suitable *B/D* ratio is chosen from the design charts.
4. The seismic passive earth pressure resistance due to various components is calculated using Eqns. 5.31, 5.36 and 5.41. The possible resistance generated for the width obtained should be sufficiently larger than the applied load. If not, then geometry should be revised, and the steps should be repeated.

5.5 Summary

Determination of seismic passive resistance of finite width structure is a complicated problem. In the present study, an accurate idealization of 3D failure wedge based on results of numerical study and previous experimental studies has been done and based on the framework of limit equilibrium method along with pseudo-static approach. Design charts for seismic passive earth pressure coefficients due to cohesion component (K_{spc}), surcharge component (K_{spq}) and unit weight component ($K_{sp\gamma}$) have been prepared by taking width of the geotechnical structure into account. Thus, the results of present study are valid for different types of geotechnical structures. Regression analysis has been performed on the huge data set created from the study in order to develop empirical correlations for the centre of log-spiral defining the failure wedge corresponding to unit weight component of resistance.

Chapter 6

PASSIVE EARTH PRESSURE RESISTANCE ON CAISSON EMBEDDED IN c-ϕ SOIL WITH SURCHARGE LOAD ASSUMING COMBINED FAILURE SURFACE

6.1 General

Soil behaviour is non-linear for most intents and purposes. The assumption of application of principle of superposition in the previous chapter also falls under this umbrella. The principle of superposition for the analysis would be accurate if the failure wedge for all the individual components is the same. Choudhury and Subba Rao (2006) determined seismic bearing capacity factors for strip footings embedded in c-ϕ soil with surcharge considering curvilinear failure surface using principle of superposition. However, it is not the case in actual field conditions. A unique failure wedge is developed under the action of all the forces which is different from the failure wedges formed under the action of a single resisting component acting individually. Subba Rao and Choudhury (2005) presented some results comparing the total passive resistance obtained from principal of superposition and that obtained from combined failure surface. No other record of consideration of combined failure surface (single failure surface developed when all the resisting components, i.e., cohesion, c; surcharge, q and unit weight γ are acting together) has been found in the existing literature.

In the present study, 3D failure wedge considered in previous chapter and depicted in Fig. 5.1 is assumed to be formed behind caisson embedded in c-ϕ soil with surcharge load of magnitude q acting upon the entire extent of failure wedge. The critical failure wedge obtained from the consideration of all resisting components acting together is further used to determine the seismic passive earth pressure coefficients due to cohesion, surcharge and unit weight components, i.e., K_{spc}, K_{spq} and $K_{sp\gamma}$ respectively. Extensive design charts have been prepared for the different resistive components. The effect of seismic acceleration coefficients on seismic passive earth pressure coefficient due to cohesion component has also been explored.

6.2 Proposed Theoretical Methodology

The proposed geometry of failure wedge and soil input parameters adopted in the present study is the same as in the previous chapter and mentioned in Table 5.1. Soil surrounding the caisson is assumed to be dry and homogeneous and soil properties are assumed to be isotropic in all directions. In addition, the soil properties (cohesion, c; adhesion, C_a; friction angle, ϕ and unit weight, γ) are assumed to be independent of seismic forces acting on the system. Limit equilibrium method of analysis has been adopted in the present study to establish force equilibrium in horizontal and vertical directions. The forces acting on any infinitesimally thin slice of failure wedge at depth z is shown in Fig. 6.1. The critical failure wedge geometry is obtained based on the action of all these forces.

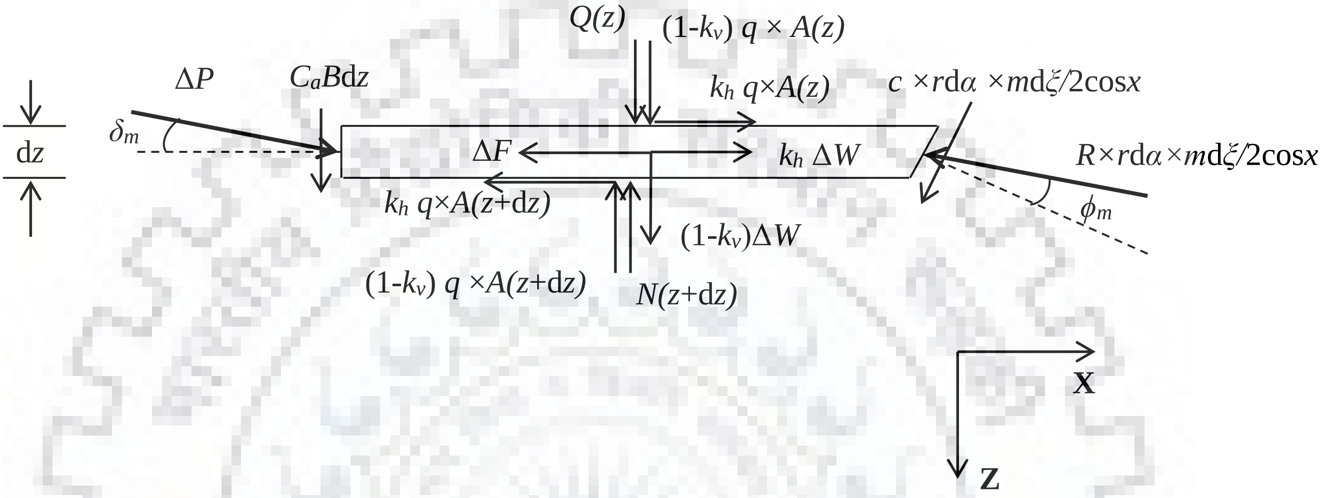

Fig. 6.1 Free body diagram of forces acting on an infinitesimally thin strip of failure wedge at depth z considering all resisting components acting together

6.2.1 Mathematical formulation of the problem

The sign convention and force notations used in this chapter is the same as it was in Chapter 5. Again, the resistive components in Y-direction cancel out each other because of geometrical symmetry about Y-axis. The resistive components due to soil reaction (ΔR_H and ΔR_V) and cohesive forces (ΔC_H and ΔC_V) of surrounding soils are defined using Eqns. (5.17) to (5.24). The force equilibrium in X and Z directions are considered to obtain the caisson forces in presence of cohesion (c), surcharge (q) and unit weight (γ) components. From Fig. 6.1, the horizontal and vertical force equilibrium equations are written as:

$$p(z)B\cos\delta\, dz - \Delta F(z) + k_h qA(z) - k_h qA(z+dz) + k_h\Delta W(z) = \Delta R_H(z) + \Delta C_H(z) \tag{6.1}$$

$$p(z)B\sin\delta\, dz + C_a Bdz + (1-k_v)\Delta W(z) + Q(z) - N(z+dz) + (1-k_v)qA(z) - (1-k_v)qA(z+dz) = \Delta R_V(z) - \Delta C_V(z) \tag{6.2}$$

$B < m\tan x$

From Eqns. (5.17c), (5.18c) and (6.1)

$$p(z)B\cos\delta\,dz - \Delta F(z) + k_h qA(z) - k_h qA(z+dz) + k_h \Delta W(z) =$$
$$Rm(z)r(z)d\alpha\frac{\cos\phi_m}{\cos x}\sin(\alpha+\alpha_o-\phi_m)\left\{\sin x - \sin\left(x-\theta(z)\right)\right\} +$$
$$m(z)r(z)d\alpha\frac{\cos(\alpha+\alpha_o-\phi_m)\{\sin x-\sin(x-\theta(z))\}}{\cos x}\times(c+R\sin\phi_m) \tag{6.3a}$$
$$p(z)B\cos\delta\,dz - \Delta F(z) + k_h qA(z) - k_h qA(z+dz) + k_h \Delta W(z) =$$
$$\frac{m(z)r(z)d\alpha\{\sin x-\sin(x-\theta(z))\}}{\cos x}\times\{c\cos(\alpha+\alpha_o-\phi_m)+R\sin(\alpha+\alpha_o)\} \tag{6.3b}$$
$$R\sin(\alpha+\alpha_o) = \Big[\{p(z)B\cos\delta\,dz - \Delta F(z) + k_h qA(z) - k_h qA(z+dz) + k_h\Delta W(z)\}\times$$
$$\frac{\cos x}{m(z)r(z)d\alpha\{\sin x-\sin(x-\theta(z))\}}\Big] - c\cos(\alpha+\alpha_o-\phi_m) \tag{6.3c}$$

From Eqns. (5.21c), (5.22c) and (6.2)

$$p(z)B\sin\delta\,dz + C_aBdz + (1-k_v)\Delta W(z) + Q(z) - N(z+dz) + (1-k_v)qA(z) -$$
$$(1-k_v)qA(z+dz) = Rm(z)r(z)d\alpha\frac{\cos\phi_m}{\cos x}\cos(\alpha+\alpha_o-\phi_m)\{\pi-2x+\theta(z)\} -$$
$$m(z)r(z)d\alpha\frac{\{\pi-2x+\theta(z)\}\sin(\alpha+\alpha_o-\phi_m)}{\cos x}\times(c+R\sin\phi_m) \tag{6.4a}$$
$$p(z)B\sin\delta\,dz + C_aBdz + (1-k_v)\Delta W(z) + Q(z) - N(z+dz) + (1-k_v)qA(z) -$$
$$(1-k_v)qA(z+dz) = \frac{m(z)r(z)d\alpha}{\cos x}\{\pi-2x+\theta(z)\}\,[R\cos(\alpha+\alpha_o) - c\sin(\alpha+\alpha_o-\phi_m)] \tag{6.4b}$$
$$R\cos(\alpha+\alpha_o) = \frac{\cos x}{m(z)r(z)d\alpha\{\pi-2x+\theta(z)\}}\{p(z)B\sin\delta\,dz + C_aBdz + (1-k_v)\Delta W(z) +$$
$$Q(z) - N(z+dz) + (1-k_v)qA(z) - (1-k_v)qA(z+dz)\} + c\sin(\alpha+\alpha_o-\phi_m) \tag{6.4c}$$

Dividing Eqn. (6.3c) by (6.4c)

$$\tan(\alpha+\alpha_o) =$$
$$\frac{\left[\{p(z)B\cos\delta dz-\Delta F(z)+k_hqA(z)-k_hqA(z+dz)+k_h\Delta W(z)\}\times\frac{\cos x}{m(z)r(z)d\alpha\{\sin x-\sin(x-\theta(z))\}}\right]-c\cos(\alpha+\alpha_o-\phi_m)}{\left[\frac{\cos x}{m(z)r(z)d\alpha\{\pi-2x+\theta(z)\}}\{p(z)B\sin\delta dz+C_aBdz+(1-k_v)\Delta W(z)+Q(z)-N(z+dz)+(1-k_v)qA(z)-(1-k_v)qA(z+dz)\}\right]+c\sin(\alpha+\alpha_o-\phi_m)} \tag{6.5a}$$

$$\Rightarrow \tan(\alpha+\alpha_o) =$$
$$\frac{[\{p(z)B\cos\delta dz-\Delta F(z)+k_hqA(z)-k_hqA(z+dz)+k_h\Delta W(z)\}\times\cos x]-c\cos(\alpha+\alpha_o-\phi_m)m(z)r(z)d\alpha\{\sin x-\sin(x-\theta(z))\}}{[\cos x\,\{p(z)B\sin\delta dz+C_aBdz+(1-k_v)\Delta W(z)+Q(z)-N(z+dz)+(1-k_v)qA(z)-(1-k_v)qA(z+dz)\}]+cm(z)r(z)d\alpha\{\pi-2x+\theta(z)\}\sin(\alpha+\alpha_o-\phi_m)}\times$$
$$\frac{\pi-2x+\theta(z)}{\sin x-\sin(x-\theta(z))} \tag{6.5b}$$

Let $HD(z) = \{\sin x - \sin(x-\theta(z))\}\tan(\alpha+\alpha_o)$ and $VD(z) = \pi - 2x + \theta(z)$

$$p(z)B\cos x\,dz\times\{\cos\delta\,VD(z) - \sin\delta\,HD(z)\} = [\cos x\;VD(z)\{\Delta F(z) - k_hq\{A(z) -$$
$$A(z+dz)\} - k_h\Delta W(z)\}] + cm(z)r(z)d\alpha VD(z)HD(z)\left\{\frac{\cos(\alpha+\alpha_o-\phi_m)}{\tan(\alpha+\alpha_o)} + \sin(\alpha+\alpha_o -\right.$$

$$\phi_m)\Big\} + \big[\cos x\, HD(z)\big\{C_a B dz + (1-k_v)\Delta W(z) + Q(z) - N(z+dz) + (1-k_v) q\{A(z) - A(z+dz)\}\big\}\big] \qquad (6.5c)$$

$$p(z)Bdz = \frac{[VD(z)\{\Delta F(z) - k_h q\{A(z) - A(z+dz)\} - k_h \Delta W(z)\}]}{\cos\delta VD(z) - \sin\delta HD(z)} + \frac{\frac{cm(z)r(z)d\alpha VD(z)HD(z)}{\cos x}\left\{\frac{\cos(\alpha+\alpha_o-\phi_m)}{\tan(\alpha+\alpha_o)} + \sin(\alpha+\alpha_o-\phi_m)\right\}}{\cos\delta VD(z) - \sin\delta HD(z)} + \frac{\big[HD(z)\big\{C_a Bdz + (1-k_v)\Delta W(z) + Q(z) - N(z+dz) + (1-k_v)q\{A(z) - A(z+dz)\}\big\}\big]}{\cos\delta VD(z) - \sin\delta HD(z)} \qquad (6.5d)$$

$B > m\tan x$

From Eqns. (5.19c), (5.20b) and (6.1)

$$p(z)B\cos\delta\, dz - \Delta F(z) + k_h qA(z) - k_h qA(z+dz) + k_h \Delta W(z) = BRr(z)\sin(\alpha+\alpha_o - \phi_m)\cos\phi_m\, d\alpha + B(c + R\sin\phi_m)\cos(\alpha+\alpha_o-\phi_m)r(z)d\alpha \qquad (6.6a)$$

$$p(z)B\cos\delta\, dz - \Delta F(z) + k_h\, qA(z) - k_h\, qA(z+dz) + k_h\, \Delta W(z) = Br(z)d\alpha[c\cos(\alpha + \alpha_o - \phi_m) + R\sin(\alpha+\alpha_o)] \qquad (6.6b)$$

$$R\sin(\alpha+\alpha_o) = \left[\frac{\{p(z)B\cos\delta dz - \Delta F(z) + k_h qA(z) - k_h qA(z+dz) + k_h\Delta W(z)\} - Br(z)d\alpha c\cos(\alpha+\alpha_o-\phi_m)}{Br(z)d\alpha}\right] \qquad (6.6c)$$

From Eqns. (5.23c), (5.24b) and (6.2):

$$p(z)B\sin\delta\, dz + C_a\, Bdz + (1-k_v)\Delta W(z) + Q(z) - N(z+dz) + (1-k_v)qA(z) - (1-k_v)qA(z+dz) = R\cos\phi_m\ \cos(\alpha+\alpha_o-\phi_m) \times r(z)d\alpha \times \{B + \frac{m(z)}{\cos x}(\pi - x - \sin x)\} - r(z)d\alpha\sin(\alpha+\alpha_o-\phi_m)\{B + \frac{m(z)}{\cos x}(\pi - x - \sin x)\} \times (c + R\sin\phi_m) \qquad (6.7a)$$

$$p(z)B\sin\delta\, dz + C_a Bdz + (1-k_v)\Delta W(z) + Q(z) - N(z+dz) + (1-k_v)qA(z) - (1-k_v)qA(z+dz) = r(z)d\alpha\left\{B + \frac{m(z)}{\cos x}(\pi - x - \sin x)\right\}[R\cos(\alpha+\alpha_o) - c\sin(\alpha + \alpha_o - \phi_m)] \qquad (6.7b)$$

$$R\cos(\alpha+\alpha_o) = \frac{\{p(z)B\sin\delta dz + C_a Bdz + (1-k_v)\Delta W(z) + Q(z) - N(z+dz) + (1-k_v)qA(z) - (1-k_v)qA(z+dz)\} + c\sin(\alpha+\alpha_o-\phi_m)r(z)d\alpha\left\{B + \frac{m(z)}{\cos x}(\pi - x - \sin x)\right\}}{r(z)d\alpha\left\{B + \frac{m(z)}{\cos x}(\pi - x - \sin x)\right\}} \qquad (6.7c)$$

$$\tan(\alpha+\alpha_o) = \frac{[\{p(z)B\cos\delta dz - \Delta F(z) + k_h qA(z) - k_h qA(z+dz) + k_h\Delta W(z)\} - Br(z)c\cos(\alpha+\alpha_o-\phi_m)d\alpha]\left\{B + \frac{m(z)}{\cos x}(\pi - x - \sin x)\right\}}{B\left[\{p(z)B\sin\delta dz + C_a Bdz + (1-k_v)\Delta W(z) + Q(z) - N(z+dz) + (1-k_v)qA(z) - (1-k_v)qA(z+dz)\} + c\sin(\alpha+\alpha_o-\phi_m)r(z)d\alpha\left\{B + \frac{m(z)}{\cos x}(\pi - x - \sin x)\right\}\right]} \qquad (6.8a)$$

Let $HD(z) = B\tan(\alpha+\alpha_o)$ and $VD(z) = B + \frac{m(z)}{\cos x}(\pi - x - \sin x)$

$$p(z)Bdz \times \{\cos\delta\, VD(z) - \sin\delta\, HD(z)\} = [VD(z)\{\Delta F(z) - k_h q\{A(z) - A(z+dz)\} - k_h \Delta W(z)\}] + cr(z)d\alpha VD(z)HD(z)\left\{\frac{\cos(\alpha+\alpha_o-\phi_m)}{\tan(\alpha+\alpha_o)} + \sin(\alpha+\alpha_o-\phi_m)\right\} + \left[HD(z)\{C_a Bdz + (1-k_v)\Delta W(z) + Q(z) - N(z+dz) + (1-k_v)q\{A(z) - A(z+dz)\}\}\right] \tag{6.8b}$$

$$p(z)Bdz = \frac{[VD(z)\{\Delta F(z) - k_h q\{A(z)-A(z+dz)\} - k_h \Delta W(z)\}]}{\cos\delta VD(z) - \sin\delta HD(z)} + \frac{cr(z)d\alpha VD(z)HD(z)\left\{\frac{\cos(\alpha+\alpha_o-\phi_m)}{\tan(\alpha+\alpha_o)} + \sin(\alpha+\alpha_o-\phi_m)\right\}}{\cos\delta VD(z) - \sin\delta HD(z)} + \frac{\left[HD(z)\{C_a Bdz + (1-k_v)\Delta W(z) + Q(z) - N(z+dz) + (1-k_v)q\{A(z)-A(z+dz)\}\}\right]}{\cos\delta VD(z) - \sin\delta HD(z)} \tag{6.8c}$$

Upon numerical integration of Eqns. (6.5d) and (6.8c) with α varying from 0 to α_f, the total caisson reaction (P_p) in presence of cohesion, surcharge and unit weight components of soil is obtained. The magnitude of P_p is then optimized with respect to initial angle of log spiral (α_o) and central angle of log spiral (α_f) using code developed in MATLAB (2021). The magnitudes of α_o and α_f corresponding to the critical condition are obtained for all input variables in order to find the individual magnitudes of seismic passive earth pressure coefficients due to unit weight component ($K_{sp\gamma}$), surcharge component (K_{spq}) and cohesion component (K_{spc}). The values of α_o and α_f corresponding to the critical failure wedge is substituted in Eqn. (5.27d) and (5.30c) and integrated to obtain K_{spc} using Eqn. (5.31). Similarly, K_{spq} is obtained from Eqn. (5.36) by substituting α_o and α_f corresponding to the critical failure wedge in Eqn. (5.33c) and (5.35c) and integrating over entire depth of failure wedge and $K_{sp\gamma}$ is calculated using Eqn. (5.41) after substitution of critical value of α_o and α_f in Eqns. (5.38) and (5.40) and integrating over entire depth of failure wedge. The seismic passive earth pressure coefficients obtained from the present study is corresponding to minimum of sum of all the resistive passive earth pressure components instead of the absolute minimum of the individual components as obtained in the previous chapter. Therefore, the present study considers the relative magnitudes of the various resisting components.

6.2.2 Validation of the proposed method

The results of the proposed methodology have been compared with the results of previous analytical studies. The magnitudes of seismic passive earth pressure coefficient due to cohesion component (K_{spc}) have been compared with the studies by Soubra (2000), Soubra and Macuh (2002), Subba Rao and Choudhury (2005) and Liu et al. (2018) and tabulated in Table 6.1. The studies by previous authors indicate that K_{spc} is independent of seismic acceleration coefficients. The present study derives critical failure wedge by considering combined failure surface due to action of all resisting components (c, q and γ). Therefore, the seismic inertial forces are also taken into consideration while defining the failure wedge and thus, affect the magnitude of seismic passive earth pressure due to cohesion component. K_{spc} obtained from present study are slightly higher in magnitude than the previous studies since the results are determined corresponding to the failure in presence of all resisting components rather than the absolute minima due to cohesion component only.

Table 6.1 Comparison of K_{spc} obtained in present study with existing literature for B=800 m, D=16 m and $k_v = 0$

			Seismic passive earth pressure coefficient due to cohesion component (K_{spc})				
ϕ_m	k_h	δ_m / ϕ_m	Soubra (2000)	Soubra and Macuh (2002)	Subba Rao and Choudhury (2005)	Liu et al. (2018)	Present Study
20°	0	0.5	3.24	4.18	3.62	3.68	4.43
		1	5.10	5.31	4.36	4.64	6.24
	0.1	0.5	3.24	4.18	3.62	3.68	4.71
		1	5.10	5.31	4.36	4.64	6.88
30°	0	0.5	12.81	6.05	5.32	5.51	6.18
		1	17.82	8.88	6.84	7.89	12.65
	0.1	0.5	12.81	6.05	5.32	5.51	7.13
		1	17.82	8.88	6.84	7.89	18.16

Similarly, Table 6.2 and Table 6.3 compares the magnitudes of seismic passive earth pressure coefficients due to surcharge and unit weight components respectively. The magnitudes of these components are also found to be in vicinity of the results of existing literature. However, some differences in magnitudes are also observed due to assumptions of curved failure surface and combined failure surface.

6.3 Present Study

In the present study, magnitudes of different seismic passive earth pressure coefficients (K_{spc}, K_{spq} and $K_{sp\gamma}$) have been tabulated for different input parameters mentioned in Table 5.4. In addition to the parameters mentioned in Table 5.4, the magnitudes of cohesion (c), surcharge (q) and unit weight (γ) adopted in the present study are 15 kN/m^2, 15 kN/m^2 and 18 kN/m^3 respectively. These coefficients have been obtained corresponding to minimum value of summation of seismic passive earth pressure forces (P_{pc}, P_{pq} and $P_{p\gamma}$). The optimization of these forces is done by varying the initial angle of log-spiral α_o between 0 to $(\pi/2 - \phi_m)$ and central angle of log-spiral α_f between 0 to $\{\pi/2 - (\phi_m + \alpha_o)\}$.

Table 6.2 Comparison of K_{spq} obtained in present study with past literature for B=800 m, D=16 m and k_v=0

			Seismic passive earth pressure coefficient due to surcharge component (K_{spq})				
ϕ_m	k_h	δ_m / ϕ_m	Soubra (2000)	Soubra and Macuh (2002)	Subba Rao and Choudhury (2005)	Liu et al. (2018)	Present Study
20°	0	0.5	2.52	2.54	2.46	2.54	2.59
		1	2.87	3.00	2.65	2.87	3.06
	0.1	0.5	2.32	-	2.37	-	2.08
		1	2.65	-	2.63	-	2.76
30°	0	0.5	4.44	4.53	4.32	4.53	4.58
		1	5.81	6.28	4.99	5.80	6.16
	0.1	0.5	4.17	-	4.21	-	4.27
		1	5.45	-	4.99	-	5.98

- : denotes that study did not present results for seismic cases

Table 6.3 Comparison of $K_{sp\gamma}$ obtained in present study with past literature for B=800 m, D=16 m and k_v=0

			Seismic passive earth pressure coefficient due to unit weight component ($K_{sp\gamma}$)					
ϕ_m	k_h	δ_m / ϕ_m	Mononobe – Okabe (1929)	Soubra (2000)	Soubra and Macuh (2002)	Subba Rao and Choudhury (2005)	Liu et al. (2018)	Present Study
20°	0	0.5	2.64	2.58	2.57	2.49	2.56	2.55
		1	3.53	3.12	3.13	2.91	3.07	2.98
	0.1	0.5	2.38	2.35	-	2.33	-	2.07
		1	3.11	2.83	-	2.76	-	2.72
30°	0	0.5	4.98	4.69	4.65	4.43	4.61	4.51
		1	10.10	6.86	6.93	5.78	6.68	5.99
	0.1	0.5	4.56	4.35	-	4.27	-	4.20
		1	9.02	6.35	-	5.57	-	5.81

- : denotes that study did not present results for seismic cases

The computation of K_{spc} was carried out corresponding to adhesion (C_a) value of ratio of tangent of δ_m and tangent of ϕ_m ($C_a/c = \tan\delta_m/\tan\phi_m$). All the numerical computations and optimization process are carried out by writing programs in MATLAB (2021). The angle x defining the shape of the failure wedge in horizontal plane has been chosen as $\phi_m \times D/B$ to take width of the caisson into account. The sequence of steps followed in the present study has been depicted through flow chart in Fig. 6.2.

6.4 Results and Discussions

The present study reveals the effect of various input parameters like soil-soil friction angle (ϕ_m), soil wall friction angle (δ_m), seismic acceleration coefficients (k_h and k_v), relative magnitudes of c, q and γ and width of caisson (B/D) on the different seismic passive earth pressure coefficients due cohesion (K_{spc}), surcharge (K_{spq}) and unit weight components ($K_{sp\gamma}$). Design charts and tables presented in this section illustrate the effects of these components.

6.4.1 Effect of relative magnitude of resisting components (c, C_a, q and γ)

Table 6.4 reflects the effect of relative magnitudes of c, q and γ on seismic passive earth pressure coefficients. It can be observed that the seismic passive earth pressure coefficient due to unit weight component is more or less insensitive (increase of 0.36% from unit weight component acting alone) to relative magnitudes of c and q. However, significant difference between absolute minima value and magnitude corresponding to combined failure surface can be observed for seismic passive earth pressure coefficient due to cohesion and surcharge components (increase of 49.67% and 4.76% respectively). This observation could be attributed to the fact that the failure wedge due to unit weight component is immune to influence of other resistive component while the failure wedge due to cohesion component acting alone is easily manipulated by seismic inertial components due to unit weight and surcharge loading. The effect of variation in magnitude of resisting components on seismic passive earth pressure coefficient due to surcharge component is intermediate, i.e., it is more sensitive than $K_{sp\gamma}$ but less sensitive than K_{spc}. It can also be observed that the increase in normalized adhesion (C_a/c) from 0 to $\tan\delta_m/\tan\phi_m$ causes increase in magnitude of K_{spc}. For the set of input parameters mentioned in Table 6.4 and for δ_m/ϕ_m=1/3 and 2/3 in the presence of surcharge loading, K_{spc} increases by 5.25% and 5.19% respectively for the increase in normalized adhesion mentioned above.

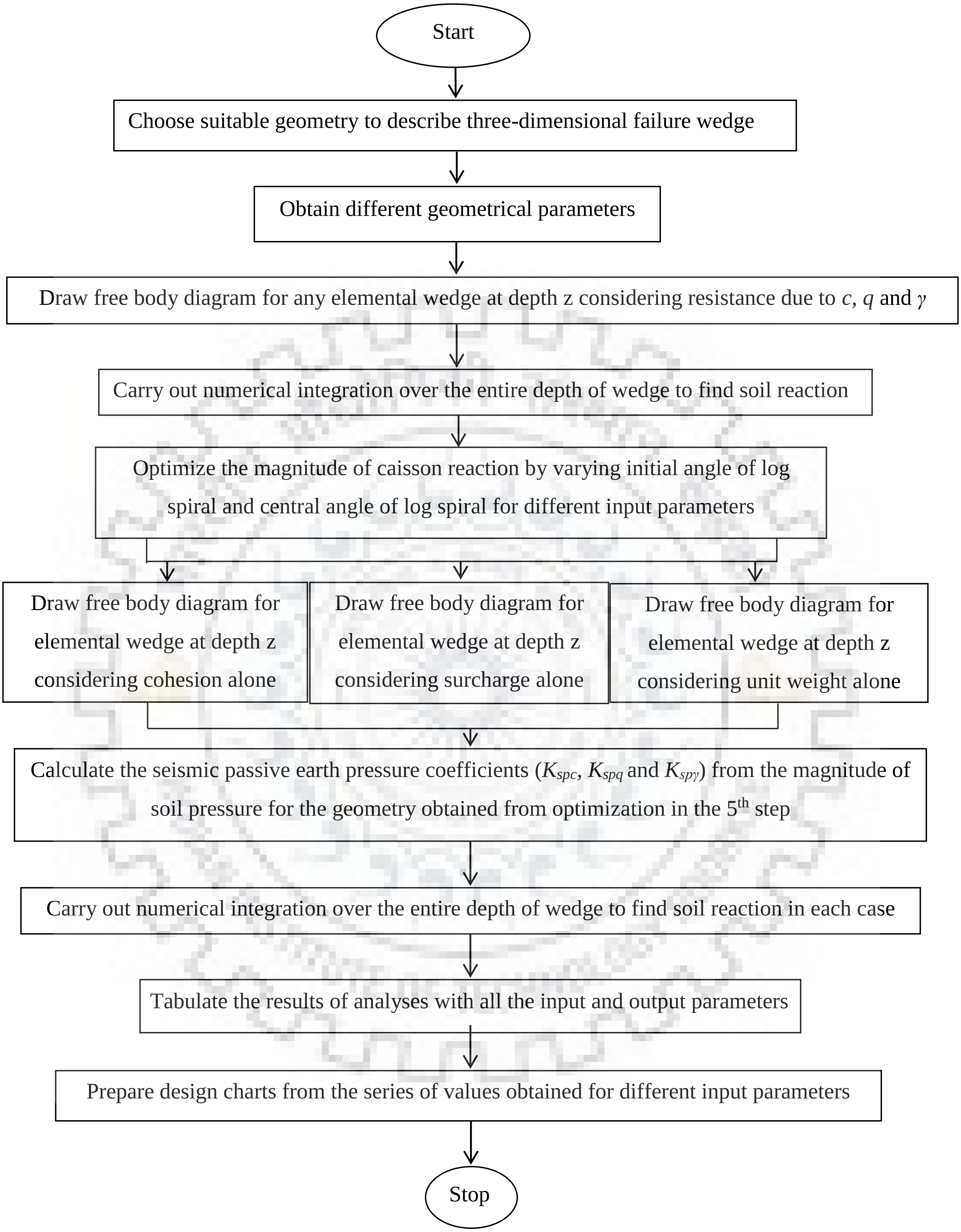

Fig. 6.2 Flow chart representing the sequence of steps in present study

Table 6.4 Magnitudes of various earth pressure coefficients for different combinations of cohesion, adhesion and surcharge for ϕ_m=30°, B=800 m, k_h=0.1 and k_v/k_h=0.5

δ/ϕ	γ (kN/m^3)	c (kN/m^2)	C_a/c	q (kN/m^2)	K_{spc}	K_{spq}	$K_{sp\gamma}$
1/3	18	0	0	0	-	-	1.756
	0	0	0	15	-	3.383	-
	18	0	0	15	-	3.401	1.756
	18	15	0	0	5.019	-	1.756
	18	15	0	15	5.427	3.467	1.758
	0	15	$\tan\delta_m/\tan\phi_m$	0	4.832	-	-
	18	15	$\tan\delta_m/\tan\phi_m$	15	5.712	3.493	1.759
2/3	18	0	0	0	-	-	4.501
	0	0	0	15	-	4.411	-
	18	0	0	15	-	4.436	4.503
	18	15	0	0	8.845	-	4.507
	18	15	0	15	10.264	4.511	4.514
	0	15	$\tan\delta_m/\tan\phi_m$	0	7.214	-	-
	18	15	$\tan\delta_m/\tan\phi_m$	15	10.797	4.621	4.517

- : denotes that the marked fields do not exist for given combination of parameters

6.4.2 Effect of mobilized soil-wall interface friction angle (δ_m)

Fig. 6.3 through Fig. 6.8 represent the effect of soil wall friction angle on $K_{sp\gamma}$ values for different combinations of horizontal seismic acceleration coefficients and mobilized soil friction angle ϕ_m. The magnitudes of $K_{sp\gamma}$, K_{spq} and K_{spc} are found to increase with increase in δ_m irrespective of k_h and ϕ_m values as was the case in previous chapter. This magnitude increase is even magnified for higher value of δ_m. In case of k_h=0.1 and k_v=k_h, for ϕ_m=15°, as δ_m is increased from 0 to $\phi_m/3$ and $2\phi_m/3$ to ϕ_m, $K_{sp\gamma}$ increases by 9.36% and 10.83% respectively while for ϕ_m=30°, as δ_m is increased from 0 to $\phi_m/3$ and $2\phi_m/3$ to ϕ_m, $K_{sp\gamma}$ increases by 29.37% and 63.03% respectively for 16m wide caisson. The increase in K_{spq} values for the same increase in δ_m values is found to be 8.81% and 10.22% respectively for ϕ_m=15° and 27.47% and 66.09% respectively for ϕ_m=30°. The increase in K_{spc} values is even more pronounced as it increases by 13.74% and 17.34% respectively for ϕ_m=15° and 54.33% and 90.53% respectively for ϕ_m=30° for the same set of input parameters. As the magnitude of δ_m increases, the soil is able to develop higher resistance through interface friction at soil-caisson boundary causing the magnitude of seismic passive earth pressure coefficients to be higher.

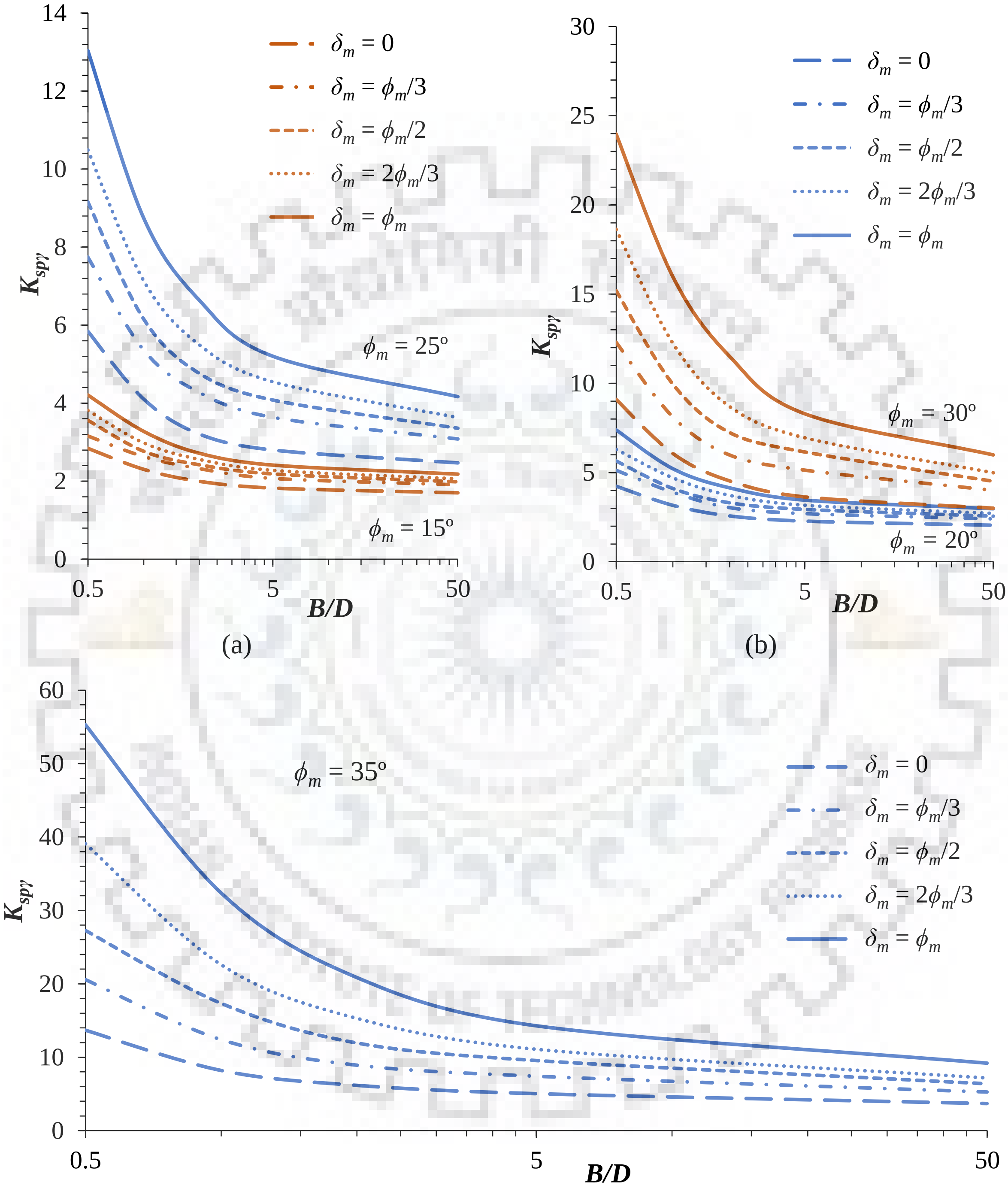

(a) (b)

(c)

Fig. 6.3 Design chart for $K_{sp\gamma}$ in static condition for different soil-wall friction angles for (a) ϕ_m=15°, 25°, (b) ϕ_m=20°, 30° and (c) ϕ_m=35°

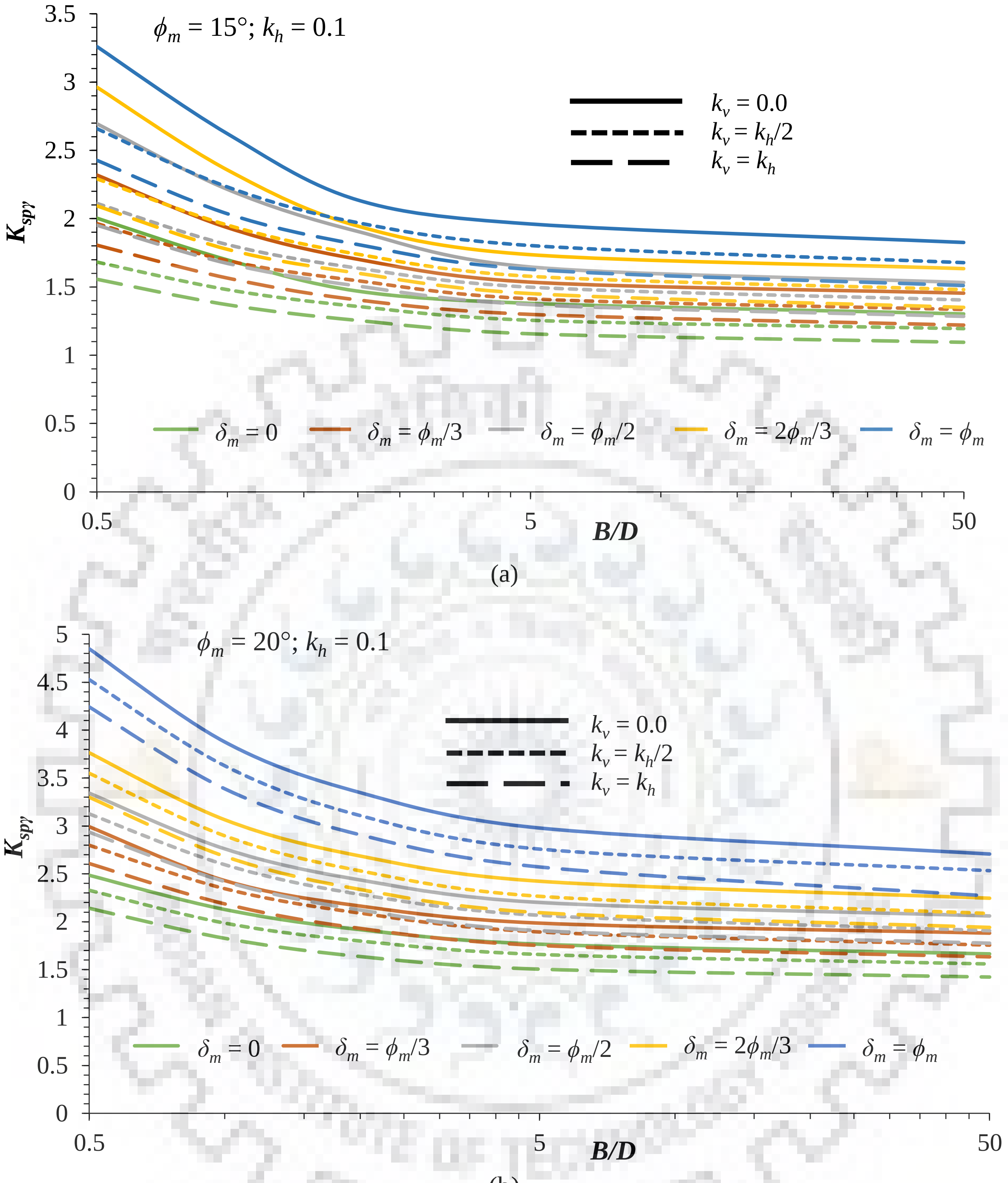

Fig. 6.4 Design chart for $K_{sp\gamma}$ in case of k_h=0.1 for different soil-wall friction angles for (a) ϕ_m=15° and (b) ϕ_m=20°

6.4.3 *Effect of mobilized soil-soil friction angle (ϕ_m)*

Fig. 6.9 to Fig. 6.11 depict the design charts highlighting the influence of mobilized soil-soil friction angle (ϕ_m) on K_{spc} values. Considering B=16 m, k_h=0.1 and k_v=k_h, for δ_m=ϕ_m/3, upon increasing ϕ_m from 15° to 20° and from 30° to 35°, the percentage increase in

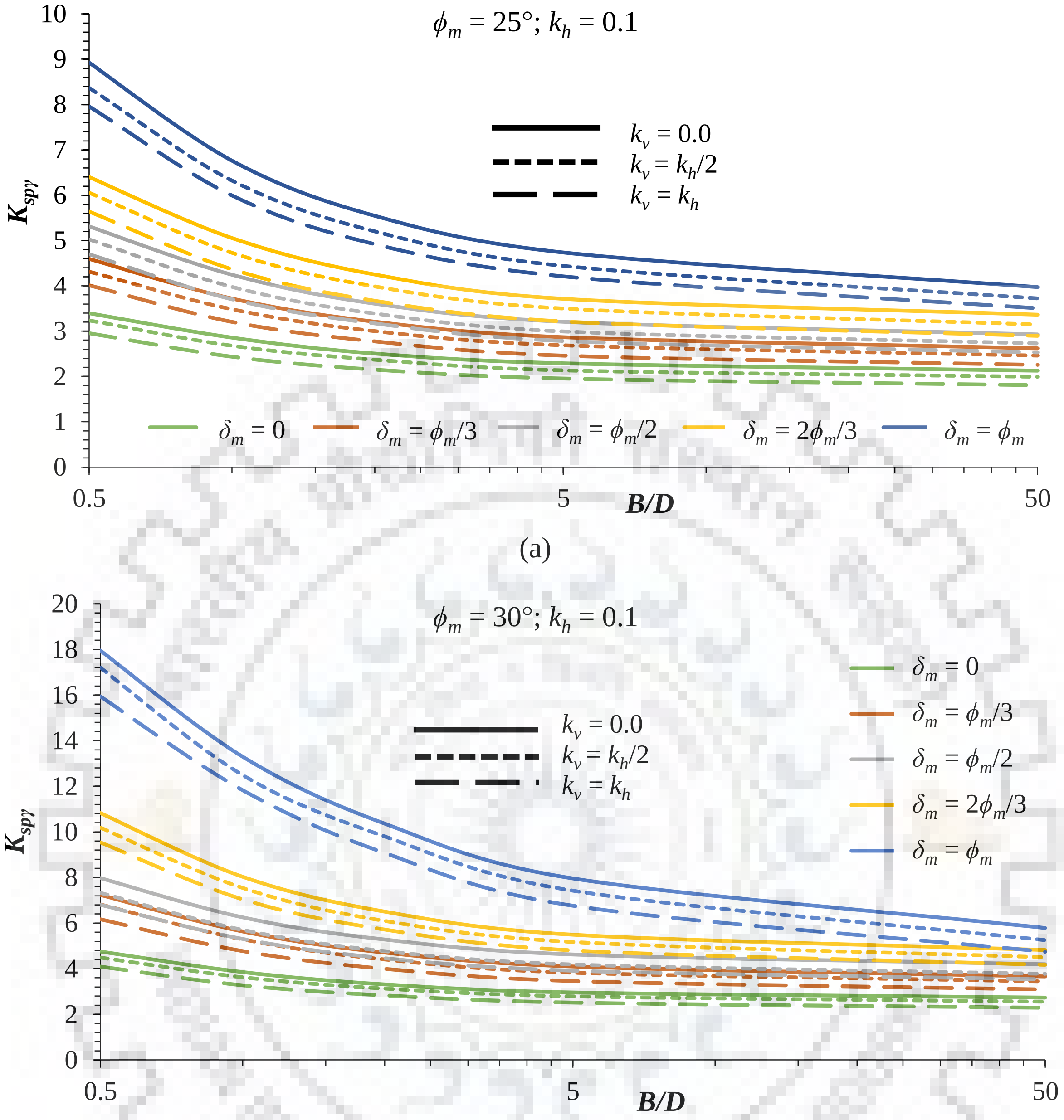

(a)

(b)

Fig. 6.5 Design chart for $K_{sp\gamma}$ in case of k_h=0.1 for different soil-wall friction angles for (a) ϕ_m=25° and (b) ϕ_m=30°

magnitude of K_{spc} is found to be 5.2% and 1.08% respectively and for $\delta_m=2\phi_m/3$, the percentage increase is 15.76% and 17.54% respectively. Again, the increase in K_{spq} magnitude is observed to be 25.8% and 23.31% respectively for $\delta_m=\phi_m/3$ and 33.58% and 39.35% respectively for $\delta_m=2\phi_m/3$. Similarly, the increase in $K_{sp\gamma}$ magnitude for $\delta_m=\phi_m/3$ case is computed as 25.94% and 24.63% respectively whereas for $\delta_m=2\phi_m/3$, the increase is 34.53% and 45.43% respectively, for the given set of input parameters. Since soil friction angle is the direct measure of soil shear strength, therefore, for the same set of input parameters, higher the magnitude of ϕ_m, higher is the seismic passive earth pressure developed. This increase is even more magnified for higher magnitudes of δ_m.

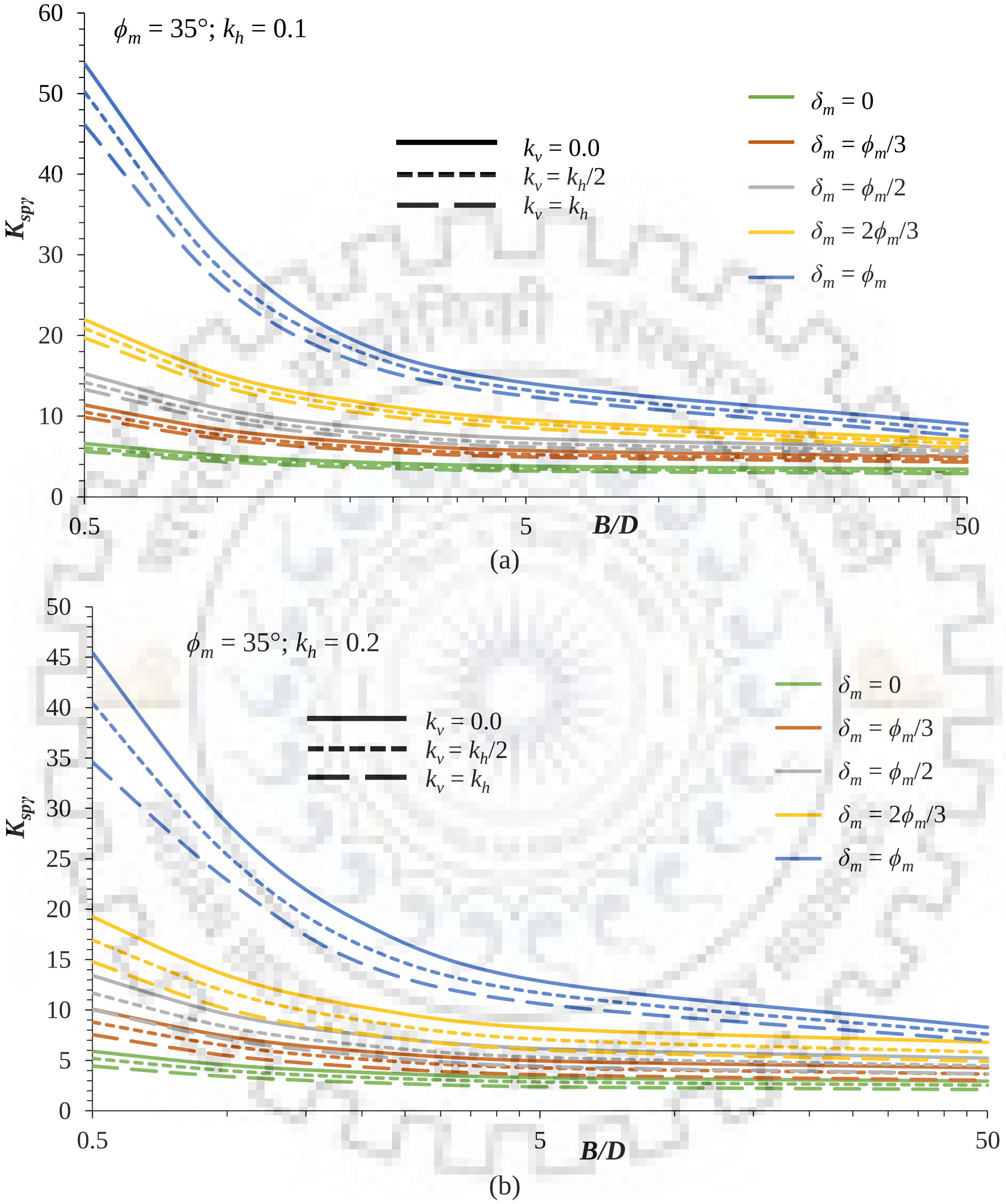

(a)

(b)

Fig. 6.6 Design chart for $K_{sp\gamma}$ in case of (a) k_h=0.1 and (b) k_h=0.2 for different soil-wall friction angles for ϕ_m=35°

6.4.4 *Effect of seismic acceleration coefficients (k_h and k_v)*

Both, horizontal and vertical seismic acceleration coefficients, have significant impact on the magnitude of K_{spq} and $K_{sp\gamma}$ since they develop inertial forces that cause instability. On the other hand, K_{spc} increases with increase in both k_h and k_v. While horizontal seismic acceleration coefficient increases K_{spc} significantly, as illustrated in Fig. 6.9 to Fig. 6.11, the effect of k_v is nominal on K_{spc} as is evident from Table 6.5.

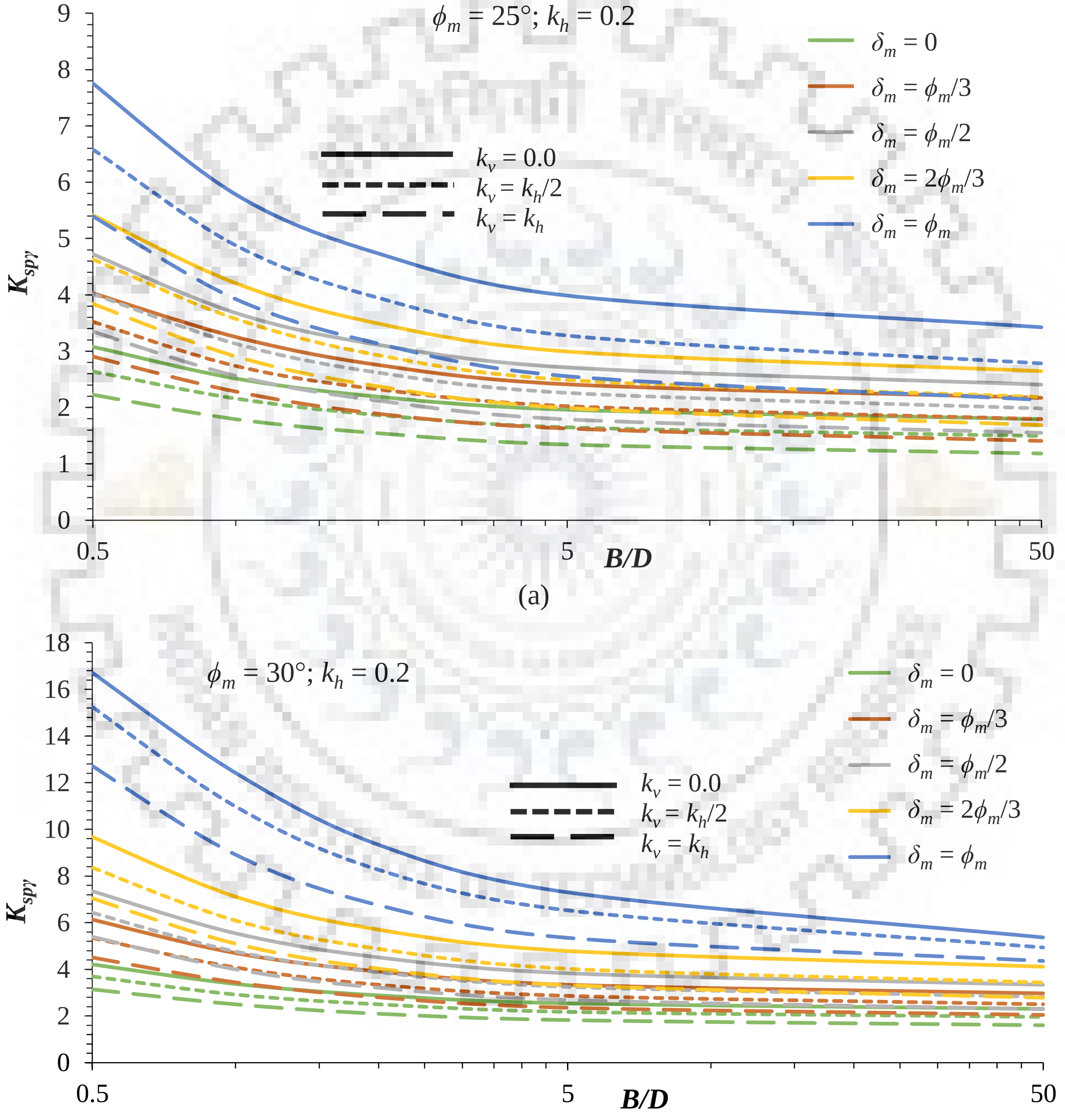

(a)

(b)

Fig. 6.7 Design chart for $K_{sp\gamma}$ in case of k_h=0.2 for different soil-wall friction angles for (a) ϕ_m=25°and (b) ϕ_m=30°

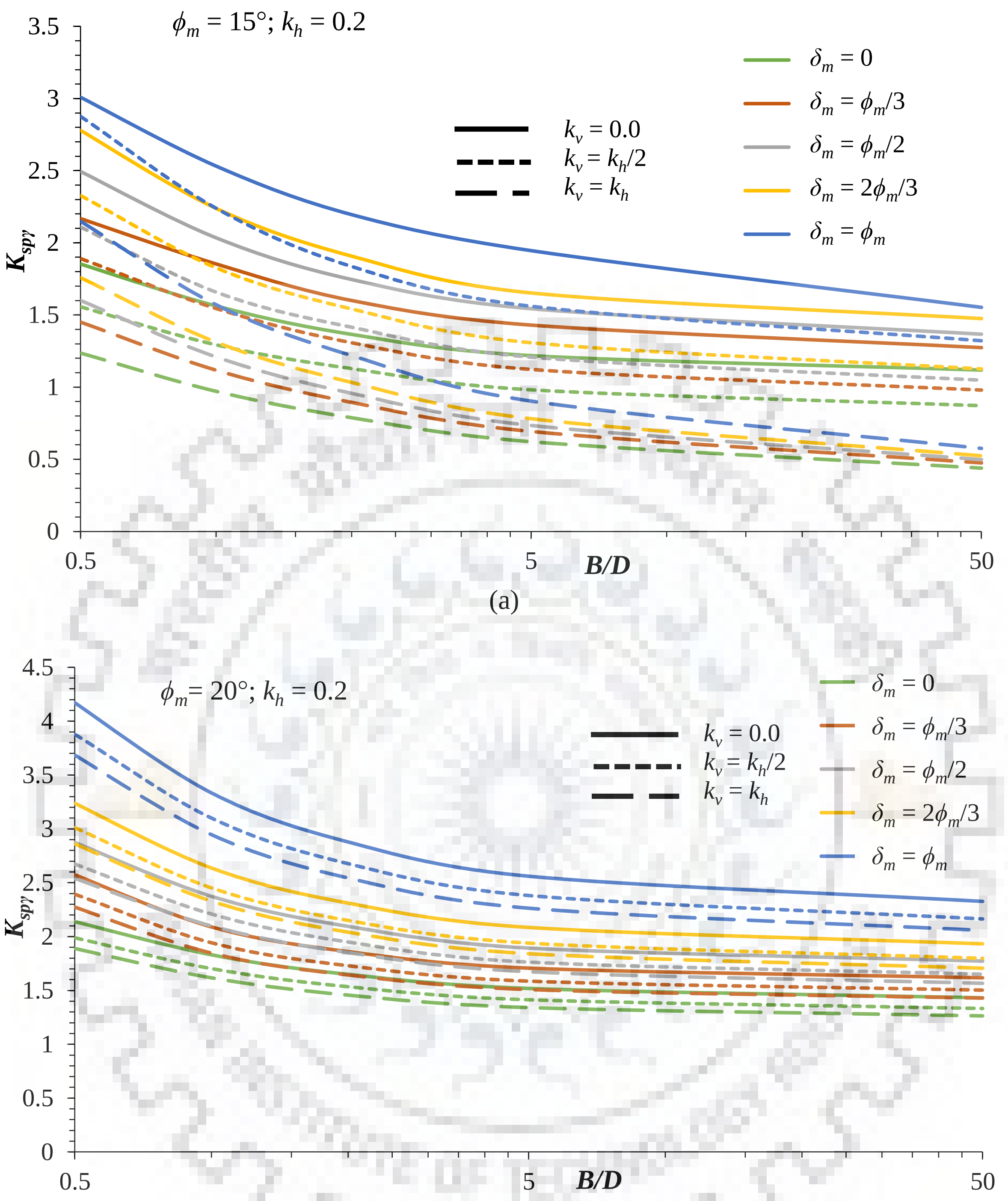

(a)

(b)

Fig. 6.8 Design chart for $K_{sp\gamma}$ in case of k_h=0.2 for different soil-wall friction angles for (a) ϕ_m=15° and (b) ϕ_m=20°

For B=16 m, k_v=k_h/2, ϕ_m=25° and δ_m=ϕ_m/3, as k_h is increased from 0 to 0.1 and 0.1 to 0.2, the magnitude of $K_{sp\gamma}$ diminishes by 20.72% and 30.91% respectively. The reduction in K_{spq} magnitudes for the same increase in k_h values are 20.47% and 30.72% respectively for the identical set of parameters.

Table 6.5 Comparison of K_{spc} obtained in present study for B/D=50 and $\delta_m=\phi_m/3$

Seismic passive earth pressure coefficient due to cohesion component (**K_{spc}**)						
k_h	ϕ_m	15°	20°	25°	30°	35°
0.1	$k_v/\ k_h = 0$	4.036	4.196	4.738	5.604	5.548
	$k_v/\ k_h = 1$	4.070	4.266	4.816	5.712	5.676
0.2	$k_v/\ k_h = 0$	4.478	4.624	5.346	6.742	6.964
	$k_v/\ k_h = 1$	4.520	4.702	5.434	6.848	7.08

The effect of k_v on seismic passive earth pressure coefficients is the same albeit with less severity. In case of ϕ_m=25°, $\delta_m=\phi_m/3$ and B=16 m, for k_h=0.1, as k_v increases from 0 to $k_h/2$ and from $k_h/2$ to k_h, the magnitude of $K_{sp\gamma}$ decreases by 9.43% and 10.22% respectively while K_{spq} diminishes by 9.07% and 9.83% respectively. However, for k_h=0.2, this reduction is much more pronounced for both K_{spq} and $K_{sp\gamma}$, i.e., 25.24% and 37.51% respectively for the above-mentioned set of input parameters.

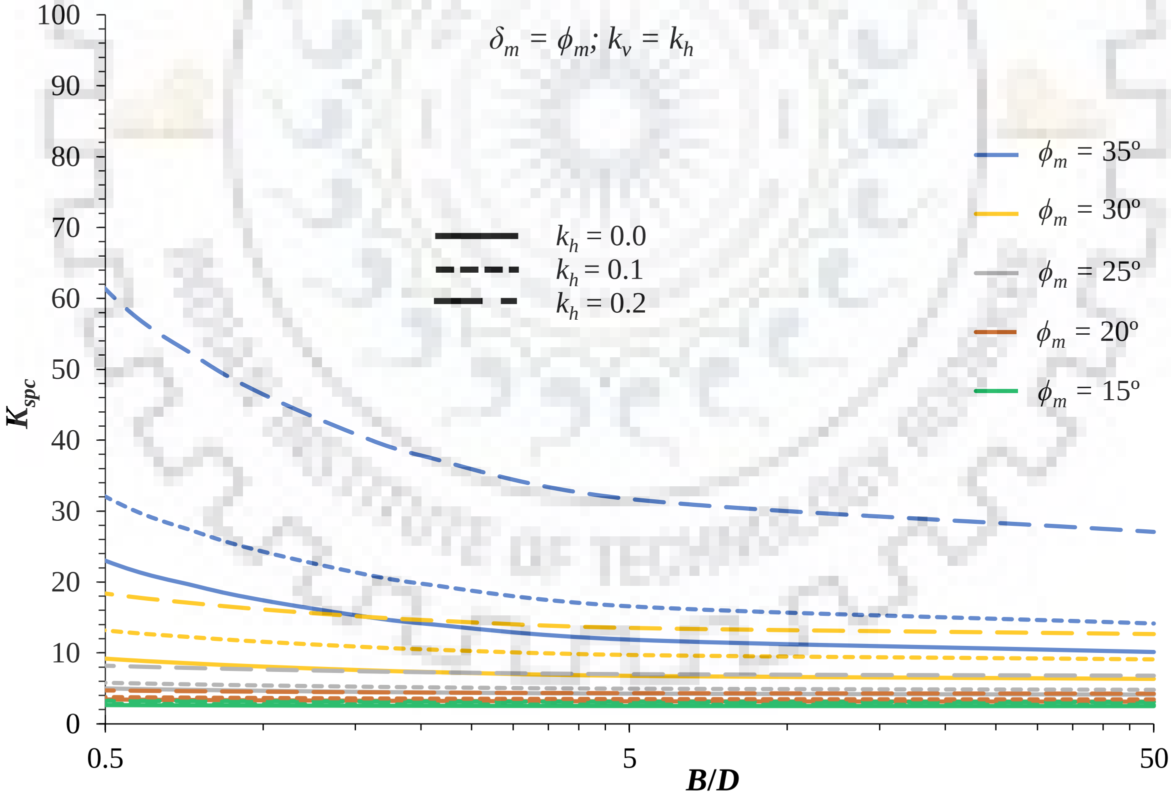

Fig. 6.9 Design chart for K_{spc} in case of $k_v=k_h$ for different mobilized soil-soil friction angles for $\delta_m=\phi_m$

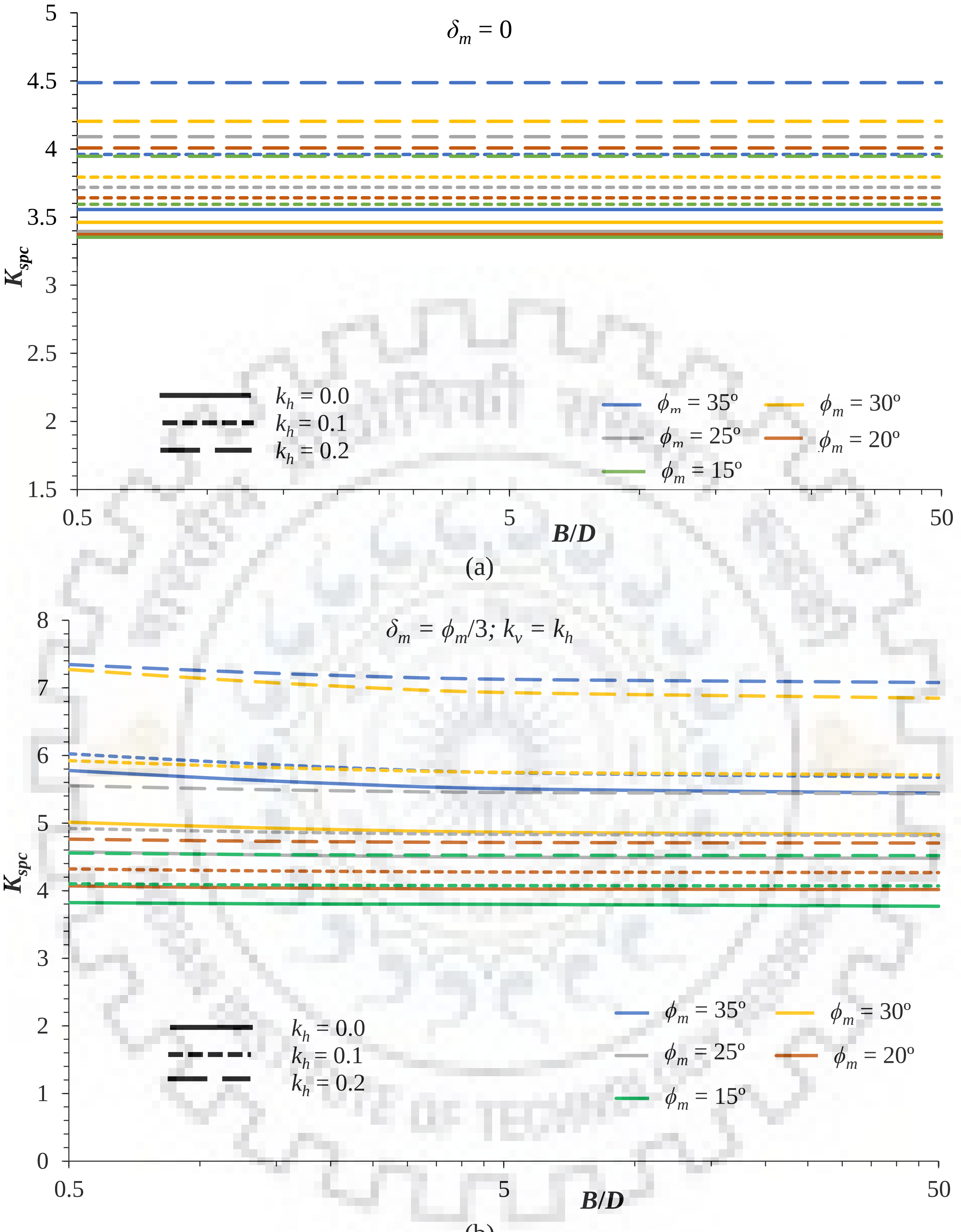

(a)

(b)

Fig. 6.10 Design chart for K_{spc} in case of k_v=k_h for different mobilized soil-soil friction angles for (a) δ_m=0 and (b) δ_m=ϕ_m/3

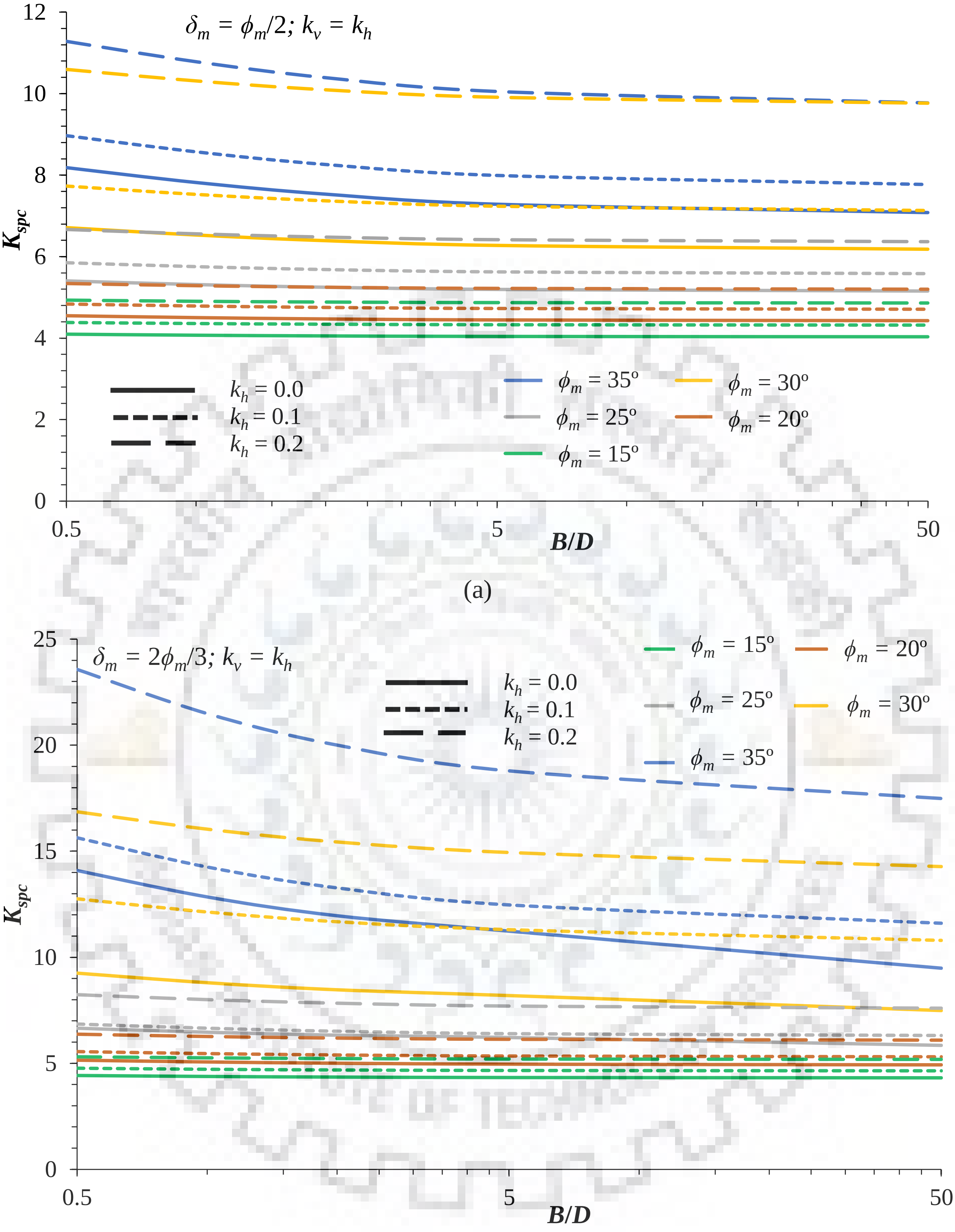

(a)

(b)

Fig. 6.11 Design chart for K_{spc} in case of k_v=k_h for different mobilized soil-soil friction angles for (a) δ_m=ϕ_m/2 and (b) δ_m =2ϕ_m/3

6.4.5 *Effect of width of caisson*

Fig. 6.12 to Fig. 6.17 show the design charts relating K_{spq} values with ratio of width of caisson to depth of failure wedge (B/D) for different values of δ_m and k_v. It could be observed that the magnitude of K_{spq} decreases as the width of caisson increases. Similar trend is followed for $K_{sp\gamma}$ and K_{spc} values. As B increases, 3-D behavior tends to convert into plane strain behavior because the volume of soil in side wedges compared to volume of wedge in front of caisson becomes smaller and smaller.

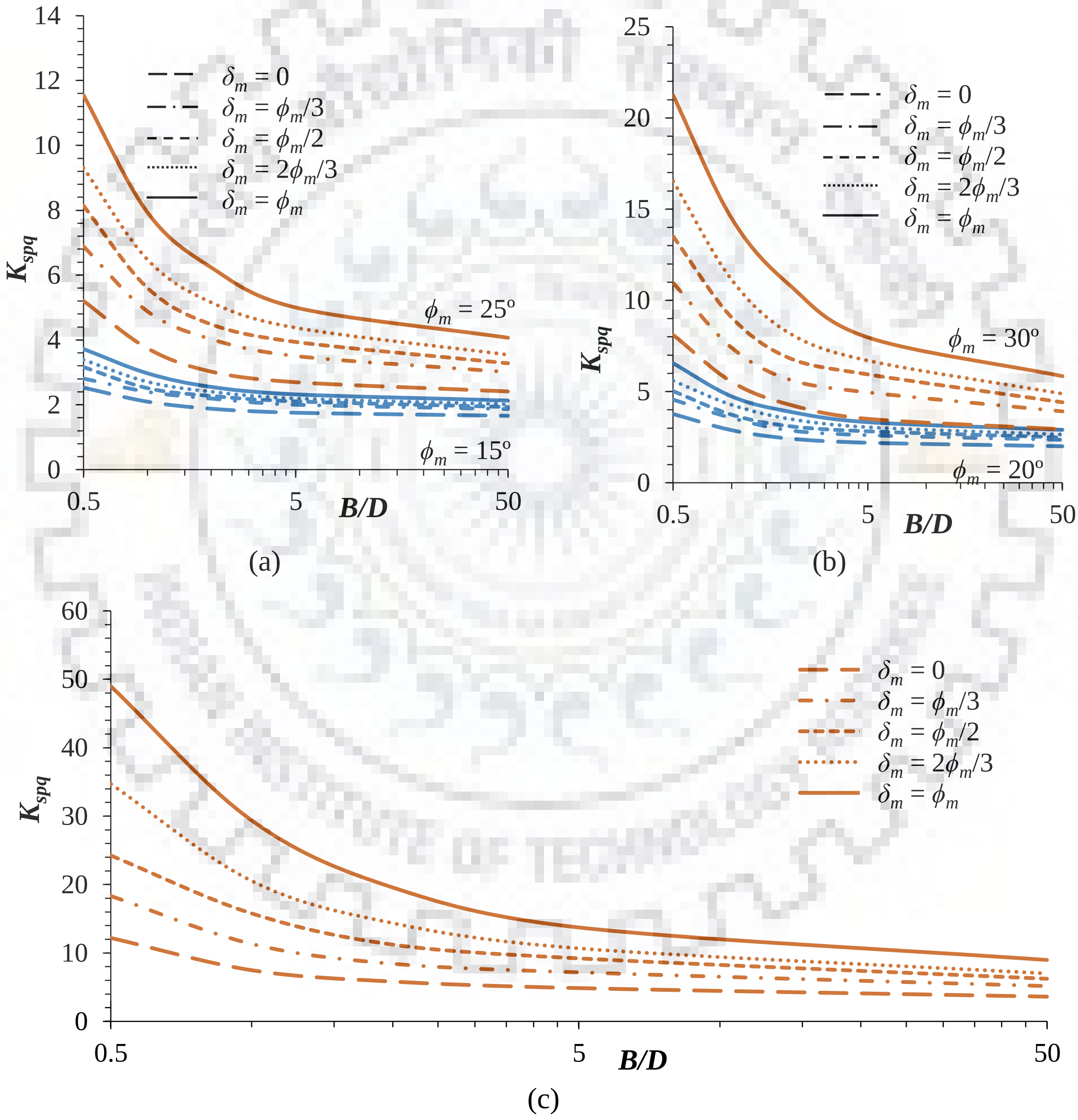

(a) (b)

(c)

Fig. 6.12 Design chart for K_{spq} under static condition for different soil-wall friction angles for (a) ϕ_m=15°, 25°; (b) ϕ_m=20°, 30° and (c) ϕ_m=35°

For ϕ_m=30°, δ_m/ϕ_m=1/3, k_h=0.1 and k_v=k_h, as B/D increases from 0.5 to 1 and from 5 to 50, the magnitude of $K_{sp\gamma}$ reduces by 22.51% and 10.15% respectively while the magnitude of K_{spq} diminishes by 20.33% and 7.26%. It is again highlighted that increasing the width of caisson reduces the sensitivity towards seismic passive earth pressure coefficients.

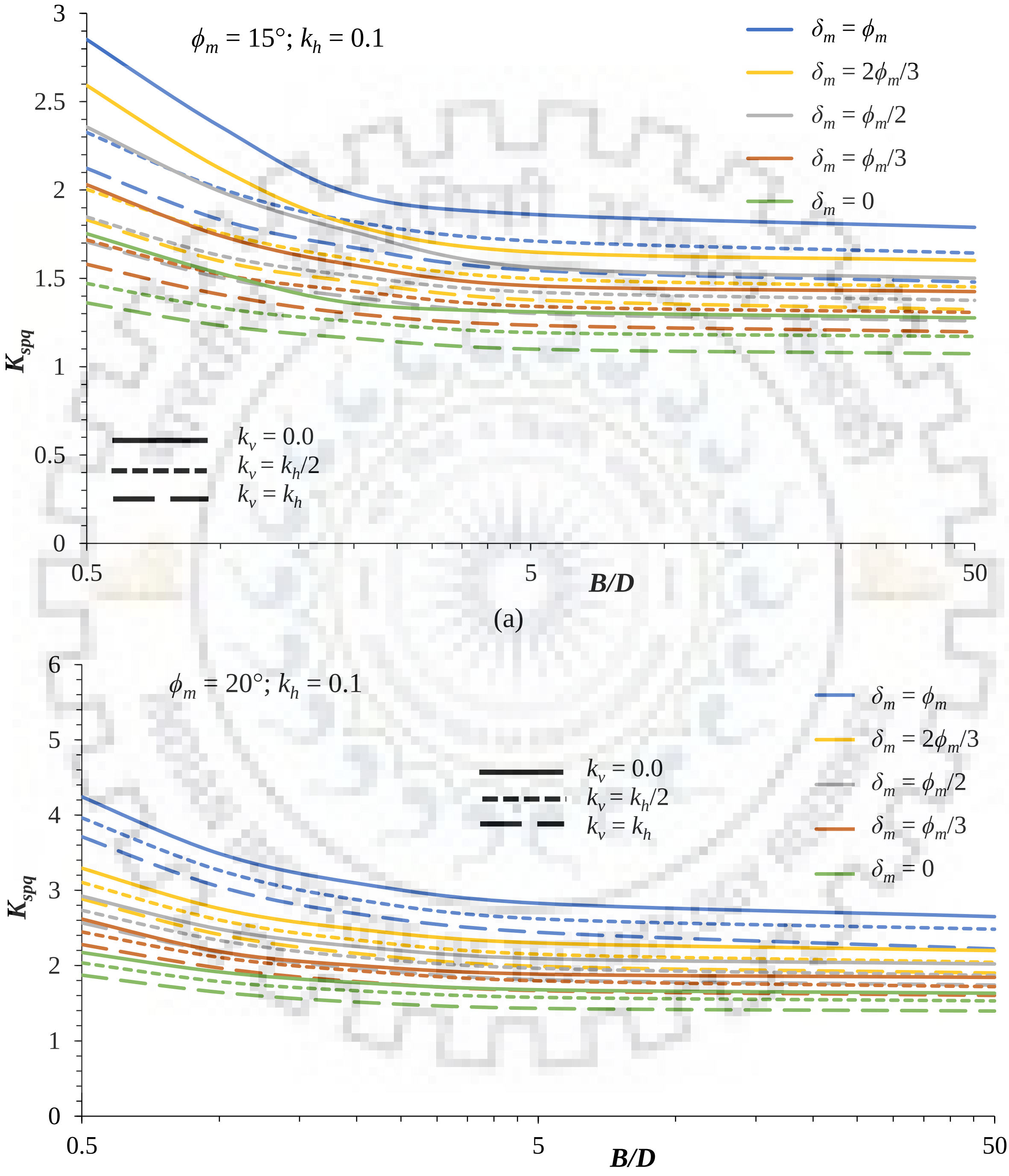

(a)

(b)

Fig. 6.13 Design chart for K_{spq} for k_h=0.1 for different soil-wall friction angles for (a) ϕ_m=15°and (b) ϕ_m=20°

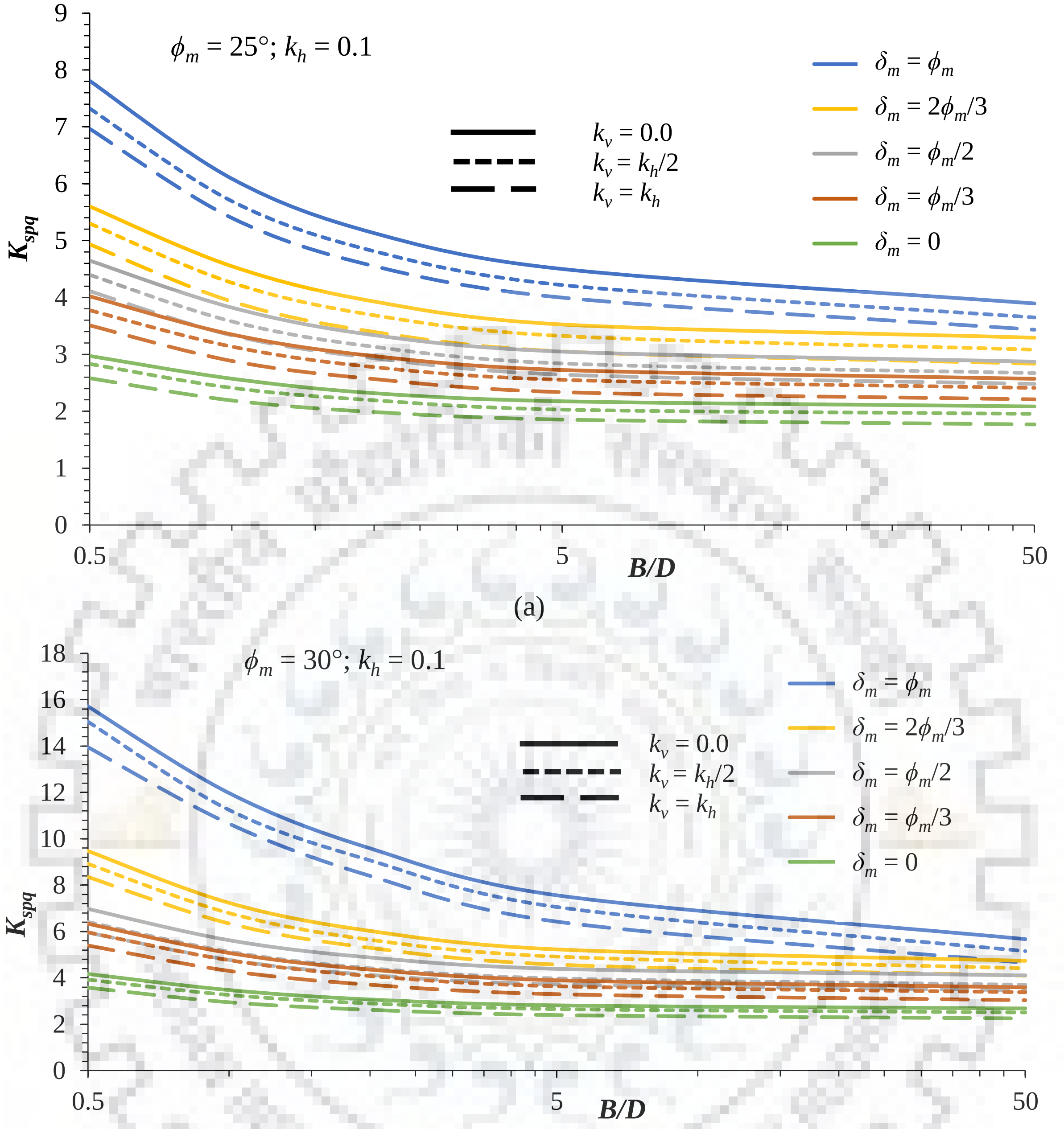

(a)

(b)

Fig. 6.14 Design chart for K_{spq} for k_h=0.1 for different soil-wall friction angles for (a) ϕ_m=25° and (b) ϕ_m=30°

6.5 Summary

The current study deals with the problem of determining passive resistance offered to a rectangular structure embedded in c-ϕ soil and acted upon by surcharge. The 3-dimensional failure wedge was idealized in a realistic manner based on the results of numerical analysis and past experimental studies. The geometry of the critical failure wedge was determined and the seismic earth pressure coefficients due to cohesion, surcharge and unit weight components were computed using limit equilibrium method for that critical geometry. This gives the true magnitudes of earth pressure coefficients at failure instead of the conservative absolute minimum values. Based on the results of the extensive study, a series of design charts have been prepared which return earth pressure coefficients for various combinations of caisson geometry, soil properties, seismic conditions and caisson-soil interface properties.

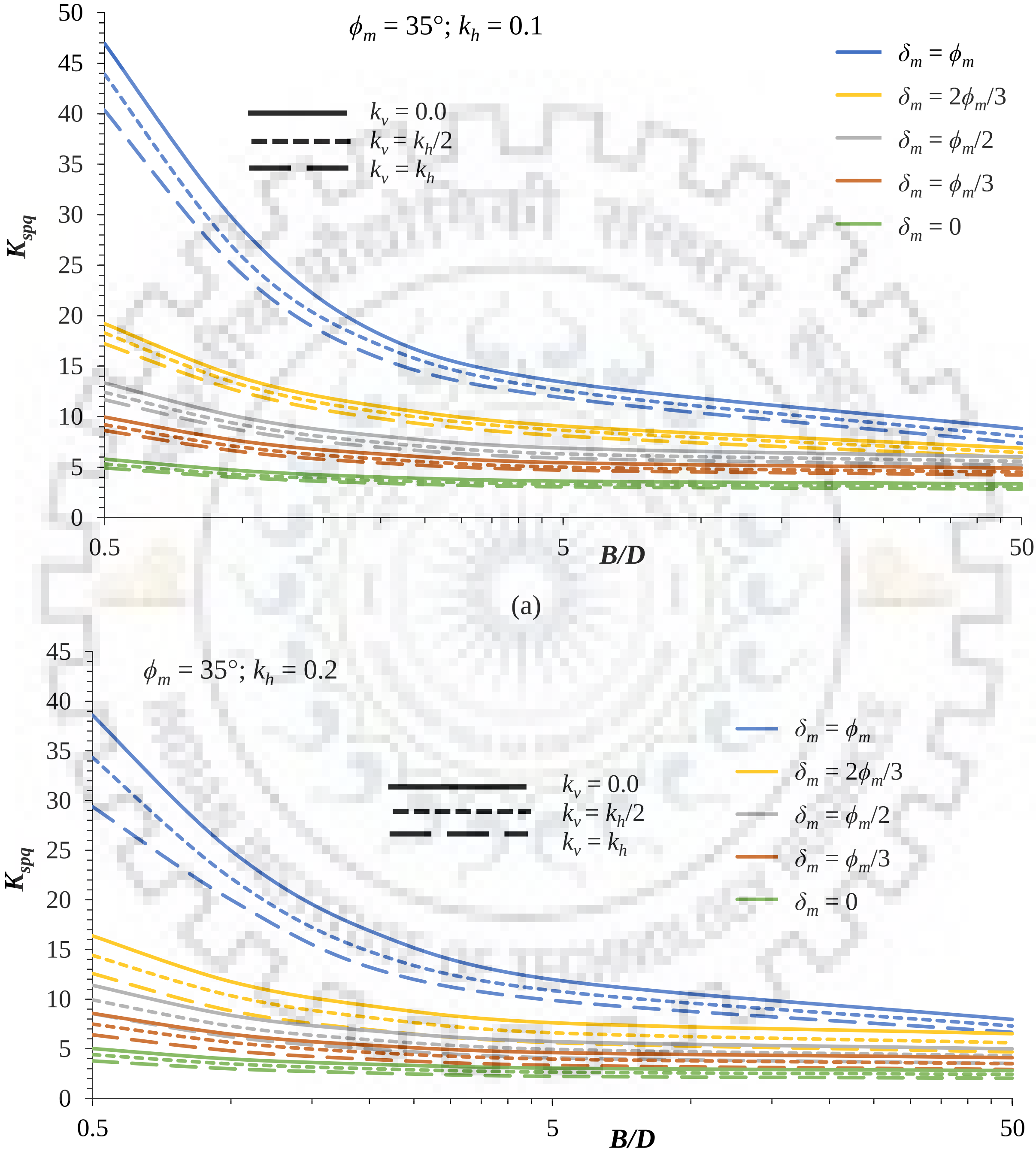

(a)

(b)

Fig. 6.15 Design chart for K_{spq} in case of (a) k_h=0.1 and (b) k_h=0.2 for different soil-wall friction angles for ϕ_m=35°

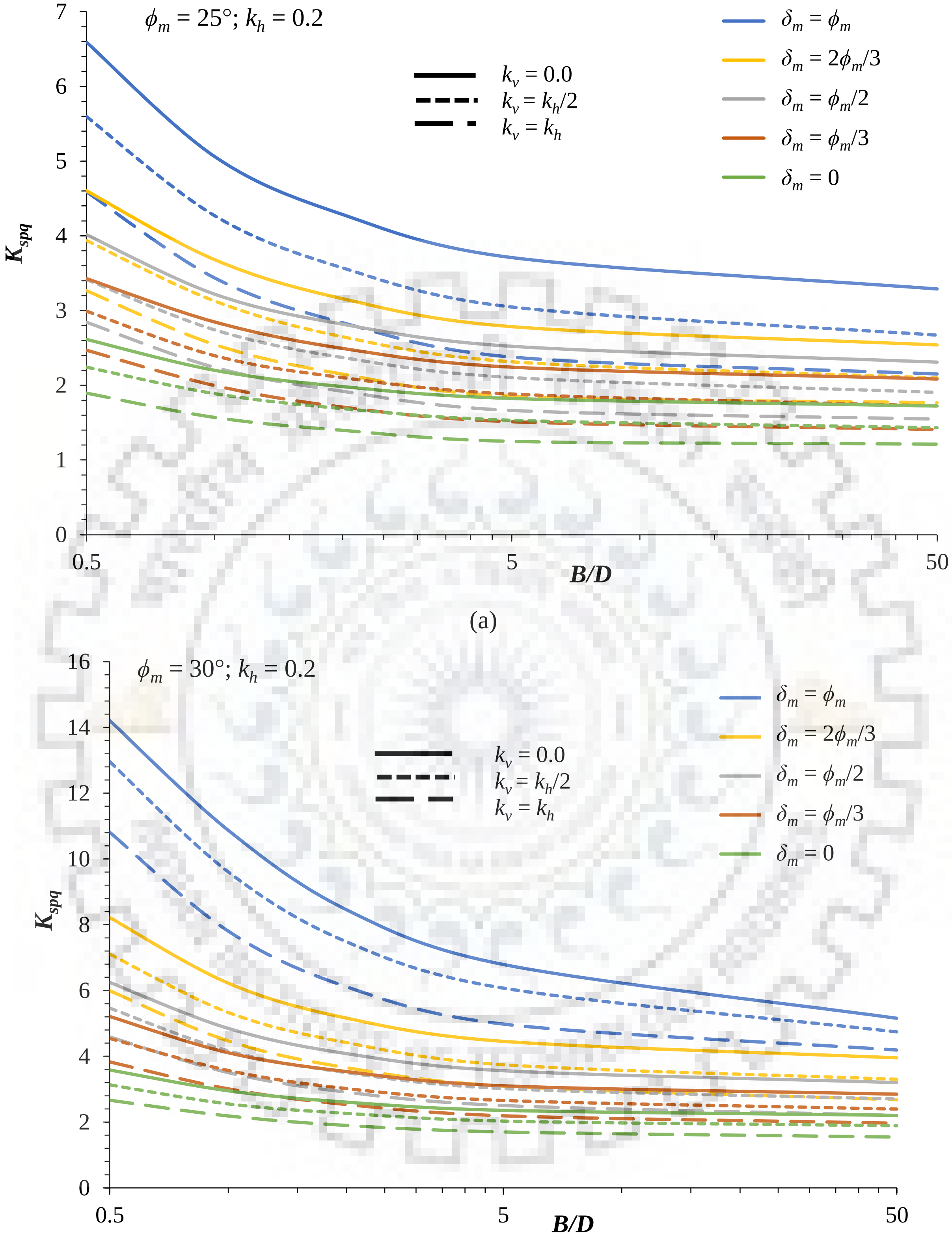

(a)

(b)

Fig. 6.16 Design chart for K_{spq} in case of k_h=0.2 for (a) ϕ_m=25°and (b) ϕ_m=30° for different soil-wall friction angles

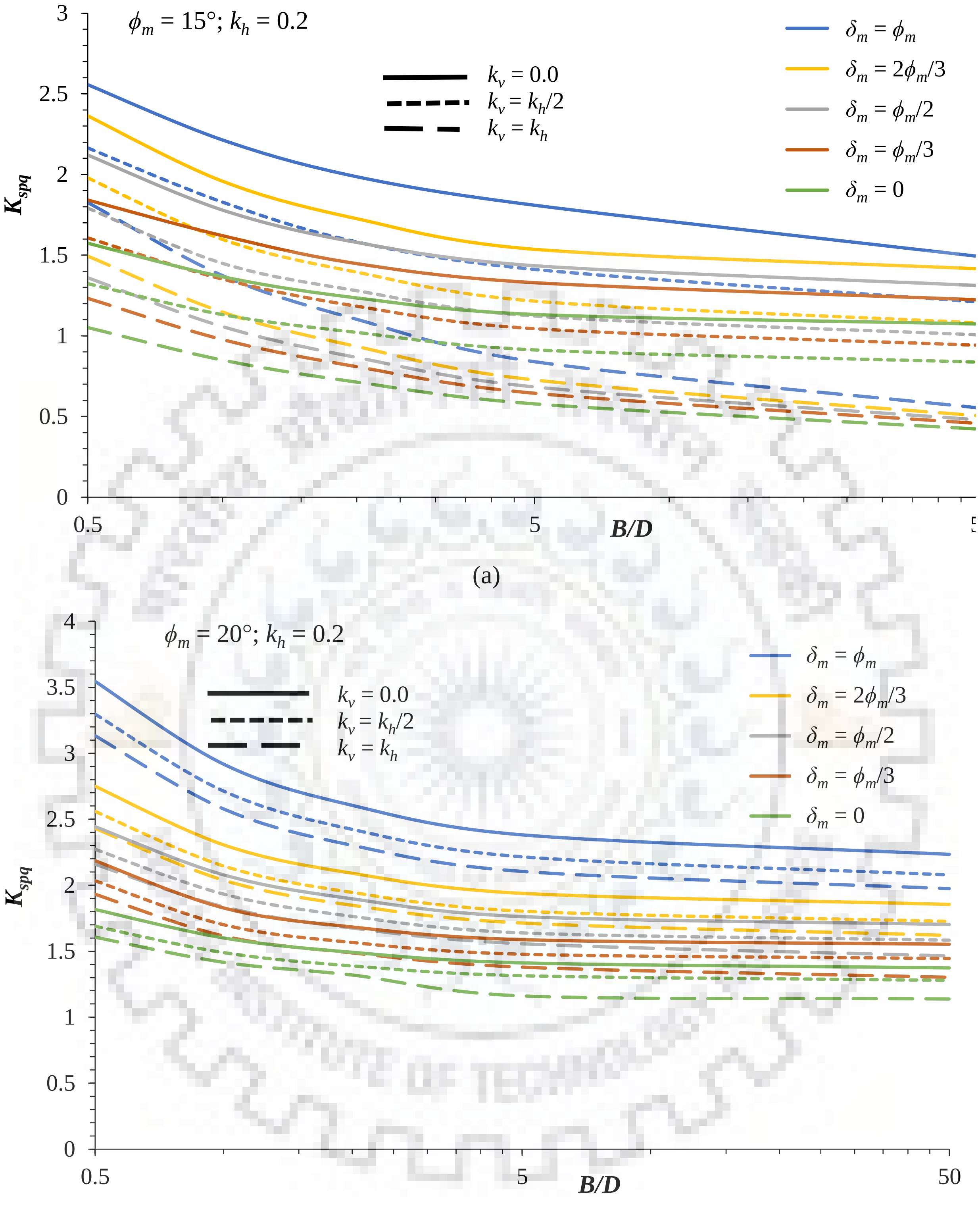

Fig. 6.17 Design chart for K_{spq} in case of k_h=0.2 for (a) ϕ_m=15°and (b) ϕ_m=20° for different soil-wall friction angles

Chapter 7

SEISMIC PASSIVE EARTH PRESSURE RESISTANCE ON CAISSON USING MODIFIED PSEUDO-DYNAMIC METHOD

7.1 General

Pseudo-static method of analysis assumes uniform horizontal and vertical seismic acceleration acting throughout the depth of a soil strata. To overcome this shortcoming, Steedman and Zeng (1990) introduced pseudo-dynamic method of analysis which allowed for amplification of earthquake waves propagating through the strata. This method was further improved by Choudhury and Nimbalkar (2005) by incorporating vertically propagating primary and shear waves. The pseudo-dynamic method still had some flaws, such as presence of shear stresses at free surface, assumption of linear variation of amplification in submerged soil and unsuitable definition of excess pore pressure ratio. The method was further updated by Bellezza (2014) where contravention of free surface was addressed. The modified pseudo-dynamic method of analysis returns the magnitude of horizontal and vertical seismic acceleration without any assumption of amplification factor. However, the studies pertaining to layered soil using modified pseudo-dynamic method is still found to be lacking. In the present study, seismic passive earth pressure coefficient has been determined for caisson embedded in layered strata with failure wedge lying in a single soil layer. The acceleration at any depth of soil layer is determined using modified pseudo dynamic method.

7.2 Proposed Methodology

The present study employs modified pseudo-dynamic approach in conjugation with limit equilibrium method of analysis. Following assumptions are made in the proposed study:

1. A rectangular caisson of length *L*, width *B* and embedment depth *d* is assumed to be embedded in layered soil such that the failure wedge of depth *D* lies entirely in cohesionless, homogeneous soil as shown in Fig. 7.1.
2. Soil is considered to be a visco-elastic material and modelled as Kelvin-Voigt solid.
3. The soil strata below the failure wedge may comprise of any number of layers.
4. Linear modified pseudo-dynamic method of analysis has been adopted to estimate propagation of earthquake waves through the soil strata (strain independent analysis).
5. Limit equilibrium method has been adopted to establish equilibrium of forces in the horizontal and vertical direction in the failure wedge.

6. The idealized failure wedge geometry has been chosen the same as in Chapter 5 and 6 and as depicted in Fig. 5.1.
7. The submerged soil conditions have been modelled based on the assumptions of Ebeling and Morrison (1992) and the hydrostatic and hydrodynamic pressure distribution has been modelled after the recommendations of Westergaard (1933).
8. The earthquake waves are assumed to be standing waves propagating vertically upwards with primary wave velocity and shear wave velocity of magnitudes v_p and v_s respectively.

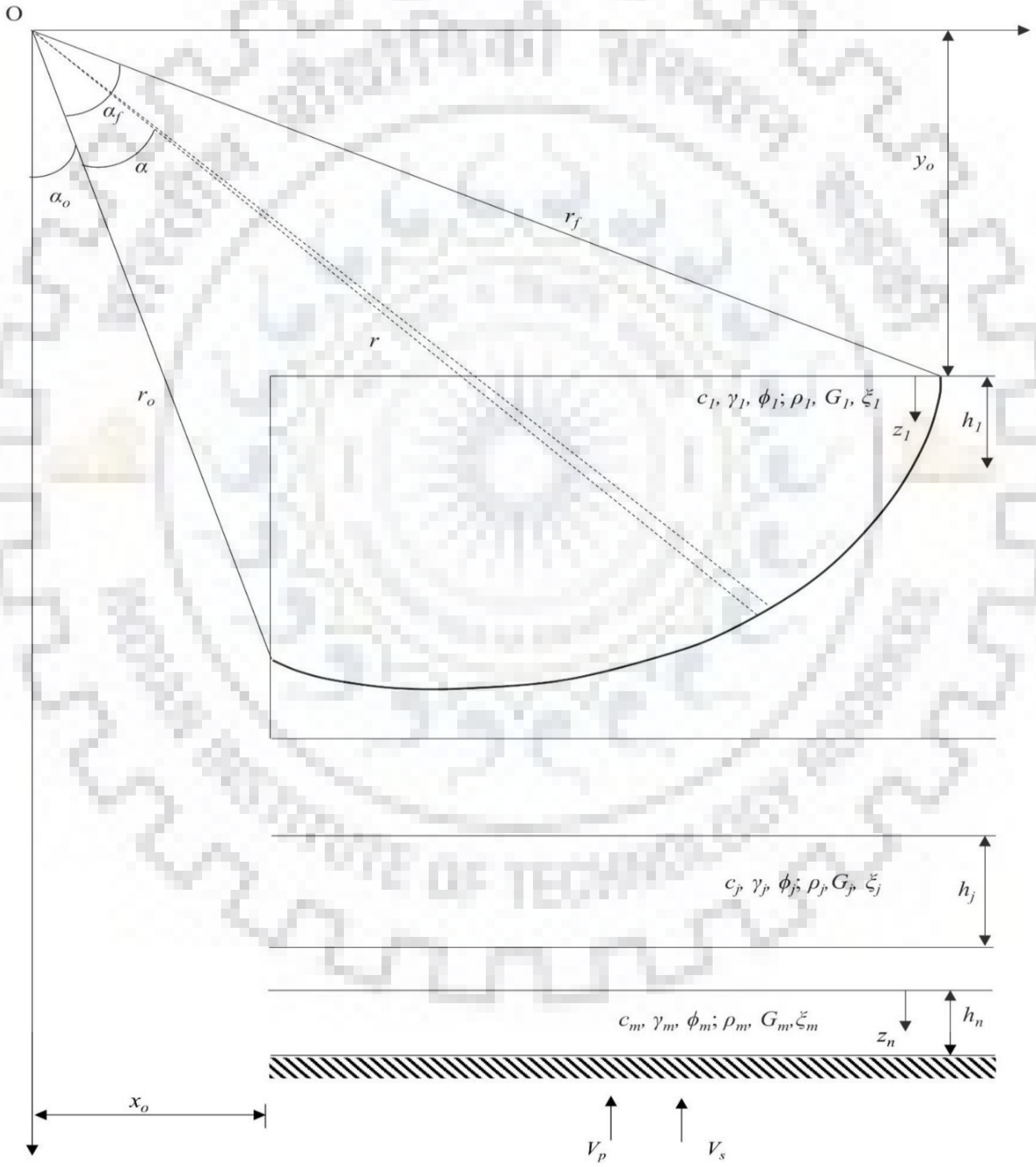

Fig. 7.1 Vertical profile of failure wedge in layered soil

7.2.1 Modified pseudo dynamic method

The shear stress developed in a Kelvin-Voigt solid is considered to be comprised of an elastic component and a viscous component. Mathematically, the shear stress in the said material is defined as:

$$\tau = G\frac{\partial u}{\partial z} + \eta_s \frac{\partial^2 u}{\partial z \partial t} \tag{7.1}$$

The general equations for wave propagation for a Kelvin-Voigt solid are given as:

$$\rho \frac{\partial^2 u_h(z,t)}{\partial t^2} = G\frac{\partial^2 u_h(z,t)}{\partial z^2} + \eta_s \frac{\partial^3 u_h(z,t)}{\partial z^2 \partial t} \tag{7.2a}$$

$$\rho \frac{\partial^2 u_v(z,t)}{\partial t^2} = (\lambda + 2G)\frac{\partial^2 u_v(z,t)}{\partial z^2} + (\eta_l + 2\eta_s) \frac{\partial^3 u_v(z,t)}{\partial z^2 \partial t} \tag{7.2b}$$

where, τ is the shear stress developed in soil at any depth z at any time t, ρ is the mass density of the soil, λ and G are the Lame's constants for soil, η_s and η_l are soil viscosities and u_h and u_v are displacements of shear and primary waves respectively [Kramer (1996)].

Harmonic horizontal ($u_{bh} = u_{ho} \times e^{i\omega t}$) and vertical ($u_{bv} = u_{vo} \times e^{i\omega t}$) base shaking is considered at bedrock level. For harmonic motion of amplitude u_h at any depth z, displacement at any depth z at time t is given as:

$$u_h(z,t) = u_h(z) \times e^{i\omega t} \tag{7.3}$$

Substituting Eqn. (7.3) into Eqn. (7.2a) and differentiating with respect to time,

$$(G + i\omega\eta_s)\frac{\partial^2 u_h}{\partial z^2} = -\rho\omega^2 u_h \tag{7.4}$$

$$\eta_s = \frac{2G}{\omega}\xi_s \tag{7.5}$$

where ξ_s is the damping ratio of soil and ω is the angular frequency of motion

From Eqn. (7.4) and (7.5),

$$(G + i2G\xi_s)\frac{\partial^2 u_h}{\partial z^2} = -\rho\omega^2 u_h \tag{7.6a}$$

$$G^* = G(1+2i\xi_s); \qquad v_s^* = G^*/\rho \qquad \text{and} \qquad k_s^* = \omega/v_s^* \tag{7.6b}$$

$$\frac{\partial^2 u_h}{\partial z^2} = -k_s^{*2} u_h \tag{7.6c}$$

The general solution of the differential equation (7.6) is of the form:

$$u_h(z,t) \;=\; Ae^{i(\omega t + k_s^* z)} + Be^{i(\omega t - k_s^* z)} \tag{7.7}$$

where A and B are the amplitudes of the waves travelling in $-z$ and $+z$ directions respectively. Therefore, for layered soil as shown in Fig. 7.1:

Wave displacement in j^{th} layer,

$$u_{hj}(z,t) \;=\; A_j e^{i(\omega t + k_{js}^* z_j)} + B_j e^{i(\omega t - k_{js}^* z_j)} \tag{7.8a}$$

where, ω is the angular frequency of the vertically propagating standing waves

$k_{js}^* = \omega/v_{sj}^*$; $v_{sj}^* = G_j^*/\rho_j$ and $G_j^* = G_j(1+2i\xi_{sj})$ are complex wave number, complex shear wave velocity and complex shear modulus respectively. A_j and B_j for each layer are determined using following boundary conditions:

1. Shear stress at ground surface is zero.

   $\Longrightarrow \tau = 0$ at $z = 0$ (7.9a)

2. Displacement at bottom of j^{th} layer and top of $(j+1)^{\text{th}}$ layer are equal.

   $\Longrightarrow u_j(h_j,t) = u_{j+1}(0,t)$ (7.9b)

3. Shear stress at bottom of j^{th} layer = Shear stress at top of $(j+1)^{\text{th}}$ layer.

   $\Longrightarrow \tau_j(h_j,t) = \tau_{j+1}(0,t)$ (7.9c)

4. Displacement at base of bottom layer = Input harmonic displacement.

   $\Longrightarrow u_n(h_n,t) = u_{bh}$ (7.9d)

From 1st boundary condition,

Substituting Eqn. (7.8a) in Eqn. (7.1) and equating to zero for $j = 1$,

$$A_1 = B_1 = A \tag{7.10}$$

From 2nd boundary condition,

$$A_j e^{i(\omega t + k_{js}^* h_j)} + B_j e^{i(\omega t - k_{js}^* h_j)} = \left(A_{j+1} + B_{j+1}\right) e^{i\omega t} \tag{7.11}$$

From 3rd boundary condition,

$$iG_j k_j^* \left[A_j e^{i(\omega t + k_{js}^* h_j)} - B_j e^{i(\omega t - k_{js}^* h_j)}\right] = iG_{j+1} k_{j+1}^* \left[A_{j+1} - B_{j+1}\right] e^{i\omega t} \tag{7.12a}$$

$$A_{j+1} - B_{j+1} = \alpha_j^* \left[A_j e^{i(\omega t + k_{js}^* h_j)} - B_j e^{i(\omega t - k_{js}^* h_j)}\right] \tag{7.12b}$$

where, $\alpha_j^* = \frac{G_j k_j^*}{G_{j+1} k_{j+1}^*} = \frac{\rho_j v_{sj}^*}{\rho_{j+1} v_{s,j+1}^*}$ is known as the complex impedance ratio

Solving Eqns. (7.11) and (7.12b),

$$A_{j+1} = \frac{1}{2}\left[A_j\left(1 + \alpha_j^*\right) e^{ik_{js}^* h_j} + B_j\left(1 - \alpha_j^*\right) e^{-ik_{js}^* h_j}\right] \tag{7.13a}$$

$$B_{j+1} = \frac{1}{2}\left[A_j\left(1 - \alpha_j^*\right) e^{ik_{js}^* h_j} + B_j\left(1 + \alpha_j^*\right) e^{-ik_{js}^* h_j}\right] \tag{7.13b}$$

Let $a_j = \frac{A_j}{A}$ and $b_j = \frac{B_j}{A}$

From 4th boundary condition,

$$A_n e^{i(\omega t + k_{ns}^* h_n)} + B_n e^{i(\omega t - k_{ns}^* h_n)} = u_{ho} e^{i\omega t} \tag{7.14a}$$

$$A\left[a_n e^{ik_{ns}^* h_n} + b_n e^{-ik_{ns}^* h_n}\right] = u_{ho} \tag{7.14b}$$

$$A = \frac{u_{ho}}{\left[a_n e^{ik_{ns}^* h_n} + b_n e^{-ik_{ns}^* h_n}\right]} \tag{7.14c}$$

$$u_{hj}(z,t) = \frac{u_{ho}}{\left[a_n e^{ik_{ns}^* h_n} + b_n e^{-ik_{ns}^* h_n}\right]} \times \left(a_j e^{ik_{js}^* z_j} + b_j e^{-ik_{js}^* z_j}\right) e^{i\omega t} \tag{7.15a}$$

Again, differentiating twice with respect to time,

$$a_{hj}(z,t) = \frac{a_{ho}}{\left[a_n e^{ik_{ns}^* h_n} + b_n e^{-ik_{ns}^* h_n}\right]} \times \left(a_j e^{ik_{js}^* z_j} + b_j e^{-ik_{js}^* z_j}\right) e^{i\omega t} \tag{7.15b}$$

$$a_{vj}(z,t) = \frac{a_{vo}}{\left[a_n e^{ik_{np}^* h_n} + b_n e^{-ik_{np}^* h_n}\right]} \times \left(a_j e^{ik_{jp}^* z_j} + b_j e^{-ik_{jp}^* z_j}\right) e^{i\omega t} \tag{7.15c}$$

where, $a_{ho} = k_h g = -\omega^2 u_{ho}$ and $a_{vo} = k_v g = -\omega^2 u_{vo}$

Transfer function relates displacement amplitude of one layer with other. It is a measure of amplification of displacement of waves between any two layers. The transfer function thus relating displacement at top of j^{th} layer to top of p^{th} layer is obtained by substituting $z_j = z_p = 0$ in Eqn. (7.15a).

$$\Rightarrow F_{j,p} = \left|\frac{u_{hj}}{u_{hp}}\right| = \frac{a_j + b_j}{a_p + b_p} \tag{7.16}$$

Since $a_{hj} = \omega^2 u_{hj}$, the ratio of acceleration at top of two layers is equal to the ratio of displacements. Therefore, the magnitude of transfer functions is equal to the ratio of acceleration at top of j^{th} layer and p^{th} layer.

7.2.2 Formulation of the problem

The geometry of idealized failure wedge in the present study is the same as considered in Chapter 5 and 6. The horizontal and vertical seismic inertial forces are different from that in previous chapters. In the present study, the real parts of a_{hj} and a_{vj} obtained from Eqns. (7.15 b,c) in the top layer, i.e., a_{hz} and a_{vz} are used for calculation of seismic inertial forces in the failure wedge as mentioned in Eqns. (7.17a,b). Horizontal and vertical seismic inertial forces (ΔQ_h and ΔQ_v) on an infinitesimally thin failure wedge at any depth z as shown in Fig. 7.2 are defined as:

$$\Delta Q_h(z,t) = M(z) \times a_{hz}(z,t) \tag{7.17a}$$

$$\Delta Q_v(z,t) = M(z) \times a_{vz}(z,t) \tag{7.17b}$$

where, $M(z)$ is the mass of the infinitesimally thin failure wedge at depth z.

Substituting seismic inertial forces $k_h \Delta W$ by ΔQ_h and $k_v \Delta W$ by ΔQ_v in Eqn. 5.40,

$$p(z,t)B\mathrm{d}z = \frac{\left[\left\{\left(\Delta W(z) - \Delta Q_v(z,t) + Q(z) - N(z+dz)\right) \times HD(z)\right\} - \left(\left(\Delta Q_h(z,t) - \Delta F(z)\right) \times VD(z)\right)\right]}{\left(\cos\delta_m \times VD(z)\right) - \left(\sin\delta_m \times HD(z)\right)} \tag{7.18}$$

For $B < m\tan x$:

$HD(z) = \left\{\sin x - \sin\left(x - \beta(z)\right)\right\} \tan(\alpha + \alpha_o - \phi_m)$ and $VD(z) = \pi - 2x + \beta(z)$

For $B > m\tan x$:

$HD(z) = B\tan(\alpha + \alpha_o - \phi_m)$ and $VD(z) = B + \frac{l(z)}{\cos x}(\pi - x - \sin x)$

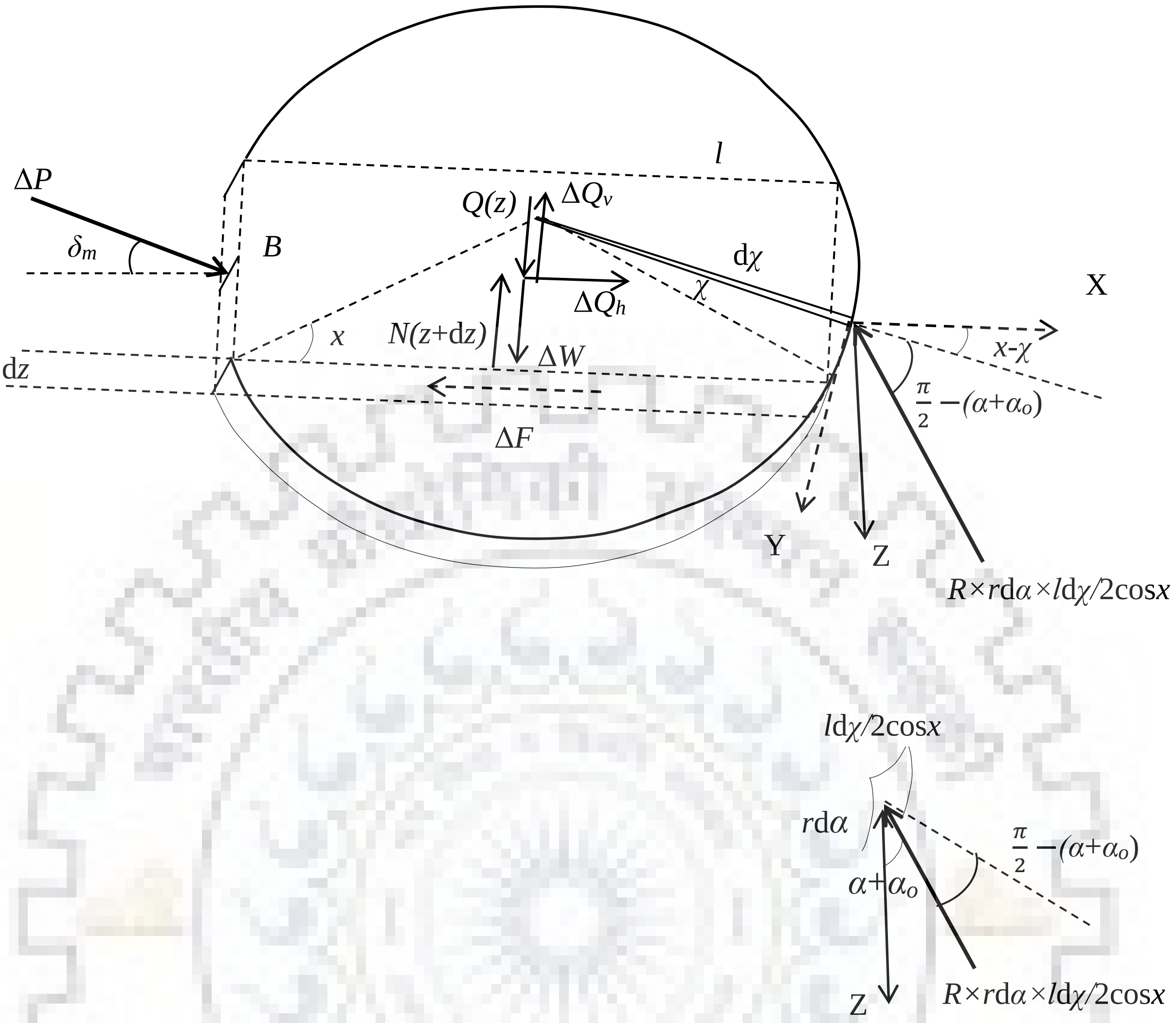

Fig. 7.2 Free body diagram of forces acting on infinitesimal strip of failure wedge

Upon integration of Eqn. (7.18) with respect to *z*, the magnitude of total caisson reaction due to unit weight component ($P_{p\gamma}$) can be determined. Since *z* is a function of initial angle of log-spiral (α_o) and angle subtended by log-spiral (α_f) and ΔQ_h and ΔQ_v are functions of time *t*, $P_{p\gamma}$ is a function of α_o, α_f and *t*. Therefore, in order to obtain the average magnitude of seismic passive earth pressure coefficient ($K_{sp\gamma}$) over entire depth of failure wedge, $P_{p\gamma}$ is minimized with respect to α_o, α_f and *t*. $K_{sp\gamma}$ is then defined as:

$$\frac{1}{2}K_{sp\gamma}\gamma D^2 \times B = P_{p\gamma} \tag{7.19a}$$

$$K_{sp\gamma} = \frac{2P_{p\gamma}}{\gamma B D^2} \tag{7.19b}$$

7.2.3 Modification in formulation for submerged soil

For submerged soil conditions, modifications are made to unit weight of soil for computation of different forces. Based on the permeability of soil, the pore water is classified as either free water (high permeability and water is free to move relative to soil skeleton) or restrained water (low permeability with no relative movement between soil and water). The unit weight of soil mass used to determine self weight of wedge (ΔW), horizontal component of tangential force (ΔF), overburden pressure force (Q) and normal reaction (N) are also modified based on the mobility of water with respect to soil skeleton.

- For computing weight of wedge and overburden pressure, unit weight of soil (γ) is taken as $\gamma_{sub}\times(1-r_u)$ for both free and restrained conditions where r_u is excess pore pressure ratio and γ_{sub} is submerged unit weight [Ebeling and Morrison (1992); Kramer (1996)].
- For computing $\Delta Q_h(z,t)$, unit weight of soil (γ) is taken as γ_{sat} for restrained water condition and γ for free water condition where γ_{sat} and γ are saturated unit weight and dry unit weight respectively [Matsuzawa et al. (1985)].
- For computing $\Delta Q_v(z,t)$, unit weight of soil (γ) is taken as γ_{sub} for both free and restrained water conditions [Rajesh and Choudhury (2017)].

For computation of total lateral pressure in restrained water conditions, summation of hydrostatic pressure with seismic earth pressure is done as water is at rest with respect to surrounding soil. However, for free water condition, hydrodynamic pressure suggested by Westergaard (1933) is also taken into consideration along with hydrostatic pressure and passive earth pressure to obtain total lateral pressure. Matsuzawa et al. (1985) expanded upon Westergaard's (1933) study and gave expression for hydrodynamic pressure distribution along depth of wall as:

$$p_{hdyn} = \frac{7}{8} k_h \gamma_w (Hz)^{0.5} \tag{7.20a}$$

Integrating over entire depth, the hydrodynamic pressure force is obtained as:

$$P_{hdyn} = \frac{7}{12} k_h \gamma_w H^2 \tag{7.20b}$$

Hydrostatic pressure distribution along depth of caisson is computed as:

$$p_{hst} = (\gamma_w + \gamma_{sub} r_u) z \tag{7.21}$$

7.2.4 Validation of the proposed methodology

The seismic passive earth pressure coefficients obtained from present study have been compared with the results of previous studies in Table 7.1. Mononobe-Okabe method

[Mononobe and Matsuo (1929)] is the pseudo-static extension of Coulomb's method [Coulomb (1776)]. Biswas and Choudhury (2019) assumed the 3D planar failure surface and used pseudo-static approach in conjugation with the limit equilibrium method for determination of passive earth pressure coefficients. Lancellotta (2007) used lower bound 2D limit analysis to determine earth pressure coefficients. Pain et al. (2017) adopted modified pseudo-dynamic method for 2D analysis of wall. Biswas and Choudhury (2021) also used modified pseudo-dynamic method for the 3D analysis of caissons but considered simplified planar failure wedge. For comparison of results, width of caisson $B>>D$ has been chosen to simulate plane strain conditions present during 2D analyses. ϕ_m=30°, k_v=0.5 k_h, $\omega H/v_s$=0.94, v_p=1.87v_s and ξ=0.1 has been adopted as the input parameters in the comparison.

Table 7.1 Comparison of $K_{sp\gamma}$ obtained in present study with past literature for plane strain conditions, ϕ_m=30° and k_v=0

		Seismic passive earth pressure coefficient ($K_{sp\gamma}$)					
k_h	δ_m / ϕ_m	Mononobe – Okabe (1929)	Lancellotta (2007)	Pain et al. (2017)	Biswas and Choudhury (2019)	Biswas and Choudhury (2021)	Present Study
0	0	3	3	-	3	3	3
	1/3	4.143	3.886	-	4.143	4.143	3.994
	1/2	4.976	4.288	-	4.977	4.977	4.497
0.1	0	2.671	2.791	2.558	2.666	2.554	2.201
	1/3	3.622	3.615	3.384	3.616	3.426	3.028
	1/2	4.312	3.988	3.88	4.307	4.057	3.599
0.2	0	2.326	2.498	2.066	2.315	2.058	1.754
	1/3	3.081	3.237	2.648	3.064	2.647	2.311
	1/2	3.627	3.571	3.035	3.608	3.071	2.733

- : denotes that values are not reported by the authors

It is evident from the results in Table 7.1 that the present study returns much conservative results compared to previous studies. The assumption of realistic shape of failure wedge and use of modified pseudo-dynamic method, which returns higher magnitude of seismic inertial forces, is the reason for low magnitudes of the seismic earth pressure coefficient in the present study. Comparison of total earth pressure with centrifuge test results of Olson et al. (2017) and modified pseudo-dynamic study of Biswas and Choudhury (2021) has been illustrated in Fig. 7.3 along with the parameters. The passive earth pressure from the present method is found to be on the conservative side compared to the other studies.

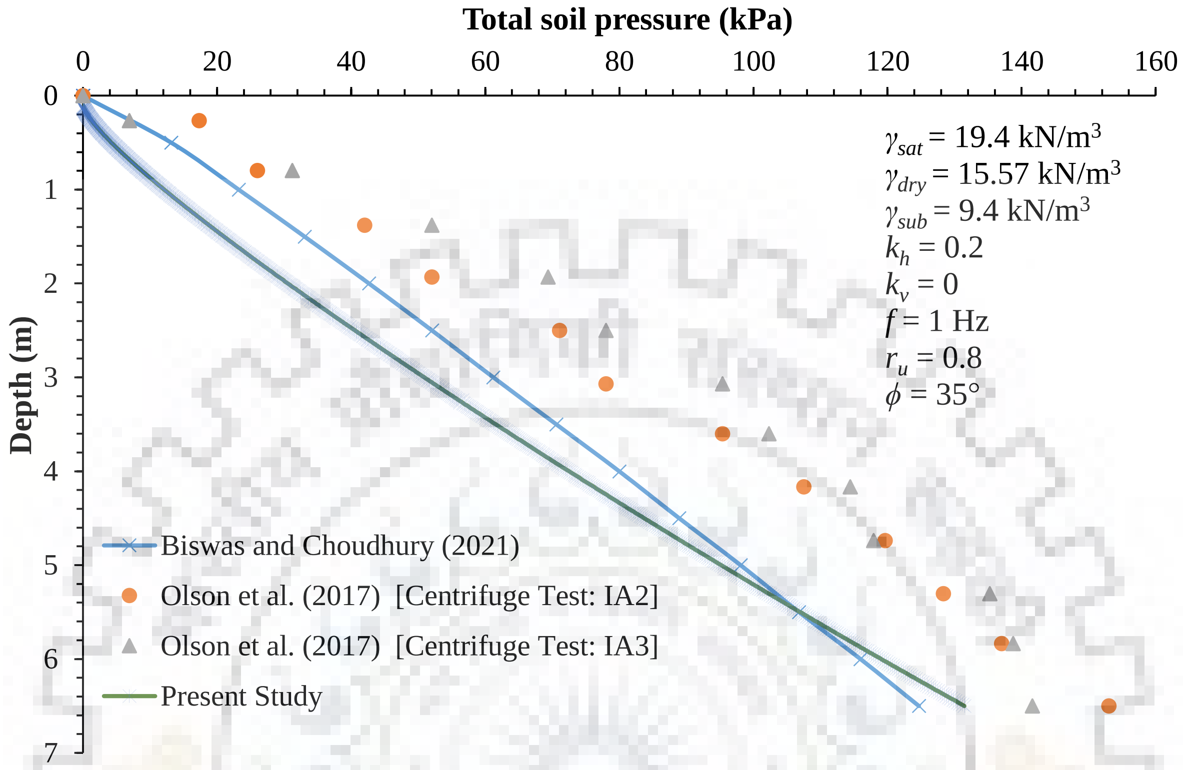

Fig. 7.3 Comparison of results of present study with results of experimental [Olson et al. (2017)] and theoretical analysis [Biswas and Choudhury (2021)]

7.3 Present Study

In the present study, a database comprising seismic passive earth pressure coefficient due to unit weight component ($K_{sp\gamma}$) has been developed for different input parameters as tabulated in Table 7.2. The computations have been carried out by writing programs in MATLAB (2021). Failure wedge depth (D) has been considered as $d/2.2$ as per recommendations of Olson et al. (2017), where d is the total depth of caisson. The magnitude of tangential stress coefficient (λ) has been adopted as the Rankine passive earth pressure coefficient for a given mobilized soil friction angle (ϕ_m) [Biswas and Choudhury (2019, 2021)]. The seismic passive earth pressure coefficients are obtained by optimizing the magnitudes of $P_{p\gamma}$ with respect to α_o, α_f and t, which are varied between 0 to $\pi/2-\phi_m$, 0 to $\pi/2-(\phi_m+\alpha_o)$ and 0 to $2\pi/\omega$ respectively. The correlation between primary wave velocity (v_p), shear wave velocity (v_s) and Poisson's ratio (ν) in an elastic medium is as stated below:

$$\frac{v_p}{v_s}=\sqrt{\frac{2-2\nu}{1-2\nu}} \tag{7.22}$$

For dry sand, v has been chosen as 0.3 whereas for submerged soil conditions, v has been adopted as 0.495. This gives $v_p = 1.87\ v_s$ for dry conditions and $v_p = 10\ v_s$ for submerged soil conditions. Design charts have been prepared for the input parameters mentioned in Table 7.2 to show the parametric variation of $K_{sp\gamma}$. In addition, the nature of transfer function has also been reported for layered soil.

Table 7.2 Input parameters considered in the present study for top layer of soil

Properties	**Values**
Dry unit weight (γ)	15.7 kN/m^3
Saturated unit weight (γ_{sat})	19.13 kN/m^3
Mobilized soil friction angle (ϕ_m)	15°, 20°, 25°, 30°, 35°
Mobilized soil-wall friction angle (δ_m)	0, $\phi_m/3$, $\phi_m/2$, $2\phi_m/3$, ϕ_m
Excess pore pressure ratio (r_u)	0, 0.2, 0.4
Damping ratio (ξ)	0.1, 0.15, 0.2
Normalized shear wave velocity ($\omega H/v_s$)	0.94
Horizontal seismic acceleration coefficient (k_h)	0, 0.1, 0.2
Vertical seismic acceleration coefficient (k_v)	0, $k_h/2$, k_h

7.4 Results and Discussions

The present study reflects the effects of soil-soil friction angle, soil-wall friction angle, seismic acceleration coefficients, damping ratio, effect of mobility of pore water, excess pore pressure ratio on seismic passive earth pressure coefficient. The variation of volume of failure wedge per unit width of caisson with caisson geometry has also been explored. Following observations have been made from the results of present study.

7.4.1 Acceleration profile and transfer function

Fig. 7.4 shows the amplification of earthquake waves at different magnitudes of normalized frequency ($\omega H/v_s$) for homogeneous soil resting on elastic rock. It can be observed that the peak amplification occurs corresponding to $\omega H/v_s$ value close to $\pi/2$. The frequency corresponding to this peak is the fundamental frequency [Kramer (1996)] as it corresponds to resonance in the surrounding soil media causing passive resistance to be minimum. The peak of the acceleration amplification curve is observed to diminish by 33.23% and 49.79% as damping ratio (ξ) increases from 0.1 to 0.15 and 0.2 respectively, since higher value of ξ causes more energy dissipation for seismic waves travelling through the soil strata. However, the amplification of acceleration is found to be insensitive to damping ratio (ξ) for $\omega H/v_s < 3\pi/10$. It is also known that the amplification is in phase for $\omega H/v_s < \pi/2$ and out of phase for $\omega H/v_s > \pi/2$ [Kramer (1996); Pain et al. (2017); Biswas and Choudhury (2021)].

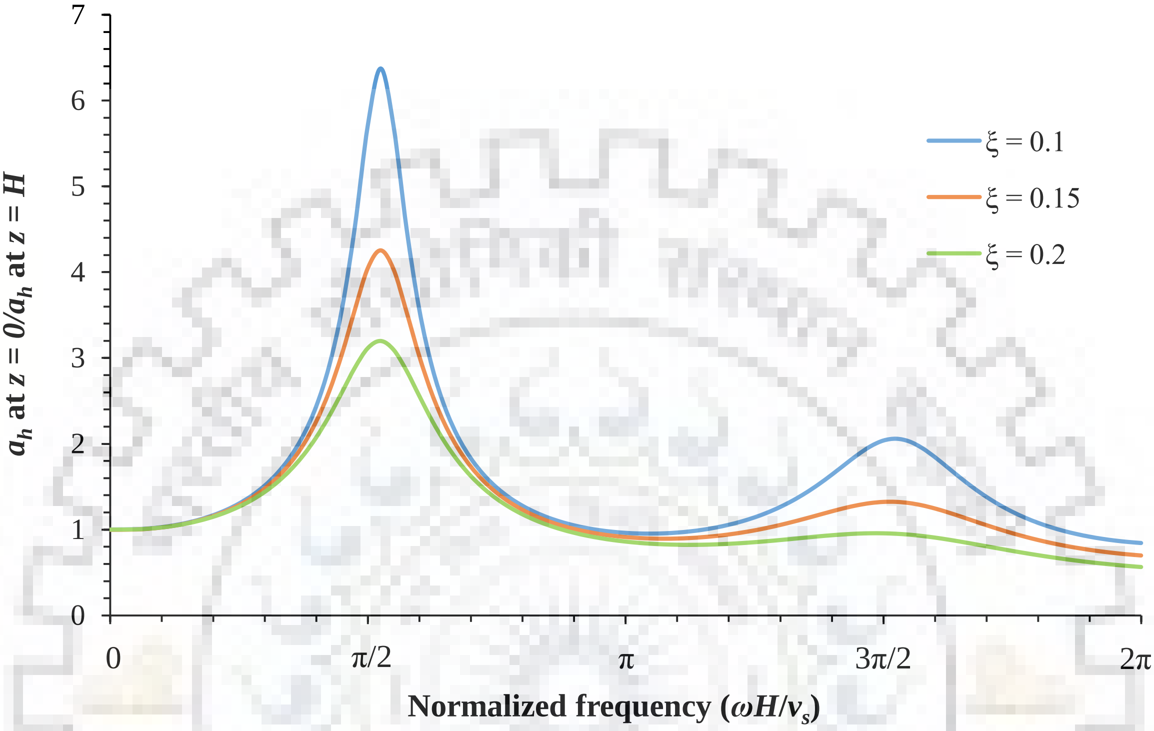

Fig. 7.4 Variation of ratio of a_h at ground level to bed rock level with normalized frequency

Therefore, the present study has been conducted for $\omega H/v_s = 3\pi/10 = 0.94$. The average magnitude of damping ratio (ξ) of various layers (varying between 0.1 and 0.2) is 0.14. Fig. 7.5(a) shows the amplification of earthquake waves at top with respect to bedrock level for 5-layered strata. It can be observed that 10 peaks (2 peaks corresponding to resonance in each layer) are formed through the entire strata corresponding to natural frequency of each layer. Fig. 7.5(b) represents the acceleration profile through the layered soil while Fig. 7.5(c) shows the variation of transfer function of acceleration at top of 1st layer with respect to 2nd, 3rd and 4th layer. The seismic wave velocity reduces as it moves through softer soil which causes its acceleration amplitude to increase to maintain its specific energy. The applied base acceleration of 0.2g is found to amplify to 0.28g at ground surface, over the depth of the strata with visible changes in slope at interface of each layer. The non-linear nature of acceleration profile can be observed which highlights the importance of modified pseudo-dynamic method compared to pseudo-dynamic method which considered an amplification factor. It can also be observed that transfer function curve for 1st layer with respect to 2nd layer (TF12) has 2 peaks as it deals with interaction in a single layer. Similarly, TF13, TF14 and TF15 have 4, 6 and 8 peaks respectively.

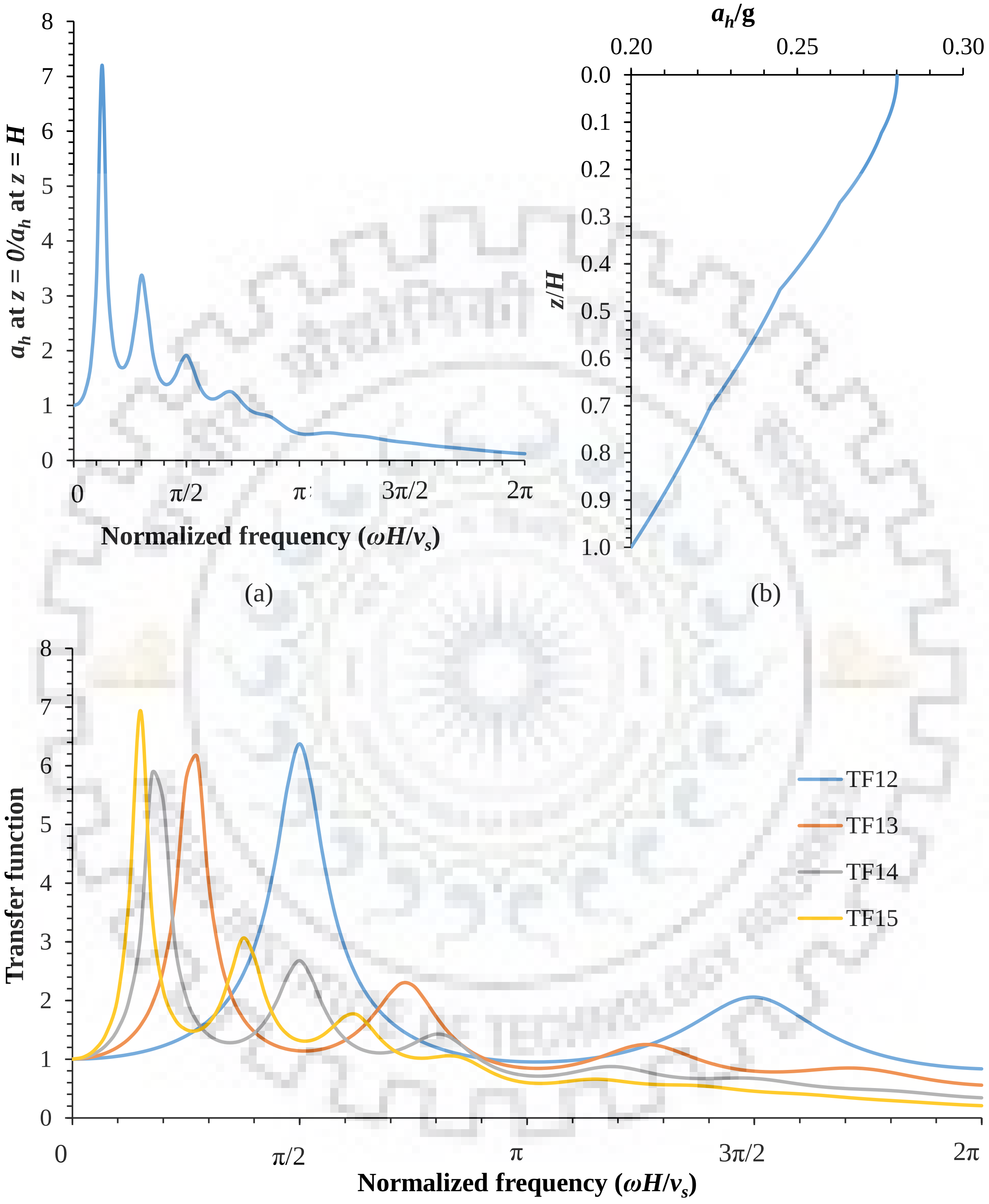

(a)

(b)

(c)

Fig. 7.5 Behavior of earthquake waves in 5-layered soil in terms of (a) acceleration amplification (b) acceleration profile with depth for k_h=0.2 and (c) transfer function

7.4.2 Effect of mobilized soil-wall interface friction angle (δ_m)

Fig. 7.6 through Fig. 7.11 depict the design charts for $K_{sp\gamma}$ for different combinations of horizontal and vertical seismic acceleration coefficients and mobilized soil friction angle for ξ=0.1. Irrespective of the magnitude of k_h, k_v and ϕ_m values, $K_{sp\gamma}$ is found to increase with δ_m.

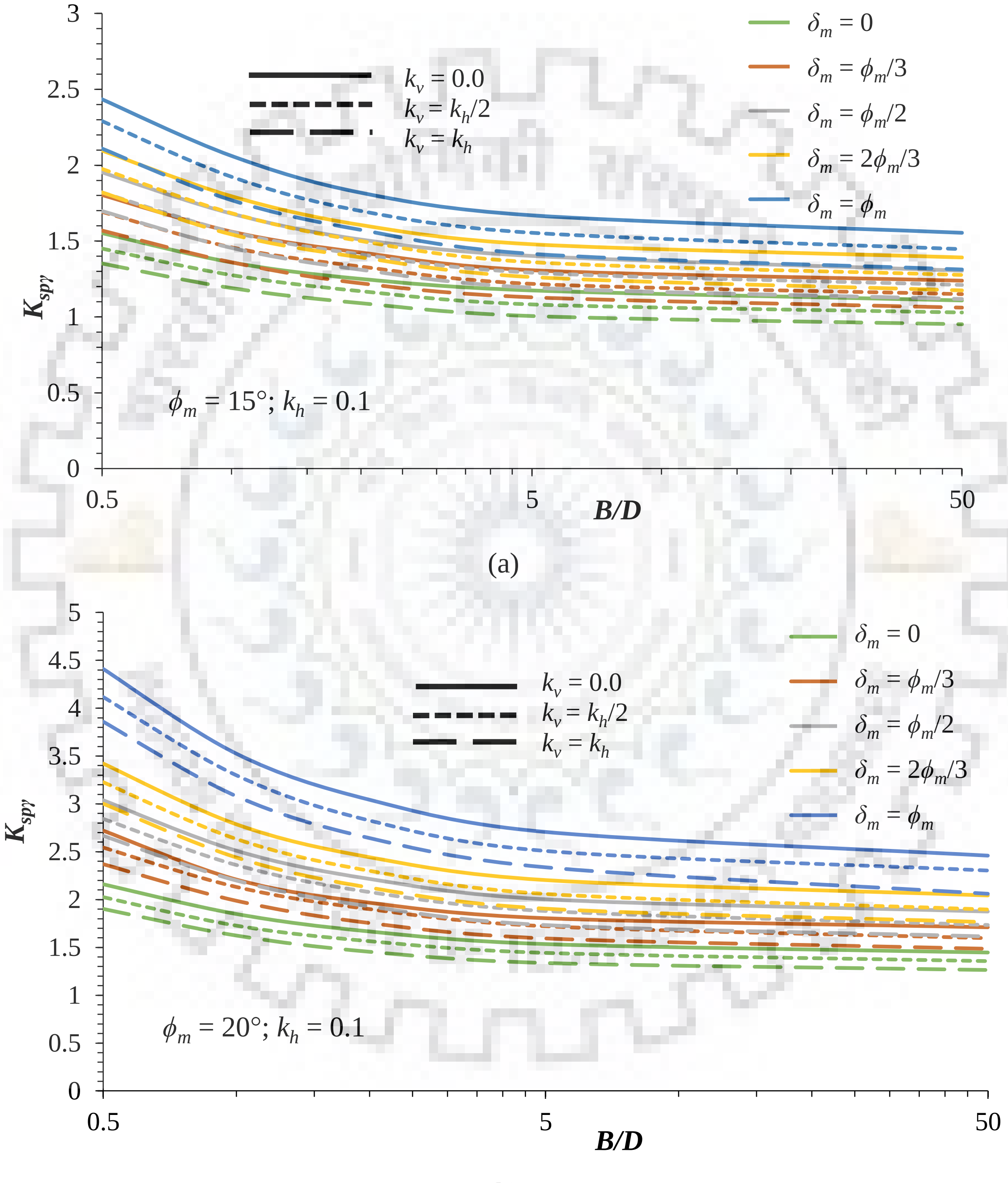

(a)

(b)

Fig. 7.6 Design chart for $K_{sp\gamma}$ in case of k_h=0.1, ξ=0.1 for different soil-wall friction angles and k_v values for (a) ϕ_m=15° and (b) ϕ_m=20°

The increase is more significant for higher magnitude of ϕ_m. In case of k_h = 0.1and k_v=k_h, for ϕ_m=15°, as δ_m is increased from 0 to ϕ_m/3 and 2ϕ_m/3 to ϕ_m, $K_{sp\gamma}$ increases by 14.27% and 14.64% respectively while for ϕ_m=30°, as δ_m is increased from 0 to ϕ_m/3 and 2ϕ_m/3 to ϕ_m, $K_{sp\gamma}$ increases by 48.43% and 67.85% respectively for B/D=1.

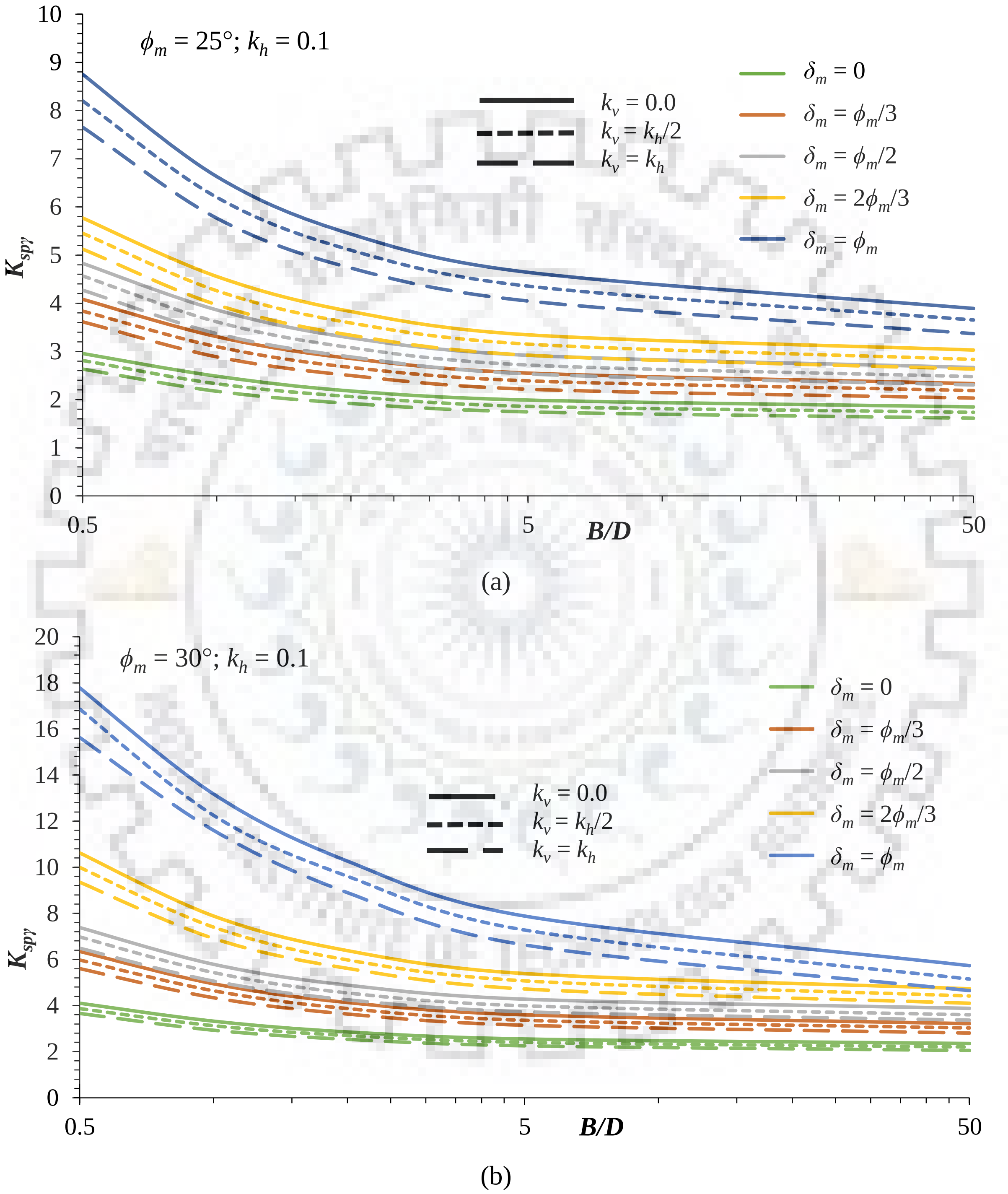

Fig. 7.7 Design chart for $K_{sp\gamma}$ in case of k_h=0.1, ξ=0.1 for different soil-wall friction angles and k_v values for (a) ϕ_m=25° and (b) ϕ_m=30°

As the magnitude of δ_m increases, the soil is able to develop higher resistance through interface friction at soil-caisson boundary causing the magnitude of seismic passive earth pressure coefficients to be higher. Fig. 7.9 shows the effect of δ_m on the ratio of volume per unit width of 3D failure wedge to volume per unit width under plane strain conditions for different soil-wall friction angles. It can be observed that the ratio increases with soil-wall friction angle suggesting that larger volume of side wedge is developed for higher magnitude of δ_m. It can also be observed that the ratio of 3D $K_{sp\gamma}$ to plane strain $K_{sp\gamma}$ increases at a much steeper rate than the ratio of volume per unit width of 3D failure wedge to volume per unit width under plane strain conditions. While the percentage increase in ratio of volume per unit width of 3D and plane strain conditions is 26.1%, 46.1% and 56.7% for δ_m=0, ϕ_m/3 and ϕ_m/2 respectively, when B/D reduces to 0.5, the increase in $K_{sp\gamma}$ value for the same set of input parameters is 83.3%, 106.5% and 120.5% respectively.

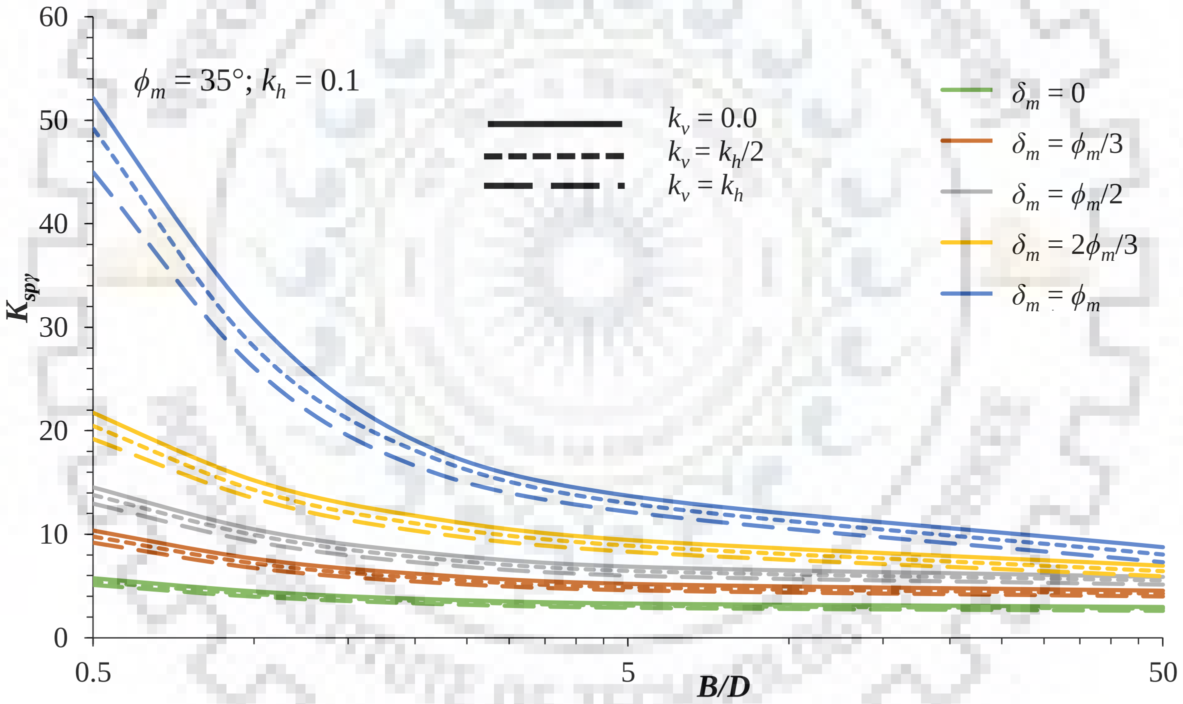

Fig. 7.8 Design chart for $K_{sp\gamma}$ in case of k_h=0.1, ξ=0.1 for different soil-wall friction angles and k_v values for ϕ_m=35°

7.4.3 Effect of mobilized soil-soil friction angle (ϕ_m)

Passive earth pressure coefficients are found to increase with increase in soil friction angles. Just as in the case of soil-wall friction angle, the increase in magnitude of $K_{sp\gamma}$ is more prominent for higher magnitude of δ_m. For B/D=1, k_h=0.1, k_v=0.5k_h and δ_m=ϕ_m/3, upon increasing ϕ_m from 15° to 20° and from 30° to 35°, the percentage increase in $K_{sp\gamma}$ was found to be 46.13% and 55% respectively and for δ_m=2ϕ_m/3, the percentage increase was 56.35% and 93.32% respectively. Since soil friction angle is the direct measure of soil shear strength, therefore, for the same set of input parameters, higher the magnitude of ϕ_m, higher is the seismic passive earth pressure developed.

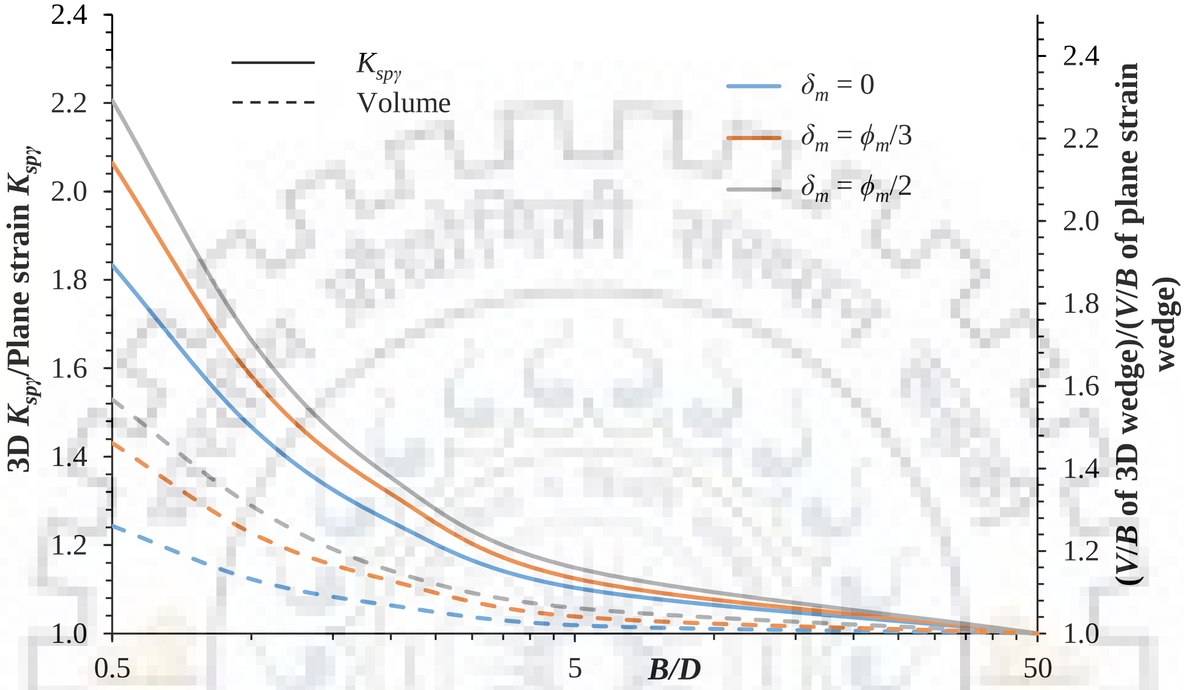

Fig. 7.9 Relative variation of $K_{sp\gamma}$ and V/B with respect to plane strain condition in case of ϕ_m=30°, k_h=0.2, k_v=0 and ξ=0.1 for different mobilized soil-wall friction angles

7.4.4 Effect of seismic acceleration coefficients (k_h and k_v)

Horizontal and vertical seismic acceleration coefficients have significant impact on the magnitude of $K_{sp\gamma}$ since it develops inertial forces that cause instability. The acceleration profile of earthquake, which generate seismic inertial forces, has been discussed in the previous section. For B/D=1, k_v=k_h/2, ϕ_m=25° and δ_m=ϕ_m/3, as k_h is increased from 0 to 0.1 and 0.1 to 0.2, the magnitude of $K_{sp\gamma}$ diminishes by 41.75% and 22.09% respectively. The effect of k_v on seismic passive earth pressure coefficient is less sensitive than that of k_h. In case of ϕ_m=25°, δ_m=ϕ_m/2 and B/D=1, for k_h=0.1, as k_v increases from 0 to k_h/2 and from k_h/2 to k_h, the magnitude of $K_{sp\gamma}$ decreases by 6.37% and 6.83% respectively. However, for k_h=0.2, this reduction is much more pronounced, i.e., 14.86% and 18.28% respectively for the above-mentioned set of input parameters.

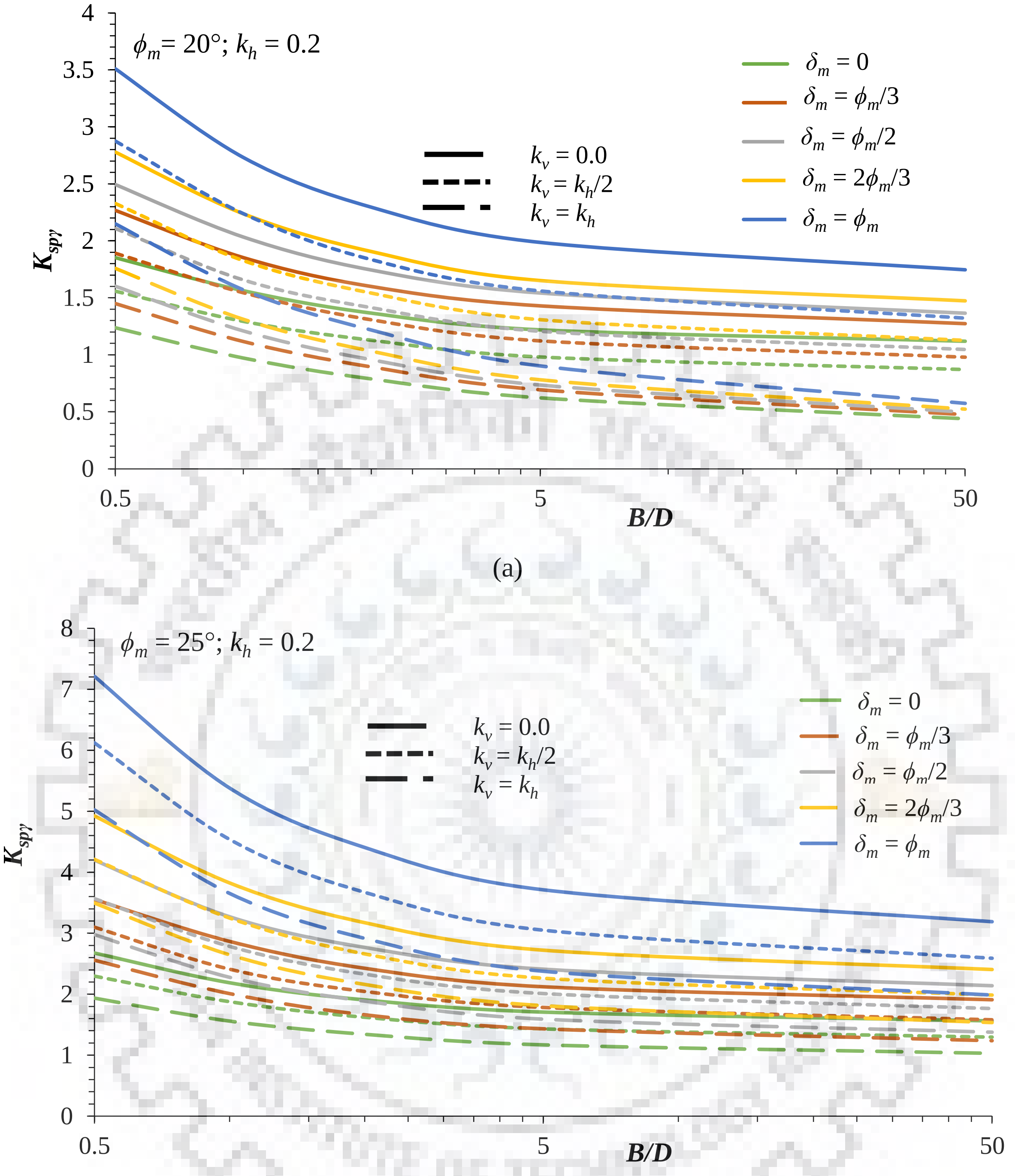

(a)

(b)

Fig. 7.10 Design chart for $K_{sp\gamma}$ in case of k_h=0.2, ξ=0.1 for different soil-wall friction angles and k_v values for (a) ϕ_m=20°and (b) ϕ_m=25°

7.4.5 Effect of width of caisson (B)

It can be observed from Fig. 7.9 that the ratio of volume of failure wedge per unit width of caisson decreases with increase in *B/D* ratio of caisson and converges at 1 for all values of δ_m, i.e., 3D behavior of caisson reduces to plane strain behaviour as the *B/D* ratio

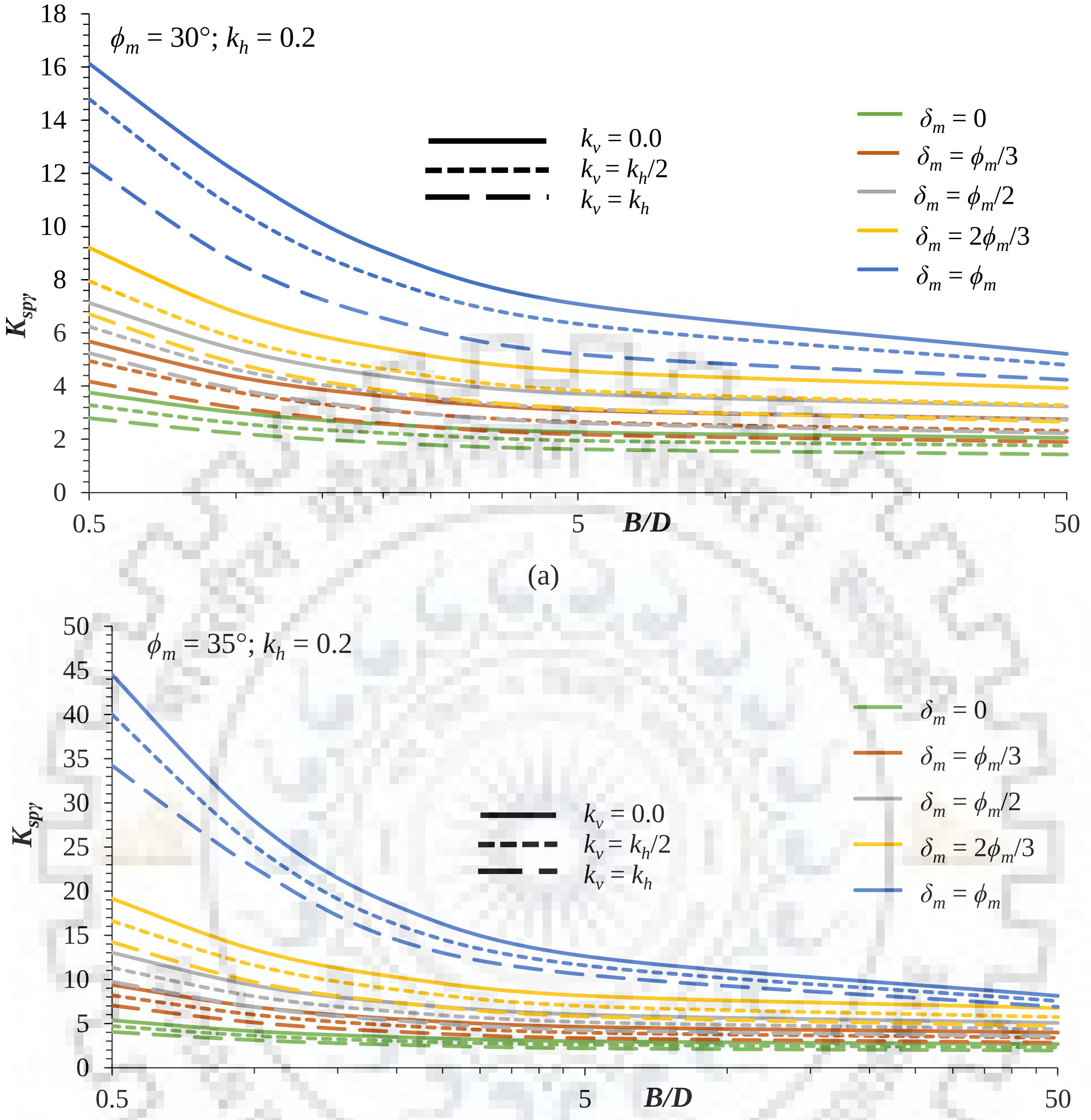

(a)

(b)

Fig. 7.11 Design chart for $K_{sp\gamma}$ in case of k_h=0.2, ξ=0.1 for different soil-wall friction angles and k_v values for (a) ϕ_m=30°and (b) ϕ_m=35°

increases. The magnitude of $K_{sp\gamma}$ is observed to decrease as the width of caisson increases irrespective of other input parameters. For k_h=0.1, k_v=0, ϕ_m=25°, δ_m/ϕ_m=0.5 and ξ=0.1, the magnitude of $K_{sp\gamma}$ diminishes by 20.05% and 8.67% as the *B/D* ratio increases from 0.5 to 1 and 5 to 50 respectively. This also reflects that the sensitivity of increase of width on $K_{sp\gamma}$ reduces as the width increases. With increase in *B/D*, volume per unit width of caisson decreases which in turn is able to mobilize resistance from smaller volume of surrounding soil.

7.4.6 *Effect of excess pore pressure ratio (r_u) and damping ratio (ξ)*

Table 7.3 and Table 7.4 shows the variation of $K_{sp\gamma}$ with ξ for different soil submergence states and soil-wall friction angles at r_u=0.2. Since the normalized frequency for the analysis was chosen in such a way that the effect of ξ on amplification of acceleration was nominal, ξ has barely any effect on the magnitudes of $K_{sp\gamma}$. For ϕ_m=30°, $\delta_m=\phi_m/3$, r_u=0.2, k_h=0.1 k_v=0, $\omega H/v_s$=0.94 and B/D=1 the seismic passive earth pressure coefficient increases by 0.31% and 0.71% respectively for dry soil; 0.58% and 0.88% respectively for submerged soil with free water condition and 1.12% and 2.86% respectively for submerged soil with restrained water condition. Higher magnitude of damping ratio directly leads to lower amplification of seismic acceleration through the soil strata. This causes overall reduction in seismic inertial forces which leads to increase in seismic passive earth pressure coefficient. Furthermore, $K_{sp\gamma}$ is found to decrease for a given set of input parameters as the surrounding soil varies from dry to submerged soil with free water and submerged soil with restrained water. For the same set of parameters as mentioned above and ξ=0.1, the seismic passive earth pressure coefficient reduces by 2.99% and 22.19% respectively as soil submergence condition changes from dry to submerged with free water and submerged with restrained water. Presence of pore water causes reduction in shear strength of soil which in turn reduces the passive resistance offered.

Table 7.3 Variation of $K_{sp\gamma}$ with damping ratio and soil submergence for ϕ_m=30°, $\delta_m=\phi_m/3$, r_u=0.2, k_h=0.1 and k_v=0, $\omega H/v_s$=0.94

	Seismic passive earth pressure coefficient ($K_{sp\gamma}$)								
Damping ratio (ξ) →	0.1	0.15	0.2	0.1	0.15	0.2	0.1	0.15	0.2
B/D ↓	Dry soil			Submerged, free water			Submerged, restrained water		
0.5	6.179	6.197	6.22	6.034	6.074	6.124	4.932	4.996	5.094
1	4.812	4.827	4.846	4.668	4.695	4.709	3.744	3.786	3.851
2	4.093	4.057	4.074	3.893	3.915	3.951	3.088	3.107	3.192
5	3.557	3.569	3.584	3.358	3.385	3.352	2.612	2.655	2.68
50	3.22	3.218	3.232	2.989	2.983	2.996	2.312	2.326	2.377

Table 7.4 Variation of $K_{sp\gamma}$ with damping ratio and soil-wall friction angle for ϕ_m=30°, r_u=0.2, k_h=0.1 and k_v/k_h=0.5, $\omega H/v_s$=0.94

	Seismic passive earth pressure coefficient ($K_{sp\gamma}$)								
Damping ratio (ξ) →	0.1	0.15	0.2	0.1	0.15	0.2	0.1	0.15	0.2
B/D ↓	δ_m = 0			δ_m = ϕ_m/3			δ_m = ϕ_m/2		
0.5	3.798	3.809	3.823	5.830	5.849	5.872	7.398	7.423	7.454
1	3.092	3.101	3.113	4.533	4.548	4.567	5.654	5.674	5.699
2	2.667	2.676	2.686	3.851	3.865	3.882	4.699	4.716	4.738
5	2.402	2.410	2.410	3.365	3.355	3.370	4.049	4.064	4.084
50	2.210	2.218	2.228	3.041	3.053	3.067	3.637	3.629	3.647

For ϕ_m=30°, $\delta_m=\phi_m/3$, r_u=0.2, ξ=0.15, k_h=0.1, k_v=0 and *B*/*D*=1, as the soil changes from dry to submerged soil with free water and submerged soil with restrained water, the $K_{sp\gamma}$ value reduces by 3.29% and 21.57% respectively. It is also observed from Fig. 7.12 that with increase in r_u, the magnitude of $K_{sp\gamma}$ decreases. As r_u increases from 0 to 0.2 and 0.4, $K_{sp\gamma}$ is found to reduce by 13.41% and 41.49% respectively at *B/D*=1 and 12.98% and 52.35% respectively at *B/D*=50. Fig. 7.13 shows the effect of submergence of soil on volume increase per unit width for varying width of caisson which reflects that the volume change per unit width decreases more steeply for dry soil compared to submerged soil, i.e., as the width of caisson reduces, larger volume of soil per unit width of caisson, normalized with respect to volume per unit width in plane strain condition, would fail compared to that for submerged soil.

7.5 Summary

The current study deals with the problem of determining passive resistance offered to a rectangular structure embedded in cohesionless layered soil with failure wedge lying in a single soil layer using modified pseudo-dynamic method. Realistic geometry of failure wedge has been chosen based on previous experimental study and results of numerical study in previous chapters. The acceleration profile through various soil layers has been determined using modified pseudo-dynamic method. The study also provides with the methodology to determine transfer function between various layers in layered strata. Design charts for various soil and seismic parameters have been presented for different widths of caisson. The change in volume per unit width of failure wedge has also been analyzed for various input parameters to demonstrate the effect of volume of side wedge and consideration of 3D failure wedge.

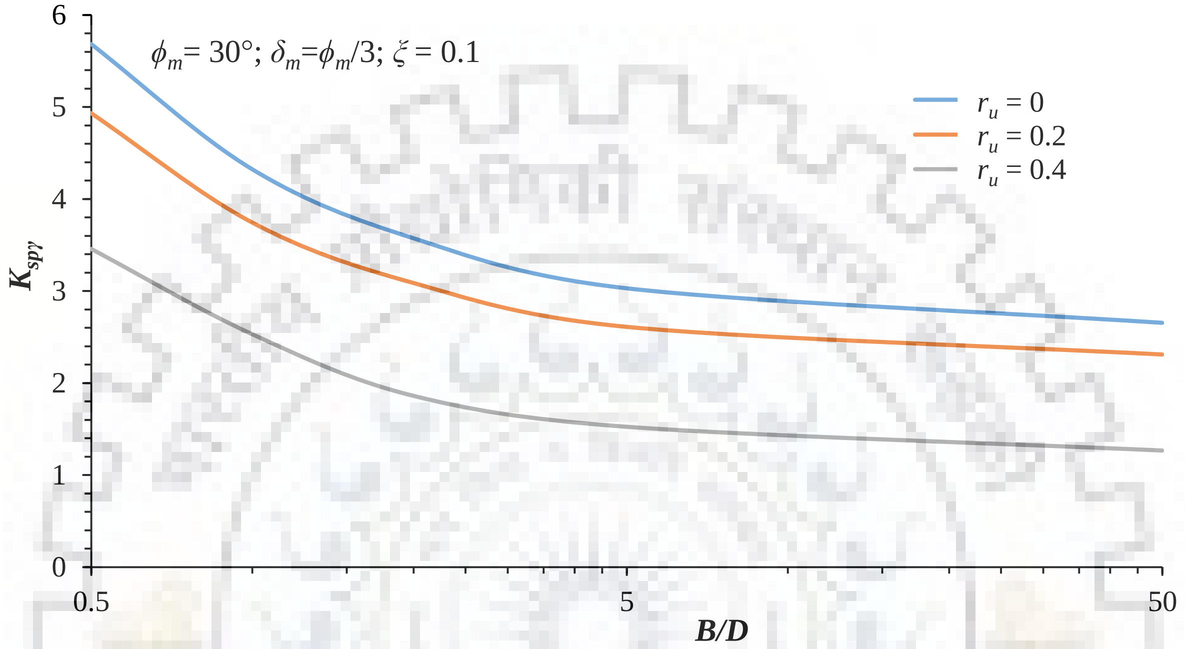

Fig. 7.12 Effect of excess pore pressure ratio on $K_{sp\gamma}$ for submerged soil with restrained water

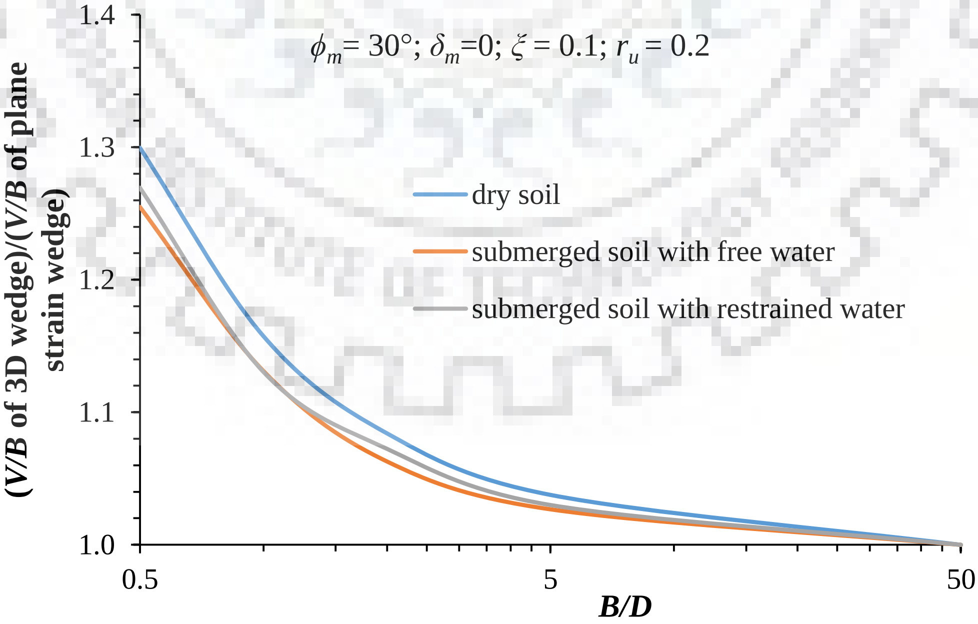

Fig. 7.13 Effect of soil submergence condition on volume of failure wedge

Chapter 8

SEISMIC PASSIVE EARTH PRESSURE COEFFICIENT FOR CAISSON IN LAYERED SOIL USING MODIFIED PSEUDO DYNAMIC METHOD

8.1 General

In field, soil is heterogeneous in nature and may have several layers with varying properties. In the past, several researchers have explored the analysis of walls [Shi et al. (2016), Santhoshkumar and Ghosh (2021a,b)] and slopes [Kumar and Samui (2006), Qin and Chian (2017), Hazari et al. (2020)] in layered soil under static and seismic conditions. Hazari et al. (2020) proposed a method for analysis of layered soil slopes using modified pseudo-dynamic method. However, these studies considered 2D plane strain analysis. So far, none of the studies have considered theoretical 3D analysis of caisson in layered soil. In the present study, modified pseudo-dynamic method of analysis has been used to compute acceleration profile in layered strata and hence determine seismic passive earth pressure coefficient ($K_{sp\gamma}$) for caisson in cohesionless layered soil considering polylinear failure wedge. The analysis has been performed for both dry and submerged soil conditions.

8.2 Proposed Theoretical Methodology

A rectangular caisson of length L, width B and embedment depth H is considered to be embedded in layered cohesionless soil with different soil properties and resting on rigid rock. A polylinear failure wedge is assumed to be formed behind the caisson as shown in Fig. 8.1. The soil in any layer of failure wedge is assumed to be homogeneous and soil properties are assumed to be isotropic in all directions in a given layer. The assumptions regarding wave propagation and boundary conditions in modified pseudo-dynamic method is the same as in Chapter 7. Therefore, the formulation for acceleration and transfer functions come out to be the same as in previous chapter and given by Eqn. 7.15 and 7.16. However, the formulation for seismic passive earth pressure resistance will be different in the present proposed methodology due to consideration of a different failure wedge geometry as mentioned in the succeeding sections. Limit equilibrium method of analysis is adopted for the said formulation to establish equilibrium of forces in horizontal and vertical directions. The critical failure wedge geometry is obtained by optimizing the angle of wedge with the horizontal in each layer from bottom to top because the extent of failure wedge in upper layers is dependent on extent of failure wedge in lower layers as will be evident from the formulation in subsequent section.

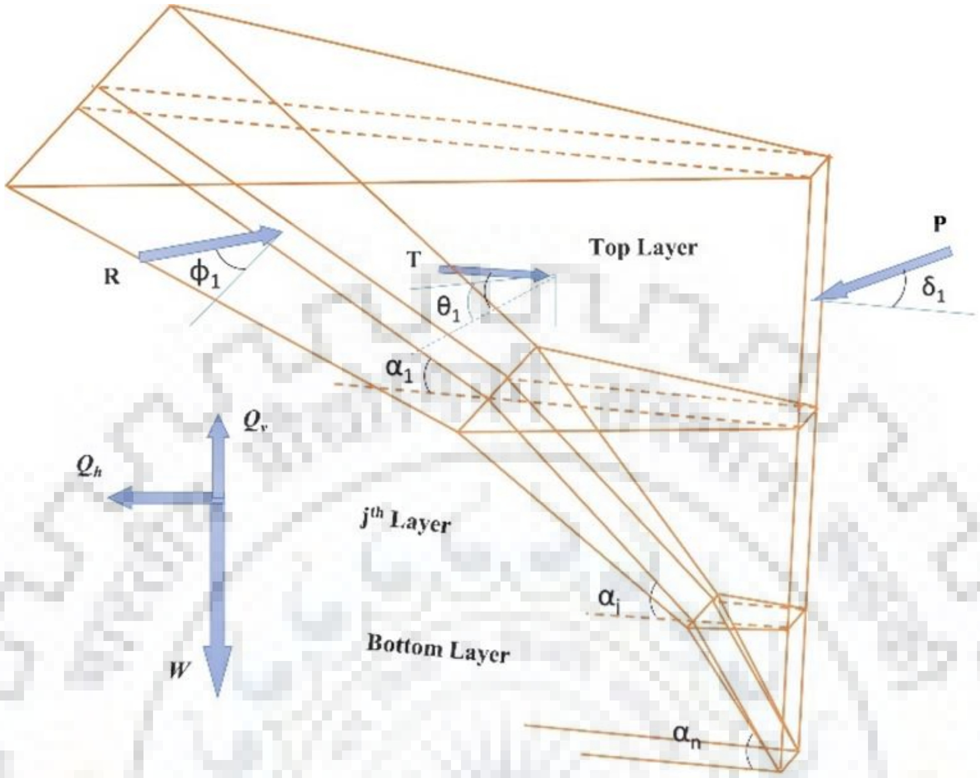

Fig. 8.1 3D polylinear failure wedge assumed in the present study

8.2.1 Formulation of the problem

Fig. 8.2 depicts the bottom failure wedge geometry to be used for computation of seismic passive earth pressure resistance on caisson. The failure wedge in layer j, with depth h_j, unit weight γ_j soil friction angle ϕ_j, is inclined at an angle α_j with the horizontal and the fanning angle defining side wedges is θ_j. Since the direction of all the forces in any layer is uniform, the free body diagram of entire layer can be considered. The seismic inertial forces at any depth are calculated as product of mass of failure wedge at any depth and the seismic acceleration at that depth. From Fig. 8.2, the volume of failure wedge at any depth is computed as follows:

At any depth z_n from the top of n^{th} layer,

$$\tan\alpha_n = \frac{h_n - z_n}{m(z_n)} \qquad \Rightarrow m(z_n) = \frac{h_n - z_n}{\tan\alpha_n} \tag{8.1}$$

$$\tan\theta_n = \frac{m_s(z_n)}{m(z_n)} \tag{8.2a}$$

$$m_s(z_n) = m(z_n)\tan\theta_n = \frac{h_n - z_n}{\tan\alpha_n}\tan\theta_n \tag{8.2b}$$

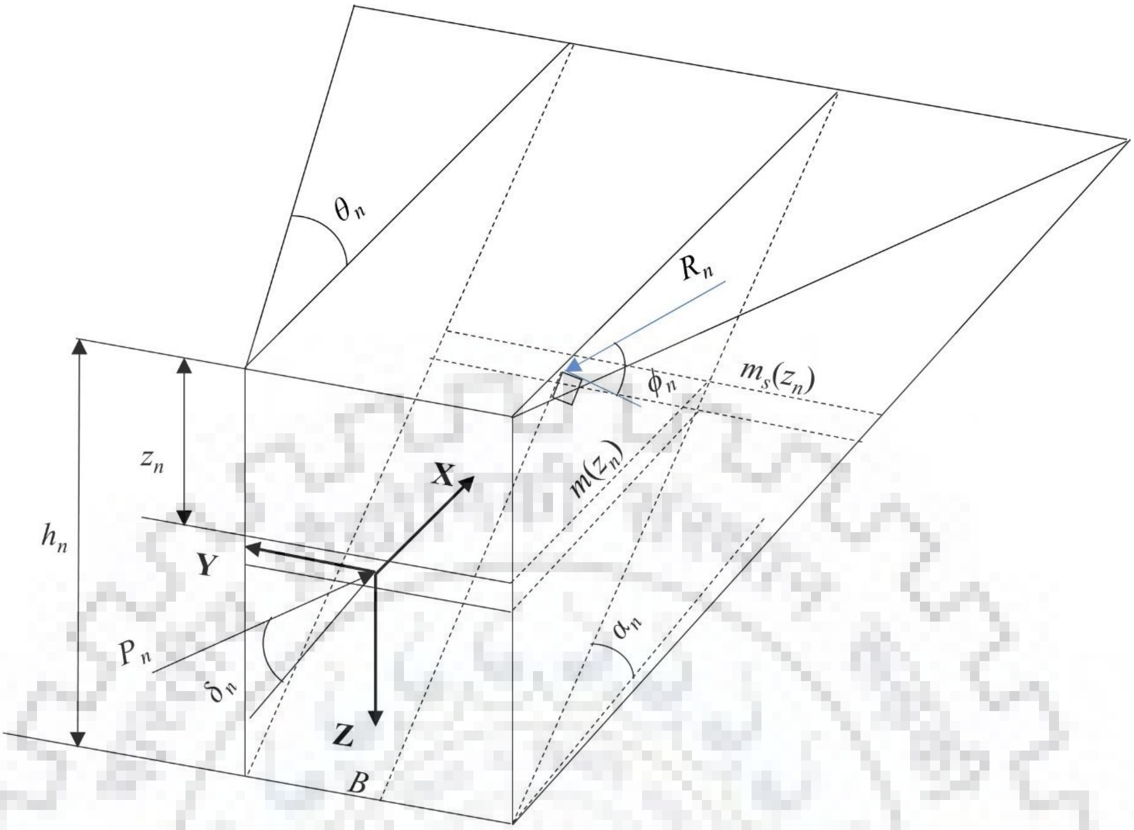

Fig. 8.2 Geometry of bottom wedge to compute seismic passive earth pressure resistance

Volume of elemental wedge of thickness dz_n at depth z_n is computed as:

$$dV_n = \frac{1}{2} \times \{B + (B + 2m_s(z_n))\} \times m(z_n) \times \mathrm{d}z_n = (B + m_s(z_n)) \times m(z_n) \times \mathrm{d}z_n \qquad (8.3a)$$

$$V_n = \int_{z_n=0}^{z_n=h_n} (B + m_s(z_n)) \times m(z_n) \times \mathrm{d}z_n \qquad (8.3b)$$

$$V_n = \int_{z_n=0}^{z_n=h_n} \left(B \times \frac{h_n - z_n}{\tan\alpha_n} \times \mathrm{d}z_n\right) + \int_{z_n=0}^{z_n=h_n} \frac{h_n - z_n}{\tan\alpha_n} \tan\theta_n \times \frac{h_n - z_n}{\tan\alpha_n} \times \mathrm{d}z_n \qquad (8.3c)$$

$$V_n = \left(\frac{B}{\tan\alpha_n} \times \frac{(h_n - z_n)^2}{-2}\right) + \frac{(h_n - z_n)^3}{-3\tan^2\alpha_n} \times \tan\theta_n \qquad (8.3d)$$

Within limits of integration, the volume of wedge is found as:

$$V_n = \frac{B{h_n}^2}{2\tan\alpha_n} + \frac{{h_n}^3 \tan\theta_n}{3\tan^2\alpha_n} = \frac{{h_n}^2}{\tan\alpha_n}\left(\frac{B}{2} + \frac{h_n \tan\theta_n}{3\tan\alpha_n}\right) \qquad (8.3e)$$

The extent of failure wedge in front of caisson ($m(z)$) in layers above the bottom layer is directly dependent upon $m(z)$ at top of bottom layer.

$$m(z_{n-1}) = \frac{h_n}{\tan\alpha_n} + \frac{h_{n-1} - z_{n-1}}{\tan\alpha_{n-1}} \qquad (8.4a)$$

Similarly, $m(z)$ at any depth in layer j is determined as:

$$m(z_j) = \sum_{i=j+1}^{n} \frac{h_i}{\tan\alpha_i} + \frac{h_j - z_j}{\tan\alpha_j} \qquad (8.4b)$$

$$dV_j = (B + m_s(z_j)) \times m(z_j) \times \mathrm{d}z_j \qquad (8.4c)$$

Area of failure wedge in horizontal plane at depth z_j (A_{zj}) in layer j is determined by Eqn. (8.4e). The area of failure at top of j^{th} layer is thus represented as A_{oj} and the area at bottom of failure wedge of j^{th} layer is represented as A_{hj}.

$$A_{z_j} = \frac{dV_j}{dz_j} = \left(B + m_s(z_j)\right) \times m(z_j) \tag{8.4d}$$

$$A_{z_j} = \left[B + \left\{\sum_{j+1}^{n} \frac{h_i}{tan\ \alpha_i} + \frac{(h_j - z_j)}{tan\ \alpha_j}\right\} tan\ \theta\right] \times \left\{\sum_{j+1}^{n} \frac{h_i}{tan\ \alpha_i} + \frac{(h_j - z_j)}{tan\ \alpha_j}\right\} \tag{8.4e}$$

The tangential stress coefficient (λ) is used to calculate the horizontal component of tangential force on any layer (F_j). The tangential stress coefficient is defined as the ratio of tangential stress to vertical stress at any depth. For any layer j, F_j is obtained as follows:

$$\lambda_j = \frac{\sigma_t}{\sigma_v} = \frac{\sigma_t \times m(z_j)\mathrm{d}z_j}{\gamma z \times m(z_j)\mathrm{d}z_j} = \frac{dT_j}{\gamma z \times m(z_j)\mathrm{d}z_j} \tag{8.5a}$$

where, T_j is the tangential force acting on both side wedges on the j^{th} layer of failure wedge as shown in Fig. 8.1. The horizontal component of T_j acting in X-direction (F_j) is computed to establish equilibrium of forces in horizontal direction.

$$dT_j = \lambda_j \times \left(\gamma_j z_j + \sum_{1}^{j-1} \gamma_i h_i\right) \times m(z_j)\mathrm{d}z_j \tag{8.5b}$$

$$dF_j = 2dT_j sin\theta cos\theta = 2\lambda_j \times \left(\gamma_j z_j + \sum_{1}^{j-1} \gamma_i h_i\right) \times m(z_j)\mathrm{d}z_j \times sin\theta cos\theta \tag{8.5c}$$

$$F_j = \int_{z_j=0}^{z_j=h_j} 2\lambda_j \times sin\theta cos\theta \times \left(\gamma_j z_j + \sum_{1}^{j-1} \gamma_i h_i\right) \times m(z_j)\mathrm{d}z_j \tag{8.5d}$$

The weight of any layer (W_j) is calculated by integrating the weight of an infinitesimal volume of failure wedge at depth z_j and thickness dz_j over the entire depth of the layer.

$$W_j = \gamma_j dV_j = \gamma_j \times \left(B + m_s(z_j)\right) \times m(z_j) \times \mathrm{d}z_j \tag{8.6}$$

The seismic acceleration profile at any depth is obtained as per the modified pseudo dynamic method formulation in the previous chapter. The horizontal and vertical seismic inertial force in any layer is obtained by integrating the product of mass of infinitesimally thin failure wedge at depth z with horizontal seismic acceleration and vertical seismic acceleration at that depth respectively over entire depth of the layer.

$$Q_{h_j} = \int_0^{h_j} \rho_j dV_j \times a_{h_j} \tag{8.7a}$$

$$Q_{v_j} = \int_0^{h_j} \rho_j dV_j \times a_{v_j} \tag{8.7b}$$

where ρ_j is the mass density of the soil layer. The overburden pressure force (Q_j) applied by preceding layers and normal reaction (N_j) offered to any layer by the subsequent layers is determined using Eqn. (8.8).

$$Q_j = \sum_{i=1}^{i=j-1} \gamma_i h_i \times A_{o_j} \tag{8.8a}$$

$$N_j = \sum_{i=1}^{i=j} \gamma_i h_i \times A_{hj} \tag{8.8b}$$

Fig. 8.1 depicts the direction of all the forces acting on any layer. Knowing the formulation for all the force components in any layer *j*, the horizontal and vertical force equilibrium equation can be written as follows:

$$\sum H = 0 \qquad \Rightarrow P_j cos\delta_j - F_j + Q_{h_j} = R_j cos\left\{\frac{\pi}{2} - \left(\alpha_j + \phi_j\right)\right\} = R_j sin\left(\alpha_j + \phi_j\right) \tag{8.9a}$$

$$\sum V = 0 \qquad \Rightarrow P_j sin\delta_j + W_j - Q_{v_j} + Q_j - N_j = R_j cos\left(\alpha_j + \phi_j\right) \tag{8.9b}$$

Dividing Eqn. (8.9a) by Eqn. (8.9b)

$$\frac{P_j cos\delta_j - F_j + Q_{h_j}}{P_j sin\delta_j + W_j - Q_{v_j} + Q_j - N_j} = tan\left(\alpha_j + \phi_j\right) \tag{8.10a}$$

$$P_j cos\delta_j - P_j sin\delta_j tan\left(\alpha_j + \phi_j\right) = \left(W_j - Q_{v_j} + Q_j - N_j\right) tan\left(\alpha_j + \phi_j\right) - \left(Q_{h_j} - F_j\right) \tag{8.10b}$$

$$P_j = \frac{\left(W_j - Q_{v_j} + Q_j - N_j\right) tan\left(\alpha_j + \phi_j\right) - \left(Q_{h_j} - F_j\right)}{\left\{cos\delta_j - sin\delta_j tan\left(\alpha_j + \phi_j\right)\right\}} \tag{8.10c}$$

8.2.2 Computation of seismic passive earth pressure coefficient ($K_{sp\gamma}$) for generalized n-layered strata

In the present study, the critical failure wedge is obtained by minimizing the seismic passive earth pressure resistance P_j in different layers. The process is initiated by minimizing the seismic passive earth pressure resistance in the bottom layer to obtain optimum value α_n. Thereafter, α_{n-1} is optimized by minimizing the magnitude of seismic passive earth pressure force from bottom 2 layers. The process is continued till the critical geometry of failure wedge in all the layers is obtained. In order to obtain the equivalent seismic passive earth pressure coefficient ($K_{sp\gamma}$) of the entire strata, the total seismic passive earth pressure resistance obtained from the analysis is equated to the area of pressure distribution diagram considering linear earth pressure distribution and signifying constant magnitude of earth pressure coefficient throughout the strata.

$$\sum_1^n P_j = \left(\frac{1}{2} K_{sp\gamma} \times \gamma_1 h_1^2\right) + \left[\frac{1}{2} K_{sp\gamma} \times \{(\gamma_1 h_1) + (\gamma_1 h_1 + \gamma_2 h_2)\} \times h_2\right] + \cdots + \left[\frac{1}{2} K_{sp\gamma} \times \left\{\sum_1^{j-1}(\gamma_i h_i) + \sum_1^{j}(\gamma_i h_i)\right\} \times h_j\right] + \cdots + \left[\frac{1}{2} K_{sp\gamma} \times \left\{\sum_1^{n-1}(\gamma_i h_i) + \sum_1^{n}(\gamma_i h_i)\right\} \times h_n\right] \tag{8.11a}$$

$$\Rightarrow \sum_1^n P_j = \frac{1}{2} K_{sp\gamma} \times \left[(\gamma_1 h_1^2) + \left[\left\{(\gamma_1 h_1) + \sum_1^2(\gamma_i h_i)\right\} \times h_2\right] + \cdots + \left[\left\{\sum_1^{j-1}(\gamma_i h_i) + \sum_1^{j}(\gamma_i h_i)\right\} \times h_j\right] + \cdots + \left[\left\{\sum_1^{n-1}(\gamma_i h_i) + \sum_1^{n}(\gamma_i h_i)\right\} \times h_n\right]\right] \tag{8.11b}$$

$$K_{sp\gamma} = \frac{2 \times \sum_1^n P_j}{\left[(\gamma_1 h_1^2) + \left[\left\{(\gamma_1 h_1) + \sum_1^2(\gamma_i h_i)\right\} \times h_2\right] + \cdots + \left[\left\{\sum_1^{n-1}(\gamma_i h_i) + \sum_1^{n}(\gamma_i h_i)\right\} \times h_n\right]\right]} \tag{8.11c}$$

The formulation mentioned in the preceding section is valid for dry soil in front of caisson. The provisions mentioned in previous chapter (section 7.2.3) are used to account for submergence of soil for both free water and restrained water conditions.

8.2.3 Validation of the proposed theoretical model

The present study deals with the computation for seismic passive earth pressure coefficient for caisson embedded in *n*-layered soil strata. No direct experimental or theoretical studies are found in existing literature for caissons in layered soil or retaining wall in more than 2 layers barring Shi et al. (2016). Therefore, the results for the present model have been validated against results for retaining wall supporting 2-layered soil strata by Santhoshkumar and Ghosh (2021) and compared with results of specific cases studied by Shi et al. (2016). In addition, the results have also been compared with results for homogeneous soil by choosing n=1 in the present study.

Santhoshkumar and Ghosh (2021) computed the seismic passive earth pressure coefficient for retaining wall in 2-layered cohesionless soil using method of stress characteristics in conjugation with pseudo-static approach for computation of seismic forces. The results for varying ratio of soil friction angles in top and bottom layer is compared in Fig. 8.3 for h_1/h_2=1, γ_1/γ_2=0.83, δ/ϕ=2/3, k_v=0 and B/H=5000. The results show that the magnitude of seismic passive earth pressure coefficient obtained in the present study is more sensitive to seismic acceleration coefficient than the study by Santhoshkumar and Ghosh (2021). This trend may be attributed to higher seismic inertial forces obtained in the present study due to amplification of acceleration through the soil strata as opposed to constant seismic acceleration assumed by Santhoshkumar and Ghosh (2021).

Shi et al. (2016) have proposed a method of analysis of retaining wall supporting layered backfill but have not presented generalized results, i.e., the magnitude of seismic active and passive earth pressure force and resistance has been computed for 2 combinations of site conditions. The authors have computed passive resistance offered to retaining wall for the parameters mentioned in Table 8.1. The magnitude of total seismic passive resistance obtained from present study have been compared with the results by Shi et al. (2016). The resistance due to cohesion component has been computed as per results from Chapter 5. The input parameters mentioned in Table 8.1 have been substituted in the formulations proposed above to obtain seismic passive resistance for different seismic conditions and compared with the study by Shi et al. (2016), as given in Table 8.2. The results of proposed method are found to be slightly conservative but in good agreement with the results of Shi et al. (2016).

Furthermore, the proposed model has been reduced to single layer and the results are compared with the results of existing studies for single layer as mentioned in

Table **8.3**. The proposed model returns the same results as Mononobe and Matsuo (1929) and Biswas and Choudhury (2019) for static cases because of assumption of similar failure geometry while returns more conservative results for seismic cases because of application of modified pseudo-dynamic method as opposed to pseudo-static approach considered by the other researchers.

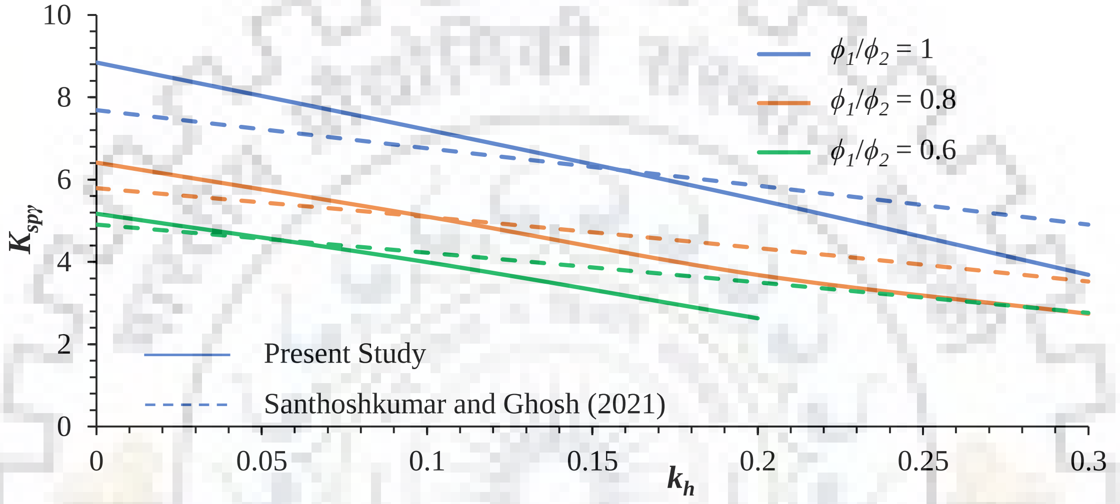

Fig. 8.3 Comparison of results of present study with Santhoshkumar and Ghosh (2016)

Table 8.1 Soil properties adopted by Shi et al. (2016)

	Soil friction angle (ϕ)	Unit weight (γ) [kN/m^3]	Cohesion (c) [kN/m^2]
H_1 = 1m	30°	16.5	0
H_2 = 2m	10°	18	15
H_3 = 3m	20°	19	10

Table 8.2 Comparison for seismic passive earth pressure with Shi et al. (2016)

k_h	k_v	δ (°)	Passive resistance (kN/m)	
			Shi et al. (2016)	Present study
0.1	0.1	0	670	662.3
0.1	0.1	10	846.6	827.5
0.2	0.1	0	627.6	620.6
0.2	0.1	10	792	776.4

Table 8.3 Comparison of results for homogeneous soil strata derived from present study with existing literature for k_v=0 and plane strain conditions

ϕ	δ/ϕ	k_h	Seismic passive earth pressure coefficient ($K_{sp\gamma}$)					
			Mononobe and Matsuo (1929)	Soubra (2000)	Lancelotta (2007)	Liu et al. (2017)	Biswas and Choudhury (2019)	Present Study
20°	0	0	2.04	2.04	2.04	2.04	2.04	2.04
		0.1	1.888	1.89	1.872	-	1.888	1.802
	1/3	0	2.414	2.39	2.349	2.38	2.414	2.414
		0.1	2.196	2.19	2.155	-	2.196	2.075
	1/2	0	2.635	2.58	2.477	2.56	2.635	2.635
		0.1	2.379	2.35	2.273	-	2.379	2.237
30°	0	0	3	3	3	3	3	3
		0.1	2.821	2.82	2.802	-	2.821	2.726
	1/3	0	4.143	4.05	3.886	4.02	4.143	4.143
		0.1	3.83	3.77	3.630	-	3.829	3.665
	1/2	0	4.977	4.69	4.288	4.61	4.977	4.977
		0.1	4.562	4.35	4.005	-	4.562	4.345

-: suggests that studies were conducted for static conditions only

8.3 Present Study

The present deals with the development of a theoretical model for determination of seismic passive earth pressure resistance offered to a caisson embedded in layered cohesionless soil. Modified pseudo-dynamic method has been adopted to determine acceleration profile of seismic waves. The shear wave velocity and primary wave velocity are bound by Poisson's ratio. For dry soil, the Poisson's ratio has been considered as 0.3 and for submerged soil, Poisson's ratio has been assumed to be 0.495. This gives v_p=1.87v_s for dry conditions and v_p=10v_s for submerged soil conditions. The fanning angle θ has been chosen equal to ϕ/2 for the analysis [Bowman (1958); Biswas and Choudhury (2021)] and tangential stress coefficient (λ) has been assumed to be equal to Rankine's passive earth pressure coefficient [Liu et al. (2009)]. The depth of failure wedge (D) has been adopted as H/2.2 according to the recommendations of Olson et al. (2017). Furthermore, in order to minimize the effect of damping ratio (ξ) while keeping the amplification of seismic waves in realistic range, the magnitude of normalized frequency ($\omega H/v_s$) has been chosen as 0.94 which gives $\omega H/v_p$=0.5. While the formulation has been derived for any number of layers, the parametric study has been performed for caisson of depth 22m embedded in 5-layered soil and resting on rigid rock, with 10m deep failure wedge. 2 of the layers are assumed to lie below the failure wedge while a maximum of 3 layers is assumed to accommodate the failure wedge. Curved failure surfaces are recommended for rough walls by previous researchers. However, planar failure surface is found to return seismic passive earth pressure coefficient for $\delta \leq \phi/2$ with reasonable degree of accuracy. In field, the magnitude of soil-wall friction angle is found to lie in the said range. Therefore, the present study considers $\delta \leq \phi/2$ for the analysis. Different input parameters considered in the present study are mentioned in Table 8.4.

Table 8.4 Input properties used in the present study

Parameter	Value
Unit weight of bottom layer of failure wedge (γ_3)	18kN
γ_1/γ_3, γ_2/γ_3	0.9,1
Soil friction angle of bottom layer of failure wedge (ϕ_3)	25°, 30° and 35°
ϕ_1/ϕ_3, ϕ_2/ϕ_3	0.6, 0.7, 0.8, 0.9 and 1
Soil-wall friction angle (δ/ϕ)	0, 1/3 and 1/2
Width of structure (B/H)	0.2, 0.5, 1, 5, 500
Seismic horizontal acceleration coefficient (k_h)	0, 0.1 and 0.2
Seismic vertical acceleration coefficient (k_v)	0, 0.5k_h and k_h
H_1:H_2 for 2-layered failure wedge	1:4, 2:3, 3:2, 4:1
H_1:H_2:H_3 for 3-layered failure wedge	1:2:3, 1:1:1
Excess pore pressure ratio (r_u)	0, 0.2 and 0.3

8.4 Results and Discussions

The analyses have been conducted to determine seismic passive earth pressure coefficient for various combinations of input parameters mentioned in Table 8.4. The study also presents the failure wedge geometry for various input parameters. The effect of various input parameters has been mentioned in detail in the succeeding sections.

8.4.1 Effect of soil-wall friction angle (δ)

The seismic passive earth pressure coefficient in the proposed model is found to increase with increasing soil-wall friction angle irrespective of the number of layers, relative depths and soil friction angle of layers, submergence of soil or seismic conditions. Fig. 8.4 to Fig. 8.9 reflect the effect of soil-wall friction angle on seismic passive earth pressure coefficient. It is found that the seismic passive earth pressure coefficient increases by 36.83% and 19.89% as δ increases from 0 to $\phi/3$ and $\phi/2$ respectively for ϕ=30°, k_h=0.2, k_v=0 and B/D=1 for failure wedge lying in single layer of soil. Similar trend was observed for failure wedge lying in 2-layered and 3-layered soil. For H_1/H_2=2/3 in 2-layered soil, the increase is 36.03% and 18.91% for ϕ_1/ϕ_2=0.8, k_h=0.1, k_v=0 and B/D=1 and for H_1:H_2:H_3=1:2:3 with ϕ_1: ϕ_2: ϕ_3=3:4:5 for ϕ_3=30°, k_h=0.1, k_v=0 and B/D=1, the increase is 33.44% and 17.89% when δ increases from 0 to $\phi/3$ and $\phi/2$ respectively.

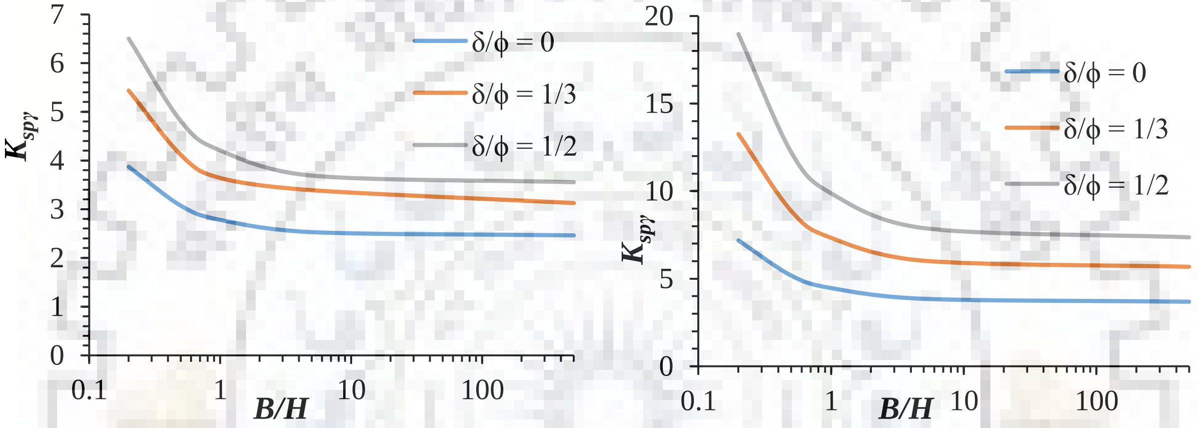

(a) (b)

Fig. 8.4 Variation of seismic passive earth pressure coefficient for failure wedge in single layer under static conditions for (a) ϕ=25° and (b) ϕ=35°

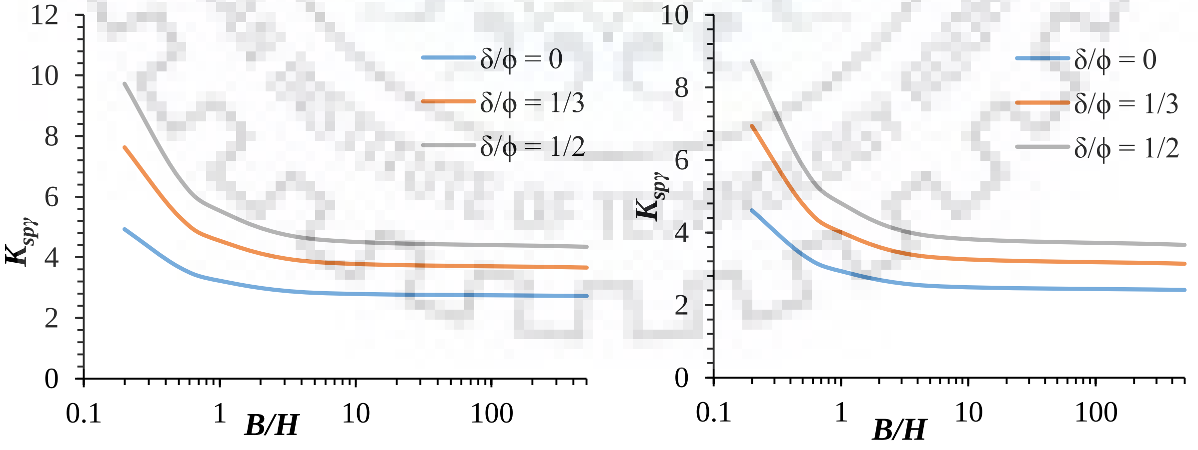

(a) (b)

Fig. 8.5 Variation of seismic passive earth pressure coefficient for failure wedge in single layer with ϕ=30°, k_v=0 for (a) k_h=0.1 and (b) k_h=0.2

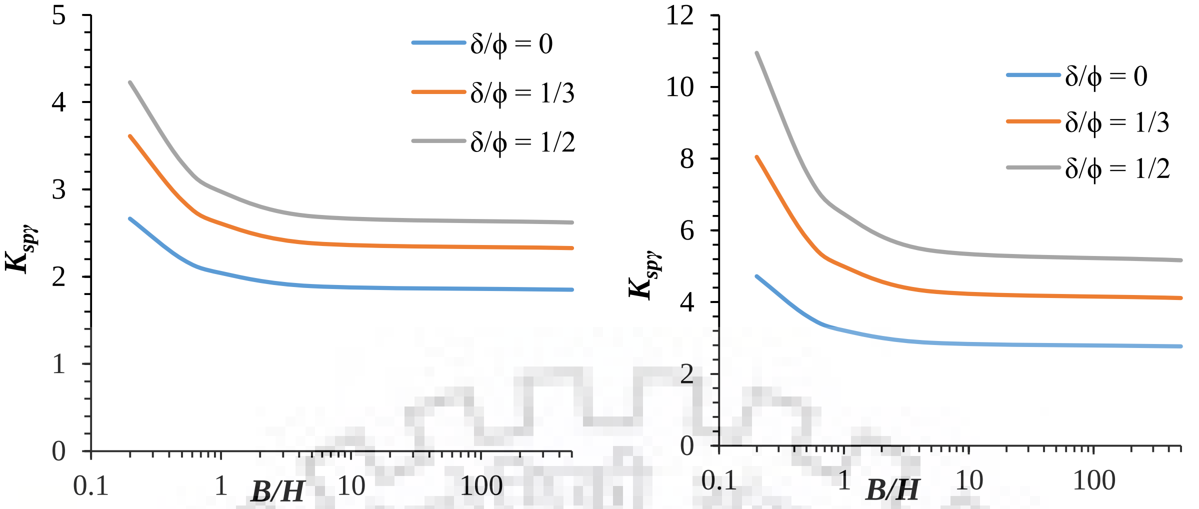

(a) (b)

Fig. 8.6 Variation of seismic passive earth pressure coefficient for failure wedge in 2 layers with H_1:H_2=2:3 and ϕ_1:ϕ_2=4:5 under static conditions for (a) ϕ=25° and (b) ϕ=35°

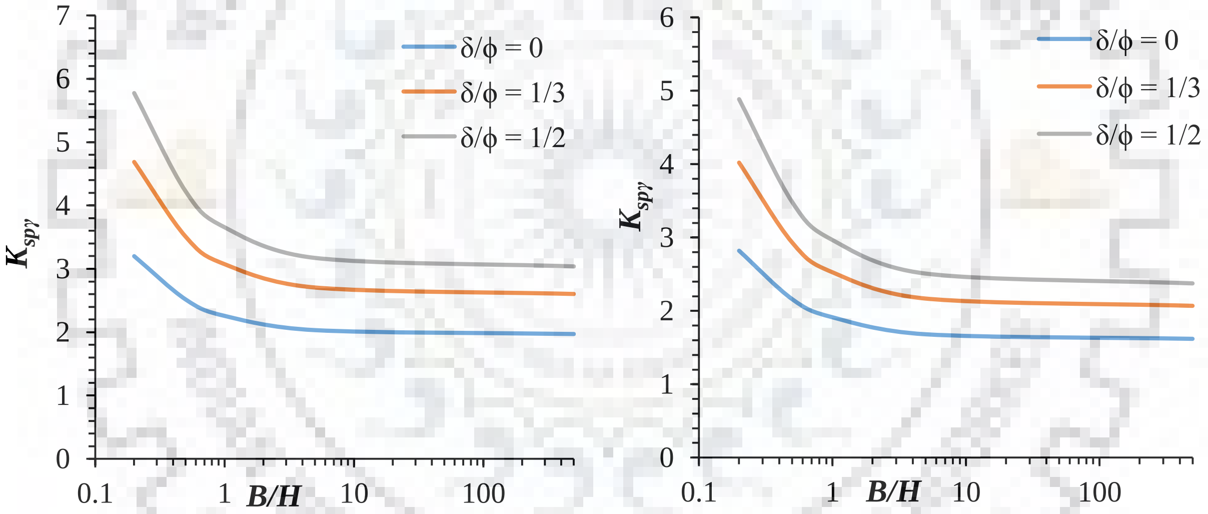

(a) (b)

Fig. 8.7 Variation of seismic passive earth pressure coefficient for failure wedge in 2-layers with ϕ_2=30°, k_v=0 with H_1:H_2=2:3 and ϕ_1:ϕ_2=4:5 for (a) k_h=0.1 and (b) k_h=0.2

Similarly, Fig. 8.10 reflects the volume change of failure wedge with change in soil-wall friction angle and vertical seismic acceleration coefficient for 3-layered soil with H_1:H_2:H_3=1:2:3 and ϕ_1:ϕ_2:ϕ_3=8:9:10 for ϕ_3=35° and k_h=0.1. It can be observed that strength is derived from larger volume of soil as soil-wall friction angle increases. The extent of failure wedge increases by 12.75% and 24.53% as δ increases from 0 to ϕ/3 and ϕ/2 respectively at top of soil strata. These increases in magnitude are 14.44% and 28.66% and 16.95% and 37.77% at top of 2nd and 3rd layer respectively, for the variation of δ as mentioned earlier.

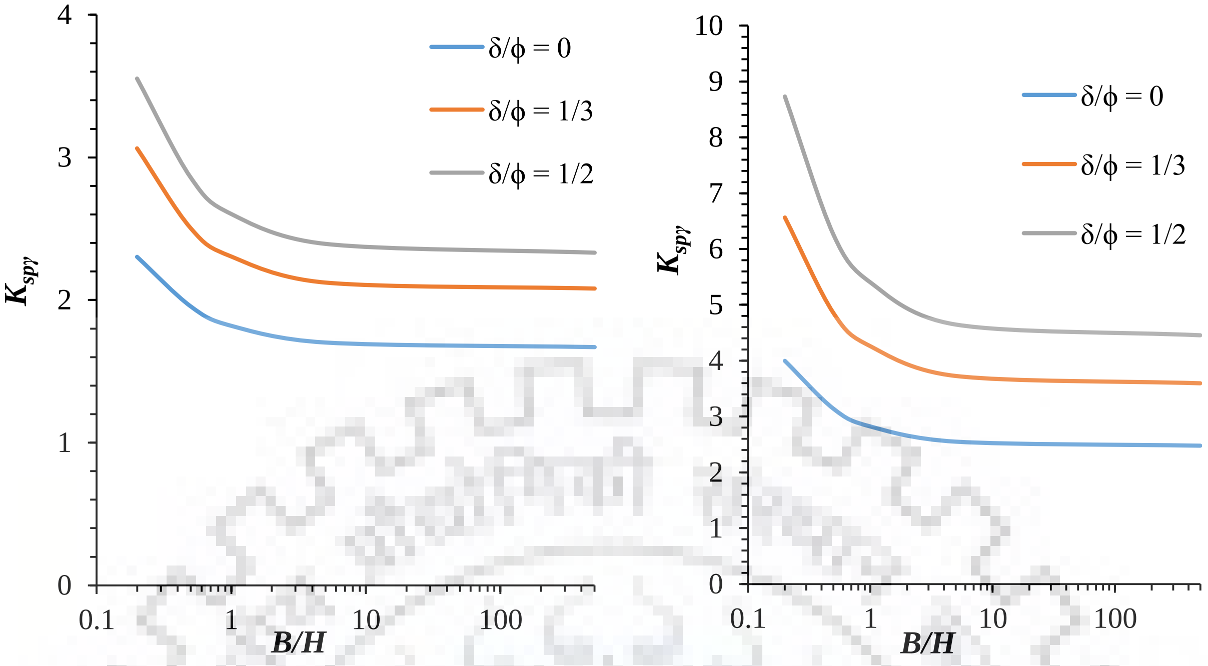

(a) (b)

Fig. 8.8 Variation of seismic passive earth pressure coefficient for failure wedge in 3 layers for H_1:H_2:H_3=1:2:3 with ϕ_1:ϕ_2:ϕ_3=3:4:5 under static conditions for (a) ϕ_3=25° and (b) ϕ_3=35°

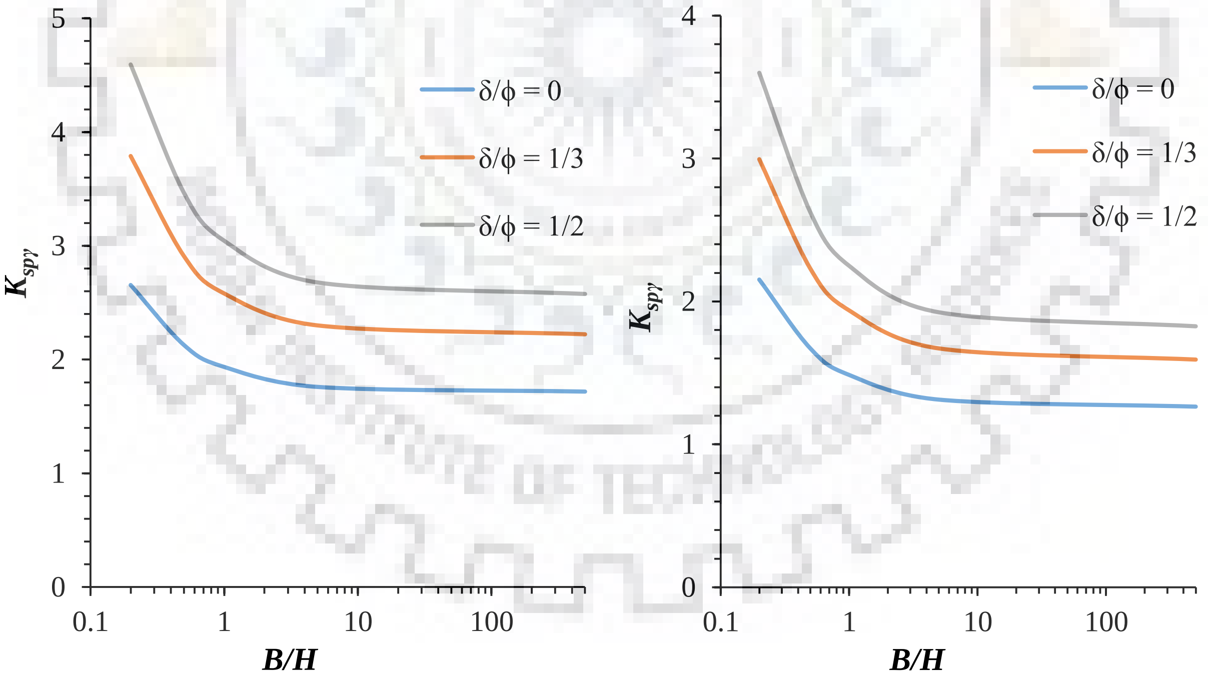

(a) (b)

Fig. 8.9 Variation of seismic passive earth pressure coefficient for failure wedge in 3 layers with ϕ=30°, k_v=0 for H_1:H_2:H_3=1:2:3 with ϕ_1: ϕ_2: ϕ_3=3:4:5 for (a) k_h=0.1 and (b) k_h=0.2

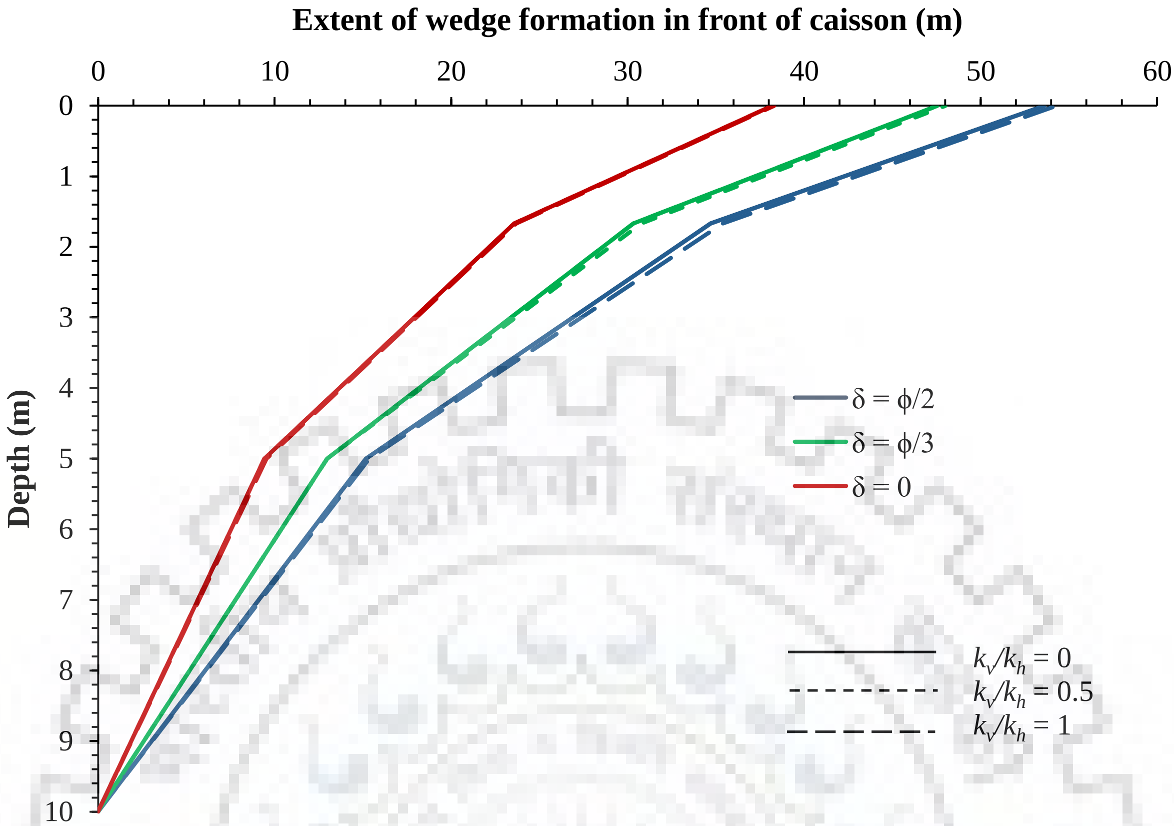

Fig. 8.10 Extent of failure wedge formation in front of caisson for varying soil-wall friction angle

8.4.2 Effect of soil-soil friction angle (ϕ)

Soil-soil friction angle (ϕ) has the same incremental effect on seismic passive earth pressure coefficient as soil-wall friction angle. Fig. 8.11 to Fig. 8.16 depict the variation of $K_{sp\gamma}$ with change in ϕ for different input parameters. For k_h=0.1, k_v/k_h=0.5, δ/ϕ=1/3 and B/H=1, the seismic passive earth pressure coefficient increases by 40.6% and 105.95% as ϕ increases from 25° to 30° and 35° respectively for failure wedge lying entirely in single layer. For failure wedge extending up to 2 layers with H_1:H_2=2:3 and ϕ_1:ϕ_2=4:5, the increase in magnitude of $K_{sp\gamma}$ for the above-mentioned increment of ϕ_2 is 39.23% and 98.56% respectively. The increment for 3-layered soil is much more violent as the increase in $K_{sp\gamma}$ magnitude is 117.51% and 229.29% respectively for soil profile with H_1:H_2:H_3=1:2:3 and ϕ_1: ϕ_2: ϕ_3=3:4:5. This high sensitivity is observed because of steep decline in $K_{sp\gamma}$ value for ϕ_3=25° as the soil friction angle in top layer reduces to 15°. Fig. 8.17 shows variation of extent of failure wedge in front of caisson lying in 3-layered soil for different soil friction angles for H_1:H_2:H_3=1:2:3 and ϕ_1:ϕ_2:ϕ_3=8:9:10, ϕ_3=35° under static condition.

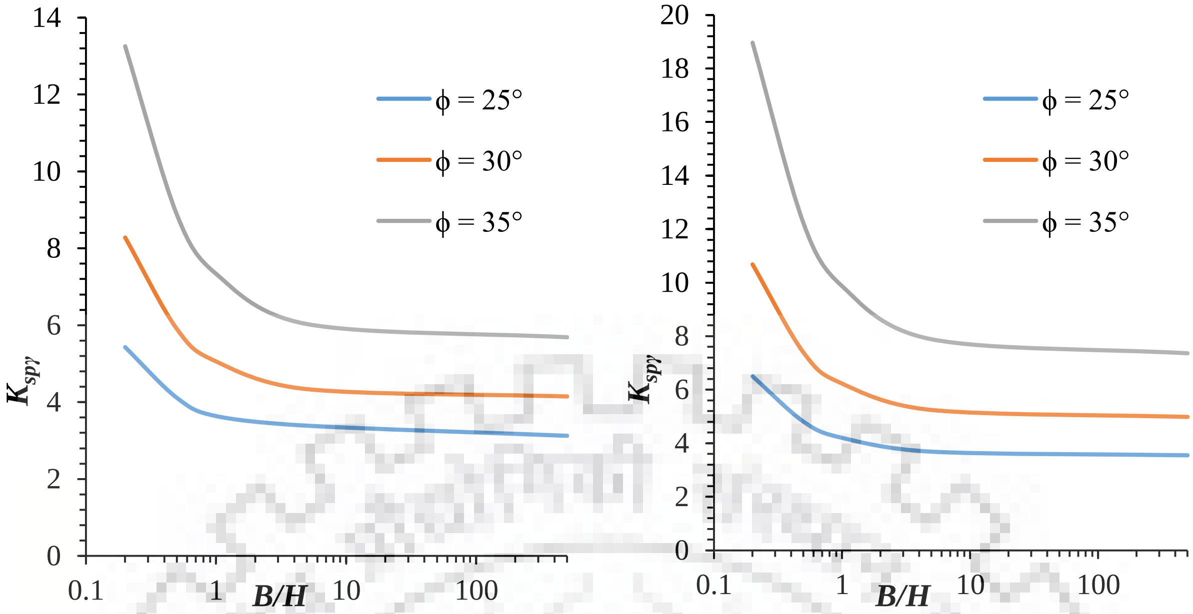

(a) (b)

Fig. 8.11 Variation of seismic passive earth pressure coefficient for failure wedge in single layer under static conditions for (a) $\delta=\phi/3$ and (b) $\delta=\phi/2$

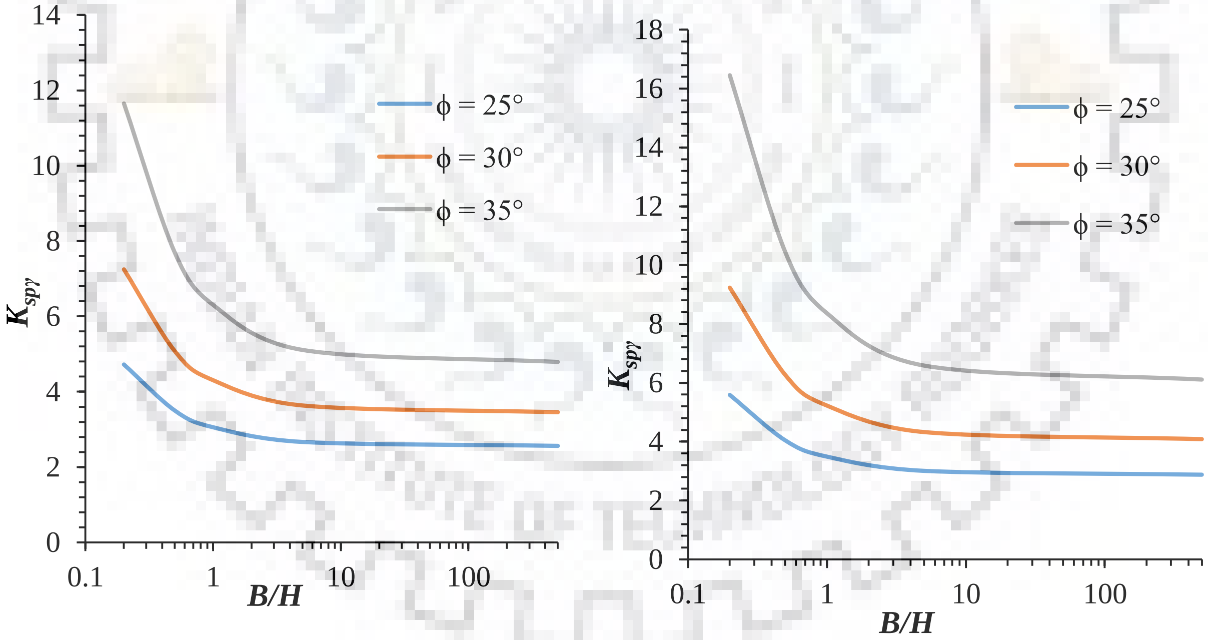

(a) (b)

Fig. 8.12 Variation of seismic passive earth pressure coefficient for failure wedge in single layer for k_h=0.1, k_v/k_h=0.5 for (a) $\delta=\phi/3$ and (b) $\delta=\phi/2$

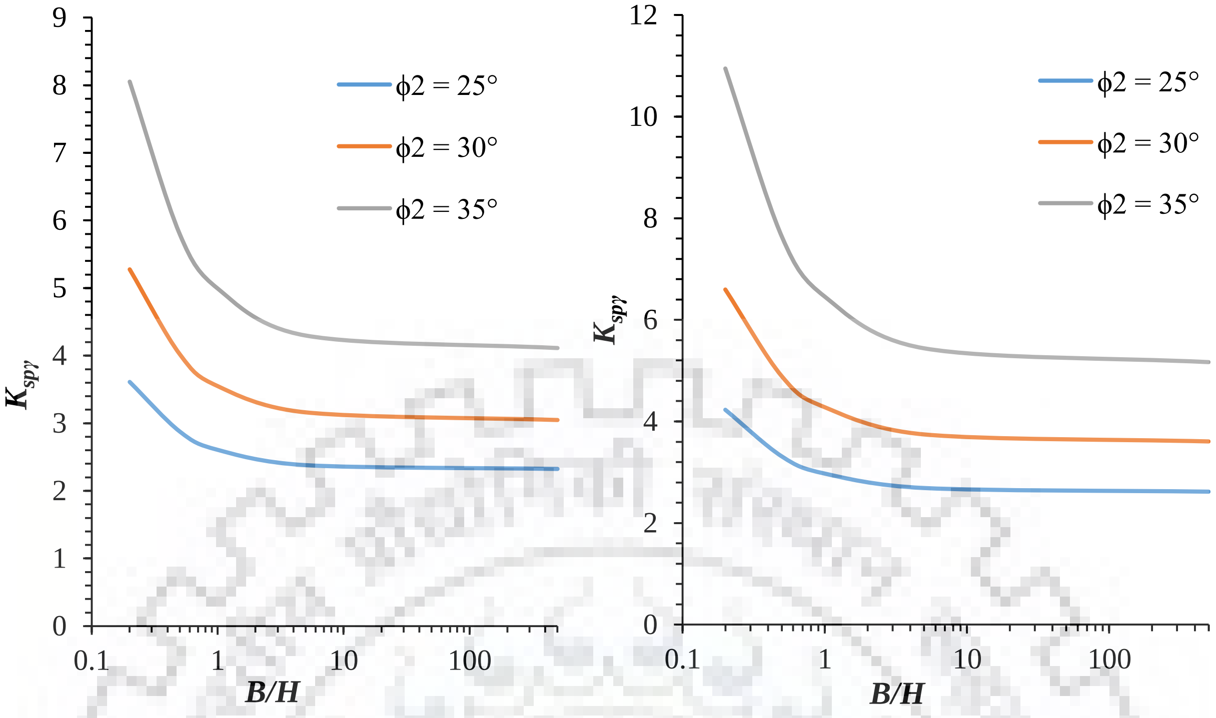

(a) (b)

Fig. 8.13 Variation of seismic passive earth pressure coefficient for failure wedge in 2 layers with H_1:H_2=2:3 and ϕ_1:ϕ_2=4:5 under static conditions for (a) $\delta=\phi/3$ and (b) $\delta=\phi/2$

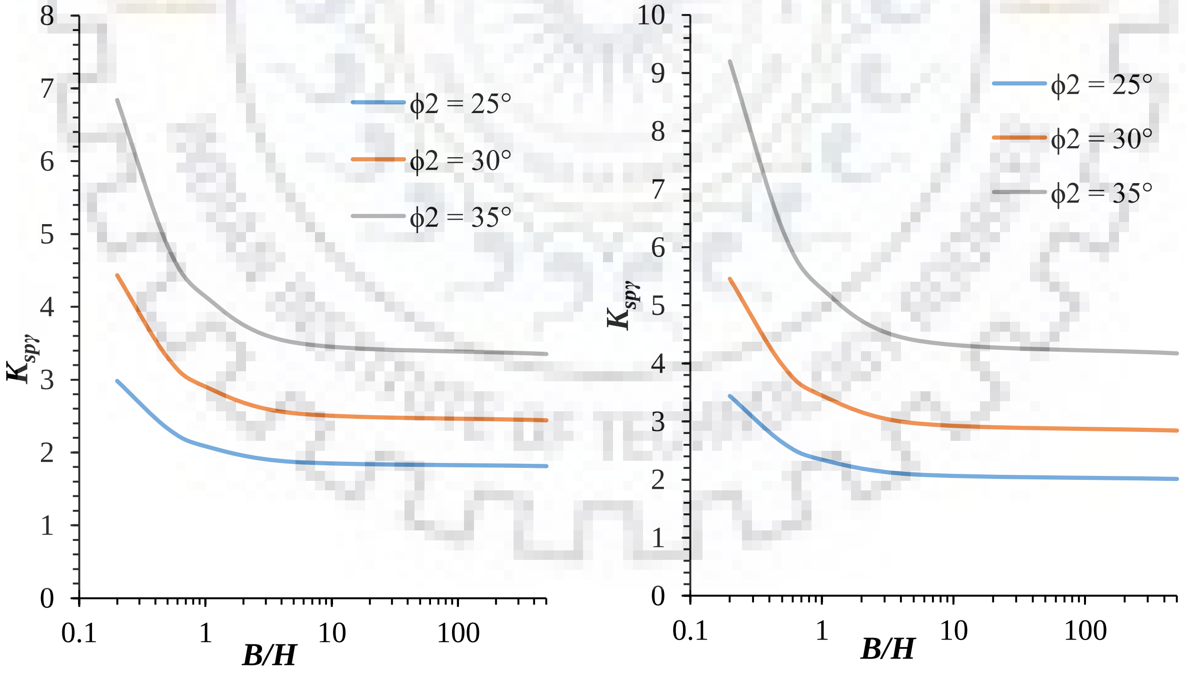

(a) (b)

Fig. 8.14 Variation of seismic passive earth pressure coefficient for failure wedge in 2 layers with k_h=0.1, k_v/k_h=0.5 with H_1:H_2=2:3 and ϕ_1:ϕ_2=4:5 for (a) $\delta=\phi/3$ and (b) $\delta=\phi/2$

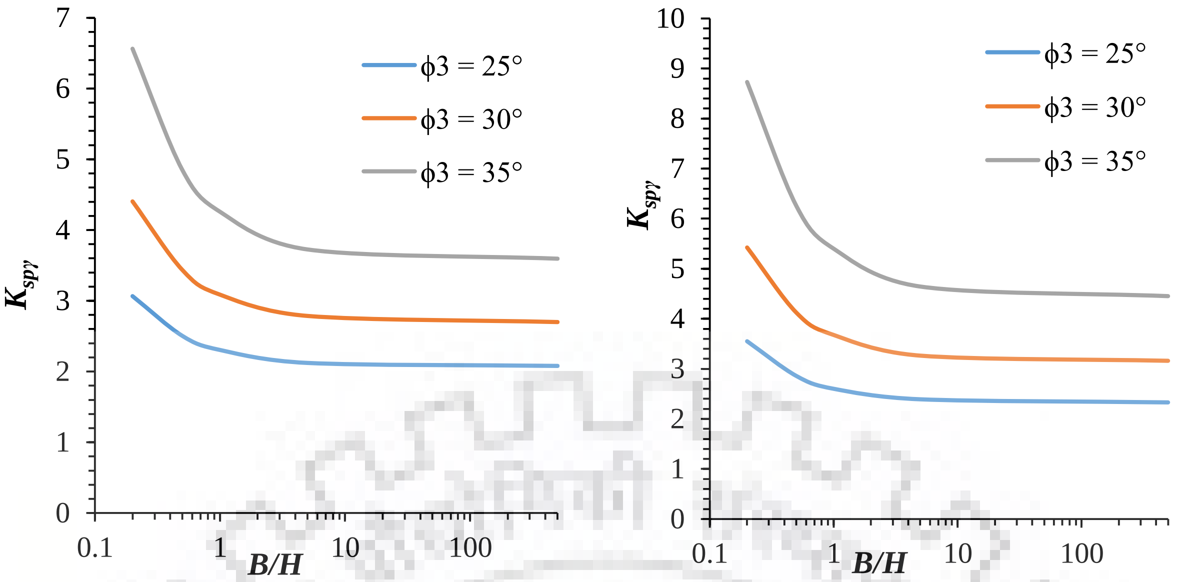

(a) (b)

Fig. 8.15 Variation of seismic passive earth pressure coefficient for failure wedge in 3 layers under static conditions for H_1:H_2:H_3=1:2:3, ϕ_1: ϕ_2: ϕ_3=3:4:5 for (a) $\delta=\phi/3$ and (b) $\delta=\phi/2$

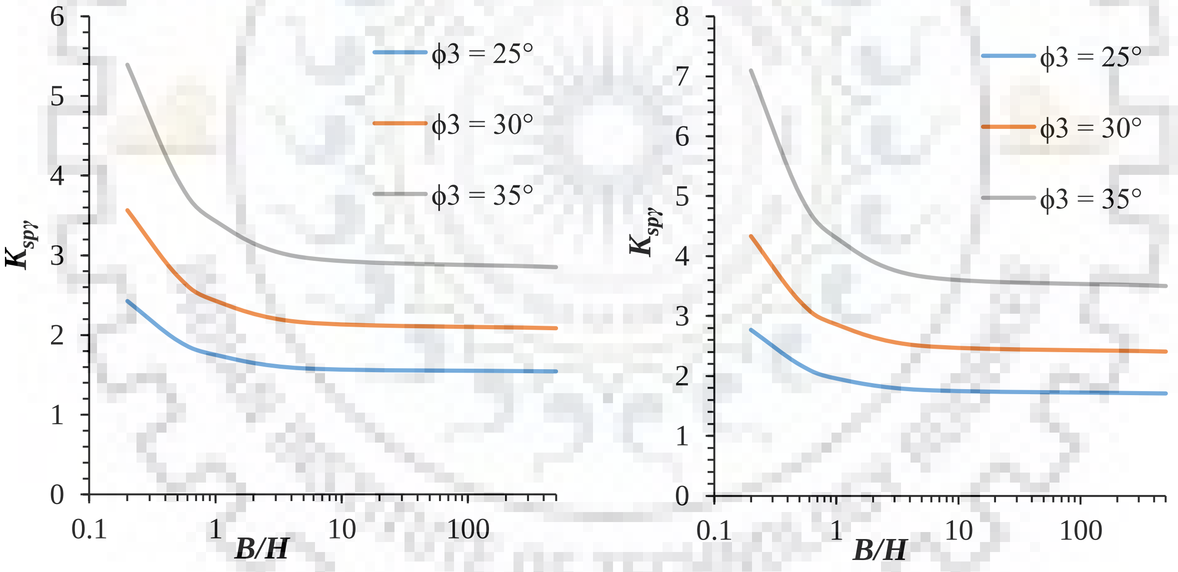

(a) (b)

Fig. 8.16 Variation of seismic passive earth pressure coefficient for failure wedge in 3 layers with k_h=0.1, k_v/k_h=0.5 for H_1:H_2:H_3=1:2:3, ϕ_1: ϕ_2: ϕ_3=3:4:5 for (a) $\delta=\phi/3$ and (b) $\delta=\phi/2$

It can again be observed that larger volume of soil contributes to provide passive resistance as soil-soil friction angle increases. The extent of failure wedge increases by 4.52% and 10.26% as ϕ_3 increases from 25° to 30° and 35° respectively at top of soil strata. These increases in magnitude are 9.53% and 20.15% respectively at top of 2nd layer and 16.77% and 34.16% respectively at the top of 3rd layer.

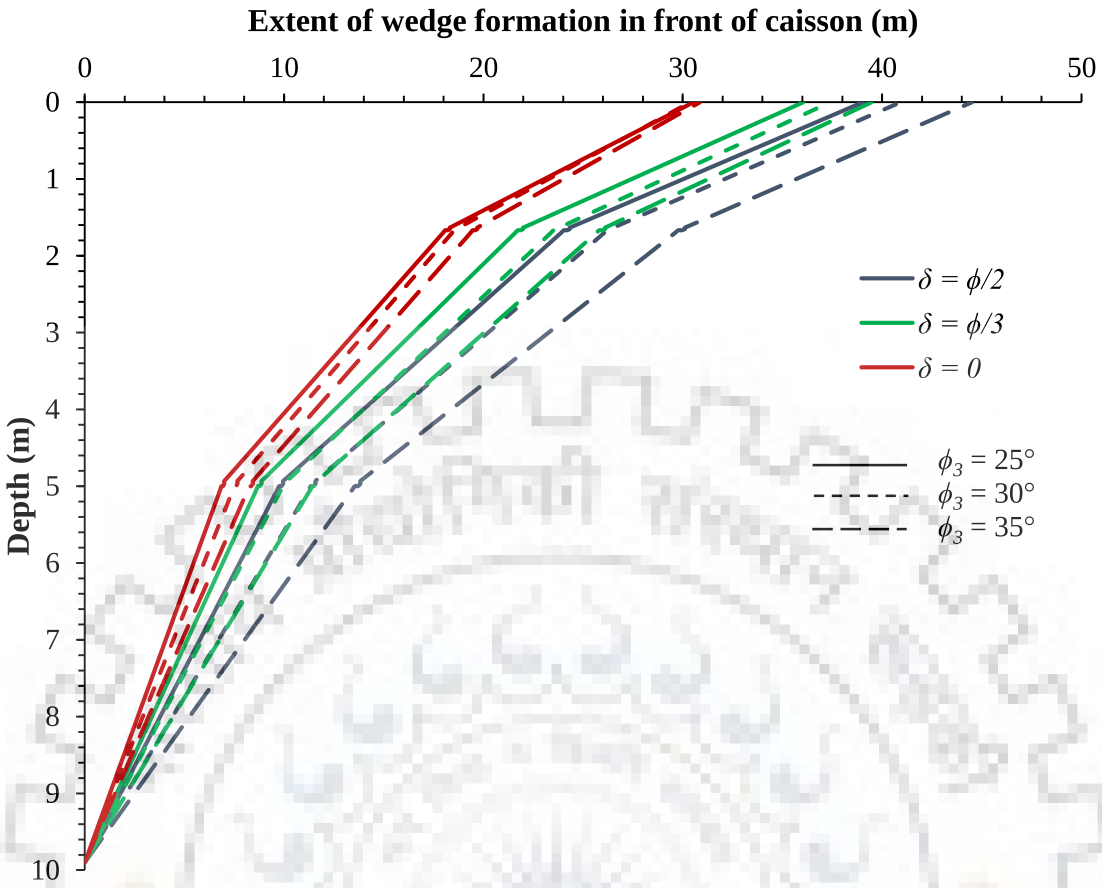

Fig. 8.17 Extent of failure wedge formation in front of caisson for varying soil-soil friction angle under static conditions

8.4.3 *Effect of seismic acceleration coefficients (k_h and k_v)*

The seismic acceleration coefficients dictate the magnitude of seismic inertial forces acting on the failure wedge at any location. In the current study, modified pseudo-dynamic method has been employed to determine acceleration profile in different layers based on the magnitudes of primary and shear wave velocity, base acceleration amplitude, damping ratio and normalized frequency. The seismic inertial forces are directly proportional to the seismic acceleration coefficients. Therefore, as the seismic acceleration coefficients increases, net resistive forces decreases and seismic passive earth pressure coefficient decreases. Fig. 8.18 to Fig. 8.23 depict the variation of seismic passive earth pressure coefficient with horizontal and vertical seismic acceleration coefficients (k_h and k_v respectively). It can be observed by merely a glance to Fig. 8.18 and Fig. 8.19 that $K_{sp\gamma}$ is much more sensitive towards k_h than k_v. It is found that seismic passive earth pressure coefficient diminishes by 20.12% and 40.72% as k_h increases from 0 to 0.1 and 0.2 respectively for ϕ=35°, δ/ϕ=1/2, k_v=k_h, B/H=1 when failure wedge is formed in homogeneous soil. For same set of soil properties and caisson geometry, when k_v/k_h is increased from 0 to 0.5 and 1 for k_h=0.1, the percentage reduction in $K_{sp\gamma}$ is determined as 5.47% and 10.92% respectively which suggests that k_h is a more dominant parameter than k_v during seismic analysis of caissons.

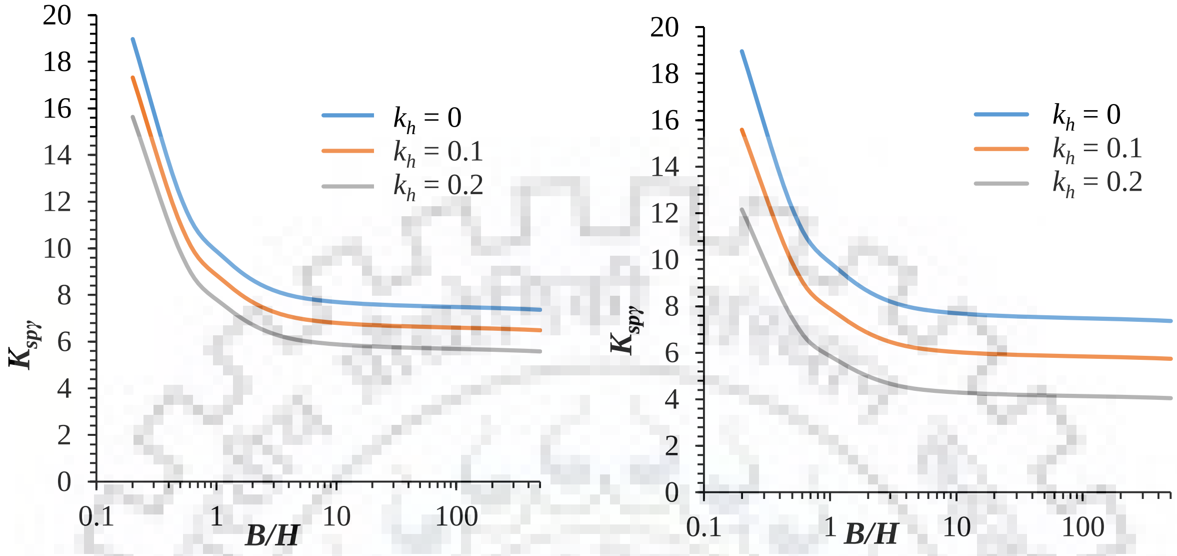

(a) (b)

Fig. 8.18 Variation of seismic passive earth pressure coefficient with k_h for failure wedge in single layer for ϕ=35°, δ/ϕ=1/2 and (a) k_v=0 and (b) k_v=k_h

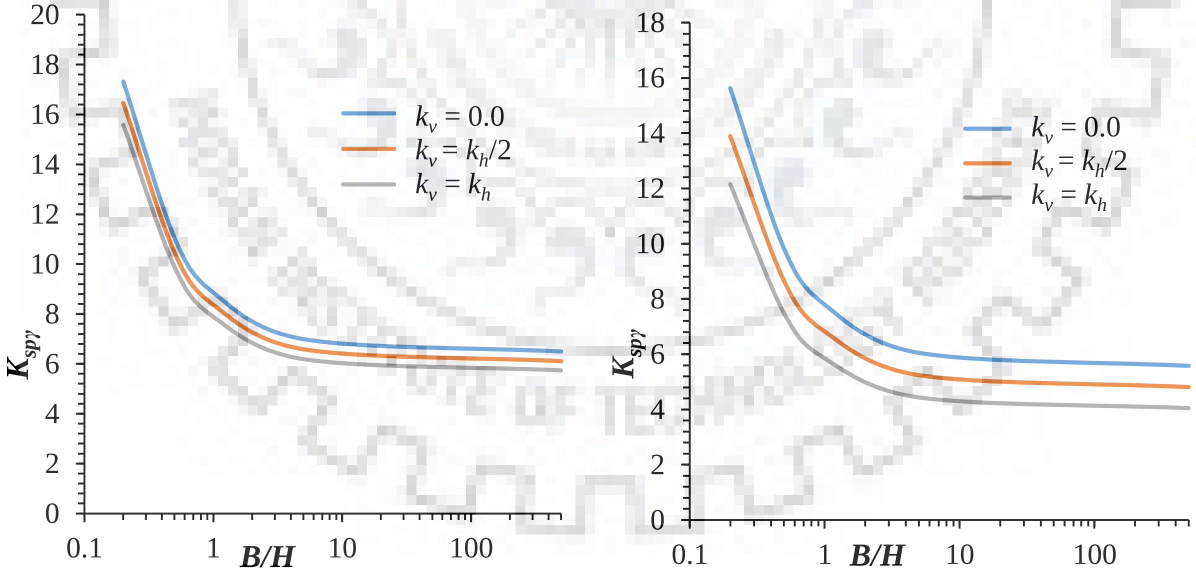

(a) (b)

Fig. 8.19 Variation of seismic passive earth pressure coefficient with k_v for failure wedge in single layer for ϕ=35°, δ/ϕ=1/2 and (a) k_h=0.1 and (b) k_h=0.2

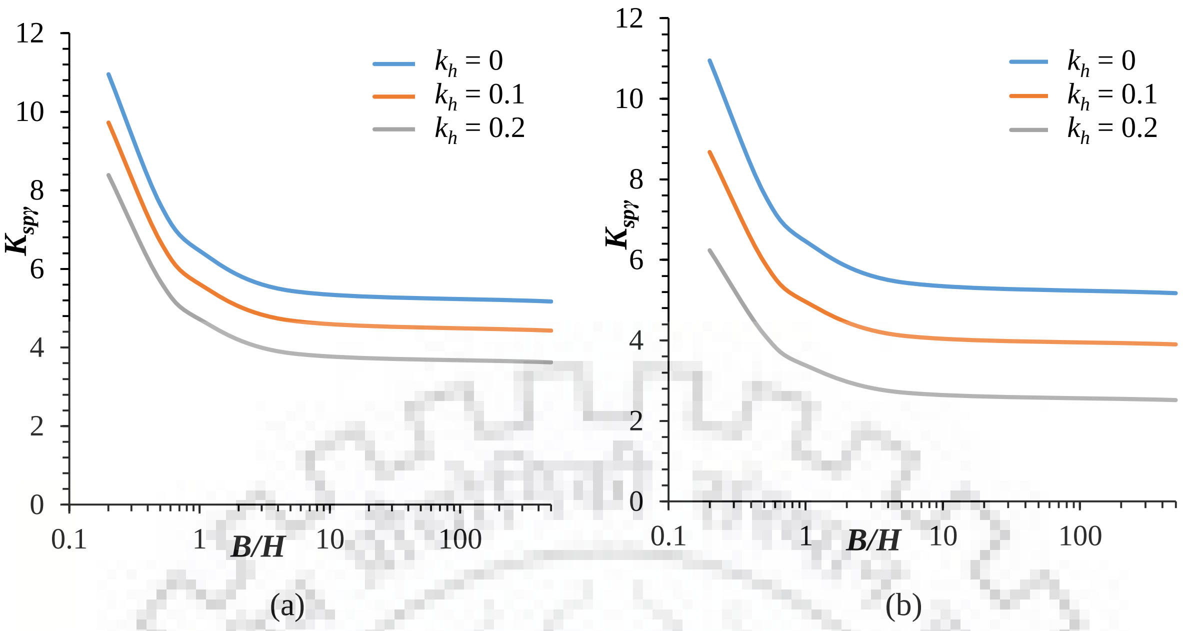

Fig. 8.20 Variation of seismic passive earth pressure coefficient with k_h for failure wedge in 2 layers with H_1:H_2=2:3 and ϕ_1:ϕ_2=4:5 for ϕ=35°, δ/ϕ=1/2 and (a) k_v=0 and (b) k_v=k_h

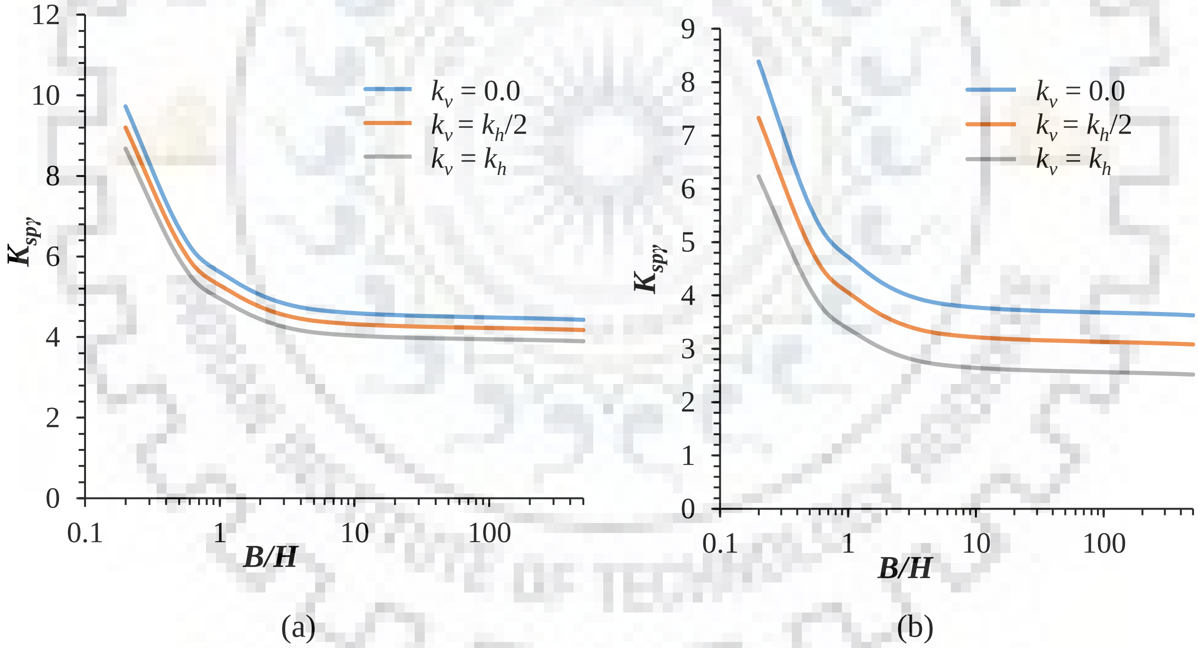

Fig. 8.21 Variation of seismic passive earth pressure coefficient with k_v for failure wedge in 2 layers with H_1:H_2=2:3 and ϕ_1:ϕ_2=4:5 for ϕ=35°, δ/ϕ=1/2 and (a) k_h=0.1 and (b) k_h=0.2

For 2-layered failure wedge, the reduction in $K_{sp\gamma}$ when k_h increases from 0 to 0.1 and 0.2 is 13.13% and 26.93% respectively for ϕ=35°, δ/ϕ=1/2, k_v=0 and B/H=1. The reduction is 5.81% and 11.62% when k_v/k_h increases from 0 to 0.5 and 1 respectively for same of input parameters and k_h=0.1. The decrease for 3-layered failure wedge is 15.22% and 32.38% for increasing k_h and 6.07% and 11.79% respectively for increasing k_v for the input parameters mentioned for 2-layered failure wedge. This suggests that as the number of layer increases, the sensitivity of $K_{sp\gamma}$ towards k_h and k_v also increases. Fig. 8.10 illustrates that extent of failure wedge in front of caisson is roughly insensitive to k_v.

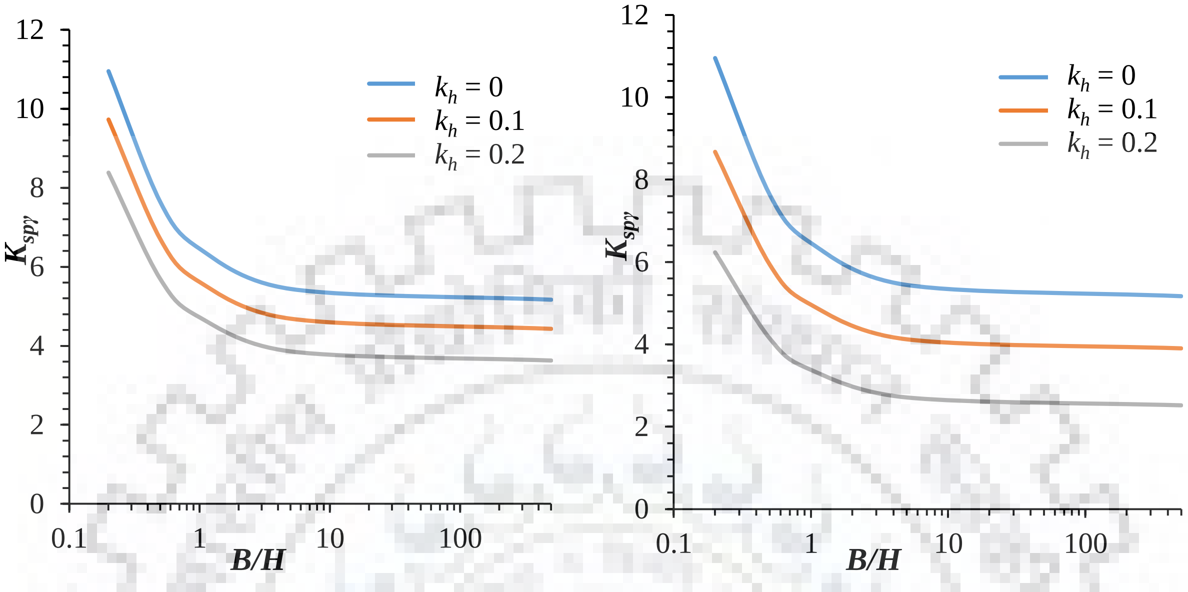

(a) (b)

Fig. 8.22 Variation of seismic passive earth pressure coefficient with k_h for failure wedge in 3 layers for H_1:H_2:H_3=1:2:3, ϕ_1: ϕ_2: ϕ_3=3:4:5 with ϕ_3=35°, δ/ϕ=1/2 and (a) k_v=0 and (b) k_v=k_h

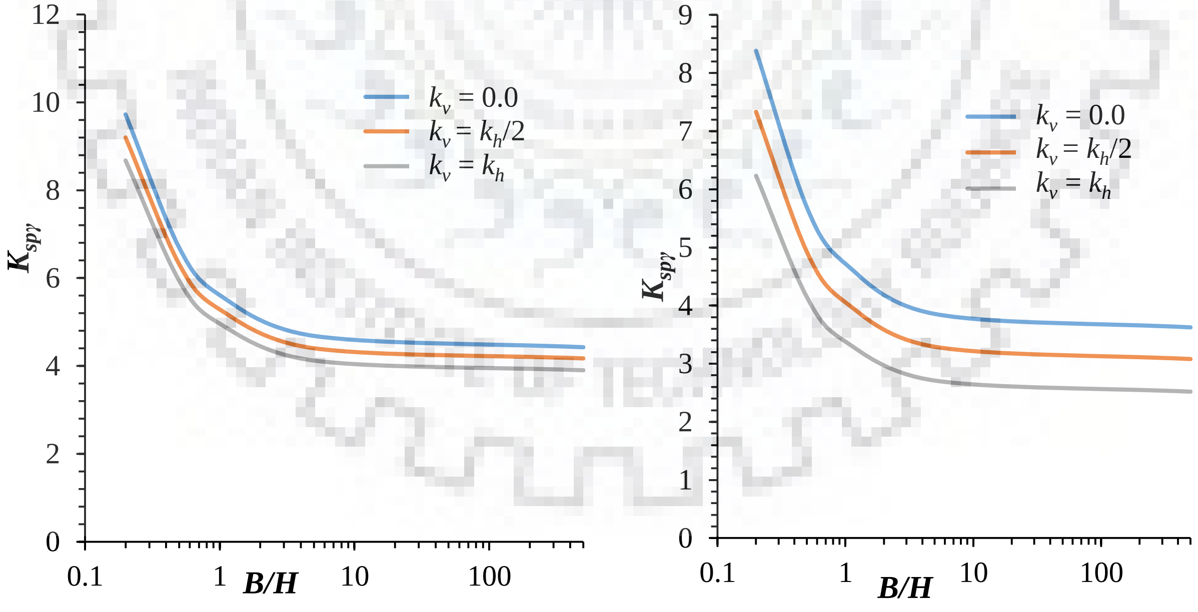

(a) (b)

Fig. 8.23 Variation of seismic passive earth pressure coefficient with k_v for failure wedge in 3 layers with H_1:H_2:H_3=1:2:3, ϕ_1: ϕ_2: ϕ_3=3:4:5 for ϕ=35°, δ/ϕ=1/2 and (a) k_h=0.1 and (b) k_h=0.2

Larger volume of soil falls in the failure wedge as the magnitude of k_h increases as is evident from Fig. 8.24 which suggests that strength from larger volume of wedge is mobilized to counter the horizontal seismic inertial force. The extent of failure wedge increases by 14.17% and 35.71% as k_h increases from 0 to 0.1 and 0.2 respectively at top of soil strata for ϕ=35°, δ/ϕ=1/2 and k_v=0. These increases in magnitude are 10.15% and 25.47% respectively at top of 2nd layer and 6.5% and 15.21% respectively at the top of 3rd layer. The increasing magnitude of volume suggests that volume of soil failing at top is increasing at accelerated rate owing to amplification of acceleration amplitude as the earthquake waves move upward.

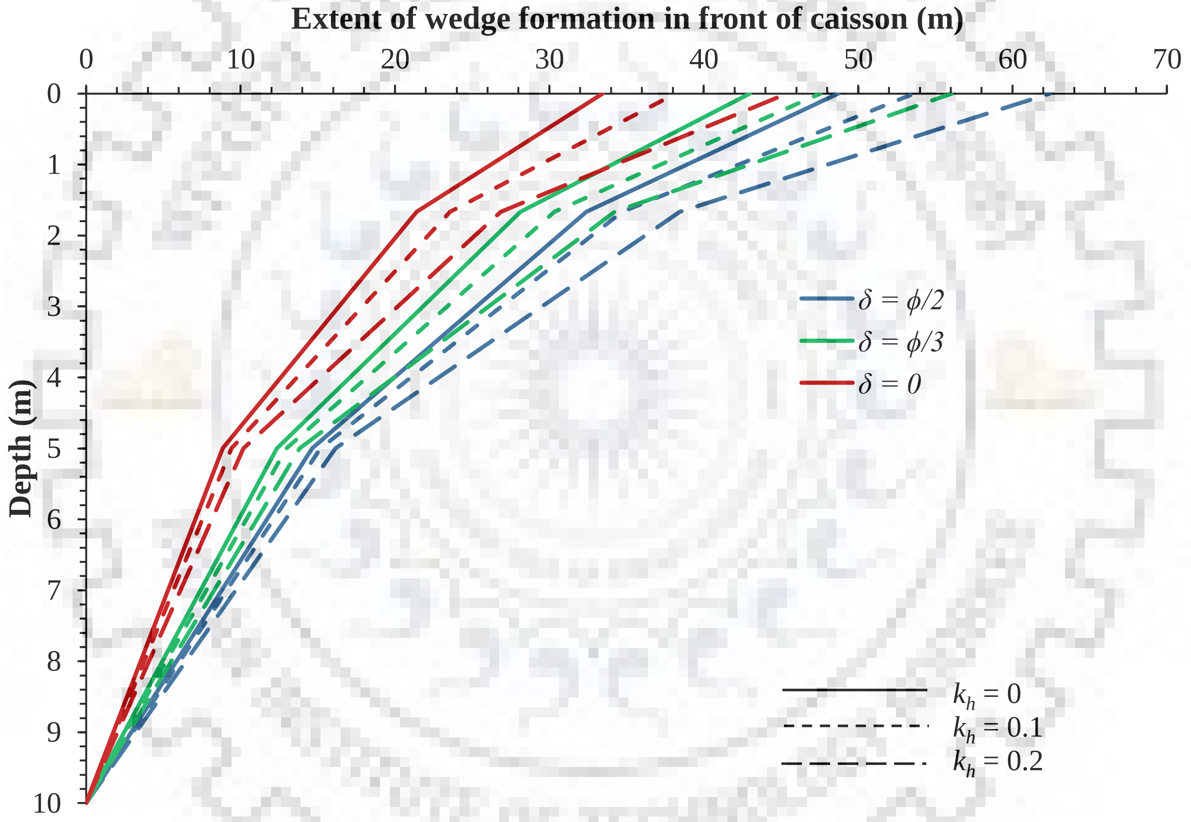

Fig. 8.24 Extent of failure wedge formation in front of caisson for varying horizontal seismic acceleration coefficient

8.4.4 Effect of submergence of soil and excess pore pressure ratio (r_u)

Presence of pore water reduces the shear strength of soil by development of pore water pressure. Higher the excess pore water pressure developed; more will be reduction in shear strength. Therefore, dry soil provides maximum soil resistance followed by submerged soil with free water wherein excess pore water pressure is instantaneously dissipated. In case of submerged soil with restrained water, excess pore water pressure accumulates faster than it dissipates since the mobility of pore water is very limited in this condition. Fig. 8.25 to Fig. 8.27 represent the effect of submergence of soil and excess pore water ratio on seismic passive earth pressure coefficient.

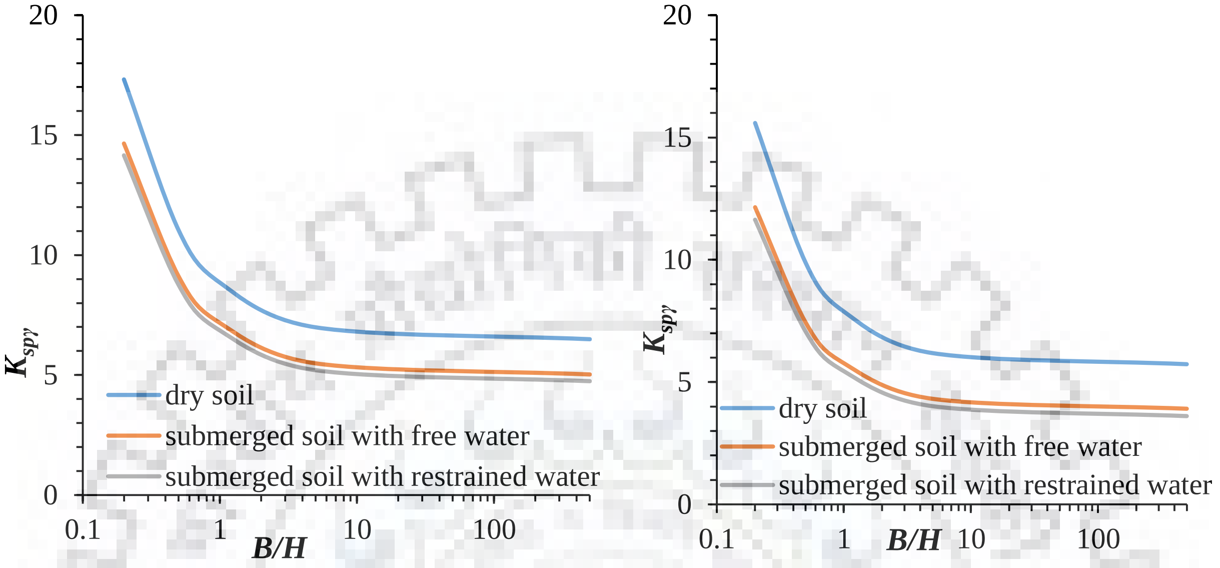

(a) (b)

Fig. 8.25 Variation of seismic passive earth pressure coefficient with soil submergence state for ϕ=35°, δ/ϕ=1/2, k_h=0.1, r_u=0.3 and (a) k_v/k_h=0 and (b) k_v/k_h=1

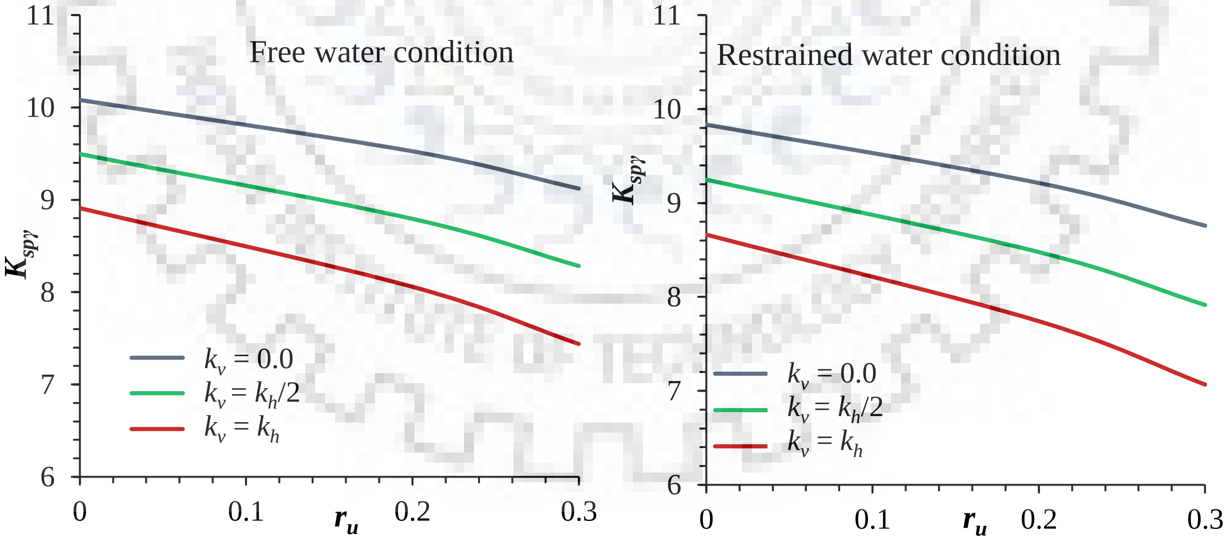

(a) (b)

Fig. 8.26 Variation of seismic passive earth pressure coefficient with excess pore water pressure ratio for ϕ=35°, δ/ϕ=1/2, k_h=0.1, B/H=0.5 for different k_v/k_h for (a) free water condition and (b) restrained water condition

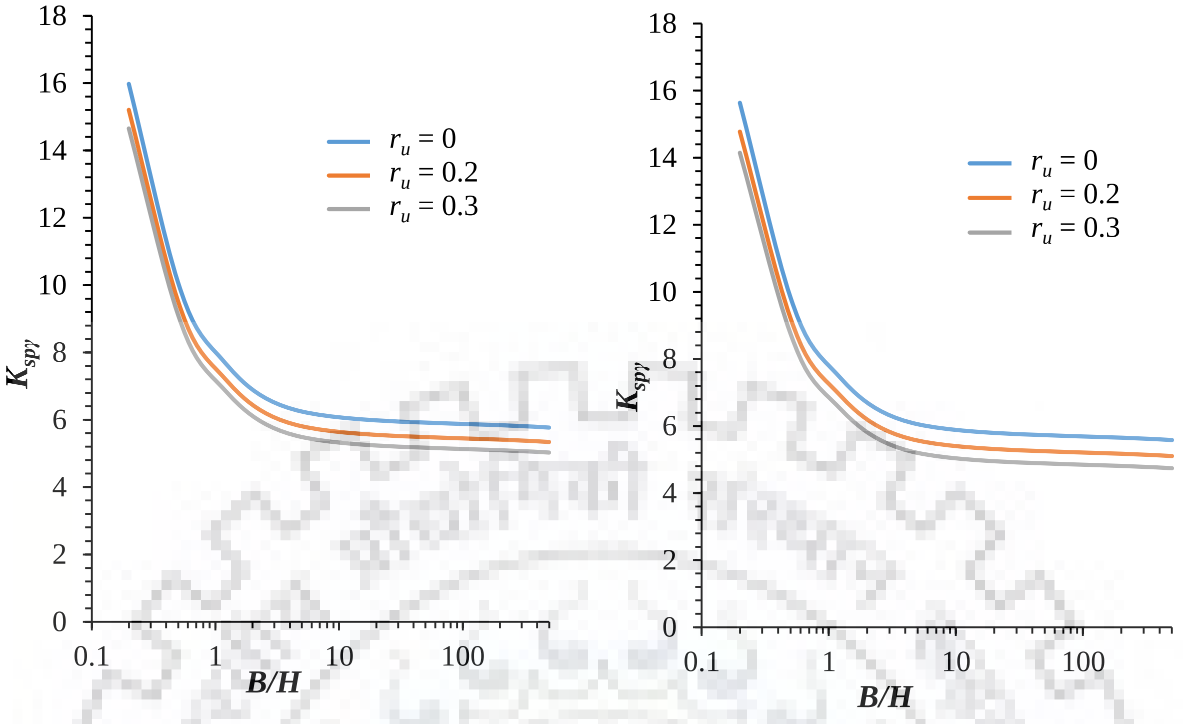

(a) (b)

Fig. 8.27 Variation of seismic passive earth pressure coefficient with ϕ=35°, δ/ϕ=1/2, k_h=0.1, for different excess pore pressure ratio for (a) free water and (b) restrained water condition

It is observed that there is a significant reduction in seismic passive earth pressure coefficient when soil changes to submerged state from dry conditions. However, the effect is mild when mobility of pore water changes from free to restrained. The percentage reduction in magnitude of $K_{sp\gamma}$ when soil changes from dry to submerged with free water and submerged with restrained water is obtained as 18.92% and 22.53% respectively for wedge in single layer with ϕ=35°, δ/ϕ=1/2, k_h=0.1, k_v=0 and B/H=1. In submerged soil, the seismic passive earth pressure coefficient also diminishes with increasing excess pore pressure ratio (r_u), which determines the extent by which effective stress decreases leading to reduction in shear strength. For k_h=0.1, k_v=k_h, ϕ=35°, δ/ϕ=1/2 and B/H=0.5, $K_{sp\gamma}$ reduces by 9.57% and 16.53% as r_u increases from 0 to 0.2 and 0.3 respectively in free water condition and 10.65% and 18.46% in restrained water condition.

The extent of failure wedge increases by 37.89% and 157.67% for submerged soil with free water condition and restrained water condition respectively, compared to dry soil at top of soil strata for ϕ=35°, δ/ϕ=1/2, k_h=0.1, k_v=0 and B/H=1. These increases in magnitude are 25.63% and 39.91% respectively, at top of 2nd layer and 9.41% and 13.93% respectively, at the top of 3rd layer as depicted in Fig. 8.28.

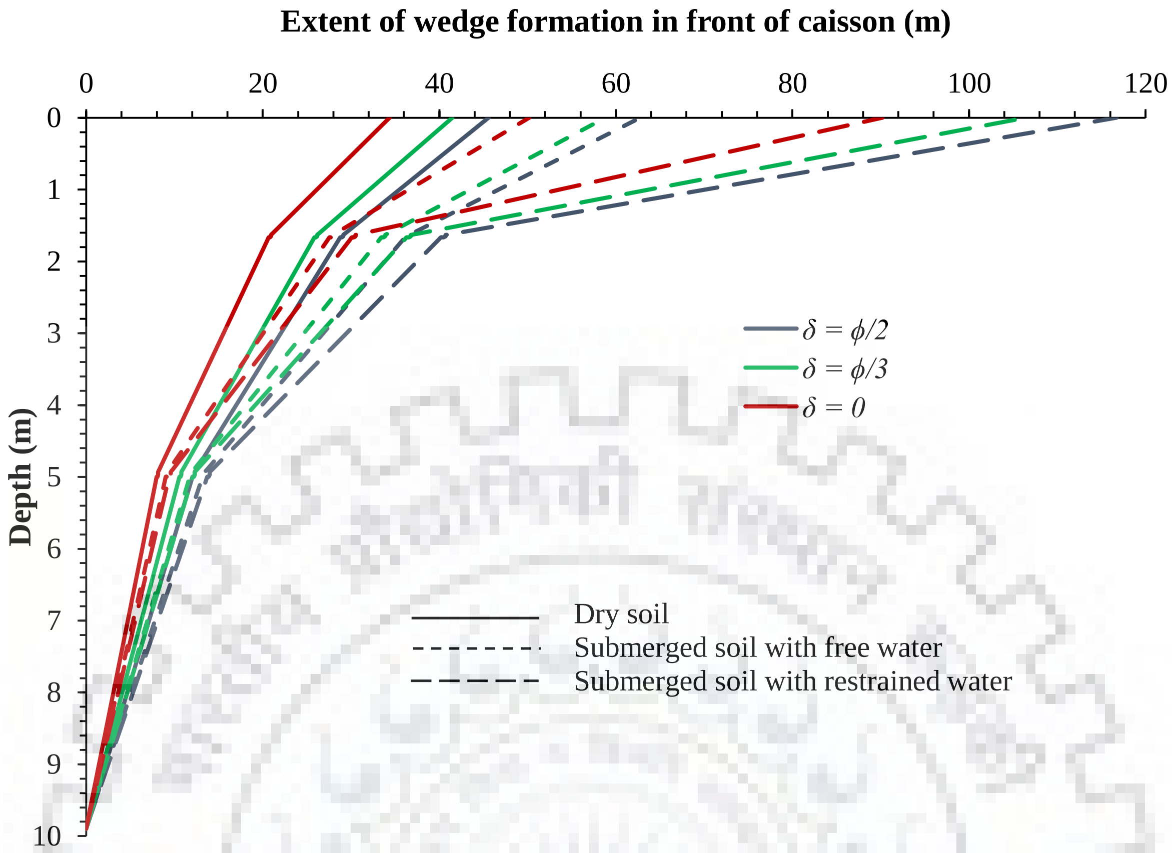

Fig. 8.28 Extent of failure wedge formation in front of caisson for different soil submergence states

Fig. 8.29 illustrates the change in failure wedge profile in vertical plane as the magnitude of excess pore pressure ratio varies. The extent of failure wedge increases by 5.26% and 11.28% when r_u increases from 0 to 0.2 and 0.3 respectively for submerged soil with free water condition at top of soil strata for ϕ=35°, δ/ϕ=1/2, k_h=0.1, k_v=0 and B/H=1. The increase in magnitude is 6.46% and 14.03% respectively at top of 2nd layer and 2.59% and 5.31% respectively at the top of 3rd layer as depicted in Fig. 8.29.

8.4.5 Effect of width of caisson (B)

The effect of increase in width of caisson is to reduce the seismic passive earth pressure coefficient. As the width of caisson increases, the volume of failure wedge per unit width of caisson decreases as seen in the previous chapter, i.e., 3D behaviour of failure wedge gradually changes into plane strain behaviour. Therefore, as the width of caisson increases, the percentage contribution of volume of failure mobilizing its strength decreases, thereby causing the seismic passive earth pressure coefficient to decrease. Fig. 8.18 to Fig. 8.23 highlight the points made above.

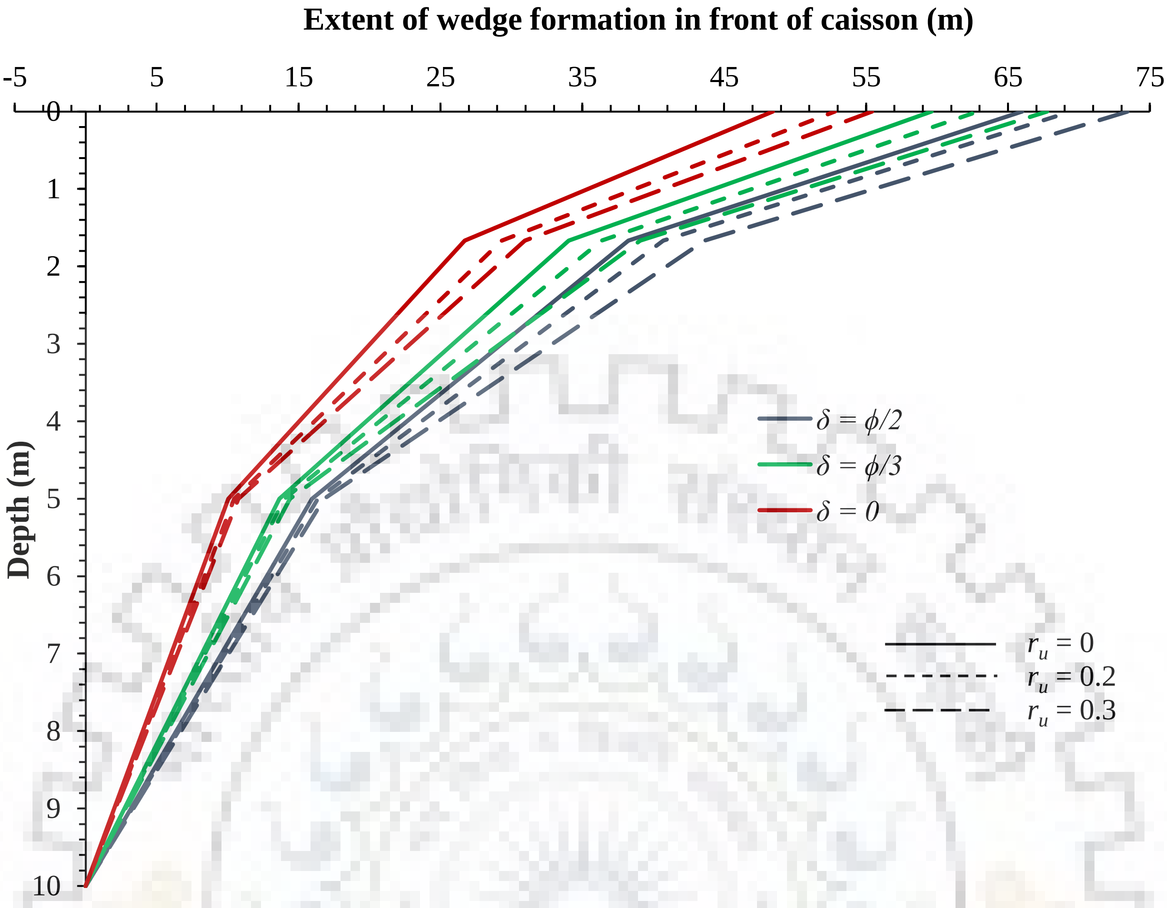

Fig. 8.29 Extent of failure wedge formation in front of caisson for different excess pore pressure ratio

It is found that seismic passive earth pressure coefficient decreases by 32.25% and 43.68% as B/H increases from 0.2 to 0.5 and 1 respectively for ϕ=30°, δ/ϕ=1/2, k_h=0.1 and k_v=k_h when failure wedge is formed in homogeneous soil. Similarly, for failure wedge extending up to 2 layers with H_1:H_2=2:3 and ϕ_1:ϕ_2=4:5, the decrease in magnitude of $K_{sp\gamma}$ for the above-mentioned increment of B/H is 27.4% and 37.43% respectively. The reduction for 3-layered soil is even milder as the decrease in $K_{sp\gamma}$ magnitude is 25.22% and 34.38% respectively for soil profile with H_1:H_2:H_3=1:2:3 and ϕ_1: ϕ_2: ϕ_3=3:4:5.

The failure wedge profile in vertical plane is also found to vary with change in width of caisson. The horizontal extent of failure wedge in front of caisson is observed to increase by 9.18% and 25.59% when B/H increases from 0.5 to 1 and 5 respectively at top of soil strata for ϕ=35°, δ/ϕ=1/2, k_h=0.1, k_v=0. The increase in magnitude is 8.39% and 22.32% respectively at top of 2nd layer and 6.28% and 13.28% respectively at the top of 3rd layer as depicted in Fig. 8.30.

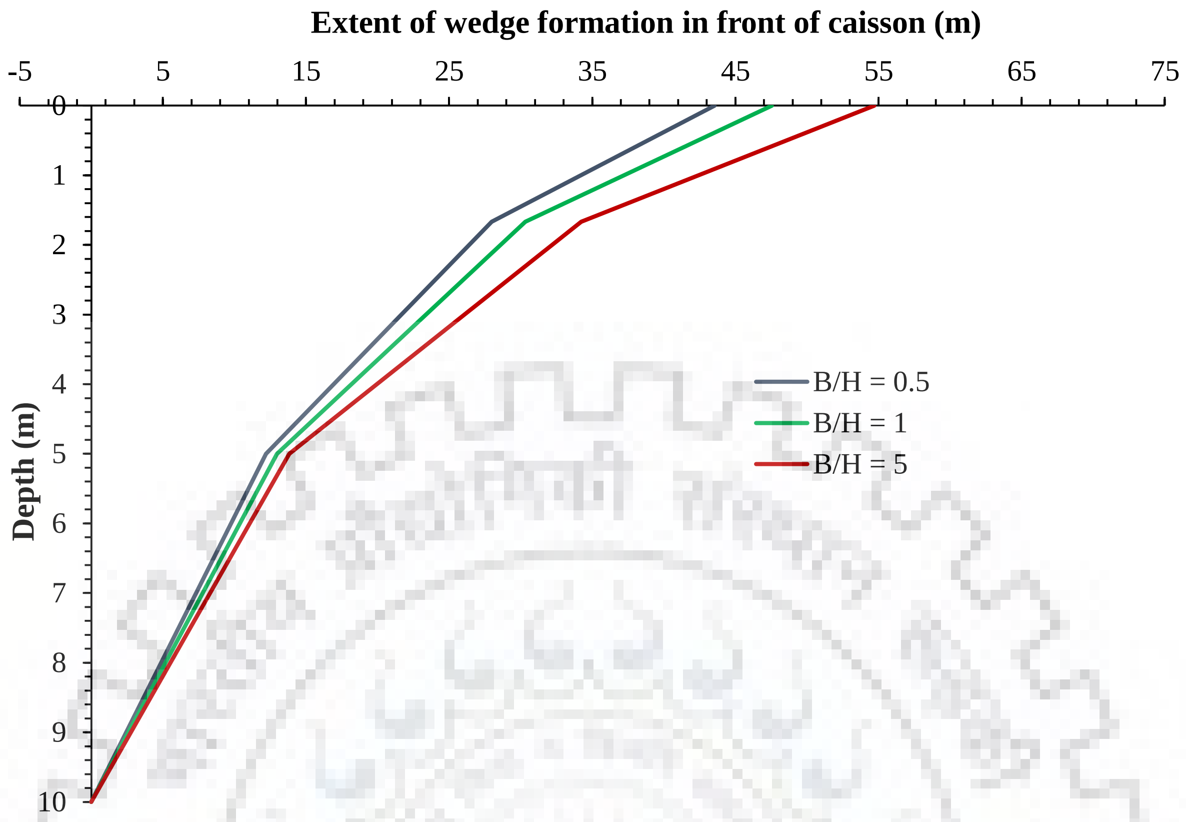

Fig. 8.30 Extent of failure wedge formation in front of caisson for different width of caisson

8.4.6 Effect of relative depth of layers

The relative depth of different layers of soil strata containing the failure wedge also has significant influence on the seismic passive earth pressure coefficient for the strata. The study has analyzed the effect of different combinations of depths of layers along with the soil friction angle in those layers on seismic passive earth pressure coefficient. Fig. 8.31 to Fig. 8.33 demonstrate the effect of relative depth and soil friction angle in different layers of the soil strata containing failure wedge. It can be seen that the magnitude of seismic passive earth pressure coefficient decreases as the number of layers in failure wedge increases. For soil friction angle of bottom layer of failure wedge equalling 30°, k_h=0.1, k_v=0 and δ=0, the seismic passive earth pressure decreases by 26.28% and 35.02% when number of layers increase from 1 to 2 and H_1/H_2 increases from 0 to 1/4 and 2/3 respectively as shown in Fig. 8.31. For 2-layered failure wedge with ϕ_1/ϕ_2=0.8 with ϕ_2=30°, k_h=0.1, k_v=0 and $\delta=\phi/2$, the seismic passive earth pressure coefficient decreases by 13.03% and 17.82% as H_1/H_2 increases from 1/4 to 2/3 and 3/2 respectively. Greater share of failure wedge depth lies in weaker soil in this condition causing the seismic passive earth pressure coefficient to decrease as H_1/H_2 increases.

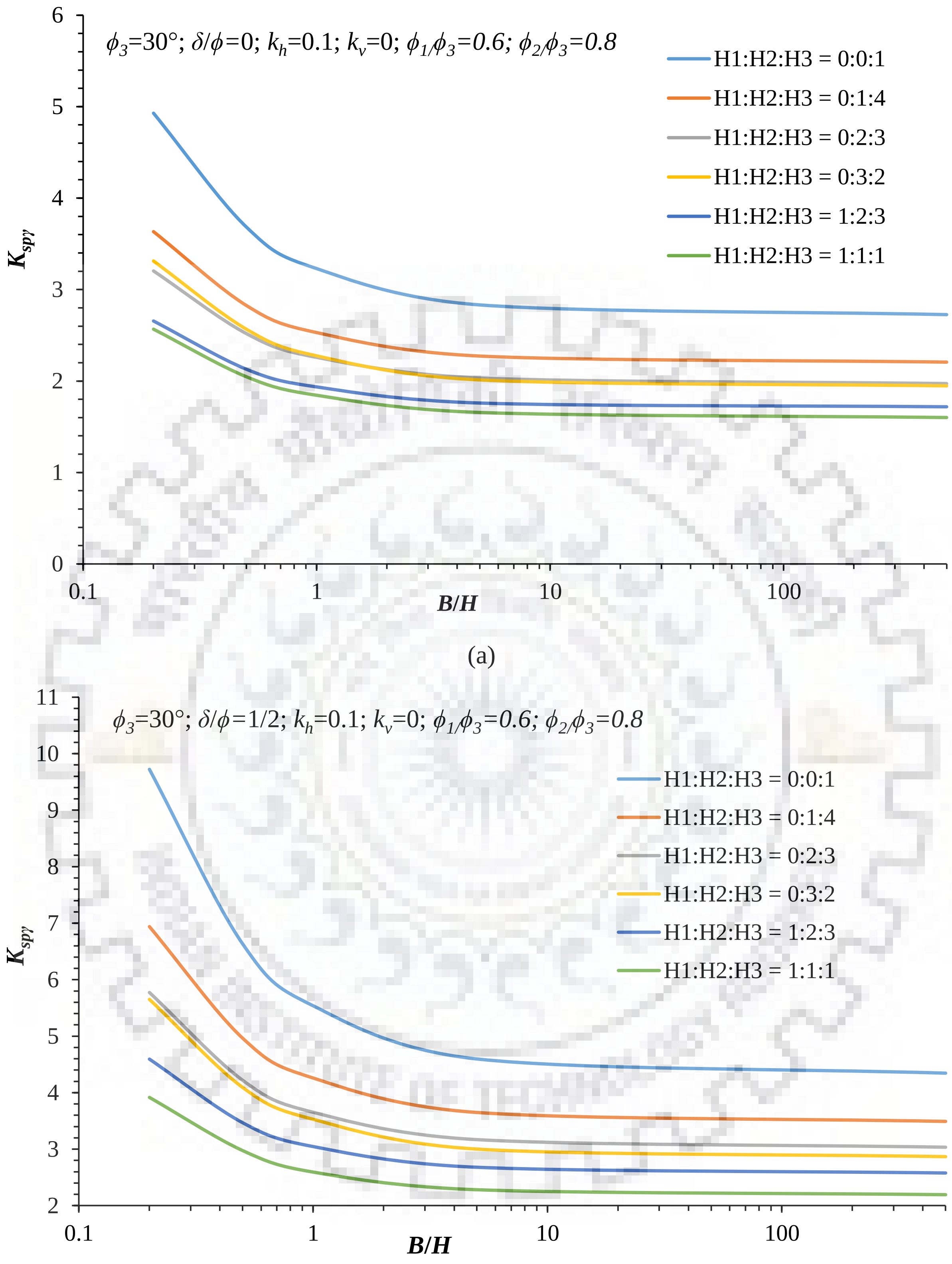

(a)

(b)

Fig. 8.31 Variation of seismic passive earth pressure coefficients for different relative depths of layers for (a) δ/ϕ=0 and (b) δ/ϕ=1/2

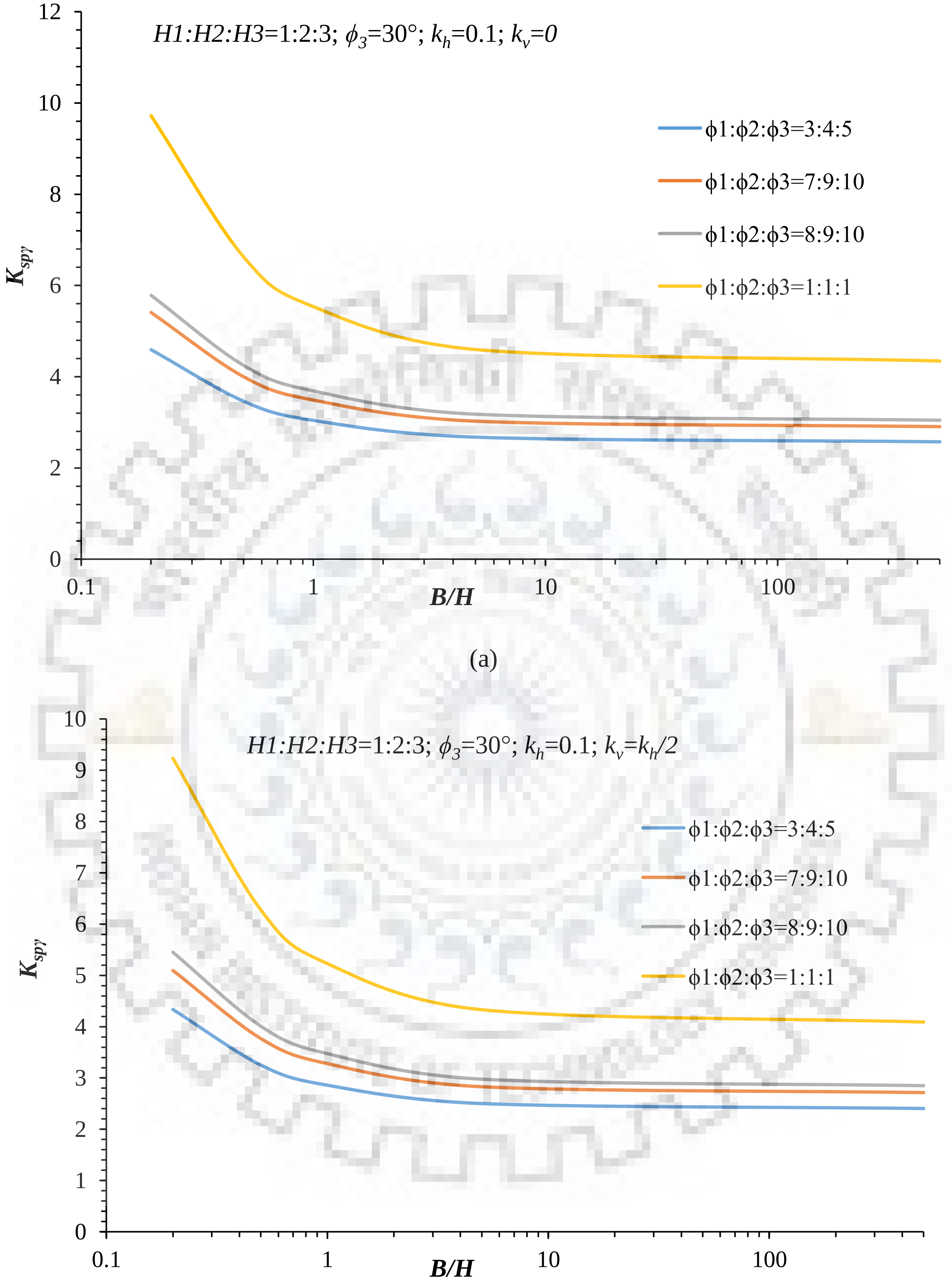

(a)

(b)

Fig. 8.32 Variation of seismic passive earth pressure coefficients for different relative soil friction angles of layers for (a) k_v=0 and (b) k_v=k_h/2

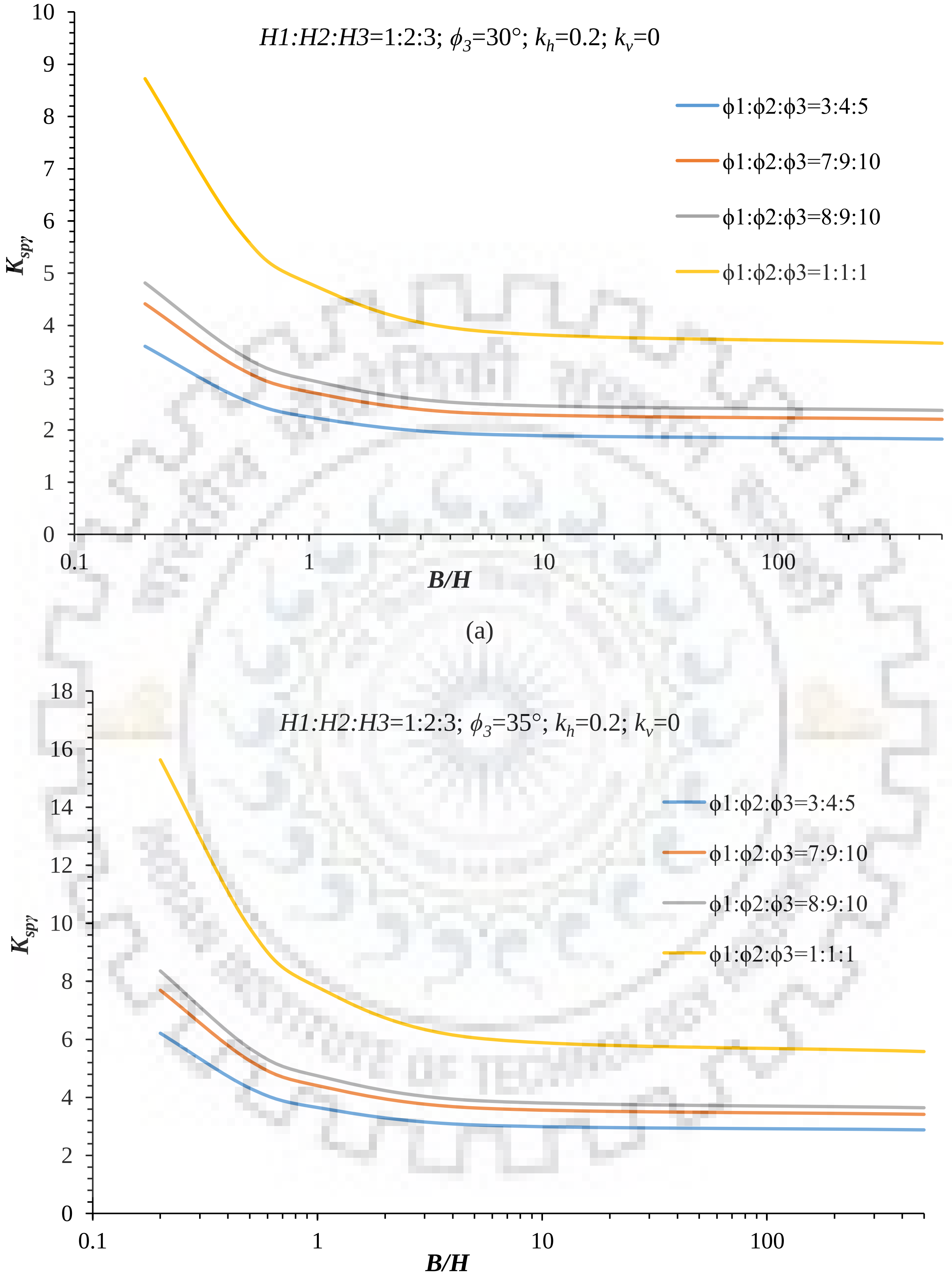

(a)

(b)

Fig. 8.33 Variation of seismic passive earth pressure coefficients for different relative soil friction angles of layers for (a) ϕ_3=30° and (b) ϕ_3=35°

It is also evident that the magnitude of seismic passive earth pressure coefficient would decrease if the magnitude of soil friction angle decreases as seen in Fig. 8.32 and Fig. 8.33. For 3-layered failure wedge with H_1:H_2:H_3=1:2:3, ϕ_3=30°, k_h=0.1, k_v=0, B/H=0.5 and $\delta=\phi/2$, the seismic passive earth pressure increases by 15.44%, 22.62% and 91.34% when ϕ_1:ϕ_2:ϕ_3 changes from 3:4:5 to 7:9:10, 8:9:10 and 1:1:1 (homogeneous soil) respectively. For ϕ_3=35°, k_h=0.2, and all other parameters remaining the same, the seismic passive earth pressure increases by 23.81%, 34.62% and 151.73% respectively for the same change in ϕ_1:ϕ_2:ϕ_3.

8.5 Summary

This chapter deals with the problem of determining seismic passive earth pressure coefficient for caisson embedded in layered cohesionless soil. The study presents formulation for computation of seismic passive earth pressure coefficient for soil strata with any number of layers. Modified pseudo-dynamic approach has been used to determine the acceleration profile using linear ground response analysis. The study has been carried out to consider caisson embedded in both dry and submerged soil depending on the permeability of the soil. Furthermore, width of structure is also considered in the study so that it can be applicable for rigid geotechnical structures for a series of widths. The effect of soil friction angle, soil-wall friction angle, seismic acceleration coefficients, excess pore pressure ratio have also been explored on the seismic passive earth pressure coefficient and vertical profile of failure wedge. Finally, the effect of relative depth of various layers and relative soil friction angle of layers on has been investigated on seismic passive earth pressure coefficient. The study should be helpful for design engineers and researchers when dealing with the problem of geotechnical structures embedded in layered soil considering dynamic soil properties.

Chapter 9

CONCLUSIONS

9.1 General

Caisson is a very important foundation system with capabilities to support wide array of loads by virtue of its huge mass and stiffness. Therefore, various aspects related to caisson which were either previously unexplored or less studied have been identified through extensive literature review. Numerical studies using finite-element method-based computer program ABAQUS has been conducted and elaborated in this thesis. The results of the numerical modelling, which show that caissons are rigid foundation systems and return the shape of failure wedge in horizontal and vertical plane, have been further used to develop theoretical model under variety of conditions to better study the response of caissons. Theoretical studies have been conducted to explore caissons in c-ϕ soil with surcharge considering 3D log-spiral failure wedge. Analysis of caissons in generalized n-layered cohesionless soil considering 3D polylinear failure wedge and using modified pseudo-dynamic method has been conducted to throw light on lesser-known aspects of caisson behaviour.

9.2 Comparison of Results from Different Theoretical Studies

Pseudo-static and modified pseudo-dynamic approaches have been used to determine seismic passive earth pressure coefficients under different conditions. The pseudo-static analysis conducted in Chapter 5 considers principle of superposition to be valid so that total passive resistance due to all resistive components [cohesion (c), surcharge (q) and unit weight (γ)] acting together is equal to sum of each component acting individually (c=0, q=0 and $\gamma \neq 0$), (c=0, $q \neq 0$ and γ=0) and ($c \neq 0$, q=0 and γ=0). Therefore, individual minimum value of seismic passive earth pressure coefficients for a given set of soil, soil-wall interface and seismic parameters are returned by the study without taking relative magnitude of c, q and γ into account. On the other hand, the pseudo-static analysis in Chapter 6 considers failure surface with all the resisting components acting together. The seismic passive earth pressure coefficient is then obtained based on failure wedge obtained considering impact of relative magnitude of c, q and γ. Therefore, magnitude of seismic passive earth pressure coefficients from the proposed model in Chapter 6 is always greater than or equal to that in Chapter 5.

The modified pseudo-dynamic method considers amplification of seismic acceleration through the soil strata. The seismic passive earth pressure coefficient obtained from model proposed in Chapter 7 uses this method with consideration of 3D log-spiral failure wedge. However, the seismic passive earth pressure coefficient in Chapter 8 is obtained by considering 3D polylinear failure surface obtained by sequentially optimizing the passive earth pressure in different layers. For the purpose of comparison of results obtained from proposed model in Chapter 8, the number of layers has been reduced to 1. Table 9.1 compares the results from various theoretical models proposed in the present study. It reflects that the magnitude of $K_{sp\gamma}$ obtained from modified pseudo-dynamic method with 3D log-spiral failure surface is minimum amongst all the proposed models. It is also seen that as the magnitude of δ/ϕ increases, the magnitude of $K_{sp\gamma}$ increases more compared to other models. It is also observed that the magnitude of $K_{sp\gamma}$ obtained from combined failure surface model is always greater than individual failure surface model.

Table 9.1 Comparison of results from various theoretical methods used in the present study for k_v=0 and B/D=1

Input parameters			**Seismic passive earth pressure coefficient due to unit weight component ($K_{sp\gamma}$)**			
ϕ(°)	δ/ϕ	k_h	Pseudo-static analysis considering individual failure wedge	Pseudo-static analysis considering combined failure wedge (c=15 kPa, q=15 kPa and γ=18 kN/m^3)	Modified pseudo-dynamic analysis for log-spiral failure wedge (ξ=0.14)	Modified pseudo-dynamic analysis for planar failure wedge (ξ=0.14)
30	0	0.1	3.127	3.151	2.696	3.055
		0.2	2.501	2.520	2.233	2.579
	1/3	0.1	4.410	4.443	3.868	4.301
		0.2	3.334	3.359	3.087	3.506
	1/2	0.1	4.772	4.820	4.545	5.230
		0.2	3.871	3.909	3.758	4.189
35	0	0.1	3.993	4.023	3.565	3.940
		0.2	3.318	3.342	3.016	3.388
	1/3	0.1	6.257	6.303	5.820	6.300
		0.2	5.129	5.167	4.771	5.232
	1/2	0.1	8.057	8.126	7.811	8.369
		0.2	6.527	6.592	6.337	6.828

9.3 Conclusions from the Present Study

Following major conclusions are drawn from the objectives undertaken and work conducted in the thesis.

9.3.1 Numerical modelling of caisson in layered soil to develop generalized 3D interaction diagrams

- Caissons are rigid foundation system as evidenced by the linear nature of load-displacement diagram thereby indicating caissons undergo rigid body rotation and translation.
- For the same magnitude of vertical load, caisson with lower magnitude of soil-wall friction angle fails at smaller magnitude of lateral load and moment. A caisson-soil system with larger magnitude of δ will be better suited to resist higher magnitude of external lateral loads and moments.
- Higher magnitude of soil-wall friction angle tends to stabilize the caisson as it diminishes caisson displacements. In the present study, this phenomenon has been reflected through maximum and minimum base pressure, tilt of caisson, point of rotation and interaction curves.
- Horizontal seismic acceleration coefficient is more dominant factor in deciding failure load combination than vertical seismic acceleration coefficient. The increase in tilt of caisson as k_h increases from 0 to 0.1; 0 to 0.2 and from 0 to 0.3 is as high as 20.75%, 54.9% 136.35% respectively, for a given loading combination. For the same loading combination, the increase in tilt of caisson when k_v/k_h increases from 0 to 0.5 and 0 to 1 is very small and around 1.46% and 2.97% respectively.
- The depth of point of rotation of caissons for a particular vertical load and horizontal seismic acceleration coefficient tends to converge towards a common point for different k_v/k_h ratios.
- Lateral loads, including horizontal seismic force, have higher influence in inducing yielding of soil as compared to vertical loads. Lateral loading causes large displacement of caissons causing the surrounding soil to fail as evidenced by tilt, shift and maximum and minimum base pressure variations.

- The 3-axis interaction diagram reflect that increase in lateral load, and seismic acceleration coefficients destabilizes the caisson while increase in soil-wall friction angle and vertical load adds to the stability.

9.3.2 Numerical modelling of caisson in layered soil to determine load sharing behaviour

- The normalization of resistive forces with respect to applied lateral and vertical loading reveals the non-linear response of surrounding soil to external loading, along width of caisson. The effect of lateral and vertical load on horizontal and vertical skin friction is found to be linear along depth of caisson, i.e., equal increment in normalized resistive force for increment in applied lateral load and vertical load.
- The magnitude of all the resistive forces on all faces of caisson is found to increase with lateral load and vertical load, but normalization of horizontal skin friction and vertical skin friction forces on side faces of caisson reduces its magnitude with increase in loading.
- The magnitudes of normalized horizontal and vertical skin friction and base reaction decreases with increase in soil-wall friction angle and vertical seismic acceleration coefficient while the magnitude of normalized base friction increases with increasing soil-wall friction angle and reduces with increasing vertical seismic acceleration coefficient. However, the effect of vertical seismic acceleration coefficient (k_v) on all the resisting forces is nominal. Increasing the magnitude of k_v from 0 to $k_h/2$ and k_h for V=800kN, $\delta=\phi$ and k_h=0.1, the reduction in normalized base pressure is 2.93% and 5.89% respectively for Q/V=0.25 and 3.31% and 7.1% respectively for Q/V=0.75.
- Normalized shear force diagrams suggest lower demand of normalized lateral resistive forces to act on caisson for increasing soil-wall friction angle and higher demand of normalized lateral resistive forces for increasing lateral load, vertical load and seismic acceleration coefficients.
- Empirical correlation for percentage of resisting moment provided by sides of caisson has been obtained by extensive regression analysis based on the detailed data set obtained from ABAQUS and calculations made for obtaining resisting moments.

9.3.3 Seismic passive earth pressure resistance on caisson embedded in c-ϕ soil with surcharge load using method of superposition

- K_{spq} and $K_{sp\gamma}$ values diminishes with increase in horizontal and vertical seismic acceleration coefficients as they exert additional inertial forces which causes larger wedge of soil to fail. However, the magnitude of K_{spc} remains unaffected by change in k_h and k_v. In case of ϕ_m=25°, δ_m=ϕ_m/3 and B=16 m, for k_h=0.1, as k_v increases from 0 to k_h/2 and from k_h/2 to k_h, the magnitude of $K_{sp\gamma}$ decreases by 9.43% and 10.22% respectively while K_{spq} diminishes by 9.07% and 9.83% respectively. However, for k_h=0.2, this reduction is much more pronounced for both K_{spq} and $K_{sp\gamma}$, as a reduction of 25.24% and 37.51% respectively is observed in $K_{sp\gamma}$ for the above-mentioned set of input parameters.
- The seismic passive earth pressure coefficients increase with increasing magnitudes of soil friction angle (ϕ_m) and soil-wall friction angle (δ_m) as they are direct indicative of strength of surrounding soil and bonding between soil and structure respectively. The increase in seismic passive earth pressure coefficients is much more significant for higher magnitudes of ϕ_m and δ_m.
- The magnitude of seismic passive earth pressure coefficients decreases with increase in B/D ratio. As the width of caissons increase, the 3-D behaviour tends to convert into plane strain behavior because the volume of soil in side wedges with respect to volume of wedge in front of caisson keeps diminishing. Therefore, the magnitude of extra soil resistance per unit width of caisson keeps decreasing with increase in width of structure.
- The present study returns slightly conservative magnitudes of seismic passive earth pressure coefficients compared to the actual values at failure, as these are absolute minimum values obtained using principle of superposition assuming each component is acting alone in absence of the other two.

9.3.4 Seismic passive earth pressure resistance on caisson embedded in c-ϕ soil with surcharge load assuming combined failure surface

- The magnitude of K_{spc} increases with increasing k_h and k_v values as the larger surface area of failure wedge generates higher cohesive resistance. The magnitude of seismic passive earth pressure coefficients due to cohesion component was found to have nominal sensitivity towards vertical seismic acceleration coefficient.

- K_{spq} and $K_{sp\gamma}$ values diminishes with increase in horizontal and vertical seismic acceleration coefficients as they exert additional inertial forces which causes larger wedge of soil to fail. For $B = 16$ m, $k_v = k_h/2$, $\phi_m = 25°$ and $\delta_m = \phi_m/3$, as k_h is increased from 0 to 0.1 and 0.1 to 0.2, the magnitude of $K_{sp\gamma}$ diminishes by 20.72% and 30.91% respectively. The reduction in K_{spq} magnitudes for the same increase in k_h values are 20.47% and 30.72% respectively for the identical set of parameters.
- The magnitude of earth pressure coefficients diminishes with increase in B/D ratio. As the width of caissons increase and plane strain conditions start prevailing, the sensitivity of the coefficients with respect to B/D diminishes. For $B/D \geq 5$, these coefficients remain mostly insensitive to width for all combinations of input parameters.
- The present study returns the practical magnitudes of earth pressure coefficients at failure which are slightly higher than their absolute minimum values because the present study assumes a single failure surface for all the resisting parameters acting together, which is the actual case in field conditions.
- The design charts prepared in the present study reflect the seismic passive earth pressure coefficients when cohesion, surcharge and unit weight components interact with each other as opposed to minimum values of coefficients acting alone on individual failure surface which is an impractical assumption.

9.3.5 *Seismic passive earth pressure resistance on caisson using modified pseudo-dynamic method*

- Volume per unit width (V/B) of caisson increases with decrease in width of caisson since the relative volume of side wedge compared to volume of wedge increases. V/B of caisson also increases with increase in soil friction angle, soil-wall friction angle, horizontal and vertical seismic acceleration coefficients and excess pore pressure ratio. In addition, V/B ratio decreases nominally with increase in damping ratio (ξ).
- Seismic passive earth pressure coefficient ($K_{sp\gamma}$) increases significantly with decrease in width of caisson since the V/B ratio increases and provides additional resistance. In other words, 3D behaviour of failure wedge becomes more and more dominant as the width of caisson decreases.
- Submergence of soil also causes the $K_{sp\gamma}$ value to decrease. While the decrease is marginal for free water condition, the reduction in magnitude is significant for

restrained water condition. For ϕ_m = 30°, $\delta_m = \phi_m/3$, r_u = 0.2, ξ = 0.15, k_h = 0.1, k_v = 0 and B/D = 1, as the soil changes from dry to submerged soil with free water and submerged soil with restrained water conditions, the $K_{sp\gamma}$ value reduces by 3.29% and 21.57% respectively.

- $K_{sp\gamma}$ decreases with increase in excess pore pressure and the reduction is much higher for higher values of r_u. As r_u increases from 0 to 0.2 and 0.4, $K_{sp\gamma}$ is found to reduce by 13.41% and 41.49% respectively for ϕ_m = 30°, $\delta_m = \phi_m/3$, r_u = 0.2, ξ = 0.15, k_h = 0.1, k_v = 0 and B/D = 1.
- $K_{sp\gamma}$ increases with increase in ϕ_m and δ_m but decreases with increase in seismic acceleration coefficients. Nominal increase is also observed with increase in damping ratio (ξ) since it diminishes the extent of amplification of earthquake waves.

9.3.6 Seismic passive earth pressure coefficient for caisson in layered soil using modified pseudo dynamic method

- The proposed model calculates the magnitude of seismic passive earth pressure coefficient for *n*-layered cohesionless soil supporting a rectangular caisson. The effect of soil friction angle, soil-wall friction angle, horizontal and vertical seismic acceleration coefficient, effect of submergence, excess pore pressure ratio, width of caisson and relative depth and relative soil friction angle has been presented. The study can thus provide seismic passive resistance offered by soil layers with different relative depth and relative soil friction angle for a multitude of parameters.
- The magnitude of seismic passive earth pressure coefficient ($K_{sp\gamma}$) increases with increase in soil friction angle and soil-wall friction angle. For H_1/H_2=2/3 in 2-layered soil, the increase in $K_{sp\gamma}$ is 36.03% and 18.91% respectively when δ increases from 0 to $\phi/3$ and $\phi/3$ to $\phi/2$ for ϕ_2=30°, ϕ_1/ϕ_2=0.8, k_h=0.1, k_v=0 and B/D=1. The increase is 33.44% and 17.89% respectively for 3-layered soil with H_1:H_2:H_3=1:2:3 and ϕ_1: ϕ_2: ϕ_3=3:4:5, for ϕ_3=30°, k_h=0.1, k_v=0 and B/D=1.
- The seismic passive earth pressure coefficient reduces with increase in both horizontal and vertical seismic acceleration coefficients. The seismic passive earth pressure coefficient diminishes by 20.12% and 40.72% as k_h increases from 0 to 0.1 and 0.2 respectively for ϕ=35°, δ/ϕ=1/2, k_v=k_h, B/H=1 when failure wedge is formed in homogeneous soil. For same set of soil properties and caisson geometry, when k_v/k_h is increased from 0 to 0.5 and 1 for k_h=0.1, the percentage reduction in $K_{sp\gamma}$ is

determined as 5.47% and 10.92% respectively which suggests that k_h is a more dominant parameter than k_v during seismic analysis of caissons.

- Submergence of soil causes $K_{sp\gamma}$ value to reduce. The percentage reduction in magnitude of $K_{sp\gamma}$ when dry soil changes to submerged with free water and submerged with restrained water is 18.92% and 22.53% respectively for wedge in single layer with ϕ=35°, δ/ϕ=1/2, k_h=0.1, k_v=0 and B/H=1.
- In submerged soil, the seismic passive earth pressure coefficient also diminishes with increasing excess pore pressure ratio (r_u). For k_h=0.1, k_v=k_h, ϕ=35°, δ/ϕ=1/2 and B/H=0.5, $K_{sp\gamma}$ reduces by 9.57% and 16.53% as r_u increases from 0 to 0.2 and 0.3 respectively in free water condition and 10.65% and 18.46% in restrained water condition.
- The extent of failure wedge in front of caisson increases with increasing ϕ, δ, k_h, r_u and width of caisson. The extent of failure wedge is also increased upon submergence of dry soil. However, it is found to be unaffected with increase in k_v values.

9.4 Contributions from the Present Study

Following major contributions have been made to the existing research work from the present study:

- Development of generalized 3D interaction diagram relating vertical load-lateral load-moment (V-Q-M) at failure based on numerical analysis of caisson in layered soil with consideration of pore water pressure.
- Determination of variation of various resistive forces acting on different faces of caisson under varying loading, soil-wall friction angle and seismic acceleration coefficients and development of empirical correlation for percentage of resisting moment shared by sides of caisson.
- Formulation and design charts for seismic passive earth pressure coefficients considering individual and combined failure surface for different resisting components, i.e., cohesion, unit weight and surcharge component.
- Modified pseudo-dynamic analysis of caisson highlighting the effect of width of caisson considering 3D log-spiral failure wedge obtained from numerical study.
- Formulation for pseudo-dynamic analysis of caisson embedded in n-layered cohesionless strata reflecting the effect of relative depths and soil friction angles of layers.

- Parametric study of variation of extent of failure wedge in front of caisson for variation of a wide array of input parameters and its effect on seismic passive earth pressure coefficient.

Table 9.2 Comparison of merits, demerits and reliability of the various theoretical models

Model → / Criterion ↓	Pseudo-static analysis considering individual failure wedge	Pseudo-static analysis considering combined failure wedge	Modified pseudo-dynamic analysis for log-spiral failure wedge	Modified pseudo-dynamic analysis for planar failure wedge
Merits	Simple	Considers the magnitudes of resisting components	Considers effects of excess pore pressure and damping ratio	Simple
	Less computational effort required	Considers a unique failure wedge for all components	Considers both dry and submerged conditions	Effectively models layered soil
	Assumes realistic shape of failure wedge	Reports variation of seismic passive earth pressure coefficient due to cohesion with k_h and k_v	Considers acceleration variation with depth	Considers acceleration variation with depth
Demerits	Considers different failure wedge for different components for failure in same stratum	Acceleration variation is not accounted	Rigorous analysis	Accuracy reduces at higher δ
	Acceleration variation is not accounted	High computational effort required	Considers cohesionless soil only	Considers cohesionless soil only
Reliability	Moderate	Fair	High	High

9.5 Limitations of the Present Study

Some of the identified limitations of the present study are mentioned below.

- Use of traditional Mohr-Coulomb model for modelling of sand during numerical study.
- Variation of caisson geometry, embedment depth and soil friction angle has not been considered in the numerical study.
- Linear ground response analysis has been adopted for obtaining the acceleration profile in various layers in modified pseudo dynamic analysis.
- Surcharge load and cohesion of soil has not been considered in the modified pseudo-dynamic analysis

9.6 Scope for future work

Following studies may be undertaken in the future:

- Dynamic numerical analysis of caisson in presence of pore water may be performed to capture response to lateral spreading induced from liquefaction.
- Consideration of equivalent linear or non-linear ground response for modified pseudo-dynamic analysis will be able to capture soil behaviour with more accuracy.
- Theoretical study of caisson in layered c-ϕ soil using modified pseudo-dynamic method considering 3D log-spiral failure wedges and subjected to surcharge load.
- Wave loading may be taken into consideration as a dynamic load for the analysis of caisson.

REFERENCES

- Ahmad, S.M. and Choudhury, D. (2009). “Seismic design factor for sliding of waterfront retaining wall.” *Proceedings of the Institution of Civil Engineers-Geotechnical Engineering*, 162 (5): 269-276.
- Al-Ramthan, A.Q.O. and Aubeny, C.P. (2020). “Numerical investigation of the performance of caissons in cohesive soils under cyclic loading.” *International Journal of Geomechanics, ASCE*, 20 (5), 04020042_1-11, doi: 10.1061/(ASCE)GM.1943-5622.0001650.
- Ashour, M., Norris, G. and Pilling, P. (1998). “Lateral loading of a pile in layered soil using the strain wedge model.” *Journal of Geotechnical and Geoenvironmental Engineering*, 124 (4), 303–315. doi: 10.1061/(ASCE)1090-0241(1998)124:4(303).
- Banerjee, P.K. and Gangopadhyay, S. (1960). “Study on the stability of well foundations for major bridges.” *Journal of the Indian Roads Congress*, 22: 588-600.
- Bellezza, I. (2014). “A new pseudo-dynamic approach for seismic active soil thrust.” *Geotechnical and Geological Engineering*, 32: 561:576. doi: 10.1007/s10706-014-9734-y.
- Bellezza, I. (2015). “Seismic active earth pressure on walls using a new pseudo-dynamic approach.” *Geotechnical and Geological Engineering*, 33: 795-812. doi: 10.1007/s10706-015-9860-1.
- Bellezza, I., D’Alberto, D. and Fentini, R. (2012). “Pseudo-dynamic approach for active thrust of submerged soils.” *Proceedings of the Institution of Civil Engineers - Geotechnical Engineering*, 165 (5), 321-333. doi: 10.1680/geng.10.00103.
- Beredugo, Y.O. and Novak, M. (1972). “Coupled horizontal and rocking vibration of embedded footings.” *Canadian Geotechnical Journal*, 9: 477-497.
- Biswas, S. and Choudhury, D. (2019). “Seismic soil resistance for caisson design in sand.” *Proceedings of the Institution of Civil Engineers - Geotechnical Engineering*, 172 (1), 67-75. doi: 10.1680/jgeen.17.00195.
- Biswas, S. and Choudhury, D. (2020). “Behavior of caisson foundations under lateral loading in layered cohesive soil.” *In Geo-Congress 2020: Foundations, Soil Improvement, and Erosion, Geotechnical Special Publication (GSP) No. 315,* ASCE, 23-32. doi: 10.1061/9780784482780.003.

- Biswas, S. and Choudhury, D. (2021). “Caissons in cohesionless soils considering 3D wedge under earthquake loading.” *International Journal of Geomechanics, ASCE*, 20 (12), 04020221_1-9, doi: 10.1061/(ASCE)GM.1943-5622.0001862.
- Biswas, S. and Manna, B. (2018). “Experimental and theoretical studies on the nonlinear characteristics of soil-pile systems under coupled vibrations.” *Journal of Geotechnical and Geoenvironmental Engineering*, 144 (3): 04018007_1-14. doi: 10.1061/(ASCE)GT.1943-5606.0001850.
- Boominathan, A., Ramana, C.H., Bühler, M.M. and Gudehus, G. (2004). “Study on performance of pile walls using laminar shake box.” *In Proceedings of 13th World Conference on Earthquake Engineering*, Vancouver, B.C., Canada.
- Bowman, E.R. (1958). “Investigation of the Lateral Resistance to Movement of a Plate in Cohesionless Soil.” *Doctoral Dissertation*, University of Texas at Austin, Austin, TX, USA.
- Broms, B.B. (1964). “Lateral resistance of piles in cohesionless soils.” *Journal of Soil Mechanics and Foundations Division*, 90 (3): 123–156.
- Brown, D.A., Turner, J.P. and Castelli, R.J. (2010). “Drilled shafts: construction procedures and LRFD design methods.” NHI course no. 132014, *Geotechnical engineering circular no. 10*, New York, USA.
- Caltabiano, S., Cascone, E. and Maugeri, M. (2012). “Static and seismic limit equilibrium analysis of sliding retaining walls under different surcharge conditions.” *Soil Dynamics and Earthquake Engineering*, 37: 38-55. doi: 10.1016/j.soildyn.2012.01.015.
- Chandrasekaran, S.S., Boominathan, A. and Dodagoudar, G.R. (2013). “Dynamic response of laterally loaded pile group in clay” *Journal of Earthquake Engineering*, 17 (1): 33-53. doi: 10.1080/13632469.2012.711957.
- Chatterjee, K., Choudhury, D. and Poulos, H.G. (2015). “Seismic analysis of laterally loaded pile under influence of vertical loading using finite element method.” *Computers and Geotechnics*, 67, 172–186. doi: 10.1016/j.compgeo.2015.03.004.
- Chatterjee, S., Mana, D.S.K., Gourvenec, S. and Randolph, M.F. (2014). “Large-deformation numerical modeling of short-term compression and uplift capacity of offshore shallow foundations.” *Journal of Geotechnical and Geoenvironmental Engineering*, 140 (3): 04013021_1-10. doi: 10.1061/(ASCE)GT.1943-5606.00010.
- Chaudhary, B., Hazarika, H., Murakami, A. and Fujisawa, K. (2018). “Mitigation of earthquake-induced damage of breakwater by geogrid-reinforced foundation.” *Marine*

Georesources and Geotechnology, 36 (7): 827-840. doi: 10.1080/1064119X.2017.1391902

- Choudhury, D. and Ahmad, S. (2007). "Design of waterfront retaining wall for the passive case under earthquake and tsunami." *Applied Ocean Research*, 29: 37-44. doi: 10.1016/j.apor.2007.08.001
- Choudhury, D. and Chatterjee, S. (2006). "Dynamic active earth pressure on retaining structures." *Sadhana,* 31: 721-730. doi: 10.1007/BF02716891.
- Choudhury, D. and Nimbalkar, S. (2005). "Seismic passive resistance by pseudo-dynamic method." *Géotechnique,* 55 (9): 699-702. doi: 10.1680/geot.2005.55.9.699.
- Choudhury, D. and Subba Rao, K.S. (2006). "Seismic bearing capacity of shallow strip footings embedded in slope." *International Journal of Geomechanics*, 6 (3): 176-184. doi: 10.1061/(ASCE)1532-3641(2006)6:3(176).
- Chowdhury, I., Tarafdar, R., Ghosh, A. and Dasgupta, S.P. (2017). "Dynamic soil structure interaction of bridge piers supported on well foundations." *Soil Dynamics and Earthquake Engineering*, 97: 251-265. doi: 10.1016/j.soildyn.2017.03.005.
- Coulomb, C.A. (1776). "Essai sur une application des regles des maximis et minimis a quelques problemes de statique relatifs a l'architecture." *Memoires de l'Academie Royale pres Divers Savants*, 7, Paris.
- Ebeling, R.M., Morrison Jr, E.E. (1992). "The seismic design of water-front retaining structures." *Technical Report No. ITL-92-11*. Washington DC: US Army Corp of Engineers.
- EN: 1991-1-6 (2005). "Eurocode 1 – Actions on structures part 1-6: General actions – Actions during execution." *European Committee for Standardization*, Brussels.
- EN: 1997-1 (2004). "Eurocode 7 – Geotechnical design part 1: General rules." *European Committee for Standardization,* Brussels.
- EN:1990 (2002). "Eurocode - Basis of structural design." *European Committee for Standardization,* Brussels.
- Fu, D., Zhang, Y. and Yan, Y. (2020). "Bearing capacity of a side rounded suction caisson foundation under general loading in clay." *Computers and Geotechnics,* 123: 103543_1-15. doi: 10.1016/j.compgeo.2020.103543.
- Fukumoto, Y., Yoshida, J., Sakaguchi, H. and Murakami, A. (2014). "The effects of block shape on the seismic behavior of dry-stone masonry retaining walls: A numerical

investigation by discrete element modeling." *Soils and Foundations*, 54 (6): 1117-1126. doi: 10.1016/j.sandf.2014.11.007.

- Gadre, A. and Dobry, R. (1998). "Lateral cyclic loading centrifuge tests on square embedded footing." *Journal of Geotechnical and Geoenvironmental Engineering*, 124(11): 1128–1138. doi: 10.1061/(ASCE)1090-0241(1998)124:11(1128).
- Gaudio, D. and Rampello, S. (2016). "Dynamic soil-structure intreraction of bridge-pier-caisson foundations." *Procedia Engineering*, 158: 146-151. doi: 10.1016/j.proeng.2016.08.420.
- Gaudio, D. and Rampello, S. (2020). "Equivalent seismic coefficients for caisson foundations supporting bridge piers." *Soil Dynamics and Earthquake Engineering*, 129: 105955_1-14. doi: 10.1016/j.soildyn.2019.105955.
- Gerolymos, N., Zafeirakos, A. and Karapiperis, K. (2015). "Generalized failure envelope for caisson foundations in cohesive soil: Static and dynamic loading." *Soil Dynamics and Earthquake Engineering*, 78: 154-174. doi: 10.1016/j.soildyn.2015.07.012
- Gerolymos, N. and Gazetas, G. (2006a). "Winkler model for lateral response of rigid caisson foundations in linear soil." *Soil Dynamics and Earthquake Engineering*, 26: 347-361. doi: 10.1016/j.soildyn.2005.12.003.
- Gerolymos, N. and Gazetas, G. (2006b). "Development of winkler model for static and dynamic response of caisson foundations with soil and interface nonlinearities." *Soil Dynamics and Earthquake Engineering*, 26: 363-376. doi: 10.1016/j.soildyn.2005.12.002.
- Gerolymos, N. and Gazetas, G. (2006c). "Static and dynamic response of massive caisson foundations with soil and interface nonlinearities-validation and results." *Soil Dynamics and Earthquake Engineering*, 26: 377-394. doi: 10.1016/j.soildyn.2005.12.001.
- Hazari, S., Ghosh, S. and Sharma, R.P. (2020). "New pseudo-dynamic analysis of two-layered cohesive-friction soil slope and its numerical validation." *Frontiers of Structural and Civil Engineering*, 14 (6): 1492-1508. doi: 10.1007/s11709-020-0679-3.
- HEC-18 (2012). "Evaluating scour at bridges." *Federal Highway Administration*, Virginia, USA.
- Indian Railway Standards (1985). "Manual on the design and construction of well and pile foundations." *Research Designs and Standards Organisation*, Lucknow, India.

- IRC 45 (1972). “Recommendations for estimating the resistance of soil below the maximum scour level in the design of well foundations of bridges.” *The Indian Roads Congress*, New Delhi, India.
- IRC 78 (2014). “Standard specifications and code of practice for road bridges-section VII: foundations and substructures.” *Indian Roads Congress*, New Delhi, India.
- IS: 3955 (1967). “Indian standard code of practice of design and construction of well foundation.” *Bureau of Indian Standard*, New Delhi.
- Jawaid, S.M.A. and Madhav, M.R. (2013). “Analysis of axially loaded short rigid composite caisson foundation based on continuum approach.” *International Journal of Geomechanics*, 13 (5): 636-644. doi: 10.1061/(ASCE)GM.1943-5622.0000185.
- Jalbi, M.S. and Bhattacharya, S. (2018). “Closed form solution for the first natural frequency of offshore wind turbine jackets supported on multiple foundations incorporating soil-structure interaction.” *Soil Dynamics and Earthquake Engineering*, 113: 593-613. doi: 10.1016/j.soildyn.2018.06.011.
- Jaya, V., Dodagoudar, G.R. and Boominathan, A. (2008). “Seismic soil structure interaction analysis of tall slender structures.” *International Journal of Geotechnical Engineering*, 2 (4): 381-393. doi: 10.3328/IJGE.2008.02.04.381-393.
- Karapiperis, K. and Gerolymos, N. (2014). “Combined loading of caisson foundations in cohesive soil: Finite element versus winkler modeling.” *Computers and Geotechnics*, 56: 100-120. doi: 10.1016/j.compgeo.2013.11.006.
- Kelly, R.B., Houlsby, G.T. and Byrne, B.W. (2006). “A comparison of field and laboratory tests of caisson foundations in sand and clay.” *Géotechnique*, 56(9): 617-626. doi: 10.1680/geot.2006.56.9.617.
- Kondner, R.L. and Cunningham, J.A. (1963). “A lateral stability of rigid poles partially embedded in sand.” *Highway Research Record No. 39*: 49-67.
- Kramer, S.L. (1996). “Geotechnical earthquake engineering.” Upper Saddle River, NJ, Prentice-Hall.
- Krishna, A.M. and Bhattacharjee, A. (2017) “Behavior of rigid faced reinforced soil retaining walls subjected to different earthquake ground motions” *International Journal of Geomechanics*, 17 (1): 06016007_1-14. doi: 10.1061/(ASCE)GM.1943-5622.0000668.

- Kumar, S.S., Krishna, A.M. and Dey, A. (2017). "Evaluation of dynamic properties of sandy soil at high cyclic strains." *Soil Dynamics and Earthquake Engineering*, 99: 157-167. doi: 10.1016/j.soildyn.2017.05.016.
- Kumar, J. and Samui, P. (2006). "Stability determination for layered soil slopes using the upper bound limit analysis." *Geotechnical and Geological Engineering*, 24: 1803-1819. doi: 10.1007/s10706-006-7172-1.
- Lancellotta, R. (2007). "Lower-bound approach for seismic passive earth resistance." *Géotechnique*, 57 (3): 319-321. doi: 10.1680/geot.2007.57.3.319
- Lazard, A. (1957). "Limit of overturning moment of isolated foundations." *Proceedings of IV International Conference on Soil Mechanics and Foundation Engineering*, London, 1: 349-354.
- Liu, F.Q. (2014). "Lateral earth pressure acting on circular retaining walls." *International Journal of Geomechanics*, 14 (3): 04014002_1-12. doi: 10.1061/(ASCE)GM.1943-5622.0000291
- Liu, F.Q., Wang, J.H. and Zhang, L.L. (2009). "Axi-symmetric active earth pressure obtained by the slip line method with a general tangential stress coefficient." *Computers and Geotechnics*, 36: 352-358. doi: 10.1016/j.compgeo.2008.02.002
- Liu, S., Xia, Y., and Liang, L. (2018). "A modified logarithmic spiral method for determining passive earth pressure." *Journal of Rock Mechanics and Geotechnical Engineering*, 10, 1171-1182. doi: 10.1016/j.jrmge.2018.03.011.
- Loli, M., Anastasopoulos, I., Bransby, M.F., Ahmed, W. and Gazetas, G. (2011). "Caisson foundations subjected to reverse fault rupture: centrifuge testing and numerical analysis." *Journal of Geotechnical and Geoenvironmental Engineering*, 137 (10): 914-925. doi: 10.1061/(ASCE)GT.1943-5606.0000512.
- Manna, B. and Baidya, D.K. (2009). "Vertical vibration of full-scale pile-analytical and experimental study." *Journal of Geotechnical and Geoenvironmental Engineering*, 135 (10): 1452-1461. doi: 10.1061/ASCEGT.1943-5606.0000110.
- Manna, B. and Baidya, D.K. (2010a). "Dynamic nonlinear response of pile foundations under vertical vibrations-theory versus experiment." *Soil Dynamics and Earthquake Engineering*, 30: 456-469. doi: 10.1016/j.soildyn.2010.01.002.
- Manna, B. and Baidya, D.K. (2010b). "Nonlinear dynamic response of piles under horizontal excitation." *Journal of Geotechnical and Geoenvironmental Engineering*, 136 (12): 1600-1609. doi: 10.1061/ASCEGT.1943-5606.0000388.

- Matsuzawa, H., Ishibashi, I., Kawamura, M. (1985). "Dynamic soil and water pressures on submerged soils." *Journal of Geotechnical Engineering,* 111 (10): 1161-1176. doi: 10.1061/(ASCE)0733-9410(1985)111:10(1161), 1161–1176
- Mita, A. and Luco, J.E. (1989). "Dynamic response of a square foundation embedded in an elastic half-space." *Soil Dynamics and Earthquake Engineering*, 8 (2): 54-67. doi: 10.1016/S0267-7261(89)80013-2.
- Murakami, A., Setsuyasu, T. and Arimoto, S. (2005). "Mesh-free method for soil-water coupled problem within finite strain and its numerical validity." *Soils and Foundations*, 45 (2): 145-154. doi: 10.3208/sandf.45.2_145.
- MATLAB (2021). Version 9.10.0.1739362 (R2021a). *The MathWorks Inc.*, Natick, Massachusetts, U.S.A.
- Mononobe, N. and Matsuo, O. (1929). "On the determination of earth pressure during earthquakes." *In Proceedings of the World Engineering Congress,* Tokyo, Japan, 179–187.
- Murakami, A., Wakai, A. and Fujisawa, K. (2010). "Numerical methods." *Soils and Foundations,* 50 (6): 877-892. doi: 10.3208/sandf.50.877.
- Murthy, V.N.S. (2016). "Advanced foundation engineering." *CBS Publishers,* New Delhi, India.
- Muszynski, M.R., Olson, S.M., Hashash, Y.M.A. and Phillips, C. (2014). "Repeatability of centrifuge tests containing a large, rigid foundation subjected to lateral spreading." *ASTM Geotechnical Test Journal*, 37 (6): 1–14. doi: 10.1520/GTJ20130093.
- Mylonakis, G., Nikolaou, S. and Gazetas, G. (2006). "Footings under seismic loading: analysis and design issues with emphasis on bridge foundations." *Soil Dynamics and Earthquake Engineering*, 26: 824-853.
- Novak, M., Nogami, T. and Aboul-Ella, F. (1978). "Dynamic soil reactions for plane strain case." *Journal of the Engineering Mechanics Division, ASCE,* 104(4): 953-959.
- Olson, S.M., Hashash, Y.M., Muszynski, M.R. and Phillips C. (2017). "Passive wedge formation and limiting lateral pressures on large foundations during lateral spreading." *Journal of Geotechnical and Geoenvironmental Engineering,* 143(7): 04017027_1-13.
- Pain, A., Choudhury, D. and Bhattacharyya, S.K. (2015). "Seismic stability of retaining wall-soil sliding interaction using modified pseudo-dynamic method." *Géotechnique Letters*, 5: 56-61. doi: 10.1680/geolett.14.00116.

- Pain, A., Choudhury, D., Bhattacharyya, S.K., (2017). “Seismic passive earth resistance using modified pseudo-dynamic method.” *Earthquake Engineering and Engineering Vibration*, 16: 263-274. doi: 10.1007/s11803-017-0381-1.
- Pender, E.B. (1947). “The lateral support afforded to pier founded on sand.” *Journal of Institution of Engineers*, Australia, 19 (7).
- Prater, E.G. (1977). “An examination of some theories of earth pressure on shaft linings.” *Canadian Geotechnical Journal*, 14 (1), 91–106. doi: 10.1139/t77-007.
- Puzrin, A.M., Alonso, E.E. and Pinyol, N.M. (2010). “Caisson Failure Induced by Liquefaction: Barcelona Harbour, Spain. In: Geomechanics of Failures.” *Springer, Dordrecht,* pp-85-148. doi: 10.1007/978-90-481-3531-8_5
- Qin, C. and Chian, S.C. (2017). “Kinematic stability of a two-stage slope in layered soils.” *International Journal of Geomechanics*, 17 (9): 06017006_1-12. doi: 10.1061/(ASCE)GM.1943-5622.0000928
- Ralli, R., Manna, B. and Datta, M. (2022). “Dynamic behavior of single steel-driven vertical and batter piles under horizontal excitations: Field model testing.” *Journal of Geotechnical and Geoenvironmental Engineering*, 148 (1): 04021177_1-25. doi: 10.1061/(ASCE)GT.1943-5606.0002726.
- Rajesh, B.G. and Choudhury, D. (2017). “Seismic passive earth resistance in submerged soils using modified pseudo-dynamic method with curved rupture surface.” *Marine Georesources and Geotechnology*, 35 (7): 930-938. doi: 10.1080/1064119X.2016.1260077.
- Ranjan, G. and Rao, A.S.R. (2004). “Basic and applied soil mechanics.” *New Age International Publishers,* New Delhi, India.
- Roscoe, K.H. (1957). “A comparison of tied and free pier foundation.” Proceedings of IV International Conference on Soil Mechanics and Foundation Engineering, London, 1: 419-423.
- Santhoshkumar, G., Ghosh, P. and Murakami, A. (2019). “Seismic active resistance of a tilted cantilever retaining wall considering adaptive failure mechanism.” *International Journal of Geomechanics*, 19 (8): 04019086_1-11. doi: 10.1061/(ASCE)GM.1943-5622.0001470.
- Santhoshkumar, G. and Ghosh, P. (2021a). “Closed-form solution for seismic earth pressure on bilinear retaining wall using method of characteristics.” *Journal of Earthquake Engineering,* 25 (6): 1171-1190. doi: 10.1080/13632469.2019.1570880

- Santhoshkumar, G. and Ghosh, P. (2021b). "Passive resistance of retaining walls supporting layered cohesionless backfill: a plasticity approach." *Journal of Geotechnical and Geoenvironmental Engineering*, 147 (8): 06021008_1-9. doi: 10.1080/13632469.2019.1570880.
- Sharda, S.C. (1975). "Response of well foundations under horizontal loads." *PhD Thesis*, School of Research and Training in Earthquake Engineering, University of Roorkee, India.
- Shi, H., Jinxing, G. and Yanqing, Z. (2016). "Earth pressure of layered soil on retaining structures." *Soil Dynamics and Earthquake Engineering*, 83: 33-52. doi: 10.1016/j.soildyn.2015.12.015.
- Shuku, T., Murakami, A., Nishimura, S., Fujisawa, K. and Nakamura, K. (2012). "Parameter identification for cam-clay model in partial loading model tests using the particle filter." *Soils and Foundations*, 52 (2): 279-298. doi: 10.1016/j.sandf.2012.02.006.
- SIMULIA. (2014). "ABAQUS documentation." *Providence*, RI: Dassault Systèmes.
- Solov'ev, N.B. (2008). "Use of limiting-equilibrium theory to determine the bearing capacity of soil beneath the blades of caissons." *Soil Mechanics and Foundation Engineering*, 45 (2), 39-45. doi: 10.1007/s11204-008-9006-z.
- Soubra, A.H. (2000). "Static and seismic passive earth pressure coefficients on rigid retaining structures." *Canadian Geotechnical Journal*, 37, 463–478. doi: 10.1139/t99-117.
- Soubra, A.H. and Regenass, P. (2000). "Three-dimensional passive earth pressures by kinematical approach." *Journal of Geotechnical and Geoenvironmental Engineering, ASCE*, 126 (11): 969-978. doi: 10.1061/(ASCE)1090-0241(2000)126:11(969).
- Soubra, A.H., and Macuh, B. (2002). "Active and passive earth pressure coefficients by a kinematical approach." *Proceedings of the Institution of Civil Engineering: Geotechnical Engineering*, 155 (2), 119-131. doi: 10.1680/geng.2002.155.2.119.
- Steedman, R.S., Zeng, X. (1990). "The influence of phase on the calculation of pseudo-static earth pressure on a retaining wall." *Géotechnique*, 40 (1): 103-112. doi: 10.1680/geot.1990.40.1.103.
- Stobie, J. (1930). "Pole footings." *Journal of the Institution of Engineers, Australia*, 2: 58-63.

- Subba Rao, K.S. and Choudhury, D. (2005). "Seismic passive earth pressures in soils." *Journal of Geotechnical and Geoenvironmental Engineering*, 131 (1), 131–135. doi: 10.1061/(ASCE)1090-0241(2005)131:1(131).
- Tsigginos, C., Gerolymos, N., Assimaki, D. and Gazetas, G. (2008). "Seismic response of bridge pier on rigid caisson foundation in soil stratum." *Earthquake Engineering and Engineering Vibrations*, 7: 33-44. doi: 10.1007/s11803-008-0825-8.
- Terzaghi, K. (1943). "Theoretical soil mechanics." John Wiley and Sons Inc., New York.
- Varun, Assimaki, D. and Gazetas, G. (2009). "A simplified model for lateral response of large diameter caisson foundations-linear elastic formulation." *Soil Dynamics and Earthquake Engineering*, 29: 268-291.
- Westergaard, H.M. (1933). "Water pressures on dams during earthquakes." *Transactions of ASCE*, 95: 418-433.
- Wolf, C.V. (1933). "Members wholly or partly buried and subjected to lateral forces." *Concrete and Construction Engineering*, 28 (11).
- Zaman, M.M., Desai, C.S. and Drumm, E.C. (1984). "Interface model for dynamic soil-structure interaction." *Journal of Geotechnical Engineering*, 110 (9): 1257-1273. doi: 10.1061/(ASCE)0733-9410(1984)110:9(1257).
- Zhong, R. and Huang, M. (2013). "Winkler model for dynamic response of composite caisson-piles foundations: Lateral response." *Soil Dynamics and Earthquake Engineering*, 55: 182-194. doi: 10.1016/j.soildyn.2013.09.017.

LIST OF PUBLICATIONS

From the research work carried out for Ph.D. and given in this report, the following publications have been published/accepted/communicated.

In Referred International Journals:

1. **Mohit Kumar** and Kaustav Chatterjee (2021). “Generalized interaction diagrams for caisson foundations in layered soil under seismic conditions.” *International Journal of Geomechanics*, ASCE, USA, **21**(8), 04021135_1-14. (Q1, SCI Indexed, Impact factor: 3.819/2020). doi: 10.1061/(ASCE)GM.1943-5622.0002079.

2. **Mohit Kumar** and Kaustav Chatterjee (2022). “Seismic stability analysis of caissons under earthquake forces considering 3-D log-spiral failure surface.” *Natural Hazards Review*, ASCE, USA. doi: 10.1061/(ASCE)NH.1527-6996.0000588 (Q1, SCI Indexed, Impact factor: 3.169/2021) [Accepted for publication and in press]

3. Kaustav Chatterjee, Deepankar Choudhury and **Mohit Kumar** (2022). “Influence of depth of liquefiable soil layer on dynamic response of pile group subjected to vertical load.” *Bulletin of Earthquake Engineering*, Springer, Netherlands, **20**(1), 113-142. (Q1, SCI Indexed, Impact factor: 3.827/2021) doi: 10.1007/s10518-021-01253-3.

4. **Mohit Kumar** and Kaustav Chatterjee (2022). “Modified pseudo-dynamic based soil-structure interaction of caisson with a novel 3D failure wedge.” *Computers and Geotechnics*, Elsevier, UK. [Communicated and under review]

5. **Mohit Kumar** and Kaustav Chatterjee (2022). “The influence of earthquake loading on passive resistance for caisson in cohesionless soil with a novel 3D failure wedge.” *Journal of Earthquake Engineering*, Taylor and Francis, UK. [Communicated and under review]

6. **Mohit Kumar** and Kaustav Chatterjee (2022). “Estimation of seismic earth pressure coefficients for caissons in c-ϕ soils with a 3D log-spiral failure wedge.” *Ocean Engineering*, Elsevier, UK. [Communicated and under review]

7. **Mohit Kumar** and Kaustav Chatterjee (2022). “Seismic passive earth pressure resistance for caisson in layered soil using modified pseudo-dynamic approach.” *International Journal for Numerical and Analytical Methods in Geomechanics*, John Wiley & Sons Ltd., UK. [Communicated and under review]

8. **Mohit Kumar** and Kaustav Chatterjee (2022). “Load sharing behaviour of caisson foundations in layered soil under seismic conditions.” *International Journal of Geomechnaics*, ASCE, USA. [Communicated and under review]

In Geotechnical Special Publications of ASCE:

9. **Mohit Kumar** and Kaustav Chatterjee (2020). “A numerical study on lateral load response of caissons in static conditions.” *In Geo-Congress 2020: Foundations, Soil Improvement and Erosion, Geotechnical Special Publication 315*, ASCE, Minneapolis, Minnesota, USA, 15–22.

10. **Mohit Kumar** and Kaustav Chatterjee (2023). “Effect of seismic acceleration coefficients on seismic passive earth pressure coefficient due to cohesion.” *In Geo-Congress 2023, Geotechnical Special Publication*, ASCE, Los Angeles, California, USA. [Communicated and under review]

In Referred International Conferences:

11. **Mohit Kumar** and Kaustav Chatterjee (2022); “Pseudo-static stability analysis of caisson in porous media.” *Proceedings of 7th International Young Geotechnical Engineers Conference (7th iYGEC)*, April 29-May 1, 2022, Sydney, Australia, 155-160.

12. **Mohit Kumar** and Kaustav Chatterjee (2019); “Pseudo-static analysis of caissons to determine critical loading ratio.” *Proceedings of 7th International Conference on Earthquake Geotechnical Engineering (7th ICEGE)*, CRC Press, June 17-20, 2019, Rome, Italy, Paper ID: 10230.

In Referred National Conferences:

13. **Mohit Kumar** and Kaustav Chatterjee (2020); “A comparative study on various codes and current practices for design of caissons.” In: Prashant, A., Sachan, A., Desai, C. (eds) Advances in Computer Methods and Geomechanics. Lecture Notes in Civil Engineering, vol 55. Springer, Singapore. https://doi.org/10.1007/978-981-15-0886-8_29.

Other Publications

From other parallel research works during PhD (but not related to the topic of PhD research work), the following papers have been published/accepted/communicated.

14. Nitin Ishwarappa Bailappanavar, **Mohit Kumar** and Kaustav Chatterjee (2021). “Effect of stone columns on strength and consolidation characteristics of black cotton soil.” *KSCE Journal of Civil Engineering*, **25**(4), 1214-1228. (Q2, SCI Indexed, Impact factor: 2.199/2020)